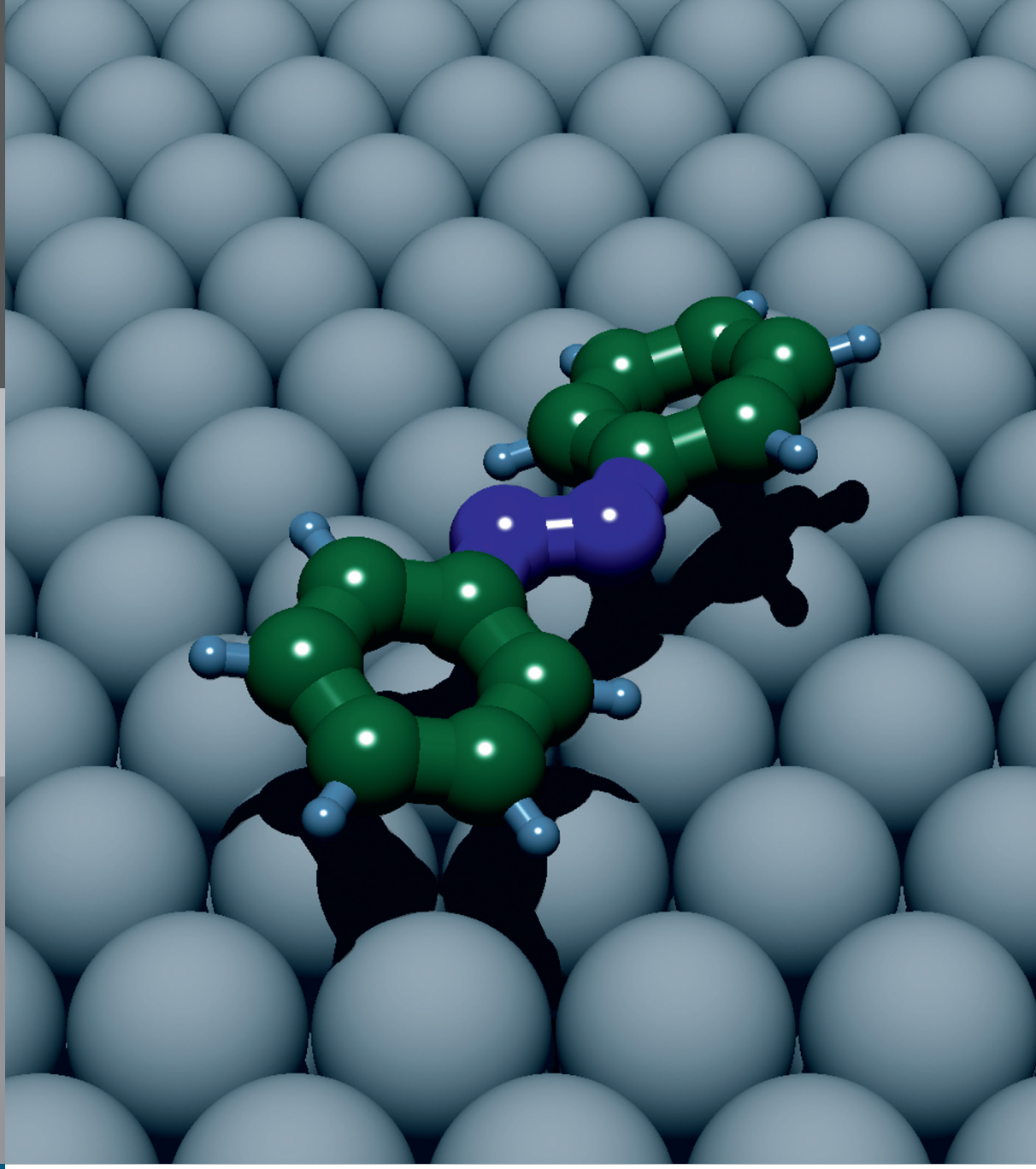


Study of Molecule-Metal Interfaces by Means of the Normal Incidence X-ray Standing Wave Technique

Giuseppe Mercurio

Member of the Helmholtz Association

JÜLICH
FORSCHUNGSZENTRUM

Study of Molecule-Metal Interfaces by Means of the Normal Incidence X-ray Standing Wave Technique

Von der Fakultät für Mathematik, Informatik und Naturwissenschaften der RWTH Aachen University zur Erlangung des akademischen Grades eines Doktors der Naturwissenschaften genehmigte Dissertation

vorgelegt von

Master of Science in Physics Engineering

Giuseppe Mercurio

aus Reggio Calabria

Berichter: Universitätsprofessor Dr. F. S. Tautz

Universitätsprofessor Dr. U. Klemradt

Tag der mündlichen Prüfung: 11. Juli 2012

Diese Dissertation ist auf den Internetseiten der Hochschulbibliothek online verfügbar.

Forschungszentrum Jülich GmbH
Peter Grünberg Institute (PGI)
Functional Nanostructures at Surfaces (PGI-3)

Study of Molecule-Metal Interfaces by Means of the Normal Incidence X-ray Standing Wave Technique

Giuseppe Mercurio

Schriften des Forschungszentrums Jülich
Reihe Schlüsseltechnologien / Key Technologies Band / Volume 49

ISSN 1866-1807 ISBN 978-3-89336-816-7

Bibliographic information published by the Deutsche Nationalbibliothek.
The Deutsche Nationalbibliothek lists this publication in the Deutsche Nationalbibliografie; detailed bibliographic data are available in the Internet at http://dnb.d-nb.de.

Publisher and Distributor:	Forschungszentrum Jülich GmbH Zentralbibliothek 52425 Jülich Phone +49 (0) 24 61 61-53 68 · Fax +49 (0) 24 61 61-61 03 e-mail: zb-publikation@fz-juelich.de Internet: http://www.fz-juelich.de/zb
Cover Design:	Grafische Medien, Forschungszentrum Jülich GmbH
Printer:	Grafische Medien, Forschungszentrum Jülich GmbH
Copyright:	Forschungszentrum Jülich 2012

Schriften des Forschungszentrums Jülich
Reihe Schlüsseltechnologien / Key Technologies Band / Volume 49

D 82 (Diss., RWTH Aachen, University, 2012)

ISSN 1866-1807
ISBN 978-3-89336-816-7

The complete volume is freely available on the Internet on the Jülicher Open Access Server (JUWEL) at http://www.fz-juelich.de/zb/juwel

Neither this book nor any part of it may be reproduced or transmitted in any form or by any means, electronic or mechanical, including photocopying, microfilming, and recording, or by any information storage and retrieval system, without permission in writing from the publisher.

Ai miei genitori, Nino e Nella

Acknowledgements

This work would have not been possible without the greatly appreciated assistance and collaboration of many people. First of all, I would like to thank my PhD mentor Professor Frank Stefan Tautz for believing in me and for giving me the opportunity to work in his research group. Moreover, I am extremely thankful to him for having taught me the joy and the fun of doing research. I would also like to thank Professor Uwe Klemradt for accepting to co-referee this Dissertation and for the stimulating questions.

I am very grateful to all my colleagues from Peter Grünberg Institut-3, especially Dr. Sergey Subach for the scientific support during my PhD, to PD Christian Kumpf and Dr. Tomoki Sueyoshi for the fruitful scientific discussions, to Mirko Müller and Martin Willenbockel for sharing an office with me in a friendly atmosphere and for their much appreciated effort in improving my German.

This work is the result of many collaborations. In particular, I would like to thank the collaborators from Freie Universität Berlin, Prof. Martin Wolf, Prof. Petra Tegeder, Dr. Felix Leyssner, Dr. Sebastian Hagen, Dr. Isabel Martin, Christopher Bronner, Matthias Koch for joining several beamtimes and performing the thermal desorption spectroscopy experiments. I am very thankful to Prof. Karsten Reuter, Dr. Jelena Jelic, Dr. Jörg Meyer from Technische Universität München and to Dr. Erik R. McNellis from Fritz Haber Institute for performing the theoretical calculations and for their patience and availability in explaining the details of their calculations to me. I am also grateful to Prof. Moritz Sokolowski, Oliver Bauer, Benjamin Fiedler, Christoph H. Schmitz, Maria Buchholz from Universität Bonn with whom we shared several beamtimes and scientific discussions, and who performed SPA-LEED experiments. Discussions with Oliver Bauer are gratefully acknowledged. Special thanks go to Prof. Steven L. Tait, Hilmar Adler from Indiana University and to Dr. Sebastian Stepanow, Dr. Alexander Langner from Prof. Klaus Kern's group at the Max Planck Institute for Solid State Research in Stuttgart for joining the synchrotron experi-

ments and for their appreciative interest in reading the chapter concerning terephthalic acid on Cu(100). I would like also to thank Christian Weiss and Dr. Ruslan Temirov (Forschungszentrum Jülich) for their collaboration in carrying out STM experiments. I thank Dr. Olga Neucheva for the help in the preparation of the Ag(111) crystals at Jacobs University Bremen and during the beamtime in which molecular switches were investigated. The experiments performed at the European Synchrotron Radiation Facility (ESRF) would have not been possible without the invaluable help of Dr. Jörg Zegenhagen, Dr. Blanka Detlefs, Dr. Yanyu Mi, Helena Isern, Lionel André and all the staff. Fruitful discussions with Dr. Ingo Kröger, Benjamin Stadtmüller and PD Christian Kumpf about the fitting algorithms of Torricelli are gratefully acknowledged. I am very grateful to my friend Dr. Giannis Koutsou for introducing me to the python scripting language and for supporting me, together with Dr. Sandipan Mohanty, in my first steps in programming. I also owe a great deal to my friend Dr. Sandipan Mohanty for having made the transition to Linux much easier, for always being available to help me and for being a very good friend.

Finally, this work would have been much more difficult without the infinite love and encouragement of my parents, Nino and Nella, my sister Laura and my brother Dario. The writing of the thesis would have been definitely much harder without the understanding, the support and the love of Özlem, who also brought light to the most stressful days, and to whom go my greatest thanks. To conclude, I am grateful to all my friends, especially Alex and Rosanna, for making Jülich such a happy place.

Abstract

This work investigates the geometric and chemical properties of different molecule-metal interfaces, relevant to molecular electronics and functional surfaces applications, by means of the normal incidence x-ray standing wave (NIXSW) technique. All NIXSW data are analysed by means of the newly developed open-source program Torricelli, which is thoroughly documented in the thesis.

In order to elucidate the role played by the substrate within molecule-metal interfaces, the prototype organic molecule 3,4,9,10-perylene-tetracarboxylic-dianhydride (PTCDA) on the Ag(110) surface is investigated. The molecule results more distorted and at smaller bonding distances on the more reactive Ag(110) surface, in comparison with the Ag(100)[1] and the Ag(111)[2] substrates. This conclusion follows from the detailed molecular adsorption geometry obtained from the differential analysis of both carbon and oxygen atoms.

Subsequently, the chemisorptive PTCDA/Ag(110) interaction is tuned by the co-deposition of an external alkali metal, namely K. As a consequence, the functional groups of PTCDA unbind from the surface, which, in turn, undergoes major reconstruction. In fact, the resulting nanopatterned surface consists of alternated up and down reconstructed Ag terraces covered by PTCDA molecules partly unbound with respect to the pure molecular phase.

Within the context of the functional surfaces, the interaction of the molecular switches azobenzene (AB) and 3,3,5,5-tetra-tert-butyl-azobenzene (TBA) adsorbed on the Ag(111) surface is investigated. The bonding distance of TBA, only slightly greater compared to AB, indicates that the desired geometric decoupling of the photochromic moiety to enable the switching in the adsorbate state does not occur.[3] In particular, the measured structural parameters of nitrogen, in excellent agreement with the dispersion-corrected DFT-PBE calculations,[4] suggest that both molecules are in the *trans* isomerization. Moreover, an accurate adsorption geometry of AB

and TBA, including the carbon atoms, is obtained by means of the vector analysis in the Argand diagram. This method allows the multiple molecular degrees of freedom to be explored and provides the conformations that best agree with NIXSW data.

Other functional surfaces that are appealing for molecular electronics applications are the 2D metal-organic networks. In this work, the self-assembled monolayer of the prototypical molecular ligand terephthalic acid (TPA) on the Cu(100) surface, prior to additional metal deposition, is examined. NIXSW data reveal a significantly distorted molecule with the carboxylate groups covalently bound to the Cu atoms underneath and the carbon backbone arc-like bent. This evidence suggests an intermolecular interaction mediated by the substrate, as also supported by HREELS measurements.[5] Finally, the disagreement between the experimental adsorption geometry and the DFT-PBE prediction motivates further theoretical studies to improve the understanding of this prototypical molecule-metal interface.

Contents

Acknowledgements IV

Abstract VI

1 Introduction 1

2 The normal incidence x-ray standing wave technique 5

2.1 Fundamentals of XSW 5
2.2 The standing wave 7
2.3 XSW detection: photoelectrons 9
2.4 Basics of an XSW experiment 10
2.5 Coherent position and coherent fraction 13
2.6 Experimental set-up 16

3 Torricelli 19

3.1 Introduction 19
3.2 Preparing reflectivity and electron yield profiles for fitting 21
3.3 Fitting the reflectivity 22
3.3.1 The fitting function 22
3.3.2 Calculation of the ideal reflectivity R_{theo} and phase ϕ_{theo} . . . 25
3.3.3 Calculation of the structure factors 29
3.4 Fitting the electron yield profile 38
3.4.1 Fitting the coherent position and fraction 38
3.4.2 Calculation of the nondipolar correction parameters 40
3.4.3 Fitting the asymmetry parameter Q 45
3.5 Error analysis of the coherent position and fraction 48
3.6 Overview and conclusions 52

4 PTCDA on Ag(110) 55
4.1 Introduction . . . 55
4.2 Experimental details . . . 57
4.2.1 PTCDA deposition and coverage estimation . . . 57
4.2.2 XPS acquisition parameters of NIXSW experiments . . . 60
4.2.3 XPS background . . . 62
4.2.4 Line shapes of the fitting components . . . 63
4.3 Experimental results . . . 66
4.3.1 Carbon . . . 66
4.3.1.1 Two-component model . . . 66
4.3.1.2 Multicomponent model . . . 71
4.3.2 Oxygen . . . 82
4.4 Discussion . . . 88
4.4.1 Interpretation of PTCDA coherent fraction . . . 88
4.4.2 Adsorption geometry of PTCDA on Ag(110) . . . 91
4.5 Conclusions . . . 99

5 K-doped PTCDA on Ag(110) 101
5.1 Introduction . . . 101
5.2 NIXSW study . . . 102
5.2.1 Experimental details . . . 102
5.2.1.1 Potassium deposition and coverage estimation . . . 102
5.2.1.2 XPS acquisition parameters of NIXSW experiments . 104
5.2.1.3 XPS background . . . 106
5.2.1.4 Line shapes of the fitting components . . . 108
5.2.2 Experimental results . . . 109
5.2.2.1 Carbon . . . 109
5.2.2.2 Oxygen . . . 114
5.2.2.3 Potassium . . . 118
5.2.2.4 Silver . . . 120
5.2.3 Discussion of NIXSW results . . . 122
5.3 LEED study . . . 126
5.3.1 Experimental results . . . 126
5.3.1.1 Role of K amount . . . 129
5.3.1.2 Additional diffraction spots . . . 131
5.3.1.3 Role of annealing step . . . 133
5.3.2 Discussion of LEED results . . . 134

5.4 STM study . . . 136
5.4.1 Experimental details . . . 136
5.4.2 *Low* K coverage results . . . 137
5.4.2.1 Overview . . . 137
5.4.2.2 X phase . . . 137
5.4.3 *Intermediate* K coverage results: stripe phase . . . 139
5.4.3.1 Introduction . . . 139
5.4.3.2 Real space and reciprocal space images . . . 140
5.4.3.3 Vertical properties of the stripe phase . . . 145
5.4.3.4 Lateral properties of the stripe phase . . . 148
5.4.3.5 Potassium fingerprint . . . 149
5.4.4 Summary of STM results . . . 153
5.5 UPS and XPS study . . . 155
5.5.1 Experimental details . . . 155
5.5.2 Work function results . . . 157
5.5.3 XPS results . . . 159
5.5.4 Discussion of UPS and XPS results . . . 160
5.6 Structural model . . . 167
5.6.1 Description of the structural model . . . 167
5.6.2 Discussion of the structural model . . . 169
5.7 Conclusions . . . 177

6 Molecular switches on Ag(111) 179
6.1 Introduction . . . 179
6.2 Experimental details . . . 181
6.2.1 Sample preparation . . . 181
6.2.2 XPS acquisition parameters of NIXSW experiments . . . 183
6.2.3 XPS background . . . 184
6.2.4 Line shapes of the fitting components . . . 185
6.3 Experimental results . . . 186
6.3.1 Introduction . . . 186
6.3.2 Silver . . . 186
6.3.2.1 Ag3*d* . . . 187
6.3.2.2 Ag3*d* plasmons . . . 189
6.3.3 Azobenzene . . . 193
6.3.3.1 Nitrogen . . . 193
6.3.3.2 Carbon . . . 200

6.3.4 TBA . . . 202
6.3.4.1 Nitrogen . . . 202
6.3.4.2 Carbon . . . 209
6.4 Discussion . . . 211
6.4.1 Discussion of azobenzene experimental results . . . 211
6.4.1.1 Introduction . . . 211
6.4.1.2 A novel interpretative scheme of NIXSW results . . . 212
6.4.1.3 NIXSW adsorption model of azobenzene/Ag(111) . . . 224
6.4.1.4 Comparison of NIXSW and DFT adsorption models 226
6.4.2 Discussion of TBA experimental results . . . 230
6.4.2.1 Introduction . . . 230
6.4.2.2 Comparison of NIXSW results with DFT calculations 231
6.4.2.3 NIXSW simulations of TBA/Ag(111) . . . 233
6.4.2.4 NIXSW adsorption model of TBA/Ag(111) . . . 240
6.5 Conclusions . . . 245

7 Terephthalic acid on Cu(100) 249
7.1 Introduction . . . 249
7.2 Experimental details . . . 252
7.2.1 Sample preparation and coverage estimation . . . 252
7.2.2 XPS acquisition parameters of NIXSW experiments . . . 255
7.2.3 XPS background . . . 256
7.2.4 Line shapes of the fitting components . . . 257
7.3 Experimental results . . . 258
7.3.1 Carbon . . . 258
7.3.2 Oxygen . . . 266
7.3.3 Copper . . . 269
7.4 Discussion . . . 273
7.4.1 Adsorption geomety of deprotonated TPA on Cu(100) . . . 273
7.4.2 Comparison of NIXSW data with DFT calculations . . . 282
7.5 Conclusions . . . 294

8 Summary and conclusions 297

A Technical details and code of Torricelli 301
A.1 Introduction . . . 301
A.2 Preparing reflectivity and electron yield profiles for fitting . . . 302
A.2.1 Technical details . . . 302

A.2.2 Code 304
A.3 Fitting the reflectivity 306
A.3.1 Technical details 306
A.3.2 Code 307
A.4 Calculating the ideal reflectivity 310
A.4.1 Technical details 310
A.4.2 Code 311
A.5 Calculating the structure factors 318
A.5.1 Technical details 318
A.5.2 Code 320
A.6 Fitting the electron yield profile: coherent position and fraction . . . 325
A.6.1 Technical details 325
A.6.2 Code 327
A.7 Calculating the nondipolar correction parameters 331
A.7.1 Technical details 331
A.7.2 Code 332
A.8 Fitting the electron yield profile: the asymmetry parameter Q 334
A.8.1 Technical details 334
A.8.2 Code 335

Bibliography **355**

List of Figures

2.1 Kinematical and dynamical theory of diffraction 6
2.2 The standing wave 7
2.3 The XSW experiment 12
2.4 Argand diagram representation of P_c and F_c 15
2.5 NIXSW experimental set-up 16

3.1 "Import Files" section of Torricelli 21
3.2 Schematic representation of the double crystal monochromator 22
3.3 Reflectivity of a Si(111) monochromator crystal 23
3.4 "Fit Reflectivity" section of Torricelli 25
3.5 Forward scattering, H and $\bar{H}$ reflections in a crystal 27
3.6 Reflectivity curve without and with absorption 28
3.7 "Calculate Reflectivity" section of Torricelli 29
3.8 Calculated sample and monochromator reflectivities 30
3.9 Fcc and diamond structures 35
3.10 "Structure Factors" section of Torricelli 37
3.11 "Fit Fc and Pc" section of Torricelli 39
3.12 Photoelectron angular distribution: forward/backward asymmetry . . 41
3.13 Representation of the four conditions for the simple ndp expression . 42
3.14 "Nondipolar Parameters" section of Torricelli 44
3.15 N1s XPS, Y and R of AB multilayer 46
3.16 "Fit Q" section of Torricelli 47
3.17 Two components XPS fitting model 49
3.18 Scatter plot of two parameters distribution 51
3.19 "Overview" section of Torricelli 53

4.1 Chemical structure of PTCDA 55
4.2 LEED images of PTCDA/Ag(110) 59
4.3 Definition of background properties: $AvWidth$ 62
4.4 C1s XPS of PTCDA/Ag(110): two-component model 67

4.5 Two-component C Argand diagram of PTCDA/Ag(110) 68
4.6 Two-component C Y of PTCDA/Ag(110) 69
4.7 C1s HR-XPS of a PTCDA film 72
4.8 Multi component C MR-XPS and LR-XPS of PTCDA/Ag(110) . . . 74
4.9 Multicomponent C Argand diagram of PTCDA/Ag(110): all prep. . . 77
4.10 Multicomponent C Argand diagram of PTCDA/Ag(110): 2^{nd} prep. . 78
4.11 Multicomponent C Y of PTCDA/Ag(110) 79
4.12 O1s XPS of PTCDA/Ag(110) 83
4.13 O Y of PTCDA/Ag(110) 85
4.14 O Argand diagram of PTCDA/Ag(110) 86
4.15 Side-view representation PTCDA/Ag(110) 92
4.16 Side view and top view of PTCDA/Ag(110): interatomic distances . . 93
4.17 LUMO of PTCDA 95
4.18 Rhombic PTCDA island on the Ag(110): intermolecular interactions . 97
4.19 Schematic illustration of PTCDA/Ag(110) 99

5.1 PTCDA unbinding from the surface upon K deposition 101
5.2 O1s PE spectra: beam damage 105
5.3 PE spectra of an NIXSW experiment 107
5.4 C1s HR-XPS of K+PTCDA/Ag(110) 110
5.5 C Argand diagram of K+PTCDA/Ag(110) 111
5.6 C Y of K+PTCDA/Ag(110) 112
5.7 O1s HR-XPS of K+PTCDA/Ag(110) 114
5.8 O Y of K+PTCDA/Ag(110) 115
5.9 O Argand diagram of K+PTCDA/Ag(110) 116
5.10 K1s XPS and Y of K+PTCDA/Ag(110) 118
5.11 K and Ag Argand diagram of K+PTCDA/Ag(110) 119
5.12 Ag3d and AgMNV XPS, Y and R of K+PTCDA/Ag(110) 121
5.13 Scale model of PTCDA and K-doped PTCDA adsorbed on Ag(110) . 122
5.14 Scale model of K+PTCDA/Ag(110) with cov and vdW radii 123
5.15 Diffraction pattern of different preparations of K+PTCDA/Ag(110) . 128
5.16 *Low*, *intermediate* and *high* K coverage SPA-LEED images 130
5.17 SPA-LEED line scans 131
5.18 LEED images before and after annealing 133
5.19 Overview STM image at *low* K coverage 137
5.20 STM image of PTCDA in brickwall and X phase 138
5.21 Real space and reciprocal space stripe phase images 141
5.22 Stripe phase area with 4-row and 3-row superstructures 142

5.23 Zoom of the crack between two stripe phase domains 143
5.24 Diffraction spots of K+PTCDA phases 143
5.25 ×4 and ×3 superstructures at *low* and *intermediate* K coverage . . . 144
5.26 Vertical properties of the stripe phase 146
5.27 STM image of a tip-destroyed stripe phase area 147
5.28 Lateral properties of the stripe phase 148
5.29 Stripe phase imaged at different bias 150
5.30 Zoom of different bias STM image 151
5.31 Schematic model of K+PTCDA/Ag(110) based on STM images . . . 152
5.32 Scheme to illustrate how Φ is measured 158
5.33 UPS cutoff and valence band region 159
5.34 C1s, K2p, O1s XPS of PTCDA and K+PTCDA 160
5.35 Φ and E_b changes of PTCDA and K+PTCDA 162
5.36 Side view and top view of the K+PTCDA/Ag(110) structure model . 168
5.37 Side view of the K+PTCDA/Ag(110) structure model 174
5.38 Expected and actual K+PTCDA/Ag(110) geometries 177

6.1 Azobenzene photoisomerization reaction 179
6.2 Expected schematic adsorption geometry of AB and TBA on Ag(111) 180
6.3 Thermal desorption spectra of AB and TBA adsorbed on Ag(111) . . 182
6.4 Ag3d XPS, Ag3$d_{5/2}$ electron yield, reflectivity 187
6.5 Argand diagram of Ag3$d_{5/2}$ P_c and F_c 188
6.6 XPS fitting model of the Ag3d-plasmons 190
6.7 Argand diagram of Ag3d-plasmons P_c and F_c. 191
6.8 Ag3d-plasmons electron yields 192
6.9 XPS fitting model of AB N1s+Ag3d-plasmons 194
6.10 XSW-XPS spectra of AB N1s+Ag-plasmons 196
6.11 Photoelectron yield N1s and Ag3d-plasmons electron yields 197
6.12 Argand diagram of AB N1s and Ag3d plasmons P_c and F_c. 198
6.13 XPS and electron yield of AB C1s 200
6.14 Argand diagram of AB C1s P_c and F_c 201
6.15 XPS fitting model of TBA N1s 203
6.16 XSW-XPS spectra of TBA N1s+Ag3d-plasmons 204
6.17 TBA N1s and Ag3d plasmons electron yields 206
6.18 Argand diagram of TBA N1s and Ag3d-plasmons P_c and F_c 207
6.19 XPS and electron yield of TBA C1s 209
6.20 Argand diagram of TBA C1s P_c and F_c 209
6.21 AB butterfly adsorption model 213

6.22 Polar and cartesian coordinates in the Argand diagram 215
6.23 Vector sum in the Argand diagram 216
6.24 Actual and calculated P_c and d_c as a function of $\widetilde{\omega}$ 218
6.25 *Sum* vectors around $\widetilde{\omega} = 40°$ 219
6.26 Argand diagram of the calculated P_c^* (C) and F_c^* (C) 220
6.27 Vector analysis to determine $\widetilde{\omega}$ 221
6.28 Vector analysis to determine β 223
6.29 Possible adsorption geometries of AB/Ag(111) 225
6.30 DFT desorption energy curves and experimental point 227
6.31 Schematic adsorption geometry of TBA/Ag(111) 230
6.32 DFT optimized geometry of TBA/Ag(111) 232
6.33 TB-down configuration of TBA/Ag(111): $\widetilde{\omega}$ 234
6.34 TB-down configuration: P_c^* (C) and F_c^* (C) for $-5° \leq \widetilde{\omega} \leq 90°$ 234
6.35 TB-down configuration of TBA/Ag(111): γ 236
6.36 TB-down configuration: P_c^* (C) and F_c^* (C) for $-15° \leq \gamma \leq 35°$ 236
6.37 TB-up configuration of TBA/Ag(111): $\widetilde{\omega}$ 237
6.38 TB-up configuration: P_c^* (C) and F_c^* (C) for $-5° \leq \widetilde{\omega} \leq 25°$ 237
6.39 TB-up/down configuration of TBA/Ag(111): $\widetilde{\omega}$ 239
6.40 TB-up/down configuration: P_c^* (C) and F_c^* (C) for $0° \leq \widetilde{\omega} \leq 90°$ 239
6.41 Possible adsorption geometries of TBA/Ag(111) 241
6.42 NIXSW schematic adsorption geometry of AB and TBA on Ag(111) . 246

7.1 Molecular structure of terephthalic acid (TPA) 249
7.2 Expected geometry of TPA/Cu(100): top view and side view 250
7.3 Molecular model of TPA and deprotonated TPA 252
7.4 LEED images of Cu(100) and TPA/Cu(100) 253
7.5 C1*s* and O1*s* XPS of monolayer TPA/Cu(100) 254
7.6 High resolution C1*s* of TPA monolayer 259
7.7 C1*s* HR-XPS and Sum-fast-XPS of TPA/Cu(100) 260
7.8 Yield curve of a satellite peak 261
7.9 C Y of TPA/Cu(100) 262
7.10 C Argand diagram of TPA/Cu(100) 263
7.11 O1*s* HR-XPS and Y of TPA/Cu(100) 266
7.12 O Argand diagram of TPA/Cu(100) 267
7.13 Cu2*p* XPS, Y and R of Cu(100) 270
7.14 CuLMM Auger spectrum and Y 271
7.15 Cu2*p* and CuLMM Argand diagram 272
7.16 Adsorption geomety of deprotonated TPA/Cu(100) 273

7.17 Simulations of the aromatic ring distortion 276
7.18 Scale model of TPA/Cu(100): interatomic distances 278
7.19 NIXSW, PBE and PBE-D side view of TPA/Cu(100) scale model . . 283
7.20 Side view of TPA/Cu(100): definition of α, β, γ and δ 284
7.21 Top view of deprotonated TPA/Cu(100): hydrogen bonds 288
7.22 Single molecule, head-to-head, side-to-side and full layer configurations 291
7.23 Top view of deprotonated TPA/Cu(100): the buckling of the Cu atoms 292
7.24 Expected and actual top view and side view of TPA/Cu(100) 294

A.1 "Import Files" section of Torricelli: technical details 303
A.2 "Fit Reflectivity" section of Torricelli: technical details 306
A.3 "Calculate Reflectivity" section of Torricelli: technical details 311
A.4 "Structure Factors" section of Torricelli: input files 318
A.5 "Structure Factors" section of Torricelli: calculations completed 319
A.6 "Fit Fc and Pc" section of Torricelli: initial fitting parameters 326
A.7 "Fit Fc and Pc" section of Torricelli: yield is fitted 327
A.8 "Non Dipolar Parameters" section of Torricelli: input files 331
A.9 "Nondipolar Parameters" section of Torricelli: calculations completed 332
A.10 "Fit Q" section of Torricelli: technical details 335

List of Tables

3.1 Summary of all calculated structure factors 37
3.2 Summary of all nondipolar correction parameters used 44

4.1 PTCDA and PTCDA+K coverage estimations 59
4.2 XPS acquisition parameters of PTCDA/Ag(110) 60
4.3 Two-component C P_c and F_c of PTCDA/Ag(110) 70
4.4 C binding energies of HR-XPS and LR-XPS models 75
4.5 Multicomponent C P_c and F_c of PTCDA/Ag(110) 81
4.6 O binding energies of HR-XPS and LR-XPS models 83
4.7 O P_c and F_c of PTCDA/Ag(110) 87
4.8 Summary of d_c and F_c of PTCDA/Ag(110) 88
4.9 Cov radii, vdW radii and interatomic distances of PTCDA/Ag(110) . 93
4.10 Comparison of experimental and theoretical adsorption heights 94

5.1 Photoionization cross sections σ of C1s and K2p 103
5.2 K coverage estimation 103
5.3 PTCDA superstructures parameters 104
5.4 XPS acquisition parameters of K+PTCDA/Ag(110) 105
5.5 Signal-to-background ratio of all measured PE spectra 107
5.6 C P_c and F_c of K+PTCDA/Ag(110) 113
5.7 O P_c and F_c of K+PTCDA/Ag(110) 117
5.8 K P_c and F_c of K+PTCDA/Ag(110) 118
5.9 Ag3d and AgMNV P_c and F_c of K+PTCDA/Ag(110) 120
5.10 Cov radii, vdW radii and interatomic distances of K+PTCDA/Ag(110) 123
5.11 PTCDA/Ag(110) and K+PTCDA/Ag(110) NIXSW results 124
5.12 E_b and ΔE_b of PTCDA and K+PTCDA core levels 164
5.13 Coordination number of the substrate atoms 175

6.1 XPS acquisition parameters of AB and TBA on Ag(111) 183
6.2 XPS background properties of AB and TBA on Ag(111) 184

6.3 P_c and F_c of Ag3$d_{5/2}$ . . . 188
6.4 P_c and F_c of Ag3d-plasmons . . . 191
6.5 P_c and F_c of AB N1s and Ag3d-plasmons . . . 199
6.6 P_c and F_c of AB C1s . . . 201
6.7 P_c and F_c of TBA N1s and Ag3d-plasmons . . . 208
6.8 P_c and F_c of TBA C1s . . . 210
6.9 Summary of AB NIXSW results . . . 212
6.10 Cov radii, vdW radii and interatomic distances of AB/Ag(111) . . . 226
6.11 Summary of TBA NIXSW results . . . 230
6.12 Cov radii, vdW radii and interatomic distances of TBA/Ag(111) . . . 242

7.1 TPA coverage estimation . . . 253
7.2 XPS acquisition parameters of TPA/Cu(100) . . . 255
7.3 BG type of $AvWidth$ of TPA/Cu(100) PE spectra . . . 256
7.4 C P_c and F_c of TPA/Cu(100) . . . 265
7.5 O P_c and F_c of TPA/Cu(100) . . . 267
7.6 Cu2p P_c and F_c of Cu(100) . . . 271
7.7 C and O NIXSW results of TPA/Cu(100) . . . 274
7.8 Cov radii, vdW radii and interatomic distances of TPA/Cu(100) . . . 279
7.9 Comparison NIXSW–DFT: adsorption heights . . . 282
7.10 NIXSW, PBE and PBE-D values of angles α, β, γ and δ . . . 284
7.11 Comparison NIXSW–DFT: interatomic distances . . . 285
7.12 Comparison DFT–NIXSW: H-bonds . . . 287
7.13 TPA adsorption energies per molecule . . . 289
7.14 Summary of H and S interactions in each configuration . . . 291

List of Acronyms

AB	Azobenzene
a.u.	arbitrary units
BG	Background
DFT	Density functional theory
DOS	Density of states
E_b	Binding energy
E_{Bragg}	Bragg energy
E_k	Kinetic energy
fcc	face-centered cubic
FFT	Fast Fourier transform
FWHM	Full width half maximum
GUI	Graphical user interface
HOMO	Highest occupied molecular orbital
HREELS	High-resolution electron energy loss spectroscopy
HR-XPS	High-resolution x-ray photoemission spectroscopy
HS-XPS	High statistics x-ray photoemission spectroscopy
IFFT	Inverse fast Fourier transform
LEED	Low-energy electron diffraction
LR-XPS	Low resolution x-ray photoemission spectroscopy
LUMO	Lowest unoccupied molecular orbital
MCP-LEED	Micro-channel plate low-energy electron diffraction
MR-XPS	Medium resolution x-ray photoemission spectroscopy
ndp	Nondipolar correction parameters
NEXAFS	Near-edge x-ray absorption fine structure
NIXSW	Normal incidence x-ray standing wave
OLED	Organic light emitting device
OPVC	Organic photovoltaic cell
OTFT	Organic thin film transistor

PBE	Perdew Burke Ernzerhof functional
PBE-D	Perdew Burke Ernzerhof dispersion corrected functional
PBE+TS	PBE plus Tkatchenko and Sheffeler dispersion corrections
PE	Photoemission
PTCDA	3,4,9,10-perylene-tetracarboxylic-dianhydride
SPA-LEED	Spot profile analysis low-energy electron diffraction
STM	Scanning tunneling microscope
TBA	3,3′,5,5′-tetra-tert-butyl-azobenzene
TCNQ	Tetracyano-p-quinodimethane
TPA	Terephthalic acid
TPD	Temperature-programmed desorption
UHV	Ultrahigh vacuum
UPS	Ultraviolet photoemission spectroscopy
vdW	van der Waals
XPS	X-ray photoemission spectroscopy
XSW	X-ray standing wave
XSW-XPS	PE spectrum of an x-ray standing wave experiment
Y	Electron yield

1 Introduction

In the last decade, functional surfaces based on self-assembled monolayers of organic molecules have attracted relevant scientific interest due to their fascinating applications in different fields such as molecular electronics, sensing and catalysis.[6,7] Among the numerous possible applications, the most successful is the organic light emitting device, or OLED, currently used in color displays.[8] In recent years, organic thin film transistors (OTFTs) and organic photovoltaic cells (OPVCs) have also experienced in the recent years great improvements that make them worthy of consideration for practical devices.[9–13]

With the realization of these organic-based devices, in which the first molecular layer of the organic thin film is in direct contact with a metal surface, the strong dependence of the overall device characteristics on the local geometric, chemical and electronic structure of the molecule-metal interface became increasingly evident.[14,15] In particular, the specific bonding of the molecules to the electrodes is crucial for the device properties.[16] In order to allow the controlled engineering of organic devices, the electronic structure, the chemical properties and the electrical behavior of the organic-metal interfaces must be fully understood. Therefore, a direct investigation of the interface chemistry is of paramount importance.[17]

The bonding distance represents a sensitive gauge of the molecule-metal interaction because it provides a direct insight into the chemistry of the interface. The normal incidence x-ray standing wave technique (NIXSW) is a powerful tool for determining the vertical position of molecules, adsorbed on metal surfaces with a typical accuracy of approximately 0.05 Å (see e.g., references[2,18,19]). Since bonding distances define the chemistry of the molecule-metal interface, they represent a relevant output parameter of ab initio calculations. Therefore, experimental adsorption heights resulting from NIXSW measurements on prototypical interfaces can also be used to benchmark different density functional theory (DFT) schemes and determine the ones with predictive power for similar systems. While an excellent agreement

between measured and calculated structures is found for physisorbed molecules, as shown in chapter 6, the same semiempirical corrected DFT cannot accurately predict the adsorption geometry of a strongly chemisorbed molecule, as reported in chapter 7. NIXSW bonding distances thus constitute invaluable data for mindfully guiding the next improvements in DFT approaches for organic molecules adsorbed at metal surfaces.

The basic principles of the NIXSW technique, which was introduced by Batterman and Cole[20] and developed mainly by Woodruff[21] and Zegenhagen,[22] are summarized in chapter 2. All standing wave data reported in this dissertation were analyzed by means of the free and open-source program Torricelli, which is documented in chapter 3 and appendix A. With the aim of determining otherwise inscrutable molecular structural details that may turn out crucial for understanding the corresponding functionality, a more accurate analysis scheme of NIXSW data was developed. This approach proves particularly useful for large organic molecules with multiple degrees of freedom, as shown in chapter 6.

Among all organic molecules, 3,4,9,10-perylene-tetracarboxylic-dianhydride (PTCDA) is most extensively studied, because it is considered to be a prototype of π-conjugated molecules with the anhydride moieties as functional end groups.[23] In order to determine the influence of different metal faces on the molecular bonding configuration, PTCDA was investigated on the Ag(111)[2] and Ag(100)[1] surfaces. With the goal of exploring the influence of a more open surface on the local versus extended bonding of the molecular functional groups, and of completing the series of experiments on the low index surfaces, an NIXSW study of PTCDA/Ag(110) is carried out and reported in chapter 4. Remarkably, a significant influence of the underlying substrate on the geometry and chemistry of the molecule-metal interface is found.

Within the context of functional surfaces, molecular switches, i.e., molecules whose properties can be reversibly switched between different states by light, can be employed, e.g., for information storage[24] or as light-driven actuators.[25] However, to exploit their functionality, not only in solution but also in the technologically relevant solid state phase, understanding the structural and electronic properties of the molecules connected to metal electrodes is essential. Azobenzene (AB) and its derivatives are promising candidates for applications. Their switching behavior is well understood in solution,[26,27] but not yet when in contact with a surface. In particular, it is still unclear why 3,3′,5,5′-tetra-*tert*-butyl-azobenzene (TBA) switches

on Au(111),[28,29] but not on Ag(111).[30] In order to shed light on the interaction between the photochromic molecules and the metal substrates, bonding distances of AB/Ag(111) and TBA/Ag(111) are measured. The data analysis is carried to the extreme by means of a thorough inspection of the corresponding molecular degrees of freedom in order to find the adsorbed structure in better agreement with experimental results, as reported in chapter 6.

Furthermore, other promising functional surfaces result from the combination of different molecular building blocks and metal atoms that yield a great variety of self-assembled supramolecular architectures with a vast scope of tailored properties.[7] These 2D metal-organic networks generate a nanopatterned substrate that can be used as templates for nanoelectronic devices,[31–33] as sensors for specific biomolecules,[7,34] or as magnetic storage media.[35] In order to tailor and control the functionality of the metal-organic network, the delicate balance of intermolecular and molecule-surface interactions of the fundamental building block prior to metal deposition must be understood. For this purpose, the basic ligand terephthalic acid (TPA) adsorbed on Cu(100) is investigated. A detailed structural analysis of NIXSW data and DFT calculations, aimed at understanding the competing interactions leading to a long-range ordered superstructure, is reported in chapter 7.

Finally, the effect of an alkali metal on a molecule-metal interface is thoroughly investigated in the 2D metal-organic network K+PTCDA/Ag(110). Upon K deposition and annealing, PTCDA partly unbinds from the substrate and, at the same time, a major reconstruction transforms Ag(110) into a nanopatterned surface, as reported in chapter 5. The investigation of the K+PTCDA/Ag(110) interface by means of NIXSW, XPS, UPS, LEED and STM provides both a structural model and a complete picture of the mechanism leading to the nanopatterning of the surface and the tuning of the molecular bonding.

2 The normal incidence x-ray standing wave technique

2.1 Fundamentals of XSW

The x-ray standing wave (XSW) technique is a powerful tool for investigating the structural properties of molecular adsorbates on metal surfaces. It exploits the combination of x-ray diffraction and inelastic x-ray scattering (photoelectric effect, Auger effect, fluorescence). The coherent interference of incident and diffracted waves generates a standing wave inside and above the crystal, and from the characteristic scattering response of atoms within the standing wave field, their spatial distribution can be determined.

One of the main advantages of XSW is that long-range order of the adsorbate under study is not required, as it is for other diffraction technique, such as low-energy electron diffraction (LEED). The more stringent requirement is a sufficiently perfect crystal with low mosaicity and thus a strong reflection resulting from the constructive interference of multiply diffracted beams. In general, there are two theories which can be used study x-ray diffraction. The first one, the kinematical theory, treats the scattering from each volume element in the sample as being independent of that of other volume elements (Figure 2.1a). The second one, the dynamical theory,[20] takes into account the multiple interplay of the beams diffracted within a crystalline region and must be used when diffraction from large perfect crystals is considered (Figure 2.1b). One of the main conceptual fundamentals of the dynamical theory is to consider the total wave field inside a crystal where diffraction is taking place, although one may naively and, for the sake of simplicity, refer to incident and diffracted waves. The reason for treating the total wave field as a unit follows from the fact that incident and diffracted waves are coherently coupled. If the diffracting region is so small and the reflection so weak that multiple interplay of the diffracted

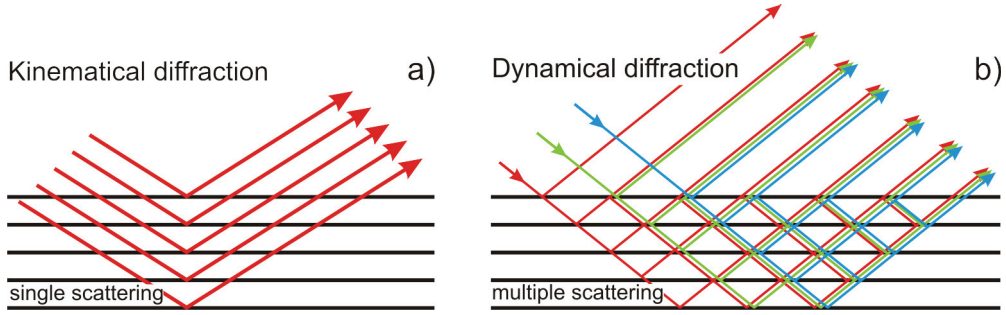


Figure 2.1: (a): schematic representation of the kinematical theory of diffraction, where single scattering events occur at each Bragg plane and different volume elements are treated independently. (b): schematic representation of the dynamical theory of diffraction, where the incident beam is forward scattered, Bragg reflected outside the crystal and Bragg back reflected inside the crystal at each Bragg plane, and the multiply diffracted beams interfere constructively to form the reflected output beam.

beams cannot occur, then the dynamical theory yields essentially the same results as the kinematical theory.

In our experiments, we employ the *normal incidence* x-ray standing wave technique[21,36] in order to relax the strict demand for a highly perfect crystal, as will be explained in detail in section 2.4. As a consequence, the incident direction of the x-ray beam is almost perpendicular to the diffraction planes, although not necessarily normal to the surface of the sample. Note also that all the following theory and discussion referring to XSW is also valid for NIXSW.

In section 2.2, the theoretical basis of XSW is summarized. For a thorough mathematical formulation of the XSW theory we refer to the review paper by Zegenhagen,[22] while for the specific details of the NIXSW variant and its potential we refer to the reviews by Woodruff.[21,36] In section 2.3 we then focus on the detection method of XSW, in our case x-ray photoemission spectroscopy (XPS). Subsequently, the basic principles of an XSW experiment are discussed (section 2.4) and two resulting structural parameters, coherent position and coherent fraction, are interpreted (section 2.5). Finally, experimental details of the set-up employed to perform NIXSW measurements are reported in section 2.6.

2.2 The standing wave

Let us consider an x-ray wave $\mathscr{E}_0$ incident on a perfect single crystal. If the Bragg condition (equation 2.11) is satisfied, a Bragg-reflected wave $\mathscr{E}_H$ will appear on the same face of the crystal. The superposition of the two coherently coupled traveling x-ray waves generates an x-ray standing wave, as shown in Figure 2.2a. If we assume the two waves to be planar, linearly polarized and with parallel electric field vectors, they can be fully characterized by the complex amplitude of the electric field of the electromagnetic wave:

$$\mathscr{E}_0 = E_0 \exp\left[2\pi i \left(\nu_0 t - \boldsymbol{K}_0 \cdot \boldsymbol{r}\right)\right] \tag{2.1}$$

and

$$\mathscr{E}_H = E_H \exp\left[2\pi i \left(\nu_H t - \boldsymbol{K}_H \cdot \boldsymbol{r}\right)\right]. \tag{2.2}$$

Here, ν is the frequency of the radiation, $\boldsymbol{K}$ is the propagation vector and $\boldsymbol{r}$ is a coordinate vector with respect to an arbitrary origin. Given $|\boldsymbol{K}| = \lambda^{-1}$ and assuming $\lambda_0 = \lambda_H = \lambda$, it follows that $|\boldsymbol{K}_0| = |\boldsymbol{K}_H|$. Furthermore, the propagation vector of the incident and Bragg-reflected wave are related by the following equation:

$$\boldsymbol{K}_H = \boldsymbol{K}_0 + \boldsymbol{H} \tag{2.3}$$

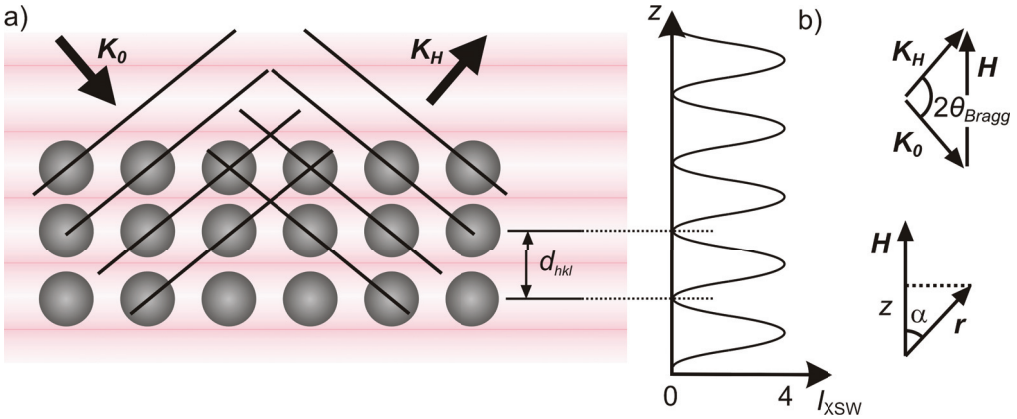


Figure 2.2: (a): schematic representation of a crystal substrate where diffraction is taking place. $\boldsymbol{K}_0$, the wave vector of the incident wave, and $\boldsymbol{K}_H$, the wave vector of the diffracted wave, fulfill the equation $\boldsymbol{H} = \boldsymbol{K}_H - \boldsymbol{K}_0$, where $2\pi\boldsymbol{H}$ is a vector of the reciprocal space, and $|\boldsymbol{H}| = (d_{hkl})^{-1}$. d_{hkl} is the spacing of the hkl Bragg planes. θ_{Bragg} is the angle formed by the incident (diffracted) wave vector and the Bragg plane. (b): I_{XSW} displayed as a function of the z axis ($\perp$ Bragg planes). The limits $(1 \pm 1)^2$ of I_{XSW} follow from the interference of two waves with amplitude normalized to 1.

where $2\pi\boldsymbol{H}$ is the reciprocal space vector associated with the specific Bragg reflection from the (hkl) scatterer planes, separated by d_{hkl}. For orthorhombic crystals in which all angles are equal ($\alpha = \beta = \gamma = 90°$), and a, b, c are the lattice constants:

$$d_{hkl} = \sqrt{\frac{1}{\left(\frac{h}{a}\right)^2 + \left(\frac{k}{b}\right)^2 + \left(\frac{l}{c}\right)^2}}. \tag{2.4}$$

In the case of fcc crystals, e.g., Ag, Cu, Au, then $a = b = c$. Note that in equations 2.1 and 2.2 the amplitudes E_0 and E_H are also complex numbers because they contain a phase factor, as expressed by the equation 2.13.

From the superposition of $\mathscr{E}_0$ and $\mathscr{E}_H$, it follows that the total wavefield of the x-ray standing wave is:

$$\mathscr{E} = \mathscr{E}_0 + \mathscr{E}_H = E_0 \exp\left[2\pi i\left(\nu t - \boldsymbol{K}_0 \cdot \boldsymbol{r}\right)\right] + E_H \exp\left[2\pi i\left(\nu t - \boldsymbol{K}_H \cdot \boldsymbol{r}\right)\right]. \tag{2.5}$$

Normalizing the amplitude of the incident x-ray flux to 1, it can be derived[22] that the intensity of the x-ray standing wave at a position $\mathbf{r}$ of the real space is:

$$I_{XSW} = \frac{\mathscr{E}\mathscr{E}^*}{|E_0|^2} = \left|1 + \left(\frac{E_H}{E_0}\right)\exp\left(-2\pi \mathrm{i}\boldsymbol{H} \cdot \boldsymbol{r}\right)\right|^2 \tag{2.6}$$

where E_0 and E_H are the incident and reflected complex amplitudes of the electric field of the electromagnetic wave, and $\boldsymbol{H}$ is the reciprocal lattice vector associated to the specific Bragg reflection from the (hkl) scatterer planes, separated by d_{hkl}. Since $|\boldsymbol{H}| = (d_{hkl})^{-1}$, then $\boldsymbol{H} \cdot \boldsymbol{r} = z/d_{hkl}$ (see Figure 2.2), where z is the vertical distance of the real-space point defined by $\boldsymbol{r}$ from the nearest Bragg plane below, and equation 2.6 can be written as:

$$I_{XSW} = \left|1 + \left(\frac{E_H}{E_0}\right)\exp\left(-2\pi \mathrm{i}\frac{z}{d_{hkl}}\right)\right|^2. \tag{2.7}$$

At the Bragg condition the intensity of the x-ray standing wave is spatially modulated by a sine function (d_{hkl}-periodic) along the direction of $\boldsymbol{H}$, while is constant along the direction perpendicular to $\boldsymbol{H}$, as illustrated by the shaded areas in Figure 2.2a. Therefore, the scattering response of an atom inside this standing wave field differs according to its vertical position relative to the scatterer planes.

2.3 XSW detection: photoelectrons

Having introduced the general properties of the x-ray standing wave, i.e., our probe, we turn now to the discussion of the possible ways to detect the XSW through the inelastic scattering of our probe from atoms whose spatial distribution is to be determined. In particular, we limit the consideration to the photoelectric effect and briefly focus on the consequent decay processes, i.e., Auger effect and fluorescence.

If the incident photon energy $h\nu$ is greater than the sum of the electron binding energy E_b and the work function Φ, i.e., $h\nu > E_b + \Phi$, the electron is emitted. From the detection of photoelectrons emitted by atoms at position z, i.e., the electron yield ($Y(z)$), we can measure the absorption ($I_a(z)$) of the XSW from a given element at z, in other words:

$$Y(z) \propto I_a(z) \tag{2.8}$$

Moreover, it can be shown that the photon absorption is proportional, within the dipole approximation (see section 3.4.2), to the intensity of the standing wave field (equation 2.6):[22]

$$I_a(z) \propto I_{XSW}(z) \tag{2.9}$$

As a consequence, the following proportionality between the electron yield and the XSW intensity holds:

$$Y(z) \propto I_{XSW}(z)\,. \tag{2.10}$$

This represents the link between our local probe, i.e., the XSW, and the measured electron yield corresponding to a given spatial distribution of atoms located at different z positions above a metal substrate.

The advantages of detecting photoelectrons, instead of Auger electrons or x-ray fluorescence, are as follows:

- The photoemission process is exclusively initiated by the XSW field, while Auger electrons and fluorescence may be initiated by secondary electrons, in which case equation 2.10 is no longer valid.
- Photoelectrons are surface sensitive for sufficiently low energies (especially below 1 keV) with a probing depth dictated by their mean free path.[37] The same is true for Auger electrons, but not for the fluorescence signal.
- Furthermore, photoelectrons are both element-specific and bonding-environment-

specific. In other words, if the chemical shift of a core level of an element is large enough to be detected, it is possible to separately analyze the absorption profiles of photoemission lines of the same element in different chemical environments. This opportunity has been widely used in our studies and examples are reported in chapters 4, 5 and 7.

2.4 Basics of an XSW experiment

Having learned that $Y(z) \propto I_{XSW}(z)$, we will show in the section below that the standing wave shifts along the z direction (Figure 2.2a) as the incoming photon energy E is varied. Therefore, Y can be used to locate photoemitters relative to the lattice planes. From the dynamical theory of diffraction it follows that the incident beam is diffracted, hence an XSW exists, for a $finite$ range of incident angles or energies, beyond the one defined by Bragg's law:

$$\lambda_{Bragg} = 2d_{hkl} \sin(\theta_{Bragg}). \tag{2.11}$$

In particular, in the dynamical theory, the full width at half maximum (FWHM) W_θ of a symmetrical Bragg reflection is proportional to $\tan(\theta_{Bragg})$.[22] As the θ_{Bragg} approaches $\frac{\pi}{2}$, W_θ would approach ∞. This obviously does not occur; in fact for $\theta_{Bragg} \simeq \frac{\pi}{2}$ some approximations of the dynamical theory cease to be valid and new appropriate expressions should be employed.[38] Nonetheless, as $\theta_{Bragg} \to \frac{\pi}{2}$ (NIXSW), W_θ significantly increases, and the larger range of reflection allows the strict condition on the crystal mosaicity to be relaxed. This is indeed the main advantage of the NIXSW variant, compared to the general XSW technique. For $\theta_{Bragg} \simeq \frac{\pi}{2}$, W_θ is thus sufficiently large that it can be scanned by a fine tuning of the incident photon energy around the Bragg energy, defined as:

$$E_{Bragg} = \frac{hc}{\lambda_{\mathrm{Bragg}}}. \tag{2.12}$$

Note that although in our experiments the incident angle θ is fixed and the photon energy E is varied, it is possible to perform the same measurements by tuning the incident angle.[22]

As the incident photon energy is scanned through the finite range of energies including E_{Bragg}, the phase ϕ of $\frac{E_H}{E_0}$ varies. Since incident and diffracted wave are coherent,

the ratio of their complex amplitudes can be expressed as:

$$\frac{E_H}{E_0} = \sqrt{R}\exp\left(\mathrm{i}\phi\right) \tag{2.13}$$

where ϕ defines the phase relationship between E_H and E_0, and has values between π ($\mathrm{h}\nu \ll E_{Bragg}$) and 0 ($\mathrm{h}\nu \gg E_{Bragg}$). Because of the coherence, ϕ is independent of space and time. R relates the amplitudes of E_H and E_0, and represents the reflectivity. Its values go from $R = 0$ (no reflection) to $R = 1$ (total reflection). If we replace the ratio $\frac{E_H}{E_0}$ in equation 2.7 with equation 2.13, we have:

$$I_{XSW} = \left|1 + \sqrt{R}\exp\left(\mathrm{i}\phi - 2\pi\mathrm{i}\frac{z}{d_{hkl}}\right)\right|^2 \tag{2.14}$$

or

$$I_{XSW}\left(z, E\right) = 1 + R\left(E\right) + 2\sqrt{R\left(E\right)}\cos\left(\phi\left(E\right) - 2\pi\frac{z}{d_{hkl}}\right), \tag{2.15}$$

where R and ϕ are functions of the energy E and their expressions are reported in equations 3.9, 3.12 and 3.13, respectively. Upon a complete scan of the incident photon energy through the Bragg condition, the phase ϕ of $\frac{E_H}{E_0}$ changes by π, which corresponds to a rigid translation of the XSW of $z = \frac{d_{hkl}}{2}$ along the direction antiparallel to $\boldsymbol{H}$, as shown in Figure 2.3 b1, b2, c1, c2. As a consequence, the absorption yield (I_a) of an atom located at a given position z in the XSW will vary accordingly.

Let us assume that atoms A and B are located at the Bragg plane and $\frac{d_{hkl}}{2}$ above it, respectively, as illustrated in Figure 2.3. If the photon energy $h\nu$ is far below the Bragg energy (E_{Bragg}), the amplitude of the reflectivity is 0 (Figure 2.3 a3) and, assuming that there is no absorption inside the crystal, the intensity of the incident x-ray wave is constant throughout the substrate and above it (Figure 2.3 a1, a2). Therefore, the absorption yield of atom A and that one of atom B are identical and normalized to 1 (Figure 2.3 a4), i.e., the intensity of the incident x-ray wave (Figure 2.3 a2). If the absorption in the crystal is neglected, for the simple interference of two beams the limiting intensity values, relative to the incident beam intensity, are $(1 \pm 1)^2 = 0$ and 4. These are also the extreme values of the absorption yield (I_a), assuming a direct proportionality between I_{XSW} and I_a (equation 2.9).

As the photon energy reaches the Bragg energy ($h\nu \gtrsim E_{Bragg}$), the incident wave is diffracted, the reflectivity increases and the standing wave forms (Figure 2.3 b1, b2). Its nodal planes coincide with the Bragg planes, in this case, also the atomic planes; in fact I_a (B) decreases, while its antinodes are midway between two Bragg

planes; in fact I_a (A) increases, as reported in Figure 2.3 b4.

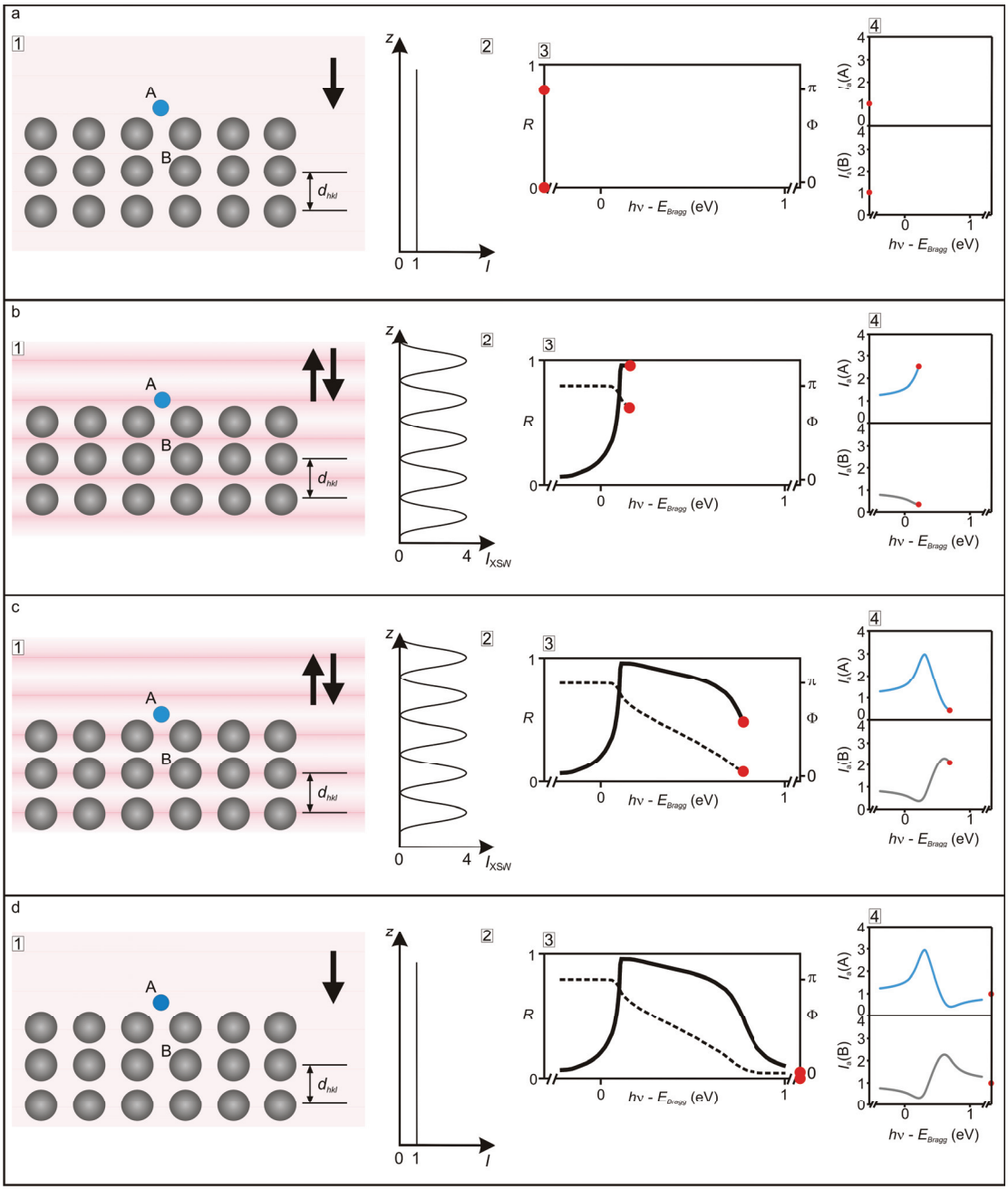


Figure 2.3: Representation of the formation and extinction of the XSW in a crystal (a1, b1, c1, d1) in four different steps, characterized by photon energy $h\nu \ll E_{Bragg}$ (a), $h\nu \gtrsim E_{Bragg}$ (b), $h\nu > E_{Bragg}$ (c) and $h\nu \gg E_{Bragg}$ (d). In each panel, the intensity of the incident x-ray wave (a2, d2) or of the x-ray standing wave (b2, c2) is displayed as a function of the z position and illustrated in figures a1, b1, c1, d1. The corresponding reflectivity R and phase ϕ (taken from Figure 5a of ref.[22]) are reported in figures a3, b3, c3, d3. The absorption profiles of atom A, located $\frac{d_{hkl}}{2}$ above the Bragg plane, and of atom B, located at the Bragg plane, are reported in figures a4, b4, c4, d4.

As $h\nu$ is scanned through the Bragg condition ($h\nu > E_{Bragg}$) the phase ϕ shifts, while the amplitude of the reflectivity is still large, although lower than in the previous scenario (Figure 2.3 c3). In fact, the XSW is still present but its nodal and antinodal planes are $\frac{d_{hkl}}{2}$ shifted (compared to the previous step) so that atom A is now at the node while atom B lies at the antinode of the XSW, with corresponding changes in the absorption yield (Figure 2.3 c4).

Finally, for $h\nu \gg E_{Bragg}$, the amplitude of the reflectivity is again 0; there is no diffraction, hence no XSW (Figure 2.3 d1, d2, d3). The absorption profiles (Figure 2.3 d4) are back to the values characteristic of the incident beam (1). The phase ϕ here has completed the shift and equals 0. Note that the asymmetric shape of the reflectivity accounts for x-ray absorption inside the substrate, which is larger as the XSW antinodes approach the atomic planes.

In the section above, we analyzed the behaviour of the XSW, of the reflectivity R and of the phase ϕ of the ratio $\frac{E_H}{E_0}$ while the incident photon energy is scanned through the Bragg condition, as is performed in an XSW experiment. We have also reported, as an example, the absorption intensity of two atoms located at different vertical positions with respect to the Bragg planes. Remarkably, atom A and atom B have very different absorption profiles. This is indeed the essence of the XSW technique. In fact, the strong correlation between the absorption profile and the vertical distance of an absorber with respect to the scatterer planes allows retrieval of the structural properties, i.e., spatial distribution, of an adsorbate starting from the corresponding absorption yield.

2.5 Coherent position and coherent fraction

In equation 2.15, we have seen the intensity of the XSW at a specific atomic position z. In reality, the vertical position of an absorber is never specified by a single value because of the thermal vibrations and possibly multiple adsorption sites. For this reason, we introduce a distribution of occupied distances z so that $\int_0^{d_{hkl}} f(z)\,dz = 1$, where $f(z)\,dz$ is the fraction of absorbers located at z within a range dz. Hence, I_{XSW} (proportional to the electron yield Y) becomes:

$$I_{XSW} = 1 + R + 2\sqrt{R} \int_0^{d_{hkl}} f(z) \cos\left(\phi - 2\pi \frac{z}{d_{hkl}}\right) dz. \tag{2.16}$$

which can be written as:[36]

$$I_{XSW} = 1 + R + 2F_c\sqrt{R}\cos\left(\phi - 2\pi P_c\right). \tag{2.17}$$

where two structural parameters are defined: the coherent position, P_c, and the coherent fraction, F_c. P_c and F_c by definition have values between 0 and 1.

In particular, the coherent position $P_c = \frac{z}{d_{hkl}}$ represents an average vertical distance of the absorber from the nearest extended Bragg plane underneath. From the fact that $2\pi P_c$ is an argument of the 2π-periodic cosine function, the modulo-1 periodicity of P_c follows. As a consequence, only the vertical position of the absorber with respect to the nearest extended Bragg plane underneath can be determined, but not its absolute distance from the surface. In practice, this is usually not a problem, because only one of the possible adsorption heights is plausible; hence the ambiguity is removed.

According to the following expression of equation 2.17:

$$I_{XSW} = F_c\left[1 + R + 2\sqrt{R}\cos\left(\phi - 2\pi P_c\right)\right] + \left(1 - F_c\right)\left(1 + R\right) \tag{2.18}$$

F_c can be interpreted as the fraction of absorbers with coherent position P_c, while $(1 - F_c)$ represents the fraction of the incoherent sum of the incident and reflected waves.

There are several possible sources of "incoherence". If the mosaicity of the crystal is large, the coherence of the standing wave decreases significantly. Moreover, even in the presence of a perfect crystal, the substrate atoms will never occupy a single position because of the thermal vibrations, which can be taken into account by the Debye-Waller factor (section 3.3.3). Thermal vibrations of the adsorbate atoms will also cause a decrease in the coherent fraction.

Besides vibrations of atoms around a defined adsorption site, in reality, adsorbate atoms can have also different vertical positions with respect to the extended Bragg plane, for reasons such as multiple adsorption sites or non-flat adsorption geometry of the molecules. In these more complex situations, it becomes more convenient to perform a Fourier analysis. In particular, the Fourier component $\tilde{f}_{\boldsymbol{H}}$ of the absorber

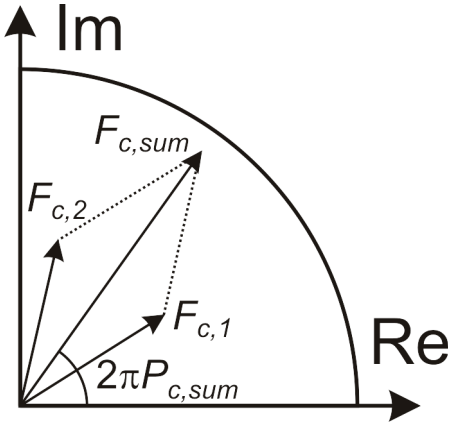


Figure 2.4: Argand diagram representation in the complex plane of two vectors corresponding to coherent positions $P_{c,1}$ and $P_{c,2}$, and coherent fraction $F_{c,1}$ and $F_{c,2}$, respectively. Their vector sum has length $F_{c,sum}$ and forms an angle $2\pi P_{c,sum}$ with the positive real axis, according to equation 2.21.

site distribution $f(z)$ projected along $\boldsymbol{H}$ is:

$$\tilde{f_{\boldsymbol{H}}} = \int_0^{d_{hkl}} f(z) \exp\left(2\pi \mathrm{i} \frac{z}{d_{hkl}}\right) dz, \tag{2.19}$$

where the real part of the right-hand side of equation 2.19 coincides with the integral term in equation 2.16. Since $\tilde{f_{\boldsymbol{H}}}$ is a complex quantity, it can be written as:

$$\tilde{f_{\boldsymbol{H}}} = F_c \exp\left(2\pi \mathrm{i} P_c\right), \tag{2.20}$$

where F_c and P_c are the amplitude and phase of the Fourier component, respectively. Therefore, $\tilde{f_{\boldsymbol{H}}}$ can be represented as a vector in an Argand diagram with length F_c and direction defined by the angle $2\pi P_c$ with the positive real axis (see Figure 2.4). Interestingly, if a sufficiently complete set of $\tilde{f_{\boldsymbol{H}}}$ is measured by XSW, the real space spatial distribution $f(z)$ can be obtained directly by Fourier inversion of the measured Fourier components. This is the essence of the XSW imaging technique.[39]

If two atoms of the same element equally occupy distances $z_1 = P_{c,1} \times d_{hkl}$ and $z_2 = P_{c,2} \times d_{hkl}$ with coherent fractions $F_{c,1} = F_{c,2} = 0.5$, the sum of the corresponding vectors in the Argand diagram is:

$$F_{c,sum} \exp\left(2\pi \mathrm{i} P_{c,sum}\right) = F_{c,1} \exp\left(2\pi \mathrm{i} P_{c,1}\right) + F_{c,2} \exp\left(2\pi \mathrm{i} P_{c,2}\right), \tag{2.21}$$

as illustrated in Figure 2.4. The result of an XSW experiment on such configuration of atoms would then be an absorption profile as in equation 2.17 with $P_c = P_{c,sum}$ and $F_c = F_{c,sum}$.

In chapter 6, we will show how the vector analysis in the Argand diagram allows much deeper insights to be obtained into the adsorption geometry of large organic molecules on metal substrates, and permits important structural details to be investigated that would otherwise remain unexplored.

2.6 Experimental set-up

NIXSW experiments described in detail in chapters 4, 5, 7 and 6 were performed at the ID32 beamline of the European Synchrotron Radiation Facility (ESRF). Figure 2.5 shows a top-view section of the ultrahigh vacuum (UHV) chamber, in which experiments were carried out.[19] The substrate sample is attached to a vertical manipulator through a sample holder. The manipulator has five degrees of freedom: x, y, z, θ and ϕ, as indicated in Figure 2.5. The leak valve is used to insert Ar gas, which is then ionized and sputtered onto the sample surface in order to clean it before the molecules to be investigated are evaporated from a Knudsen cell. To control the residual gas in the chamber and to monitor the deposition of adsorbate

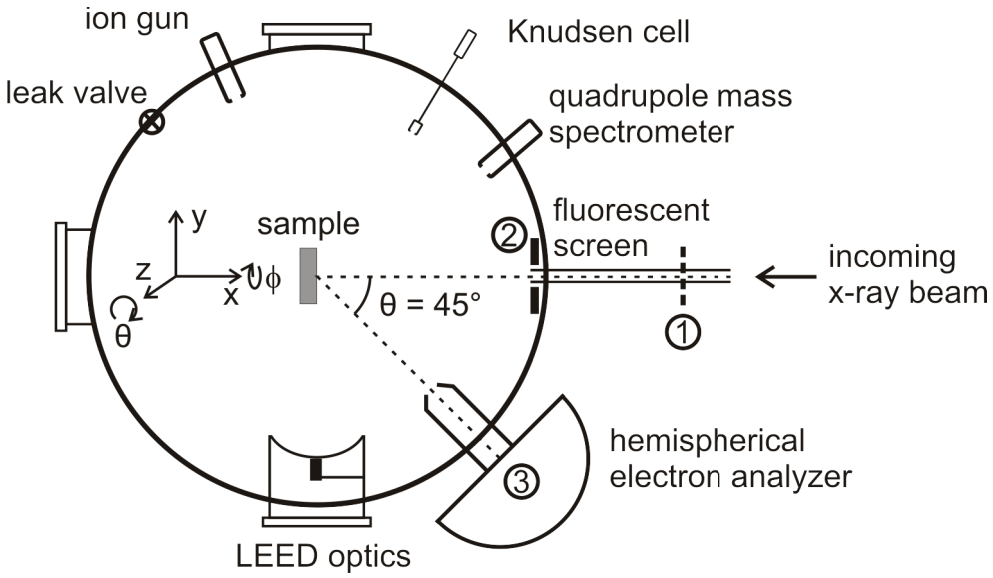


Figure 2.5: Top-view section of the UHV chamber in ID32 (ESRF) in which NIXSW experiments reported in chapters 4, 5, 7 and 6 were performed. For details about each component, see text.

on the sample, a quadrupole mass spectrometer is used. The LEED set-up is used to inspect the molecular superstructure formed on the crystal sample. Note that given this experimental set-up, LEED experiments, together with XPS, are the only ones which can be done both in a home lab and at the synchrotron in order to ensure that NIXSW experiments are performed on the same desired molecular structure.

Moreover, the experimental set-up of the chamber is designed to perform NIXSW experiments specifically. In fact, the incident x-ray beam is directed almost perpendicular to the Bragg planes of the sample and the diffracted beam hits the fluorescent screen (point 2 in Figure 2.5), where its intensity is measured by means of a photodiode and the corresponding fluorescent spot can be visualized. Photoelectrons are detected by a PHI hemispherical analyzer (point 3 in Figure 2.5) that forms an angle of $\theta = 45°$ with the x-ray beam direction.

During an NIXSW experiment, for each photon energy scanned, we measure:

- a quantity proportional to the intensity of the incoming x-ray beam, measured after the beam crosses the last slit before entering the UHV chamber, at point 1 in Figure 2.5. Since the intensity of the x-ray beam is not constant during the experiments, the knowledge of this parameter is essential for accurate normalization of the reflectivity and the absorption yield.
- a quantity proportional to the reflectivity R,
- an XPS spectrum of an element core level, from which the photoelectron yield (Y), i.e., integrated PE intensity after background subtraction, is derived.

In the following chapter 3 we will see how it is possible to determine the two structural parameters (P_c, F_c) starting from the XPS and reflectivity measurements, normalized by the beam intensity, by means of the Torricelli program.

3 Torricelli

3.1 Introduction

Torricelli is a software designed for the analysis of XSW data. While the XSW technique has been employed for several decades, to our knowledge no free, open source, and particularly well-documented program for conducting XSW data analysis exists to date. The intent of Torricelli is therefore an attempt to fill this gap.

XSW experimentalists usually seek the spatial distribution of a certain atomic species. As we have seen in section 2.5, the spatial distribution of each atomic species can be partially described by two parameters, the coherent position P_c and the coherent fraction F_c. The main target of Torricelli is to determine this pair of parameters in the most accurate way, and also provide the corresponding errors, as explained in section 3.5.

In section 2.4 we have learned that there is a strong correlation between (P_c, F_c) and the absorption profile $I_a(z) \propto I_{XSW}(z)$. Since in our experiments we detect either photoelectrons or Auger electrons (section 2.6), we talk more specifically of electron yield profile Y. Therefore, on the basis of equation 2.10 and 2.17 we can write:

$$Y_{exp} = 1 + R_{theo} + 2F_c\sqrt{R_{theo}}\cos(\phi_{theo} - 2\pi P_c). \tag{3.1}$$

where Y_{exp} is the experimental electron yield, derived from the XPS spectra measured for each photon energy scanned during NIXSW experiments. R_{theo} and ϕ_{theo} are the theoretical square modulus and phase of the ratio $\frac{E_H}{E_0}$ (equation 2.13) respectively. A thorough description of how R_{theo} and ϕ_{theo} are calculated is reported in section 3.3.2. In ideal conditions, if R_{theo} and ϕ_{theo} were equal to the respective experimental quantities, it would be sufficient to fit the experimental Y with the right side of equation 3.1 in order to find the two unknown parameters (P_c, F_c).

However, in reality there are several "non-idealities" to be taken into account that can significantly affect the result of the fitting, e.g., the mosaicity of the crystal, the non-perfectly monochromatic incident x-ray beam, and other items that are explained in detail in section 3.3.1. Nevertheless, since we measure the reflectivity (section 2.6), all the non-idealities associated with the experimental set-up and the sample can be included in the analysis.

Our strategy is then to determine the functional F_{ni} (from non-idealities) that satisfies the equation:

$$R_{exp} = NF_{ni}\left[R_{theo}\right] + \Delta R, \tag{3.2}$$

where N and ΔR are a normalization factor and an offset, respectively. The fitting of the experimental reflectivity will be discussed in more detail in section 3.3.

Subsequently, the functional F_{ni} from the previous step is used to take into account all the non-idealities that propagate to the electron yield, proportional to I_{XSW}. Therefore, equation 3.1 can be written as:

$$Y_{exp} = MF_{ni}\left[1 + R_{theo} + 2F_c\sqrt{R_{theo}}\cos\left(\phi_{theo} - 2\pi P_c\right)\right], \tag{3.3}$$

where the only two unknown variables are P_c and F_c. Y_{exp} is then fitted using the fitting function on the right side of equation 3.3 and (P_c, F_c) are found, as explained in section 3.4. The assumption behind the use of the same function F_{ni} for R_{exp} and Y_{exp} is that the electron analyzer does not include further non-idealities, which are expected to be mainly due to the optical properties of the incident beam and the non-perfect quality of the crystal.

In summary, the present chapter can be divided in two main parts. The first one deals with the fitting of the experimental reflectivity according to equation 3.2 (section 3.3.1), and therefore with the calculation of the theoretical reflectivity and phase (section 3.3.2), in turn based on the knowledge of the structure factors (section 3.3.3). The second part treats the fitting of the experimental electron yield according to equation 3.3 to determine (P_c, F_c) (section 3.4). After a discussion of the nondipolar correction parameters (section 3.4.2), the fitting of Y_{exp} to determine the asymmetry parameter Q is described in section 3.4.3. Before reflectivity and electron yield can be fitted, the raw experimental data need to be normalized by the x-ray beam intensity as reported in section 3.2 below.

3.2 Preparing reflectivity and electron yield profiles for fitting

This first part of the program, shown in Figure 3.1, represents the interface between the measured data and their analysis. In this section, experimental reflectivity and electron yield profile are normalized by the intensity of the incoming x-ray beam. In particular, the electron yield can be given by:

- the integrated area of the XPS spectrum after background subtraction (*Region*);
- the area of one fitting component;
- the sum of two or more fitting components.

Torricelli allows any of the options listed above to be selected. This feature is particularly useful to differentiate signals of different atomic species or to sum components of the same atomic species, as will be shown in chapters 4-6. Details about the operation of this section of Torricelli, including the main parts of the code, can be found in section A.2.

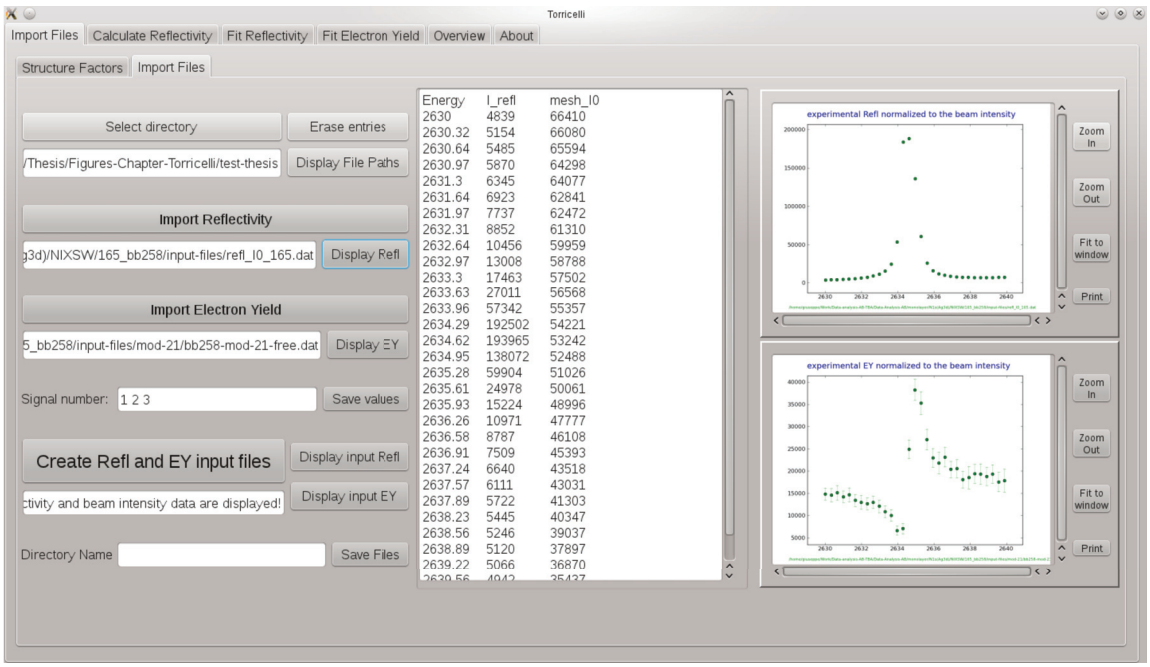


Figure 3.1: "Import Files" section of Torricelli where reflectivity and electron yield data are imported and normalized by the intensity of the incoming x-ray beam. Normalized signals are displayed in the two figures on the right. Details of this part of the program are presented in section A.2.

3.3 Fitting the reflectivity

3.3.1 The fitting function

The experimental reflectivity R_{exp} is fitted by the following equation:

$$R_{exp}(E) = \underline{N}\left[G(\underline{\sigma}) \otimes R_m^2 \otimes R_{theo}\right]\Big|_{(E+\underline{\Delta E})} + \underline{\Delta R}, \tag{3.4}$$

where the fitting function on the right side has four fitting parameters (underlined). R_{theo} and R_m are the theoretical reflectivities of the sample and of the monochromator crystal respectively, calculated as described in section 3.3.2. $G(\underline{\sigma})$ is a Gaussian function with width σ. N is a normalization factor. ΔE is an energy shift. ΔR is a reflectivity offset. In the section below we argue why the fitting function in equation 3.4 is employed to model the experimental reflectivity. In practice, this is equivalent to discussing the main causes of non-idealities and their corresponding mathematical model.

- In our experimental set-up, before reaching the sample crystal, the incoming x-ray beam goes through a double crystal monochromator as shown in Figure 3.2, in order to select the desired energy from the spectrum of the input beam. The monochromator consists of two identical single crystals (in our case Si(111)) parallel to each other so that the output beam is always parallel to the input beam. Due to the x-ray absorption in the crystal, the asymmetric shape of the monochromator crystal reflectivity (figures 3.3 and 3.8) is transferred to the beam intensity. Therefore, to accurately model the experimental reflectivity, the monochromator reflectivity must be taken into account.

  If E_0, E_1 and E_2 are the complex amplitudes of the incoming, singly-diffracted

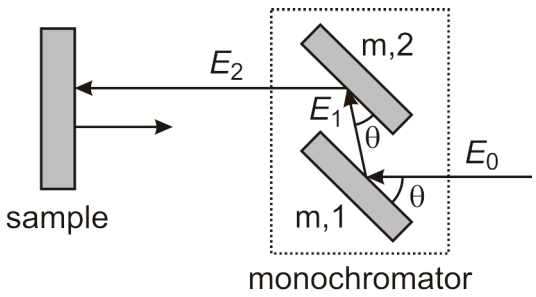


Figure 3.2: (a): schematic representation of the double crystal monochromator, formed by two parallel Si(111) crystal in our experimental set-up (section 2.6), and the sample crystal.

and doubly-diffracted (outgoing) x-ray waves respectively, the reflectivity of the double crystal monochromator can be written as:

$$\left|\frac{E_2}{E_0}\right|^2 = \left|\frac{E_2}{E_1}\frac{E_1}{E_0}\right|^2 = \left|\frac{E_2}{E_1}\right|^2 \left|\frac{E_1}{E_0}\right|^2 = R_{m,2}R_{m,1} = R_m^2, \tag{3.5}$$

assuming that the two crystals are perfectly identical, hence $R_{m,2} = R_{m,1} = R_m$, and parallel to each other. The parallelism of the two crystals scattering planes leads to the multiplication of the corresponding reflectivities $R_{m,1}$ and $R_{m,2}$. In fact, each incoming beam, with photon energy $h\nu$ and incident angle θ (Figure 3.2) that fulfill the Bragg condition (equation 2.11) of the first monochromator crystal, is Bragg reflected with an output intensity modulated by $R_{m,1}$ (Figure 3.3a). Similarly, the Bragg-reflected beam from the first crystal will form the same angle θ (because of the parallelism) with the second crystal; hence its intensity will be analogously modulated by $R_{m,2} = R_{m,1}$, as shown in Figure 3.3b. Therefore, in mathematical terms, the resulting effect will be as if the incoming beam is diffracted by a crystal with reflectivity R_m^2, illustrated in Figure 3.3c. In contrast, the same geometrical relation does not hold between the monochromator

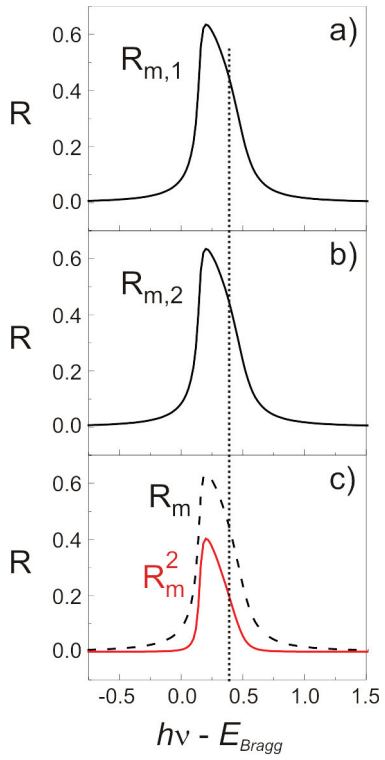


Figure 3.3: Si(111) reflectivity profile $R_{m,1}$ (a) and $R_{m,2}$ (b) of the two monochromator crystals, and the square of the monochromator crystal reflectivity R_m^2 calculated for $h\nu = 2629.89$ eV (Figure 3.8b,d).

crystals and the sample crystal. As a consequence, we must take into account the asymmetry of the monochromator reflectivity through the convolution:

$$R_m^2 \otimes R_{theo} \tag{3.6}$$

where both R_{theo} and R_m can be calculated, as described in section 3.3.2.

- In the ideal case the incoming x-ray beam is perfectly monochromatic, but in reality this is not the case. We take this into account by convoluting the reflectivity with a Gaussian function:

$$G(\sigma) \otimes R_m^2 \otimes R_{theo}, \tag{3.7}$$

assuming a Gaussian intensity distribution around the selected photon energy for the radiation coming from the undulator. Note that σ is one of the fitting parameter in equation 3.4. Moreover, $G(\sigma)$ also models the mosaicity of the monochromator and sample crystals, which may lead to a further broadening of the reflectivity curve.

- In order to align the experimental energy scale with the one of the reflectivity calculations, the energy shift ΔE is introduced as one of the fitting parameters.

- Furthermore, what we actually measure as reflectivity is the drain current that replaces the electrons photoemitted from a fluorescent reflectivity plate (Figure 2.5) by the x-ray beam diffracted at the sample crystal. Therefore, a normalization factor N has to be included in the fitting function as a fitting parameter.

- In order to measure the full dynamic range of the reflectivity, an electrical offset is introduced. Hence, the offset ΔR is added to the fitting function as the last fitting parameter.

To conclude, the resulting fitting function, used to take experimental non-idealities into account for the fitting of the electron yield as well, is:

$$F_{ni} = G(\underline{\sigma}) \otimes R_m^2\big|_{(E+\underline{\Delta E})}, \tag{3.8}$$

where the areas of $G(\underline{\sigma})$ and R_m^2 are normalized to 1 (section A.3.2, lines 7-8, and A.4.2, lines 312-314) so that only the shape of the profile (but not the area) of the sample reflectivity is affected by the convolution with F_{ni}.

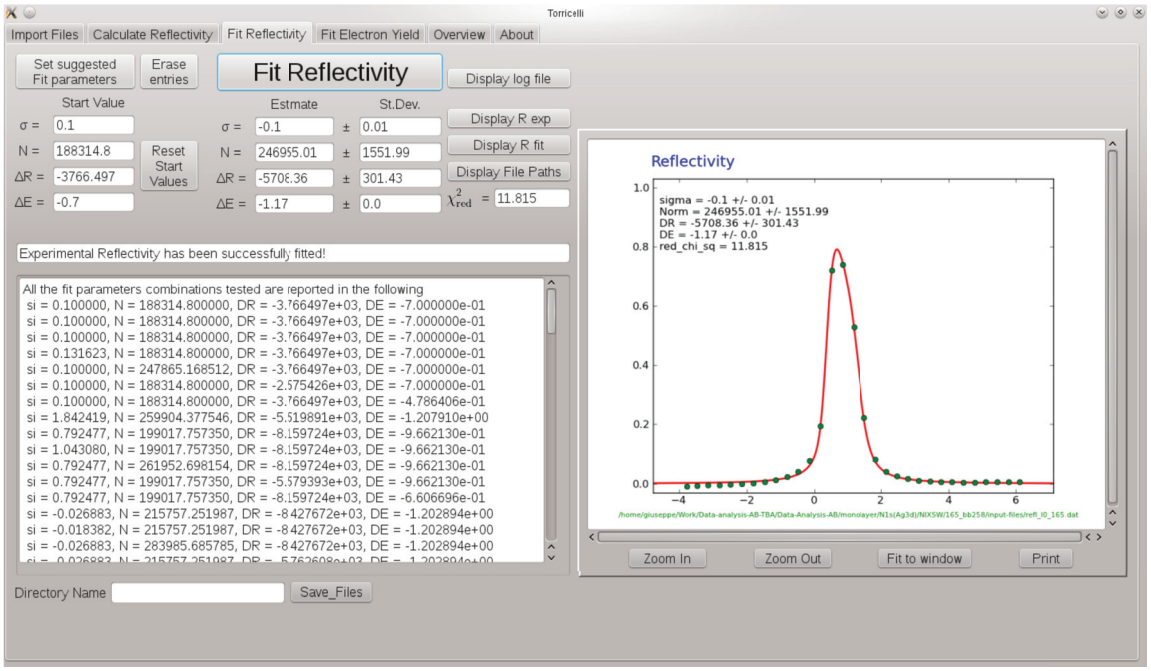


Figure 3.4: "Fit Reflectivity" section of Torricelli. Technical details are reported in section A.3.

Figure 3.4 shows the section of Torricelli in which the fitting of the experimental reflectivity is performed, along with details about its practical operation and corresponding code can be found in section A.3.

3.3.2 Calculation of the ideal reflectivity R_{theo} and phase ϕ_{theo}

Torricelli calculates the ideal reflectivity and phase of the sample crystal (R_{theo}, ϕ_{theo}) and of the monochromator crystal (R_m, ϕ_m). They are employed for the calculation of the fitting function for the experimental reflectivity (section 3.3.1).

Equation 103 of Batterman and Cole[20] is used to calculate the reflectivity:

$$R = \left|\frac{E_H}{E_0}\right|^2 = |b| \left|\eta \pm \left(\eta^2 - 1\right)^{1/2}\right|^2 \frac{F_H}{F_{\bar{H}}}. \tag{3.9}$$

In equation 3.9, b is defined as $b = \frac{\gamma_0}{\gamma_H}$, where $\gamma_0 = \mathbf{n} \cdot \mathbf{s}_0$ and $\gamma_H = \mathbf{n} \cdot \mathbf{s}_H$, with $\mathbf{s}_0$ and $\mathbf{s}_H$ the unit vectors of the incident and diffracted beam directions, and $\mathbf{n}$ the normal to the diffraction planes, assumed to be parallel to the surface. In the case of Bragg reflection, since the angles of the incident and outgoing x-ray beam with the surface of the crystal are the same, $b = -1$, and $|b| = 1$. According

to equation 2.4 of the review paper by Woodruff,[21] the parameter η is given by:

$$\eta = \frac{-2\left(\Delta E/E\right)\sin^2\left(\theta_{Bragg}\right) + \Gamma F_0}{|P|\,\Gamma\left(F_H F_{\bar{H}}\right)^{\frac{1}{2}}}, \tag{3.10}$$

where:

- ΔE is the energy difference between the photon energy E ($h\nu$) and the Bragg energy E_{Bragg}.
- θ_{Bragg} is the angle formed by the incident (diffracted) x-ray beam and the scattering planes when Bragg's law is fulfilled.
- P is the polarization factor equal to 1 for the σ polarization state, where the electric field $\boldsymbol{E}$ is perpendicular to the plane defined by the wave vectors $\boldsymbol{K}_0$ and $\boldsymbol{K}_H$.
- The parameter Γ relates the dielectric constant with the electron density inside the crystal and is defined as:[20]

  $$\Gamma = \left(\frac{e^2}{4\pi\varepsilon_0 mc^2}\right)\frac{\lambda_{Bragg}^2}{\pi V}, \tag{3.11}$$

  where $r_e = \frac{e^2}{4\pi\varepsilon_0 mc^2}$ is the classical electron radius equal to $2.818\ 10^{-18}$cm and V is the volume of the crystal unit cell.
- F_0, F_H and $F_{\bar{H}}$ are the structure factors for the $0 = (0,0,0)$, $H = (h,k,l)$ and $\bar{H} = (-h,-k,-l)$ reflection. The 0, H and $\bar{H}$ reflections represent the forward scattering of the incident beam, the Bragg reflection outside the crystal and the Bragg back-reflection inside the crystal respectively, as illustrated in Figure 3.5. These are the three phenomena simultaneously present inside a nearly perfect crystal, for which the dynamical diffraction theory must be employed. A detailed description of their calculation is reported in section 3.3.3. Note that $F_H = F_{\bar{H}}$, if the crystal is centrosymmetric (e.g., fcc crystals) and if the origin of the Bravais lattice is located at the symmetry center (section 3.3.3).

To understand the relation between the shape of the reflectivity curve R (Figure 3.6) and equation 3.9, we analyze three different cases depending on the value of parameter η, which is real (η') in case of non-absorbing crystal. Subsequently, the case of absorption in the crystal is treated. We point out here the presence of two solutions for the reflectivity as expressed in equation 3.9, the positive and the negative branch. Below we will see how to solve this apparent dilemma.

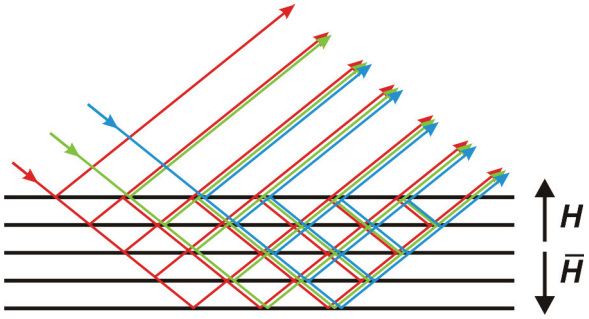


Figure 3.5: Schematic representation of the forward scattering of the Bragg reflection $H = (h, k, l)$ outside the crystal and of the Bragg reflection $\bar{H} = (-h, -k, -l)$ inside the crystal.

- If ΔE is large and negative, η is large and positive. The positive branch of equation 3.9 would give $R \gg 1$; therefore the correct solution is the one with the negative sign that gives $R \to 0$, hence no reflected beam.

- As ΔE goes through zero and becomes positive, η decreases to $+1$, i.e., $2\,(\Delta E/E)\,\sin^2\,(\theta_{Bragg}) = \Gamma F_0 - |P|\,\Gamma\,(F_H F_{\bar{H}})^{\frac{1}{2}}$, and $R = 1$. This point is the beginning of the total reflection. For all the values of η between $+1$ and -1, equation 3.9 is equal to 1, as shown in Figure 3.6. At $\eta = -1$, $2\,(\Delta E/E)\,\sin^2\,(\theta_{Bragg}) = \Gamma F_0 + |P|\,\Gamma\,(F_H F_{\bar{H}})^{\frac{1}{2}}$, and R is still unity. Note that the center of the reflectivity curve occurs at $\eta = 0$, i.e., $2\,(\Delta E/E)\,\sin^2\,(\theta_{Bragg}) = \Gamma F_0$. The displacement with respect to the beginning of total reflection is due to an index of refraction effect.[20]

- Finally, as ΔE increases, η becomes increasingly larger and negative. In this case, the negative branch of equation 3.9 would again give $R \gg 1$; thus the physically meaningful solution is the one with the positive sign that yields $R \to 0$, hence no reflected beam.

In case of absorption in the crystal, the structure factors F_0, F_H and $F_{\bar{H}}$ become complex and the reflectivity curve changes as follows: the reflectivity is generally lower compared to the non-absorbing crystal, and the reduction of the reflected intensity is enhanced at the high energy side, as shown in Figure 3.6b. The asymmetry of the reflectivity curve comes from a stronger absorption in the crystal due to the spatial shift of the XSW towards the atomic planes as the incident photon energy is scanned through the Bragg condition (see Figure 2.3).

Having discussed in detail how the theoretical reflectivity is calculated and its physical properties, we turn now to the calculation of ϕ_{theo}. To calculate the phase, we employ the formula 2.10-2.12 from the review paper by Zegenhagen,[22] namely:

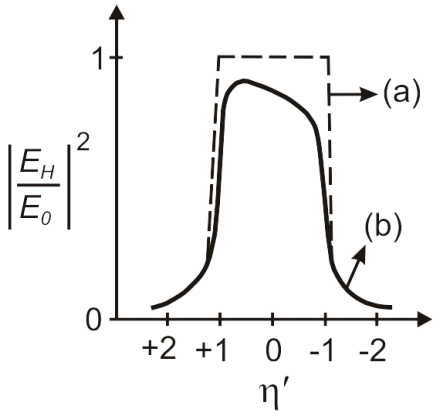


Figure 3.6: Figure 30 from Batterman and Cole:[20] reflectivity as a function of η', i.e., the real part of η. (a): curve for zero absorption. (b): curve in presence of absorption in the crystal.

$$\phi = \begin{cases} \varphi & \text{for } \mathrm{Re}\,(E_H/E_0) > 0 \\ \varphi + \pi & \text{for } \mathrm{Re}\,(E_H/E_0) < 0 \end{cases}, \tag{3.12}$$

where

$$\varphi = \arctan\left[\frac{\mathrm{Im}\,(E_H/E_0)}{\mathrm{Re}\,(E_H/E_0)}\right]. \tag{3.13}$$

In order to calculate the phase of the sample crystal, it is necessary to calculate the ratio of the electric field amplitudes of the electromagnetic waves $\frac{E_H}{E_0}$, and the sign of its real part. From equation 103 of Batterman and Cole[20] it follows that:

$$\frac{E_H}{E_0} = \sqrt{|b|}\left(\eta \pm \left(\eta^2 - 1\right)^{1/2}\right)\sqrt{\frac{F_H}{F_{\bar{H}}}}. \tag{3.14}$$

Assuming the crystal to be centrosymmetric ($\sqrt{\frac{F_H}{F_{\bar{H}}}} = 1$, read above), we can then focus on the first two factors on the right side of equation 3.14. Since $\sqrt{|b|} = \sqrt{1} = \pm 1$ and $\left(\eta \pm (\eta^2 - 1)^{1/2}\right)$ also has two branches (one for + and one for −), mathematically, $\frac{E_H}{E_0}$ has four possible solutions. However, it can be shown that the only physical solutions are those corresponding to $\sqrt{|b|} = -1$. In fact, $\sqrt{|b|} = +1$ provides a discontinuous ϕ function with singularities, which is hence unphysical.

In summary, both the reflectivity and the phase have two possible solutions. In order to determine which is the actual reflectivity and phase, we employ the fact that the reflectivity by definition must have a value between 0 and 1. In particular, for each photon energy $E = h\nu$, the reflectivity and phase will correspond to the positive [negative] solution, if the positive [negative] solution of the reflectivity has

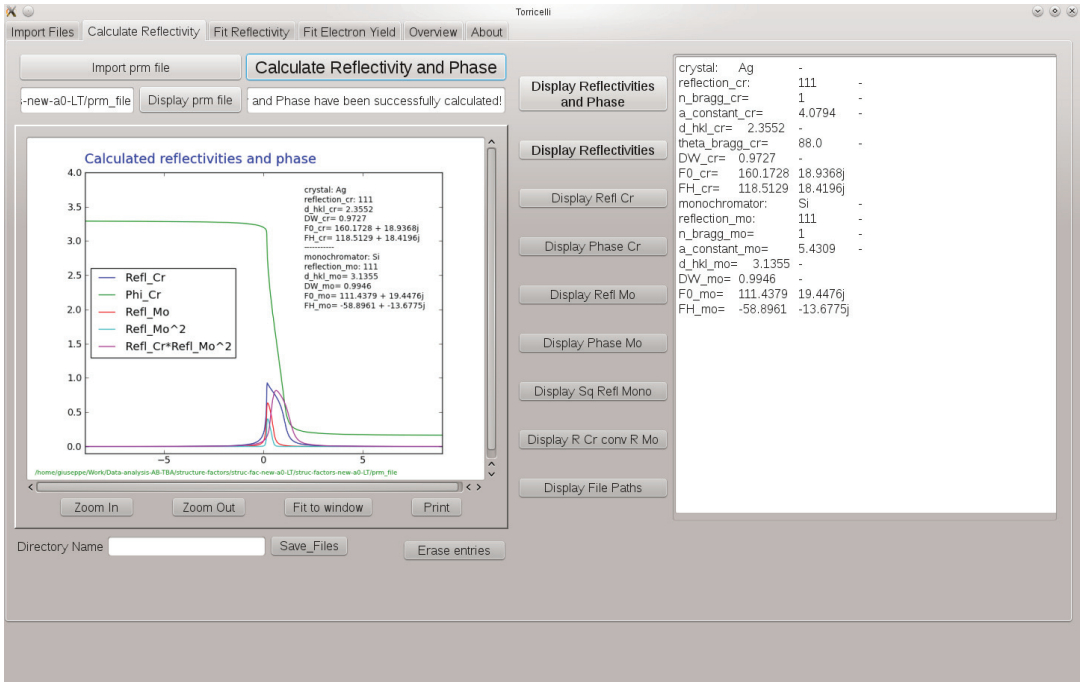


Figure 3.7: "Calculate Reflectivity" section of Torricelli. Technical details are reported in section A.4.

a value between 0 and 1 (see section A.4.2, lines 245-265).

We have seen how Torricelli calculates the reflectivity and phase of the sample and monochromator crystal. Figure 3.7 shows an example of the program page with the quantities calculated in the "Calculate Reflectivity" section, i.e., R_{theo}, ϕ_{theo}, R_m, R_m^2 and $R_{theo} \otimes R_m^2$. A summary of the latter quantities calculated for Ag(110), Ag(111) and Cu(100), i.e., the crystals employed for our NIXSW experiments, is shown in Figure 3.8. These reflectivities are those used to fit the corresponding experimental reflectivity and electron yield according to equations 3.4 and 3.42. The respective structure factors are reported in Table 3.1.

3.3.3 Calculation of the structure factors

In section 3.3.2 we explained that to calculate the crystal reflectivity and phase, knowledge of the structure factors F_H is essential. If we assume that atoms behave as rigid spheres with respect to their charge densities, F_H can be written as:[20]

$$F_H = \sum_n f_n \exp\left(-M_n\right) \exp\left(+2\pi \mathrm{i} \boldsymbol{H} \cdot \boldsymbol{r}_n\right) \tag{3.15}$$

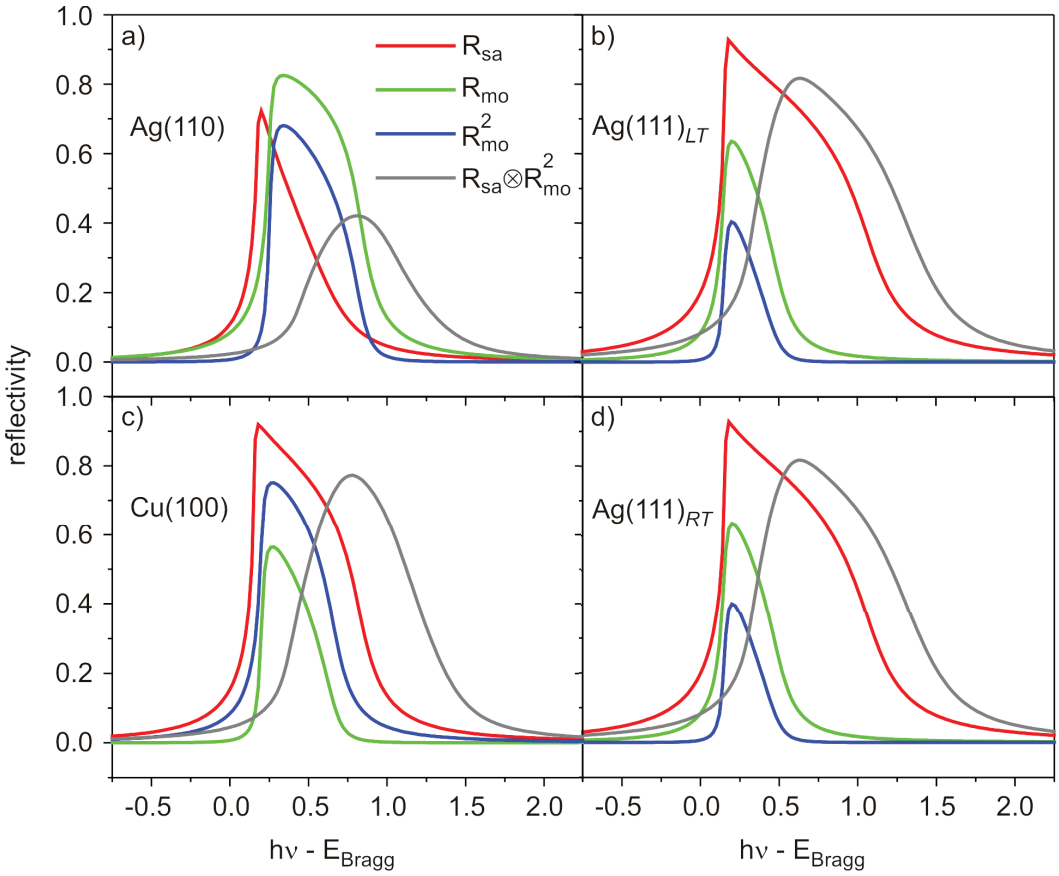


Figure 3.8: R_{theo}, R_m, R_m^2 and $R_{theo} \times R_m^2$ calculated for Ag(110) (a), Ag(111) (at 210 K $\rightarrow$ *LT*) (b), Ag(111) (at 300 K $\rightarrow$ *RT*) (d) and Cu(100) (c). Note that $Ag(111)_{LT}$ and $Ag(111)_{RT}$ reflectivities are practically identical, since the difference between the corresponding structure factors is negligible (see Table 3.1).

where f_n is the atomic scattering factor (see below), $\exp(-M_n)$ is the Debye-Waller factor (see below) and $\boldsymbol{r}_n$ is the position of the n^{th} atom in the unit cell. The reciprocal vector $\boldsymbol{H}$ can be written as:

$$\boldsymbol{H} = h\mathbf{b}_1 + k\mathbf{b}_2 + l\mathbf{b}_3, \tag{3.16}$$

where $\mathbf{b}_1$, $\mathbf{b}_2$, $\mathbf{b}_3$ are the reciprocal lattice vectors defining the unit cell in the reciprocal space, and h, k, l are the Miller indices associated with the reciprocal lattice point $2\pi\boldsymbol{H}$. In the case of crystals formed by one single element, equation 3.15 becomes:

$$F_H = f \exp(-M) \sum_n \exp(+2\pi \mathrm{i} \boldsymbol{H} \cdot \boldsymbol{r}_n) = f \exp(-M)\, S \tag{3.17}$$

In the section below, we will see the three factors in equation 3.17, i.e., f, $\exp(-M)$ and S, are calculated.

Atomic scattering factors *f*

The interaction of an x-ray with an atom (e.g., photoabsorption and scattering) can be accurately described by the complex atomic scattering factor. The atomic scattering factor f is defined as the factor that must multiply the amplitude scattered by a single free electron to yield the total amplitude coherently scattered by the particular atom, and it can be expressed as:

$$f = f_1 + f_2 \tag{3.18}$$
$$= f_0 + \Delta f' + \mathrm{i}\Delta f'' \tag{3.19}$$
$$= f_0(\theta) - Z + f_1(0) + \mathrm{i}f_2(0) \tag{3.20}$$

In equation 3.19 f_0, $\Delta f'$ and $\Delta f''$ are defined as follows:

- f_0 is the atomic form factor, tabulated in reference[40] as a function of the atomic number Z and $\frac{\sin(\theta)}{\lambda} = \frac{1}{2d_{hkl}}$. It can be shown that f approaches Z for small values of $\frac{\sin(\theta)}{\lambda}$.[41]

- $\Delta f'$ and $\Delta f''$ are the real and imaginary part of the dispersion correction, i.e., the correction of the atomic scattering factor for x-ray energies close to the absorption threshold. In particular, $\Delta f''$ represents a small shift in phase of the scattered radiation. Since the dependence of $\Delta f'$ and $\Delta f''$ on the angle θ is much smaller than that of f_0, the two correction terms are considered here to be angle independent.[41,42]

In equation 3.20, the angular dependence of the single terms is explicit. This is also the expression used in Torricelli. In particular, $f_1(0)$ and $f_2(0)$ are the angle-independent atomic scattering-factor components, tabulated as function of the photon energy in reference[42] (Figure A.4, display panel 2). Note that $f_0(\theta)$, $f_1(0)$ and $f_2(0)$ values are interpolated by the program to find the ones corresponding to a specific Bragg energy (see section A.5.2, lines 113-123, 97-108 and 203-212, 186-197, for the sample and the monochromator crystals, respectively).

Equation 3.20 is the general expression of the atomic scattering factor for all photon energies of interest and for all scattering angles. If the x-ray energy is far from

any absorption edge in the atom, $f_2(0) = 0$ and $f_1(0) \to Z$, hence equation 3.20 becomes:

$$f = f_0(\theta). \tag{3.21}$$

Moreover, for small values of $\frac{\sin(\theta)}{\lambda}$, $f_0(\theta)$ approaches Z, hence equation 3.20 becomes:

$$f = f_1(0) + \mathrm{i} f_2(0) \tag{3.22}$$

close to an absorption edge, and it further simplifies to

$$f = Z \tag{3.23}$$

far from an absorption edge.

As mentioned in section 3.3.2, the structure factors must be calculated for forward scattering $0 = (0,0,0)$, $H = (h,k,l)$ and $\bar{H} = (-h,-k,-l)$ reflection (Figure 3.5). Therefore, the respective atomic scattering factors must be also calculated. In particular, $\theta = 0$ for forward scattering, hence $\frac{\sin(\theta)}{\lambda} = 0$ and

$$f_{000} = f_1(0) + \mathrm{i} f_2(0). \tag{3.24}$$

In case of reflection H or $\bar{H}$, the atomic scattering factor is:

$$f_{hkl} = f_{-h-k-l} = f_0(\theta) - Z + f_1(0) + \mathrm{i} f_2(0). \tag{3.25}$$

The real and imaginary parts of f_{hkl} are calculated as reported in section A.5.2 (lines 125-126 and 214-215). These latter calculations also include the Debye-Waller factor, which will be discussed below.

Debye-Waller factor

Torricelli provides two different approaches for calculating the Debye-Waller factor $\exp(-M)$. The first assumption, valid for both methods, is that lattice vibrations are harmonic (or quasi-harmonic). The other approximations and the formula employed are reported below.

- ***M* according to Warren.**[41] According to formula 11.77 of Warren[41], M is given by:

$$M = \frac{6h^2 T}{mk\Theta_M^2}\left[\Phi(x) + \frac{x}{4}\right]\left(\frac{\sin\theta_{\mathrm{Bragg}}}{\lambda_{\mathrm{Bragg}}}\right)^2 \tag{3.26}$$

where h is the Planck's constant; m is the atomic mass of the crystal atom expressed in $g \cdot mol^{-1}$; k is the Boltzmann's constant; and T is the crystal temperature. Θ_M is an average characteristic temperature defined as:

$$\frac{3}{\Theta_M^2} = \frac{1}{\Theta_l^2} + \frac{2}{\Theta_t^2} \tag{3.27}$$

according to equation 11.76 of Warren,[41] where Θ_l and Θ_t are characteristic temperatures for the longitudinal and transverse waves. A significant approximation is to use the tabulated Debye temperature Θ_D as Θ_M, although they are differently defined and their difference may be not only negligible. The function of x in equation 3.26 can be expanded as:

$$\Phi(x) + \frac{x}{4} = 1 + \frac{x^2}{36} - \frac{x^4}{3600} + ... \tag{3.28}$$

according to equation 11.75 from Warren,[41] where $x = \frac{\Theta_M}{T}$. Finally, $\frac{\sin\theta_{\text{Bragg}}}{\lambda_{\text{Bragg}}} = \frac{1}{2d_{hkl}}$ defines Bragg's law for the selected hkl-reflection.

The code calculation of the Debye-Waller factor according to Warren[41] is reported in section A.5.2 (lines 84-91 and 173-180).

- ***M* according to Sears and Shelley.**[43] A second model for calculating the Debye-Waller factor, proposed by Sears and Shelley,[43] is based on the phonon density-of-states curves obtained from neutron inelastic scattering measurements. The advantage of this model is that it allows the Debye-Waller factor to be determined with a high level of accuracy at any temperature. The parameter M is defined as follows:

$$M = \frac{39.904}{m\nu_m} J(y) \left(\frac{\sin\theta_{\text{Bragg}}}{\lambda_{\text{Bragg}}}\right)^2 \tag{3.29}$$

where m is the atomic mass in $g \cdot mol^{-1}$; ν_m is the maximum phonon frequency in THz (values are tabulated in reference[43]); $J(y)$ is a function of $y = \frac{T}{T_m}$ (T_m is the Debye temperature also tabulated in reference[43]), and is expressed as:

$$J(y) = \begin{cases} f_{-1} + \left(\frac{\pi^2}{3}\alpha y^2\right) & y < 0.2 \\ 2f_{-2}y + \frac{1}{6y} - \frac{f_2}{360y^3} & y \geq 0.2 \end{cases} \tag{3.30}$$

where f_{-1}, f_{-2} and α are tabulated parameters.[43] Note that for $H = (0,0,0)$, $M = 0$ and $\exp(-M) = 1$. For more details about the model on which the

formulas above are based, we refer to Sears and Shelley[43]. The corresponding code is reported in section A.5.2 (lines 279-307).

The geometrical factor *S*

The last term of equation 3.17 to be discussed is the geometrical factor S, defined as:

$$S = \sum_n \exp\left(2\pi \mathrm{i} \boldsymbol{H} \cdot \boldsymbol{r}_n\right). \tag{3.31}$$

In the following, we will now show how to express S in a simpler and more useful form. We express the cell vectors $\boldsymbol{r}_n$ that define the atomic positions in terms of their components along the unit cell vectors $\mathbf{a}_1$, $\mathbf{a}_2$, $\mathbf{a}_3$ (Figure 3.9a) by means of the coordinates x_n, y_n and z_n, as follows:

$$\boldsymbol{r}_n = x_n\mathbf{a}_1 + y_n\mathbf{a}_2 + z_n\mathbf{a}_3. \tag{3.32}$$

If we substitute equations 3.16 and 3.32 in equation 3.31, we obtain:

$$\begin{aligned} S &= \sum_n \exp\left[2\pi \mathrm{i}\left(h\mathbf{b}_1 + k\mathbf{b}_2 + l\mathbf{b}_3\right) \cdot \left(x_n\mathbf{a}_1 + y_n\mathbf{a}_2 + z_n\mathbf{a}_3\right)\right] \\ &= \sum_n \exp\left[2\pi \mathrm{i}\left(hx_n + ky_n + lz_n\right)\right]. \end{aligned} \tag{3.33}$$

The simplified expression of equation 3.33 reveals the strict dependence of the structure factors on the position of atoms inside the unit cell and on the specific hkl-reflection.

In order to calculate the reflectivity and phase of a crystal, three structure factors F_0, F_H and $F_{\bar{H}}$ need to be calculated (section 3.3.2). As a consequence, three different reciprocal space vectors need to be considered: $H = (0, 0, 0)$, $H = (h, k, l)$ and $H = (-h, -k, -l)$. For this purpose, Torricelli calculates the structure factors for any hkl-reflection (section A.5). In contrast, regarding the positions of the unit cell atoms, it is limited to the two classes of crystals with fcc and diamond structures. In fact, this does not actually constitute a limitation because it covers the great majority of the sample substrate crystals (e.g., Ag, Cu, Au) and of the monochromator crystals (e.g., Si, Ge). Moreover, we are planning to extend this functionality of the program to the calculation of structure factors for any crystals.

For centrosymmetric crystals (e.g., fcc and diamond structures) $F_H = F_{\bar{H}}$ if the

origin of the Bravais lattice is located at the symmetry center. To take advantage of this simplification, the origin of the lattice space has to be properly chosen. Figure 3.9 shows the unit cell and the corresponding atomic positions $\boldsymbol{r}_n$ that satisfy the latter requirement for both an fcc (panel a) and a diamond structure (panel b), so that $F_H = F_{\bar{H}}$. In particular, for an fcc crystal with one atom per unit cell and $\boldsymbol{r}_n$ as in Figure 3.9a, for forward scattering $[H = (0,0,0) = 0]$ we have:

$$S_{000} = \sum_{n=1}^{4} \exp\left[2\pi \mathrm{i}\,(0 \cdot x_n + 0 \cdot y_n + 0 \cdot z_n)\right] = 4, \tag{3.34}$$

while for hkl-reflection and analogously for $(h{-}k{-}l)$-reflection, we have:

$$S_{hkl} = S_{-h-k-l} = \sum_{n=1}^{4} \exp\left[2\pi \mathrm{i}\,(h \cdot x_n + k \cdot y_n + l \cdot z_n)\right]. \tag{3.35}$$

On the other hand, for a diamond structure with two atoms per unit cell and $\boldsymbol{r}_n$ as in Figure 3.9b, and specifically for the (111) reflection, as in the case of the Si(111) double crystal monochromator used for our experiments, in the case of forward scattering we have:

$$S_{000} = \sum_{n=1}^{8} \exp\left[2\pi \mathrm{i}\,(0 \cdot x_n + 0 \cdot y_n + 0 \cdot z_n)\right] = 8, \tag{3.36}$$

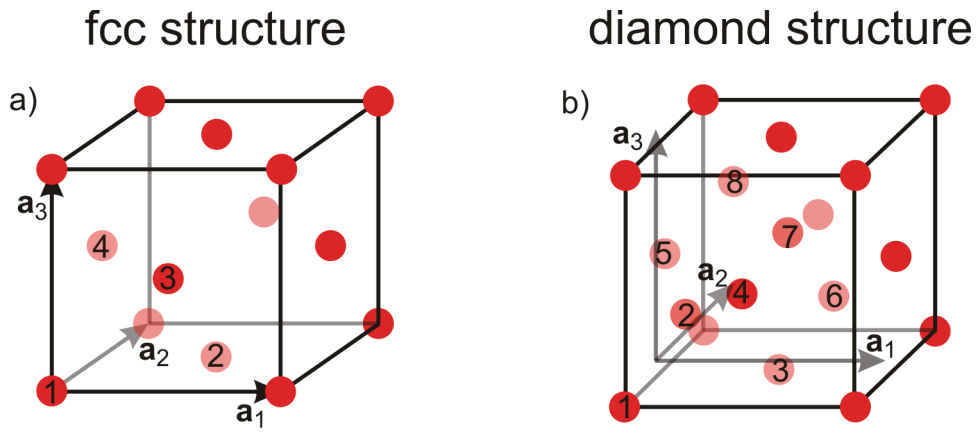


Figure 3.9: fcc (a) and diamond (b) crystal structures with corresponding lattice unit vectors $\mathbf{a}_1$, $\mathbf{a}_2$ and $\mathbf{a}_3$. The vectors $\boldsymbol{r}_n$ defining the atomic positions in terms of their components x_n, y_n and z_n along the unit cell vectors are reported below. (a): $\boldsymbol{r}_1 = (0,0,0)$, $\boldsymbol{r}_2 = (1/2,1/2,0)$, $\boldsymbol{r}_3 = (1/2,0,1/2)$, $\boldsymbol{r}_4 = (0,1/2,1/2)$. (b): $\boldsymbol{r}_1 = (-1/8,-1/8,-1/8)$, $\boldsymbol{r}_2 = (1/8,1/8,1/8)$, $\boldsymbol{r}_3 = (3/8,3/8,-1/8)$, $\boldsymbol{r}_4 = (3/8,-1/8,3/8)$, $\boldsymbol{r}_5 = (-1/8,3/8,3/8)$, $\boldsymbol{r}_6 = (5/8,5/8,1/8)$, $\boldsymbol{r}_7 = (5/8,1/8,5/8)$, $\boldsymbol{r}_8 = (1/8,5/8,5/8)$.

while for 111-reflection and analogously for $(-1-1-1)$-reflection, we have:

$$S_{111} = S_{-1-1-1} = \sum_{n=1}^{8} \exp\left[2\pi \mathrm{i}\left(h \cdot x_n + k \cdot y_n + l \cdot z_n\right)\right] = 8\cos\left(\frac{3}{4}\pi\right). \tag{3.37}$$

Final expressions of F_H

To conclude, in the section below, we summarize in the following the expressions of the structure factors practically used to calculate the reflectivity and phase of the sample and monochromator crystal.

Under the assumptions that the crystal consists of only one element, it is centrosymmetric with the origin of the Bravais lattice at the symmetry center and lattice vibrations can be considered harmonic, the structure factors of the sample crystal are:

$$F_0 = 4f_1\left(0\right) + \mathrm{i}4f_2\left(0\right) \tag{3.38}$$

for forward scattering (see section A.5.2, lines 109-111), and

$$\begin{aligned} F_H = F_{\bar{H}} &= \left[f_0\left(\theta\right) - Z + f_1\left(0\right)\right]\exp\left(-M\right)\sum_{n=1}^{4}\exp\left[2\pi\mathrm{i}\left(h \cdot x_n + k \cdot y_n + l \cdot z_n\right)\right] \\ &+ \mathrm{i}f_2\left(0\right)\exp\left(-M\right)\sum_{n=1}^{4}\exp\left[2\pi\mathrm{i}\left(h \cdot x_n + k \cdot y_n + l \cdot z_n\right)\right] \end{aligned} \tag{3.39}$$

for hkl-reflection (see section A.5.2, lines 152-155).

The structure factors of the monochromator crystal are:

$$F_0 = 8f_1\left(0\right) + \mathrm{i}8f_2\left(0\right) \tag{3.40}$$

for forward scattering (see section A.5.2, lines 198-200), and

$$\begin{aligned} F_H = F_{\bar{H}} &= \left[f_1\left(0\right) - \left(Z - f_0\right)\right] \cdot \exp\left(-M\right) \cdot 8\cos\left(\frac{3}{4}\pi\right) \\ &+ \mathrm{i}f_2\left(0\right) \cdot \exp\left(-M\right) \cdot 8\cos\left(\frac{3}{4}\pi\right) \end{aligned} \tag{3.41}$$

for hkl-reflection (see section A.5.2, lines 216-222).

structure factors					
	hkl	d_{hkl}	$\exp(-M)$	F_0	F_H
Ag(110)	220	1.4444	0.9295	$173.6963 + i47.221$	$98.5871 + i43.891$
Si(111)	111	3.1355	0.9946	$115.2807 + i8.3872$	$-61.5988 + i5.8987$
Ag(111)_{LT}	111	2.3552	0.9727	$160.1728 + i18.9368$	$118.5129 + i18.4196$
Si(111)	111	3.1355	0.9946	$111.4379 + i19.4476$	$-58.8961 - i13.6775$
Ag(111)_{RT}	111	2.3593	0.973	$160.2389 + i18.9853$	$118.6963 + i18.472$
Si(111)	111	3.1355	0.9946	$111.3976 + i19.5021$	$-58.8678 - i13.7158$
Cu(100)	200	1.8075	0.9507	$115.6085 + i10.7221$	$78.3926 + i10.1937$
Si(111)	111	3.1355	0.9946	$114.765 + i12.4686$	$-61.2361 - i8.7691$

Table 3.1: Summary of the hkl-reflection, of the Bragg plane spacing d_{hkl}, of the Debye-Waller factor $\exp(-M)$, and of the structure factors F_0 and F_H relative to the sample and monochromator crystals employed in the NIXSW experiments reported in chapters 4, 5, 6, and 7. Ag(111)_{LT} and Ag(111)_{RT} refer to the low temperature (210 K) and room temperature NIXSW experiments of AB/Ag(111) and TBA/Ag(111), respectively. Note that since $S = 0$ for (110) reflection of Ag and for (100) reflection of Cu, the respective higher order reflections (220) and (200) are considered.[41]

All the structure factors and Debye-Waller factors employed to calculate the ideal reflectivities of Ag(110), Ag(111) (at 210 K $\rightarrow$ LT), Ag(111) (at 300 K $\rightarrow$ RT), Cu(100) corresponding to experimental data in chapters 4–7 are reported in Table 3.1. In conclusion Figure 3.10 shows the section of Torricelli in which structure factors are calculated. Technical details about its operation and the corresponding code are reported in section A.5.

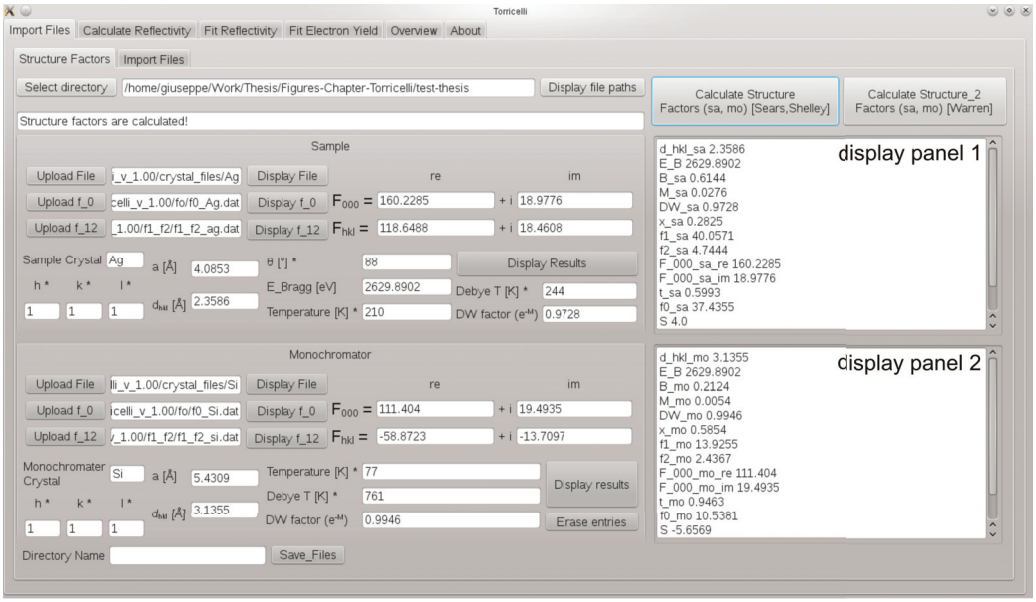


Figure 3.10: "Structure Factors" section of Torricelli. Corresponding code and technical details are reported in section A.5.

3.4 Fitting the electron yield profile

3.4.1 Fitting the coherent position and fraction

The strong correlation between the spatial distribution of a certain atomic species (P_c, F_c) (section 2.5) and the intensity of the XSW (I_{XSW}), equation 2.17, on the one hand, and the proportionality of the electron yield profile to I_{XSW} (section 2.3, equation 2.10), on the other hand, allow the experimental determination of P_c and F_c. The equation employed to fit the experimental electron yield Y_{exp} is:

$$\begin{aligned} Y_{exp} &= \underline{M} \times \left[1 + S_R R_{theo} + 2\underline{F_c}\sqrt{R_{theo}}\,|S_I| \cos\left(\phi_{theo} - 2\pi\underline{P_c} + \Psi\right)\right] \\ &\quad \otimes G(\sigma) \otimes R_m^2\big|_{(E+\Delta E)}, \end{aligned} \tag{3.42}$$

where S_R, $|S_I|$ and Ψ are the so-called nondipolar correction parameters. Their calculation is described in section 3.4.2. It was shown in several studies[18,19,44–47] that the dipole approximation of the electron, interacting with the incident and diffracted x-ray beams, may be too crude and thereby provide significantly altered structural parameters (P_c, F_c). To this end, Vartanyants and Zegenhagen[44] developed the expression of the photoelectron yield generated by initial s-electrons within the quadrupole approximation. The result is in the square brackets of equation 3.42 and will be referred below as the ideal electron yield (see equation 3.1). For $S_R = |S_I| = 1$ and $\Psi = 0$ the expression in the square brackets is valid also for electron yield resulting from Auger electrons, for which the nondipolar effect does not exist (see section 3.4.2), as well as for a fluorescence absorption profile, provided that $I_a \propto I_{XSW}$ (section 2.3).

The "non-idealities" associated with the experimental set-up, as discussed in section 3.3.1, are taken into account by means of the convolution of the ideal electron yield (equation 3.1) with the function $F_{ni} = G(\sigma) \otimes R_m^2\big|_{(E+\Delta E)}$ (equation 3.8). The functional F_{ni} results from the fit of the experimental reflectivity, as reported in section 3.3.1, and is defined so that both $G(\sigma)$ and R_m^2 have area normalized to 1. In this way, only the electron yield profile, but not its area, is modified by the convolution with F_{ni}. Note that the function F_{ni} also contains the energy shift ΔE, resulting from the fit of the experimental reflectivity, and is necessary to align the theoretical energy scale of the ideal electron yield and the experimental energy scale of Y_{exp}.

If we again focus on equation 3.42, we note that S_R, $|S_I|$ and Ψ can be calculated (section 3.4.2); R_{theo}, ϕ_{theo} and R_m can also be calculated, as shown in section 3.3.2; $G(\sigma)\big|_{(E+\Delta E)}$ results from the fit of R_{exp} (section 3.3.1). Therefore, the only three unknown variables are the normalization factor M, the coherent position P_c and the coherent fraction F_c. The latter three parameters are found as a result of the fit of Y_{exp} with the fitting function on the right side of equation 3.42.

Furthermore, Torricelli provides not only the best fit value but also the corresponding standard deviation of each fitting parameter. The uncertainty associated with P_c and F_c defines the degree of accuracy with which they are determined, and more importantly, is directly correlated with the uncertainty of the experimental electron yield, as explained in more detail in section 3.5.

Figure 3.11 shows the section of the Torricelli where the electron yield is fitted. Technical details and the corresponding code are reported in sections A.6.1 and A.6.2, respectively.

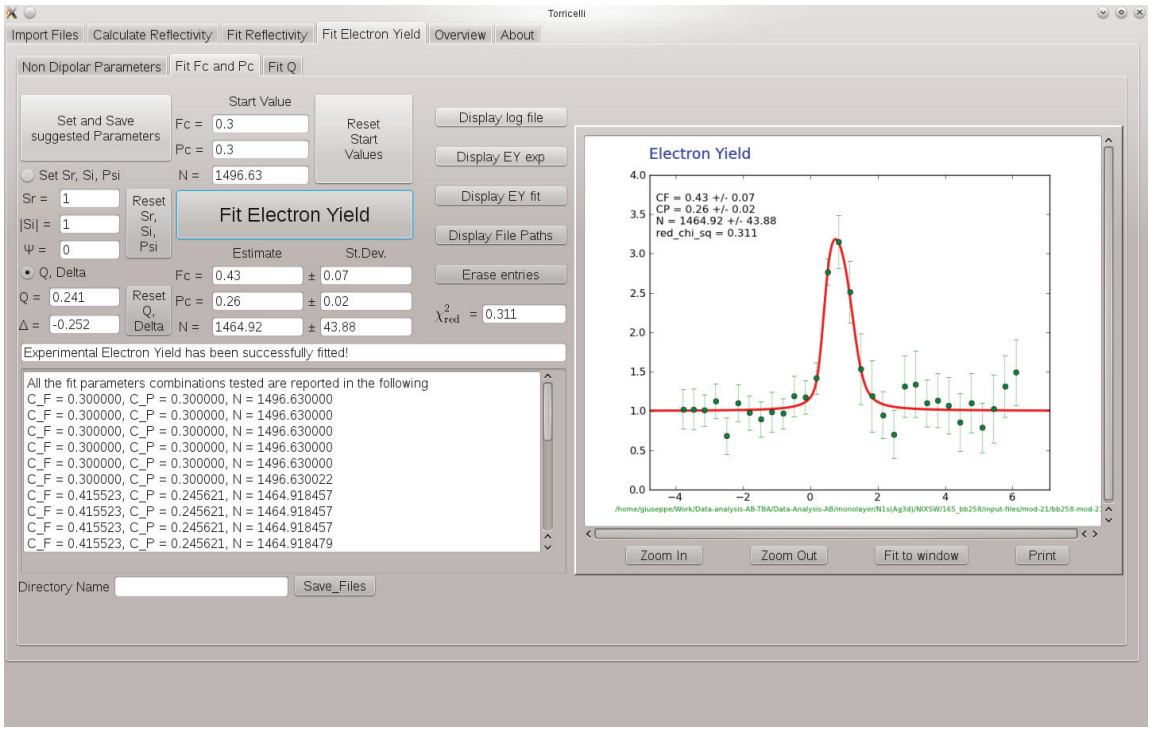


Figure 3.11: "Fit Fc and Pc" section of Torricelli. Operation and technical details are reported in section A.6.

3.4.2 Calculation of the nondipolar correction parameters

In section 2.3 we state that the absorption profile and in particular the photoelectron yield profile is proportional to the intensity of the XSW within the dipole approximation. In the section below, the validity of this approximation is discussed and the corresponding correction terms are introduced.

In the non-relativistic limit, the absorption intensity of a photon plane wave $\mathbf{E} = \mathbf{e}E_0 \exp(\mathrm{i}\boldsymbol{K}\boldsymbol{r} - i\omega t)$ by an atom with concomitant ejection of a bound electron into a continuum state is proportional to the square modulus of the matrix element:[47]

$$M_{fi} =< f \left|\exp(\mathrm{i}\boldsymbol{K}\boldsymbol{r})(\mathbf{e}\hat{p})\right| i >, \tag{3.43}$$

where $\boldsymbol{K}$ is the wave vector of the incident photon (with magnitude $|\boldsymbol{K}| = 2\pi/\lambda$), and $\hat{p} = -\mathrm{i}\hbar\nabla$ is the momentum operator. In the long wavelength limit $\lambda \gg a$ (where a is the average size of the electron bound state) the exponential can be expanded in a Taylor series as:

$$\exp(\mathrm{i}\boldsymbol{K}\boldsymbol{r}) = 1 + \mathrm{i}\boldsymbol{K}\boldsymbol{r} - \frac{1}{2}(\boldsymbol{K}\boldsymbol{r})^2 - ..., \tag{3.44}$$

which is equivalent to a multipole expansion. In particular, the first term represents the electric dipole and the second one the electric quadrupole and the magnetic dipole transitions. For the photoelectric effect, we take into account only the electric transitions. As will be clear in the following, in the specific case of photoabsorption excited by XSW and detected by angular resolved photoemission spectroscopy, both the dipole and the quadrupole terms must be taken into account and yield the matrix element:

$$M_{fi} = M_{fi}^{D} + M_{fi}^{Q}(\mathbf{s}), \tag{3.45}$$

where $\mathbf{s} = \boldsymbol{K}/|\boldsymbol{K}|$ is the unit propagation vector.

For soft x-rays, with photon energies of the order of 3 keV, the variation of the electromagnetic wave field of the incident wave over the spatial extent of the photoemission initial state wave function is small. Therefore, the dipole approximation should be valid for our NIXSW experiments and the nondipole effects should become important only for hard x-rays of $20 - 40$ keV.

This general rule fails in the case of angular resolved photoemission, when the pho-

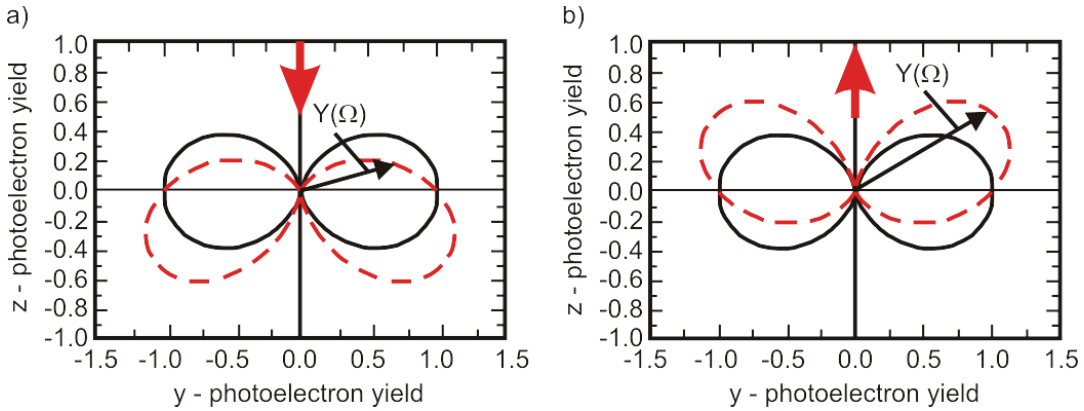


Figure 3.12: Figure 9a from reference:[44] the photoelectron angular distribution in the backscattering geometry. The angular distribution of photoelectrons excited only by the incoming beam (a) and only by the reflected beam (b) with the quadrupole contribution (red dashed line) and without the quadrupole contribution (black solid line), i.e., within the dipole approximation. Note that y and z axis are oriented as in Figure 3.13.

toemission signal is detected only in one particular direction, for the two following reasons:

- First, the matrix element of the photoemission process corresponding to the quadrupole term depends on the propagation vector of the electromagnetic wave, as shown in equation 3.45.
- Second, in an NIXSW experiment, there are simultaneously incident and reflected x-ray waves with opposite propagation directions (Figure 2.2a).

As a consequence, the photoemission cross sections for the absorption of the incident photon plane wave and of the reflected photon plane wave are different, as illustrated in Figure 3.12. In this case, the photoemission signal is not proportional to the total x-ray absorption, and hence not proportional to the intensity of the XSW at the absorbing atom.

In summary, for photon energies in the range of few keV as well, in the case of angular resolved photoemission, the nondipole effects can significantly modify the photoemission angular dependence and must be taken into account for accurate analysis of NIXSW data, as shown by many recent studies.[18,19,44–47] Note that nondipolar correction parameters are more relevant for light elements (e.g., C, N, O) and photoemitted electrons with large kinetic energy ($\gtrsim$1000 eV), while they become negligible for heavy elements (e.g., Cu, Ag, Au) and small kinetic energies, as the systematic study of Lee et al.[18] revealed.

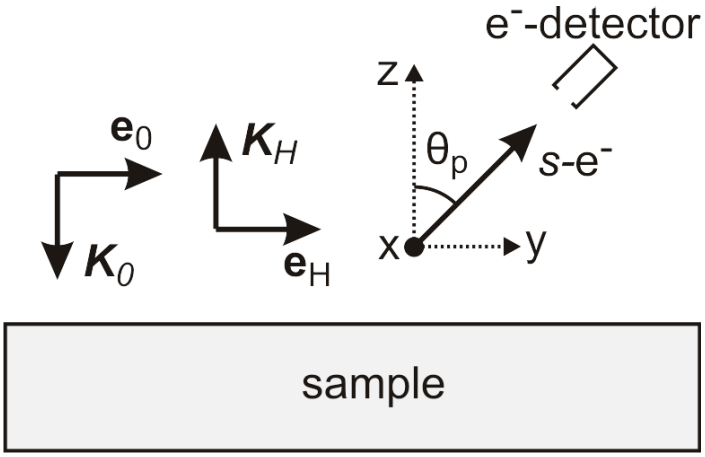


Figure 3.13: Scheme representing the four conditions under which the nondipolar correction parameters can be expressed as in equations 3.47, 3.48 and 3.49. Both the polarization vectors ($\mathbf{e}_H \parallel \mathbf{e}_0$) and the wave vectors ($\boldsymbol{K}_H = -\boldsymbol{K}_0$) are reported in the figure. The direction of the detected photoemitted s-electrons (s-e$^-$) together with the angle θ_p formed with the direction z perpendicular to the sample surface is also marked in the figure.

Vartanyants and Zegenhagen[44] derived the general form of the photoelectron yield function for an atom in an XSW field:

$$Y = 1 + S_R R + 2\,|S_I|\,\sqrt{R} F_c \cos\left(\phi - 2\pi P_c + \Psi\right) \tag{3.46}$$

where S_R and $S_I = |S_I| \exp(\mathrm{i}\Psi)$ are related to the square modulus of the matrix elements of the photoemission process.[47] S_R, $|S_I|$ and Ψ can be expressed in a simple and useful form if the conditions detailed in the following are satisfied:

- Condition 1: σ-polarization, the electric field $\mathbf{E}$ is perpendicular to the plane of incidence defined by the wave vectors $\boldsymbol{K}_0$ and $\boldsymbol{K}_H$ (see Figure 3.13).
- Condition 2: backscattering, i.e., $\boldsymbol{K}_0 = -\boldsymbol{K}_H$ (see Figure 3.13).
- Condition 3: the photoelectron detector is in the plane of the polarization vectors ($\mathbf{e}_0 \parallel \mathbf{e}_H$) and the wave vectors (Figure 3.13).
- Condition 4: s initial state.

If conditions 1-4 are fulfilled, S_R, $|S_i|$ and Ψ can be written as:

$$S_R = \frac{1+Q}{1-Q}, \tag{3.47}$$

$$|S_I| = \frac{\sqrt{1 + Q^2 \tan^2(\Delta)}}{1 - Q}, \tag{3.48}$$

$$\Psi = \arctan(Q \tan(\Delta)). \tag{3.49}$$

These equations are also the formulas employed in Torricelli (section A.7.2, lines 46-49 and 76-79) for the calculation of the nondipolar correction parameters. Q is defined as the forward/backward asymmetry parameter[45] and can be expressed as:

$$Q = \frac{\gamma}{3} \cos(\theta_p), \tag{3.50}$$

where γ is one of the angular distribution parameters, calculated in the framework of the quadrupole approximation and tabulated.[48,49] In the geometry according to conditions 2 and 3, θ_p is the angle between the direction of the photoemitted electrons and the wave vector $\boldsymbol{K}_H$. In all the experiments reported in chapters 4, 5, 6 and 7, $\theta_p = 45°$. Δ is defined as the difference between the partial phase shifts δ_p and δ_d for the p- and d- asymptotic wave:

$$\Delta = \delta_d - \delta_p. \tag{3.51}$$

The values of the scattering phase shifts δ_p and δ_d are available from ab initio calculations.[50] Note that although we have three nondipolar correction parameters in the generalized equation 3.46, from equations 3.47, 3.48 and 3.49 it follows that only two of them are independent. We can therefore refer either to (S_R, $|S_I|$, Ψ) or to (Q, Δ).

Having reported all the equations for the calculation of the nondipolar correction parameters, we now explain how this operation is actually carried out in Torricelli. First, the kinetic energy of the photoemitted electron is calculated (section A.7.2, lines 30-38), knowing the Bragg energy and the binding energy of the s core level. Subsequently, γ corresponding to the kinetic energy calculated above is interpolated (section A.7.2, lines 39-41) on the basis of the tabulated values from references.[48,49] The third step is to calculate Q from equation 3.50 and Δ from equation 3.51, knowing δ_p and δ_d from reference[50] (section A.7.2, lines 42-45). Finally, S_R, $|S_I|$ and Ψ are calculated from equations 3.47, 3.48 and 3.49 (section A.7.2, lines 46-49 and 76-79).

All NIXSW data reported in chapters 4, 5, 6, and 7 are analyzed using the nondipolar parameters calculated as explained above and summarized in Table 3.2. This

nondipolar parameters							
	PTCDA/Ag(110) K+PTCDA/Ag(110)			AB/Ag(111) TBA/Ag(111)		TPA/Cu(100)	
E_{Bragg} (eV)	4294.59			2629.89		3431.9	
line	C1s	O1s	K1s	C1s	N1s	C1s	O1s
E_b (eV)	288	538	3611	288	403	288	538
E_k (eV)	4006.59	3756.59	683.59	2341.89	2226.89	3143.9	2893.9
γ	1.421	1.351	0.281	1.061	1.022	1.249	1.174
δ_p	0.6928	0.8720	−0.0794	0.7993	0.9074	0.7397	0.9324
δ_d	0.5267	0.6445	−1.2006	0.5879	0.6553	0.5544	0.6764
Q	0.335	0.319	0.066	0.250	0.241	0.294	0.277
Δ	−0.166	−0.228	−1.121	−0.211	−0.252	−0.185	−0.256
S_R	2.007	1.935	1.142	1.667	1.635	1.834	1.765
$\lvert S_I \rvert$	1.506	1.471	1.081	1.336	1.320	1.419	1.386
Ψ	−0.056	−0.074	−0.137	−0.054	−0.062	−0.055	−0.072

Table 3.2: Summary of the binding energy E_b of the core-level lines measured by XPS during our NIXSW experiments, followed by the corresponding kinetic energy E_k depending on the Bragg energy E_{Bragg} of each experiment. For each core-level line, the corresponding angular distribution parameter γ and the phase shifts δ_p and δ_d for the p- and d- asymptotic wave are reported. Finally a list of the two sets of the respective nondipolar correction parameters (Q, Δ) and (S_R, $|S_I|$, Ψ) employed to analyzed NIXSW data is reported.

procedure is strengthened by the good agreement between the nondipolar correction parameters measured (section 3.4.3) by Gerlach et al.[19] using the same experimental

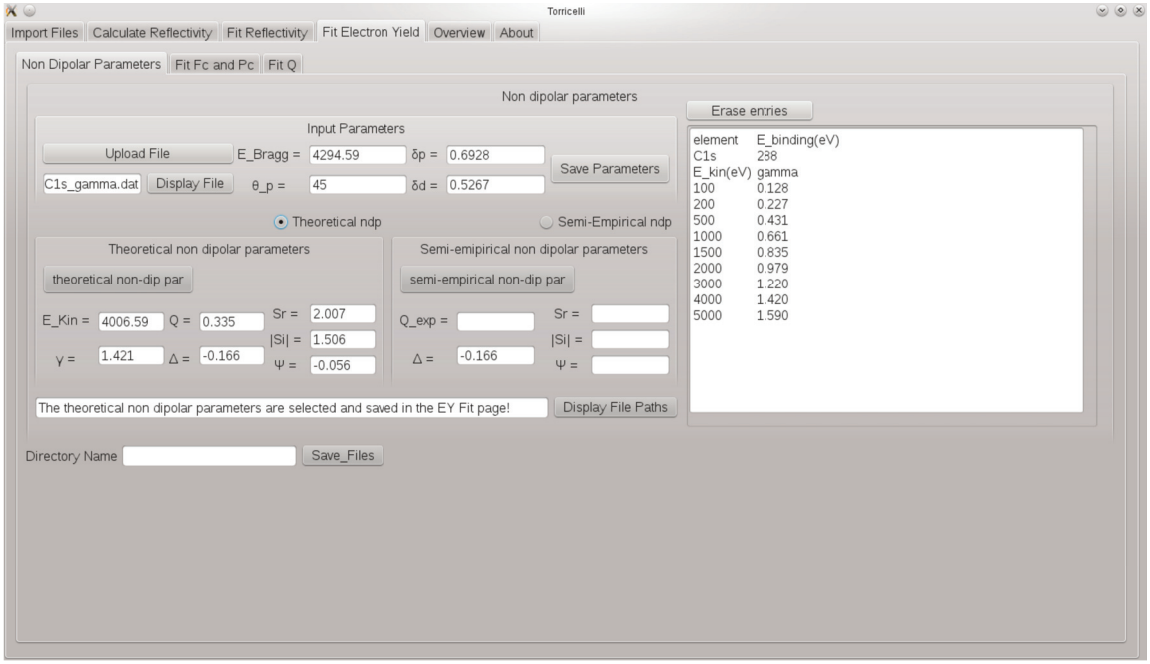


Figure 3.14: "Nondipolar Parameters" section of Torricelli. Operation and technical details are reported in section A.7.

set-up as in our experiments (section 2.6) and the theoretical predictions,[47] obtained following the same approach detailed above.

Figure 3.14 shows the section of Torricelli devoted to the calculation of the nondipolar parameters. Technical details are reported in section A.6.

3.4.3 Fitting the asymmetry parameter Q

While the sensitivity of the NIXSW experiment monitored by angular resolved photoemission to the nondipolar effects requires the knowledge of the corresponding parameters for an accurate structural analysis, at the same time, it offers a means to measure these parameters. In particular, there are two methods for determining the asymmetry parameter Q, and hence γ, by means of NIXSW.

The first approach consists of two NIXSW experiments performed on the same well-defined structure. One is monitored by Auger electrons that are insensitive to the nondipolar effects, as they have no memory of the photon propagation direction. The other is monitored by photoelectrons that, in contrast, intrinsically carry the information regarding the nondipolar terms. From the first Auger-monitored NIXSW experiment the two structural parameters (P_c, F_c) can be determined. Determining the asymmetry parameter Q on the basis of the experimental photoemission-monitored electron yield (second experiment) and the previously found structural parameters is thus straightforward. We assume here that the phase shift difference Δ is known from ab initio calculations[50] or from experiments.[18] In section 7.3.3, although we did not fully apply this first approach, the comparison between Cu2p and CuLMM electron yields is discussed and the difference in (P_c, F_c) is ascribed to the fact that nondipolar parameters are not taken into account in the analysis of Cu2p data. Note that equations 3.47, 3.48 and 3.49 are valid only for initial s-states; for other initial subshells the theory becomes more complicated and a simple and useful formulation is still missing.

The second approach consists of preparing an incoherent overlayer with respect to the hkl-reflection planes, so that $F_c = 0$ and equation 3.1 becomes:

$$Y_{exp} = 1 + \frac{1+Q}{1-Q}R. \tag{3.52}$$

In this case a single measurement suffices to retrieve the asymmetry parameter

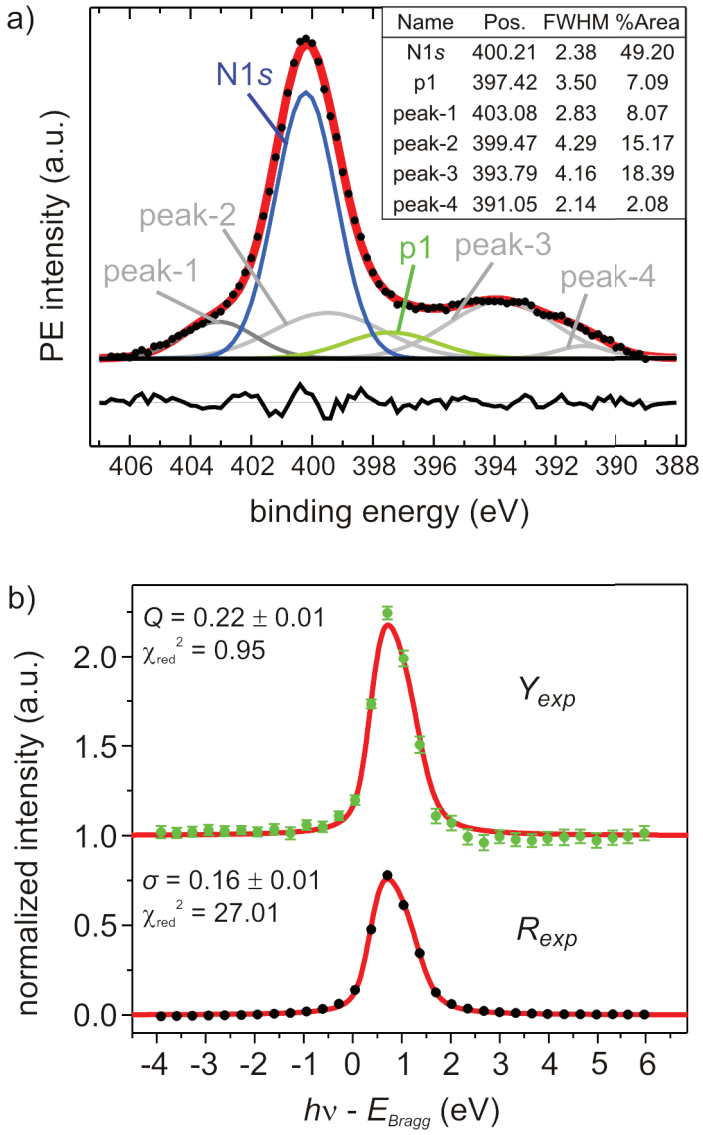


Figure 3.15: (a): sum of 31 XSW-XPS spectra of N1s+Ag-plasmons acquired in one NIXSW experiment. Ag3d-plasmons (peak-1, peak-2, peak-3, peak-4, see section 6.3.2.2): light gray line. N1s: blue line. p1: green line. Background: straight black line. Residuals (black line below the spectrum) result from the subtraction of the whole spectrum (black dots) and the sum of all fitting components (thick red line). Table: position (eV), FWHM (eV), and relative area (%) of the fitting components N1s, p1, peak-1, peak-2, peak-3, peak-4 of model in panel d. (b): fit of the the N1s experimental electron yield and the experimental reflectivity. Results of the fit, i.e., Q and σ, are reported in the figure together with the corresponding χ^2_{red}.

Q. The fitting function used in Torricelli is found by setting $F_c = 0$ in equation 3.42, and replacing S_R with equation 3.47:

$$Y_{exp} = \underline{N} \times \left(1 + \frac{1+\underline{Q}}{1-\underline{Q}} R_{theo}\right) \otimes G(\sigma) \otimes R_m^2\big|_{(E+\Delta E)}. \tag{3.53}$$

All the considerations reported in section 3.4 are valid here as well. The only difference is in the fitting parameters, here represented by the normalization factor N and the asymmetry parameter Q.

This second approach was employed to experimentally determine the asymmetry parameter Q relative to the photoemission of N1s electrons of multilayer azobenzene/Ag(111) (chapter 6). Figure 3.15a shows the XPS spectrum obtained from the sum of all spectra measured during one NIXSW experiment and reveals the presence of a N1s peak that is much more intense than in the monolayer preparation (Figure 6.9). The electron yield profile of the N1s signal is reported in Figure 3.15b and the fit with the fitting function in equation 3.53 provides the asymmetry parameter $Q = 0.22 \pm 0.01$, slightly lower than the calculated one, 0.241 (Table 3.2). This small discrepancy is assigned to the possible residual coherence of the azobenzene molecules in the multilayers with respect to the (111) Bragg planes, parallel to the surface. In fact, to prevent this, a trick often used to guarantee the incoherence of the overlayer is to employ hkl-reflection planes steeply inclined with respect to the crystal surface. Evidence of a residual coherence, i.e., $F_c \approx 0$ and not $F_c = 0$, is derived from the observation that the low energy tail of Y_{exp} is located above the fitting curve and the high energy tail below it, whereas the reflectivity data points R_{exp} are located almost perfectly on the fitting curve. This confirms our initial conjecture and led us to consider the theoretical one for this case as well, where experimental

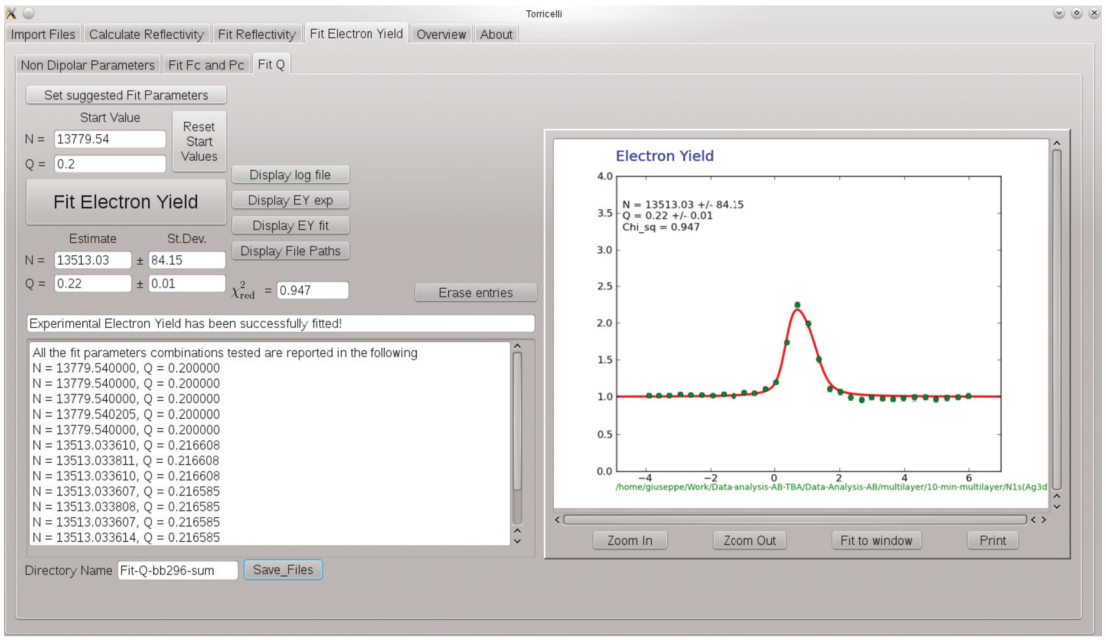


Figure 3.16: "Fit Q" section of Torricelli. Technical details are reported in section A.8.

Q value is available.

In conclusion, Figure 3.16 shows the section of Torricelli where the fitting of the Y_{exp} to determine Q is implemented. To learn more about the operation of this section of the program and the corresponding code, please consult sections A.8.1 and A.8.2, respectively.

3.5 Error analysis of the coherent position and fraction

Although NIXSW structural parameters (P_c, F_c) are interpreted as quantitative properties of the analyzed elemental species, in general little attention has been given to the statistical precision or uncertainty (error) associated with the corresponding values. A quantitative analysis of XPS spectra usually involves both random and systematic uncertainties.[51]

Examples of systematic errors are those caused by:

- a poor focus of the electron analyzer and the beam at the sample, due to a possible drifting of the incident x-ray beam during experiments. In these cases, due to the misalignment of the x-ray beam and the analyzer focus, the intensity of the incoming beam may not be related to the measured electron yield. This leads to an erroneous normalization of the yield profile.
- uncertainties in the nondipolar correction parameters,
- an incorrect decomposition of an XPS spectrum.

In contrast, random errors should mainly follow from the Poisson counting statistics, assumed to be valid in the case of electron detection.[51] Systematic uncertainties are usually larger than the random ones, however in a comparative study of two or more spectra, acquired under the same measurement conditions with the same instrument, random errors become important and ultimately define the significance of a parameter resulting from the fit of a PE spectrum. The rest of the section will mainly focus on the uncertainty related to the random noise.

Error bars of the order of 0.05 Å are often quoted[18,19] for the adsorption height

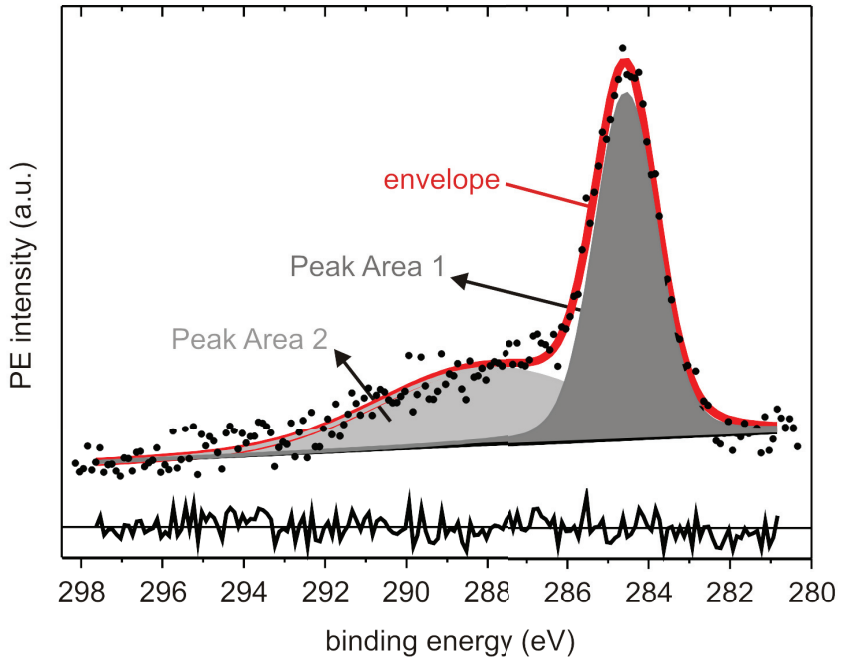


Figure 3.17: Photoemission spectrum of C1*s* core level of PTCDA/Ag(110) (see Figure 4.4), including an XPS fitting model consisting of two overlapping components and a linear background.

derived from the coherent position. However, to our knowledge a proper error propagation analysis from the PE spectrum to (P_c, F_c) has not yet been undertaken. In this dissertation, a careful analysis of the statistical errors is implemented. It is based on the the analysis software CasaXPS[52] which calculates the uncertainty of a fitting component area, even in case of overlapping peaks when uncertainties are likely to be correlated. The standard deviation of each electron yield point, corresponding to the scanned photon energies, results from the error analysis in CasaXPS and serves an input for Torricelli, namely in the χ^2 formula (section A.6.2, lines 89-92).

The steps followed to determine the uncertainty of a fitting component area are summarized below. For better understanding, we focus initially, as an example, on a C1*s* spectrum (Figure 3.17) and we will later extend our conclusions to a more general case. The spectrum is fitted by means of the least-squares Marquardt algorithm implemented in CasaXPS[52] using two components with overlapping tails. Our goal is to estimate the uncertainty associated with each component area. If an XPS spectrum is measured multiple times, the expected value of the peak area is given by the average over the set of measurements and the uncertainty is represented

by the square root of the peak areas' variance, according to Poisson statistics. To achieve a good statistics, numerous measurements of the same spectrum should be performed. Since this is not very practical and sometimes even impossible, due to the radiation damage of the sample or simply due to the limited amount of beamtime, when only a single spectrum is available to estimate the area of a peak, the expected value and the corresponding uncertainty are calculated using Monte Carlo simulations, assuming that the noise in the spectral data obeys a Poisson distribution. Monte Carlo error analysis proceeds as follows:

1) First, the noise of the original spectrum is removed by replacing the raw spectrum with the envelope of the fitting components. In this way, the synthesized spectrum is obtained.

2) Second, for each count N corresponding to a given binding energy (Figure 3.17), a random number generator produces normally distributed noise (i.e., Gaussian noise) with average and standard deviation equal to N and $\sqrt{N}$, according to Poisson statistics. In fact, for a large numbers of counts, the normal distribution is a good approximation of the Poisson distribution, which applies to counting experiments such as the one considered here.[53] The generated noise is then added to each point of the synthetic spectrum from point 1).

3) Following the approach described in point 2), 400 synthetic spectra with random generated noise are created. Subsequently, these spectra are fitted with the XPS model developed on the raw data. As a result, a set of fitting parameters differing due to the influence of the random noise is generated. In the section below we explain how the uncertainty of each peak area is determined.

For the purpose of discussion, the XPS fitting model of the spectrum in Figure 3.17 has positions and FWHM fixed, and only the peak areas are free to vary. Our goal is to determine the uncertainty of the peak areas. For this purpose, Monte Carlo simulation is performed and for each of the 400 spectra generated as explained above, the two fitted peak areas are provided and displayed in Figure 3.18. We define as *confidence region* the ellipse that contains 68.3% of the total distribution around the center. Both the shape of the confidence region and the confidence level are customary in scientific usage.[55] The ratio of the ellipse dimensions $\frac{\alpha}{\beta}$ follows from the principal axes analysis. The next step is to generate 400 ellipses with ratios of the diagonals $\frac{\alpha}{\beta}$, centered at the center of mass of the distribution and passing through each of the distribution points. In this way, each ellipse corresponds to one point. Subsequently, the distribution points are ordered in terms of distance of the corresponding ellipse from the center. The ellipse (blue in Figure 3.18) containing

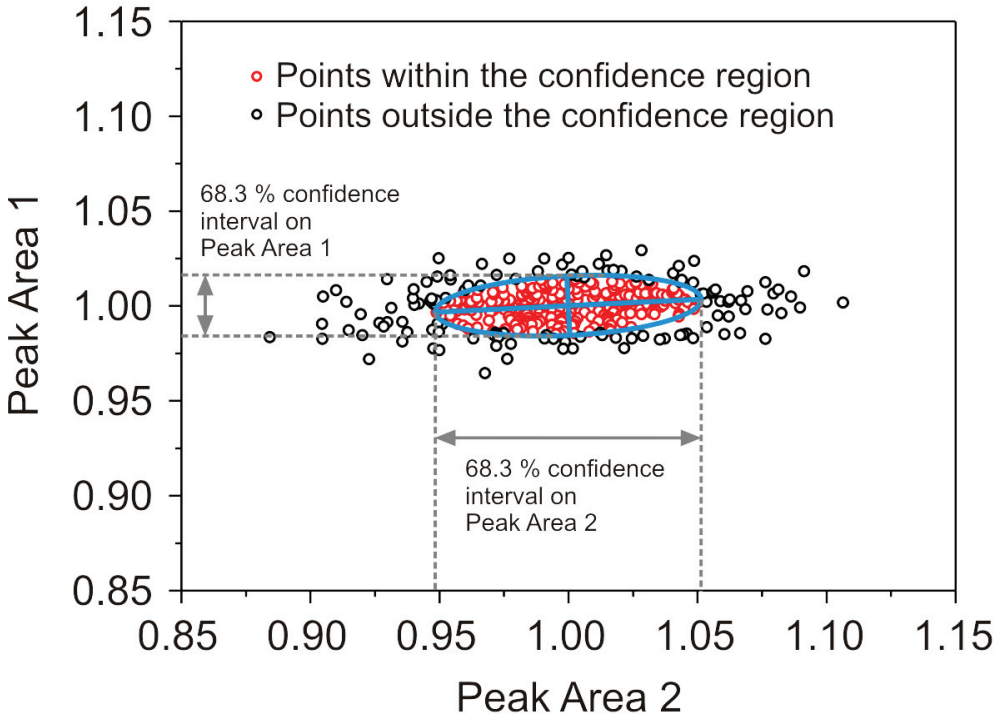


Figure 3.18: Scatter plot of the parameter sets (Peak Area 1, Peak Area 2) resulting from the fitting of 400 Monte Carlo simulated spectra, on the basis of the raw spectrum in Figure 3.17. The blue ellipse contains all the parameter sets enclosed in the confidence region including 68.3% of the points around the center of mass of the distribution. The distribution points within the confidence region are red; those outside are black. The confidence intervals of the two parameters are marked with dashed grey lines. The principal axes are marked with the blue straight lines. Mathematically, the principal axes can be determined as the eigenvectors for a matrix resulting from the minimization of the squared sum of the distance of each point in the scatter plot from a line crossing the centroid.[54]

68.3% of the distribution points (red in Figure 3.18) represents our confidence region. Therefore, projecting the extremes of the confidence region on each axis yields the confidence interval for each of the two peak areas, as illustrated in Figure 3.18.

In the presence of m free-fitting parameters, Monte Carlo simulation provides a distribution in the m-dimensional space. Analogous to the 2D case, the confidence region is defined as the ellipsoid that includes 68.3% of the distribution points around the centroid, i.e., center of mass in m dimensions. Similarly, the confidence interval of each parameter is determined by projecting the extremes of the ellipsoid on the corresponding axis. We note that the uncertainties obtained in this manner take into account all the fitting parameters simultaneously, and not just one at a time; therefore, it is representative of the correlation among fitting parameters of overlapping peaks (e.g., Figure 3.17). Further details about the implementation of this

error analysis in CasaXPS are available in reference.[54]

A possible alternative to the Monte Carlo method involves using the inverse of the Hessian matrix, resulting from the χ^2 minimization, to obtain the uncertainty of each fitting parameter directly. However, the Monte Carlo method is preferable because it allows the influence of the noise on the background and in turn on the peak area to be taken into account. In particular, the background is largely affected by the noise if its extremes are pinned to only one count at a specific binding energy (see Figure 4.3). In this case, each simulated spectrum will have a different background and this reflects directly on the peak area. In fact, one of the largest source of uncertainty associated with a component area is the uncertainty of the background.[56] This is why in order to simultaneously reduce the background uncertainty and increase the peak area accuracy, the background is usually averaged over a chosen number of points,[57] as explained in section 4.2.3.

A proper determination of the error corresponding to the fitting component area, i.e., photoelectron yield, is essential, because that value directly enters the χ^2 formula whose minimization provides (P_c, F_c) and the corresponding uncertainty (section A.6.2, lines 89-92). Therefore, through the propagation of the errors, the uncertainty of the structural parameters is also representative of the peak area standard deviation of the measured spectrum, determined via the Monte Carlo method described above.

3.6 Overview and conclusions

The last section of Torricelli shows an overview of all the results. In particular, the fitted experimental profiles (reflectivity and electron yield) and the corresponding fitted parameters (plus standard deviations and χ^2_{red}) are reported together with the normalized raw data from the "Import Files" section, as shown in Figure 3.19.

In this chapter, all the steps that are followed in order to go from the raw data to the structural parameters (P_c, F_c) are described in detail. We focus particularly on the formula employed by Torricelli and on the underlying assumptions that may limit their applicability. A brief mention of the graphical user interface (GUI) is also provided throughout this chapter; more detailed description of the GUI can be found in appendix A.



Figure 3.19: "Overview" section of Torricelli.

Having provided a tool for analyzing NIXSW data, we can present the experimental results regarding the investigated systems, i.e., PTCDA/Ag(110) (chapter 4), K+PTCDA/Ag(110) (chapter 5), AB/Ag(111) and TBA/Ag(111) (chapter 6), and TPA/Cu(100) (chapter 7).

4 PTCDA on Ag(110)

4.1 Introduction

Organic molecules have opened up a large field of possible applications for electronic devices as light emitting diodes,[58–62] organic field-effect transistor,[63,64] and solar cells.[65,66] Among other organic molecules that are technologically relevant in the field of *molecular electronics*, 3,4,9,10-perylene-tetracarboxylic-dianhydride (PTCDA) has been widely studied as a prototype of π-conjugated molecules due to its structure, which consists of a perylene core and two functional groups (Figure 4.1). In particular, among other molecule-substrate interfaces, PTCDA/Ag(110) has been extensively investigated[67–75] and can be considered to be a model system for studying the interplay between:

- chemical and Coulomb interaction between oxygen atoms of the PTCDA anhydride groups and silver surface atoms;
- charge transfer metal $\leftrightarrow$ adsorbate;

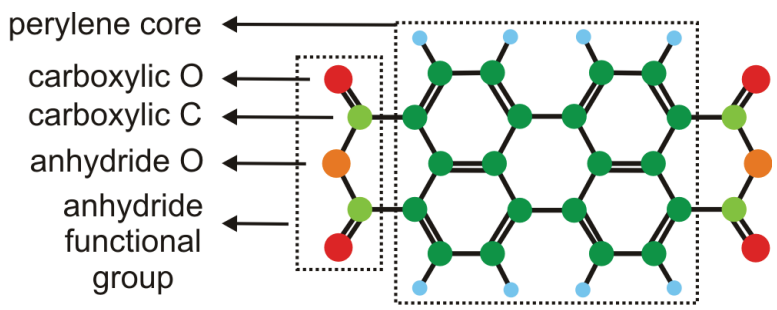


Figure 4.1: Chemical structure of 3,4,9,10-perylene-tetracarboxylic-dianhydride (PTCDA). The molecule is subdivided in a perylene core, consisting of carbon atoms (dark green) and hydrogen atoms (light blue) and two anhydride functional groups, which in turn consist of two carboxylic oxygens (red) doubly bonded to the carboxylic carbons (light green), and one anhydride oxygen (orange).

- long-range electrostatic and van der Waals (vdW) forces acting between the substrate and the molecules, and among the molecules;
- energetic penalty due to distortion of the gas-phase molecular geometry upon adsorption;
- Pauli repulsion between occupied orbitals of adsorbate and substrate.

Moreover, PTCDA adsorbs flat[75] at a unique adsorption site and assembles on Ag(110) in the *brickwall* commensurate phase (see Figure 4.18). The unit cell of PTCDA monolayer on Ag(110) contains only one molecule; it has an area of 141 Å^2 and only one rotational domain with the long molecular axis oriented along the [001] direction. The interaction with the substrate is thus rather strong and we will mainly focus on this aspect in relation with experimental data. Nevertheless, intermolecular interactions, often overlooked for PTCDA/Ag(110), will be also discussed.

In the following sections, after reporting on experimental details of the measurements, NIXSW data are presented. Subsequently, the resulting adsorption geometry of PTCDA is also discussed in the light of previous experimental data that, in some cases, will be reinterpreted on the basis of our present results. Finally, a bonding mechanism for PTCDA/Ag(110) is presented, which will represent the starting point for the next step, i.e., tuning the molecule-substrate interaction via coadsorption of an alkali metal (chapter 5).

4.2 Experimental details

In this section, experimental details concerning sample preparation, measurement settings and data analysis are provided. The section is organized as follows: in the first part, experiments performed on different PTCDA/Ag(110) preparations are described and the corresponding coverage estimation is presented. In the second part, XPS data acquisition parameters of NIXSW experiments are discussed in general and values relative to PTCDA/Ag(110) are reported. The third part regards issues and solutions concerning the XPS background definition. Finally, in the fourth part, the line shapes of XPS fitting components examined. NIXSW experiments were performed at the beamline ID32 (ESRF, Grenoble) together with S. Subach, F. S. Tautz (Forschungszentrum Jülich) and O. Bauer, C. H. Schmitz, M. Buchholz, M. Sokolowski (Universität Bonn).

4.2.1 PTCDA deposition and coverage estimation

Our goal is to perform NIXSW experiments on less than one monolayer (= 1 ML) of brickwall PTCDA/Ag(110)[68–70,75] in order to investigate the adsorption geometry and the direct interaction of PTCDA with the most open low index Ag surface. The main features of PTCDA preparation are summarized below. With XPS and LEED, it is observed that the first PTCDA layer cannot be desorbed from Ag(111) and Ag(110) before dissociation at more than 550 K;[75,76] therefore a submonolayer can be obtained only by direct deposition and not by desorption of excess molecules. However, on the Ag(111) surface it is possible to obtain one monolayer of herringbone PTCDA by desorption of multilayers,[69,75] but if PTCDA multilayers are desorbed from the Ag(110) surface, the result is a monolayer consisting of two molecular phases, brickwall and herringbone[77,78] (see Figure 4.2b). Therefore, the only way to fulfill our original requirement of preparing a submonolayer of brickwall PTCDA/Ag(110), without additional molecular phases, is to directly deposit less than 1 ML of molecules on the surface. This procedure makes sample preparation more difficult because the possibility of ending up with multilayers cannot be excluded.

NIXSW experiments on PTCDA/Ag(110) were carried out in two beamtimes: in April 2008 and February 2009. Results from the April 2008 beamtime will not be discussed, because coverage estimate (Table 4.1) reveals that experiments were performed on a film consisting of approximately three PTCDA layers. The correspond-

ing structural parameters are therefore averaged over molecules located in each of the three layers; hence the information about the direct interaction of PTCDA with the Ag(110) substrate is lost. The rest of the chapter will focus on NIXSW data from the February 2009 beamtime (F'09_1, F'09_1a, F'09_2, see Table 4.1).

Preparation of the brickwall PTCDA phase[70] consists of several steps. At first, the Ag(110) single crystal is cleaned by repeated cycles of argon ion sputtering and annealing at 600 °C. The cleanness of the crystal is checked by LEED and XPS. PTCDA molecules are successively evaporated from a Knudsen cell on the Ag substrate kept at room temperature. Finally, the sample is annealed at 150 °C (well below the desorption temperature of multilayers[70,75]) for several minutes in order to increase the homogeneity of the molecular layer.

In order to estimate the coverage of the sample the following formula,[79] describing the relation of photoemission intensities I of two lines j and j' with kinetic energies E_k and E'_k emitted by the two elements Z and Z′, is considered:

$$\frac{I\left(j,Z\right)}{I\left(j',Z'\right)}=\frac{\sigma\left(j,Z\right)C\left(Z\right)\lambda\left(E_k\right)T\left(E_k\right)\exp\left[-\left\langle d\right\rangle/\lambda\left(E_k\right)\right]}{\sigma\left(j',Z'\right)C(Z')\lambda\left(E'_k\right)T\left(E'_k\right)\exp\left[-\left\langle d'\right\rangle/\lambda'\left(E'_k\right)\right]}. \tag{4.1}$$

In equation 4.1, σ is the photoionization cross section; C(Z) and C(Z′) are the atomic concentrations of the elements Z and Z′, respectively; λ is the mean electron escape depth; T is the factor accounting for the analyzer transmission; and finally, the exponential factor describes the attenuation of the electron intensity through a surface layer of effective thickness $\langle d\rangle$ and $\langle d'\rangle$ for photoelectrons from elements Z and Z′, respectively.

The thickness of the PTCDA layer is estimated by comparing the integrated photoemission peak intensity of C1s and Ag3d lines, I(C1s) and I(Ag3d), respectively. Since the kinetic energy (E_k) of C1s photoelectrons is only 2% larger than Ag3d photoelectrons, electron escape depth and analyzer transmission is assumed to be approximately equal for these two lines; therefore the corresponding factors λ and T cancel each other out. Moreover, since we are dealing with approximately one monolayer of PTCDA the thickness of the layer crossed by substrate photoelectrons is $\langle d'\rangle \approx \langle d\rangle \approx 0$, where $\langle d\rangle$ is approximated with zero because we did not deposit much more that 1 ML. As a consequence, both exponential terms are approximately 1. Within the approximations discussed above, equation 4.1 reduces to the following relation between the concentration of carbon and silver, estimated through C1s and

PTCDA and PTCDA+K preparations				
abbr.	beamtime	preparation	coverage [ML]	C_C/C_O
N'04	Nov. 2004	PTCDA / Ag(111)	1.00 ± 0.08	
A'08	Apr. 2008	PTCDA / Ag(110)	3.09 ± 0.25	6.59 ± 0.85
F'09_1	Feb. 2009	1^{st} PTCDA / Ag(110)	1.32 ± 0.10	7.16 ± 0.41
F'09_1a	Feb. 2009	annealed @ 350 °C (5 min)	0.94 ± 0.08	11.12 ± 0.98
F'09_2	Feb. 2009	2^{nd} PTCDA / Ag(110)	0.89 ± 0.09	5.84 ± 0.50

Table 4.1: PTCDA coverages and C_C/C_O ratio for PTCDA/Ag(111) and PTCDA/Ag(110) relative to different preparations and different beamtimes. Both the coverages and the C_C/C_O ratios are estimated on the basis of core levels PE intensities (equation 4.2).

Ag3d lines, respectively:

$$\frac{C\,(\mathrm{C1}s)}{C\,(\mathrm{Ag3}d)} \propto \frac{I\,(\mathrm{C1}s)}{I\,(\mathrm{Ag3}d)} \cdot \frac{\sigma(\mathrm{Ag3}d)}{\sigma(\mathrm{C1}s)}. \tag{4.2}$$

We consider as a reference of 1 ML the ratio $C\,(\mathrm{C1}s)\,/C\,(\mathrm{Ag3}d)$ estimated for an earlier beamtime preparation (N'04, see Table 4.1) of PTCDA/Ag(111), resulting from the thermal desorption of a multilayer[80] (see above). The different densities of the first molecular layer on Ag(111), $8.35 \times 10^{13}\mathrm{molecules} \cdot \mathrm{cm}^{-2}$, and Ag(110), $7.07 \times 10^{13}\mathrm{molecules} \cdot \mathrm{cm}^{-2}$, are also taken into account[69] (see Table 5.3) and the coverage values in Table 4.1 are corrected accordingly.

In the February 2009 beamtime, NIXSW measurements were performed on two PTCDA/Ag(110) preparations. The first one (F'09_1) apparently corresponds to the desired brickwall phase,[77] judging from the LEED image in Figure 4.2a. However, coverage estimation reveals that the sample consists of approximately 1.3 ML

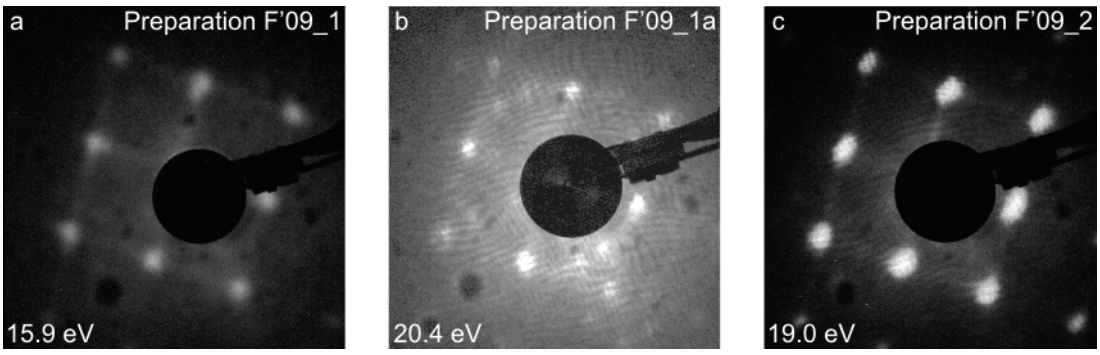


Figure 4.2: LEED images of sample preparations F'09_1 (a), F'09_1a (b), F'09_2 (c). The corresponding electron beam energy is reported on each image.

PTCDA, with a ratio $C_C/C_O = 7.16 \pm 0.41$ almost two times the stoichiometric value of 4 (PTCDA contains 24 C atoms and 6 O atoms, see Figure 4.1). This suggests the presence of contamination on the surface in addition to PTCDA. After annealing the sample at 350 °C for 5 minutes, in order to desorb molecules of the second layer, the coverage indeed decreases to 0.94 (F'09_1a, Table 4.1). However, at the same time, the C_C/C_O ratio increases to 11.12, approximately three times the stoichiometric value, which suggests that part of the molecules undergoes dissociation upon annealing with consequent desorption of oxygen.[70] Moreover, the corresponding LEED image (Figure 4.2b) shows additional faint spots that can be related to the presence of the herringbone phase in addition to the brickwall phase.[77] In the second preparation (F'09_2), a sample coverage of 0.89 ± 0.09 is directly obtained upon PTCDA deposition on the Ag(110) surface. The corresponding LEED image (Figure 4.2c) testifies that molecules assemble in the brickwall phase, and the C_C/C_O ratio is closer to the stoichiometric value.

4.2.2 XPS acquisition parameters of NIXSW experiments

NIXSW data consist of a set of x-ray PE spectra, measured at different photon energies, which contain the structural information about the system under study. To be able to extract such information, it is fundamental to set the XPS acquisition parameters in an optimal manner. There are five main parameters which can be set in order to tune the properties of the measured PE spectra:

- First, the pass energy which is related to the resolution ΔE of the analyzer. The

XPS data acquisition parameters				
element	C1s		O1s	
XPS type	HS	XSW	HS	XSW
$h\nu$ window [eV]	-	5	-	5
$h\nu$ step [eV]	-	0.10	-	0.10
E_k window [eV]	40	31	20	26
E_k step [eV]	0.1	0.2	0.1	0.2
time/step [ms]	500	100	500	100
pass energy [eV]	47	47	47	47
repeats	4	6	13	7

Table 4.2: XPS data acquisition parameters of HS (High Statistics) and XSW-XPS spectra adopted for experiments of preparations $F'09_1$, $F'09_1a$ and $F'09_2$ (Table 4.1). Photon energy window and photon energy step of the NIXSW scan, plus kinetic energy window, kinetic energy step, time per step, pass energy and number of repeats are reported for PE spectra of C1s and O1s lines.

lower the pass energy, the better the resolution.

- Second, the size of the kinetic energy window of the photoemitted electrons detected by the analyzer. A large energy window is desirable for a better definition of the background.
- Third, the energy step, which is the energy distance between two adjacent data points. The smaller the energy step, the more accurate the fitting of PE spectra will be.
- Fourth, the time per step, which is the acquisition time of one data point. A longer time per step improves the statistics of the spectrum.
- The fifth and last parameter is the number of repeats, i.e., the number of times a spectrum is measured before being averaged.

To maximize the statistics and improve the resolution, it is desirable to acquire PE spectra with low pass energy, large kinetic energy window, small energy step, long time per step and high number of repeats. However, this would imply a very long acquisition time that may induce beam damage (for instance, dissociation or desorption, see sections 5.2.1.2 and 5.5.1), especially in organic layers, besides the practical unavailability of the x-ray beam for an indefinite time. Therefore, a compromise needs to be found between the limited acquisition time (constrained by the beamtime and integrity of the molecular layer), on the one hand, and the resolution and statistics necessary to resolve possible core-level chemical shifts, on the other.

In Table 4.2 we report XPS acquisition parameters relative to two different kinds of PE spectra, called HS (High Statistics) and XSW. The first, HS-XPS, are photoemission spectra devoted to the development of the C1s and O1s XPS fitting models. The second, XSW-XPS, are the PE spectra measured during an NIXSW experiment. HS photoemission spectra are recorded with longer time/step (500 ms) and smaller E_k step (0.1 eV), thus with higher statistics compared to XSW-XPS. Moreover, the larger E_k window allows a better definition of the background (section 4.2.3). The employment of the same pass energy (47 eV) for HS- and XSW-XPS enables the transfer of the fitting model developed for HS spectra to XSW spectra without further adjustment of the components FWHM (see section 7.3.1). Furthermore, as we will see in sections 4.3.1.2 and 4.3.2, the compromise achieved with the XPS acquisition settings reported in Table 4.2 is sufficient to discern carbon and oxygen species of PTCDA in different chemical environments.

4.2.3 XPS background

The photoelectron yield of an adsorbate signal (for example, C1s or O1s line) is defined as the difference between the PE spectrum and the background (BG), i.e., the PE intensity coming from the substrate. It is therefore important to properly define the background in order not to include part of the substrate signal in the photoelectron yield of the adsorbate signal. Otherwise, the corresponding structural parameters of the adsorbate atom would be altered by the substrate contribution.

In all the PE spectra discussed in this chapter a linear BG is adopted, since there is no evidence of other background types, such as a Shirley BG.[81] The software used to analyze the XPS data (CasaXPS[52]) defines the linear background as a straight line $L(E)$ crossing the two values I_1 and I_2 corresponding to the energies E_1 and E_2 located at the boundaries of the selected energy window (Figure 4.3)

$$L(E) = I_1 \frac{E_2 - E}{E_2 - E_1} + I_2 \frac{E - E_1}{E_2 - E_1}. \tag{4.3}$$

Since the PE intensity of each single data point is susceptible to noise, to prevent it from affecting the background, the intensities I_1 and I_2 at the end points E_1

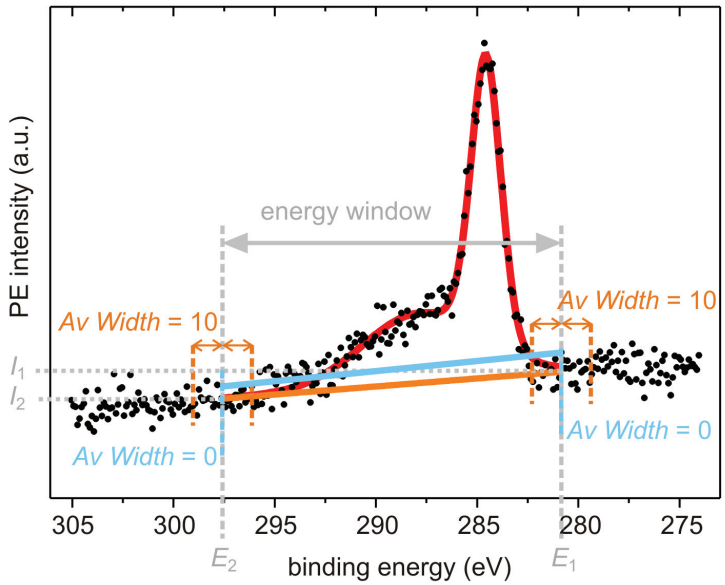


Figure 4.3: Illustration of the energy window (gray) where the background is defined, and of two linear backgrounds corresponding to $AvWidth = 10$ (orange) and $AvWidth = 0$ (blue).

and E_2 can be modified through the parameter $AvWidth$, as explained in the following. If $AvWidth = 0$, the values I_1 and I_2 are set equal to the intensity of the spectrum $I(E)$, where E is the closest energy value to E_1 and E_2, respectively (see blue line in Figure 4.3). If the $AvWidth$ is greater than zero, the number of data points specified by $AvWidth$ to the left and to the right of the data point otherwise used are averaged to determine the intensities I_1 and I_2 employed to compute the background. For instance, in Figure 4.3, I_1 and I_2 of the orange background result from the average of 10 data points to the left and 10 data points to the right of the closest data point at energies E_1 and E_2, respectively. The intensity of the boundary values of the Shirley BG are defined in the same way.

If the energy window of the PE spectrum is so large that the end points E_1 and E_2 are far enough from the PE peak, then it is better to set a larger $AvWidth$ so that a larger number of intensities is averaged to compute I_1 and I_2. As a result, the background will be more robust against the noise. In fact, in Figure 4.3 the orange BG ($AvWidth = 10$) is clearly more accurate than the blue one ($AvWidth = 0$). However, usually the energy window $E_2 - E_1$ where the background is defined is only slightly larger than the energy interval where the PE peak appears. In this case $AvWidth$ is limited by the close presence of the signal and it is set in order not to also average intensities of the signal for the definition of I_1 and I_2.

Once the background is defined, the difference between the whole PE spectrum and the background yields the *Region* signal. If *Region* includes contributions from atoms located at different vertical positions, the corresponding coherent position P_c refers to the average distance of the same atoms from the surface Bragg plane (with one exception discussed in section 6.4.1.2).

4.2.4 Line shapes of the fitting components

Before discussing the line shape of the fitting components, it is useful to make a clear distinction between photoemission lines, also called main peaks, and satellite peaks. Due to shakeup processes, satellite components, can be easily distinguished in PE spectra because they appear at higher binding energies than the corresponding main peaks. In the work of Schöll et al.,[82] where high-resolution PE spectra of various condensed organic molecules are compared, satellite peaks are assigned to shakeup processes caused by excitations of valence electrons upon sudden creation of a core hole. The satellite intensity is influenced by different factors re-

lated to the reaction of the electronic system upon ionization and can be divided into:

- intramolecular contributions which determine the ability of the molecular electronic system to react on core-hole creation;
- intermolecular contributions, which are responsible for the influence of the molecular surrounding on the electronic response in the condensed phase.

In particular, the satellite intensity depends on the number of aromatic rings, so that a larger aromatic ring system entails higher satellite intensities. The polarity of the molecule also plays an important role, so that the larger the polarity, the larger the satellite intensities because of the increased intermolecular screening. Unless differently specified in the following chapters, we attribute satellite components to shakeup processes, as explained above. We turn now to the discussion of the line shapes of main and satellite components.

The line shape of core-level peaks is the result of a combination of the physics involved in the photoemission process and the measurement process. Ideally, the measurement process, which includes instrumental response, x-ray line shape and thermal broadening, can be described by a Gaussian function. On the other hand, a Lorentzian function is used to model the lifetime broadening due to the uncertainty principle relating lifetime and energy of the photoemitted electrons. The functions used by the XPS fitting software (CasaXPS[52]) are:

$$G\left(x,E,F\right)=exp\left[-4ln\left(2\right)\left(\frac{x-E}{F}\right)^{2}\right] \tag{4.4}$$

$$L\left(x,E,F\right)=\frac{1}{1+4\left(\frac{x-E}{F}\right)^{2}} \tag{4.5}$$

where the peak energy E and width F of the functions are fit parameters. For the photoemission lines, we use Voigt profiles approximated by the sum or linear combination of a Gaussian and a Lorentzian, defined as follows:

$$SGL\left(x,E,F,m\right)=\left(1-\frac{m}{100}\right)G\left(x,E,F\right)+\frac{m}{100}L\left(x,E,F\right) \tag{4.6}$$

where m represents the percentage of Lorentzian contribution and $100-m$ the percentage of Gaussian contribution to the linear combination. For PE spectra discussed in this chapter, the best fits result from photoemission lines modeled by Voigt

functions with 20% Lorentzian contribution, while satellite peaks are fitted by pure Gaussian functions.

Furthermore, we note that a test to verify the effect of the fitting component line shape on the structural parameters has been carried out for C1s data of K+PTCDA/ Ag(110) (section 5.2.2.1). In particular, one of the satellite peaks ($Sat1$, see Figure 5.4) is fitted with a linear combination of Gaussian and Lorentzian ($m = 30\%$), and also with a pure Gaussian ($m = 0\%$). Despite the different line shapes used, the resulting structural parameters turn out to be identical within the error. Therefore, we conclude that for our purpose of extracting the photoelectron yield of a given PE peak, the specific line shape of the fitting component does not play a crucial role in the determination of the coherent position and the coherent fraction.

4.3 Experimental results

In this section, NIXSW results of PTCDA/Ag(110) are reported. In particular, XPS fitting models of C1s and O1s core levels are derived and described. The corresponding electron yields and structural parameters (P_c, F_c) are presented and discussed. Silver results will be presented in section 5.2.2.4, since both PTCDA/Ag(110) and K+PTCDA/Ag(110) were prepared on the same silver crystal (section 5.2.1.1), but we can already anticipate that both P_c and F_c are approximately 1. For the discussion of the resulting adsorption geometry of PTCDA, we refer to section 4.4.

4.3.1 Carbon

Two different XPS fitting models for C1s spectra are developed and employed. The first one, a two-component model (section 4.3.1.1), aims to determine the average distance of PTCDA carbon atoms from the Ag(111) surface. Interestingly, the corresponding NIXSW results suggest the possibility to differentiate carbon atoms within the PTCDA molecule. Hence, a second multicomponent model (section 4.3.1.2) is developed with the aim of distinguishing between the vertical positions of carbon atoms in the functional groups and in the perylene core of PTCDA. In the following subsections each of these two models is described in detail.

4.3.1.1 Two-component model

XPS fitting model

The C1s PE spectrum reported in Figure 4.4 is acquired with higher statistics than XSW-XPS for a more accurate development of the XPS fitting model, as explained in section 4.2.2. In a first approximation, this C1s spectrum consists of an intense peak at approximately 284.6 eV and a broad satellite at higher binding energies. Therefore, the simplest fitting model consists of two components: a prominent peak called $Main$, located at the C1s photoemission line; and a broad peak called Sat, tentatively assigned to a satellite component (see section 4.2.4). The background of C1s spectra is set to be linear with $AvWidth = 5$ (section 4.2.3).

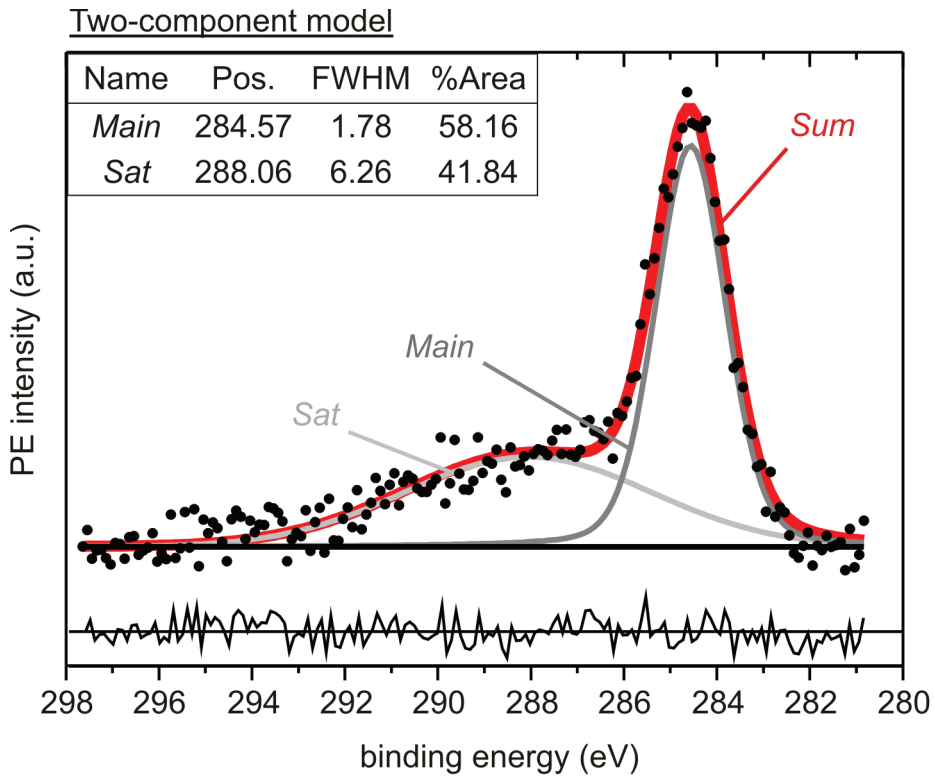


Figure 4.4: C1s HS-XPS (pass energy = 47 eV, energy window = 40 eV, energy step = 0.1 eV, time/step = 0.5 ms, repeats = 4) measured at $h\nu = 4280$ eV. In the inset table, position (eV), FWHM (eV), and relative area (%) of the fitting components *Main* (dark gray line) and *Sat* (light gray line) are reported. *Sum* (red line) is the sum of *Main* and *Sat*. The residuals (thin black line below the spectrum) result from the subtraction of the whole spectrum (black dots) and *Sum*.

Photoelectron yield

The model described above is applied to C1*s* XSW-XPS spectra of preparations F'09_1, F'09_1a and F'09_2 (section 4.2.1) leaving the position, the FWHM and the area of each component free to be fitted. No constraint is set in order to have more degrees of freedom for a better fit of the whole PE spectrum.

We investigate the photoelectron yield of four signals, namely *Main*, *Sat*, *Sum* (= *Main* + *Sat*) and *Region* (= spectrum − background). The corresponding structural parameters are summarized in Table 4.3 and in the Argand diagrams of Figure 4.5. If we compare results from different preparations we can observe several features common to all four signals. In particular, preparation F'09_1a obtained from annealing of preparation F'09_1 is characterized by lower coherent fraction and higher coherent position than the parent preparation F'09_1. This can be the result of two concomitant phenomena, on the one hand, the decomposition of PTCDA molecules due to the high annealing temperature (section 4.2.1), and on the other

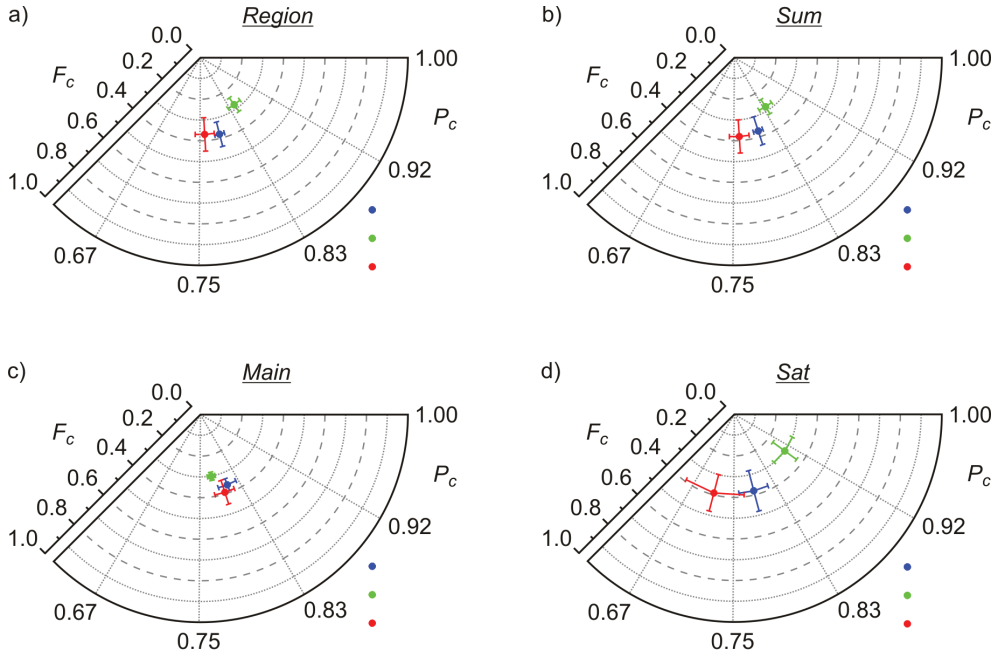


Figure 4.5: Argand diagram of *Region* (a), *Sum* (b), *Main* (c), *Sat* (d) structural parameters (P_c, F_c) for the three different preparations F'09_1 (blue), F'09_1a (green) and F'09_2 (red) (section 4.2.1).

hand, the coexistence of two molecular phases, brickwall and herringbone[77,78] (see Figure 4.2b). At the same time, all signals of preparation F'09_1 have approximately the same coherent fraction but higher coherent position as compared to preparation F'09_2. These results are difficult to interpret because while a difference in P_c between the 0.89 ML and 1.32 ML preparations of PTCDA/Ag(110) can be expected, it is not clear why the F_c is not affected and keeps constant despite the sizable difference in the estimated sample coverage. Since we are interested in the submonolayer of PTCDA/Ag(110), we now analyze the photoelectron yields of *Main*, *Sat*, *Sum* and *Region* of the preparation F'09_2 (Figure 4.6) in more detail.

When inspecting Figure 4.6, we notice a sizable difference in the error bars of the four photoelectron yield profiles. A detailed description of how error bars of a photoelectron yield data point are defined is provided in section 3.5. We briefly recall here that the error of a component area is given by its standard deviation, calculated on the basis of the fit of Monte Carlo-simulated raw XSW-XPS spectra. If we move the focus on the actual profiles in Figure 4.6, the similarity between *Region* and *Sum* signals, as well as the dissimilarity between *Main* and *Sat* signals is notable. The tendency remains the same, although the difference is not so large for the other data sets either: F'09_1(1), F'09_1(2) and F'09_2(1) (Table 4.3). The average structural parameters of *Region* and *Sum* are identical within the errors and provide an

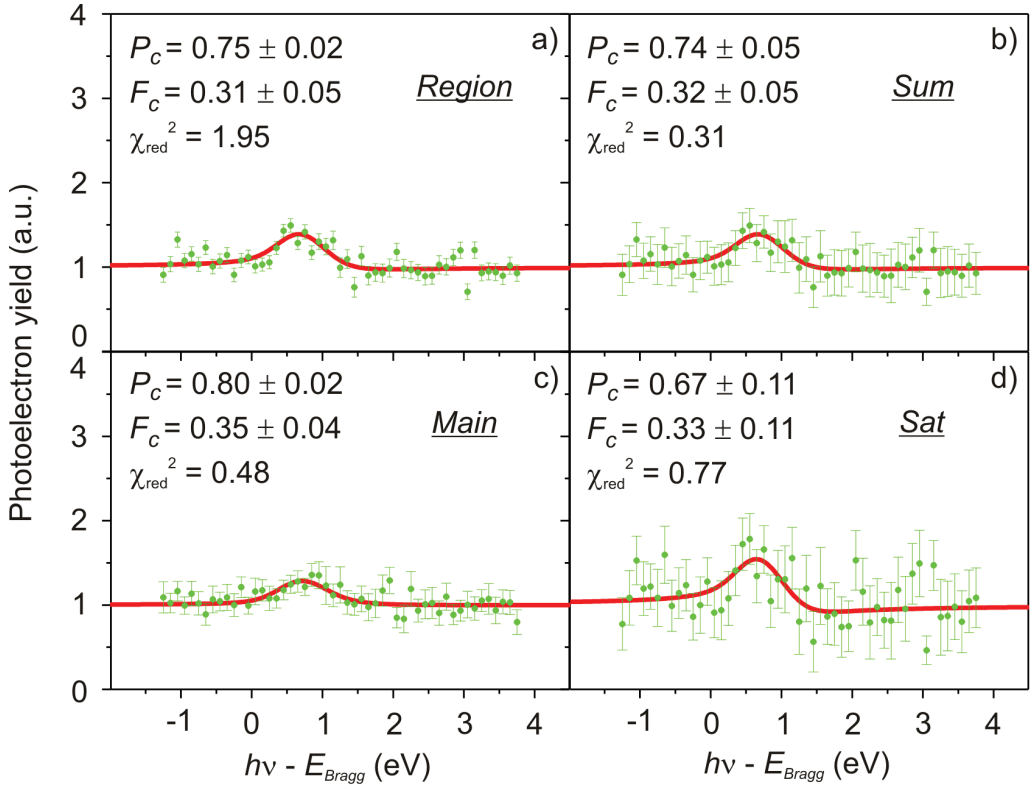


Figure 4.6: Photoelectron yield of *Region* (a), *Sum* (b), *Main* (c), *Sat* (d) signals (green dots and relative error bars) of data set F'09_2(2) (Table 4.3), displayed as a function of the photon energy relative to the Bragg energy (4288.5 eV). Fitting curve (red) together with results of the fit: coherent position (P_c), coherent fraction (F_c), and reduced χ^2 are also reported for each profile.

average distance of carbon atoms from the Bragg surface plane of approximately 2.54 Å with coherent fraction of 0.38. The fact that F_c and P_c of *Region* and *Sum* coincide is a direct consequence of the fit of *Main* and *Sat* without any constraints in position, FWHM and area, so that the two fitting components can adapt more easily to best fit the spectrum.

The average coherent position of the *Main* component, 0.80, corresponds to an average distance from the surface Bragg plane of 2.60 Å. In contrast, *Sat* has coherent position equal to 0.71 which corresponds to an average carbon height of 2.47 Å, 0.13 Å smaller than the *Main* component. Although *Main* and *Sat* signals have the same coherent fraction (0.39), their significantly different coherent positions indicate the presence of a chemically shifted carbon species located at a different vertical position. We aim to distinguish the carbon atoms at different adsorption heights using a more complex fitting model described in the following section 4.3.1.2.

Two-component model: NIXSW results												
First Preparation												
C1s	*Region*			*Sum*			*Main*			*Sat*		
data set	P_c	d_c	F_c	P_c	d_c	F_c	P_c	d_c	F_c	P_c	d_c	F_c
F'09_1(1)	0.79 (1)	2.59 (1)	0.33 (3)	0.80 (1)	2.60 (1)	0.32 (3)	0.82 (1)	2.63 (1)	0.34 (2)	0.78 (3)	2.57 (4)	0.31 (6)
F'09_1(2)	0.79(1)	2.59(1)	0.42(4)	0.79(1)	2.59(1)	0.42(3)	0.79(1)	2.59(1)	0.38(1)	0.79(2)	2.59(3)	0.45(6)
Average	0.79(1)	2.59(1)	0.38(6)	0.80(1)	2.59(1)	0.37(7)	0.81(2)	2.61(3)	0.36(3)	0.79(3)	2.58(4)	0.38(10)
F'09_1a	0.85(2)	2.67(3)	0.28(4)	0.84(2)	2.66(3)	0.28(4)	0.78(1)	2.57(1)	0.30(2)	0.90(4)	2.74(6)	0.30(7)
Second Preparation												
C1s	*Region*			*Sum*			*Main*			*Sat*		
data set	P_c	d_c	F_c	P_c	d_c	F_c	P_c	d_c	F_c	P_c	d_c	F_c
F'09_2(1)	0.77(1)	2.56(1)	0.43(4)	0.77(1)	2.56(1)	0.44(4)	0.80(1)	2.60(1)	0.43(3)	0.75(3)	2.53(4)	0.44(7)
F'09_2(2)	0.75(2)	2.53(3)	0.31(5)	0.74(2)	2.51(3)	0.32(5)	0.80(2)	2.60(3)	0.35(4)	0.67(5)	2.41(7)	0.33(11)
Average	0.76(2)	2.54(2)	0.37(8)	0.76(2)	2.53(3)	0.38(8)	0.80(2)	2.60(2)	0.39(6)	0.71(6)	2.47(8)	0.39(9)

Table 4.3: Coherent position (P_c), coherent fraction (F_c) and distance d_c (Å) from the surface Bragg plane, calculated as $(P_c{+}1)\times d_{\mathrm{Ag(110)}}$ (where $d_{\mathrm{Ag(110)}} = 1.44$ Å) are reported for *Region*, *Sum*, *Main* and *Sat* signals. The structural parameters (P_c, F_c, d_c) refer to two data sets of F'09_1 preparation (plus the corresponding average values), to the data set of F'09_1a preparation and to the two data sets of F'09_2 preparation (plus the corresponding average values). Preparations F'09_1, F'09_1a and F'09_2 are discussed in section 4.2.1.

4.3.1.2 Multicomponent model

Having observed different structural parameters (P_c, F_c) for $Main$ and Sat of the two-component model (section 4.3.1.1), we now develop a multicomponent XPS model with the aim of differentiating PTCDA carbon atoms in different chemical environments and presumably at different vertical positions. Subsequently, the corresponding NIXSW results are presented and discussed.

XPS fitting model

The multicomponent XPS fitting model is derived on the basis of three C1s PE spectra of PTCDA, namely HR-XPS, MR-XPS and LR-XPS. These three spectra are measured in three different UHV chambers, on different systems and with different photon sources and electron analyzers. Their names HR (high resolution), MR (medium resolution) and LR (low resolution) follow from the ability to resolve the fine structures of the measured spectra. For the reasons already discussed in section 4.2.2, it was not possible to acquire PE spectra in NIXSW experiments with a resolution that would allow a direct and clear evidence of chemically shifted carbon species to develop an accurate XPS fitting model, hence the name LR-XPS. Therefore, we consider two more PE spectra (HR- and MR-XPS), acquired with higher resolution to enable the differentiation of multiple PTCDA carbon species. In the following, C1s fitting models of HR- and MR-XPS are described.

The HR-XPS, reported in Figure 4.7, is a high-resolution C1s PE spectrum measured by Schöll et al.[82] on a PTCDA thin film (above ten layers) deposited on Ag(111). The spectrum was recorded at the U49/1-PGM undulator beam line of BESSY-II, with photon energy of 335 eV and with an analyzer resolution of $\Delta E = 0.08$ eV. The schematic chemical structure of the PTCDA molecule sketched in Figure 4.7 points out the presence of four chemically different carbon atoms. In particular, there are the carbon atoms of the functional groups with bonds to carbon and oxygen atoms ($C1$), the connecting carbon atoms between the functional groups and the perylene core ($C2$), the carbon atoms of the aromatic core that are bonded to three other ring carbons ($C3$), and finally the carbon atoms bonded to two carbons and one hydrogen ($C4$). In the work of Schöll et al.[82] a complete and unambiguous assignment of the C1s photoemission lines to the different PTCDA carbon species is achieved and corroborated by singles and doubles configuration interaction (SDCI) calculations.[82] The result is a fitting model ($Schöll$ model) in perfect agreement with the

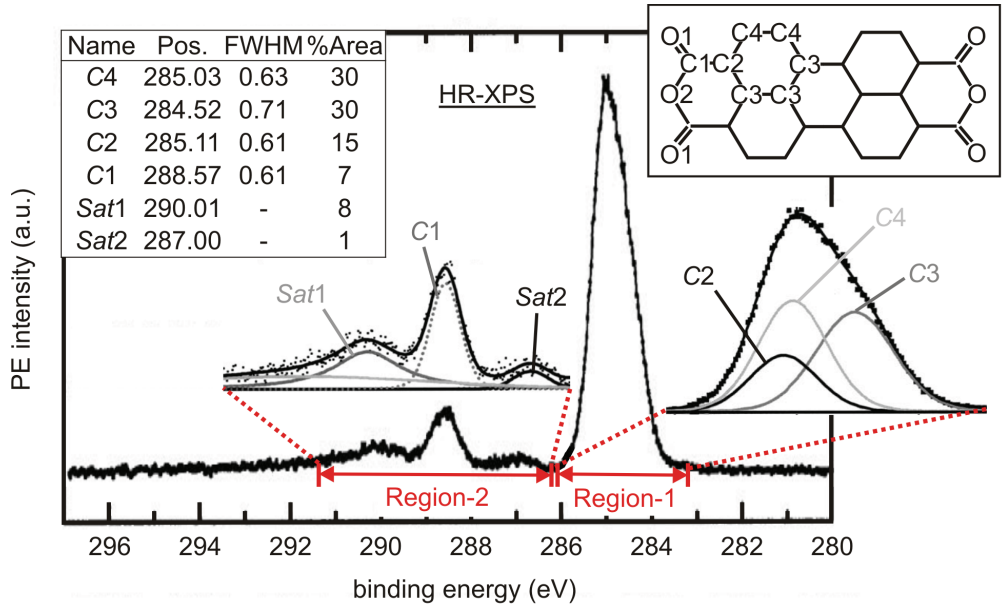


Figure 4.7: figure from Schöll et al.[82]: C1*s* HR-XPS of a PTCDA film (more than 10 layers) deposited on Ag(111). The enlarged regions of the spectrum show the fitting model and the assignment of the peaks. The table on the upper left summarizes position (eV), FWHM (eV), and relative area (%) of each fitting component. A scheme of PTCDA molecule including the nomenclature of the different carbon species is illustrated in the upper right corner.

stoichiometry of PTCDA, so that:

$$(C1 + Sat1) : C2 : C3 : C4 = 4 : 4 : 8 : 8 \tag{4.7}$$

where $Sat1$ is the shakeup satellite (section 4.2.4) of the component $C1$. The satellite $Sat2$ of $C2$, $C3$, $C4$ peaks can be disregarded in equation 4.7 due to its low intensity; in fact it represents only 1% of the entire C1*s* PE area (see table in Figure 4.7). The relative energy positions of $C2$, $C3$ and $C4$ peaks result from the comparison of C1*s* PE spectra of five different π-conjugated organic molecules (including PTCDA), while the higher binding energy of $C1$ carbons can be rationalized in a simple initial-state picture. In particular, the highly electronegative oxygens withdraw electrons and therefore reduce the charge density at the covalently bonded carbons $C1$, hence inducing a significant chemical shift of the C1*s* line toward higher binding energies. The XPS fitting model of the C1*s* HR-XPS will be referred to below as the *Schöll* model.

The HR-XPS is measured on a PTCDA thin film; thus the resulting *Schöll* model is characteristic of PTCDA molecules that are not in direct contact with the metal sub-

strate. We can expect a redistribution of the C1s PE intensity if the organic molecule is in direct contact with the metal surface due to molecular chemisorption and substantially different intermolecular interactions than in a thin film. Hence, the binding energies of the photoemission lines and the satellite structure in the C1s PE spectra (MR-XPS and LR-XPS) measured on a submonolayer PTCDA/Ag(110) are expected to differ from the *Schöll* model developed for multilayers of PTCDA/Ag(111). Bearing this in mind, we now describe the MR-XPS spectra and the corresponding fitting model.

The MR-XPS, reported in Figure 4.8a, is the medium resolution C1s spectrum measured on a submonolayer PTCDA/Ag(110) by Willenbockel et al..[83] The spectrum was recorded using a monochromated Al Kα lab source (1486 eV) and the R4000 Scienta analyzer, with a resulting average resolution of $\Delta E = 0.65$ eV, estimated as the FWHM of the Ag3d$_{5/2}$ line. The *Schöll* model is applied to MR-XPS without setting any constraint in positions, FWHM and areas of the fitting components reported in the table of Figure 4.7. The resulting MR-XPS fitting model (Figure 4.8a) fulfills the stoichiometric ratios of equation 4.7. The main difference between MR-XPS and HR-XPS is the absence of $Sat2$ and the shift of $C1$ toward lower binding energies of approximately 1 eV. We attribute this latter feature, in an initial-state picture, to the different chemical environment of carboxylic carbons ($C1$) due to the fact that oxygen atoms can now directly interact with the surface Ag atoms, with a consequent weakening of the C=O double bond. Moreover, the MR-XPS fitting model has a broader $C2$ component compared to $C3$ and $C4$ in order to fit the shoulder of the main photoemission line without introducing an additional component. The satellite structure is also different than in the *Schöll* model. In fact, $Sat1$, the satellite peak of $C1$, has smaller area and two additional satellite peaks ($Sat2$ and $Sat3$) appear at the high binding energy tail of the C1s spectrum. The MR-XPS model just described is then applied to the LR-XPS.

The LR-XPS, reported in Figure 4.8b, is the low-resolution C1s spectrum of a submonolayer PTCDA/Ag(110) and is identical with the HS-XPS mentioned in sections 4.2.2 and 4.3.1.1. The spectrum was recorded at the ID32 undulator beam line of ESRF, with photon energy 4280 eV and with an average resolution of $\Delta E = 1.25$ eV, estimated as the FWHM of the Ag3d$_{5/2}$ line. In order to fit the low-resolution PE spectrum and develop the C1s model for XSW-XPS spectra, several constraints have to be set. In particular, the relative areas of $C2$, $C3$ and $C4$ are fixed as dictated by the stoichiometry of the molecule (equation 4.7) and their relative FWHMs are fixed

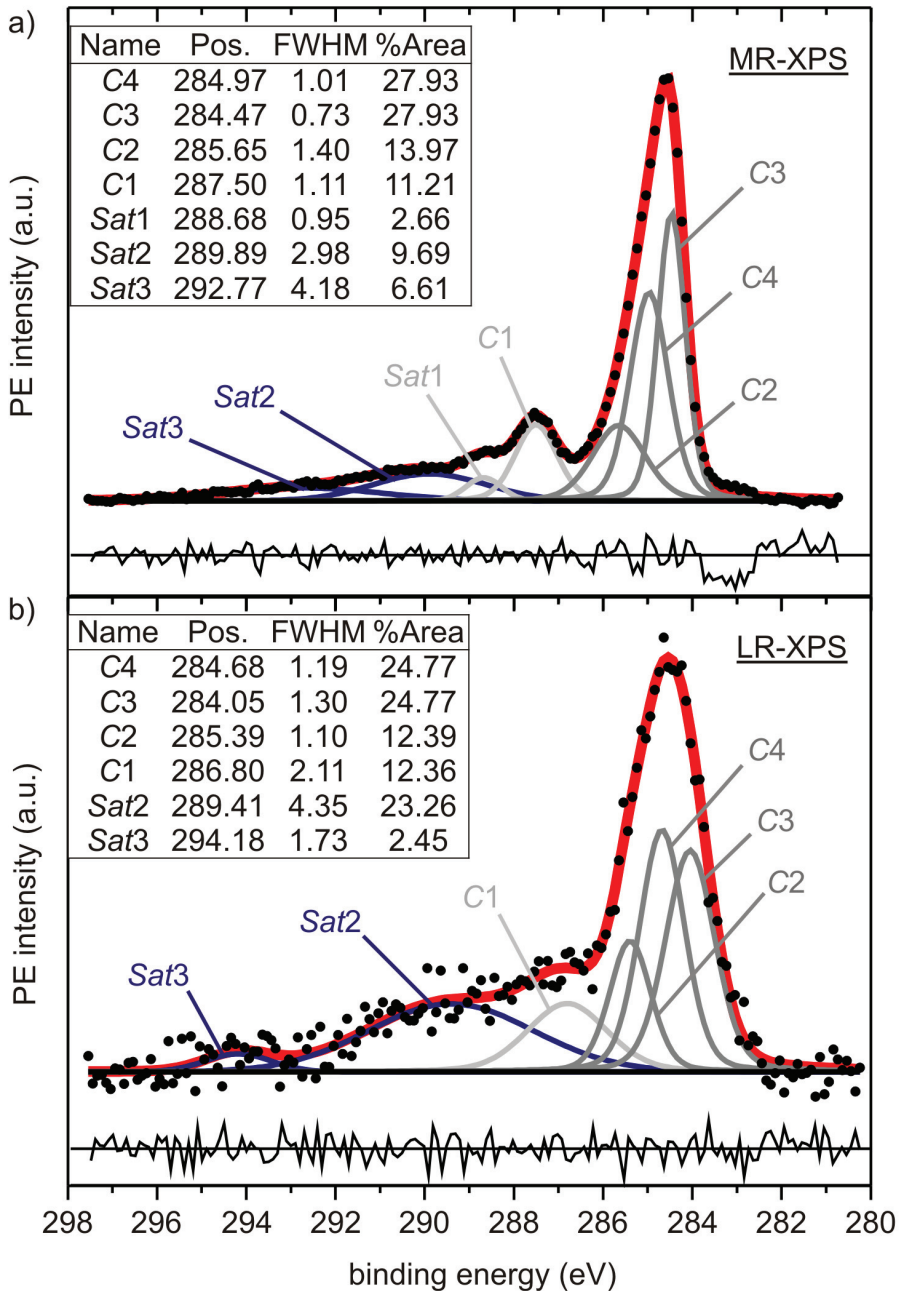


Figure 4.8: (a): MR (medium resolution) C1*s* PE spectrum of submonolayer PTCDA/Ag(110), measured by M. Willenbockel, T. Sueyoshi, S. Subach (Forschungszentrum Jülich). This spectrum is the sum of 26 spectra measured with the following settings: pass energy = 200 eV, energy window = 20 eV, energy step = 0.1 eV, time/step = 0.5 ms, repeats = 10. (b): LR (low resolution) C1*s* PE spectrum of submonolayer PTCDA/Ag(110) (pass energy = 47 eV, energy window = 40 eV, energy step = 0.1 eV, time/step = 0.5 ms, repeats = 4) measured with $h\nu = 4280$ eV. *Sum* (thick red line) is the sum of all components: $C2$, $C3$, $C4$ (dark gray line), $C1$ and $Sat1$ (light gray line), $Sat2$ and $Sat3$ (blue line) . The background is marked by a straight black line. The residuals (thin black line below the spectrum) result from the subtraction between the whole spectrum (black dots) and *Sum* (thick red line).

C1s	HR-XPS[82]	LR-XPS	
component	E_b (eV)	E_b (eV)	ΔE_b
$C4$	285.03	284.68	−0.35
$C3$	284.52	284.05	−0.47
$C2$	285.11	285.39	+0.28
$C1$	288.57	286.80	−1.77

Table 4.4: Binding energies of $C1$, $C2$, $C3$ and $C4$ components of HR-XPS[82] and LR-XPS fitting models. ΔE_b is the difference of binding energies between LR-XPS and HR-XPS components.

as in the *Schöll* model (table of Figure 4.7). The resulting LR-XPS fitting model has $C1$, $C2$, $C3$ and $C4$ components areas in perfect agreement with equation 4.7 that reflects the stoichiometry of PTCDA.

We discuss now the LR-XPS fitting model in more detail and in comparison with both HR-XPS and MR-XPS fitting models, from which it follows. In Table 4.4 we report the binding energy (E_b) shifts of the main components. The shift of $C3$ and $C4$ toward lower binding energies are assigned to the screening effect of the substrate that is irrelevant in the multilayer spectrum (HR-XPS). However, this argument does not hold for the shift of $C2$ toward higher binding energies by 0.28 eV. This apparent contradiction can be explained by the fact that the overall shapes of the C1s photoemission lines in HR-XPS and LR-XPS are substantially different. In fact, in the first case, the spectrum presents a shoulder at the low binding energy side, at approximately 284 eV, while in both MR-XPS and LR-XPS the shoulder switches to the high binding energy side, at approximately 285.5 eV. This effect can be a consequence of a different and more poorly resolved satellite structure responsible for the increased PE intensity in the region between the main C1s line and $C1$, as shown more clearly in Figure 4.8a. In order to fit this portion of the spectrum, the position of $C2$ thus comes out slightly shifted compared to the *Schöll* model.

To conclude the analysis of the main carbon components, we observe that $C1$ has the largest binding energy shift of 1.77 eV toward lower binding energies. This feature was already observed in the MR-XPS and is assigned to the different chemical environment of carboxylic carbons due to the direct interaction of carboxylic oxygens with the Ag atoms, as discussed in section 4.4.2. Moreover, due to the lower resolution compared to MR-XPS and HR-XPS, it is not possible to distinguish $Sat1$. Therefore, a broader $C1$ peak takes into account also its satellite $Sat1$.

Moving to the higher binding energy portion of the C1s spectrum, we note that

the still relatively small $Sat2$ area in MR-XPS is further increased in LR-XPS and represents 23.26% of the entire C1s spectrum. We attribute this additional feature (absent in the HR-XPS) to the different electronic structure of PTCDA at the surface as compared to the thin film. This also implies a different reaction to the creation of a core-hole; hence a different satellite structure.[82] Finally, $Sat3$ decreases in area in comparison with MR-XPS model and represents only a negligible 2.45% of the total area at the high binding energy tail.

In general, since LR-XPS and MR-XPS are both measured on submonolayer PTCDA/Ag(110), the differences between the respective fitting models are attributed to the very different data acquisition settings. Because of the lower resolution and lower statistics of LR-XPS and the consequent difficulty to differentiate carbon species, MR-XPS is reported here as evidence of the presence of chemically shifted C1s photoemission lines and to support the LR-XPS fitting model derived above.

Photoelectron yield

The LR-XPS fitting model described above is applied to XSW-XPS spectra measured on preparations F'09_1, F'09_1a and F'09_2. Positions and FWHMs of all fitting components, reported in the table of Figure 4.8 and corresponding to the best fit of LR-XPS, are fixed. In contrast, areas are left free to be fitted, with two exceptions: the areas of $C2$ and $C3$ are fixed to be half of and the same as the area of $C4$ respectively, in agreement with the stoichiometry of PTCDA. Since the areas of $C2$, $C3$ and $C4$ are related to each other by a fixed ratio, their photoelectron yield profile will be identical; therefore in the following we will refer to their sum $C234 = C2 + C3 + C4$. In the rest of the discussion we will focus on the structural parameters of the following signals: $Region$ (= spectrum − Sum); Sum (= $C234 + C1 + Sat2 + Sat3$); $C234$; $C1$; $Sat2$ and $Sat3$.

Table 4.5 summarizes all structural parameters of the signals mentioned above for the three preparations F'09_1, F'09_1a and F'09_2. The corresponding visual representation is given by the Argand diagrams of Figure 4.9. Panels a and b show the structural parameters of $Region$ and Sum. Their similarity, reflected in the photoelectron yield curves of Figure 4.11 a and b, proves that the envelope (Sum) of LR-XPS fitting model accurately fits the single spectra of NIXSW data sets, as already noted for the two-component model where components have no constraints (section 4.3.1.1). The Argand diagram of $C234$ (Figure 4.9c) presents slightly higher coherent fraction and lower coherent position for F'09_2 preparation compared to F'09_1

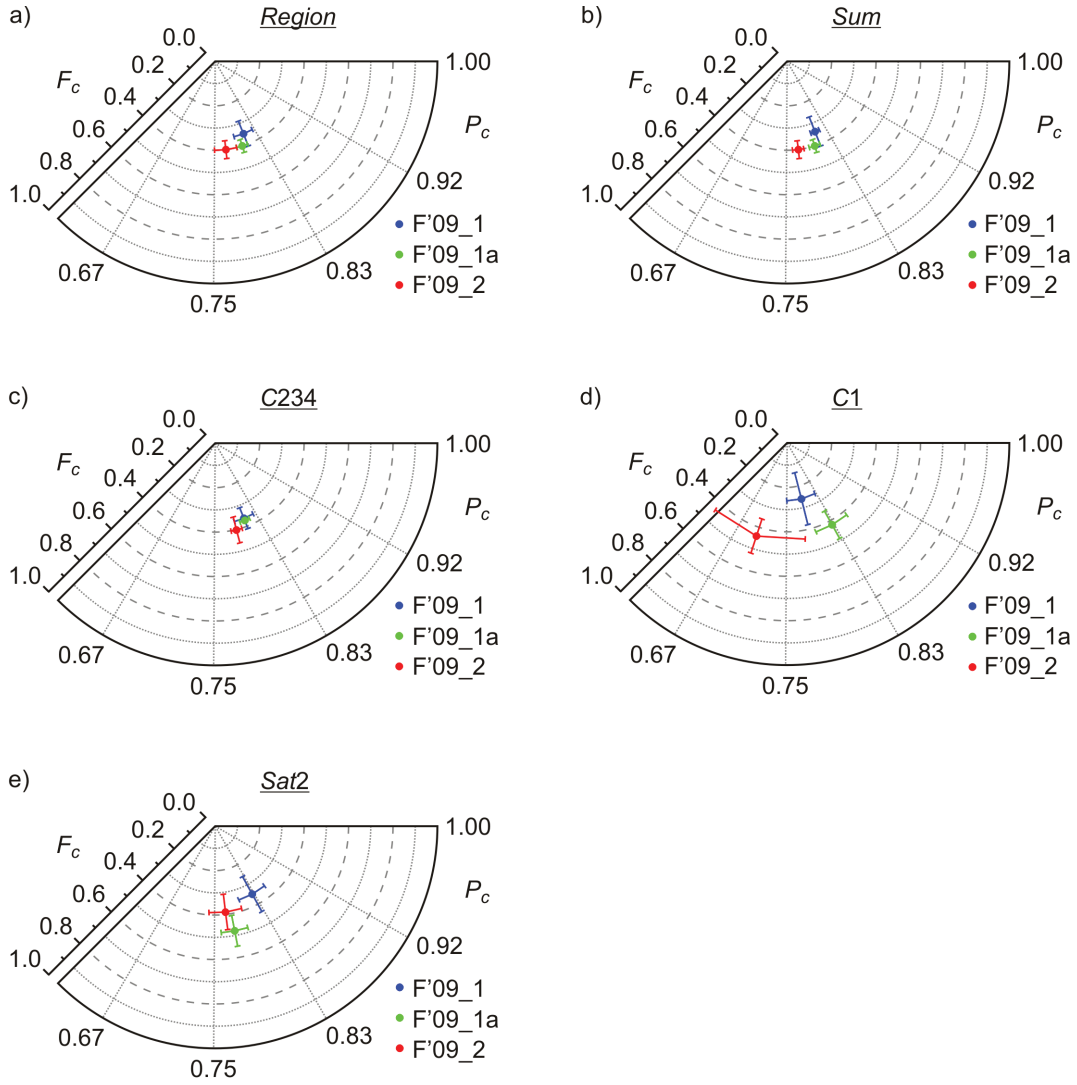


Figure 4.9: Argand diagram of *Region* (a), *Sum* (b), $C234$ (c), $C1$ (d) and $Sat2$ (e) structural parameters (P_c, F_c) for the three different preparations F'09_1 (blue), F'09_1a (green) and F'09_2 (red) (section 4.2.1).

and F'09_1a preparations, characterized by identical values within the errors. On the other hand, the $C1$ signal (Figure 4.9d) presents notably different structural parameters for each of the three preparations. In particular, the lower F_c of $C1$ in the F'09_1 preparation compared to F'09_1a preparation can be explained by the presence of approximately 30% of the second PTCDA layer above the first one (see section 4.2.1). However, along the lines, we would also expect a lower fraction of the corresponding $C234$ signal, while $C234$ of F'09_1 and F'09_1a preparations have the same coherent fraction, as shown in Figure 4.9c. This once more confirms the difficult interpretation of results from preparations with more than 1 ML PTCDA, since we have access only to average values, and cannot distinguish between carbon contribution from PTCDA molecules in different layers because of the small chem-

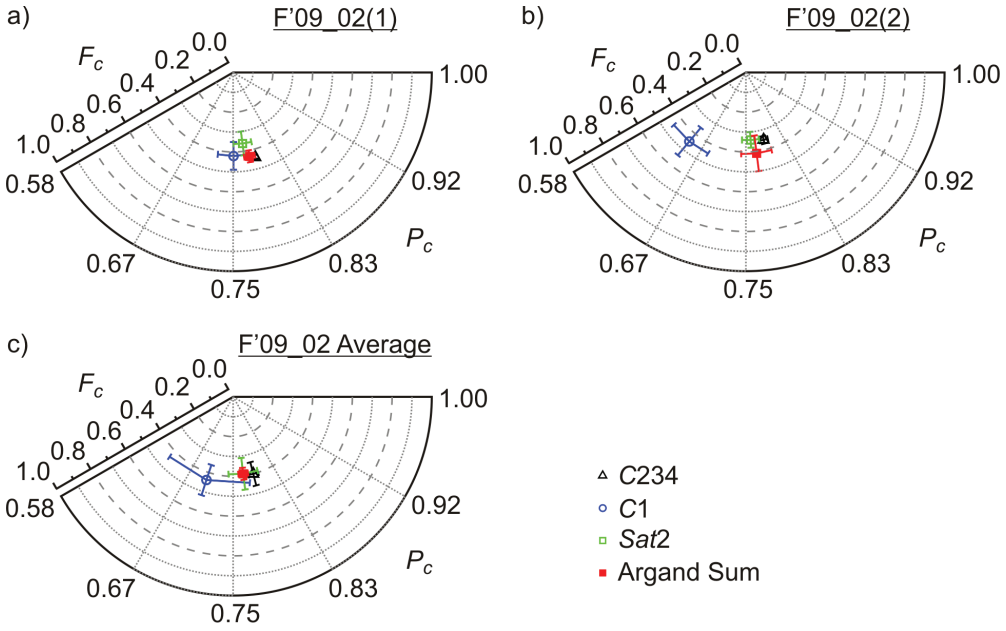


Figure 4.10: Argand diagram of $C234$ (empty black triangle), $C1$ (empty blue circle) and $Sat2$ (empty green square) structural parameters (P_c, F_c) relative to the two F'09_2 preparation data sets, and their average values. The sum (filled red square) $5 \times C234 + 1 \times C1$ is also reported in the Argand diagrams (a-c).

ical shifts of multilayer peaks and the small amount of molecules in the second layer.

We focus now on the F'09_2 preparation. The lower coherent position of $C1$ (Figure 4.9d) compared to $C234$ (Figure 4.9c) with the similar coherent fraction of approximately 40% is remarkable. The significantly larger error bar of the coherent position of $C1$, as compared to $C234$ and $Sat2$ (Figure 4.10c), follows from the approximately 10% difference in P_c of $C1$ between the two F'09_2 data sets, as shown in Figure 4.10a,b and in Figure 4.11e,f. We attribute this rather pronounced scatter of $C1$ data points of different data sets to the smaller signal-to-noise ratio compared to $C234$ and $Sat2$. However, we note that both F'09_2(1) and F'09_2(2) data sets provide carboxylic carbons ($C1$) below the perylene core, and due to the lack of further experiments that may lean towards results from one or the other data set, we will refer in the following to their average (Table 4.5 and Figure 4.10) for the discussion of PTCDA adsorption geometry (section 4.4.2).

$Sat2$ is introduced as a satellite component and indeed, it includes contributions from carbon atoms of the perylene core and of the functional group. In particular, Figure 4.10 reports the weighted Argand sum of $C234$ and $C1$ vectors, i.e.,

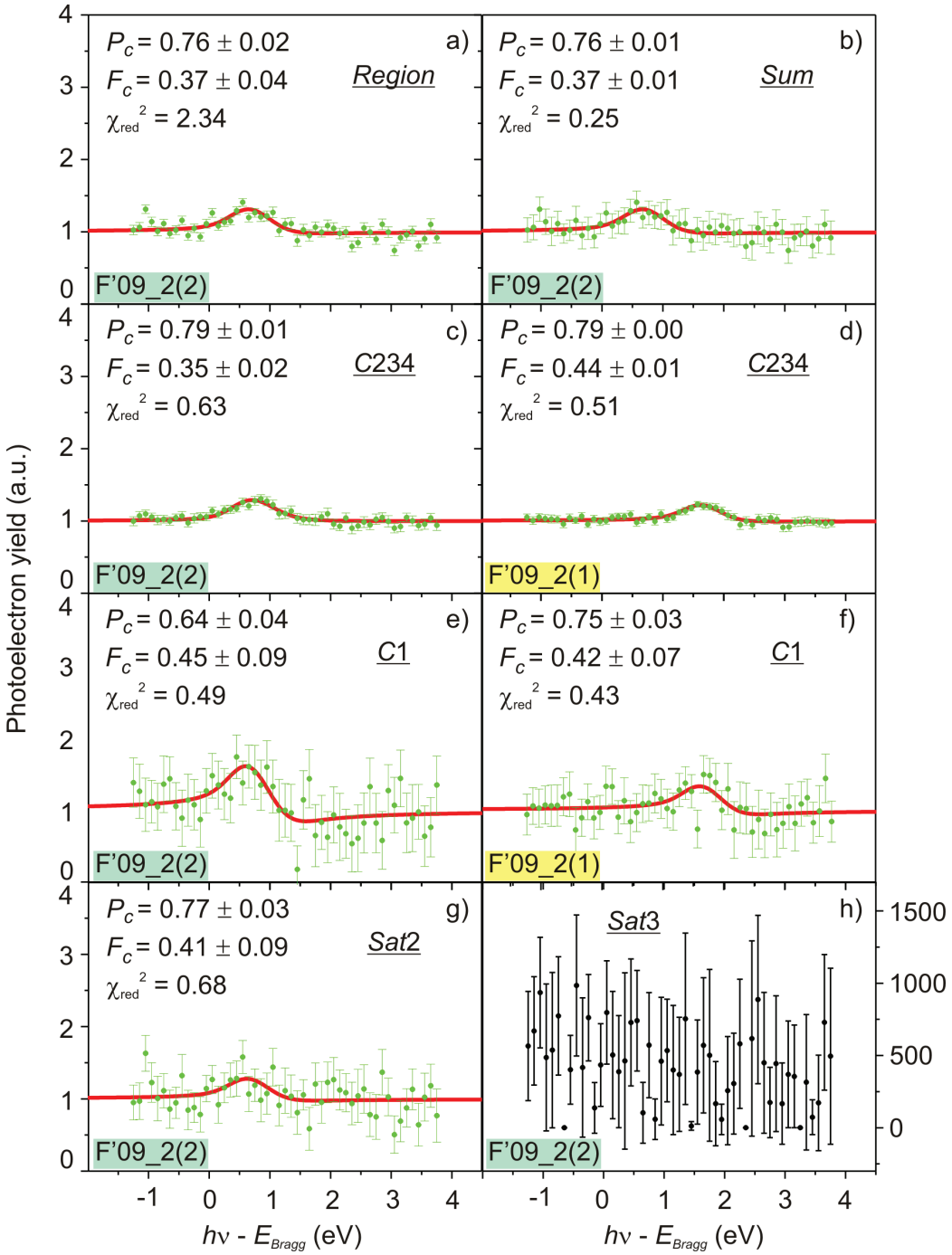


Figure 4.11: Photoelectron yield of *Region* (a), *Sum* (b), $C234$ (c), $C1$ (e), $Sat2$ (g) and $Sat3$ (h) signals (green dots and relative error bars) of F'09_2(2) preparation (labeled with green background), displayed as a function of the photon energy relative to the Bragg energy (4288.5 eV). Photoelectron yield of $C234$ (d), $C1$ (f) relative to F'09_2(1) (labeled with yellow background) preparation are also reported for comparison. Fitting curve (red) together with results of the fit: coherent position (P_c), coherent fraction (F_c), and reduced χ^2 are reported for profiles (a-g). $Sat3$ signal is not fitted and it is displayed in an arbitrary unit scale after normalizing each data point by the corresponding photon beam intensity.

$5 \times C234 + 1 \times C1$, and it shows that, while the agreement with $Sat2$ is not excellent for the single data sets (Figure 4.10a,b), it is considerably improved for the average values (Figure 4.10c). Therefore, the structural parameters of $Sat2$ suggest that the satellite component consists of photoemission contributions from both $C234$ and $C1$ carbons, in proportions which could not be more specifically determined. Finally, $Sat3$ due to the very low signal-to-noise ratio provides a very noisy electron yield profile (Figure 4.11h) which does not provide any structural information.

To conclude, we have shown that it is possible to differentiate PTCDA carbon atoms of the functional groups ($C1$) from those of the aromatic core ($C2$, $C3$, $C4$). In particular, $C1$ carbon atoms result at 2.45 ± 0.11 Å from the surface Bragg plane, approximately 0.14 Å lower than the carbon atoms of the aromatic core, located at 2.59 ± 0.01 Å. In section 4.4, adsorption geometry of PTCDA/Ag(110) will also be discussed in light of the position of oxygen atoms, to which we now turn in the next section 4.3.2.

Multicomponent model: NIXSW results

First Preparation

C1s	*Region*			*Sum*			$C234$			$C1$			$Sat2$		
data set	P_c	d_c	F_c	P_c	d_c	F_c	P_c	d_c	F_c	P_c	d_c	F_c	P_c	d_c	F_c
F'09_1(1)	0.82 (1)	2.63 (1)	0.30 (3)	0.82 (1)	2.63 (1)	0.29 (2)	0.82 (1)	2.63 (1)	0.32 (1)	0.81 (5)	2.61 (7)	0.17 (7)	0.83(3)	2.64(4)	0.28(5)
F'09_1(2)	0.79(1)	2.59(1)	0.39(3)	0.80(1)	2.60(1)	0.39(2)	0.79(0)	2.59(0)	0.39(1)	0.77(3)	2.56(4)	0.34(6)	0.82(2)	2.63(3)	0.41(6)
Average	0.81(2)	2.61(3)	0.35(6)	0.81(1)	2.62(2)	0.34(7)	0.81(2)	2.61(3)	0.36(5)	0.79(4)	2.59(6)	0.26(12)	0.83(3)	2.64(4)	0.35(9)
F'09_1a	0.80(1)	2.60(1)	0.40(3)	0.80(1)	2.60(1)	0.40(3)	0.81(1)	2.61(1)	0.37(1)	0.83(3)	2.64(4)	0.42(7)	0.78(2)	2.57(3)	0.48(7)

Second Preparation

C1s	*Region*			*Sum*			$C234$			$C1$			$Sat2$		
data set	P_c	d_c	F_c	P_c	d_c	F_c	P_c	d_c	F_c	P_c	d_c	F_c	P_c	d_c	F_c
F'09_2(1)	0.78(1)	2.57(1)	0.42(3)	0.78(1)	2.57(1)	0.44(1)	0.79(0)	2.59(0)	0.44(1)	0.75(3)	2.53(4)	0.42(7)	0.77(2)	2.56(3)	0.36(6)
F'09_2(2)	0.76(2)	2.54(3)	0.37(4)	0.76(1)	2.54(1)	0.35(2)	0.79(1)	2.59(1)	0.35(2)	0.64(4)	2.37(6)	0.45(9)	0.77(3)	2.56(4)	0.41(9)
Average	0.77(2)	2.56(2)	0.40(4)	0.77(1)	2.56(2)	0.40(4)	0.79(1)	2.59(1)	0.40(6)	0.70(8)	2.45(11)	0.44(8)	0.77(3)	2.56(4)	0.39(8)

Table 4.5: Coherent position (P_c), coherent fraction (F_c) and distance d_c (Å) from the surface Bragg plane, calculated as $(P_c+1)\times d_{\mathrm{Ag(110)}}$ (where $d_{\mathrm{Ag(110)}} = 1.44$ Å) are reported for *Region*, *Sum*, $C234$, $C1$ and $Sa2$ signals. The structural parameters (P_c, F_c, d_c) refer to the two data sets of F'09_1 preparation (plus corresponding average), to the data set of F'09_1a preparation and to the two data sets of F'09_2 preparation (plus corresponding average). Preparation F'09_1, F'09_1a and F'09_2 are discussed in section 4.2.1.

4.3.2 Oxygen

XPS fitting model

O1s PE spectrum, reported in Figure 4.12, consists of two peaks representing oxygen atoms in two different chemical environments. In particular, PTCDA contains oxygen atoms doubly bonded to one $C1$ carbon (Figure 4.7) and oxygen atoms singly bonded to two $C1$ carbons, called carboxylic and anhydride oxygens, respectively (Figure 4.1). Since PTCDA molecules have four carboxylic and two anhydride oxygen atoms (Figure 4.7), their ratio is carboxylic : anhydride = 2 : 1. On the basis of this simple argument, we can assign, in a first approximation, the photoemission peak at higher binding energy in Figure 4.12 to anhydride oxygens, while the peak at lower binding energies corresponds to carboxylic oxygens.

The O1s XPS fitting model is developed on the basis of the high statistics spectrum (section 4.2.2) of Figure 4.12. The PE spectrum is deconvoluted into four components, namely a $Main$ and a Sat component for each oxygen species. The $Main$ components represent the two most prominent O1s photoemission lines, $Carb$-$Main$ and An-$Main$, while the Sat components stand for their satellite features (section 4.2.4), $Carb$-Sat and An-Sat, respectively. According to our fitting model, $Carb$-Sat and An-Sat are at 2.17 eV and 2.20 eV higher binding energies respectively than their $Main$ peaks, with an area approximately 19% and 17% of the corresponding $Main$ peaks area. The FWHMs of both carboxylic and anhydride $Main$ components are fixed to be identical. Given these constraints, our O1s fitting model fulfills the stoichiometric ratio:

$$(Carb\text{-}Main + Carb\text{-}Sat) : (An\text{-}Main + An\text{-}Sat) = 2 : 1. \tag{4.8}$$

The background of the O1s spectrum is set to be linear with $AvWidth = 8$ (section 4.2.3). To prevent the noise from affecting the background definition, a larger $AvWidth$ and a smaller energy window compared to C1s spectra (section 4.3.1.1) are set.

Within their high resolution XPS study of multilayer PTCDA/Ag(111), Schöll et al.[82] also investigated the O1s photoemission line. In particular, the anhydride peak is found at approximately the same binding energy (533.40 eV) as in our XPS fitting model (see Table 4.6). In contrast, in our HS-XPS data, the carboxylic component is registered at approximately 0.75 eV lower binding energy than in the HR-XPS

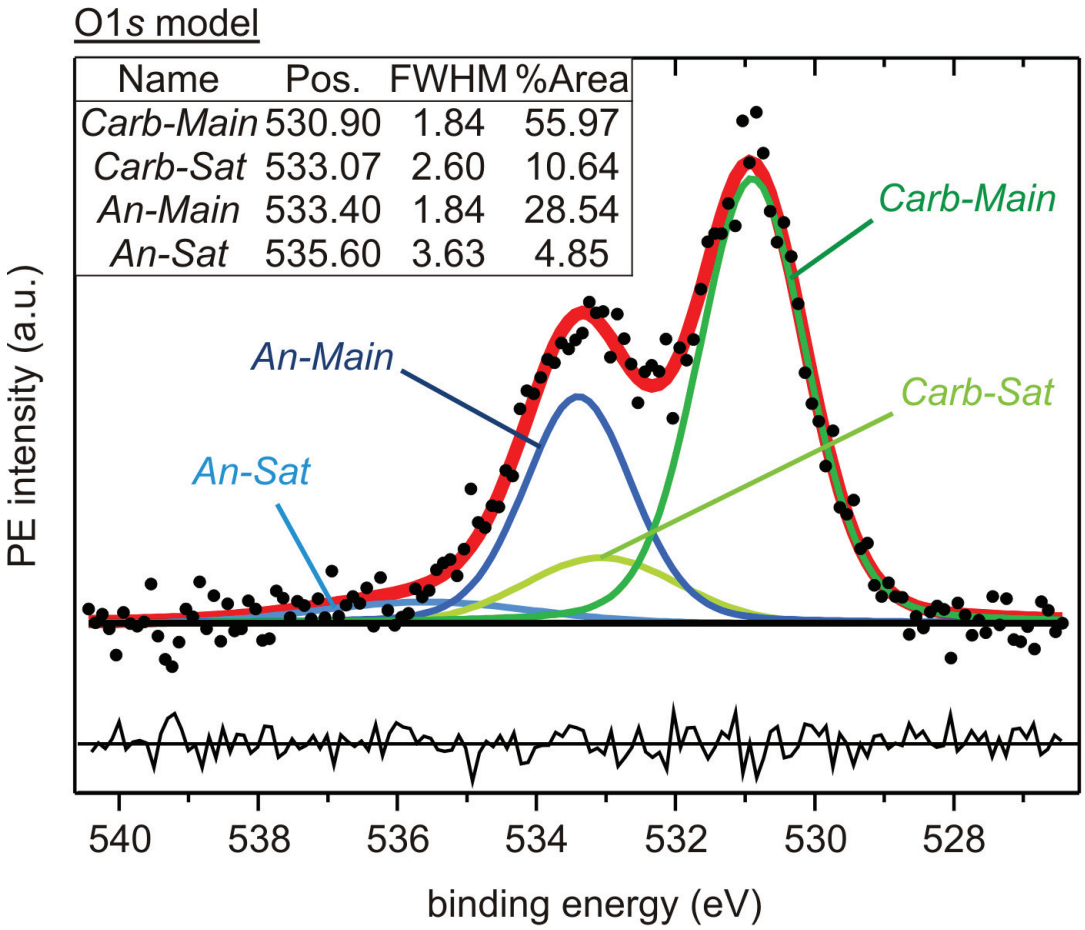


Figure 4.12: O1s HS-XPS (pass energy = 47 eV, energy window = 20 eV, energy step = 0.1 eV, time/step = 0.5 ms, repeats = 13) measured with $h\nu = 4280$ eV. Positions (eV), FWHM (eV), and relative areas (%) of the fitting components *Carb-Main* (dark green), *Carb-Sat* (light green), *An-Main* (dark blue) and *An-Sat* (light blue) are reported in the inset table. The envelope (*Sum*) is marked by the red line. The background is indicated by the straight black line. The residuals (thin black line below the spectrum) result from the subtraction of the sum of all fitting components (*Sum*, thick red line) and the whole spectrum (black dots).

O1*s*	HR-XPS[82]	HS-XPS	
component	E_b (eV)	E_b (eV)	ΔE_b
Carb-Main	531.65	530.90	−0.75
Carb-Sat	533.97	533.07	−0.90
An-Main	533.41	533.40	−0.01
An-Sat	537.72	535.60	−2.12

Table 4.6: Binding energies of *Carb-Main*, *Carb-Sat*, *An-Main* and *An-Sat* components of the O1*s* HR-XPS from the work of Schöll et al.[82] and our HS-XPS fitting model (Figure 4.12). ΔE_b is the difference of binding energies between HS-XPS and HR-XPS components.

model. This differential shift of the carboxylic O1*s* line suggests a more pronounced modification of the carboxylic oxygen chemical state as compared to the anhydride state upon direct contact of PTCDA with the Ag(110) surface. This preliminary conclusion will be confirmed in the discussion of section 4.4.2. However, we should mention here that both carboxylic and anhydride oxygens deviate from the plane of the molecule due to interaction with the Ag substrate. This makes the interpretation of the binding energy shifts more difficult, because they reflect the superposition of several contributions: a rather strong interaction of the whole anhydride group with the surface, resulting in a rearrangement of the molecular electronic structure; the screening of the core electrons from the metallic substrate; the very different intermolecular interactions for a PTCDA molecule in the submonolayer compared to the multilayer case. The same qualitative argument is invoked to rationalize the binding energy shifts of the satellite peaks corresponding to the carboxylic and anhydride main components. In fact, as already seen in the C1*s* spectrum (section 4.3.1.2), for O1*s* spectrum as well, the satellite structure significantly deviates from the high-resolution spectrum measured on a PTCDA thin film[82] (Table 4.6).

Photoelectron yield

The O1*s* XPS fitting model described above is applied to the three data sets of the F'09_2 preparation (section 4.2.1), keeping positions and FWHM of each component fixed, and also fixing the area of *Sat* peaks relative to the corresponding *Main* peaks. As a consequence, we will consider the sum of the carboxylic components $Carb\text{-}Main + Carb\text{-}Sat$ $(= Carb)$ and the sum of the anhydride components $An\text{-}Main + An\text{-}Sat$ $(= An)$. Moreover, we will analyze two more signals: *Region* (= spectrum − background) and Sum $(= Carb + An)$.

The structural parameters of the signals *Region*, *Sum*, *Carb* and *An* are summarized in Table 4.7. If we compare structural parameters of *Region* and *Sum*, we see that *Sum* always presents a slightly larger coherent position and coherent fraction than *Region*. This may be an indication of systematic errors in our fitting model. However, since the percentage difference is lower than 9% and within the error bars, the agreement between *Region* and *Sum* results is considered to be satisfactory.

The differential analysis of *Carb* and *An* provides carboxylic oxygen atoms at 2.32±0.05 Å with a coherent fraction of 21%, and anhydride oxygens at 2.41±0.06 Å

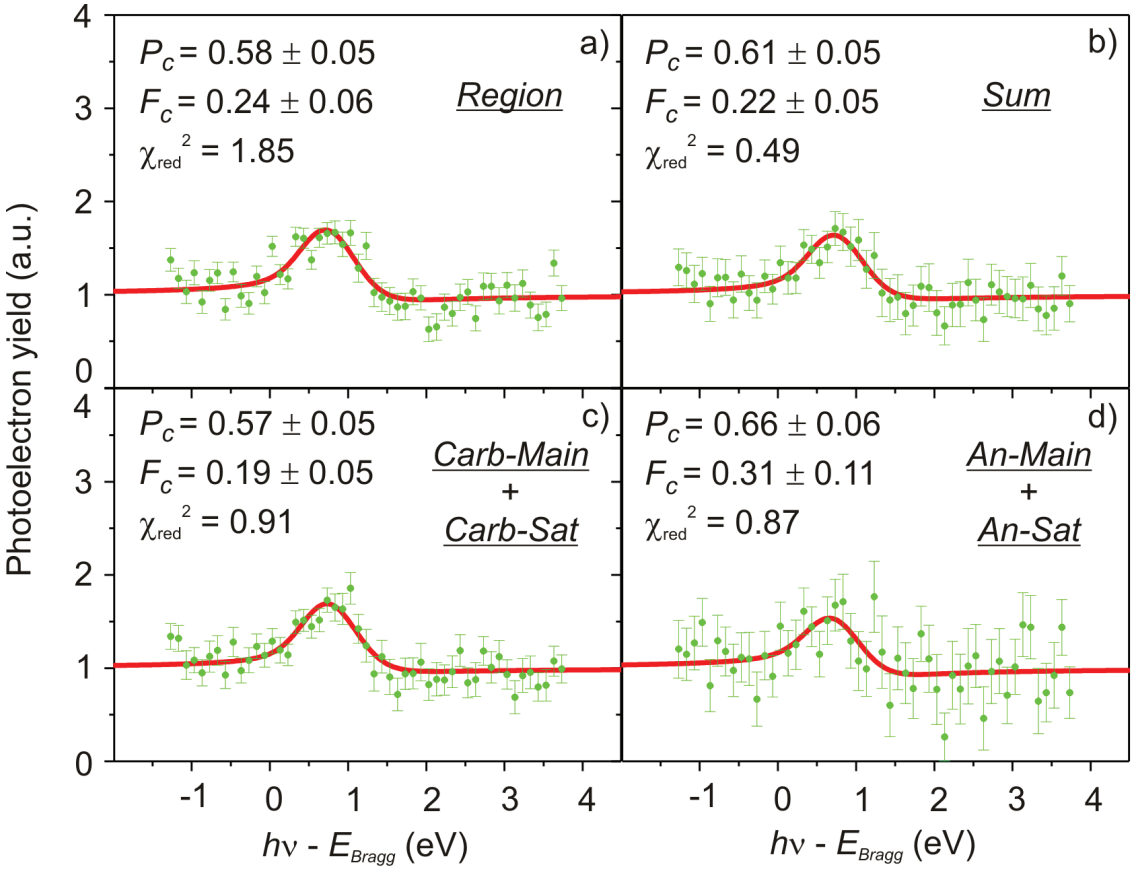


Figure 4.13: Photoelectron yield of *Region* (a), *Sum* (b), *Carb-Main*+*Carb-Sat* (c) and *An-Main*+*An-Sat* (d) signals (green dots and relative error bars) of data set F'09_2(3) (Table 4.7), displayed as a function of the photon energy relative to the Bragg energy (4288.5 eV). Fitting curve (red) together with results of the fit, coherent position (P_c), coherent fraction (F_c), and reduced χ^2, are also reported for each profile.

with a coherent fraction of 34%. Interestingly, carboxylic oxygens are approximately 0.10 Å closer to the surface than the anhydride ones, and with a substantially lower coherent fraction, as displayed in the Argand diagram in Figure 4.14.

To prove the self-consistency of the fitting model used, the Argand sum $2 \times Carb + 1 \times An$ of carboxylic and anhydride structural parameters is calculated and compared to the *Sum* signal. From the overlap of the Argand sum (green "+" symbol) and the *Sum* (black triangle) vectors in the Argand diagram (Figure 4.14), we conclude that our fitting model is self-consistent and the photoelectron yield of the whole spectrum is perfectly described by the superposition of carboxylic and anhydride signals according to the stoichiometry of the PTCDA molecule (equation 4.8). Both carbon and oxygen NIXSW results will be discussed in the next section 4.4.

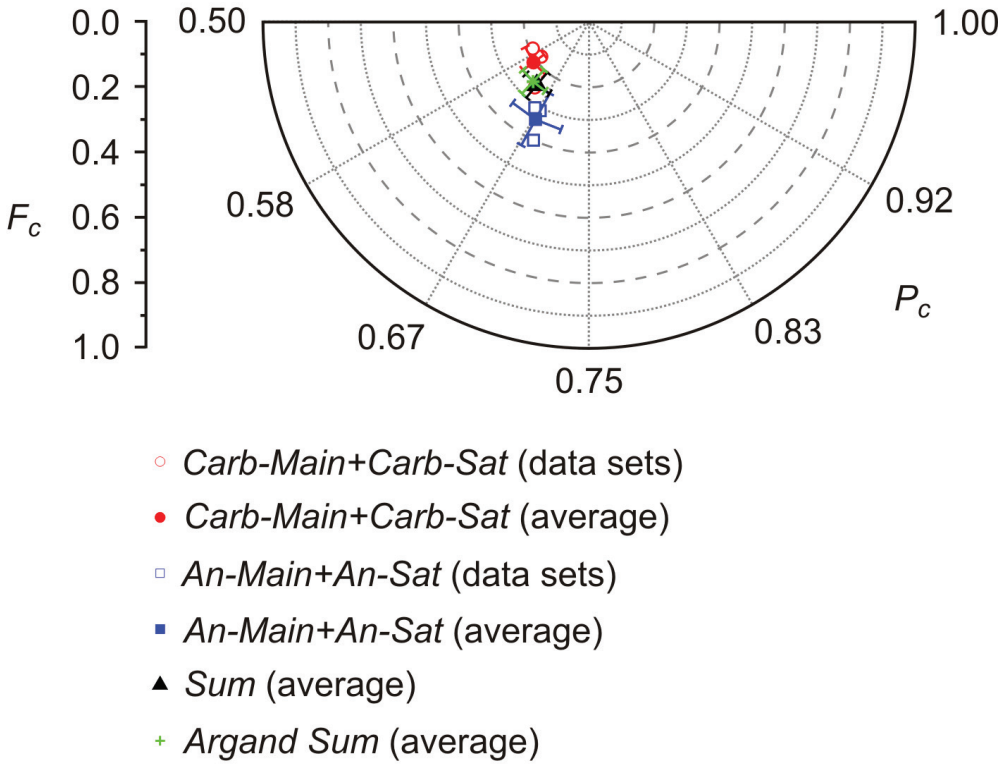


Figure 4.14: Argand diagram of $Carb\text{-}Main{+}Carb\text{-}Sat$ (= $Carb$) data sets (open red circles) and average (filled red circle), $An\text{-}Main{+}An\text{-}Sat$ (= An) data sets (open blue squares) and average (filled blue square), Sum average (filled black triangle) and Argand sum (green "+" symbol) = $2 \times Carb + 1 \times An$.

O1s model: NIXSW results												
Second Preparation												
O1s	*Region*			*Sum*			*Carb-Main+Carb-Sat*			*An-Main+An-Sat*		
data set	P_c	d_c	F_c	P_c	d_c	F_c	P_c	d_c	F_c	P_c	d_c	F_c
F'09_2(1)	0.59(4)	2.30(6)	0.21(4)	0.64(3)	2.37(4)	0.22(3)	0.60(4)	2.31(6)	0.18(4)	0.67(5)	2.41(7)	0.31(10)
F'09_2(2)	0.62(3)	2.34(4)	0.23(4)	0.66(2)	2.40(3)	0.30(3)	0.64(2)	2.37(3)	0.26(3)	0.68(2)	2.43(3)	0.40(6)
F'09_2(3)	0.58(5)	2.28(7)	0.24(6)	0.61(5)	2.33(7)	0.22(5)	0.57(5)	2.27(7)	0.19(5)	0.66(6)	2.40(9)	0.31(11)
Average	0.60(4)	2.31(6)	0.23(5)	0.64(3)	2.36(5)	0.25(5)	0.60(4)	2.32(5)	0.21(4)	0.67(4)	2.41(6)	0.34(9)

Table 4.7: Coherent position (P_c), coherent fraction (F_c) and distance d_c (Å) from the surface Bragg plane, calculated as $(P_c+1)\times d_{\mathrm{Ag(110)}}$ (where $d_{\mathrm{Ag(110)}}=1.44$ Å) are reported for *Region*, *Sum*, *Carb-Main+Carb-Sat* and *An-Main+An-Sat* signals. The structural parameters (P_c, F_c, d_c) refer to the three data sets of F'09_2 preparation (section 4.2.1), plus the corresponding average values.

4.4 Discussion

The present section is subdivided in two parts. In the first part, the relatively low coherent fraction of PTCDA is discussed and several interpretations are proposed. In the second part, we discuss the PTCDA adsorption geometry on the Ag(110) surface in the context of previous theoretical and experimental results.

4.4.1 Interpretation of PTCDA coherent fraction

Before discussing the adsorption geometry of PTCDA/Ag(110), we present several possible interpretations of the relatively low coherent fractions ($\lesssim 40\%$) of carbon and oxygen atoms summarized in Table 4.8. As already mentioned in section 2.5, the coherent fraction F_c can only take values between 0 and 1; low values can arise from dynamic (e.g., thermal vibrations) or static disorder, or from multiple site occupation.

Furthermore, it should be noted that since the coherent fraction is related to the scatter of atomic vertical positions between two consecutive extended Bragg planes, its value scales with the distance d_{hkl} between two Bragg planes, which in turn depends on the orientation (hkl) of the metal substrate and on the substrate element itself. As an example, the three low Miller indices Ag surfaces (111), (100) and (110) are considered. The corresponding distances between Bragg planes are $d_{\mathrm{Ag(111)}} = 2.36$ Å, $d_{\mathrm{Ag(200)}} = 2.04$ Å and $d_{\mathrm{Ag(220)}} = 1.44$ Å. The same absolute height difference of 0.20 Å between two atoms results in different F_c for the three Ag surfaces. In particular, the corresponding coherent fraction decreases, compared to the case in which both atoms have the same vertical position, are 3%, 5% and 10% on Ag(111), Ag(100) and Ag(110), respectively. Therefore, given the same vertical scatter of adsorbate atoms, the smaller d_{hkl}, the larger the percentage decrease of F_c.

PTCDA/Ag(110)		
	d_c	F_c
Perylene-C	2.59 (1)	0.40 (6)
Carboxylic-C	2.45 (11)	0.44 (2)
Anhydride-O	2.41 (6)	0.34 (9)
Carboxylic-O	2.32 (5)	0.21 (4)

Table 4.8: Summary of adsorption height d_c and coherent fraction F_c of PTCDA carbon and oxygen atoms.

Having defined the general framework for interpreting the F_c of adsorbates on the Ag(110) surface compared to other substrates, we now discuss several possible causes of a coherent fraction reduction for PTCDA/Ag(110).

Effect of moleuclar vibrations on F_c

Molecular vibrations, mentioned above, can affect NIXSW measurements because the photoemission process and the associated electronic relaxation occur on a time scale of 10^{-15} s, while nuclear motion relative to vibrations is approximately two orders of magnitude slower, in the range of $\sim 10^{-13}$ s. The Born-Oppenheimer approximation is thus valid for the XPS and NIXSW experiments.[84] However, molecular vibrations can only partially explain the significant reduction in the coherent fraction.[85] In fact, it can be easily calculated that an atomic vertical displacement of ± 0.10 Å from its equilibrium position, adsorbed on the Ag(110) surface, corresponds to a decrease in F_c of only 10% (see above). This suggests that other phenomena contribute to a further increase in the vertical disorder in the PTCDA submonolayer adsorbed on the Ag(110) surface. In particular, we propose that diffusion of the molecules on the metal surface may substantially decrease the overall coherent fraction of the system. Arguments supporting of our conjecture are discussed below.

Effect of molecular diffusion on F_c

A room temperature STM study of PTCDA/Ag(100)[86] suggested the presence of a disordered 2D PTCDA gas phase in equilibrium with PTCDA islands, based on the detection of a significant "noise" (pulses) in the tunneling current that is not present on the bare Ag(100) sample. A further investigation of the temporal width of the pulses in the tunneling current measured for a stationary scanning tunneling microscope tip on PTCDA/Ag(100)[87] allowed the PTCDA diffusion constant of approximately 4.0×10^3 nm^2 s^{-1} to be determined. In a related study, Ikonomov et al.[88] also concluded that the decay of PTCDA islands on Ag(100) is diffusion-limited, i.e., the diffusion rate of molecules from or to the islands is smaller than the attachment-detachment rate. As a consequence, molecules distribute only slowly on the surface and with a nonconstant density. In particular, the coverages of molecules between the PTCDA islands were measured between $\Theta = 0.0004$ and 0.02, with higher coverages near an island. These values correspond to coverages between 0.4%

and 20% of the overall PTCDA coverage of that experiment (0.10 ML), and to molecular densities between $\rho = 3.1 \times 10^{-4}$ nm^{-2} and $\rho = 3.1 \times 10^{-4}$ nm^{-2}. Therefore, a significant amount of molecules can be in an undefined position with unknown adsorption geometry diffusing on the surface.

An analogous island decay mechanism can be expected for PTCDA/Ag(110) due to the similarities with PTCDA/Ag(100). In fact, on the (110) surface as well, PTCDA molecules assemble in islands commensurate with the substrate and located far away from the step edges. Moreover, the intermolecular interaction for PTCDA/Ag(100) is attributed to both electrostatic and substrate-mediated contributions. A similar scenario can be predicted for PTCDA/Ag(110) with an even stronger substrate-mediated component and weaker electrostatic intermolecular interaction due to the head-to-head arrangement of molecules in the brickwall phase[68] (see Figure 4.18), in contrast to the T-shape superstructure of PTCDA/Ag(100)[86] with the negatively charged functional groups facing the positively charged perylene side of the molecule. From these qualitative arguments, we can therefore expect for PTCDA islands on Ag(110) surface a diffusion-limited decay with a 2D gas phase between the islands. The experimental evidence for this is given by an STM study of submonolayer PTCDA/Ag(110)[89] which shows static molecular islands at 50 K, while at 295 K, repeated STM images of the same surface area reveal the growth of larger islands at the expense of the smaller ones. This significant rearrangement of islands on the surface implies the presence of a 2D gas of mobile molecules at 295 K. Furthermore, the presence of occasional streaks of apparent height equal to that of PTCDA islands is observed with a larger density in the proximity of an island than on open terraces. This evidence strongly supports the diffusion-limited decay of PTCDA islands[88] on Ag(110) as well.

The presence of PTCDA in 2D gas phase diffusing on the surface can rationalize the relatively low coherent fraction of PTCDA/Ag(110). In fact, if molecules diffusing on the surface assume different vertical positions so that their average F_c is zero, then they represent the incoherent portion of the molecular layer, which in turn lowers the overall coherent fraction of the system. Therefore, we can interpret the adsorption heights d_c reported in Table 4.8 as the distances of atoms (forming PTCDA molecules) from the surface Bragg plane and interpret the coherent fraction as the fraction of molecules coherently adsorbed on the surface, while diffusing molecules constitute the incoherent fraction of the layer.

In light of the arguments presented above, we propose another interpretation for the decrease in the coherent fraction of CuPc/Ag(111), going from low temperatures (140-153 K) to room temperature (300 K), measured by NIXSW, and attributed by the authors[85] in part to out-of-plane vibrational modes and in part to static disorder due to a weaker interaction with the surface at higher temperatures. The F_c decrease is also found to be larger for smaller CuPc coverages. This general F_c trend can be explained by the fact that the higher the sample temperature, the larger the energy for molecular diffusion, and simultaneously the lower the coverage, the larger the surface areas for molecular diffusion. Therefore, an interesting correlation between the sample temperature, the molecular coverage and F_c seems to occur. This interpretation is corroborated by the measurement of the CuPc diffusion constant (1.7×10^4 nm^2 s^{-1})[87] on Ag(100), which is approximately four times larger than that of PTCDA on the same substrate[87] (see above). On the more closed-packed Ag(111) surface, the weaker interaction with the substrate should favor an even larger diffusion that can explain the F_c trend measured by NIXSW.

In order to further investigate the correlation between diffusion and the coherent fraction of molecular adsorbates, we plan to perform an experiment to monitor the structural parameters (P_c, F_c) of PTCDA/Ag(110) (as well as on other substrates), keeping the coverage of PTCDA fixed and changing the sample temperature. In this way, we expect to control the 2D molecular gas phase present at the surface[89] in order to systematically study the effect of molecular diffusion on the structural parameters, especially the coherent fraction, and learn about the intermolecular binding energy as well.

4.4.2 Adsorption geometry of PTCDA on Ag(110)

After having discussed the possible reasons behind the relatively low coherent fraction, we focus on the vertical positions of PTCDA carbon and oxygen atoms with respect to the Ag(110) surface (section 4.3), illustrated in Figure 4.15. In particular, the arc-like molecular geometry with the functional groups bent towards the surface is remarkable (Figure 4.15a). In fact, carboxylic [anhydride] oxygen atoms (red [orange] circles) are at 2.32 Å [2.41 Å] from the surface Bragg plane, i.e., 0.27 Å [0.18 Å] below the carbon backbone of PTCDA (Figure 4.15b). In agreement with a smaller adsorption height of the oxygen atoms, the carbon atoms of the functional groups (light green) are also located 0.14 Å lower than the PTCDA perylene core.

In order to discuss the interaction of PTCDA molecules with the Ag(110) surface, interatomic distances between molecular atoms and Ag surface atoms represent more interesting parameters than the atomic vertical positions presented above, because they allow a direct comparison with common bond lengths. To determine the interatomic distances between atoms of PTCDA and Ag surface atoms, it is necessary to know the lateral position of the adsorbed molecule with respect to the substrate. To this end, STM studies of submonolayer PTCDA/Ag(110)[68,69] reveal the orientation of PTCDA molecules within the brickwall unit cell and their position relative to the Ag substrate. In particular, PTCDA molecules are oriented with the long axis parallel to the [001] direction and their centers are located between the closed-packed Ag rows, as shown in Figure 4.16b. Due to the symmetry of adsorption site of PTCDA on Ag(110), we can limit the calculation of interatomic distances d_i between atoms of PTCDA and Ag nearest neighbors to one fourth of the molecule.

Interatomic distances of carbon [d_i (C-Ag)] and oxygen [d_i (O-Ag)] atoms from the nearest underlying Ag surface atom are reported in Figure 4.16c, and are estimated based on the atomic vertical positions resulting from NIXSW (Figure 4.15), on the atomic lateral position of the gas-phase geometry, calculated with the Gaussian03 package[90] (B3LYP functional, LANL2DZ basis set), and under the assumption that the topmost Ag layer does not relax (section 5.2.2.4). Interestingly, both carboxylic and anhydride oxygen atoms have the same distance d_i = 2.45 Å from the nearest

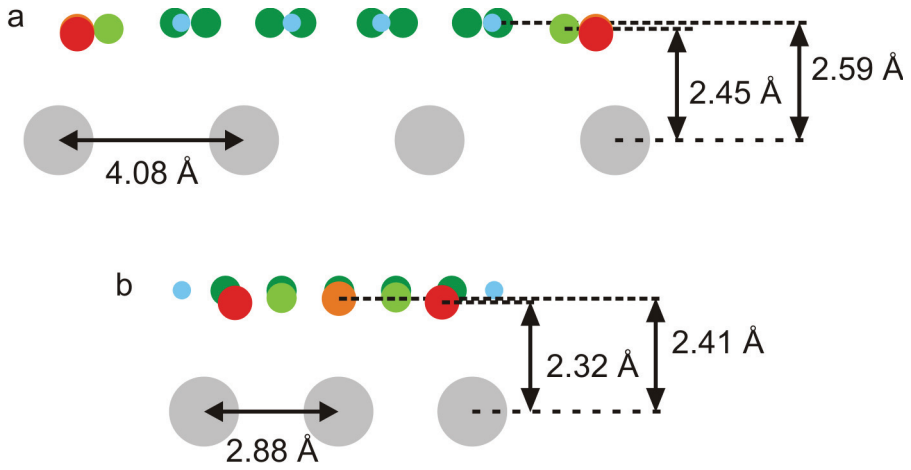
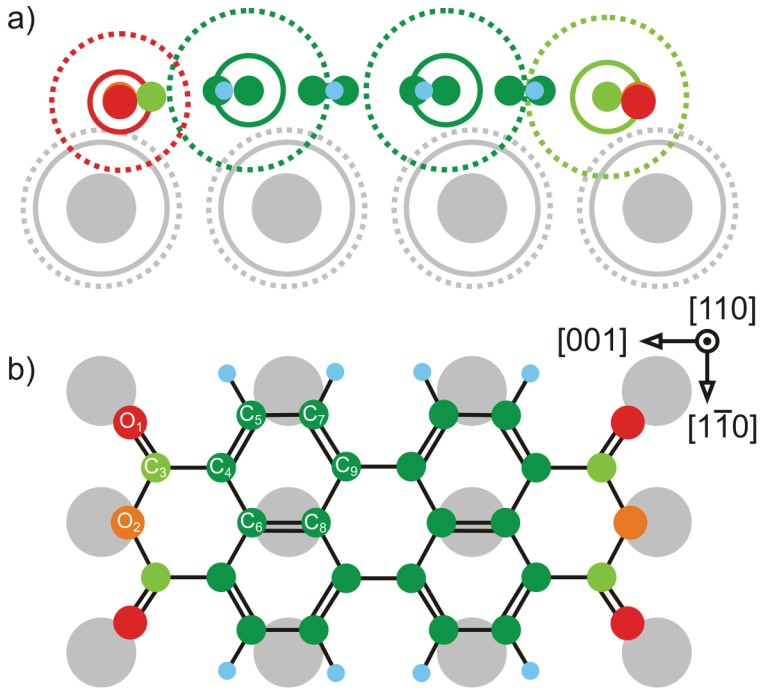


Figure 4.15: (a) side-view representation, along the short molecular axis, of PTCDA adsorbed on the topmost Ag(110) layer. Distances of carboxylic and anhydride oxygen atoms from the surface are explicitly given. (b) side-view representation, along the long molecular axis, of PTCDA adsorbed on the topmost Ag(110) layer. Distances of perylene core and end group carbon atoms from the surface are explicitly given. Interatomic distance between two adjacent Ag atoms is reported for both side-views (a,b).



c)

X	d_i(X-Ag)
O_1	2.45
O_2	2.45
C_3	2.95
C_4	3.24
C_5	2.76
C_6	2.72
C_7	2.69
C_8	2.66
C_9	3.16
$\overline{d_i(\text{O-Ag})}$	2.45
$\overline{d_i(\text{C-Ag})}$	2.92

Figure 4.16: (a): side-view representation of PTCDA/Ag(110) along the PTCDA long axis. Solid lines indicate covalent radii (C: 0.76 Å; O: 0.66 Å; Ag: 1.45 Å), dashed lines indicate vdW radii (C: 1.75 Å; O: 1.50 Å; Ag: 1.72 Å), filled circles indicate the position of the atoms. Color code: green → carbon; red → oxygen; turquoise → hydrogen; gray → silver. (b): top-view of PTCDA/Ag(110), relative lateral position of PTCDA results from calculations.[67] (c): table of interatomic distances between the specified element (numbered in panel b) and the closest underlying Ag atom, including the average among all oxygen atoms and among all carbon atoms.

X	$r^{\text{X}}_{cov} + r^{\text{Ag}}_{cov}$	$r^{\text{X}}_{vdW} + r^{\text{Ag}}_{vdW}$	$\overline{d_i(\text{X-Ag})}$	% of $(r^{\text{X}}_{cov} + r^{\text{Ag}}_{cov})$	% of $(r^{\text{X}}_{vdW} + r^{\text{Ag}}_{vdW})$
C	2.21	3.47	2.92	132	84
O	2.11	3.22	2.45	116	76

Table 4.9: Sum of covalent radii[91] $r^{\text{O}}_{cov} + r^{\text{Ag}}_{cov}$, sum of vdW radii[92] $r^{\text{O}}_{vdW} + r^{\text{Ag}}_{vdW}$ and average interatomic distances $\overline{d_i(\text{C-Ag})}$ and $\overline{d_i(\text{O-Ag})}$ for PTCDA/Ag(110) are reported, followed by the percentage of the interatomic distances with respect to the sum of covalent radii and the sum of vdW radii.

Ag atom, despite their different chemical environment within the molecule. This suggests a rather strong interaction of PTCDA oxygen atoms with Ag surface atoms, in effect bending the C-backbone and pulling the carbon atoms of the functional groups (carboxylic) closer to the surface than the perylene core.

For a better assessment of the interaction between PTCDA molecules and the Ag substrate, it is useful to compare the average interatomic distances $\overline{d_i(\text{X-Ag})}$ with the sum of covalent radii $r^{\text{X}}_{cov} + r^{\text{Ag}}_{cov}$ and the sum of vdW radii $r^{\text{X}}_{vdW} + r^{\text{Ag}}_{vdW}$, where

	Exp	MP2-Ag_{32} [67]	Δ(Theo-Exp)
C-perylene	2.59 (1)	2.69	4%
C-carboxylic	2.45 (11)	2.64	8%
ΔC	0.14	0.05	
O-carboxylic	2.32 (5)	2.50	8%
O-anhydride	2.41 (6)	2.63	9%
ΔO	0.09	0.13	

Table 4.10: Distances of perylene and carboxylic carbon atoms, carboxylic and anhydride oxygen atoms from the topmost non-relaxed Ag layer obtained from MP2 calculations by Abbasi and Scholtz[67] and NIXSW experiments (our study). Errors of experimental values are reported in brackets. Relative distance of different carbon species (ΔC) and of different oxygen species (ΔO) are also provided, together with the difference in percentage between theoretical and experimental results.

X represents either carbon (C) or oxygen (O) atoms. From the values reported in Table 4.9 we note that the average interatomic distance $\overline{d_i(\text{O-Ag})} = 2.45$ Å is only 16% (0.34 Å) larger than the sum of covalent radii $r_{cov}^{\text{O}} + r_{cov}^{\text{Ag}} = 2.11$ Å. At the same time, the average interatomic distance $\overline{d_i(\text{C-Ag})} = 2.92$ Å is 16% (0.56 Å) smaller than the sum of vdW radii $r_{vdW}^{\text{X}} + r_{vdW}^{\text{Ag}} = 3.47$ Å. In summary, on the one hand, the distance of PTCDA oxygen atoms from Ag atoms is slightly above the lower limit of the covalent bond length, and on the other hand, the average distance of PTCDA carbon atoms from Ag atoms is slightly below the upper limit of the vdW interaction length, as shown in Figure 4.16a. Both facts are consistent with a significant chemical contribution to the interaction between PTCDA molecule and Ag(110) substrate, which brings the perylene core well below the vdW interaction limit and bends the molecular plane in order to favor the interaction of the functional groups oxygen atoms with the Ag surface atoms underneath.

The general trend of PTCDA/Ag(110) adsorption heights resulting from NIXSW experiments is well reproduced by second-order Møller-Plesset theoretical calculations (MP2) of a single PTCDA molecule adsorbed on a two-layer slab of 32 Ag atoms.[67] Theoretical and experimental results are reported and compared in Table 4.10. In particular, the perylene core, i.e., the larger portion of the molecule, is predicted by MP2 calculations to be only 4% higher than experimental results. This represents good agreement if we consider that, due to the computationally expensive calculations, only a significantly reduced substrate slab is taken into account. In contrast, MP2 theory overestimates the adsorption height of the anhydride functional groups, i.e., oxygen atoms and carboxylic carbons, by approximately 0.20 Å, about 8% more than experimental values (Table 4.10). Although the calculations predict

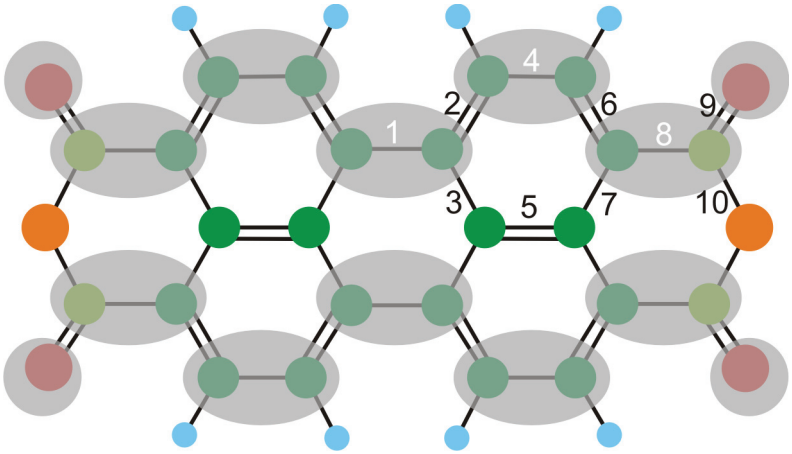


Figure 4.17: Schematic representation of PTCDA LUMO (gray-shaded circles) based on DFT calculations by Abbasi and Scholtz[67]. Some specific bonds to which we will refer in the text are labeled by numbers.

a more flattened adsorption geometry as compared to the experimental one, the main features of the adsorbed molecules, i.e., the downward bending of the molecule with C-carboxylic beneath C-perylene and O-carboxylic beneath O-anhydride, are correctly reproduced. Therefore, we consider the agreement between the experiment and the simulated geometry of PTCDA chemisorbed on Ag(110) to be satisfactory and now discuss the corresponding electronic orbitals.

According to MP2 calculations,[67] the former lowest unoccupied molecular orbital (LUMO) of the free molecule is occupied by two electrons for PTCDA/Ag(110). However, the net charge on the entire molecule is approximately $q = -0.41\,\mathrm{e}$. This indicates the existence of a compensating mechanism, transferring electronic charge back into the substrate. In fact, the analysis of the molecular orbitals assigned the reduction of the negative net charge of PTCDA to the hybridization of both LUMO and the highest occupied molecular orbital (HOMO) with the substrate orbitals. The complete filling of the LUMO and the presence of new hybrid orbitals, involving at least LUMO, HOMO and HOMO-1 is experimentally proven by UPS measurements of monolayer PTCDA/Ag(110).[75] Moreover, the back-donation of electronic charge to the substrate can be also deduced by the small (+0.08 eV) work function change of Ag(110) upon PTCDA deposition (see section 5.5.2), which is incompatible with a net charge of two electrons on the molecule. Furthermore, the additional negative net charge on the molecule induces a positive image charge in the substrate and the resulting Coulomb interaction contributes to the overall binding energy of PTCDA/Ag(110).

A direct consequence of the filling of the LUMO is the shortening of those bond lengths where LUMO has maxima (1,4,8 in Figure 4.17), with the consequence of an increased bond order (strengthening the double bond character), and the elongation of the bond length, where LUMO has anti-bonding character (2,6,9 in Figure 4.17), with the consequence of a decreased bond order (weakening the double bond character).[93] In particular, since the LUMO of PTCDA, shown schematically in Figure 4.17, has a node at the C=O double bond (9),[67] we would therefore expect an elongation of this bond length compared to the gas-phase molecule. As a consequence, the weakening of C=O double bond is in perfect agreement with a chemical interaction between carboxylic oxygens and Ag atoms, as follows from the estimation of interatomic distances (see above). Furthermore, it was noted by Rohlfing et al.[93] that in the case of a full σ bond between O and Ag, the double bond C=O would turn into a single bond C−O and the C−C bond character of the entire molecule would change, causing the same effect of the bond length variation induced by LUMO filling. In other words, the consequences of the LUMO filling observed by UPS measurements[75] and predicted by ab initio calculations[67] are consistent with and even enhanced by the formation of a O−Ag bond bearing significant chemical character. Besides the chemical interaction, so far discussed, oxygen atoms also feel the Coulomb attraction between the partial negative charges carried by them and the positive image charge of the Ag atom below.[67]

Moreover, in light of the present NIXSW results we can unambiguously attribute the shift of the C=O stretch mode[72,73] in the submonolayer PTCDA/Ag(110), as compared to the PTCDA multilayer, to a weaker double bond character resulting from the elongation of the bond length upon LUMO filling and bonding of carboxylic O to the Ag surface. An interaction of carboxylic oxygens with Ag atoms was already proposed for PTCDA/Ag(111).[2,93] From our NIXSW data on PTCDA/Ag(110), we can conclude that not only the carboxylic oxygens but rather the whole anhydride function group has a chemical interaction with the Ag surface. In fact, in contrast to PTCDA/Ag(111), where the anhydride oxygen is above the molecular plane, on the Ag(110) surface the anhydride oxygen moves below the carbon backbone and is found at the same interatomic distance (2.45 Å) from the nearest Ag atom, just like the carboxylic oxygens. This is a clear indication of the rather strong chemical and also electrostatic interaction involving all the three oxygen atoms of the PTCDA functional groups.

Furthermore, the bonding of the anhydride groups to the substrate tends to pull

the whole molecule closer to the surface into the Pauli repulsion regime. As a result of the delicate balance between the attraction of the functional groups to the surface, on the one hand, and the repulsion among filled molecular and substrate orbitals on the other hand, the PTCDA molecule adopts a downward bent arc-like geometry. An interesting indication of this distortion comes from the comparison between the coherent fraction of the carboxylic carbons and of the perylene carbons (Table 4.8). The slightly lower coherent fraction of the perylene carbons, 0.40 in contrast to 0.44 of carboxylic carbons (Table 4.8), suggests a larger static disorder within the bent C-backbone, which may be caused by the downward pulling of the anhydride groups.

So far, we have focused our attention on the molecule-substrate interaction, which undoubtedly represents the stronger contribution to the binding energy of PTCDA, but not the only one. We briefly report here about the molecule-molecule interactions. PTCDA molecules arrange on Ag(111) and on Ag(100) in the herringbone[69] and T-shape[86] structures with the negatively charged anhydride groups facing the positively charged perylene core, so that electrostatic intermolecular interaction are maximized. In contrast, due to the head-to-head molecular arrangement of PTCDA

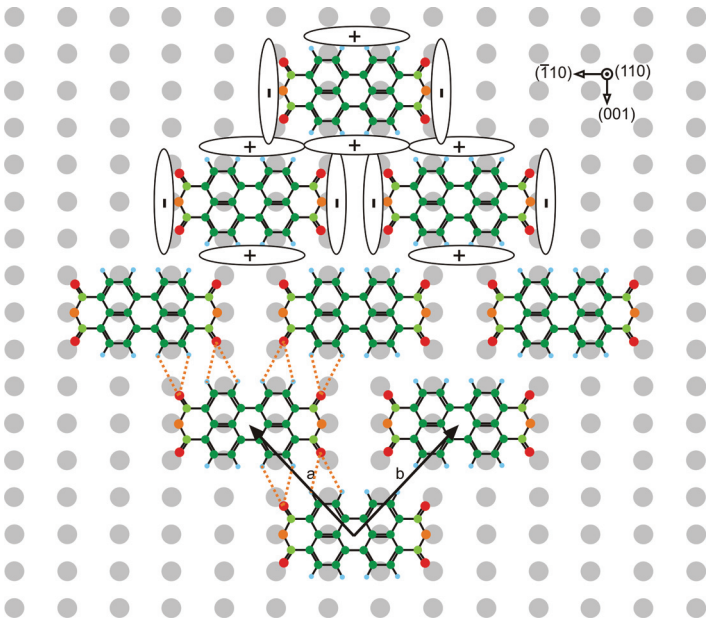


Figure 4.18: Representation of a rhombic PTCDA island on the Ag(110) topmost layer, similar to those imaged by STM.[68,69] H-bond are marked with dotted orange lines going from the carboxylic oxygens to the nearest H atoms of the neighboring molecule. PTCDA quadrupoles are indicated by "+" and "-" circled symbols close to anhydride groups and perylene core, negatively and positively charged respectively. Unit cell vectors a = b = 11.9 Å.[69]

molecules on the Ag(110) surface[68,69] (Figure 4.18), negatively charged anhydride groups face each other, and the intermolecular interactions are considered much weaker and often neglected. Given the stronger interaction of PTCDA with Ag(110) as compared to other substrates [such as Ag(111) and Ag(100)], we wish at this point to also briefly discuss the interactions among molecules. The larger distances between H and O atoms of neighboring PTCDA molecules, increased from approximately 2.3 Å on Ag(111) to approximately 3.3 Å on Ag(110), suggests the presence of much weaker H-bonds between molecules. Therefore, besides substrate-mediated interaction (see section 7.4), we attribute to long-range vdW forces and electrostatic forces among PTCDA quadrupoles the formation of rhombic islands on Ag(110),[68,69] as shown in Figure 4.18. Indeed, this is the geometric configuration which maximizes the number of nearest neighbors. Therefore, besides the strong molecule-substrate interaction, intermolecular interaction must also be present and contribute to the formation of PTCDA islands on Ag(110).

4.5 Conclusions

In this chapter, NIXSW data of submonolayer PTCDA adsorbed on Ag(110) are presented and discussed. From the PTCDA adsorption height, a rather strong chemical contribution to the PTCDA-Ag(110) interaction is deduced. Our conclusion is supported by previous TPD,[70,75] UPS,[75] NEXAFS,[75] STM[68,69] and LEED[70] experiments.

The PTCDA molecule consists of carbon and oxygen atoms in different chemical environments. NIXSW differential analysis (sections 4.3.1.2 and 4.3.2) allows the respective adsorption heights of carboxylic and perylene carbons, and of carboxylic and anhydride oxygens to be determined. This leads to the structure model in which PTCDA is anchored to the Ag substrate via chemical bonding of the anhydride functional groups, adopting an arc-like geometry with the carbon backbone bent downward (Figure 4.19).

The NIXSW structural data of PTCDA/Ag(110) support a bonding mechanism based on two main interaction channels. On the one hand, electronic charge is transferred from the substrate to the LUMO, with concomitant hybridization of molecular and substrate orbitals, and consequent back-donation of charge into the substrate. This interaction channel involves mainly the perylene core of the molecule where LUMO is primarily located. On the other hand, the functional groups of PTCDA are pulled down closer to the surface via O-Ag chemical and electrostatic interaction, with consequent bending of the C-backbone once they have reached the Pauli repulsion limit. Figure 4.19 schematically illustrates these two virtually separated, interaction channels and represents the starting point of the chapter 5, where an attempt to unbind PTCDA from the surface through K deposition is discussed.

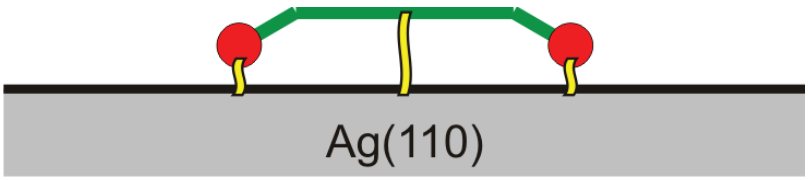


Figure 4.19: Schematic illustration of PTCDA adsorbed on Ag(110) according to NIXSW results presented in section 4.3. The yellow lines indicate the interaction (bonding) between the functional groups and perylene core of PTCDA with the Ag substrate.

5 K-doped PTCDA on Ag(110)

5.1 Introduction

In chapter 4 we studied the interaction between PTCDA molecules and the Ag(110) substrate, resulting in a chemisorptive adsorption followed by a significant distortion of the gas phase molecular geometry. With the original aim of weakening this rather strong molecule-substrate interaction, and unbinding PTCDA molecules from the Ag surface, as shown in Figure 5.1b, potassium was evaporated onto the brickwall phase of PTCDA/Ag(110). In order to investigate both structural and electronic properties of the K-PTCDA-Ag interface, several different experimental methods were employed: NIXSW, LEED, STM, UPS and XPS.

The chapter is organized as follows: First, experimental results of each of the above-mentioned techniques are presented. Then, a structural model is proposed and the *physics* behind this type of complex alkali-molecule-substrate interface is discussed. Finally, conclusions are drawn and an outlook of possible future experiments is presented.

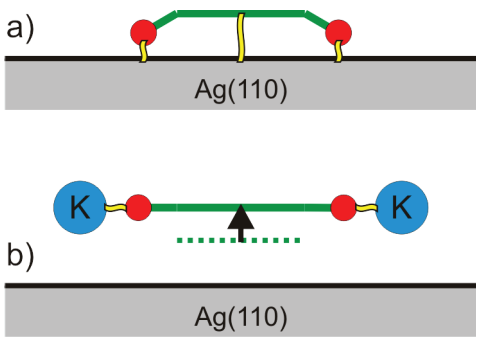


Figure 5.1: Schematic illustration of PTCDA unbinding from the surface upon K deposition. (a): side view of PTCDA adsorbed on Ag(110) according to NIXSW (chapter 4). (b): expected adsorption geometry of K and PTCDA on Ag(110). The dotted green line indicates the vertical position of the molecular plane in (a).

5.2 NIXSW study

This section concerns NIXSW results of K-doped PTCDA adsorbed on Ag(110). The first part reports on the experimental details of the sample preparation, with a particular focus on the estimation of the coverage of K deposited on the PTCDA layer. Successively, XPS data acquisition parameters of NIXSW experiments are provided. In the second part, the background and fitting components lineshapes of PE spectra are discussed. The third subsection presents all experimental results: XPS models are described together with photoelectron yield curves and corresponding structural parameters. Finally, to conclude this section, experimental data are discussed and partial conclusions are drawn, with further interpretation of NIXSW results presented in section 5.6.2.

5.2.1 Experimental details

In section 5.2.1.1, experimental details regarding the preparation of the K+PTCDA layer that was later investigated by NIXSW are reported, with a focus on the amount of K atoms relative to PTCDA molecules and on the K coverage at the Ag surface. XPS data acquisition parameters are also discussed and compared to those of the pristine PTCDA phase in section 5.2.1.2. Subsequently, the properties of XPS background and the line shapes of the fitting components are presented in sections 5.2.1.3 and 5.2.1.4, respectively. NIXSW experiments were performed at the beamline ID32 (ESRF, Grenoble) together with S. Subach, F. S. Tautz (Forschungszentrum Jülich) and O. Bauer, B. Fiedler, M. Sokolowski (Universität Bonn).

5.2.1.1 Potassium deposition and coverage estimation

NIXSW measurements of K-doped PTCDA molecules deposited on Ag(110) were performed in the February 2009 beamtime. During preparation F'09_2 (see section 4.2.1) a submonolayer (0.89 ± 0.09 ML) of PTCDA on Ag(110) was investigated with NIXSW; the results have been presented in chapter 4. Before depositing K, the integrity of the PTCDA layer was checked with XPS and LEED in order to make sure that no beam damage had occurred. Indeed, neither shift nor broadening of core-level peaks was detected and diffraction spots after NIXSW experiments were the same as before, i.e., typical of the brickwall phase (see section 4.2.1). Potassium

photoionization cross sections σ		
	Trzhaskovskaya[48]	Verner[94]
C1s	0.541	0.577
K2p	1.730 (K)	1.805 (K) [1.876 (K^+)]

Table 5.1: Photoionization cross sections σ (kb $= 10^{-21}\text{cm}^{-2}$) of C1s and K2p subshells according to Trzhaskovskaya et al.[48] and Verner et al.[94]. In the first case,[48] cross sections are linearly interpolated between tabulated values, and $\sigma(\text{K2}_p) = \sigma(\text{K2}_{p3/2}) + \sigma(\text{K2}_{p1/2})$. In the second case,[94] cross sections are calculated using analytical expressions and tabulated fit parameters. $\sigma(\text{K2}_p)$ is computed for both the neutral (K) and the singly ionized (K^+) potassium atom.

K coverage estimation			
	σ Trzhaskovskaya[48] (K)	σ Verner[94] (K)	σ Verner[94] (K^+)
$C(\text{K2}p)/C(\text{C1}s)$	0.118 ± 0.012	0.120 ± 0.009	0.116 ± 0.009
K/PTCDA	2.87 ± 0.29	2.88 ± 0.22	2.78 ± 0.22
K-density	23.13 ± 2.34	23.21 ± 1.77	22.41 ± 1.77
Θ_K	0.27 ± 0.03	0.27 ± 0.02	0.27 ± 0.02

Table 5.2: Concentration ratios $C(\text{K2}p)/C(\text{C1}s)$ of potassium and carbon are calculated as in formula 5.1 using cross sections reported in Table 5.1. The number of K atoms per PTCDA molecule (K/PTCDA) is calculated as $C(\text{K2}p)/C(\text{C1}s)$ times the number of carbon atoms in a PTCDA molecule (24). K-density (atoms $\cdot\,\text{cm}^{-2}$) is given by the average number of K atoms per PTCDA molecule (K/PTCDA) times the density of PTCDA molecular layer in the K-doped phase, $8.06 \times 10^{13}\text{molecules} \cdot \text{cm}^{-2}$ (Table 5.3). K coverage is calculated as Θ_K = K-density/Ag-density, where Ag-density $= 84.50 \times 10^{13}\text{atoms} \cdot \text{cm}^{-2}$ if only the topmost (ridge) atoms are considered.[95] Θ_K is expressed relatively to the underlying Ag layer, and not to the closed-packed K overlayer ($54 \times 10^{13}\text{atoms} \cdot \text{cm}^{-2}$), in order to be consistent with notation of Jacob et al.[95]

was evaporated from a commercial SAES Getters source, followed then by annealing for 3 minutes at 180 °C. On the system prepared in this manner LEED, XPS and NIXSW experiments were performed. We will refer to this preparation of K-doped PTCDA as F'09_2K to distinguish it from that of pristine PTCDA F'09_2 (see Table 4.1).

To estimate the coverage of K on the Ag(110) surface, either the K1s or the K2p core-level peaks could be used. We opted for the K2p line because of its proximity to the C1s core level; in fact they were measured within the same spectrum (see Figure 5.4). Since corresponding photoelectrons have similar kinetic energy, E_k-dependent terms in equation 4.1 cancel each other out, providing the simplified formula:

$$\frac{C\,(\text{K2}p)}{C\,(\text{C1}s)} \propto \frac{I\,(\text{K2}p)}{I\,(\text{C1}s)} \cdot \frac{\sigma(\text{C1}s)}{\sigma(\text{K2}p)}. \tag{5.1}$$

In contrast, the kinetic energy of K1s photoelectrons is smaller by a factor of six than

PTCDA superstructures parameters			
	PTCDA/Ag(111)	PTCDA/Ag(110)	K+PTCDA/Ag(110)
phase	Herringbone	Brickwall	Stripe
number of molecules per unit cell	2	1	1
$\mathbf{b_1}$ (Å)	19.0	11.9	15.0
$\mathbf{b_2}$ (Å)	12.6	11.9	8.6
$\gamma\,(deg)$	89.0	86.7	106.0
molecular density $\left(10^{13} molecules \cdot cm^{-2}\right)$	8.35	7.07	8.06

Table 5.3: Unit cell parameters of PTCDA/Ag(111),[69] PTCDA/Ag(110),[69] and K-doped PTCDA/Ag(110). $\mathbf{b_1}$ and $\mathbf{b_2}$ are the unit cell vectors, $\gamma\,(deg)$ is the angle between them. Molecular density is calculated as number of molecule of the unit cell per unit cell area.

that of C1s photoelectrons; hence equation 4.1 cannot be further simplified. Two different sets of photoemission cross sections (Table 5.1), relative to singly ionized or neutral K, were considered in order to assess their influence on the K coverage (Θ_{K}) value. The cross section of the K2p subshell when potassium is in the ionic state (K^+) is only 4% smaller than for the neutral atom (K), and each of the cross sections in Table 5.1 leads to identical Θ_{K} within the errors (Table 5.2). More specifically, multiplying the ratio of the atomic concentrations $C\,(\mathrm{K}2p)\,/C\,(\mathrm{C}1s)$ times the number of carbon atoms in a PTCDA molecule, 24, we obtain the average number of K atoms per molecule, equal to about 2.84 K/PTCDA (average of K and K^+ results from Table 5.2). Multiplying then the average number of K atoms per molecule times the density of PTCDA molecular layer in the K-doped phase, $8.06 \times 10^{13}\mathrm{molecules} \cdot \mathrm{cm}^{-2}$ (see Table 5.3), yields the density of potassium on the Ag(110) surface, $22.89 \times 10^{13}\mathrm{atoms} \cdot \mathrm{cm}^{-2}$. The potassium coverage of 0.27 ML is finally obtained dividing density of potassium by the density of Ag atoms in the topmost layer ($84.50 \times 10^{13}\mathrm{atoms} \cdot \mathrm{cm}^{-2}$). Θ_{K} is defined here with respect to the topmost Ag layer, instead of the closed-packed K overlayer ($54 \times 10^{13}\mathrm{atoms} \cdot \mathrm{cm}^{-2}$, $\Theta_{\mathrm{K}} = 0.42$), just to be consistent with the notation of Jacob et al.,[95] to which we will refer again in section 5.4.3.5, where we will discuss how Θ_{K} affects the electronic structure of the K-PTCDA-Ag interface.

5.2.1.2 XPS acquisition parameters of NIXSW experiments

The different data acquisition parameters were already discussed in section 4.2.2. Nevertheless some values displayed in Table 5.4 deserve further discussion. In general, all XPS data acquisition parameters of K+PTCDA phase were set in order not to exceed 30 minutes of exposure time under x-ray beam during an NIXSW experiment. This time limitation results from a careful investigation of the effect of the

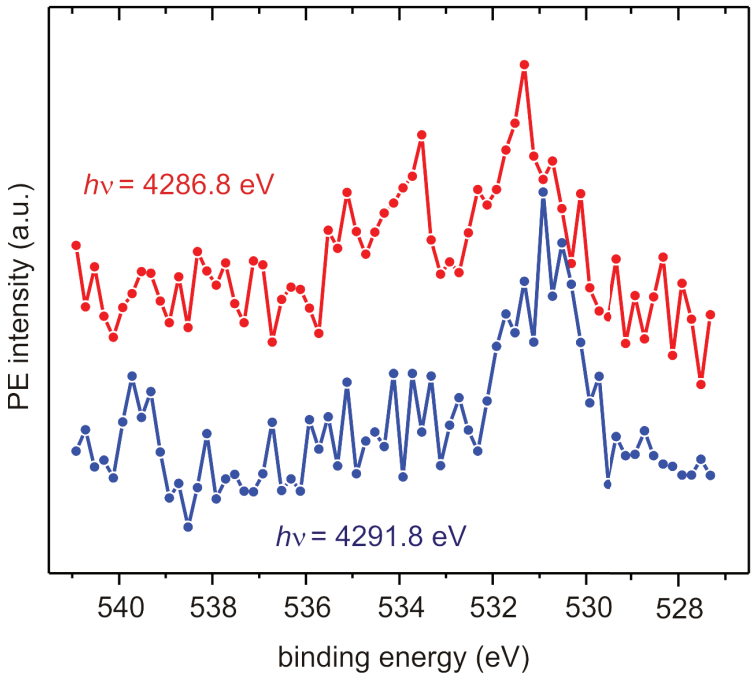


Figure 5.2: O1*s* PE spectra corresponding to the first (4286.8 eV, red) and last (4291.8 eV, blue) photon energies of a NIXSW experiment.

exposure time to the photon beam on the O1*s* PE spectrum, after realizing that one of the two chemically shifted O1*s* peaks decreases upon x-ray irradiation. This phenomenon is clearly seen in Figure 5.2, which shows the first and the last O1*s* PE spectra of a two hours NIXSW experiment. The red spectrum was measured on a spot never irradiated before, while the blue spectrum was recorded after irradiating the same spot for approximately 2 hours, applying the same acquisition parameters as for O1*s* pristine PTCDA (see Table 4.2). This peak disappearance may result from the decomposition of PTCDA molecules, so that oxygen atoms are no longer

XPS data acquisition parameters					
	C1*s*+K2*p*	O1*s*	K1*s*	Ag3*d*	AgMNV
$h\nu$ window [eV]	4	4	4	5	4
$h\nu$ step [eV]	0.15	0.15	0.15	0.10	0.15
E_k window [eV]	38.1	26.1	21	25	50
E_k step [eV]	0.3	0.3	0.3	0.2	0.3
time/step [ms]	100	100	100	100	100
pass energy [eV]	47	47	47	47	47
repeats	5	5	1	1	1

Table 5.4: Data acquisition parameters of single photoemission spectra of NIXSW experiments performed on K-doped PTCDA on Ag(110). Photon energy window, photon energy step, kinetic energy window, kinetic energy step, time per step, pass energy and number of repeats are reported for PE spectra of lines C1*s*+K2*p*, O1*s*, K1*s*, Ag3*d*, AgMNV.

in the carboxylic and anhydride state. To prevent this from happening, the time of an NIXSW scan had to be reduced as compared to experiments on PTCDA/Ag(110) (see section 4.2.2). For this purpose, the photon energy window was reduced to 4 eV, the photon energy step size as well as the E_k step size of PE spectra were increased to 0.15 eV and 0.3 eV, respectively, and finally the number of repeats was reduced to 5. In this way, it was possible to perform XSW experiments on the K+PTCDA phase as well without inducing any decomposition by the x-ray beam. No effect of the irradiation time on C1s spectrum could be observed.

It should be also remarked that since K2$p_{3/2}$ and K2$p_{1/2}$ peaks have binding energies only about 10 eV higher than the C1s core level, it was possible to measure each of the three lines in one spectrum by simply increasing the kinetic energy window by 7 eV compared to the pristine PTCDA C1s spectrum. For this reason, we will occasionally refer to the corresponding spectra as C1s+K2p spectra.

The potassium signal was also measured through K1s core level, and this is the signal chosen for extracting the distance of K atoms from the surface Bragg plane for two reasons. First, there are no additional peaks in the energy region nearby, as is the case of the K2p line, which sits on the tail of the C1s photoemission spectrum; therefore the K1s photoelectron yield can be determined more easily. Second, the simplified expression of the yield of photoelectrons emitted by an x-ray standing wave[44] is valid only if the initial state of the electron in the atom is an s-state.

Furthermore, both Ag3d and the Auger peak AgMNV were measured in order to obtain information from the silver crystal both in the bulk and at the surface, due to the very different escape depth of the corresponding photoemitted electrons having kinetic energy 3915 eV and 350 eV, respectively (see section 5.2.2.4).

5.2.1.3 XPS background

All the considerations about the importance of the background definition mentioned in section 4.2.3 are still valid here. To sum up, the determination of the background is crucial for extracting the electron yield; therefore much care needs to be taken, since it represents a very sensitive parameter which can affect the photoelectron yield and possibly introduce systematic errors. This concept is illustrated very well in Figure 5.3, where a selection of K1s photoemission spectra of an XSW experiment

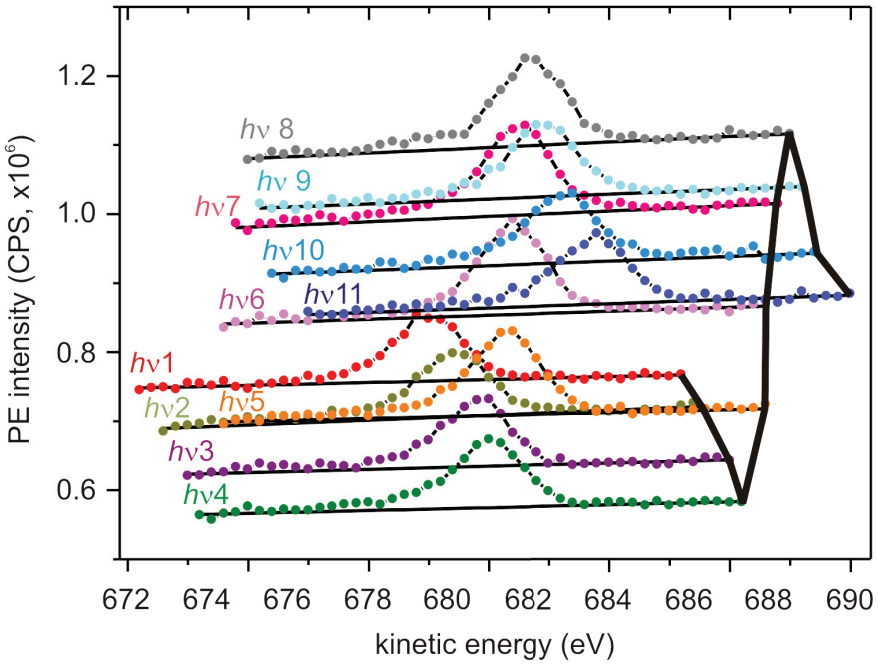


Figure 5.3: PE spectra measured at different photon energy (labeled from $h\nu 1$ to $h\nu 11$) during an NIXSW experiment and plotted as a function of the kinetic energy. The silver background intensity (thick black line), defined as the PE intensity at the upper edge of the kinetic energy window, follows the typical substrate electron yield profile (see Figure 5.12b) as photon energy changes.

are plotted. The solid black line on the right side of the figure follows the Ag background PE intensity and reproduces the typical substrate electron yield profile (see section 5.2.2.4). From this example, one can clearly see that if the BG straight line is not properly defined, part of the Ag signal may be included in the electron yield of potassium, and this will consequently alter the resulting structural parameters. In order to avoid such systematic errors, the region of the photoemission spectrum in which the electron yield is determined must be carefully defined. One of the parameters driving this choice is the background noise, which in turn is related to the signal-to-background ratio. In particular, in Table 5.5, we see that C1s and K1s peaks are about 10% of the background signal, which is sufficient to properly define the BG baseline, without being affected to a great extent by the noise, as it can

signal-to-background ratio						
	C1s	K2p	O1s	K1s	Ag3d	AgMNV
signal/background	0.12	0.03	0.03	0.11	13.86	1.49

Table 5.5: Signal-to-background ratio calculated as the ratio between the signal, given by the highest peak intensity subtracted by the intensity at lowest binding energy of the measured PE spectrum (here defined as background intensity), and the background intensity itself.

be seen in Figure 5.3 and 5.4. The region chosen is as wide as possible compatible with $AvWidth = 10$ (see section 4.2.3). On the other hand, the O1s peak is only 3% larger than the background, thus the BG noise is much more evident in this case (see Figure 5.7). In order to prevent the background noise from altering photoelectron yield data, the region chosen was the narrowest possible around the core-level peak and $AvWidth$ was reduced to 8.

Another relevant parameter is the background type. For C1s+K2p, O1s, K1s and AgMNV spectra, the background was chosen to be linear, while a Shirley type is clearly visible in Ag3d spectrum (see Figure 5.12a). This can be rationalized by looking at the signal-to-background ratio in Table 5.5. In fact only Ag3d PE intensity is more than 10 times larger than the background. Hence, the inelastically scattered Ag3d electrons have enough intensity to establish a Shirley type background.[81]

5.2.1.4 Line shapes of the fitting components

The line shapes of fitting components were already discussed in detail in section 4.2.4. For the data presented in the rest of the chapter as well, a linear combination of Gaussian (80%) and Lorentzian (20%) was used for the main peaks, while a pure Gaussian was adopted for satellite peaks. For K1s, Ag3d and AgMNV spectra there was no need to differentiate species in different chemical environments; therefore no fitting component was employed and the entire *Region* signal (see section 4.2.3) was considered as the total electron yield.

5.2.2 Experimental results

In this section, experimental NIXSW results of K-doped PTCDA on Ag(110) are reported. Carbon, oxygen, potassium and silver signals are analyzed, the model of PE spectra is described and the structural parameters of the corresponding photoelectron yields are presented and discussed.

5.2.2.1 Carbon

XPS model

In order to differentiate among the carbon atoms of K-doped PTCDA adsorbed on Ag(110), the model employed for C1s spectra of pristine PTCDA (section 4.3.1.2) was adopted in the spectrum of Figure 5.4 with a few modifications that are described below.

Since K2p lines overlap with the tail of the C1s core-level peak, two additional components representing K2$p_{3/2}$ and K2$p_{1/2}$ peaks need to be included in the model describing the photoemission spectra in the C1s energy region. K2$p_{3/2}$ line consists of four electronic levels having main total angular momentum quantum number $j = -3/2, -1/2, 1/2, 3/2$; therefore, it has twice the intensity of the K2$p_{1/2}$ line representative of $j = -1/2, 1/2$ levels. The intensity of K2$p_{3/2}$ and K2$p_{1/2}$ are thus fixed to be the first double of the second.

Another relevant difference, compared to the C1s model of pristine PTCDA (section 4.3.1.2), is the redistribution of the satellite intensity. In fact, $Sat2$ has lower intensity and a new satellite $Sat1$ appears between $C234$ (= $C2$+$C3$+$C4$) and $C1$. The introduction of $Sat1$ is necessary to fulfill the stoichiometric ratio:

$$C(perylene) : C(carboxylic) = (C234{+}Sat1) : C1 = 5 : 1 \tag{5.2}$$

where $C234$ represents the carbon atoms of the PTCDA perylene core, while $C1$ stands for the carbon atoms of the anhydride groups. The FWHM of $C1$ is much broader than the single components $C2$, $C3$, $C4$, because $C1$ includes both the main peak and its satellite. Finally, $Sat2$ is a satellite expected to include inelastically scattered electrons from both the perylene core and the carboxylic carbons. Figure 5.5 shows the Argand diagram representation of structural parameters (P_c,

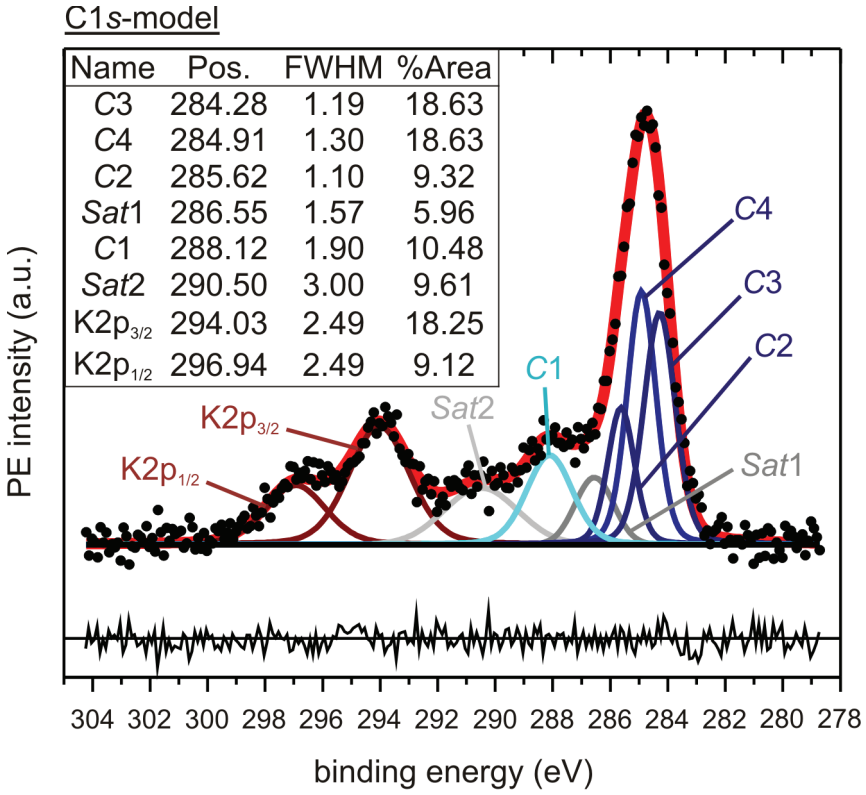


Figure 5.4: C1*s* HR-XPS (pass energy = 47 eV, energy window = 40 eV, energy step = 0.1 eV, time/step = 100 ms, repeats = 50) measured at $h\nu = 4280$ eV. In the top-left table, position (eV), FWHM (eV), and relative area (%) of the fitting components $C2$, $C3$, $C4$ (blue line), $Sat1$ (dark gray line), $C1$ (cyan line), $Sat2$ (light gray line), K2$p_{3/2}$ and K2$p_{1/2}$ (wine line) are reported. Background: thick black straight line. Residuals (thin black line) = *Envelope* (thick red line) - *counts* (black dots), are shown below the PE spectrum.

F_c) for $C234$+$Sat1$, $C1$ and $Sat2$ of data sets 4, 6, 9 (see Table 5.6) and their average, in panels a, b, c and d, respectively. The red square in each plot represents the sum of the corresponding $C234$+$Sat1$ and $C1$ Argand vectors according to the ratio of equation 5.2, namely, Argand Sum $= 5 \times (C234 + Sat1) + 1 \times C1$. In each of the plots displayed in Figure 5.5, the Argand Sum is within the error bars of $Sat2$ data point. This indicates that the satellite $Sat2$ consists of contributions from the two different carbons species in proportions very similar to the molecular stoichiometric ratio (equation 5.2).

The third difference from the model employed for the pristine PTCDA phase is the absolute position of $C2$, $C3$, $C4$, increased by 0.23 eV towards higher binding energy, while their relative position and FWHM did not change. Following the same trend, $C1$ is at binding energy 1.32 eV higher than before K deposition. As will be discussed in more detail in section 5.5, the shift towards higher binding energy is

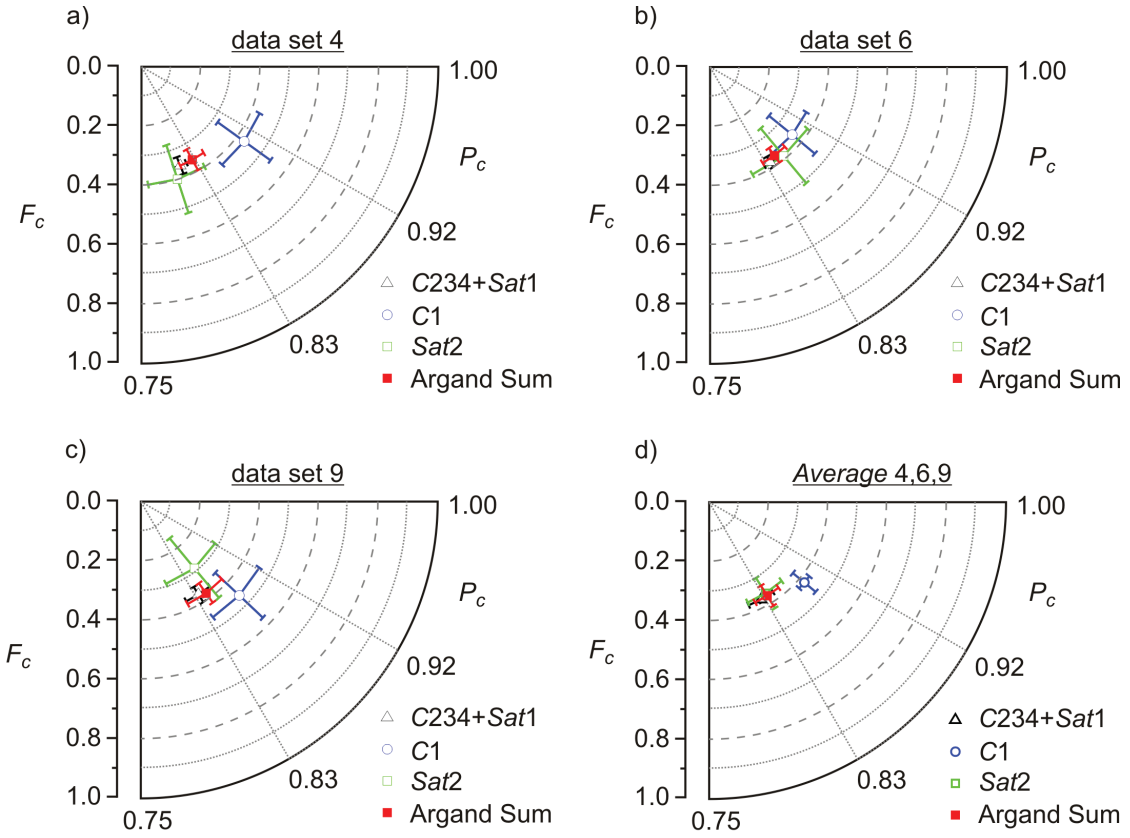


Figure 5.5: Argand diagram of $C234{+}Sat1$ (empty black triangle), $C1$ (empty blue circle), $Sat2$ (empty green square) structural parameters (P_c, F_c) with relative error bars and the Argand sum $5 \times (C234 + Sat1) + 1 \times C1$ (filled red square), of data sets 4 (a), 6 (b), 9 (c) and the *Average* 4,6,9 (d) (see Table 5.6).

attributed to the presence of positively charged potassium atoms at the molecule-metal interface.

Photoelectron yield

The model described above was applied to each photoemission spectrum of XSW experiments after the position and FWHM of each component were fixed to the values shown in the table of Figure 5.4. The areas of $C2$, $C3$ are fixed to that of $C4$ according to equation 4.7 following from the stoichiometry of the perylene core. $Sat1$ area is also fixed relatively to $C4$ area, as specified in the table of Figure 5.4, since they come from the same carbon species; thus they provide the same height information. As mentioned above, the relative intensity of the K2$p_{3/2}$ and K2$p_{1/2}$ peaks is fixed to the 2:1 ratio. The areas of $C4$, $C1$, and $Sat2$ are free to be fitted in order to detect possible height differences among different species of carbon atoms.

Figure 5.6 shows four examples of $C234{+}Sat1$, $C1$, $Sat2$ and Sum ($= C234 + Sat1 + C1 + Sat2$) electron yield profiles. All data analysis results for 9 independent data sets, measured on the preparation F'09_2K (section 5.2.1.1), are reported in Table 5.6, followed by the average over a selection of them (*Average* 4,6,9). Data sets 4, 6, 9 present the best properties, in terms of small noise, high coherent fraction and low χ^2. The other data sets were discarded because of the poor quality of the fits due to very noisy electron yields. In the rest of the chapter, we will refer to the structural parameters relative to *Average* 4,6,9. As a result, the carbon core of the molecule is at 2.64 Å from the surface and the carbon atoms of the anhydride groups are 0.09 Å higher, all with a coherent fraction of about 40%. This is the first case where carboxylic carbons are found at a distance from the surface larger than the core of PTCDA. This point will be discussed further in section 5.7.

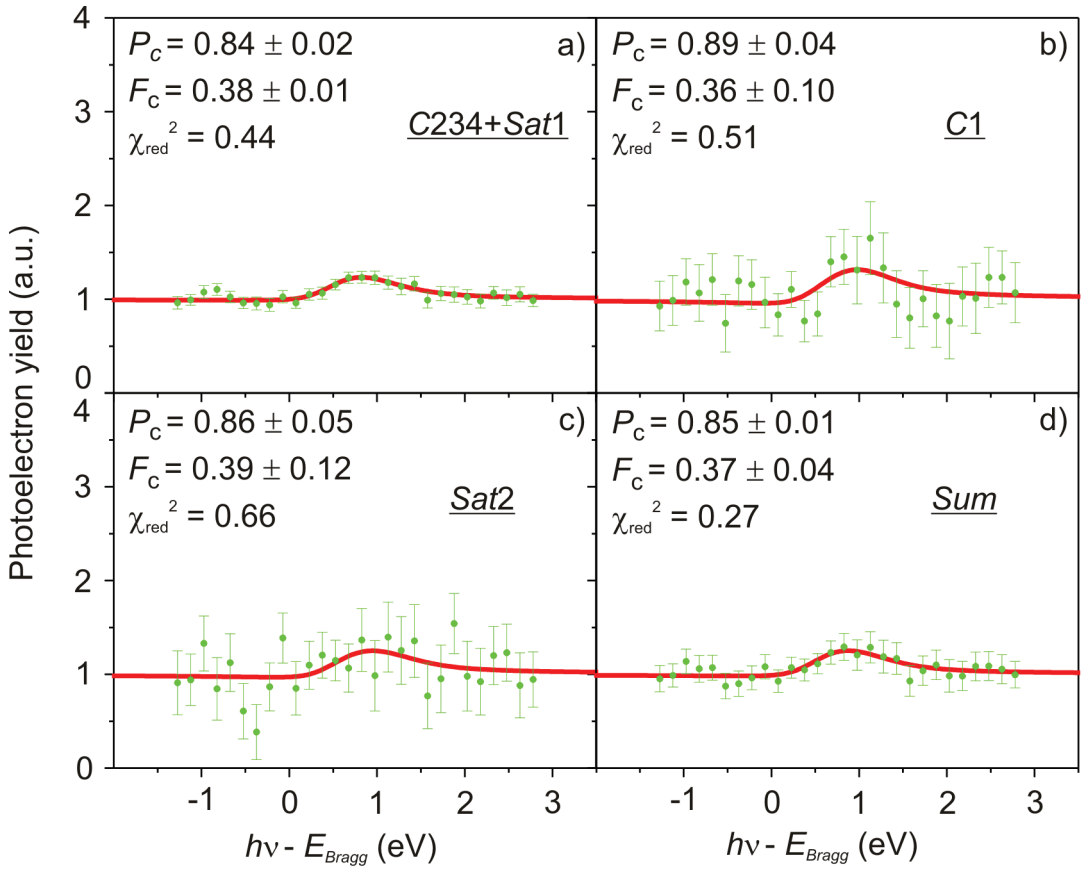


Figure 5.6: Photoelectron yields (relative to data set 6) of $C234{+}Sat1$ (a), $C1$ (b), $Sat2$ (c), Sum ($= C234 + Sat1 + C1 + Sat2$) (d) signals (green dots and relative error bars) as a function of the photon energy relative to the Bragg energy. Fitting curve (red) together with results of the fit: coherent position (P_c), coherent fraction (F_c), and reduced χ^2 are also reported for each profile.

C1s model: results												
C1s	$C234$+$Sat1$			$C1$			$Sat2$			Sum		
data set	P_c	d_c	F_c	P_c	d_c	F_c	P_c	d_c	F_c	P_c	d_c	F_c
1	0.83 (1)	2.64 (1)	0.35 (3)	0.81 (13)	2.61 (19)	0.14 (15)	0.87 (10)	2.70 (14)	0.20 (15)	0.84 (2)	2.66 (3)	0.30 (4)
2	0.83 (1)	2.64 (1)	0.39 (3)	0.89 (8)	2.73 (12)	0.24(12)	0.85 (4)	2.67 (6)	0.41 (12)	0.84 (1)	2.66 (1)	0.38 (4)
3	0.85 (1)	2.67 (1)	0.33 (2)	1.04 (19)	2.93 (27)	0.13(12)	0.86 (3)	2.69 (4)	0.46 (10)	0.86 (2)	2.69 (3)	0.32 (4)
4	0.81 (1)	2.61 (1)	0.36 (3)	0.90 (4)	2.74 (6)	0.43(11)	0.80 (4)	2.60 (6)	0.40 (12)	0.82 (1)	2.63 (1)	0.37 (3)
5	0.84 (1)	2.66 (1)	0.31 (3)	0.91 (6)	2.76 (9)	0.26(10)	0.81 (14)	2.61 (20)	0.12 (14)	0.84 (2)	2.66 (3)	0.27 (4)
6	0.84 (1)	2.66 (1)	0.38 (2)	0.89 (4)	2.73 (6)	0.36(10)	0.86 (5)	2.69 (7)	0.39 (12)	0.85 (1)	2.67 (1)	0.37 (4)
7	0.84 (1)	2.66 (1)	0.32 (2)	0.90 (5)	2.74 (7)	0.33(11)	0.86 (17)	2.69 (25)	0.10 (13)	0.85 (1)	2.67 (1)	0.29 (3)
8	0.82 (1)	2.63 (1)	0.37 (2)	0.98 (8)	2.86 (12)	0.28(12)	0.87 (5)	2.70 (7)	0.42 (13)	0.84 (1)	2.66 (1)	0.36 (2)
9	0.84 (2)	2.66 (1)	0.37 (3)	0.88 (4)	2.72 (6)	0.46(11)	0.86 (6)	2.69 (9)	0.29 (13)	0.85 (1)	2.67 (1)	0.37 (4)
Average 4,6,9	0.83 (2)	2.64 (3)	0.37 (3)	0.89 (4)	2.73 (6)	0.42 (11)	0.84 (5)	2.66 (7)	0.36 (12)	0.84 (2)	2.66 (3)	0.37 (4)

Table 5.6: Coherent position (P_c), coherent fraction (F_c) and distance d_c (Å) from the surface Bragg plane, calculated as $(P_c{+}1)\times d_{Ag(110)}$ (where $d_{Ag(110)} = 1.44$ Å) are reported for each data set labeled from 1 to 9, followed by the average values of data sets 4, 6, 9.

5.2.2.2 Oxygen

XPS model

The photoemission spectrum of the O1s core level (Figure 5.7) consists of two peaks approximately 2.5 eV from each other, similar to the O1s spectrum of the pristine PTCDA (Figure 4.12), although the relative intensity of the two peaks is notably different in the two cases. O1s PE spectrum is modeled by a main component ($Main$) and the corresponding satellite (Sat) for each of the two species: carboxylic ($Carb$) and anhydride (An) oxygen. To fulfill the stoichiometric ratio $Carb : An = 2 : 1$, the O1s XPS model of the pristine PTCDA was modified. The main difference lies in the intensity and the position of the carboxylic satellite component ($Carb$-Sat), which has about half the area of the analogous peak for PTCDA/Ag(110) and it is no longer buried under An-$Main$, instead it overlaps with $Carb$-$Main$. Comparing the absolute binding energies of the $Carb$-$Main$ and An-$Main$ of the K-doped PTCDA phase

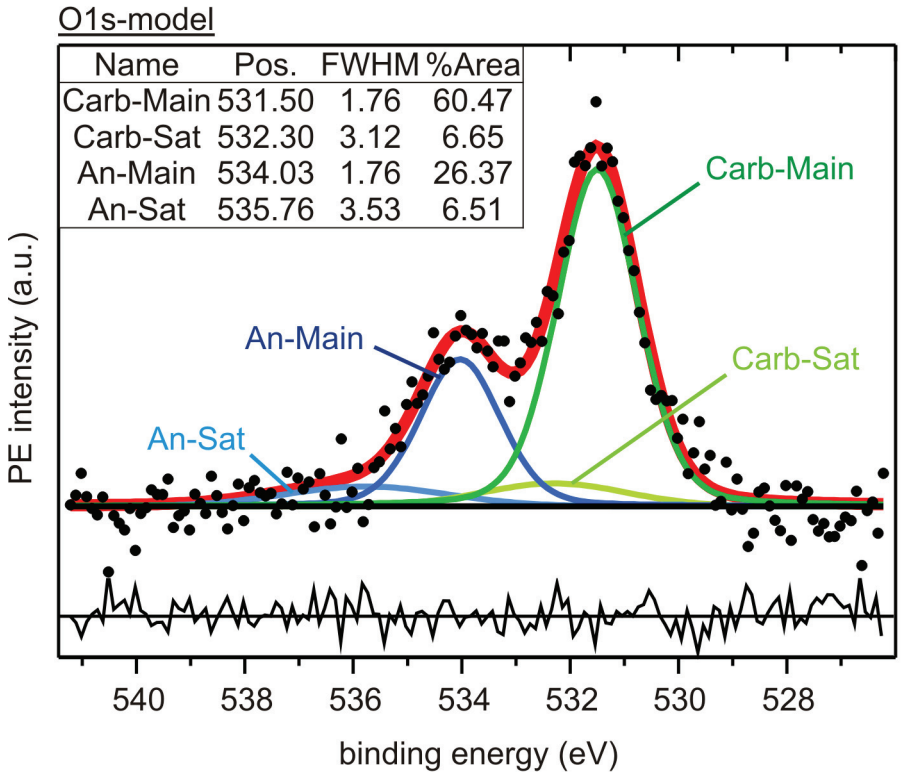


Figure 5.7: O1s HR-XPS is the sum of three spectra (pass energy = 47 eV, energy window = 20 eV, energy step = 0.1 eV, time/step = 0.1 ms, sum of repeats = 84) measured at $h\nu$ = 4280 eV. In the table on the upper left, position (eV), FWHM (eV), and relative area (%) of the fitting components (lines) $Carb$-Main (dark green), $Carb$-Sat (light green), An-Main (dark blue), An-Sat (light blue). Background: thick dark line. Residuals (thin dark line), *Envelope* (thick red line) - *counts* (black dots), are shown below the PE spectrum.

with the pure PTCDA (Figure 4.12), an increase of 0.5 eV and 0.6 eV respectively for carboxylic and anhydride oxygens is registered (see Table 5.12). This shift towards higher binding energies is attributed to the positively charged K atoms in the ionic state and will be further discussed in section 5.5.4.

Photoelectron yield and NIXSW fits

The model described above was used to fit each photoemission spectrum of XSW data sets, after fixing positions and FWHM of the four components. The areas of *Sat* peaks are also fixed relative to the corresponding *Main* components, according to the ratios reported in the table of Figure 5.7, since the *Sat* components bring the same structural information of relative *Main* peaks. Examples of the resulting photoelectron yields are shown in Figure 5.8. *Region* and *Sum* (= *Carb-*

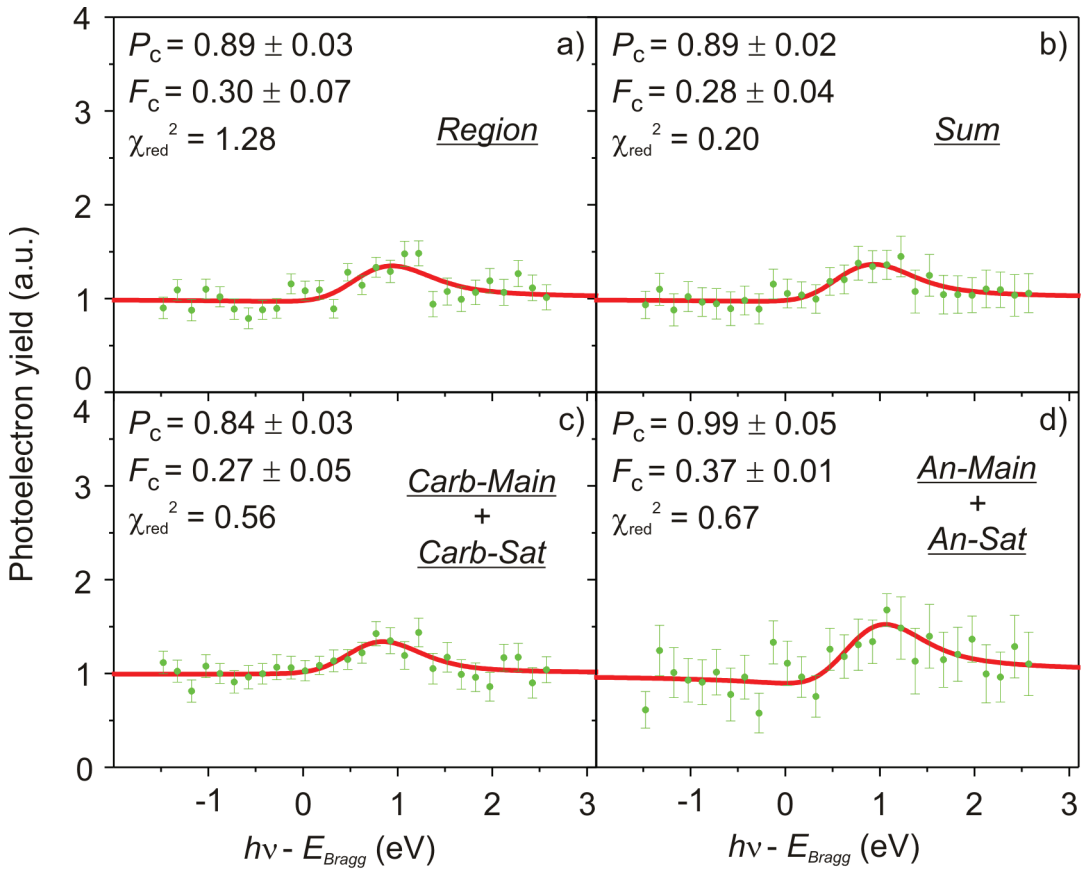


Figure 5.8: Photoelectron yield of *Region* (a), *Sum* (= *Carb-Main*+*Carb-Sat*+*An-Main*+*An-Sat*) (b), *Carb-Main*+*Carb-Sat* (c), *An-Main*+*An-Sat* (d) signals (green dots and relative error bars) as a function of the photon energy relative to the Bragg energy. Fitting curve (red) together with results of the fit: coherent position (P_c), coherent fraction (F_C), and reduced χ^2 are also reported for each profile.

Main+Carb-Sat+An-Main+An-Sat) signals provide identical results, confirming a proper definition of the background and the XPS fitting model whose envelope accurately describes O1*s* PE spectra. In contrast, electron yields of carboxylic and anhydride species show quite different profiles, reflecting different heights and coherent fractions. Table 5.7 reports all experimental results followed by average values of a selection of them (*Average* 3,5,7,8,9), to which we will refer in the rest of the chapter. The data not included in the average are characterized by poor quality fits due to particularly noisy electron yields, and consequently, the corresponding structural parameters are far from the averaged values. Carboxylic (*Carb-Main+Carb-Sat*) and anhydride (*An-Main+An-Sat*) signals have different heights and coherent fractions. Indeed, carboxylic oxygens are at 2.63 Å above the surface within the plane of the PTCDA perylene core (Table 5.6), 0.13 Å lower than the anhydride ones, and have coherent fraction of 18%, approximately half of anhydride oxygens coherent fraction. At this point we cannot yet exclude that this low coherent fraction is due to two or more oxygen species at different vertical positions. We refer to section 5.2.3, for further discussion.

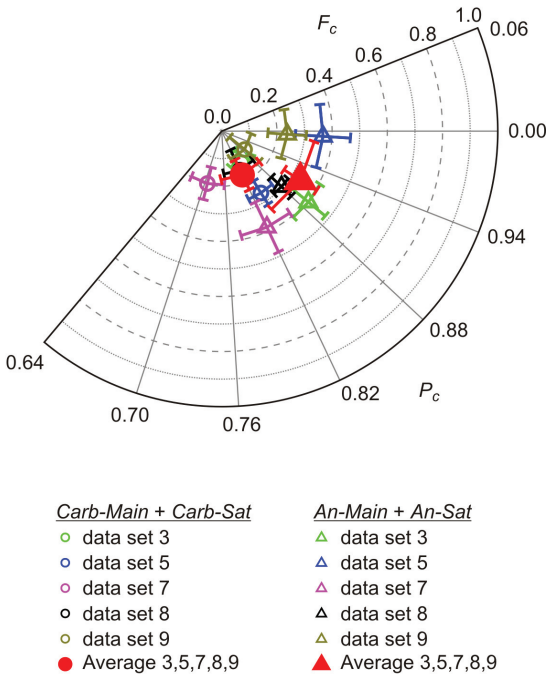


Figure 5.9: Argand diagram of *Carb-Main+Carb-Sat* (open circles) and *An-Main+An-Sat* (open triangles) structural parameters (P_c, F_c) of data sets number 3 (green), 5 (blue), 7 (cyan), 8 (magenta), 9 (dark yellow) (see Table 5.7) and the corresponding average (red).

O1s model: results												
O1s	*Region*			*Sum*			*Carb-Main+Carb-Sat*			*An-Main+An-Sat*		
data set	P_c	d_c	F_c	P_c	d_c	F_c	P_c	d_c	F_c	P_c	d_c	F_c
1	0.87 (4)	2.70 (6)	0.31 (9)	0.86 (3)	2.69 (4)	0.26 (7)	0.89 (4)	2.73 (6)	0.27 (8)	0.86 (5)	2.69 (7)	0.26 (11)
2	0.83 (4)	2.64 (6)	0.28 (9)	0.86 (2)	2.67 (3)	0.34(6)	0.85 (2)	2.67 (3)	0.37 (6)	0.86 (7)	2.69 (10)	0.25 (11)
3	0.84 (7)	2.66 (10)	0.16 (8)	0.87 (3)	2.70 (4)	0.23(5)	0.84 (5)	2.66 (7)	0.14 (5)	0.89 (3)	2.73 (4)	0.41 (8)
4	0.55 (38)	2.24 (55)	0.04 (7)	0.85 (9)	2.67 (13)	0.09(6)	0.82 (6)	2.63 (9)	0.12 (6)	0.87 (16)	2.70 (23)	0.09 (10)
5	0.89 (3)	2.73 (4)	0.30 (7)	0.89 (2)	2.73 (3)	0.28(4)	0.84 (3)	2.66 (4)	0.27 (5)	0.99 (5)	2.87 (7)	0.37 (10)
6	0.86 (14)	2.69 (20)	0.09 (10)	0.87 (6)	2.70 (9)	0.16(6)	0.87 (3)	2.70 (4)	0.28 (6)	0.37 (21)	1.98 (30)	0.10 (14)
7	0.75 (5)	2.53 (7)	0.18 (7)	0.77 (3)	2.56 (4)	0.23(5)	0.71 (5)	2.47 (7)	0.20 (6)	0.82 (4)	2.63 (6)	0.39 (10)
8	0.92 (7)	2.77 (10)	0.14 (7)	0.84 (3)	2.66 (4)	0.20(4)	0.82 (6)	2.63 (9)	0.16 (8)	0.88 (2)	2.72 (3)	0.30 (5)
9	1.00 (11)	2.89 (16)	0.13 (7)	0.96 (6)	2.83 (9)	0.15(5)	0.89 (9)	2.73 (19)	0.11 (7)	0.99 (6)	2.87 (9)	0.24 (7)
Average 3,5,7,8,9	0.88 (9)	2.72 (13)	0.18 (7)	0.87 (7)	2.70 (10)	0.22(5)	0.82 (7)	2.63 (10)	0.18 (6)	0.91 (7)	2.76 (11)	0.34 (8)

Table 5.7: Coherent position (P_c), coherent fraction (F_c) and distance d_c (Å) from the surface Bragg plane, calculated as $(P_c{+}1)\times d_{Ag(110)}$ (where $d_{Ag(110)} = 1.44$ Å) are reported for each data set labeled from 1 to 9, followed by the average values of all data sets and of 3, 5, 7, 8, 9.

5.2.2.3 Potassium

As already mentioned in section 5.2.1.2, in addition to K2p lines, the K1s photoemission peak was also measured and the structural parameters of potassium are actually extracted from this signal. The choice is mainly driven by the fact that K1s does not overlap with other core-level peaks, as is the case for K2p lines with C1s, which is why it is more straightforward to derive its electron yield. Moreover, there was no evidence of chemical shifts, thus no need to fit components in order to differentiate contributions of different species of the same element to the overall spectrum (see Figure 5.10a). Therefore, the *Region* given by the photoemission counts subtracted

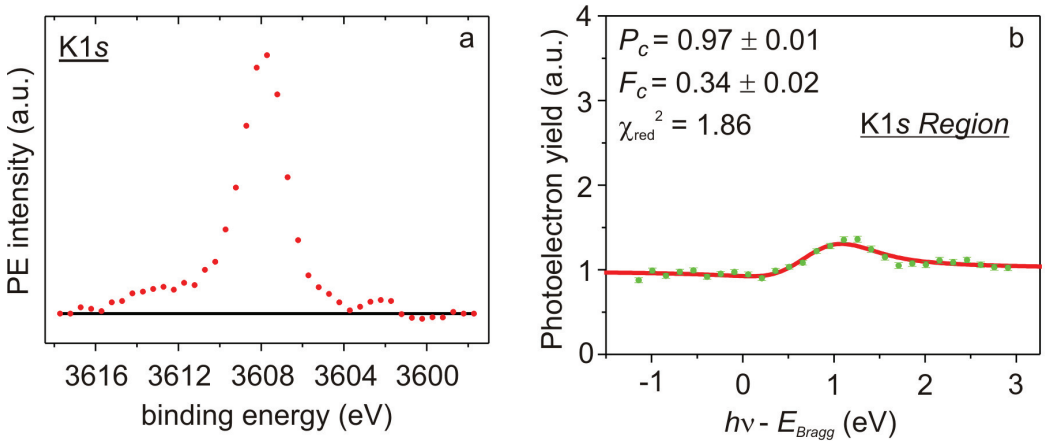


Figure 5.10: (a): K1s XPS (pass energy = 47 eV, energy window = 35 eV, energy step = 0.5 eV, time/step = 0.1 ms, repeats = 10) measured at $h\nu$ = 4280 eV. (b): photoelectron yield of K1s *Region* signal (green dots and relative error bars) as a function of the photon energy relative to the Bragg energy. Fitting curve (red) together with results of the fit: coherent position (P_c), coherent fraction (F_c), and reduced χ^2 are also reported for each profile.

K1s model: results			
K1s	*Region*		
data sets	P_c	d_c	F_c
1	0.98 (2)	1.42 (3)	0.32 (3)
2	0.97 (1)	1.40 (1)	0.34 (2)
3	0.96 (2)	1.39 (3)	0.30 (3)
4	0.99 (2)	1.43 (3)	0.27 (3)
5	1.06 (2)	1.53 (3)	0.34 (3)
6	1.03 (2)	1.49 (3)	0.38 (4)
Average	1.00 (4)	1.44 (6)	0.33 (4)

Table 5.8: Coherent position (P_c), coherent fraction (P_c) and distance d_c (Å) from the surface Bragg plane, calculated as $P_c \times d_{Ag(110)}$ (where $d_{Ag(110)}$ = 1.44 Å) are reported for each data set labeled from 1 to 6, followed by the average value of all data sets.

by the background is the photoelectron yield representative of the potassium signal (see example in Figure 5.10b).

In Table 5.8 and the Argand diagram of Figure 5.11, all K1*s* NIXSW results are summarized. Given the relatively low coherent fraction of approximately 30%, we cannot exclude the presence of more than one adsorption site for K atoms at different distances from the Ag surface. However, for the purpose of discussion, we will consider all K atoms at the same height corresponding to their average coherent position 1.00±0.04. Therefore, the corresponding vertical position of K atoms coincides with that of a Bragg plane, which, in turn, coincides with the Ag(110) atomic planes (see section 5.2.2.4). In fact, in the Argand diagram of Figure 5.11, potassium and silver data points have approximately the same coherent position. However, due to the modulo 1 ambiguity of P_c, K atoms can be either within the topmost Ag surface layer, or 1.44 Å above, or 2.88 Å above; any other possibility can be reasonably excluded. In order to discern which of these scenarios is the most plausible, it is necessary to have a full picture of the molecule-metal-substrate interface. This discussion is therefore postponed to section 5.4.3.5.

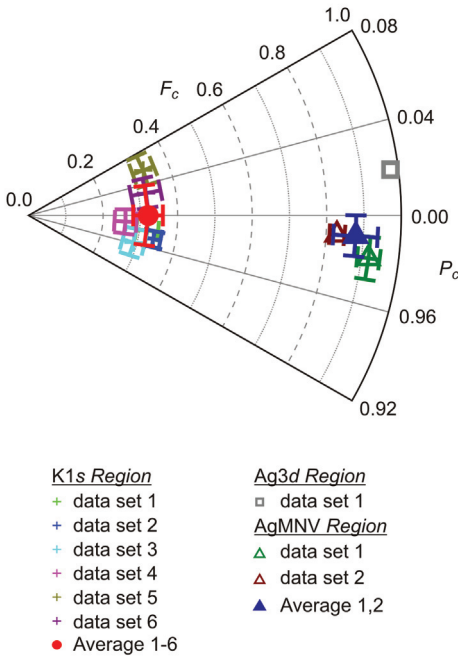


Figure 5.11: Argand diagram of K1*s* (+ symbols) structural parameters (P_c, F_c) of data sets 1-6 (see Table 5.8) and the corresponding average (full red circle). Argand diagram of AgMNV (open triangles) structural parameters (P_c, F_c) of data sets 1-2 (see Table 5.9) and the corresponding average (full blue triangle). Argand diagram of Ag3*d* (open gray square) structural parameters (P_c, F_c) of data sets 1 (see Table 5.9).

5.2.2.4 Silver

The quality of the substrate crystal can be checked by inspecting the reflectivity curve (Figure 5.12c,f). Its width and shape give an indication about the crystal mosaicity. The standing wave signal of the substrate atoms can also be used to learn about the degree of crystallinity of a metal substrate directly. Both Ag3*d* and and AgMNV Auger photoelectrons were recorded in order to compare the Ag3*d* signal coming from the deeper layers (bulk) with the more surface-sensitive AgMNV Auger line, originating from Auger electrons. In fact, kinetic energy of AgMNV photoelectrons (≈350 eV) is one order of magnitude smaller than that of Ag3*d* photoelectrons and, according to the universal curve of escape depth,[37] AgMNV PE signal probes a depth of approximately 5 Å below the surface.

In the Ag3*d* PE spectrum shown in Figure 5.12a, the energy window, in which the Shirley background is defined, is marked by the two dashed vertical lines. The electron yield of the *Region* signal (counts-background) shows an ideal substrate signal (Figure 5.12b), with coherent position equal to 1.02 and coherent fraction 0.98. This result confirms the perfect order of the Ag atoms in the bulk placed at the (110) crystal plane coinciding with the Bragg planes.

Auger photoelectrons give rise to the PE spectrum in Figure 5.12d. The average of AgMNV structural parameters, resulting from the fit of the two electron yields reported in Table 5.9, shows a 10% decrease in the coherent fraction, which goes hand in hand with a 3% decrease in the coherent position, compared to Ag3*d* data (see Argand diagram in Figure 5.11). Hence, XSW experimental results are in good

Ag results			
Ag3*d*	*Region*		
data sets	P_c	d_c	F_c
1	1.02 (0)	1.47 (0)	0.98 (0)
AgMNV	*Region*		
data sets	P_c	d_c	F_c
1	0.98 (1)	1.42 (1)	0.92 (3)
2	0.99 (0)	1.43 (0)	0.83 (2)
Average	0.99 (1)	1.42 (1)	0.88 (6)

Table 5.9: Coherent position (P_c), coherent fraction (F_c) and distance d_c (Å) from the surface Bragg plane, calculated as $P_c \times d_{Ag(110)}$ (where $d_{Ag(110)} = 1.44$ Å) are reported for each data set, followed by the average of AgMNV results.

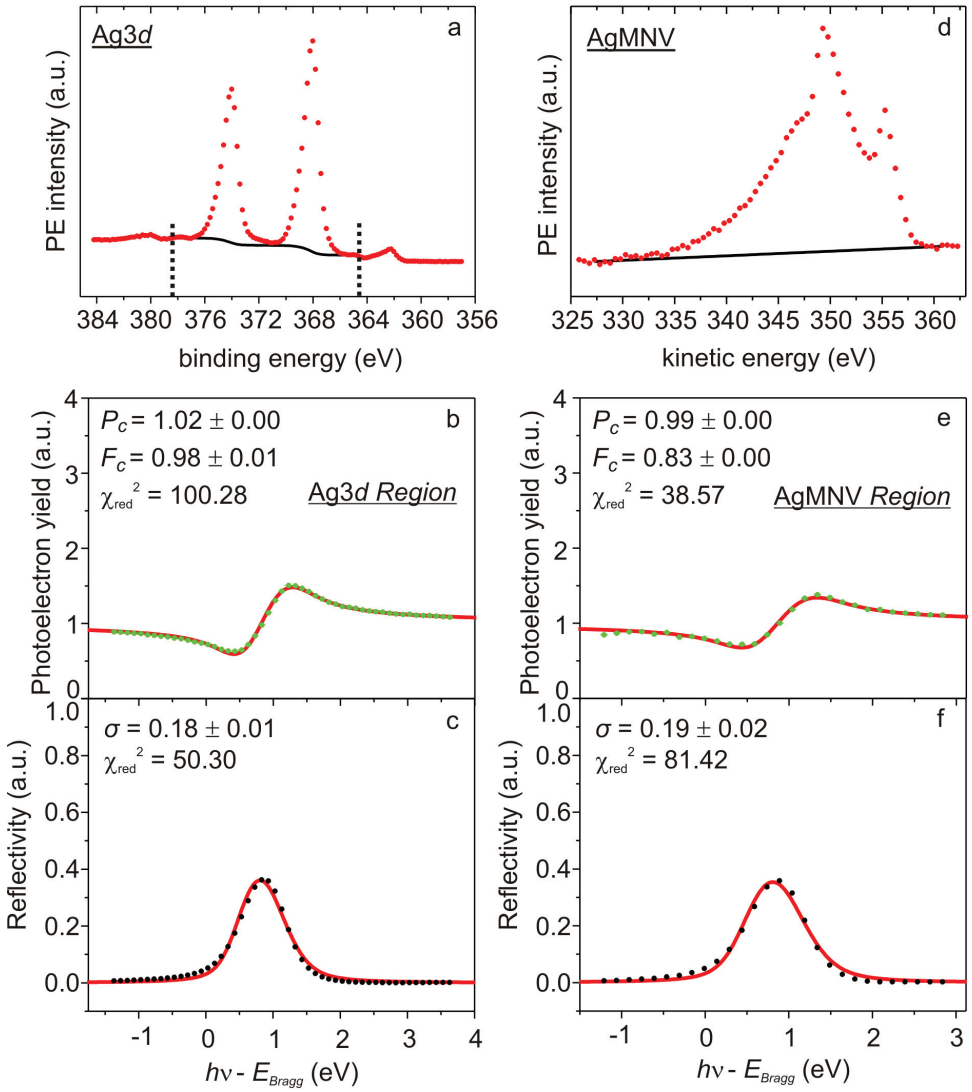


Figure 5.12: (a): Ag3*d* XPS (pass energy = 47 eV, energy window = 100 eV, energy step = 0.5 eV, time/step = 0.1 ms, repeats = 1) measured at $h\nu$ = 4280 eV. (d): AgMNV Auger spectrum (pass energy = 47 eV, energy window = 40 eV, energy step = 0.5 eV, time/step = 0.1 ms, repeats = 1) measured at $h\nu$ = 4280 eV. (b) and (e): photoelectron yields of Ag3*d* and AgMNV *Region* (green dots and relative error bars) displayed as a function of the photon energy relative to the Bragg energy. Fitting curve (red) together with results of the fits, coherent position (P_c), coherent fraction (F_c), and reduced χ^2 are also reported. (c) and (f): X-ray beam reflectivity (black dots) corresponding to NIXSW experiments in panels (b) and (e), respectively. Fitting curve (red), fitted width σ of the Gaussian function (see section 3.3.1), and reduced χ^2 are also reported on the plot.

agreement with LEED-$I(V)$ measurements[96] of the bare Ag(110) surface, from which an overall contraction of about 2% of the Ag surface including the first three atomic layers was concluded.

5.2.3 Discussion of NIXSW results

Now that we have presented all the NIXSW data regarding K-doped PTCDA adsorbed on Ag(110), we can draw some preliminary conclusions. NIXSW results will be further discussed in section 5.6.2 in the light of experimental results obtained from LEED, STM and UPS.

Because of the general low coherent fraction of NIXSW results (see Table 5.11) the presence of multiple species of the same chemical element at different vertical positions cannot be excluded. However, for the purpose of discussion we will assume d_c values to refer to the average distance of single species from the surface Bragg plane. In order to understand the role played by K atoms at the PTCDA-Ag interface, it is interesting to compare the adsorption geometry of the molecule before and after K deposition. From the long side view in Figure 5.13a, it is clear that the PTCDA molecule changes from the downward bent geometry of the pristine phase to a more flattened structure in presence of K atoms, as it is in the gas phase. Evidently the carboxylic groups are the most strongly affected by potassium deposition. In fact, the vertical shift of the oxygen atoms together with the carboxylic carbons is approximately 0.30 Å, whereas the perylene core lifts up by only 0.05 Å, as illustrated in the scale model of Figure 5.13b.

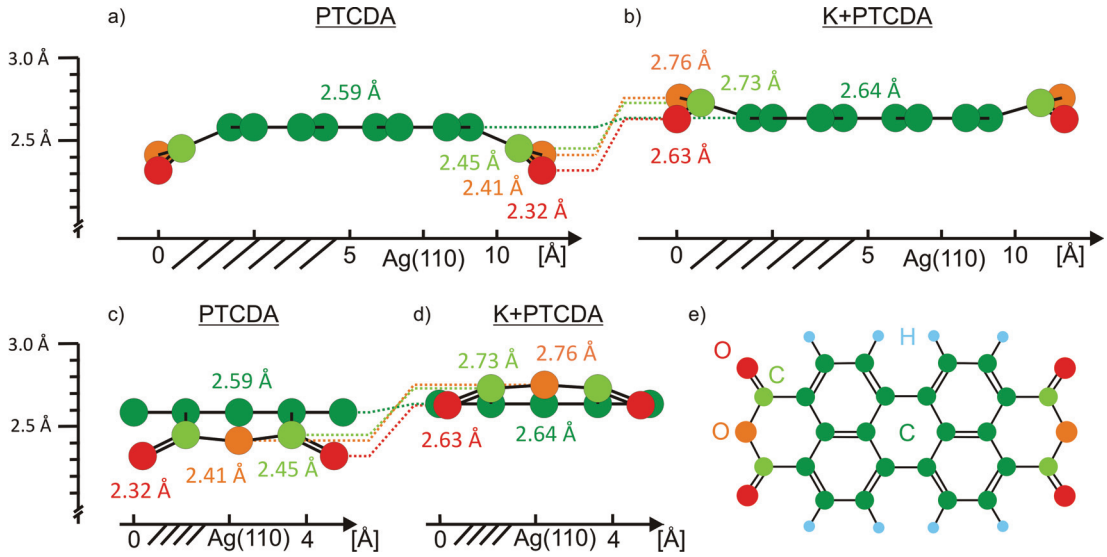


Figure 5.13: Scale model of PTCDA and K-doped PTCDA adsorbed on Ag(110): long side view (a, b); short side view (c, d); top view (e). In panels a, b, c, d only the vertical positions (from Table 5.11) are in scale, not the lateral positions of atoms. Color code: dark green → perylene-carbon; light green → carboxylic-carbon; red → carboxylic-oxygen; orange → anhydride-oxygen; light blue → hydrogen.

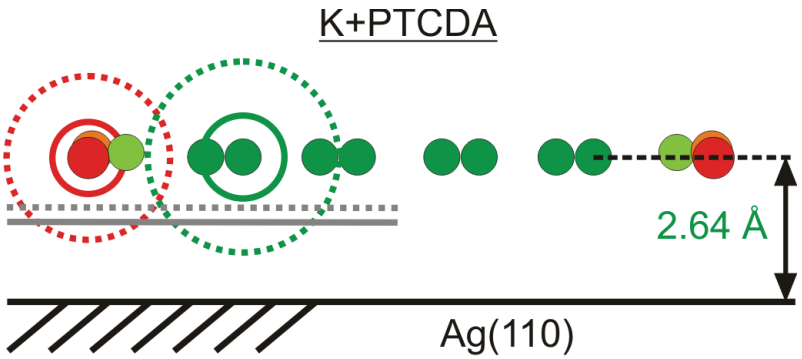


Figure 5.14: Scale model of K-doped PTCDA on Ag(110). Solid lines indicate covalent radii[91] (r^{C}_{cov} = 0.73 Å; r^{O}_{cov} = 0.66 Å; r^{Ag}_{cov} = 1.45 Å), dashed lines indicate van-der-Waals radii[92] (r^{C}_{vdW} = 1.75 Å; r^{O}_{vdW} = 1.50 Å; r^{Ag}_{vdW} = 1.72 Å), filled circles indicate the position of the atoms. Color code: dark green→perylene-carbon; light green→carboxylic-carbon; red→carboxylic-oxygen; orange→anhydride-oxygen; gray→silver.

To better understand the meaning of the atomic adsorption heights in terms of chemical interaction with the substrate we can compare the interatomic distance between oxygen and silver atoms with the sum of the corresponding covalent (r^{O}_{cov}, r^{Ag}_{cov}) and vdW radii (r^{O}_{vdW}, r^{Ag}_{vdW}). However, since the lateral position of PTCDA relative to the Ag substrate is not known, it is not be possible to precisely define the interatomic distance of molecular atoms from the next neighboring underlying Ag atoms, as it was done in section 4.4.2. Therefore, in order to define a unique quantity to compare with the average O-Ag interatomic distance for PTCDA/Ag(110), we make the two following assumptions. First, the relaxation of the topmost Ag layer (section 5.2.2.4) is disregarded. Second, oxygen atoms are assumed to be in an on-top adsorption site above Ag atoms; thus O-Ag interatomic distance is underestimated. Given those assumptions, the distance of O from the nearest Ag atom is equal to height d_c (Figure 5.13b,d). From the weighted sum of carboxylic and anhydride oxygen d_c, we obtain what we define as the O-Ag interatomic distance $\overline{d_i(\text{O-Ag})}$ = 2.67 Å for K+PTCDA/Ag(110). $\overline{d_i(\text{O-Ag})}$ is 26% larger than the sum of covalent radii $r^{O}_{cov}+r^{Ag}_{cov}$, and only 17% smaller than the sum of vdW radii $r^{O}_{vdW}+r^{Ag}_{vdW}$

	$r^{O}_{cov}+r^{Ag}_{cov}$	$r^{O}_{vdW}+r^{Ag}_{vdW}$	$\overline{d_i(\text{O-Ag})}$	% of $(r^{O}_{cov}+r^{Ag}_{cov})$[Å]	% of $(r^{O}_{vdW}+r^{Ag}_{vdW})$[Å]
PTCDA/Ag(110)	2.11	3.22	2.45	116	76
K+PTCDA/Ag(110)	2.11	3.22	2.67	126	83

Table 5.10: Sum of covalent radii[91] $r^{O}_{cov}+r^{Ag}_{cov}$, sum of vdW radii[92] $r^{O}_{vdW}+r^{Ag}_{vdW}$ and interatomic distance $\overline{d_i(\text{O-Ag})}$ for PTCDA/Ag(110) and K+PTCDA/Ag(110) are reported, followed by the percentage of the interatomic distance with respect to the sum of covalent radii and the sum of vdW radii.

	Perylene-C		Carboxylic-C		Carboxylic-O		Anhydride-O	
	d_c	F_c	d_c	F_c	d_c	F_c	d_c	F_c
PTCDA/Ag(110)	2.59 (1)	0.40 (6)	2.45 (11)	0.44 (8)	2.32 (5)	0.21 (4)	2.41 (6)	0.34 (9)
K+PTCDA/Ag(110)	2.64 (3)	0.37 (3)	2.73 (6)	0.42 (11)	2.63 (10)	0.18 (6)	2.76 (11)	0.34 (8)

Table 5.11: Summary of all NIXSW experimental results, d_c (distance from the Bragg plane) and F_c (coherent fraction), of perylene and carboxylic carbon, anhydride and carboxylic oxygen, for both PTCDA/Ag(110) and K+PTCDA/Ag(110).

(see Table 5.10). From the overlap of oxygen and silver vdW radii, it is possible to infer the presence of a chemical component contributing to the O-Ag interaction, although it is notably smaller compared to the pristine PTCDA case. This evidence suggests that K atoms cause the unbinding of the PTCDA molecule from the surface, or, more precisely, a partial unbinding of the carboxylic groups including both oxygens and carbon atoms directly bonded to them. In fact, thanks to the differential analysis of C1s photoemission peak according to the model described in section 5.2.2.1, carboxylic carbons too are found to be lifted up by 0.28 Å upon K deposition, following the trend of oxygen atoms. The PTCDA carbon skeleton lifts up as well, albeit by a smaller amount, 0.05 Å; thus its vertical position does not seem to be affected by the coadsorbed potassium atoms to a great extent.

As mentioned at the beginning of this section, the low coherent fraction of carbon and oxygen could be explained by the presence of more than one K+PTCDA superstructure, considering the average structural parameters reported in Table 5.11. However, from Table 5.11 it is also evident that both carbon and oxygen species of PTCDA/Ag(110) and K+PTCDA/Ag(110) have identical coherent fraction within the errors. This indicates that the fraction of molecules coherently adsorbed on the Ag(110) surface does not change upon K deposition. It was shown in chapter 4 that PTCDA forms a highly ordered brickwall phase with only one adsorption site on Ag(110), and there was no evidence of any additional phases. Therefore, the low coherent fraction was attributed to molecular diffusion and out-of-plane vibrational modes, as discussed in section 4.4.1. This argument would then speak against multiple species as a reason for low F_c of K+PTCDA/Ag(110).

It was shown that NIXSW experiments provide insights into the vertical geometry of the adsorbed molecule and its inner structure. This allows the effect of K atoms on the adsorption geometry of the strongly interacting PTCDA molecule on the Ag(110) surface to be analyzed. Nevertheless, at this point many questions remain unanswered. First, where are K atoms? It is not possible to solve the ambi-

guity of the K atoms height (0 Å, 1.44 Å, 2.88 Å, or above) based on standing wave data alone. In particular, it cannot be concluded whether they are within the Ag topmost layer, within the molecular layer or above it. Second, the lateral structure of the K+PTCDA phase has to be investigated, and it is not clear whether the structural data just discussed correspond to one or more coexisting phases. Third, our conjecture of molecular unbinding induced by K deposition has to be supported by additional structural and electronic data of the K-PTCDA-Ag interface. In the following sections LEED, STM and UPS results are presented and the questions addressed here will be answered.

5.3 LEED study

After having determined the vertical adsorption geometry of PTCDA on Ag(110) in the presence of coadsorbed K atoms (section 5.2), we now investigate the lateral arrangement of the K+PTCDA phase. To this end, LEED experiments were performed. In particular, the roles played by the amount of deposited K and by the annealing step were studied. This provides some valuable information about K-doped PTCDA on the Ag(110) surface.

5.3.1 Experimental results

As already mentioned in the introduction of this chapter, the K+PTCDA/Ag(110) system was investigated by several techniques: XPS, NIXSW, LEED, STM, UPS. Experiments using different techniques were performed in different UHV chambers and therefore on different preparations of the K+PTCDA phase. Nevertheless, it was always possible to perform LEED experiment on the samples studied by means of the above-mentioned methods. Therefore, the resulting K+PTCDA diffraction pattern was considered to be the fingerprint of the phase we wanted to investigate. Analysis of LEED images was conducted by means of the free software *Spot-Plotter*.[97]

In Figure 5.15a-d, we report LEED diffraction patterns of different K+PTCDA preparations in four different UHV chambers, mainly devoted to SPA-LEED, NIXSW, STM and UPS experiments, respectively. Because of the different experimental setups, the preparation procedure was slightly different in terms of the PTCDA coverage (although still in the sub-monolayer regime), and in terms of the amount of deposited K and the annealing temperature. In order to compare diffraction patterns measured at different electron beam energies, images were rescaled (without altering their aspect ratio), in order to have the same distance between the central and the lateral rows of spots. Figure 5.15e-h show the same images as those in panels a-d, but contain colored circles on top of the most intense diffraction spots. Drawing the colored circles next to each other, as in Figure 5.15i, shows that they overlap almost perfectly (except for the MCP-LEED image that presents some additional spots, further discussed in section 5.4.3.2). The small deviations along the vertical direction of SPA-LEED spots compared to the others is due to a different detection system peculiar to that technique.[98] The corresponding corrected spot profile from spot (0.0) towards Ag spot $(0,\bar{1})$ is shown in Figure 5.17.

Based on the experimental evidence that the same K+PTCDA diffraction pattern could be successfully reproduced under different experimental conditions in different UHV chambers, we deduce that SPA-LEED, NIXSW, STM and UPS experiments were performed on sample surfaces having the same, or at least very similar, lateral order and vertical structure. We can therefore conclude that results from different experimental techniques presented in this chapter should be mutually consistent and, taken together, contribute to a deeper understanding of the same K+PTCDA phase adsorbed on the Ag(110) surface.

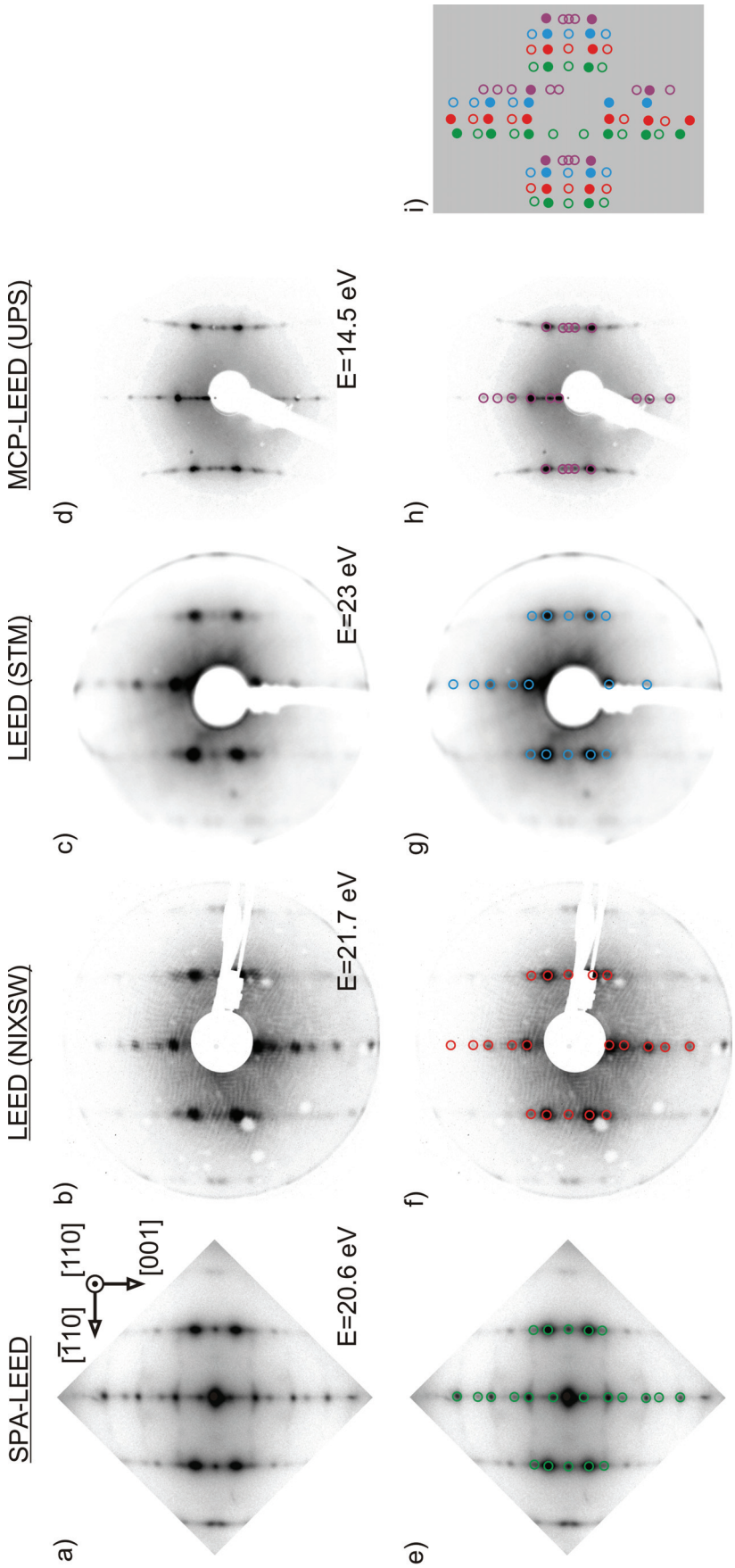


Figure 5.15: Diffraction pattern of K+PTCDA adsorbed on Ag(110). (a): SPA-LEED image (measured by O. Bauer, B. Fiedler, M. Sokolowski, Universität Bonn) and crystallographic directions, valid for each other image in the figure. (b): LEED image of the sample investigated by NIXSW. (c): LEED image of the sample studied by STM. (d): MCP-LEED image of the sample where UPS experiments were performed (measured by M. Willenbockel, T. Sueyoshi, S. Subach, Forschungszentrum Jülich). For each LEED image energy, of incident electrons is explicitly reported. (e-h): same images as the ones in panels a-d plus colored circles overlaying the diffraction spots. (i): colored circles are displayed next to each other to prove that they are representative of the same structure. Filled circles correspond to the most intense LEED spots.

5.3.1.1 Role of K amount

Having concluded that LEED images in Figure 5.15 are equivalent, we can focus on the SPA-LEED results since their better resolution allows fine features to be distinguished more clearly. Since it was not possible to determine quantitatively the amount of potassium deposited on the Ag(110) surface, we will use the terms *low*, *intermediate* and *high* K coverage in the section below.

Figure 5.16a is the SPA-LEED pattern of *low* K coverage on one monolayer of PTCDA after annealing the sample at 380 K for 5 min. Diffraction spots belonging to the brickwall superstructure of PTCDA (see Figure 4.2) are still present and brighter than the new spots appearing along the [001] direction. We therefore conclude that upon deposition of a *low* amount of K, PTCDA molecules are arranged in one or more ordered phases represented by the additional diffraction spots, besides the pre-existing brickwall superstructure, whose vectors in the reciprocal and real space are shown in Figures 5.16d and g, respectively. If an *intermediate* amount of K is deposited, followed by another annealing step, brickwall spots disappear and the previously faint spots become now much more intense (see Figure 5.16b), making it possible to determine the new fundamental unit cell formed by K-doped PTCDA layer. Figure 5.16e shows the corresponding unit cell vectors and green circles over the relative diffraction spots. A real space sketch of the K+PTCDA unit cell and its structural parameters are displayed in Figure 5.16h, where the orientation of the molecules within the unit cell results from STM experiments, as discussed in section 5.4. If a *high* amount of K is deposited on the sample which is successively annealed, the result is the absence of any ordered phase as testified by the presence of a continuous faint diffracted line between the (0,0) spot and the first order Ag substrate diffraction spots. This indicates a disordered distribution of PTCDA molecules and K atoms on the surface. Substrate diffraction spots are shown in Figure 5.16f, while the corresponding real space drawing of the topmost Ag(110) surface layer, together with its unit cell, is reported in Figure 5.16i.

A more careful look along the [001] direction in Figure 5.16b reveals the presence of some less intense spots in between those attributed to the K+PTCDA phase. Their physical origin is the object of the following section.

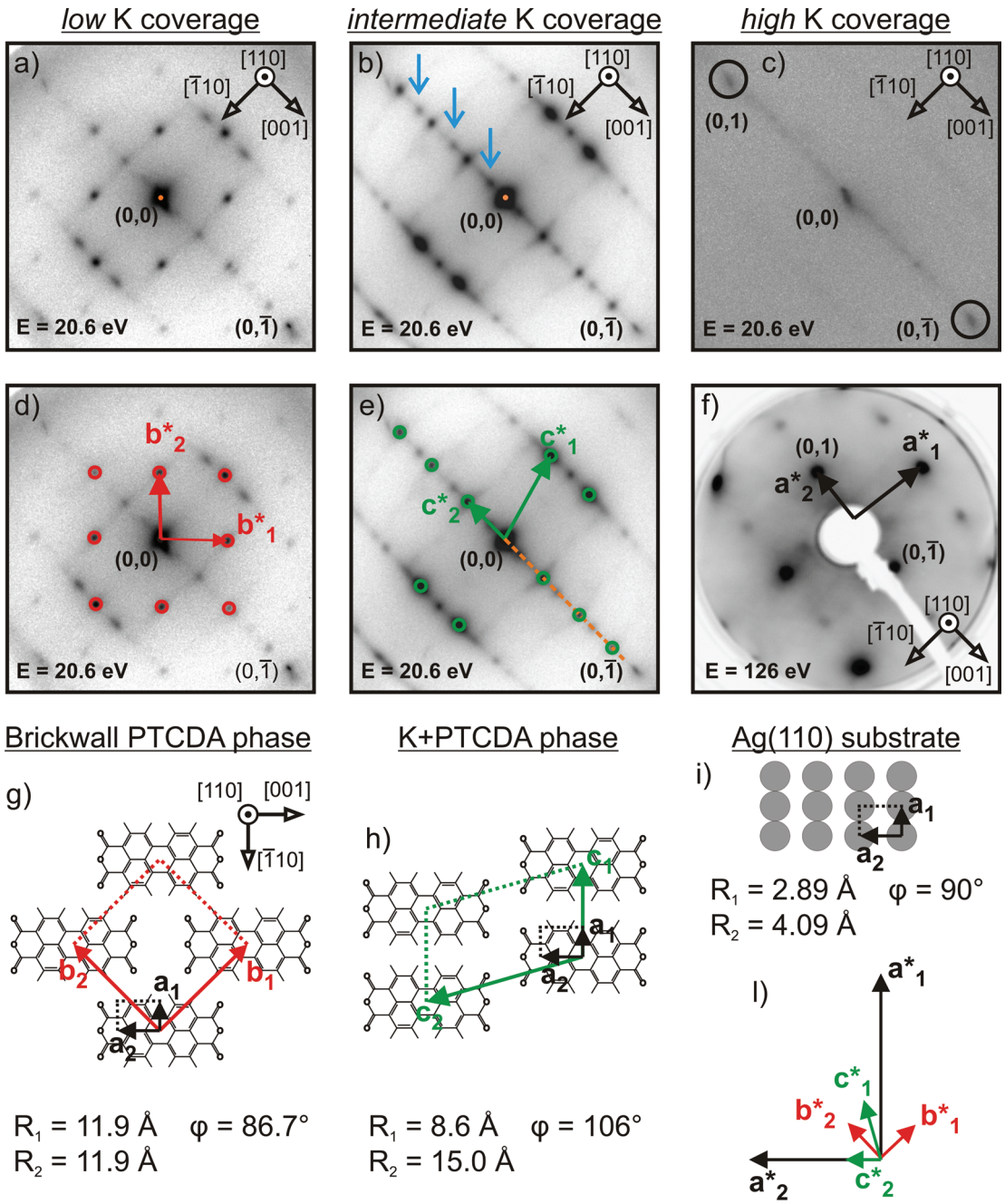


Figure 5.16: *Low* (a), *intermediate* (b) and *high* (c) K coverage SPA-LEED images, with corresponding brickwall PTCDA (d, red), K+PTCDA (e, green) and Ag(110) (f, black) unit cell vectors and circled diffraction spots, followed by real space drawing of PTCDA molecules (g,h) and Ag atoms (i) in the corresponding unit cells and by unit cell vector length (R_1, R_2) together with angle φ between them. (l): summary of Ag(110) (black), brickwall PTCDA (red), K+PTCDA (green) unit cell vectors in the reciprocal space. SPA-LEED images (a)-(e) were measured by O. Bauer, B. Fiedler, M. Sokolowski, Universität Bonn.

5.3.1.2 Additional diffraction spots

To understand the origin of the additional diffraction spots marked with a blue arrow in Figure 5.16e, two SPA-LEED line scans from the (0,0) spot to the (0,$\bar{1}$) Ag spot were further analyzed. In Figure 5.17, two experimental line profiles (red and blue lines) measured in this region, and corresponding to different preparations, are reported. The preparations differ in terms of PTCDA coverage (1 ML, red profile; 0.5 ML, blue profile), in terms of deposited K (deposition time: 105 s, red profile; 40 s, blue profile), in terms of annealing procedure (380 K for 5 min, plus 430 K for 5 min, red profile; 380 K for 5 min, plus 450 K for 5 min, blue profile).

Comparing the two SPA-LEED line scans of Figure 5.17, we observe that the blue one contains more fine structure: there are more and better resolved peaks than in the red profile, in which only two broad peaks, one relatively intense and the other very small, can be detected between two consecutive K+PTCDA diffraction

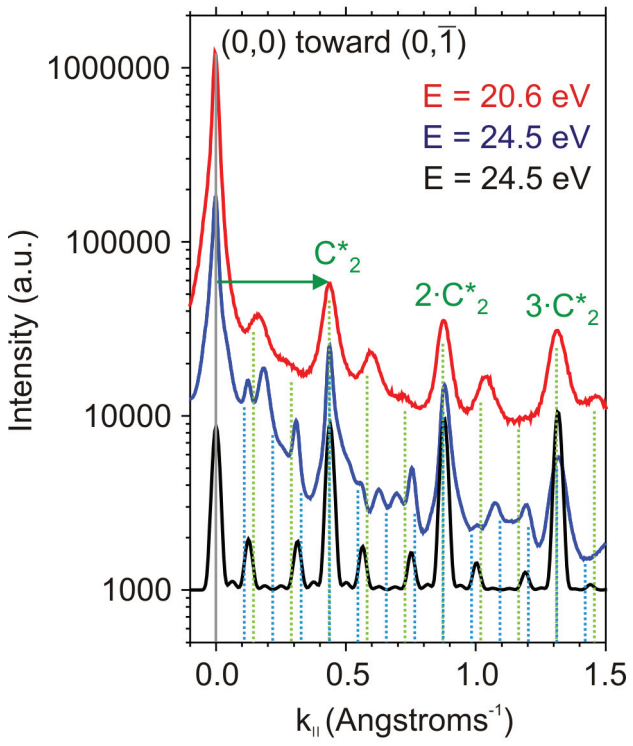


Figure 5.17: SPA-LEED line scans (red and blue lines) of two different K+PTCDA/Ag(110) preparations (see text), measured from the (0,0) spot to the (0,$\bar{1}$) Ag spot (region highlighted by the orange dashed line in Figure 5.16e). The simulated line scan (black line), plus the diffraction spots positions of ×3 and ×4 superstructures (green and blue dotted line) are also reported. The line scans were measured by O. Bauer, B. Fiedler, M. Sokolowski (Universität Bonn) and simulations were performed by M. Sokolowski.

spots (at multiple C_2^* positions). The presence of two additional peaks between the (0,0) and C_2^* spots of the red profile may indicate the existence of a real space unit cell three times larger than the K+PTCDA unit cell along the [001] direction, which would result in a diffraction spot at $k_{||}$ three times smaller than C_2^*, and corresponding higher order diffraction spots. The diffraction positions of such possible $\times 3$ superstructures are marked in Figure 5.17 by the dotted green lines. Analogously, the presence of at least four clear peaks in the blue profile between C_2^* and $2 \cdot C_2^*$ may hint at a $\times 4$ superstructure, whose unit cell along the [001] direction is four times larger than the fundamental K+PTCDA unit cell and its diffraction spot positions are highlighted by the dotted blue lines. Neither $\times 3$ nor $\times 4$ superstructures can explain the additional diffraction spots appearing along the [001] direction of our LEED patterns as shown in Figure 5.17.

However, the predicted existence of both superstructures which modulate the surface geometry of K+PTCDA phase was also confirmed by STM results, as will be shown in section 5.4. In particular, STM shows the co-existence of random arrays of $\times 3$ (T) and $\times 4$ (F) patterns. In order to understand which real space structures correspond to the measured LEED profile, the diffraction pattern of the simplest sequence (TFTFTFTF) was simulated[99] yielding the black line profile in Figure 5.17. The peak positions of the simulated curve and the blue profile are in very good agreement, although the intensities are still quite different. This limitation of the calculations may be due to the fact that K atoms are completely neglected in this first approximation, although they will contribute to the scattering process, since their positions are not precisely known. Moreover, the intensity of the diffraction peaks might be affected by the exact sequence of T and F domains, which is presently not known. If disordered sequences such as TTTFTTFFTTT are considered, then the simulated peaks become broader, while their positions are not affected to a great extent. The energy of the incident electrons also appears to have little effect on the calculated profile within the range of energy considered (20.6 eV-24.5 eV). The evidence that introducing disorder in the sequence causes the broadening of the peaks may at least partially explain the broader peaks of the red profile, although disorder alone cannot explain the different modulation in intensity of peaks in the regions between C_2^* and $2 \cdot C_2^*$ spots, and between $2 \cdot C_2^*$ and $3 \cdot C_2^*$ spots (blue curve in Figure 5.17). To rationalize this fine structure, it is presumably necessary to introduce K atoms and TF superstructure that is closer to the experimental one in the structure model whose diffraction pattern is simulated.

From this deeper analysis of the SPA-LEED profile, we learn that in addition to the fundamental K+PTCDA unit cell described in section 5.3.1.1, there are two more co-existing superstructures on the surface responsible for the additional spots which could not be easily assigned. This result is in perfect agreement with STM findings that will be presented in section 5.4.

5.3.1.3 Role of annealing step

The LEED pattern of the K+PTCDA phase (Figure 5.15a-d) is the result of K deposition on one monolayer or less than a monolayer of PTCDA, followed by annealing at a temperature of approximately 180 °C. Figure 5.18 shows a series of LEED images after K deposition with and without annealing, in order to assess the role played by the annealing step in the formation of K+PTCDA phase. Potassium

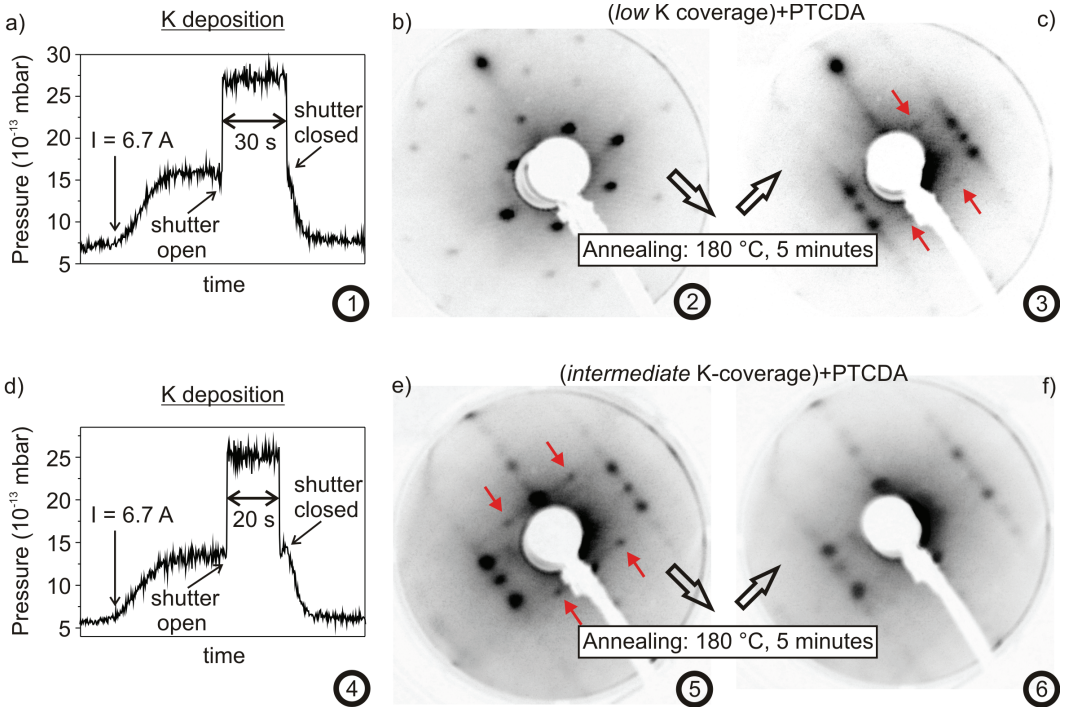


Figure 5.18: LEED images (b,c,e,f) following two consecutive depositions of K (a,d): each figure is labeled with a circled number indicating the sequence order. (a,d): vapor pressure of K, measured by a quadrupole mass spectrometer set to detect K atomic mass (39), displayed as a function of time during K deposition in the UHV chamber. Significant steps such as setting the current going through the K dispenser, and opening and closing the shutter are explicitly marked on the plots. (b): LEED image recorded immediately after K deposition of step 1. (c): LEED image after annealing the sample at 180 °C for 5 min. (e): LEED image recorded immediately after K deposition of step 4. (f): LEED image after annealing the sample at 180 °C for 5 min. Red arrows point to brickwall PTCDA diffraction spots to underline their presence.

deposition was monitored by its vapor pressure (Figures 5.18a,d), measured by a quadrupole mass spectrometer (set to record atomic mass 39). In order to better control K deposition, we built an evaporator consisting of a K dispenser (SAES getter) between two electrical contacts. Deposition temperature was monitored with a thermocouple. Deposition time was regulated with a shutter. Electric currents are reported on the plots (Figure 5.18a,d).

We will now show that the role of annealing is actually essential in the formation of the K+PTCDA phase. In fact, the LEED pattern recorded immediately after 30 s K deposition is almost indistinguishable from the one of the pure PTCDA brickwall phase, as shown in Figure 5.18b. However, after annealing at 180 °C for 5 min, the LEED pattern changes significantly and spots attributed to a K+PTCDA phase appear, while the pure PTCDA brickwall structure is still present, due to the small amount of K deposited, as already discussed in section 5.3.1.1. After another deposition, this time for 20 s on the same sample, but still before annealing, the pattern in Figure 5.18e is obtained, showing essentially the same features as Figure5.18c. Upon subsequent annealing at 180 °C for 5 min, the LEED pattern changes again, and the brickwall diffraction spots indeed disappear completely. This is an indication that the pure brickwall phase is fully converted into the K+PTCDA superstructure.

5.3.2 Discussion of LEED results

In this section we presented LEED results and showed that XPS, NIXSW, SPA-LEED, STM and UPS experiments were performed on samples obtained from different preparations nevertheless leading to the same K+PTCDA LEED pattern (see Figure 5.15). The preparation of the K+PTCDA phase proceeds in three steps: first, preparation of the PTCDA submonolayer (as reported in section 4.2.1); second, K deposition; third, annealing of the sample.

In particular, from the LEED investigation of the K+PTCDA system, it was possible to conclude that the amount of deposited K plays a crucial role. In fact, the K concentration on the surface has to be sufficient, proportionate to the coverage of PTCDA molecules, in order to convert brickwall phase into the ordered K+PTCDA phase, but below a threshold above which no ordered superstructure can be detected. Already at this point an interaction can be deduced between K and PTCDA

adsorbed on the Ag(110) surface, depending on their relative concentrations. Indeed, if only a low amount of potassium is deposited on the molecular layer, only part of the molecules contribute to form the new alkali-molecule phase, while the rest remains in the pristine PTCDA brickwall phase. The evidence that the amount of K deposited in order to achieve the desired K+PTCDA phase depends on the pre-existing concentration of PTCDA molecules is another clear indication of a correlation between potassium atoms and adsorbed molecules on the metal surface.

However, even after depositing the required amount of K on the sample, in order to trigger the phase transition from brickwall to K+PTCDA it is necessary to anneal the sample at about 180 °C for several minutes. Only then will diffraction spots of the pure PTCDA phase disappear and will K+PTCDA spots become more intense and clearly visible. The importance of annealing indicates that an energy barrier must be overcome in order to achieve the stable and ordered K+PTCDA phase. This conjecture will be confirmed and motivated when STM results are presented in section 5.4. The effect of annealing was also studied by UPS, whose experimental results are discussed in section 5.5. Here too, the strong influence of the annealing step on the electronic structure of K+PTCDA interface was found.

From a deeper analysis of SPA-LEED line profiles, corroborated by the simulation of diffraction spots starting from a simple structure model of the K+PTCDA (where K is presently ignored), it was possible to deduce the presence of two additional superstructures whose unit cell is three and four times larger than the fundamental K+PTCDA unit cell respectively along the [001] direction of the substrate. In future, LEED simulations that also include K atoms in the calculations may shine more light on the effect of the K amount on the concentration of different superstructures and consequently on the intensity of corresponding diffraction spots.

At this point, knowing that several superstructures co-exist on the surface, it is essential to investigate their structural properties and arrangement on the surface more carefully in order to check whether standing wave experiments were performed on a molecular layer at a given distance from the surface, or on several K+PTCDA phases with different vertical adsorption heights of PTCDA above the Ag(110) substrate. Moreover, the ambiguity of the K atoms' position, left by NIXSW data, still needs to be resolved in order to draw a more definite picture of the K+PTCDA structure model. For this purpose, STM experiments were performed and their results are presented in the next section.

5.4 STM study

In order to further investigate the structural properties of the K-PTCDA-Ag interface, STM experiments were performed together with C. Weiss and R. Temirov (Forschungszentrum Jülich). Two different K coverage regimes were studied, focusing in particular on the structure of different molecular phases imaged on the surface. Real space images also contributed to a better understanding of diffraction patterns presented in the LEED section and provide a strong indication of the position of K atoms within the predominant K+PTCDA phase. Therefore, the STM results presented below represent a significant step towards a structure model of the alkali-molecule-metal interface.

5.4.1 Experimental details

STM experiments were performed using a commercial CreaTec low-temperature STM/AFM, in a UHV chamber with base pressure below 2×10^{-10}mbar at a sample temperature of approximately 5 K. PTCDA molecules were evaporated from a Knudsen cell onto the Ag(110) substrate kept at room temperature. Organic molecule deposition was followed by annealing of the sample at 160 °C for 5 min. In order to be able to clean the STM tip by controlled indentation in the bare Ag surface, a PTCDA coverage of about 0.5 ML was targeted. Potassium was then deposited from a commercial SAES getter source following the procedure already described in section 5.3.1.3.

STM experiments were performed on two preparations, differing in the amount of K deposited. In the first one, not enough K atoms were deposited to convert the whole brickwall phase into K+PTCDA phase, as shown in Figure 5.18c; hence the name *low* K coverage preparation. In the second preparation, the corresponding LEED pattern (Figure 5.18f) showed no evidence of the brickwall PTCDA phase, instead, only the K+PTCDA phase could be detected, explaining the term *intermediate* K coverage preparation.

STM images referring to each of the above-mentioned sample preparations are presented and discussed in the following two sections. All experiments were performed in the constant current mode. Finally, data analysis was carried out by means of the softwares STMAFM (version 3.0, CreaTec) and WSxM.[100]

5.4.2 *Low* K coverage results

5.4.2.1 Overview

The present section concerns the *low* K coverage preparation. As already discussed in section 5.3.1.1, the LEED pattern of the K+PTCDA system depends on the amount of K deposited on the surface. In particular, when the amount of K on the surface is *low*, then both brickwall and K+PTCDA diffraction spots co-exist, together with some additional spots whose corresponding real space structure could not be further specified based on LEED experiments alone. In fact, the STM image of a large surface area displayed in Figure 5.19 reveals the presence of at least three different phases, labeled as: brickwall, X phase, stripe phase. The first is the well-known submonolayer phase of PTCDA on Ag(110) (see chapter 4). The second and third are new superstructures induced by the presence of K on the surface. The X phase is the topic of the next section 5.4.2.2, while the stripe phase is discussed in detail in the *intermediate* K coverage section 5.4.3.

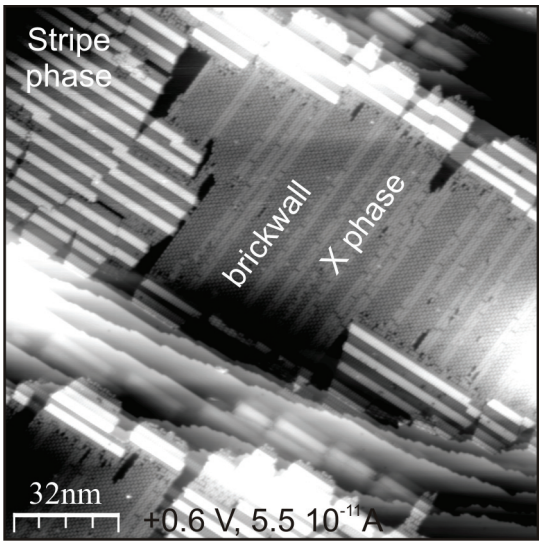


Figure 5.19: STM image of PTCDA/Ag(110) after depositing *low* coverage of K and annealing at 180 °C for 5 min. Image parameters: 160 x 160 nm^2, $I = 55$ pA, $V = 0.6$ V.

5.4.2.2 X phase

The X phase, shown in Figure 5.20a, consists of two double rows of PTCDA molecules and K atoms. Each of these double rows consists of a sequence of PTCDA pairs alternating with K atoms, giving rise to the peculiar "X": shape. The X phase alternates

with areas of brickwall phase and there is a clear relation between the two superstructures. In particular, we see that of the four PTCDA rows forming the X phase, the two external ones follow the brickwall periodicity while the two central ones, although they are shifted relatively to each other as in the brickwall phase, are also shifted with respect to the external rows by 8.6 Å along the [001] direction. Therefore, two consecutive PTCDA molecules are aligned along the [$\bar{1}$10] direction and there is enough space for K atoms to locate in the hollow site between PTCDA pairs

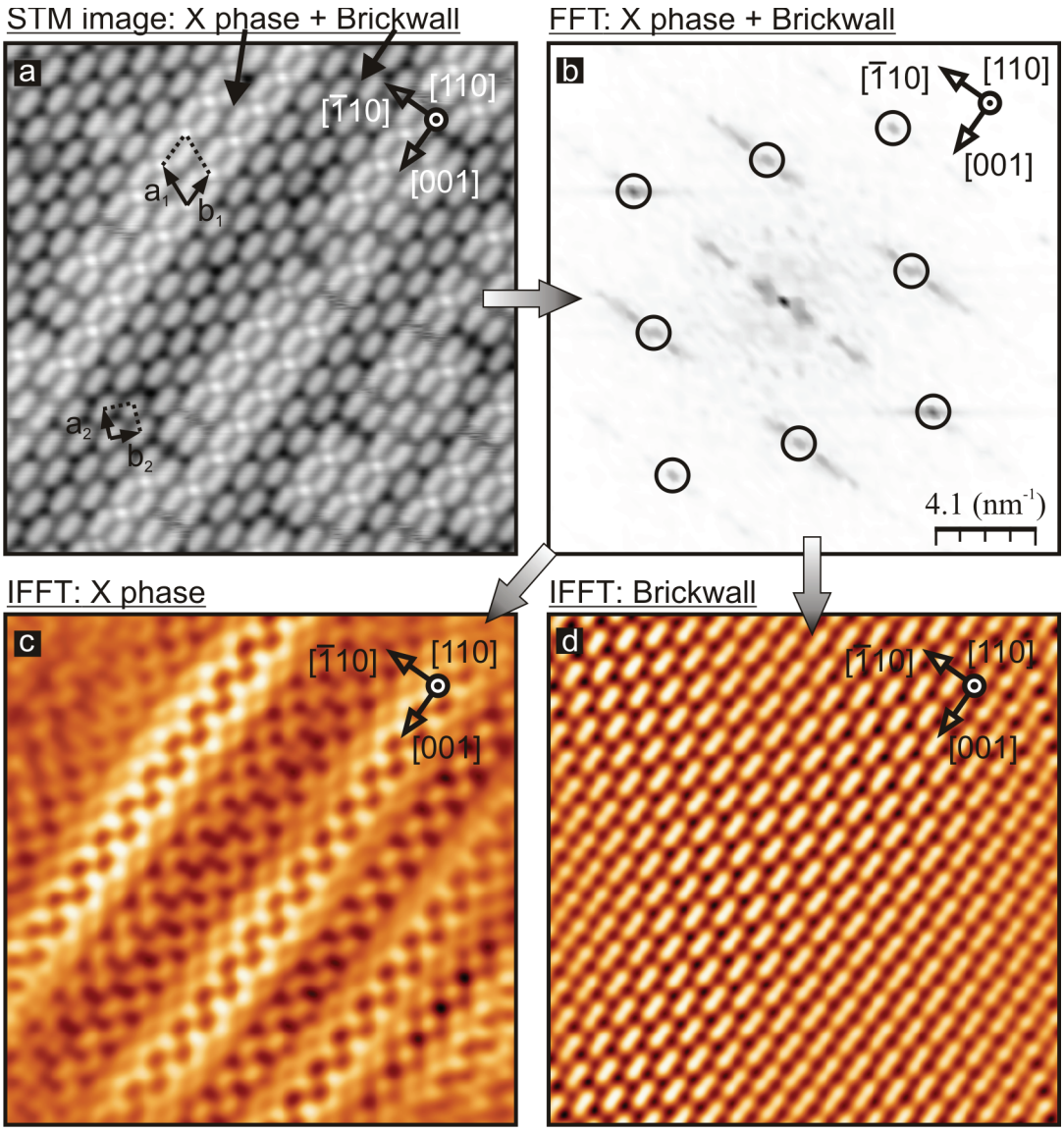


Figure 5.20: (a): STM image of PTCDA in brickwall and X phase, unit cell vectors of both superstructures are: $a_1 = 18.6$ Å, $b_1 = 15.4$ Å, $a_2 = b_2 = 11.9$ Å. (b): fast Fourier transform (FFT) of image in panel (a). (d): inverse FFT (IFFT) of the spots within the black circles. (c): IFFT of image (b) except the spots in the circles. Image parameters: (a) 20 x 20 nm^2, $I = 1.1$ nA, $V = 0.6$ V; (c) 20 x 20 nm^2; (d) 20 x 20 nm^2.

along the [001] direction. As shown in Figure 5.20a, K atoms are not always present within the X phase and it is difficult to use the term "unit cell" in this particular case, since the structure is periodic in one direction only. Nevertheless, the basic structure repeating along the [001] direction is the unit cell of vectors a_1 (18.6 Å) and b_1 (15.4 Å) marked in Figure 5.20.

In order to understand the effect of the presence of this additional X phase on the LEED pattern, a fast Fourier transform (FFT) of Figure 5.20a was calculated and its result is reported in Figure 5.20b. Inverse fast Fourier transform (IFFT) of the spots marked with circles in panel b is shown in panel d and confirms that they are representative of the brickwall phase. On the other hand, IFFT of image 5.20b, with the circled spots omitted, provides the modulation of the surface morphology corresponding to the periodicity of the X phase along the $[\bar{1}10]$ direction, as seen in panel c. The corresponding exact position of the spots in the reciprocal space is clearly dependent on the average distance between two consecutive double rows of X phase.

In conclusion, since the X phase is not strictly periodic along the $[\bar{1}10]$ direction (Figure 5.19 and 5.20a), the corresponding diffraction spots in the FFT image appear faint and broadened, and its presence cannot be detected in the LEED image recorded on the same sample preparation just before STM measurements (see Figure 5.18c). This could be due to the small concentration of X phase on the surface as compared to brickwall and stripe phase, which instead appears to predominate and to which we now turn.

5.4.3 *Intermediate* K coverage results: stripe phase

5.4.3.1 Introduction

After depositing more potassium on the sample whose STM images have been discussed above, and annealing at 180 °C for 5 min, the LEED pattern, already shown in Figure 5.18f, was obtained. The LEED image does not show any brickwall diffraction spots and indeed the corresponding STM images confirm the absence of PTCDA molecules arranged in the brickwall phase. No X phase could be registered in any of the surface areas scanned by the tip. Apparently, all PTCDA molecules contribute to the stripe phase, whose name comes from the presence of stripes of molecules with different contrast, as shown in the top right corner of Figure 5.19.

Due to the complexity of the stripe phase, the following section is divided into four parts. The first part concerns the correlation between real space STM images and the corresponding reciprocal space images, providing a new interpretation of the LEED patterns. In the second and third parts, vertical and lateral properties are analyzed, respectively. Finally, in the fourth part, the position of K atoms within the K+PTCDA phase is discussed.

5.4.3.2 Real space and reciprocal space images

The main result of the LEED analysis of the *intermediate* K coverage preparation (section 5.3.1.2) was the co-existence of the K+PTCDA phase together with a superposition of ×3 and ×4 patterns responsible for the additional diffraction spots along the [001] direction. Figure 5.21a indeed shows a K+PTCDA phase whose electronic contrast is modulated such that 4- and 3-PTCDA row structures are formed, consisting of two bright and two dark, and two bright and one dark PTCDA molecules, respectively. The alternation of brighter and darker stripes occurs along the [001] direction, while the PTCDA rows themselves are oriented along the $[\bar{1}10]$ direction.

To better understand the relation between the real space image of Figure 5.21a and the corresponding LEED pattern (Figure 5.18f), an FFT of Figure 5.21a was calculated and is displayed in panel b. The similarity to the experimental diffraction pattern of the same sample in which STM experiments were performed (Figure 5.18f) is remarkable. In sections 5.3.1.1 and 5.3.1.2 we attempted to correlate the diffraction pattern with the real space structure of the K+PTCDA phase. On the basis of STM experiments, we will now corroborate our former conclusions based on LEED data. In particular, the FFT (panel b) of the STM image in Figure 5.21a is taken into consideration and subdivided into two sets of spots. The first set (panel d) consists of the spots corresponding to the fundamental K+PTCDA unit cell, highlighted by the circles in panel b and in Figure 5.16e. The second set (panel f) is given by all the remaining spots. The IFFT images of the two sets of spots (panel d and f) are reported in panel c and e, respectively. The IFFT in panel c indeed shows the fundamental K+PTCDA unit cell already found on the basis of LEED data (see Figure 5.16e,h). Furthermore, the IFFT in panel e reveals the ×3 and ×4 patterns suspected to be responsible for the diffraction intensity between multiple C_2^* spots.

To further investigate the effect of ×3 and ×4 patterns on the diffraction spots,

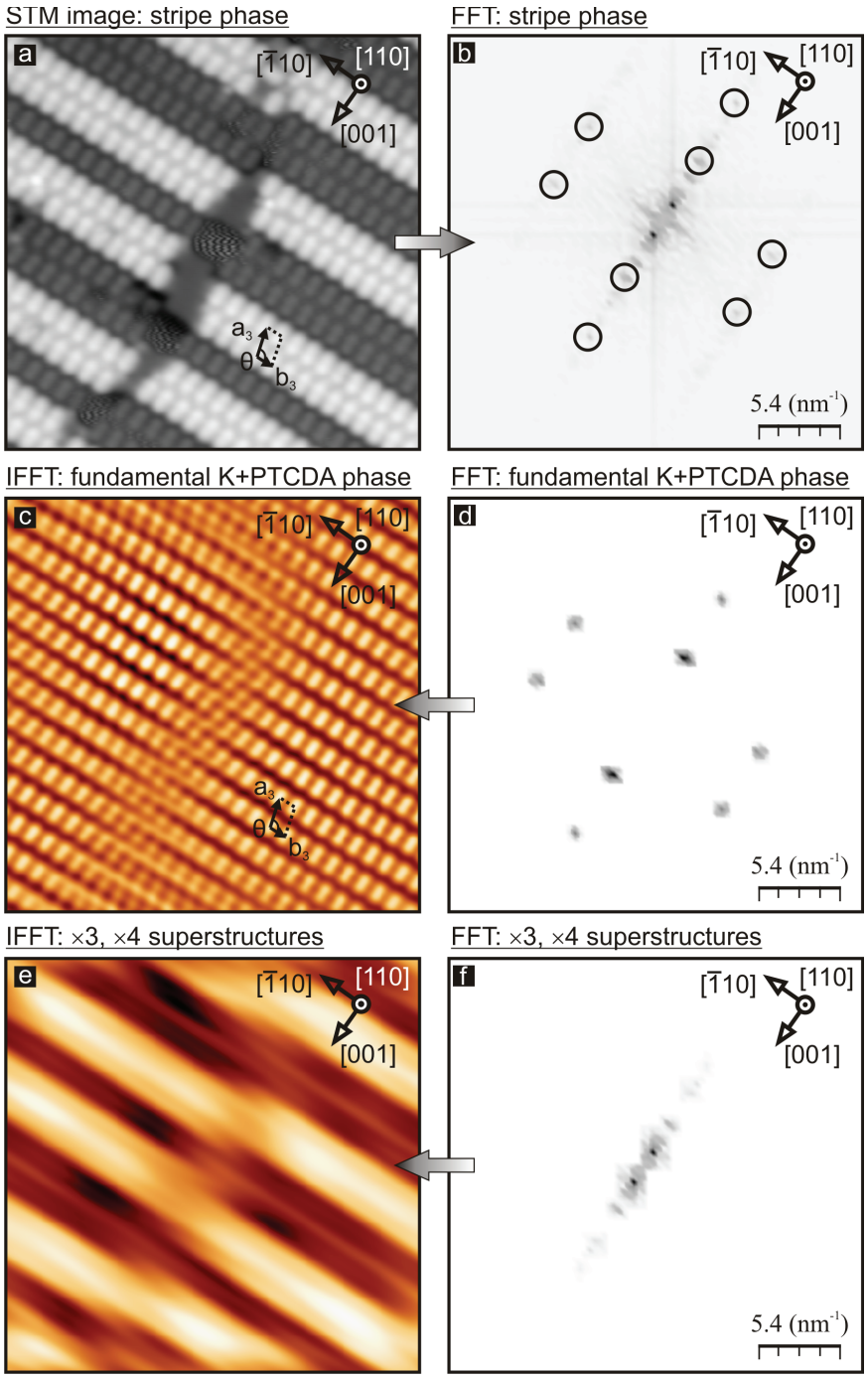


Figure 5.21: (a): STM image of two distinct domains of PTCDA in the stripe phase separated by a crack. Unit cell vectors and angle of the K+PTCDA phase: $a_3 = 15$ Å, $b_3 = 8.6$ Å, $\theta = 106°$. see Figure 5.16h. (b): FFT of the image in panel (a). (d): same FFT as in (b), containing only spots within the circles. (c): IFFT of spots in (d), representative of the fundamental K+PTCDA phase. (f): same FFT as in (b) except circled spots. (e): IFFT of image (f), showing the different contrast of the stripes. Image parameters: (a) 20 x 20 nm^2, $I = 1$ nA, $V = 0.1$ V, (c) 20 x 20 nm^2, (e) 20 x 20 nm^2.

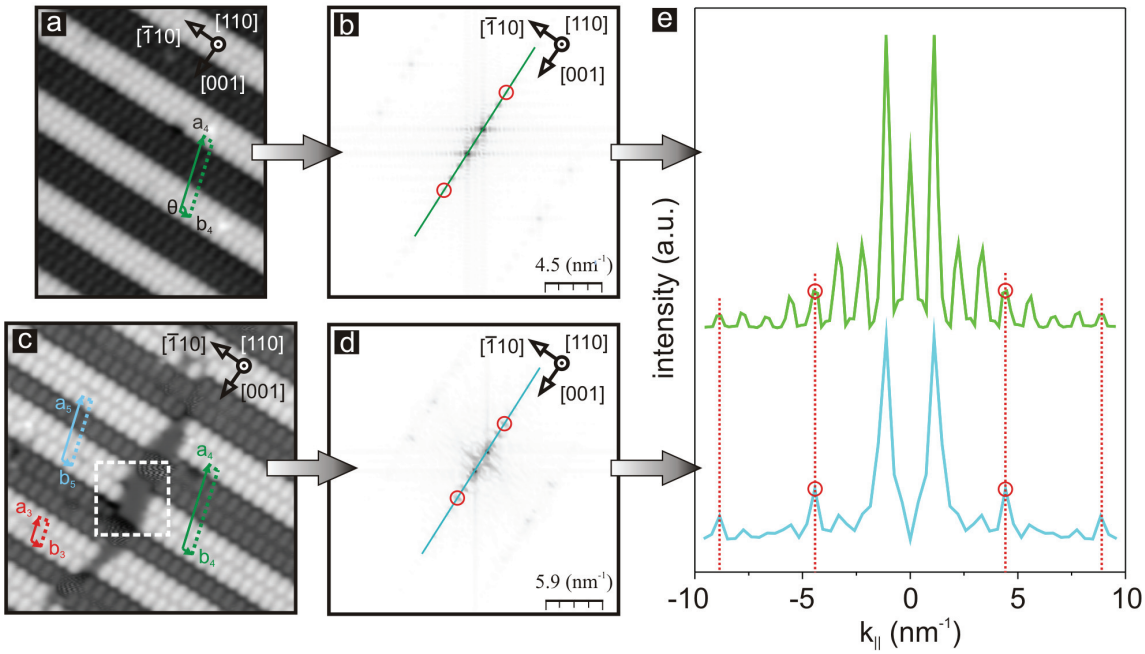


Figure 5.22: (a): STM image of a stripe phase area containing only the 4-row superstructure; corresponding FFT (b) and relative line-scan profile (e, green). (c): STM image of a stripe phase area divided by a crack and containing both 3-row and 4-row superstructures; corresponding FFT (d) and relative line-scan profile (e, cyan). Diffraction spots of the fundamental K+PTCDA phase are named in panels b, d, e and marked by red circles and dotted lines. Image parameters: (a) 18 x 23 nm^2, $I = 67$ pA, $V = 0.6$ V, (c) 20 x 20 nm^2, $I = 1$ nA, $V = 0.1$ V.

an image containing only 4-row superstructure (Figure 5.22a) and another one including both 3-row and 4-row patterns (Figure 5.22c) were considered. The FFT (panel b) of the 4-row patterned STM image (panel a) presents a series of spots along the [001] direction (green line scan in panel e) corresponding to the reciprocal vectors of a_4 (panel a) and its multiple order spots. On the other hand, the FFT line profile (cyan line scan in panel e) of the 3-row and 4-row patterned STM image (panel c) shows how 3-row patterns modify the relative intensities and the positions of spots intervening between the fundamental K+PTCDA diffraction spots (marked with dotted red lines). This result supports our suggestion formulated in section 5.3.1.2 to attribute the disagreement between experimental and simulated diffraction spots to the specific sequence of $\times 3$ and $\times 4$ superstructures.

Another effect that should not be neglected is the presence of the crack between the two domains of stripe phase (Figure 5.22c). This discontinuity contributes to the increase in disorder due to the relative shift of molecular stripes along the [001] direction, and this finally results in broader peaks, as can be seen from the comparison of line profiles in Figure 5.22e. If we look more closely inside the crack (Figure

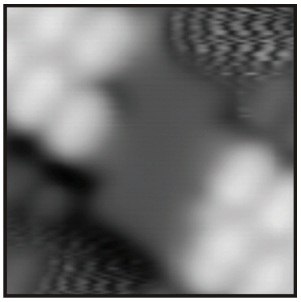


Figure 5.23: Zoom of the STM image (Figure 5.22c) within the dashed square. Image parameters: 5 x 5 nm^2, $I = 1$ nA, $V = 0.1$ V.

5.23), we observe a disruption of the surface represented by the shift of Ag atomic rows to form an antiphase boundary between the two molecular domains. A similar observation has been reported by Barth et al.[101] as a side effect of the K-induced reconstruction of Au(110), mainly observed after K deposition at approximately 450 K, whereas the formation of antiphase domain boundaries was apparently suppressed at room temperature. This can be explained by a higher energy requirement for shifting entire substrate atomic rows.

We have shown how from the analysis of the stripe phase STM images and their FFT, we can at least qualitatively explain the presence of additional spots in K+PTCDA LEED images. We will now show how the LEED pattern of the stripe phase can provide hints about the relative concentration of 3-row and 4-row patterns. Figure 5.24 displays the positions of the diffraction spots of the fundamental K+PTCDA unit cell (red), ×4 superstructure (green) and ×3 superstructure (blue), based only

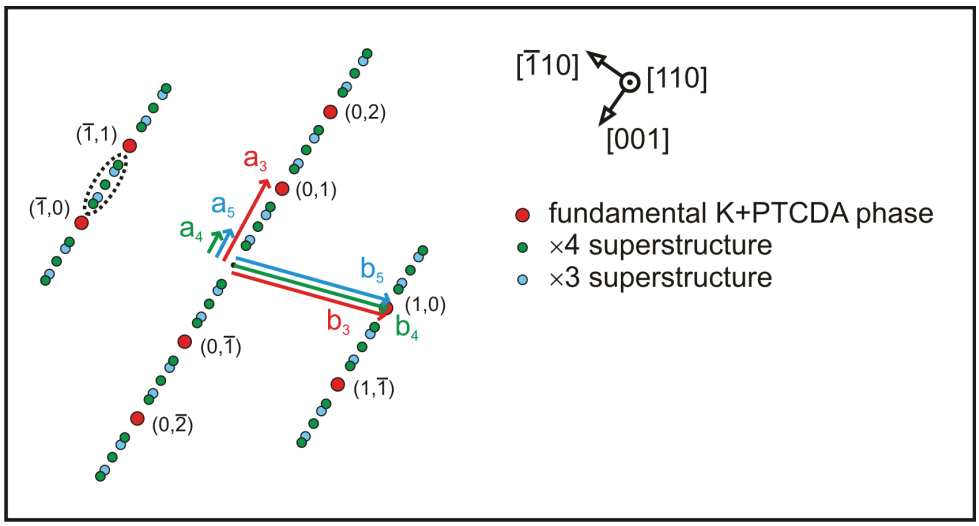


Figure 5.24: Positions of diffraction spots and unit cell vectors of the fundamental K+PTCDA phase (red), ×4 (green) and ×3 (blue) superstructures.

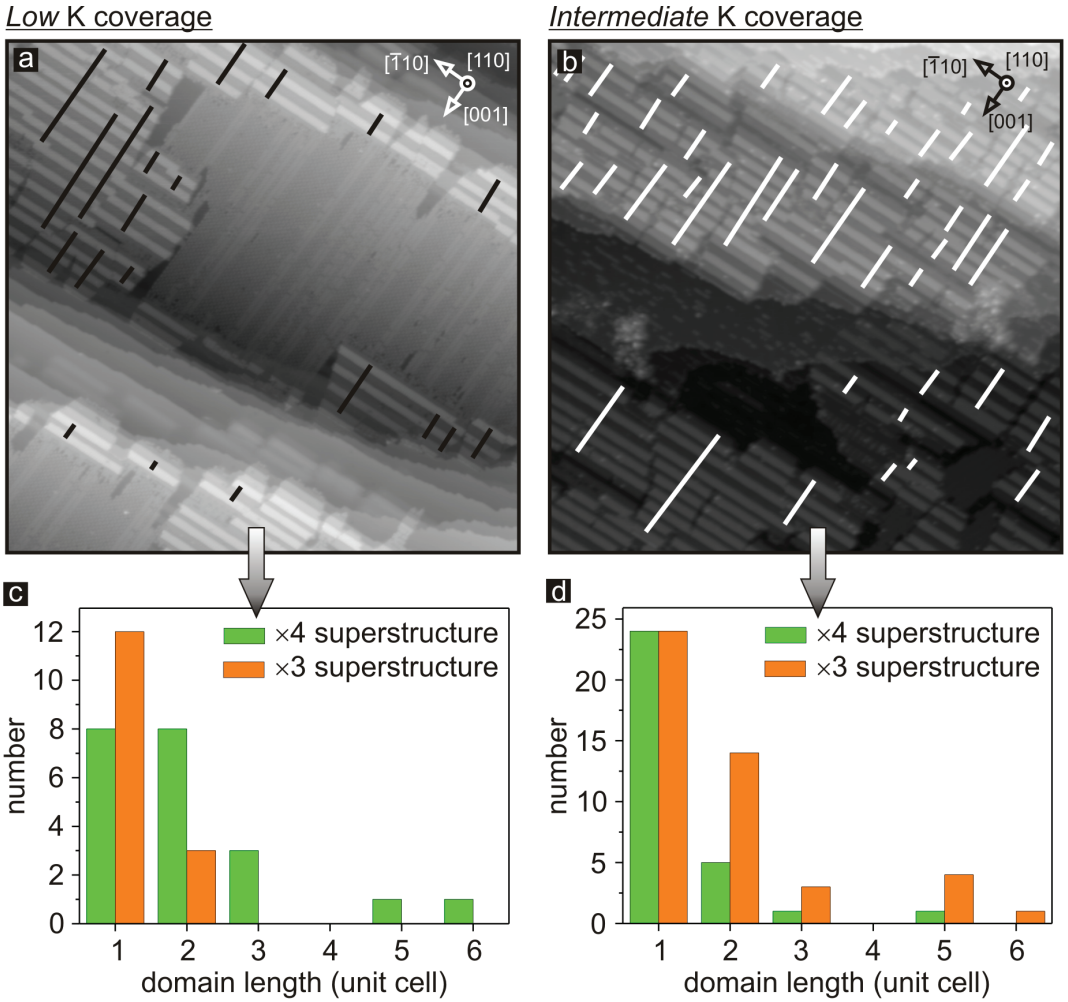


Figure 5.25: STM images of *low* K coverage (a) and *intermediate* K coverage (b) on PTCDA/Ag(110), including line scans (black and white, respectively) considered for counting the domain length of ×4 and ×3 superstructures. Bar plot (c and d, corresponding to a and b, respectively) of the number of ×4 (green) and ×3 (orange) superstructures having a given domain length. This analysis was performed by M. Willenbockel (Forschungszentrum Jülich). Image parameters: (a) 160 x 160 nm^2, $I = 55$ pA, $V = 0.6$ V, (b) 160 x 160 nm^2, $I = 0.1$ nA, $V = 0.6$ V.

on the knowledge of the corresponding unit cell geometry. In particular, this figure helps to understand the origin of the LEED spots in the region (marked by the dotted black line) between ($\bar{1}$,0) and ($\bar{1}$,1) K+PTCDA spots (red), which has not been discussed so far. Clearly, diffraction spots in this region are related to those already analyzed between spots (0,0) and (0,1); however, they have the advantage to be far enough from the (0,0) peak of the elastically scattered electrons to be analyzed without interference from the (0,0) spot. If we focus our attention on the region in the dotted circle of Figure 5.24, we can immediately conclude that in the exclusive presence of 3-row structures there would be no central green spot. Since the relative intensity of diffraction spots also depends on the relative concentration

and arrangement of 3-row and 4-row patterns, by simply looking at the ($\bar{1}$,0)-($\bar{1}$,1) region of the LEED pattern one could estimate the concentration of 3-row and 4-row patterns at the surface, based on the intensity of the central diffraction spot. Following this argument, a mere glance at Figure 5.15a-d allows us to easily notice that the LEED image measured on the same sample in which UPS experiments were carried out presents a higher intensity of ×3 spots, thus, a higher concentration of the 3-row pattern, compared to all other LEED patterns in the same figure. As a result, our finding allows the K+PTCDA sample preparation to be characterized semiquantitatively just by inspection of the corresponding LEED image.

Having realized the influence of the arrangement of ×3 and ×4 superstructures on the diffraction pattern, a careful investigation of the domain length of ×3 and ×4 patterns, in terms of number of unit cells along the [001] direction, was carried out on both *low* K coverage and *intermediate* K coverage preparations by M. Willenbockel (Forschungszentrum Jülich).[102] From this study (see Figure 5.25), we can conclude that in the *low* K coverage regime there is a greater number of ×4 superstructures with a larger domain length compared to the ×3 superstructures which appears mainly with domain length of 1. In contrast, at *intermediate* K coverage, the ×3 pattern becomes more frequent and the number of ×3 periodicity areas having longer domain length increases at the expense of the ×4 pattern, which is mainly present as a sequence of one or two unit cells along the [001] direction. There is thus a correlation between the amount of deposited K and the structure of the stripe phase. In particular, larger ×3 superstructure areas correspond to higher K concentration. This conclusion is confirmed and strengthened by photoemission data discussed in section 5.5.4. We will focus again on the position of potassium within the stripes and a structure model will be proposed and discussed in section 5.6.

5.4.3.3 Vertical properties of the stripe phase

Having proved the correlation between the additional diffraction spots besides the ones deriving from the fundamental unit cell, we can now investigate the origin of the dark/bright contrast modulation among the stripes. In Figure 5.26a, three different stripe contrasts (dark gray, light gray, white) are present, and from the line scan profile in panel b, it follows that the height difference between two neighboring stripes is 1.43 Å, the same height of a single step of the bare Ag surface (panel d), and approximately the same vertical distance between the brighter and the darker

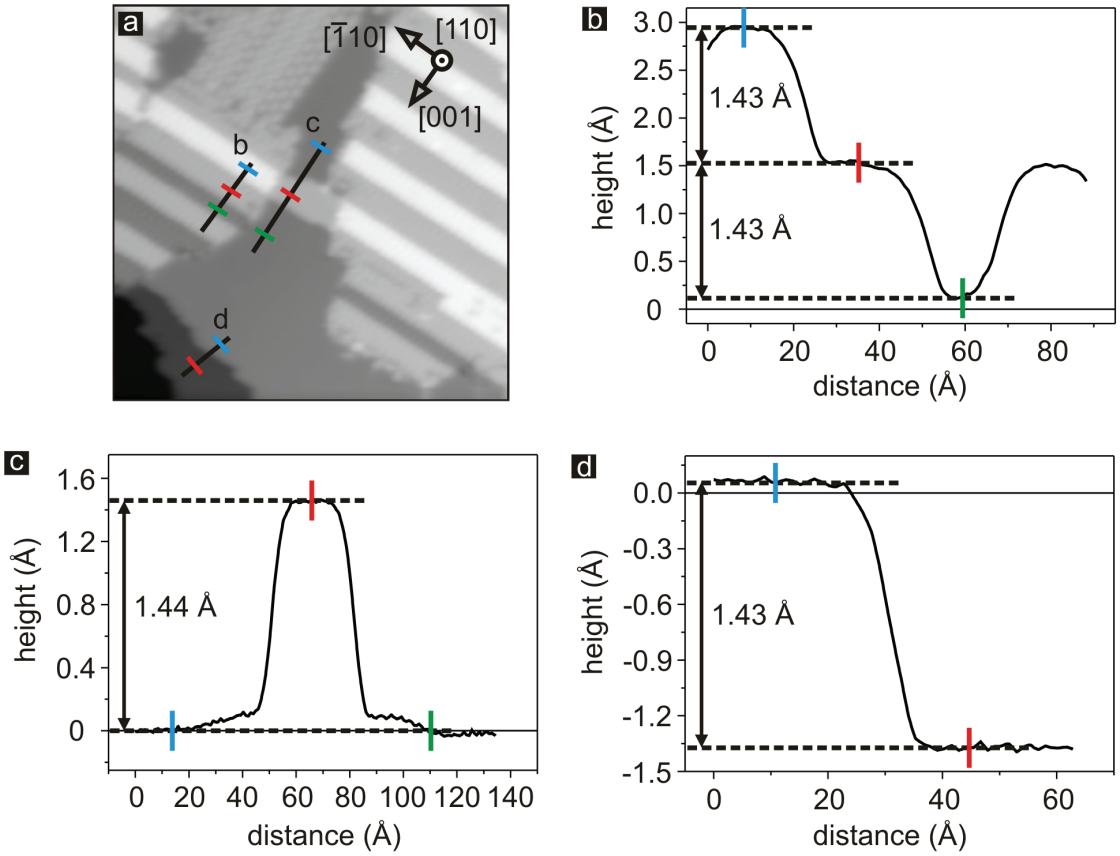


Figure 5.26: (a): STM image of *low* K coverage PTCDA/Ag(110). Line scan profiles of trajectories going over four stripes of different contrast (b), over the area between two domains of stripes (c), and over a Ag step (d). Image parameters: (a) 40 x 40 nm^2, $I = 0.5$ nA, $V = 0.1$ V.

area in the crack region between two domains of stripes (panel c). The experimental observation that apparent height difference between two stripes of different contrast is equal to the Ag(110) step height, plus the evidence that the inner contrast of the stripes is the same for brighter and darker stripes (see Figure 5.21a), strongly indicate that different stripe contrast and consequent heights are actually due to the underlying Ag substrate which defines the striped pattern on which PTCDA molecules adsorb.

To prove our conjecture an additional experiment was performed. An area containing the stripe phase and bare Ag covered with chains of K atoms was imaged (see Figure 5.27a). Then, the STM tip was used to scratch the surface in order to remove PTCDA molecules and have a closer look at the surface below. After several controlled indentations of the tip into the bare Ag surface in order to remove atoms attached during contact with the molecular layer and ultimately to prevent artifacts, the same area was imaged again (see Figure 5.27b). It appears very clear that the

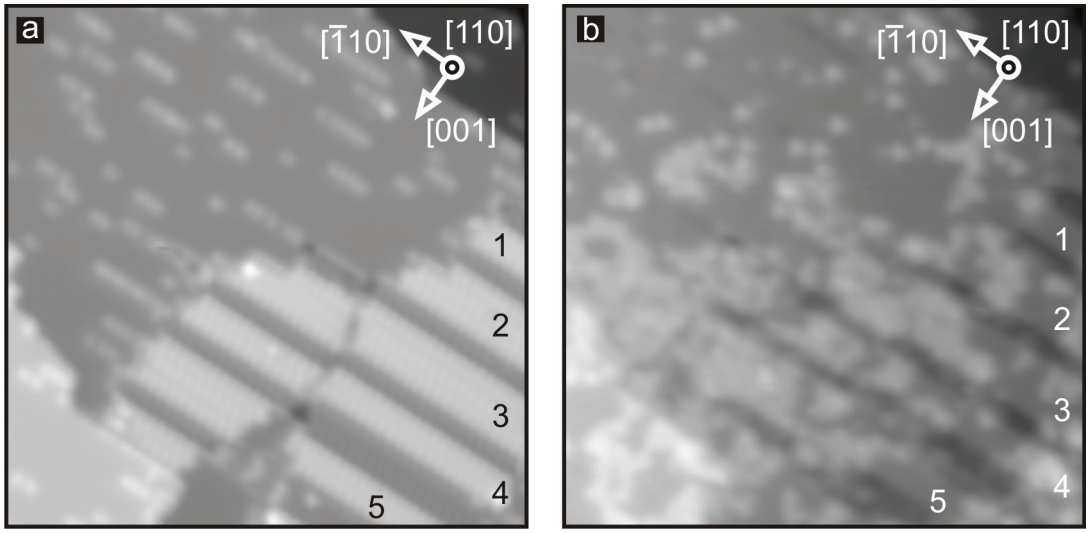


Figure 5.27: (a): STM image of an area containing stripe phase and K atoms chains on the bare Ag surface. (b): image of the same area as in (a) after having destroyed the molecular layer by scratching the surface with the STM tip. Image parameters: (a) 40 x 40 nm^2, $I = 0.7$ nA, $V = 0.6$ V, (b) 40 x 40 nm^2, $I = 0.3$ nA, $V = 0.6$ V.

Ag substrate underneath the PTCDA layer indeed has the same striped structure as the molecular phase above. We can therefore conclude that the different contrast of PTCDA stripes comes from different heights of the molecular layer following the underlying Ag substrate.

It is important to remark here that since the distance between the upper and lower stripe is exactly equal to one Ag(110) step, that is, the distance between two consecutive (110) Bragg planes, if molecules in all stripes are at the same distance from the underlying topmost Ag layer, then their height is indistinguishable by NIXSW. In fact, if molecules are at the same distance from the Bragg plane, they will have the same structural parameters as those measured by the standing wave technique. Since STM images show that PTCDA molecules have the same kind of electronic contrast within the upper and the lower stripes (Figure 5.21a), it is reasonable to expect them to have the same electronic configuration, hence to be at the same distance from the underlying Ag topmost layer and therefore contribute to the same height as measured by NIXSW. As a consequence, we can reasonably exclude that the distance of PTCDA molecules from the Ag surface measured by NIXSW is an average among different phases, and we can thus consider the standing wave results as significant in the discussion of the molecule-substrate interaction.

5.4.3.4 Lateral properties of the stripe phase

After having investigated the vertical properties of the stripe phase, we focus on its lateral properties. In particular, the width of the three different kinds of stripes, 2-rows-up, 2-rows-down, 1-row-down, was measured and the average of width values from different STM images is reported in the plot of the line profile (Figure 5.28b) corresponding to the line scan marked by the black line in Figure 5.28a.

The 1-row-down stripe has a width equal to approximately half the width of the 2-rows-down stripe, as could be expected. Surprisingly, however, the width of 2-rows-up and 2-rows-down stripes differ significantly. The average width of the lower (upper) stripe is approximately 30.6 Å (26.8 Å). This difference of approximately 4 Å detected by line profile analysis of several STM images can be rationalized by constructing a side-view scale model of the stripes. In fact, in Figure 5.28c, we see that in order to accommodate the two molecular rows of the lower stripe, seven Ag atomic rows need to be removed. This leaves behind a region that is about one Ag unit cell vector wider then the upper stripe (see Figure 5.28c).

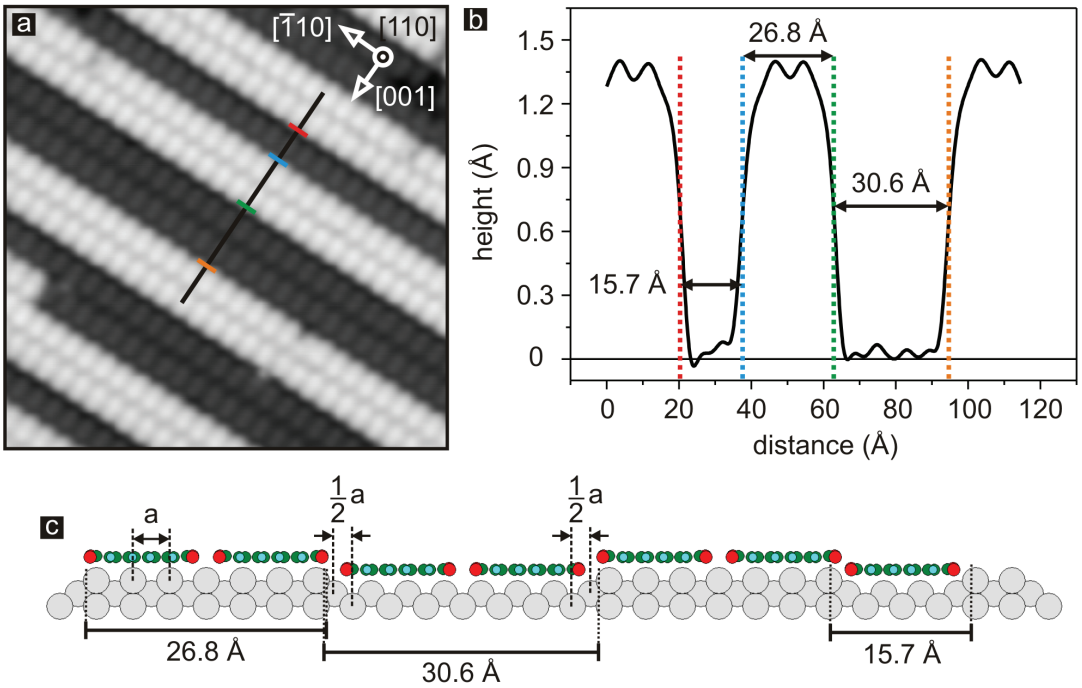


Figure 5.28: (a): STM image of a stripe phase area. (b): line scan profile of the area marked by the straight black line in panel (a), including stripes of different width. (c): side view of the structure model of the stripe phase, including both 2-rows-up+2-rows-down and 2-row-up+1-row-down structures, where a = 4.09 Å is the Ag unit cell vector. Image parameters: (a) 20 x 20 nm^2, $I = 1.1$ nA, $V = 0.6$ V.

From the structural model, constructed on the basis of the experimental evidence of different widths of up- and down-terraces, we deduce that the lateral position of PTCDA molecules relative to the Ag substrate atoms is different in the two kind of stripes. Nevertheless, despite this difference, the lateral arrangement of the molecules in the K+PTCDA unit cell remains constant and is independent of the kind of stripe. Evidently, the model presented so far disregards the presence of K atoms at the interface molecule-substrate. This aspect is discussed in the following sections and will help us to clarify the interaction between the molecular layer and the metallic surface.

5.4.3.5 Potassium fingerprint

Let us focus again on the first STM image shown in Figure 5.21a. There we see a small patch of stripe phase in which the electronic contrast clearly reveals the position of PTCDA molecules within the up- and down-terraces. By scanning the tip on the same area and applying a bias voltage of 1.5 V instead of 0.1 V, the image reported in Figure 5.29a is obtained. At this bias voltage too it is possible to distinguish stripes oriented along the $[\bar{1}10]$ direction and alternating with brighter and darker contrast along the [001] direction. Within each stripe and across each step between two stripes, the image contrast is further modulated by periodic elongated protrusions, characterized by the same unit cell as the fundamental K+PTCDA unit cell drawn in Figure 5.29a. In order to determine the position of those protrusions with respect to the PTCDA molecules, images of the same area recorded at 0.1 V and 1.5 V were compared and re-displayed in Figure 5.29b1 and b2, upper and lower panel, respectively. The schematic molecular structure of several PTCDA molecules was drawn at their corresponding positions in both the up- and down-terraces, as shown in panel b1. This molecular array was then transferred to identical positions of the lower panel. In this plot it becomes clear that the elongated protrusions (indicated by solid blue lines in panel b2) bridge parallel molecular rows within the stripes and across the steps. This reveals a clear structural correlation between the elongated protrusions and the PTCDA molecules.

For better characterization of the elongated protrusions, we look more closely at the STM image in Figure 5.29a, and we focus mainly on the area marked by the yellow square (Figure 5.30) obtained after image processing by low-pass and high-pass filter. The inspection of Figure 5.30 yields two remarks: First, the elongated protrusions appear as two distinct lobes (blue circles) in the area between the carboxylic

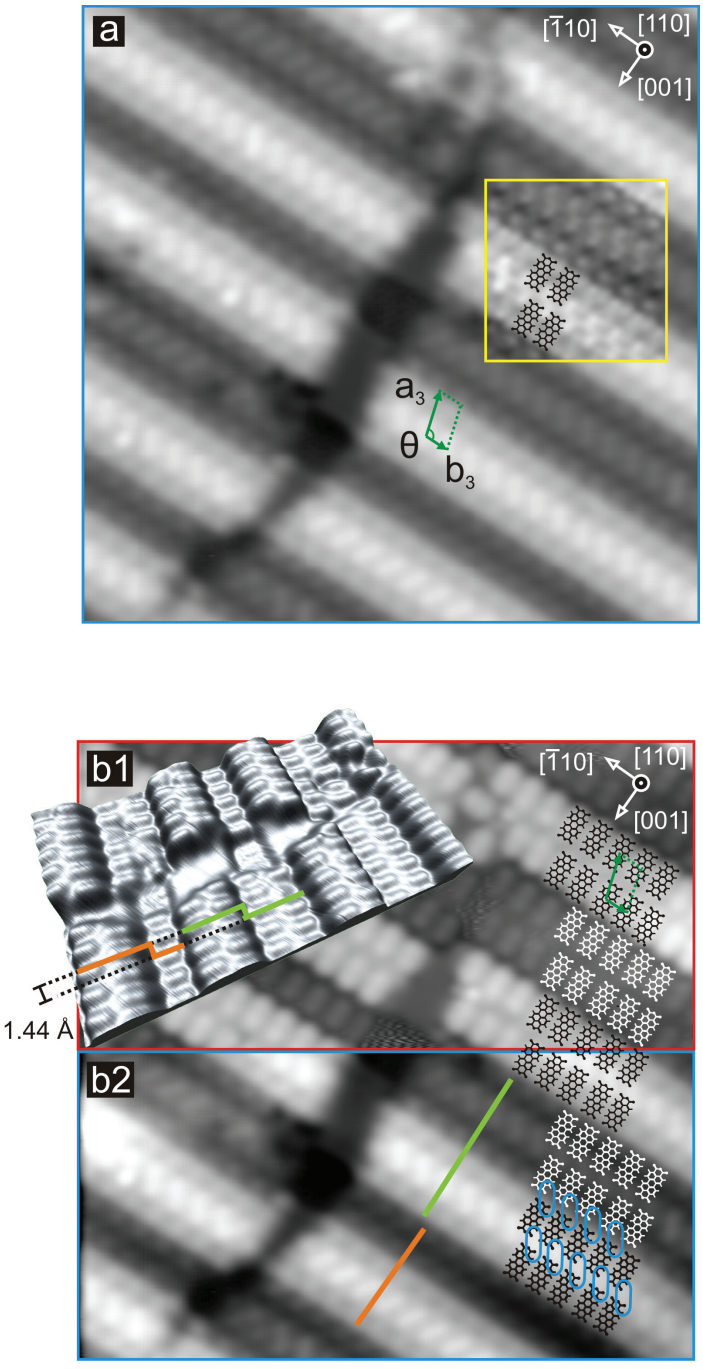


Figure 5.29: (a): STM image of the same area as in Figure 5.21a measured at bias voltage of 1.5 V (see below). The yellow square defines an area of the image processed by high-pass and low-pass filter. (b2): lower part of panel (a), thick green and orange lines correspond to the trajectories marked in the 3D plot of panel b1. (b1): upper part of Figure 5.21a, plus its 3D plot. Chemical structures of PTCDA are overlapped on the image, together with the fundamental K+PTCDA unit cell (green) and blue ellipsoids remarking the elongated protrusions underneath. Image parameters: (a) 20 x 20 nm^2, $I = 5$ nA, $V = 1.5$ V, (b1) 20 x 10 nm^2, $I = 1$ nA, $V = 0.1$ V, (b2) 20 x 10 nm^2, $I = 5$ nA, $V = 1.5$ V

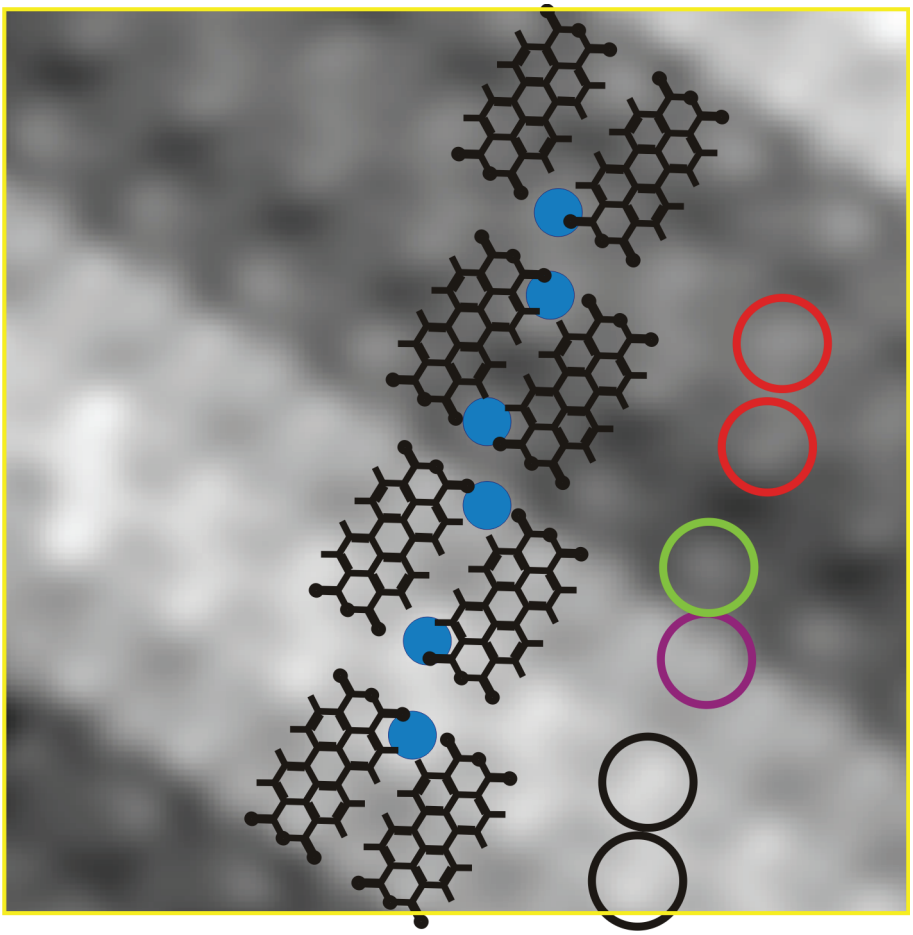


Figure 5.30: STM image of the area within the yellow square in Figure 5.29a, after processing by high-pass and low-pass filter. The schematic molecular structure of several PTCDA molecules is drawn at their corresponding position, together with filled blue circles at the position of the lobes. Lobes of different contrast are marked with circles of different colors: upper terrace (black), lower terrace (red), upper step (purple), lower step (green).

oxygen atoms of two neighboring PTCDA molecules. Second, these lobes have a different contrast and shape depending on their position with respect to PTCDA molecules and to the Ag substrate. In particular, the lobes appearing at the center of the up- and down-terraces have the same shape, however with different contrast, brighter and darker, respectively. On the other hand, the lobes appearing across the step between upper and lower terraces have a different shape in addition to slightly different contrast. From these STM images we can therefore conclude that there is a structural correlation between the elongated protrusions (consisting of two lobes) and the molecular layer. Furthermore, we suggest that the four different kind of lobes originate from potassium atoms lying under the molecular layer in slightly different chemical environment (see Figure 5.36). We will present several arguments supporting our conjecture below.

The correlation between the concentration of K and the coverage of stripe phase has been shown indirectly by the dependence of the relative concentration of ×3 and ×4 superstructures on the amount of K deposited (see section 5.4.3.2). It is therefore clear that K atoms must be somewhere within the stripes. However, STM images at 0.1 V bias voltage reveal only the presence of PTCDA molecules, although the ability to detect potassium was already shown for the X phase, from which we can conclude that potassium is not above the molecular layer. Moreover, the arrangement of molecules in the fundamental K+PTCDA unit cell prevents the possibility to accommodate K atoms within the molecular layer, at a vertical distance of 2.88 Å from the surface (see section 5.2.2.3), since it would be too close to the atoms of PTCDA. As a consequence, potassium is expected to be below the PTCDA molecules, within the topmost Ag layer in agreement with NIXSW results. Given this scenario, it is not surprising why alkali atoms cannot be imaged together with PTCDA molecules. However it is still not clear why the protrusions in Figure 5.29a and 5.30 should actually correspond to potassium atoms.

Inverse photoemission spectroscopy (IPE) study of the system K/Ag(110)[95] revealed the presence of K-induced unoccupied level appearing at 2.8 eV above E_F for K coverage $\Theta_K = 0.08$ ML. This peak grows in intensity and shifts towards the Fermi level until K coverage reaches 0.20 ML. For higher Θ_K, the peak decreases in intensity but continues to shift towards E_F. At K coverage of 0.34 ML the peak reached the Fermi level, where it remains even if coverage is further increased. Hence, IPE

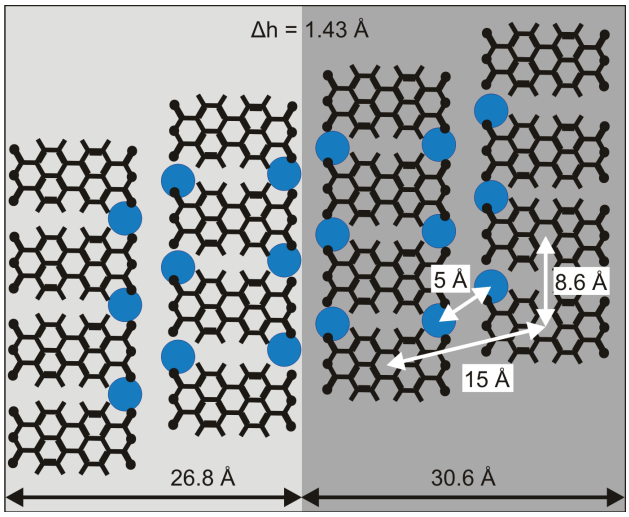


Figure 5.31: Schematic model of K and PTCDA relative positions in the up- (light gray) and down- (dark gray) terraces, including all structural information derived from STM images.

experiments show that the intensity and the energy position of the K-induced unoccupied state depends on the K coverage itself. For samples on which standing wave experiments have been carried out (see section 5.2.1.1) a K coverage of 0.27 ML was estimated. Since the LEED patterns of the XSW and STM preparations are basically identical (see Figure 5.15), we can exclude a significant difference in K concentration between the two, because it would definitely influence the diffraction pattern (see section 5.3.1.1). We can therefore assume that the STM experiments have been carried out on a K+PTCDA sample characterized by a K coverage of approximately 0.27 ML. From IPE experiments, we know that at $\Theta_K = 0.27$ ML the unoccupied density of states due to K reaches its maximum intensity at 1.5 eV above the Fermi level, exactly the energy level probed by the STM in Figure 5.29a. The bright protrusions thus originate from electrons tunneling into empty K-induced states. We can therefore conclude that inverse photoemission results support our idea of K atoms lying beneath the molecular layer embedded within the first Ag layer, as is schematically depicted in Figure 5.31. On the basis of this schematic model plus all other experimental results, a more detailed structure model will be presented in section 5.6.

5.4.4 Summary of STM results

The STM results presented in this section confirm the dependence of the K+PTCDA system on the concentration of K deposited on the surface, which was already concluded from the LEED study. In fact, experiments performed on two different preparations, depending on the K coverage, are discussed separately. Three different phases, brickwall, X phase and stripe phase, are found in the preparation characterized by *low* K coverage, while only the stripe phase could be detected in the *intermediate* K coverage preparation. This last sample preparation is characterized by the same diffraction pattern as found for samples on which standing wave and SPA-LEED experiments had been carried out.

Although only one phase could be detected from the *intermediate* K coverage images, the stripe phase is structurally complex. A careful analysis of STM images reveals the presence of $\times 3$ and $\times 4$ superstructures modulating the K+PTCDA phase, whose unit cell was presented in section 5.3.1. It was found that the intensity and position of additional spots apart from those of the K+PTCDA fundamental unit cell depend on the relative concentration of 3-row and 4-row structures, which in turn depends on the amount of K deposited on the surface, as was suggested from

LEED simulations 5.3.1.2.

Analysis of the vertical structure of the stripe phase reveals the presence of upper and lower stripes of molecules lying on up- and down-terraces vertically offset by 1.44 Å. From the same kind of inner electronic contrast of upper and lower molecular stripes, we deduce that molecules are in the same electronic configuration and at the same height relative to the substrate. This means that independent of the position of the molecule within the stripe phase, its distance from the surface is the same; therefore NIXSW data can still be interpreted as representative of PTCDA molecules in a similar adsorption state relative to the Ag surface. The analysis of the lateral structure of the stripes provides information about their width and enables us to draw a side view of the structure model representing the PTCDA layer on the up- and down-terraces.

Furthermore, although the role of the annealing step could not be specifically assessed, since all STM images were recorded only after annealing the sample, the need of additional activation energy to form the stripe phase could be inferred from the observed restructuring of the Ag surface below the molecular stripes. Finally, STM images at different bias shed more light on the possible position of K atoms in the stripe phase and suggest that K atoms are under the molecular layer within the topmost layer of Ag atoms. To support the picture of the K-PTCDA-Ag interface obtained so far, that is, mainly based on structural information, the investigation of the electronic structure needs to be carried out and this will be object of the next section.

5.5 UPS and XPS study

The following section consists of four parts. First, experimental details about sample preparation and measurement protocol are given. The second and third sections present work function and XPS data acquired by M. Willenbockel, T. Sueyoshi, S. Subach (Forschungszentrum Jülich). In the fourth section, the interpretation of experimental results in light of what has been already concluded from NIXSW, LEED, and STM is presented.

5.5.1 Experimental details

UPS ($h\nu = 21.22$ eV, He Iα) and XPS ($h\nu = 1486.6$ eV, Al Kα) experiments were performed in a UHV chamber equipped with a Scienta R4000 electron analyzer and MCP LEED. The base pressure of the UHV chamber is in the low 10^{-10}mbar range, while during XPS experiments, pressure was on the order of 1×10^{-9}mbar, and during UPS experiments it was about 6×10^{-10}mbar. All experiments were conducted keeping the sample at room temperature. The preparation and measurement procedure can be summarized in nine steps:

1) several sputtering and annealing cycles of the Ag(110) crystal followed by XPS and UPS experiments to check the cleanness of the surface,

2) evaporation of PTCDA molecules, followed by annealing at 300 °C for 5 minutes.

3) LEED experiment to check whether the diffraction pattern characteristic of the brickwall phase was obtained,

4) XPS of C1s or O1s core-level peaks, or UPS measurements,

5) K evaporation from a SAES getter dispenser,

6) XPS of C1s or O1s core-level peaks, or UPS measurements of the K+PTCDA phase, before annealing,

7) annealing of the sample at 200 °C for 10 minutes,

8) LEED experiment to check whether the diffraction pattern of K+PTCDA phase (see section 5.3.1) was obtained,

9) XPS of C1s or O1s core-level peaks, or UPS measurements of the K+PTCDA phase corresponding to the desired diffraction pattern.

It was observed that the K+PTCDA system, before the annealing step, is sensitive to the exposure to the x-ray beam. In particular, the exposure of the sample to x-rays for more than half an hour prevented the conversion of the brickwall phase to the K+PTCDA phase (sections 5.3 and 5.4) due to beam damage. For this reason, the XPS/UPS measurement time of the unannealed K+PTCDA sample was limited to not longer than 30 minutes. Since this time was insufficient to measure more than one spectrum with sufficient statistics, it was impossible to record C1s+K2p and O1s lines, and UPS of the same K+PTCDA unannealed sample. Therefore, the carbon and oxygen XPS and UPS data presented in this section refer to three different preparations, respectively. Each preparation is obtained by following exactly the same procedure summarized above and resulting in the same well reproducible LEED pattern (see Figure 5.15d). We will discuss C1s, O1s XPS and UPS data under the reasonable assumption that they refer to the same K+PTCDA phase, although they correspond to three distinct but analogous preparations.

Despite several annealing and sputtering cycles, the UPS spectrum of bare Ag(110) surface in Figure 5.33b (black line) shows a non-negligible intensity in the valence band region, apart from the typical *s*-*p* Ag band (reported in the inset of Figure 5.33b and measured using the same set-up but on another clean Ag(110) crystal). The measured valence band structure cannot be attributed to carbon, oxygen or potassium, as there was no evidence of those elements in XPS. Therefore, it must be due to some contamination of the surface which could not be further investigated. This contamination did not affect the binding energy of the C1s and O1s lines, found to be basically identical to the NIXSW preparation (see Table 5.12 in section 5.5.4), and it did not influence the work function as measured in the corresponding UPS spectrum (black line in Figure 5.33), which is 4.32 eV, and therefore very similar to the value of 4.34 eV obtained from the UPS spectrum in the inset of Figure 5.33b, where no additional structure in the valence band region was detected. As a consequence, the measured data will be still presented and discussed, focusing our attention mainly on the changes in work function and core-level binding energy shifts. In order to further investigate the valence band region of UPS spectra, and to address the effect of x-rays on the alkali-doped molecular layer, additional experiments on the same system are planned.

5.5.2 Work function results

The goal of our experiments is to investigate the work function behavior upon K deposition on the PTCDA/Ag(110), and upon subsequent annealing of the K+PTCDA phase. From UPS spectra it is possible to extract the sample work function, as depicted schematically in Figure 5.32. In particular, the work function can be expressed as:

$$\Phi_s = E_k^{cutoff} - \overline{E}_k^{F\prime} \tag{5.3}$$

where E_k^{cutoff} is the cutoff energy edge of the acquired photoemission spectrum and $\overline{E}_k^{F\prime}$ is the Fermi level of the sample density of states (DOS) (expressed in kinetic energy). Since $\overline{E}_k^{F\prime}$ can be calculated as:

$$\overline{E}_k^{F\prime} = E_k^{F\prime} - h\nu \tag{5.4}$$

where $E_k^{F\prime}$ is the Fermi level of the acquired photoemission spectrum, it follows that

$$\Phi_s = E_k^{cutoff} - (E_k^{F\prime} - h\nu) = h\nu - W. \tag{5.5}$$

$W = E_k^{cutoff} - E_k^{F\prime}$ represents the width of the whole UPS spectrum, where E_k^{cutoff} and $E_k^{F\prime}$ can be estimated from the photoemission spectrum acquired by the analyzer, as shown in Figure 5.33, and $h\nu$ is the energy of the He I excitation line (21.22 eV).

Figure 5.33a shows the cutoff region of UPS spectra measured on the bare Ag(110) surface (black), after PTCDA deposition (blue), after subsequent K deposition but before annealing (green), and finally after annealing (red) of the K+PTCDA/Ag(110) sample. Work function changes reported in the figure testify to significant differences in electronic properties between the molecule-metal interface and alkali-doped molecule-metal interface. The significant role played by the annealing step is confirmed again by the increase in the work function by 0.33 eV on annealing.

Another important aspect to be underlined here is the considerable difference in photoemission intensity between the secondary electron peak of the unannealed phase and all other curves. This evidence indicates a much higher concentration of disordered scatterers in the K+PTCDA layer before annealing, compared to after annealing and before K deposition. This observation, together with relative work function changes, will be discussed at the end of the section and will help us to

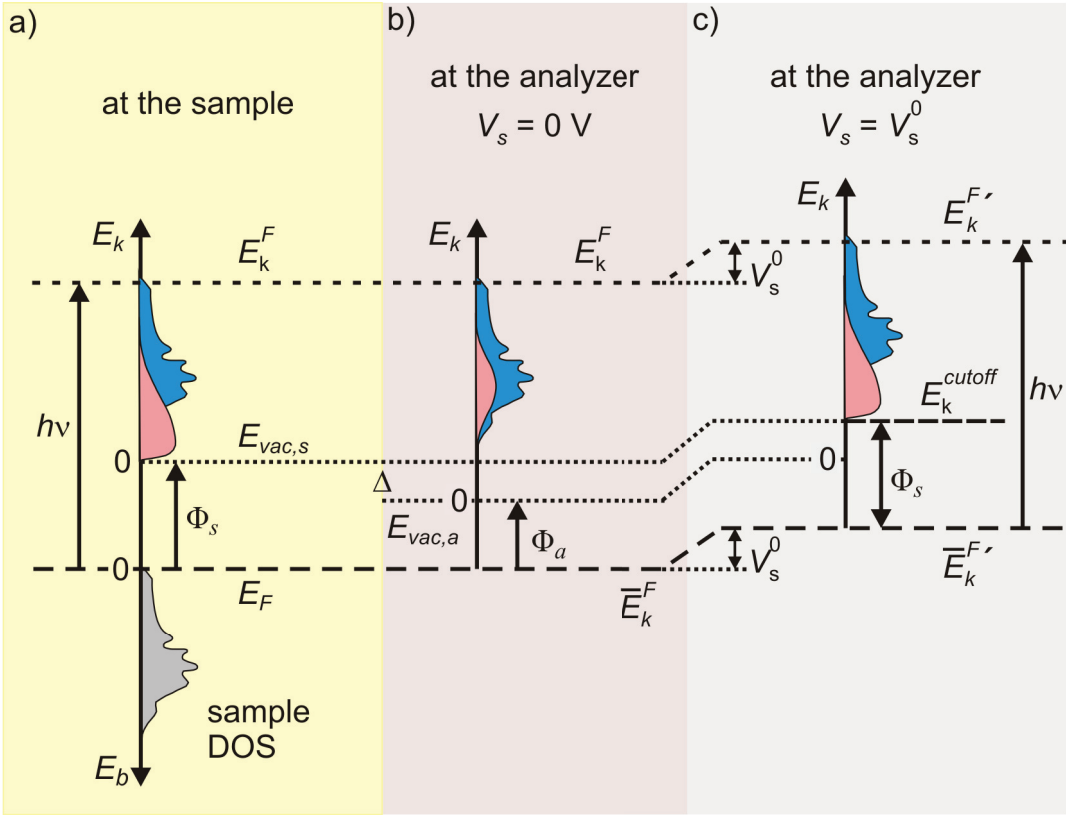


Figure 5.32: Schematic of photoemission spectroscopy to illustrate how work function is measured. The sample and the analyzer are in contact, having then the same Fermi level (E_F). Panel a (bottom): sample DOS as a function of the binding energy (E_b). E_F, vacuum level of the sample ($E_{vac,s}$) and work function of the sample (Φ_s) are marked in the figure. Panel a (top): distribution of (primary) electrons (blue) photoemitted by photons of energy $h\nu$ and (secondary) inelastically scattered electrons (pink), displayed as function of their kinetic energy (E_k). Fermi level in the kinetic energy scale is indicated by E_k^F. Panel b: distribution of photoemitted electrons measured by the analyzer of work function $\Phi_a < \Phi_s$ and with V_s (voltage applied between the sample and the first lens of the analyzer) equal to 0. Δ is the contact potential between sample and analyzer. $\overline{E}_k^F$ is the Fermi level of the sample DOS expressed in kinetic energy. If sample voltage is 0 and/or if $\Phi_a > \Phi_s$, secondary electrons with low kinetic energy will not reach the analyzer. In order to collect more secondary electrons for a better definition of the cutoff energy edge (see text), a sample voltage $V_s^0 \approx -3$ V is applied (c). Panel c: distribution of primary (blue) and secondary (pink) electrons measured by the analyzer with $V_s = V_s^0$. The corresponding Fermi level is $E_k^{F\prime} = E_k^F + V_s^0$; the secondary electron cutoff energy is indicated as E_k^{cutoff}; and $\overline{E}_k^{F\prime} = \overline{E}_k^F + V_s^0$ is the Fermi level of the sample DOS expressed in kinetic energy. The sample work function can be then estimated as $\Phi_s = E_k^{cutoff} - \overline{E}_k^{F\prime}$, hence $\Phi_s = E_k^{cutoff} - (E_k^{F\prime} - h\nu)$, where E_k^{cutoff} and $E_k^{F\prime}$ can be estimated from the acquired photoemission spectrum and $h\nu$ is the photon energy of the He I radiation line (21.22 eV).

sketch a model of K+PTCDA phase together with the XPS data, to which we now turn.

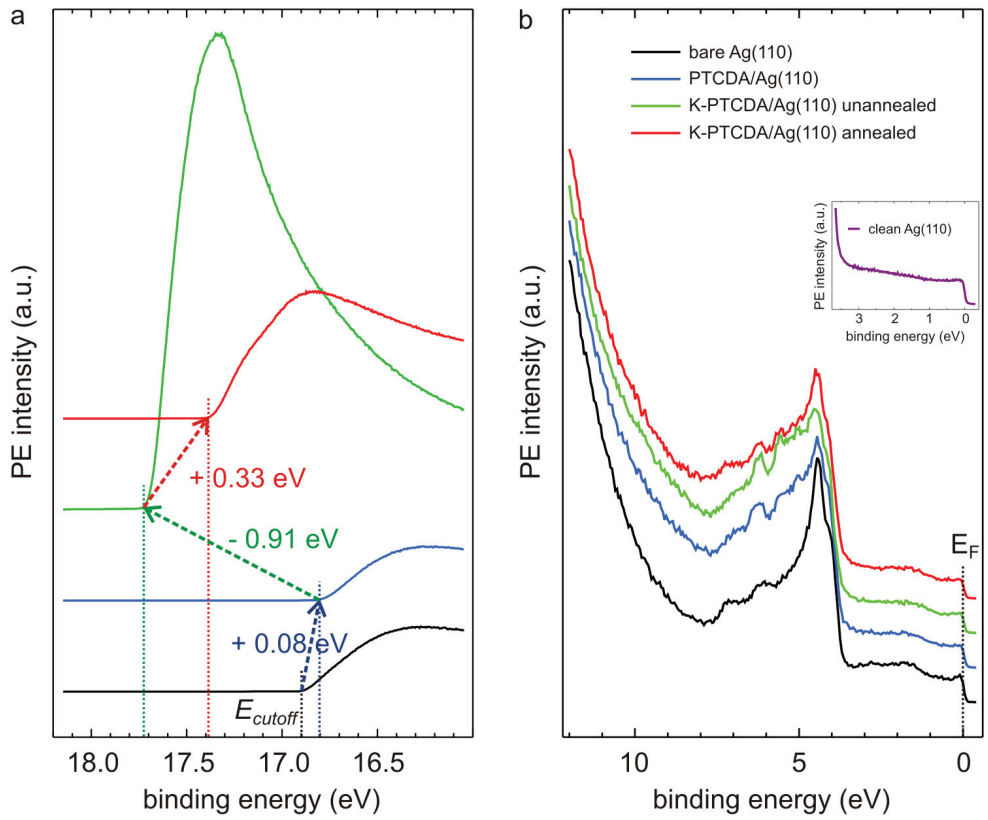


Figure 5.33: Cutoff region (a) and valence band region (b) of UPS spectra of bare Ag(110) (black), PTCDA/Ag(110) (blue), K+PTCDA/Ag(110) unannealed (green), K+PTCDA/Ag(110) annealed (red). These spectra were measured by M. Willenbockel, T. Sueyoshi, S. Subach (Forschungszentrum Jülich). Inset: valence band region of UPS spectrum measured on another clean Ag(110) crystal showing no additional structure (as black curve in panel b) apart from *s*-*p* band of the Ag substrate. This spectrum was measured by A. Delhey, T. Sueyoshi, S. Subach (Forschungszentrum Jülich).

5.5.3 XPS results

In order to have a full picture of the electronic structure of the K-PTCDA-Ag interface, XPS experiments were performed. The aim of these experiments was to investigate core-level shifts upon K deposition on the PTCDA layer, and after annealing of the sample. Combining this information with the UPS results will help us to develop a consistent model of the K+PTCDA phase.

PE spectra in the carbon region, reported in Figure 5.34a, show that the C1*s* core-level peak shifts by 0.4 eV to higher binding energy after K deposition. No detectable shift occurs after annealing. A reverse behavior is found for K2*p* peaks, which after annealing present lower binding energies by approximately 0.3 eV. However, it should be remarked that the relative intensity I_C/I_K stays constant, which indicates

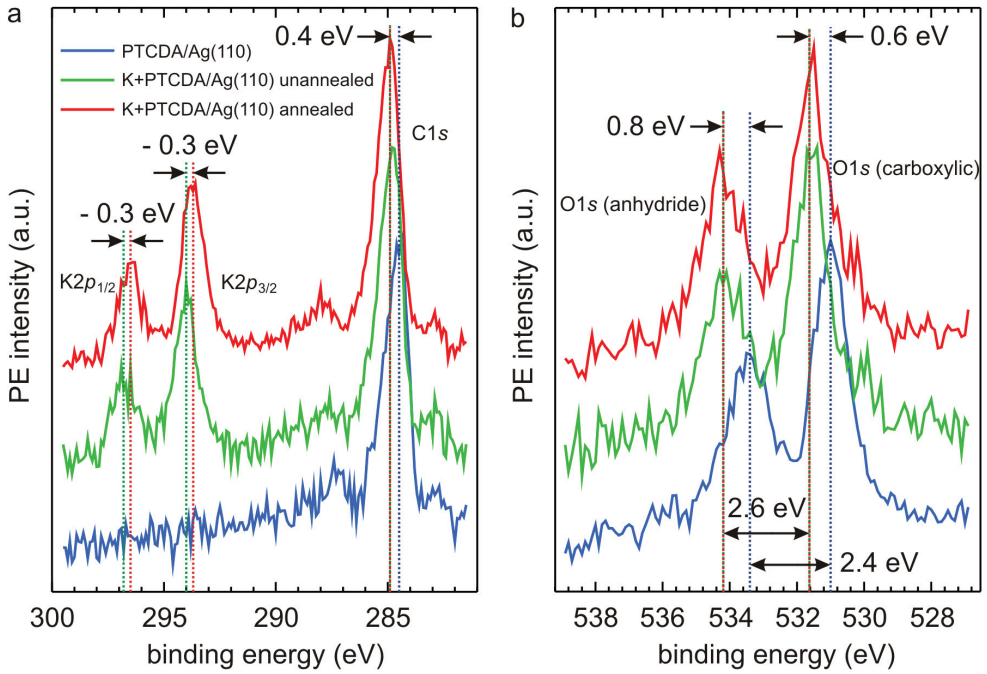


Figure 5.34: XPS spectra of C1*s* and K2*p* (a), O1*s* (carboxylic) and O1*s* (anhydride) (b) core-level peaks of PTCDA (blue), K+PTCDA unannealed (green), K+PTCDA annealed (red), deposited on the Ag(110) surface. These spectra were measured by M. Willenbockel, T. Sueyoshi, S. Subach (Forschungszentrum Jülich).

that no desorption of K atoms occurs on annealing; instead, a redistribution of K atoms at the interface can be expected. On the other hand, oxygen atoms seem to be more affected by the presence of potassium on the surface (see Figure 5.34b). In fact, upon K deposition the O1*s* carboxylic peak is measured at a binding energy that is 0.6 eV higher than in the pristine PTCDA/Ag(110). An even larger increase in the binding energy (0.8 eV) was registered for the anhydride O1*s* peak. Neither oxygen component changes its binding energy position on annealing, which may indicate that O-K interaction is not affected by the annealing of the sample. As a result of the differential shift of the two oxygen core-level lines, the chemical shift between the carboxylic and the anhydride peaks increases from 2.4 eV to 2.6 eV, while XPS in the context of NIXSW experiments provides an increase to 2.4 eV (see section 5.2.2.2 and Table 5.12). The interpretation of both XPS and UPS results will be discussed below.

5.5.4 Discussion of UPS and XPS results

In this section, work function changes, $\Delta\Phi$, and binding energy shifts of core levels, ΔE_b, presented in previous sections, are discussed with the help of the schematic ad-

sorption model presented in Figure 5.35. UPS and XPS experiments were performed in four different stages of sample preparation:

- bare Ag(110),
- after PTCDA deposition on the clean metal substrate,
- after K deposition on PTCDA/Ag(110) and before annealing,
- after annealing of the K+PTCDA/Ag(110) sample.

There are thus three distinct transitions. The goal of this section is to understand the *physics* behind the measured $\Delta\Phi$ and ΔE_b in each of the three processing steps, thereby providing an adsorption mechanism for potassium atoms on a PTCDA layer chemisorbed on the Ag(110) substrate.

Bare Ag(110) → PTCDA/Ag(110)

Work function changes induced by organic adsorbates on a metal substrate have been investigated extensively.[103–106] There are two main contributions to the work function change of an organic-metal interface, i.e., the push-back effect and the formation of a chemical dipole. Every neutral metal surface presents an intrinsic electrostatic surface dipole given by an excess electron density spilling out of the surface and an excess of positive charges inside the metal close to the surface. Both result from the "spreading" of negative charge into the free space due to the absence of the next atomic layer at the surface, as described by Smoluchowski in his seminal work.[107] This dipole is substrate dependent and it contributes to the work function of the metal.

Closed-shell molecules adsorbed on the surface push the surface electron density back into the bulk, reducing the surface dipole and thus the work function.[105,106] The closer to the surface the molecules are and the higher the coverage, the stronger the decrease in the work function due to the push-back effect. In the case of physisorption, the push-back of the electron density is the only contribution to the $\Delta\Phi$. For example, this is the case for Xe adsorption on metal surfaces, since no chemical interaction occurs.[104]

Upon PTCDA deposition on Ag(110) an increase, albeit small (+0.08 eV), in the work function is measured. This implies that the adsorption corresponds to a chemisorption process,[104] involving charge transfer from the metal substrate to the molecule and the consequent formation of a chemical surface dipole pointing towards the

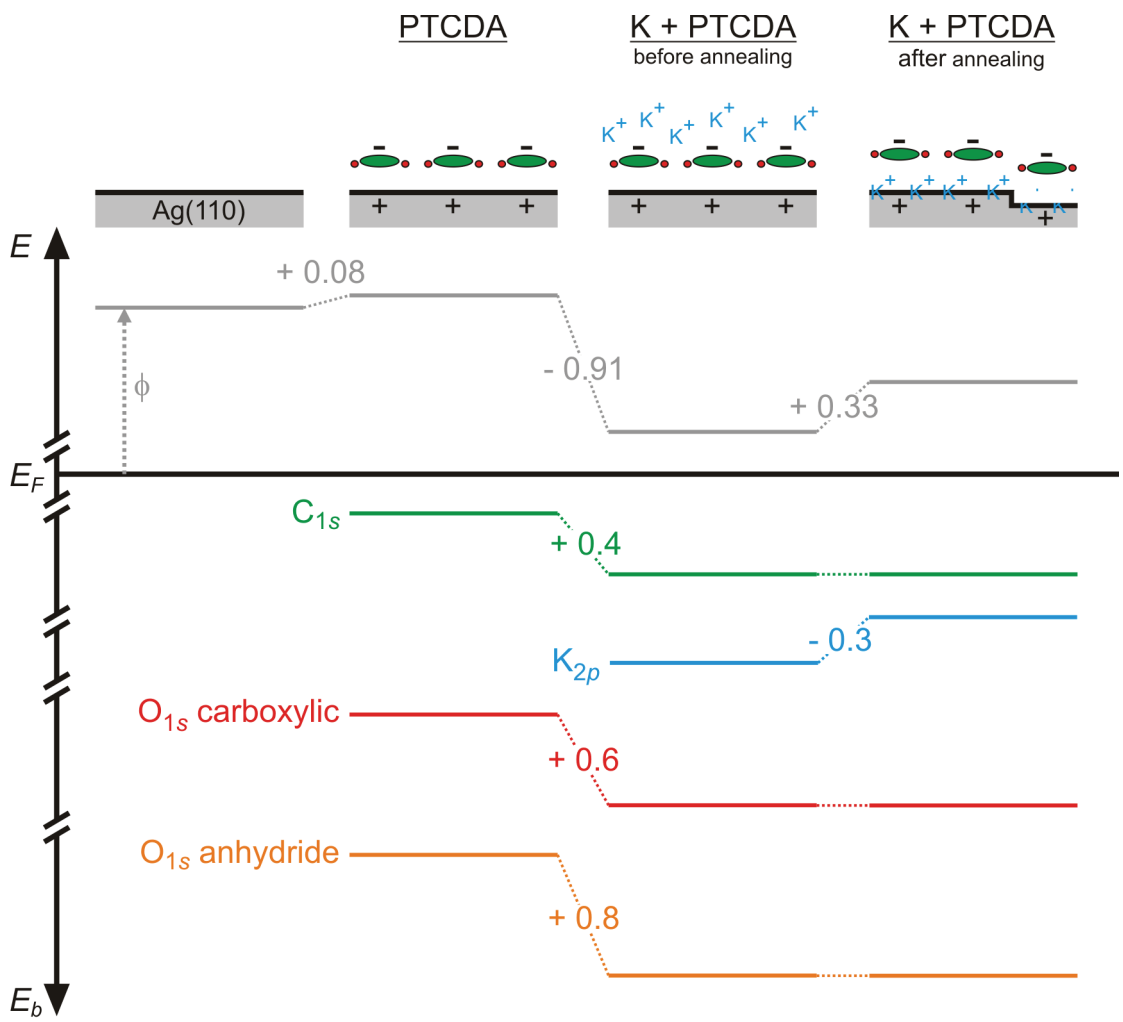


Figure 5.35: Schematic representation of clean Ag(110) surface, PTCDA deposited on Ag(110), K deposited on the PTCDA layer, K+PTCDA/Ag(110) after annealing, followed by an energy diagram to point out corresponding work function changes $\Delta\Phi$ and binding energy changes ΔE_b of C1s, K2$p_{3/2}$, O1s (carboxylic), O1s (anhydride) core-level peaks. E_F is drawn equal to the one of Ag(110), as was demonstrated by by Hill et al.[103] that for several PTCDA-metal (Mg, In, Sn, Au) interfaces the vacuum level alignment rule breaks down and Fermi level is "pinned" to that of the metal.

bulk, thus contributing to an increase in the work function. In fact, UPS measurements[75] on PTCDA/Ag(110) showed that upon adsorption, the former LUMO becomes occupied, indicating a charge transfer from the Ag substrate to the PTCDA molecule. Therefore, the increase of PTCDA/Ag(110) work function by 0.08 eV as compared to the bare Ag(110) follows from the superposition of push-back effect and chemical dipole.

PTCDA/Ag(110) → K+PTCDA/Ag(110) (before annealing)

After K deposition on PTCDA/Ag(110), UPS measurements reveal a strong de-

crease in the work function of 0.91 eV. This finding is explained by the following mechanism: K atoms transfer part of their negative charge to the substrate; thus they become positively charged. As a result, the positive partial charge of potassium and its image charge in the Ag substrate constitute an interface dipole pointing into the opposite direction of the surface metal dipole, leading to a significant decrease in the work function. In the following the arguments supporting this scenario are presented.

In XPS, we measure a binding energy of 294 eV for the K2$p_{3/2}$ core level, which is not far from the value of potassium atom in the ionic state (294.5 eV), measured upon doping C_{60} molecules with K,[108] where it is generally accepted that a total charge transfer of K4s electron to the C_{60} takes place. We can therefore expect to have K atoms at least partially ionized. However, it has still to be clarified where the negative charge goes. DFT calculations of a K-doped PTCDA crystal,[109] without considering the underlying substrate, show that the minimum total energy is found if potassium atoms transfer their outermost electrons to PTCDA molecules via the carboxylic oxygens. If this was the case, we would expect to measure the corresponding O1s peak at a lower binding energy than in the PTCDA layer. However, we register an increase in the binding energy of O1s and C1s lines. Thus, we expect K atoms to transfer their charge to the metal substrate. Hence, an electrostatic dipole, given by positively charged K atoms and their image charge in the metal, forms at the surface and is the cause for the decrease in work function.

The question arises as to why the work function decrease is so strong (0.9 eV). To answer this question, we should have a closer look at the cutoff region of UPS spectra. After K deposition and before annealing of the sample, a very strong increase in the intensity of the secondary electron peak is observed (Figure 5.33a). Secondary electrons are mainly photoelectrons from the bulk which are inelastically scattered by the overlayer before they reach the electron analyzer. In the case of a disordered adsorbate structure on the surface, one can expect an increase in the intensity of the secondary electron peak,[110] which we attribute, in our case, to the irregular distribution of K atoms on the surface. In fact, potassium atoms may be in direct contact with the metal, above the molecular layer or even within it (see Figure 5.35).

Since before the annealing step, PTCDA molecules are mainly arranged in the brick-wall phase (see section 5.3.1.3), there is enough space to accommodate K atoms in the hollow site, at the center of the unit cell, between the anhydride end groups

binding energy and binding energy shifts of core levels								
	NIXSW preparation			UPS-XPS preparation				
	PTCDA	K+PTCDA annealed	ΔE_b	PTCDA	K+PTCDA unannealed	$\Delta E'_b$	K+PTCDA annealed	$\Delta E''_b$
C1s	284.6	284.8	**+0.2**	284.5	284.9	**+0.4**	284.9	**0**
O1s (carboxylic)	531.0	531.5	**+0.5**	531.0	531.6	**+0.6**	531.6	**0**
O1s (anhydride)	533.4	534.0	**+0.6**	533.4	534.2	**+0.8**	534.2	**0**
K2$p_{3/2}$		294.0	-		294.0	-	293.7	**−0.3**

Table 5.12: Summary of binding energy (E_b) values of C1s, O1s (carboxylic), O1s (anhydride), and K2$p_{3/2}$ core levels relative to PTCDA, unannealed K+PTCDA and annealed K+PTCDA phase of NIXSW and UPS-XPS preparations. Core-level E_b shifts between the annealed K+PTCDA and the PTCDA phase of NIXSW preparation (ΔE_b), between unannealed K+PTCDA and PTCDA phase ($\Delta E'_b$) and between annealed K+PTCDA and unannealed K+PTCDA phase of UPS-XPS preparation ($\Delta E''_b$) are also reported.

of two adjacent PTCDA molecules. In this disordered array, there will be potassium atoms acting as scatterers placed at different heights above the surface. The higher the distance from the underlying substrate, the more intense the corresponding dipole and thus the decrease in the work function. DFT calculations of K atoms on SiO_2/Mo(112)[111] indeed show a linear correlation between $\Delta\Phi$ and the height of the alkali ions.

The presence of a positively charged environment surrounding the PTCDA molecules can explain the binding energy shifts of the C1s and O1s core levels towards higher values. The screening of carbon and oxygen core electrons by the partial positive charge of K atoms can actually rationalize the generally higher binding energies measured. In particular, the higher E_b shifts for O1s than for C1s lines (Table 5.12) can be explained by a closer interaction of the K atoms with the oxygens than with the carbons, as we already reported in the schematic structure model based on STM results (Figure 5.31). In support of our suggestion, DFT calculations of K-doped PTCDA thin films[109] indicate a propensity of potassium atoms to interact with oxygen atoms to form O-K-O chains; this configuration has in fact lower energy than the one where K is on top of the perylene group between two molecular planes. Furthermore, the smaller E_b shift of carboxylic oxygens (0.6 eV) compared to that of anhydride oxygens (0.8 eV) is assigned to the screening effect from the Ag substrate, which is stronger for atoms closer to the surface. It was indeed measured, for PTCDA/Ag(110) and for K+PTCDA/Ag(110) after annealing (see Figure 5.13) though not for K+PTCDA/Ag(110) before annealing, that carboxylic oxygens have smaller adsorption heights than anhydride ones.

K+PTCDA/Ag(110): (before annealing) → (after annealing)

Upon annealing of K+PTCDA/Ag(110), an increase in the work function of 0.33 eV is measured. The origin of this positive $\Delta\Phi$ is assigned to the positively charged potassium atoms which move from an irregular distribution to an ordered array of atoms beneath the molecular layer. In this way, the surface dipole induced by potassium is reduced, due to the shorter distance between positive and negative charges. As discussed in section 5.4.3, STM, XSW and IPE experiments strongly indicate that K atoms lie within the metallic surface layer. The negative shift $\Delta E_b = -0.3$ eV of the K2p binding energy is in agreement with the picture of the positively charged K atoms embedded in the topmost Ag layer, which screens their core-holes and thus decreases the corresponding binding energy. Furthermore, the much weaker intensity of the secondary peak of UPS spectrum after annealing (red line in Figure 5.33a) points to a more ordered surface, in which potassium cannot be on top of PTCDA molecules (otherwise it should have been detected by STM) or within the molecular layer (because there is not enough room to accommodate K within the stripes). Therefore, potassium must be incorporated into the first metal layer, in agreement with all experimental results. The strength of the surface dipole associated to alkali ions clearly depends on the amount of charge transferred to the metal and also on the distance of the ions from the surface itself.[111] Since after annealing, the K atoms are expected to be much closer to the surface than before annealing, the corresponding surface dipole decreases causing an overall increase in the metal work function.

Another contribution to the work function comes from the presence of the many steps in the ×3 and ×4 superstructures of the K+PTCDA phase. Dipoles associated to these steps contribute to decreasing the work function due to the deficit of electron density at the top edge of a step ("hill") and the excess of electron density at the bottom edge of the same ("valley").[107,112] Superposition of all these contributions results in an overall increase in the work function of 0.33 eV.

At the same time, the E_b of carbon and oxygen do not change as compared to the situation before annealing (Table 5.12). This can be rationalized by the presence of the same K-induced electrostatic field seen by the adsorbed PTCDA molecules. In other words, the constant E_b for C1s and O1s, upon annealing, can be explained by the same electrostatic environment surrounding PTCDA molecules. In this case, too, the differential E_b shift of oxygen atoms can be ascribed to a different substrate screening effect due to the different distance of carboxylic ($d_c = 2.63$ Å) and anhy-

dride ($d_c = 2.76$ Å) oxygens from the surface, as measured by NIXSW (see section 5.2). Moreover, from the ΔE_b and $\Delta E_b'$ values presented in Table 5.12, we observe that binding energy shifts of C1s, O1s (carboxylic) and O1s (anhydride) peaks between the annealed K+PTCDA and the pristine PTCDA phase are about 0.2 eV bigger for the UPS-XPS preparation than for the NIXSW preparation. This trend can be rationalized by a stronger electrostatic field seen by PTCDA molecules, that is induced by a higher K ion concentration in the UPS-XPS sample preparation. In fact, LEED images (see example in Figure 5.15d) of K+PTCDA annealed phase of UPS-XPS sample preparation indicate a significant presence of $\times 3$ superstructure, which goes hand in hand with a higher concentration of K atoms on the surface, as was argued in section 5.4.3. We can therefore attribute the higher ΔE_b shifts registered in the UPS-XPS preparation to more potassium atoms present at the K+PTCDA/Ag(110) interface.

5.6 Structural model

In the final section of this chapter, a structural model of K-doped PTCDA submonolayer adsorbed on Ag(110) is presented. The model is based on the experimental data reported and discussed in sections 5.2-5.5. First, the model is described, pointing out many of the results which enabled us to draw such a detailed picture of this alkali-molecule-substrate interface. Then, the main features of the model are discussed, placing our work into the context of other investigations in similar systems and attempting to understand the driving force for the observed restructuring of the surface.

5.6.1 Description of the structural model

After having presented experimental data obtained from NIXSW, LEED, STM, UPS and XPS experiments, the resulting structural model is shown in Figure 5.36. In the section below, the main features of the model are described, referring to the corresponding experimental data from which they follow.

We start from the description of the molecular layer upon K deposition. The relative lateral position of PTCDA molecules shown in Figure 5.36b comes from STM images (section 5.4.3), their corresponding unit cell is confirmed by LEED experiments (section 5.3.1.1), while their average vertical position above the Ag substrate is provided by NIXSW data (section 5.2.3). STM images also reveal the presence of brighter and darker stripes of molecules, represented in Figure 5.36a by alternating rows of up- and down-terraces of different widths, namely one or two PTCDA molecular chains. The height difference between up- and down-terraces comes from height profile analysis of STM images and equals 1.44 Å (section 5.4.3.3), one Ag monoatomic step height.

Determining the position of K atoms was rather complicated and required the use of results from NIXSW, STM, UPS and XPS. In fact, from standing wave experiments we learn that K atoms may be either on top of, within or below the molecular layer, in the latter case, embedded in the first Ag layer. STM images exclude the first two possibilities because potassium is not imaged on top of the molecular layer, neither can it be within the PTCDA molecular layer because there would not be enough space to accommodate it. Indications that K atoms are located within the topmost metal layer come from STM images at different bias (section 5.4.3.5), showing a

brighter contrast which derives from unoccupied empty states induced by potassium adsorption on Ag(110), as was reported by a previous inverse photoemission spectroscopy study.[95] This indication is further supported by work function and XPS data (section 5.5.4), both consistent with the presence of positively charged K atoms ordered below the molecular layer.

According to our structural model, K induces a missing row reconstruction of the Ag(110) surface. In particular, several topmost Ag rows are removed to make room for potassium atoms, so that the up-terrace lacks five atomic rows, while the down-terrace lacks four. The Ag atomic rows are replaced by K atomic rows of lower density (approximately 75% smaller). Furthermore, STM images (section 5.4.3.5) suggest that K atoms are not only placed underneath the molecular layer, but also near the carboxylic oxygens of PTCDA to form K-pairs, in which K atoms are separated by a distance of approximately 5 Å. This value corresponds to the distance between the two lobes of the bright protrusions bridging two PTCDA molecules (Figure 5.30).

If we now look at the lateral position of potassium relative to the metal surface, we see that according to our model, K occupies mainly the four-fold coordinated

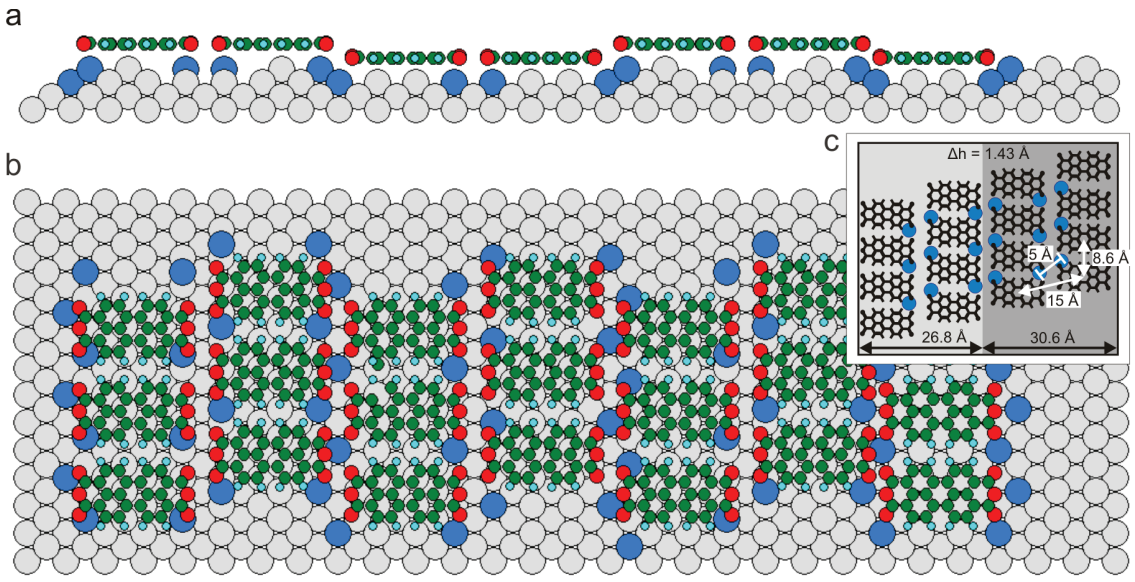


Figure 5.36: Side view (a) and top view (b) of the structure model of 2-rows-up-2-rows-down and 2-rows-up-1-row-down K+PTCDA phase including scale drawing of PTCDA molecules (carbon, green; oxygen, red; hydrogen, light blue), K atoms (blue) and the Ag substrate (gray). (c): Schematic model (Figure 5.31) of K and PTCDA relative positions in the up- (light gray) and down- (dark gray) terraces, including all structural information derived from STM images.

site of Ag(110) substrate. Only in the up-terrace alkali atoms occupy a bridge position, in order to keep the relative distance within the K-pair of approximately 5 Å. The occupation of the highest coordination site by adsorbed K atoms cannot be experimentally proven in our work, however it seems plausible since it also results from other studies of similar alkali-metal interfaces. For example, the hollow site for potassium was indeed predicted for K on Cu(110), by effective medium theory calculations,[113] and the prediction was successively confirmed by photoelectron diffraction experiments.[114]

Our experiments allowed us to deduce the relative lateral positions of K atoms and PTCDA molecules and their vertical distance from the surface (see Figure 5.36c), whereas we do not have more precise direct structural information about the lateral position of K and PTCDA relative to the substrate. However, a great deal can be learned indirectly from the different width of up- and down-terraces measured by STM (section 5.4.3.4). In fact, from the need to accommodate the same K+PTCDA phase on up- and down-terraces of different widths, the different surface reconstruction and consequently the locally different adsorption sites of PTCDA molecules and K atoms follows. In the following section, we will discuss the effect of these structural features on the main interactions at the K-PTCDA-Ag interface, with an initial focus on the K-induced reconstruction of Ag(110) mediated by PTCDA.

5.6.2 Discussion of the structural model

This section is subdivided into three parts discussed below:

- K-induced reconstruction of Ag(110),
- molecule-induced reconstruction of a metal surface,
- main interactions at the K-PTCDA-Ag interface.

K-induced reconstruction of Ag(110)

The alkali metal-induced reconstruction of Ag(110) is a very well known and extensively investigated phenomenon.[115,116] It was first reported by Hayden et al.,[117] who detected (1x2) and (1x3) reconstruction of the Ag(110) surface upon Cs deposition. In their work the driving force for the reconstruction was assigned to a

redistribution of the charge donated from the alkali metal to states in the metal surface levels near E_F. Interestingly, the appearance of reconstruction spots occurred only at room temperature, not at 80 K, indicating that the reconstruction is a thermally activated process. Frenken et al.[118] also reported on a missing row surface reconstruction of Ag(110), induced this time by the adsorption of potassium. In this case, too, the role of annealing (section 5.3.1.3) was proven by the evidence that after subsequent annealing of the sample at 400 K for several minutes, the quality of the (1x2) LEED pattern considerably improved.

In order to understand the mechanism behind the missing row reconstruction, Fu and Ho[119] performed a density functional theory study of the structural and electronic properties of the (1×1) and (1×2) structures of fcc metal (110) surfaces. Alkali metal ions were modeled by an effective external charge chosen to have a negligible overlap with the surface electronic density so that the only effect is that of an applied electric field. Above a certain threshold of induced surface electrons (≈ 0.05 e/surface-atom) the surface energy of the (1×2) structure is lower than that of the (1×1) structure; thus the surface reconstructs. The authors mainly attribute the origin of the surface reconstruction to two reasons. On the one hand, the unique (110) geometry allows the removal of alternate ($\bar{1}10$) atomic rows without breaking extra nearest-neighbor bonds, thus at a relatively low potential energy cost. On the other hand, the (1×2) structure provides a larger surface facet area for the s,p electron to spread out to lower kinetic energy. As a result, the decrease in kinetic energy of s,p electrons at the (1×2) surface exceeds the surface potential energy to remove atomic rows and the surface reconstructs.

In contrast, according to the effective medium theory study of Jacobsen and Nørskov,[113] the main contribution to the stabilization of the reconstructed fcc (110) surface comes from the electrostatic energy, which is larger the closer the atoms are. Therefore, this energy term favors the highest-coordination-number site, in agreement with our structural model. According to this theory, the alkali-induced reconstruction of a metal surface is driven by the larger stabilization electrostatic energy of an alkali atom on the reconstructed surface, due to the larger number of nearest substrate atoms (7) as compared to the unreconstructed surface (5). The limitation of these calculations[113] is that, by definition, all electron transfer effects are excluded.[119]

According to the scenario described in section 5.5.4, the K+PTCDA/Ag(110) interface presents two different phases, one before and one after annealing. Before

annealing, potassium atoms donate part of their charge to the substrate and lie mainly on top and within the molecular layer. In fact, work function measurements on this phase support the idea of having partially positively K atoms above the PTCDA layer contributing to a surface dipole pointing towards the vacuum (section 5.5.4). Moreover, the LEED pattern (see section 5.3.1.3) did not show any reconstruction spots after potassium deposition but before annealing. All these elements induce us to conclude that Ag(110) surface covered by PTCDA molecules does not reconstruct just upon alkali metal deposition. Additional thermal activation from the annealing of the sample is required for removing Ag atomic rows and rearranging PTCDA molecules. In fact, upon annealing of the K+PTCDA/Ag(110) sample, K atoms are embedded into the topmost Ag layer, inducing a major surface restructuring, resulting into up- and down-terraces, in turn, missing row reconstructed, on top of which the PTCDA layer adsorbs in the stripe phase (section 5.4.3). In summary, the reconstruction mechanism of the Ag(110) surface occurs upon charge transfer from the alkali metal to the substrate and upon adsorption of K atoms within the topmost Ag layer. Therefore, both theories[113,119] discussed above contribute to explaining the reconstruction of Ag(110) upon K and PTCDA deposition.

Molecule-induced reconstruction of a metal surface

As can be deduced from the discussion above, PTCDA molecules also play a role in the reconstruction of the Ag(110) surface induced by K adsorption. In the literature there are many examples of surface reconstruction induced exclusively by the adsorption of molecules on metal surfaces.[120–122] We report here briefly about two exemplary cases illustrating the driving force behind the restructuring process.

First, STM and LEED studies of C_{60} on Cu(110) and Ni(110) by Murray et al.[122] demonstrated a new kind of surface reconstruction, thermally activated by sample annealing at approximately 575 K, consisting of adjacent rows of C_{60} molecules vertically displaced by one monoatomic Ni(110) step height. The driving force for such process can be described as follows: upon reconstruction of the surface, the *d* states shift upward in energy due to the lower coordination of surface atoms.[123] As a consequence, the hybridization energy of the molecular LUMO and the *d* band becomes even more negative,[124] resulting in a bonding energy gain of C_{60} sufficiently large to overcome the energy spent in restructuring the surface. The absence of reconstruction on Cu(110) is ascribed to the larger separation between its *d* band and C_{60} LUMO.

Second, STM experiments on HtBDC (hexa-*tert*-butyl-decacyclene)/Cu(110)[125] revealed the presence of double rows of molecules that self-assemble after a local disruption of the surface, implying the removal of about 7 Cu atoms per molecule. The process does not occur at low temperatures, but rather does not become thermally active until room temperature. Two possible reasons for the observed restructuring are postulated. First, a steric effect induces an adaptation of the surface to the size of the adsorbed molecules in order to increase the surface interaction. Second, the reduction of the coordination number of the surface atoms causes a higher reactivity and results in a binding energy of the molecule to the substrate sufficient to exceed the energy spent for the Cu atom removal.

In the case of K+PTCDA/Ag(110), while PTCDA molecules do not induce reconstruction of the Ag surface, they significantly contribute to the final structure of the interface by defining the width of the up- and down-terraces. In fact, as it results, for example, from Figure 5.29b1 and consequently from our model in Figure 5.36, the size of the terraces along the [001] direction is enough to accommodate either one or two PTCDA molecules. Therefore, the molecular layer is also involved in the restructuring of the Ag surface. The interaction of PTCDA molecules with the reconstructed surface is discussed below, with a particular focus on the coordination number of reconstructed surface atoms, which, as recalled in the two examples above, strongly influences the surface reactivity.

Main interactions at the K-PTCDA-Ag interface

After having discussed the reconstruction of Ag(110) induced by K atoms, mediated by PTCDA molecules and activated by annealing of the sample, we focus our attention on the main interactions present at the interface, namely:

- K-Ag,
- K-K,
- K-PTCDA,
- PTCDA-PTCDA,
- PTCDA-Ag.

The interaction of K atoms with the Ag substrate is expected to be primarily electrostatic. In fact, if we assume that K atoms transfer the $4s$ outer-shell electron

to the substrate upon adsorption, then K atoms can be considered to be closed-shell ions. Hence, their interaction with surrounding Ag atoms is mainly electrostatic. The same argument applies if potassium donates only part of its external charge, although in this case, K would be only partially ionized. As described in the study of Jacobsen and Nørskov,[113] the K-Ag electrostatic energy represents the main stabilization energy of the missing row reconstructed surface. Therefore, this interaction term plays an important role in the overall energy of the interface.

In contrast, since K atoms are positively charged, K-K interaction is repulsive. However, this energy term does not play a prominent role in our system, since the smallest distance between K atoms is large enough (approximately 5 Å, see section 5.4.3.5) to prevent a strong interaction.

In order to assess the role played by potassium within the molecule-metal interaction, K-PTCDA, PTCDA-PTCDA and PTCDA-Ag interactions of K+PTCDA/Ag(110) are discussed in comparison with the pristine PTCDA/Ag(110). In this latter system (chapter 4) PTCDA is chemisorbed on Ag(110) and anchored to the substrate via the anhydride groups in a downward bent geometry, as shown schematically in Figure 5.1a. At first glance, NIXSW results of K+PTCDA/Ag(110) (see Figure 5.13) seem to indicate an unbinding of the molecule from the substrate. However, upon closer inspection, we observe that the oxygen atoms are about 0.30 Å higher compared to the pristine PTCDA phase, while the carbon backbone is lifted up by only 0.05 Å, thus within the experimental error of the method. In the following, we will discuss the effect of K atoms, first on the anhydride groups of PTCDA, then on the intermolecular interaction, and finally on the C-backbone of the molecule.

In both up- and down-terraces, K atoms induce missing row reconstruction of the Ag surface and locate within the topmost Ag layer nearby the carboxylic oxygen atoms of adjacent PTCDA molecules (section 5.4.3.5). As a result, the O-Ag interaction channel, responsible for the downward bending of the pristine PTCDA on Ag(110) is inhibited. Instead, the chemical bonding between O and Ag is possibly replaced by the electrostatic interaction of negatively polarized carboxylic oxygens with positive K ions. The vertical shift of PTCDA anhydride groups can be therefore rationalized as a direct consequence of the K-induced missing row reconstruction that prevents oxygen atoms from interacting with the Ag surface atoms. On the other hand, it is not yet clear what is behind the small height increase (0.05 Å) of the perylene core upon K deposition. From the relative position of K and PTCDA (Figure 5.36b),

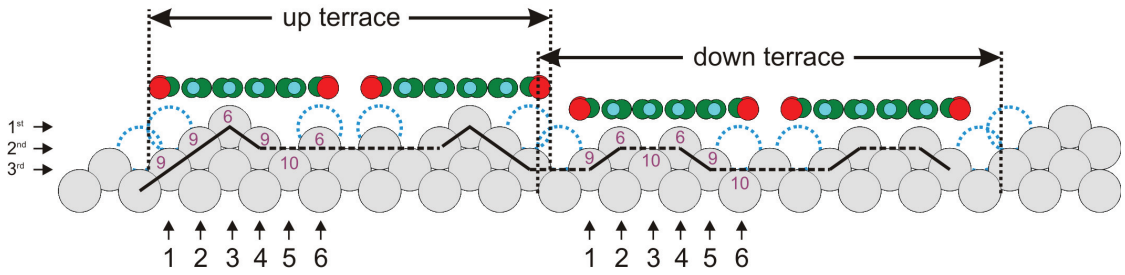


Figure 5.37: Side view of the K+PTCDA/Ag(110) structure model. Up- and down-terraces are represented together with PTCDA molecules and K atoms (dotted blue circles). Solid black lines indicate (111) facets, while black dashed lines indicate (110) facets. The surface Ag atomic rows are numbered below the figure, while the Ag atomic layer are named on the left side of the figure. Coordination number of surface Ag atoms is marked in purple on the corresponding atom.

we can exclude a direct interaction of the alkali atoms with the C-backbone of the molecule. In the attempt to shed light on this point, the intermolecular interactions are examined.

A combined NIXSW-STM-LEED-UPS study[126] revealed the importance of intermolecular interactions among PTCDA molecules on the Ag(111) surface. Intermolecular interactions are considered to be responsible for the long-range order herringbone structure of the room temperature (RT) phase, as opposed to the low-temperature (LT) (below 150 K) phase, where molecules have stronger interaction with the substrate; in fact they cluster in isolated *dendritic* islands approximately 0.06 Å closer to the surface. The total positive energy gain in going from the LT to the RT phase was attributed to the interaction energy among the molecules. In the K+PTCDA/Ag(110) stripe phase, however, the molecules are aligned such that the positively polarized hydrogen terminated perylene cores of two neighboring molecules face each other, as well as the negatively polarized oxygens of the anhydride groups. Therefore, there is no energy gain from the intermolecular interaction of the stripe phase which could justify a weaker interaction with the substrate, hence a larger distance from the surface, as occurs for PTCDA/Ag(111) in the RT phase. We therefore conclude that the key to understanding what happens to the C-backbone of PTCDA is the substrate. In order to assess the degree of interaction of the C-backbone with the reconstructed surface, we compare the coordination number (CN) and substrate layer (L) of surface atoms relative to the six atomic rows underneath PTCDA on up- and down-terraces with the corresponding values of pristine PTCDA/Ag(110) (see Figure 5.37 and Table 5.13). In particular, we draw our attention to the differently reconstructed up- and down-terraces (Figure 5.36) that will be discussed separately for this reason.

	pristine PTCDA		K+PTCDA up-terrace				pristine PTCDA		K+PTCDA down-terrace			
row	CN	L	CN	L	ΔCN	ΔL	CN	L	CN	L	ΔCN	ΔL
1	6	1^{st}	9	3^{rd}	+3	+2	10	2^{nd}	9	2^{nd}	−1	0
2	10	2^{nd}	9	2^{nd}	−1	0	6	1^{st}	6	1^{st}	0	0
3	6	1^{st}	6	1^{st}	0	0	10	2^{nd}	10	2^{nd}	0	0
4	10	2^{nd}	9	2^{nd}	−1	0	6	1^{st}	6	1^{st}	0	0
5	6	1^{st}	10	3^{rd}	+4	+2	10	2^{nd}	9	2^{nd}	−1	0
6	10	2^{nd}	6	2^{nd}	−4	0	6	1^{st}	10	3^{rd}	+4	+2

Table 5.13: Coordination number (CN) and substrate layer (L) of surface Ag atoms corresponding to the atomic rows (1-6) indicated in Figure 5.37 and relative to u-p and down-terraces of K+PTCDA/Ag(110) and pristine PTCDA/Ag(110).

In the down-terrace, four Ag atomic rows nearby the anhydride groups of the two PTCDA molecular rows are removed and replaced by less dense rows of K atoms located at the hollow site of the Ag(110) surface. As a result, the interaction between anhydride groups and Ag atoms is inhibited (see above). The surface Ag rows (2, 3, 4) directly beneath the perylene core (see Figure 5.37) are identical to those directly below pristine PTCDA on Ag(110). On the other hand, atomic rows 1 and 5, both in the second substrate layer, have a lower CN than the unreconstructed surface because of the nearby missing rows (Table 5.13). Finally, the surface atomic row corresponding to position 6 is only in the third substrate layer, preceded by K atomic row within the first layer. In summary, large part of the Ag area underneath PTCDA is identical to the unreconstructed surface, two Ag atomic rows have an even lower CN, thus are more reactive, and finally the last one is missing because it is replaced by K atoms. As a result, the interaction of the C-backbone with the Ag substrate is expected to be of similar strength to that of the pristine PTCDA. Hence, a similar adsorption height for the C-backbone of PTCDA should be expected.

In contrast, in the up-terrace, the Ag surface underneath the molecular layer is significantly different compared to the down-terrace. In order to respect the constraint of the K-PTCDA relative position, based on the schematic model deduced from STM images (Figure 5.37c), the Ag substrate needs to undergo a severe reconstruction, implying the removal of five Ag atomic rows. As a result, the up-terrace consists of four (111) facets at 45° with the surface plane located at the edges and one (110) area at the center. Consequently, the K adsorption site is also different from the hollow site of the (110) surface seen in the down-terrace. In fact, K atoms occupy the hollow site of the (111) external facets, and the bridge site of the central

(110) area. However, despite the different location of the K atoms within the topmost Ag layer, they are still placed near the carboxylic oxygen and prevent O-Ag interaction, as was already seen for the down-terrace. In contrast, the Ag surface underneath the PTCDA C-backbone is profoundly different. In particular, there is only one Ag atomic row (3) in the first layer (see Figure 5.37). The two neighboring rows (2, 4) have coordination a number (9) lower than in the unreconstructed surface (10) because they are directly next to missing Ag rows (Table 5.13). The main difference with the down-terrace lies in Ag rows 1 and 5, both in the third layer, hence practically non-interacting with the C-backbone. Finally, the second layer row 6 has a CN lower than the corresponding pristine PTCDA value, but it is directly underneath K atoms; therefore, their interaction with PTCDA molecule is partially hindered. Considering the smaller number of Ag atoms to interact with, although some of them have a lower coordination number and thus higher reactivity, PTCDA C-backbone is expected to have a weaker interaction with the Ag surface in the up-terrace. Therefore, in light of the discussion above, it is plausible to predict a slightly larger adsorption height of the PTCDA C-backbone on the up-terrace than on the down-terrace, providing as a result an average height 0.05 Å greater than for pristine PTCDA/Ag(110).

5.7 Conclusions

In this chapter, investigations of the K-PTCDA-Ag(110) interface by NIXSW, LEED, STM, UPS, and XPS were reported and discussed. STM images at *low* K coverage revealed the presence of small X phase patches (section 5.4.2.2), where K atoms were imaged within the PTCDA layer, which was consistent with our original unbinding idea (Figure 5.38b). However, it was not possible to prepare large domains of X phase in order to use NIXSW to investigate the actual unbinding of PTCDA from the Ag surface.

In contrast, K and PTCDA assemble in the so-called stripe phase, characterized by alternating up- and down-terraces of molecules on a restructured K-Ag surface, as illustrated by the structural model in Figure 5.36. In the stripe phase, our initial expectation of unbinding PTCDA molecules from the Ag(110) surface upon K deposition (Figure 5.38b) is only partly fulfilled. In fact, the anhydride groups of PTCDA are actually unbound from the surface due to the presence of K atoms beneath, within the topmost Ag layer (Figure 5.38d). However, the C-backbone of PTCDA maintains a rather strong interaction with the reconstructed surface as well, as testified by approximately the same height as in PTCDA/Ag(110), and as rationalized by a careful analysis of surface Ag coordination number (section 5.6.2).

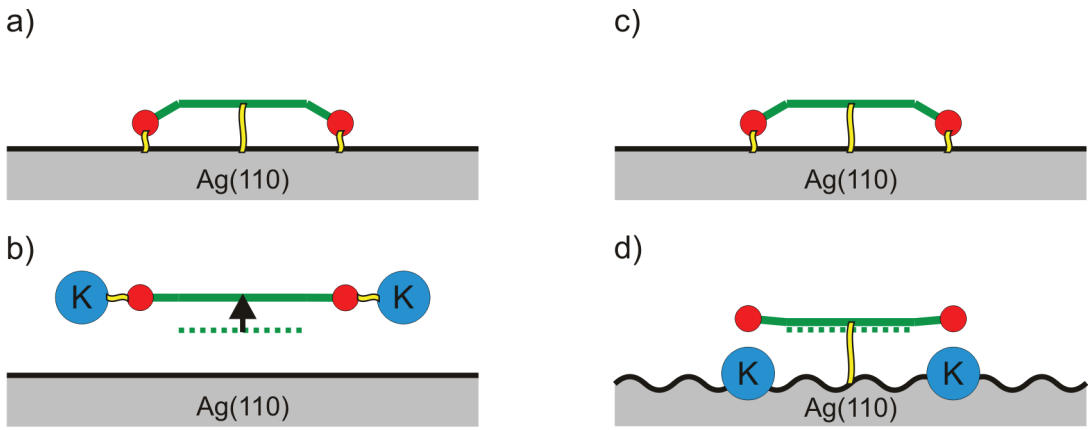


Figure 5.38: Schematic illustration of expected PTCDA unbinding from the surface upon K deposition (b) and real adsorption geometry of K and PTCDA on Ag(110) (d), according to NIXSW, LEED, STM, UPS and XPS. (a), (c): side view of PTCDA adsorbed on Ag(110) according to NIXSW (chapter 4). The dotted green line in (b) and (d) indicates the vertical position of the molecular plane in (a).

Outlook

Based on this knowledge, it would be interesting to use a bigger or smaller molecule of similar structure (for example NTCDA) to verify whether the width of the terraces can be varied by fine-tuning the size of the organic molecule. Furthermore, according to our model, one can expect to tune the interaction of the end groups O atoms with the substrate by adopting alkali metal with bigger (Cs) or smaller (Li) radius, which may induce different kind of reconstruction. Regarding the electronic properties of the K-PTCDA-Ag interface, we have shown a decrease in the work function of PTCDA/Ag(110) upon K deposition and annealing, in addition to core-level shifts consistent with the presence of an additional surface dipole. Preliminary UPS experiments[127] to investigate the valence band region revealed a shift towards higher binding energy of the former molecular LUMO as K concentration increases. Further experiments in this direction are planned to elucidate the origin of the LUMO shift. Finally, in order to fine-tune the electronic properties of submonolayer organic molecules (for instance, between metallic and semiconductive) via alkali metal deposition, a less reactive substrate such as Au(111) might be preferable. In this case, in fact, LUMO of PTCDA remains unoccupied upon adsorption on the surface;[128] thus a stronger interaction with the co-adsorbed alkali metal than with the substrate can be expected.

6 Molecular switches on Ag(111)

6.1 Introduction

The potential of a future nanotechnology motivates the study of functional organic molecules at metal surfaces. Light-driven actuators[25] and data-storage media[24] are only some of the possible applications. Azobenzene is a prototypical molecular switch that undergoes a reversible photoinduced isomerization between the planar C_{2h} symmetric *trans* isomer and the torsion-twisted C_2 *cis* isomer. This functionality makes it a possible candidate for an optically active device. While the switching mechanism in solution[26,27] and in the gas phase is well understood, the way the substrate influences the switching functionality remains unanswered. In particular, steric hindrance, electronic lifetime effects and substrate-induced changes in the optical absorption spectrum of the molecule are three possible mechanisms that can occur.[28] At the same time, new properties of the molecular switches induced by the presence of the substrate also cannot be excluded a priori.

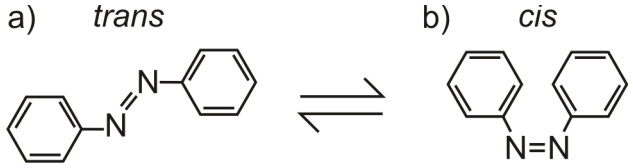


Figure 6.1: Azobenzene photoisomerization reaction between the *trans* (a) and the *cis* isomer.

In this context, azobenzene (AB) and its derivative, 3,3′,5,5′-tetra-*tert*-butyl- azobenzene (TBA) are extensively investigated on different metal surfaces. Isomerization of azobenzene on Au(111) can be achieved through different excitation mechanisms via an STM tip,[129,130] although not with light.[28] On the other hand, light-induced switching of TBA is achieved on Au(111),[28,29] but not on the Ag(111) surface.[30]

With the aim of better understanding the switching properties of photo-active

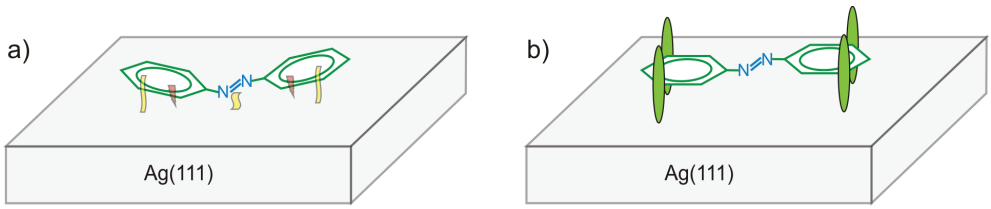


Figure 6.2: (a): Schematic representation of azobenzene/Ag(111) based on the expectation that the azo (-N=N-) bridge interacts chemically with the Ag atoms (yellow symbol) bringing the phenyl rings in the Pauli repulsive regime (red symbol) with the phenyl rings vdW attracted to the substrate, thereby leading to a butterfly-like configuration (sections 6.4.1 and 6.4.1.3). (b): Schematic representation of TBA/Ag(111) based on the "spacer leg" groups strategy of decoupling the photo-active moiety (-N=N-) from the surface.

molecules adsorbed on metal surfaces, a detailed knowledge of their adsorption geometry and molecular orientation is essential. Insights into the structural configuration will also shed light on the molecule-metal interactions (Figure 6.2a). For this purpose, NIXSW experiments are performed on AB/Ag(111) and TBA/Ag(111) with the twofold target of acquiring a detailed bonding geometry of the two prototypical molecular switches, and to verify the validity of the widely accepted strategy of using the "spacer leg" groups to decouple the photo-active moiety (-N=N-) from the substrate (Figure 6.2b).[28,29,130,131]

6.2 Experimental details

Experimental details about the preparation of AB and TBA monolayers on the Ag(111) surface are summarized and discussed in the following section 6.2.1. Subsequently, XPS data acquisition parameters, the main features of the XPS background and the line shapes of the XPS fitting components are reported in sections 6.2.2, 6.2.3 and 6.2.4, respectively. NIXSW experiments were performed at the beamline ID32 (ESRF, Grenoble) together with S. Subach, O. Neucheva, F. S. Tautz (Forschungszentrum Jülich), S. Hagen, F. Leyssner, M. Koch, P. Tegeder (Freie Universität Berlin).

6.2.1 Sample preparation

NIXSW experiments were performed under UHV conditions with a base pressure of 5×10^{-10}mbar. The Ag(111) surface is cleaned in the conventional way by several cycles of sputtering with Ar^+ ions and annealing at 820 K. The cleanness of the surface is checked by XPS before molecular deposition. AB and TBA multilayers are deposited from a home-built evaporator held at 385 K onto the Ag crystal maintained at 220 K. Subsequent annealing, with a heating rate of 1 K/s, causes the desorption of multilayers, leaving behind a monolayer of the corresponding molecules on the silver surface. The desorption rate is calibrated and controlled by a quadrupole mass spectrometer. In particular, the AB-fragment mass of 77 amu (phenyl ring ion, $C_6H_5^+$), and the TBA-fragment mass of 57 amu (butyl group ion, $C_4H_9^+$) are monitored to control desorption from the Ag surface of AB and TBA respectively.

Figure 6.3 shows the desorption spectra for AB (panel a) and TBA (panel b) of multilayer and monolayer (black line) and of multilayer (red line) only. The multiple low-temperature peaks are assigned to desorption of multilayers from the Ag surface and from the Mo mask used to fix the crystal to the sample holder. On the other hand, the broad peak at higher temperatures is attributed to the desorption of the first molecular layer. It should be noted here that the temperature scale of the plots in Figure 6.3 is not very accurate, since the thermocouple was fixed to the sample holder plate and not directly to the Ag crystal. Other temperature programed desorption (TPD) experiments[30,132] relying on temperature readings from a thermocouple directly located in a drilled hole inside the crystal show an offset of approximately 60 K. For this reason, temperature values in Figure 6.3 must be considered to be indicative and they are simply meant to point out the different

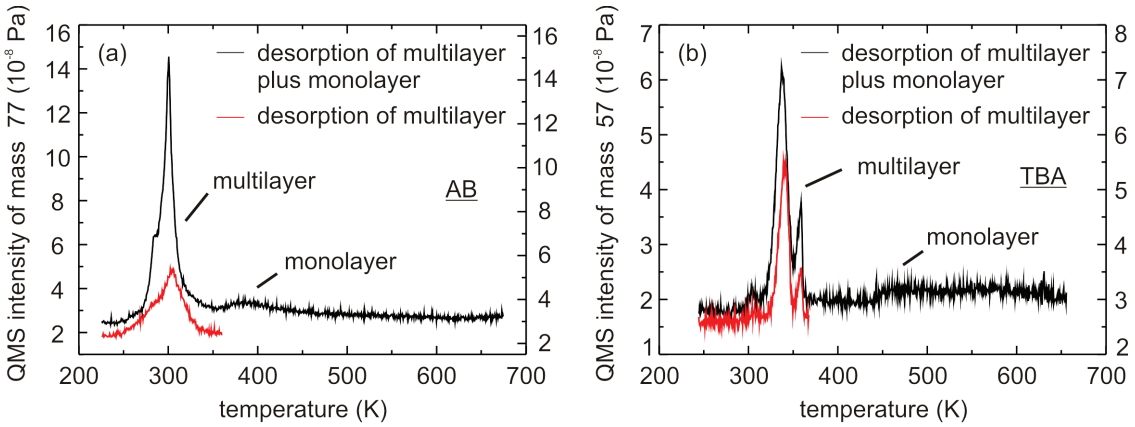


Figure 6.3: Thermal desorption spectra of AB (a) and TBA (b) adsorbed on Ag(111), recorded with a linear heating rate of 1 K/s at the AB-fragment mass of 77 amu (phenyl ring ion, $C_6H_5^+$), and TBA-fragment mass of 57 amu (butyl group ion, $C_4H_9^+$), respectively. Black line: the Ag crystal is heated up to above 650 K so that molecules in the overlayer and in the first layer are desorbed. Red line: crystal heating is interrupted right after the multilayer peak is recorded by quadrupole mass spectrometer so that a monolayer of molecules is left behind. Multilayer desorption spectra (red lines, right Y-axis) are shifted in order to have the same temperature scale as the corresponding complete desorption spectra (black lines, left Y-axis).

desorption temperatures of the monolayer phase for AB and TBA. In fact, in the case of TBA, the molecules of the first layer start to desorb only at temperatures higher than 350 K; hence it is possible to perform NIXSW experiments with the Ag crystal at room temperature. In contrast, to preserve integrity of AB monolayer and prevent the desorption of molecules, it is necessary to keep the substrate crystal at a lower temperature, 210 K, during NIXSW experiments.

Different crystal temperatures imply correspondingly different Ag lattice spacings and thus slightly different Bragg energies. On the basis of the Ag expansion ϵ at 200 K:[133]

$$\epsilon_{200} = (L_{200} - L_{293})/L_{293} = -1720\ 10^{-6} \tag{6.1}$$

and the room temperature (293 K) Ag lattice constant:

$$L_{293} = 4.08641\ \text{Å}\,[134] \tag{6.2}$$

we derive the spacings of the (111) planes at approximately 210 K, $d_{Ag(111)} = 2.3552$ Å, and the spacing at room temperature, $d_{Ag(111)} = 2.3593$ Å.

6.2.2 XPS acquisition parameters of NIXSW experiments

Acquisition parameters of PE spectra are summarized in Table 6.1. Three different kinds of photoemission spectra are considered: fast-, XSW- and survey-XPS. Before discussing the specific photoemission settings, we will focus our attention on the excitation energy of the x-ray photon beam. XSW-XPS spectra are recorded at photon energies within a 10 eV window (energy step = 0.33 eV) centered around the Bragg energy (Table 6.1). For room temperature measurements (TBA and bare Ag) $E_{Bragg} = 2627$ eV, while for low-temperature (210 K) measurements (AB) $E_{Bragg} = 2634$ eV. In order to prevent the formation of a standing wave that enhances or reduces the photoemission intensity from a specific element depending on its vertical position, both fast-XPS and survey-XPS were acquired with a photon excitation energy of 2617 eV, at least 10 eV below the corresponding Bragg energy. The remaining acquisition parameters of the three types of spectra are discussed in more detail below.

Fast-XPS is measured with the aim of checking the integrity of the molecular layer, through XPS of N1s and C1s lines, before and after NIXSW measurements, as well as the cleanness of Ag crystal after sputtering-annealing cycles and before molecular deposition. In fact, it is possible to exclude beam damage upon x-ray radiation as well as light-induced isomerization of AB and TBA, since neither core-level shifts nor line broadenings are detected in fast-XPS spectra.

XPS data acquisition parameters						
element	N1s/plasmons		C1s		Ag3d	all
XPS type	fast	XSW	fast	XSW	XSW	survey
$h\nu$ window [eV]	-	10	-	10	10	-
$h\nu$ step [eV]	-	0.33	-	0.33	0.33	-
$h\nu$ [eV]	2617	-	2617	-	2617	2617
E_k window [eV]	40	19	25	17	12	1500
E_k step [eV]	0.5	0.2	0.2	0.2	0.4	2
time/step [ms]	500	100	100	100	30	100
pass energy [eV]	94	47	47	47	29	94
repeats	4	10	5	10	1	1

Table 6.1: Data acquisition parameters of survey, fast and XSW single photoemission spectra performed on the bare Ag crystal, AB/Ag(111) and TBA/Ag(111). Photon energy window, photon energy step, photon energy, kinetic energy window, kinetic energy step, time per step, pass energy and number of repeats are reported for PE spectra of lines C1s, Ag3d, region containing N1s line and/or Ag plasmon peaks, and a wide energy window including all of the above-mentioned elements.

XSW-XPS is typically recorded with a lower pass energy (47 eV) and a smaller E_k step (0.2 eV), hand in hand with a higher number of repeats (10) and a smaller E_k window, compared to fast-XPS. The goal of XSW-XPS is to reveal the most important spectral features to allow a differential analysis of chemically shifted species. Therefore, a finer sampling of the energy window and higher resolution through a smaller pass energy are adopted. At the same time, to prevent an acquisition time that is too long, a smaller energy window and shorter time/step (100 ms) are selected. Moreover, XSW-XPS spectra of Ag3d are recorded immediately after N1s photoemission signal, within the same XSW photon energy scan, since their binding energy differs by only approximately 20 eV. Furthermore, both spin-orbit split Ag3$d_{3/2}$ and Ag3$d_{5/2}$ lines are recorded in the same spectrum with relatively high E_k step (0.4 eV), low time/step (30 ms) and one repeat. To compensate for the resulting low resolution, a smaller pass energy (29 eV) is adopted.

Finally, survey spectra are acquired in order to have a fast and full picture of a wide binding energy window. They are characterized by a wide energy window, 1500 eV, measured with low statistics and low resolution settings (i.e., high pass energy, large step size, small time/step). Their target is to check for the cleanness of the sample during measurements, i.e., to rule out adsorption of other species on the surface, and to verify the integrity of the molecular layer, for example, from the peak intensity ratio of C1s and Ag3d lines.

6.2.3 XPS background

The type and width of XPS background are discussed here. Ag3d PE spectra are the only spectra characterized by a Shirley BG. The corresponding $AvWidth$ (see section 4.2.3) is equal to 1 and it is not possible to average a larger number of data points to define the edge values of the BG line (Figure 6.4a), because Ag3d spectra are recorded with a relatively large E_k step. On the other hand, N1s and C1s fast-XPS spectra (Figure 6.6b, Figure 6.4a and Figure 6.19), measured with a wider energy window than XSW-XPS (section 6.2.2), have a linear background,

element	N1s	C1s	Ag3d
BG type	linear	linear	Shirley
$AvWidth$	2	3	1

Table 6.2: Background type and $AvWidth$ of N1s, C1s, Ag3d PE spectra measured during NIXSW experiments.

with $AvWidth = 2$ and 3, respectively.

6.2.4 Line shapes of the fitting components

For a more general discussion regarding the line shape of the components fitting core-level photoemission peaks we refer to section 4.2.4. We report here the line shape employed to fit N1*s* PE spectrum, the only one decomposed into multiple fitting components. In particular, due to the multiplicity of peaks needed to describe the whole photoemission signal, because of the overlapping Ag plasmon peaks (see section 6.3.3.1), and due to the a priori unknown nature of the fitting components, a pure Gaussian, without any Lorentzian contribution, was adopted as the line shape of each component. In contrast, C1*s* and Ag3*d* spectra are not further decomposed since there is no evidence of chemically shifted lines to differentiate. Instead, the corresponding photoelectron yield signal is given by the *Region*, the integrated area of the whole spectrum after background subtraction.

6.3 Experimental results

6.3.1 Introduction

NIXSW results of AB and TBA presented in this chapter differ slightly, but not substantially, from the ones of the respective publications (ref.[4] and ref.[3]) for several reasons presented below:

- First, in ref.[4] the N1*s* energy window of each XSW-XPS spectrum is adjusted in order to improve the fit of every single spectrum, whereas here the energy window is fixed to be the same for all the XSW-XPS spectra without further correction. This procedure is considered to be more reproducible and less arbitrary. Even though some spectra may be better fitted with a different energy window, this is taken into account by the error, which is then propagated to the coherent position and coherent fraction.
- A second reason for discrepancy is the use of different nondipolar correction parameters, calculated as described in detail in section 3.4.2, rather than using semiempirical parameters from literature.[135,136]
- Finally, the third cause of different results lies in the different fitting function of both reflectivity and photoelectron yield. In this work, we employ the algorithms of Torricelli, explained in sections 3.3 and 3.3, while in ref.[4] and ref.[3] the DARE[137] program was used.

Due to the overlap of the N1*s* core-level peak with Ag plasmon peaks, it is necessary to further investigate the photoemission signal of the latter in order to extract the nitrogen photoelectron yield. To this end, we will start from the analysis of the substrate Ag3*d* lines (section 6.3.2.1), then move to the model of the Ag plasmon peaks (section 6.3.2.2), and will finally focus on the experimental results of the adsorbed molecules AB/Ag(111) and TBA/Ag(111) in sections 6.3.3 and 6.3.4, respectively.

6.3.2 Silver

This section consists of two parts. First, Ag3*d* results are presented and taken as a reference for the substrate structural parameters; Second, the photoemission spectrum in the region where Ag plasmon peaks are expected[138] is modeled and the corresponding standing wave results are reported.

6.3.2.1 Ag3d

Both spin-orbit split Ag3$d_{5/2}$ and Ag3$d_{3/2}$ core-level lines are measured by NIXSW and shown in Figure 6.4(a). Having verified that both peaks provide identical results, we focus our attention only on the more intense 5/2 line. Figure 6.4b shows an example of the corresponding photoelectron yield, characterized by ideal substrate structural parameters, i.e., coherent position equal to 1 and coherent fraction equal to 1.

A summary of all fitted values (P_c, F_c) of the Ag signal, together with corresponding vertical position with respect to the next Bragg plane underneath are reported in Table 6.3. The Argand diagram of Figure 6.5 clearly shows that all data points are closely clustered around the average with relatively small error bars. In fact, inde-

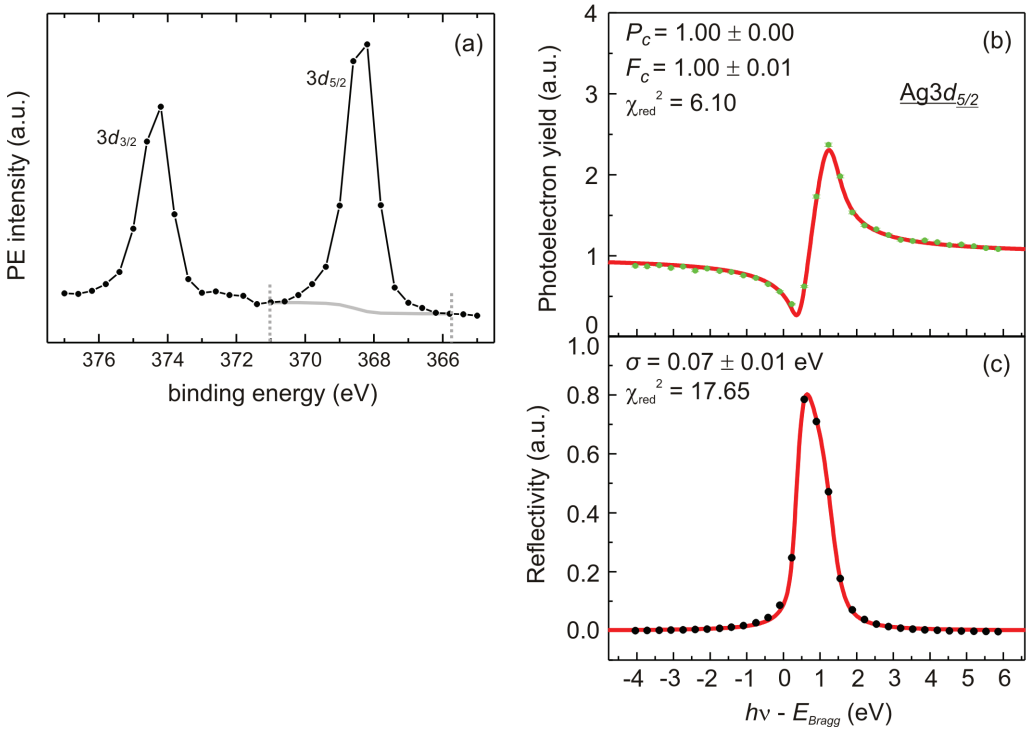


Figure 6.4: (a): Ag3d XSW-XPS spectrum (black dots, see acquisition parameters in Table 6.1) measured at $h\nu = 2623$ eV in data set TBA-1 (Table 6.3); background: gray line; the energy window where photoelectron yield is defined is marked by two dotted gray lines. (b): Ag3$d_{5/2}$ photoelectron yield (green dots and relative error bars) of data set TBA-1 (Table 6.3), displayed as a function of the photon energy relative to the Bragg energy (2627 eV). Fitting curve (red) together with results of the fit: coherent position (P_c), coherent fraction (F_c), and reduced χ^2, are displayed in the figure. (c): X-ray beam reflectivity (black dots) corresponding to experimental data displayed panel b. Fitting curve (red), fitted width σ of the Gaussian function (see section 3.3), and reduced χ^2 are also reported on the plot.

Ag results			
	Ag3$d_{5/2}$ *Region*		
data set	P_c	d_c	F_c
Clean-1	0.99 (1)	2.34 (2)	1.03 (4)
Clean-2	1.01 (0)	2.38 (0)	1.01 (1)
Clean-3	1.00 (0)	2.36 (0)	0.98 (2)
AB-1	1.01 (0)	2.38 (0)	1.05 (1)
AB-2	1.01 (0)	2.38 (0)	1.05 (1)
AB-3	1.00 (0)	2.36 (0)	1.01 (2)
TBA-1	1.00 (0)	2.36 (0)	1.00 (1)
TBA-2	1.00 (0)	2.36 (0)	1.03 (2)
Average	1.00 (1)	2.36 (2)	1.02 (2)

Table 6.3: Fitted values of Ag3$d_{5/2}$ *Region* coherent position (P_c), coherent fraction (F_c) and distance d_c (Å) from the next Bragg plane underneath , calculated as $P_c \times d_{\mathrm{Ag(111)}}$, where $d_{\mathrm{Ag(111)}} = 2.3552$ Å at 210 K (AB), and $d_{\mathrm{Ag(111)}} = 2.3593$ Å at 300 K (TBA and clean Ag).

pendently from the data set and from the presence of molecules on the Ag crystal, Ag atoms result highly ordered at each lattice plane with an average spacing of 2.36 Å. The average coherent fraction (1.02 ± 0.02) slightly exceeds the maximum physically meaningful limit of 1 (see section 2.5). This very small excess (2%) beyond the F_c upper bound can be considered to be negligible and comes from the best fit of our experimental photoelectron yield curves without setting any boundaries to the fitted parameters P_c and F_c. An indication of the good quality of the crystal also comes from the sharp reflectivity curve (Figure 6.4c) of our Ag(111) substrate. In fact, the quite narrow width of approximately 1 eV of the fitting profile and the asymmetric shape, with a lower reflectivity at higher photon energies due to absorption in the crystal (see section 3.3.2), are both indications of a small mosaicity: a fundamental requirement for accurate standing wave measurements.

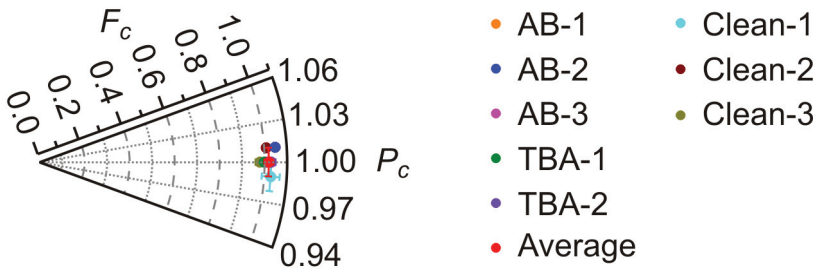


Figure 6.5: Argand diagram of Ag3$d_{5/2}$ structural parameters (P_c, F_c) with corresponding error bars of data sets reported in Table 6.3.

6.3.2.2 Ag3d plasmons

Due to the overlap of Ag3d plasmon peaks[138] in the energy window 370−410 eV and N1s core level of azobenzene located at approximately 400 eV,[139,140] it is necessary to further investigate the structure of Ag3d plasmons (Figure 6.6). Our goal is to develop an XPS model to describe the plasmon peaks of the bare Ag crystal and then transfer it to the photoemission spectra containing also the N1s line in order to obtain the nitrogen photoelectron yield by subtraction.

Before developing the XPS model itself, the energy window and the background type should be defined. In Figure 6.6b, the interesting region where Ag3d plasmon peaks appear is marked by the two dashed gray lines. Moreover, judging from the photoemission signal at lower and higher binding energies than the plasmons in Figure 6.6a,b, the background is evidently linear.

Since our ultimate aim is to model plasmon peaks to subsequently extract the N1s photoelectron yield from XSW-XPS spectra, the plasmon model is also developed for XSW-XPS spectra for reasons of consistency. In particular, to achieve better statistics, all PE spectra (recorded at different photon energies) of the three XSW data sets measured on the bare Ag crystal are added together (Figure 6.6c). This operation is valid only under the assumption (to be verified) that the photoemission signal within the selected energy window (Figure 6.6b) comes exclusively from Ag atoms. In this case, in fact, the PE intensity of each fitting component would vary in the same way as a function of the photon energy. Therefore, adding spectra measured at different $h\nu$ would not alter the the relative intensity of the peaks; it would simply improve considerably the statistics, thereby allowing a better definition of the XPS fitting model.

We are not aiming to decompose the whole PE spectrum of Figure 6.6c into multiple components and discuss their physical nature, as was done e.g., by Leiro et al.[138] Instead, we are looking for a model consisting of the smallest number of components, whose envelope best describes the plasmon PE spectrum under analysis. The proposed model consists of four peaks: Two of them are more significant and account for approximately 90% of the whole PE intensity. In addition, two minor components at each tail of the spectrum are added. Judging from the analysis of the residuals (Figure 6.6c), the envelope (red line) describes the measured data points very well.

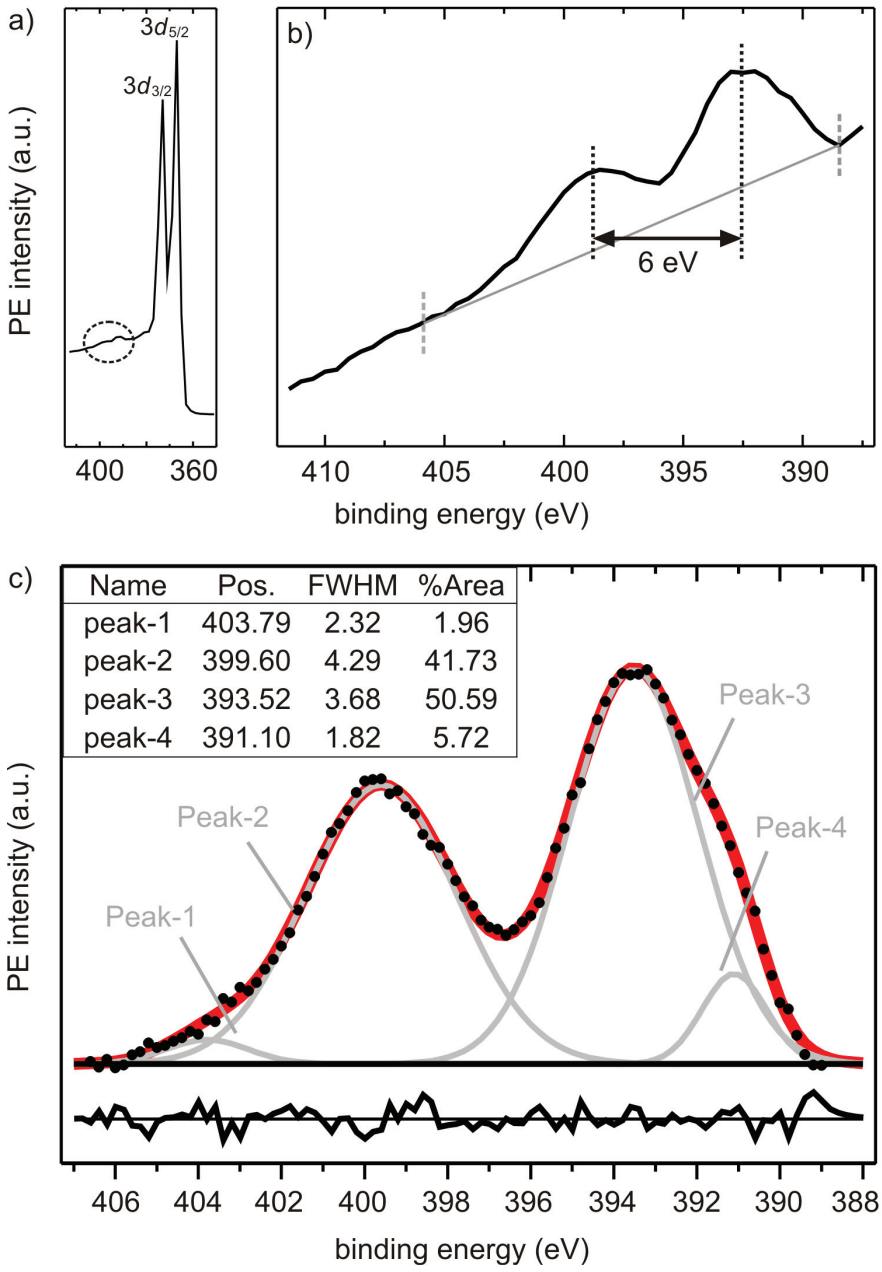


Figure 6.6: (a): sum of 14 survey-XPS spectra (black line, see acquisition parameters in Table 6.1) measured at $h\nu = 2617$ eV on the bare Ag crystal. Here only the energy window of Ag3*d* peaks is reported to highlight the presence of Ag plasmons (dashed circle). (b): sum of 14 fast-XPS spectra (black line, see acquisition parameters in Table 6.1) of the Ag3*d* plasmon peaks; background: gray line; the energy window where photoelectron yield is defined is marked by the two dashed gray lines. (c): sum of 96 XSW-XPS spectra of Ag plasmon acquired in three XSW data sets (Clean-1,2,3, see Table 6.4). Inset table: position (eV), FWHM (eV), and relative area (%) of the fitting components peak-1, peak-2, peak-3, peak-4 (gray line). Background: straight black line. Residuals (black line below the spectrum) result from the subtraction of the whole spectrum (black dots) and the sum of all fitting components (*Envelope*, thick red line).

Ag plasmon results						
	Region			peak-1-2-3-4		
data set	P_c	d_c	F_c	P_c	d_c	F_c
Clean-1	1.00 (1)	2.36 (2)	0.97 (7)	0.99 (1)	2.34 (2)	0.97 (5)
Clean-2	1.00 (1)	2.36 (2)	1.02 (3)	1.00 (1)	2.36 (2)	1.02 (2)
Clean-3	1.00 (1)	2.36 (2)	0.99 (3)	1.00 (1)	2.36 (2)	0.99 (3)
Average	1.00 (1)	2.36 (2)	0.99 (4)	1.00 (1)	2.35 (2)	0.99 (3)

Table 6.4: Fitted values of Ag coherent position (P_c), coherent fraction (F_c) and vertical distance d_c (Å) from the next Bragg plane underneath, calculated as $P_c \times d_{\mathrm{Ag(111)}}$ ($d_{\mathrm{Ag(111)}} = 2.3593$ Å), of *Region* and peak-1+2+3+4 (= peak-1 + peak-2 + peak-3 + peak-4), plus corresponding average values, reported for each of the three measured data sets: Clean-1, Clean-2 and Clean-3.

In fitting the NIXSW data sets, we follow the the original assumption that all four components are generated from Ag and fix the relative intensities of peak-1, peak-2, peak-4 to 3.9%, 82.5% and 11.3% of peak-3 (the most intense component), besides constraining the FHWM and position of each line, according to the fitted values reported in Figure 6.6c. The model described in this way was applied to each XSW-XPS of the three data sets providing the results reported in Table 6.4. In particular, the photoelectron yield profile of the sum of the four components, renamed as peak-1+2+3+4 (= peak-1 + peak-2 + peak-3 + peak-4), is analyzed. Structural parameters (P_c, F_c), both equal to 1, are typical of a substrate signal and basically identical with the ones resulting from Ag3$d_{5/2}$ core level (see Table 6.3). This would then indicate that indeed the PE signal in the energy window investigated here (388− 407 eV) originates exclusively from Ag atoms.

However, as we fix the relative intensity of the other fitting components to the one of peak-3, this may bias our results by overlooking some possible minor peak coming from some other species. To conclusively exclude this possibility, we analyze

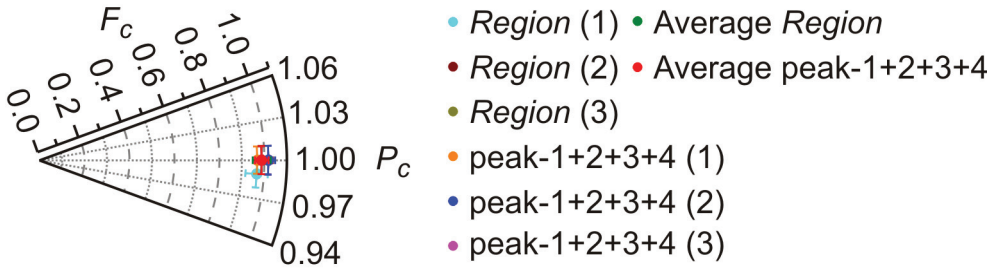


Figure 6.7: Argand diagram of *Region* and peak-1+2+3+4 (see text) structural parameters (P_c, F_c), with relative error bars, of data sets Clean-1,2,3 reported in Table 6.4 and marked in the legend.

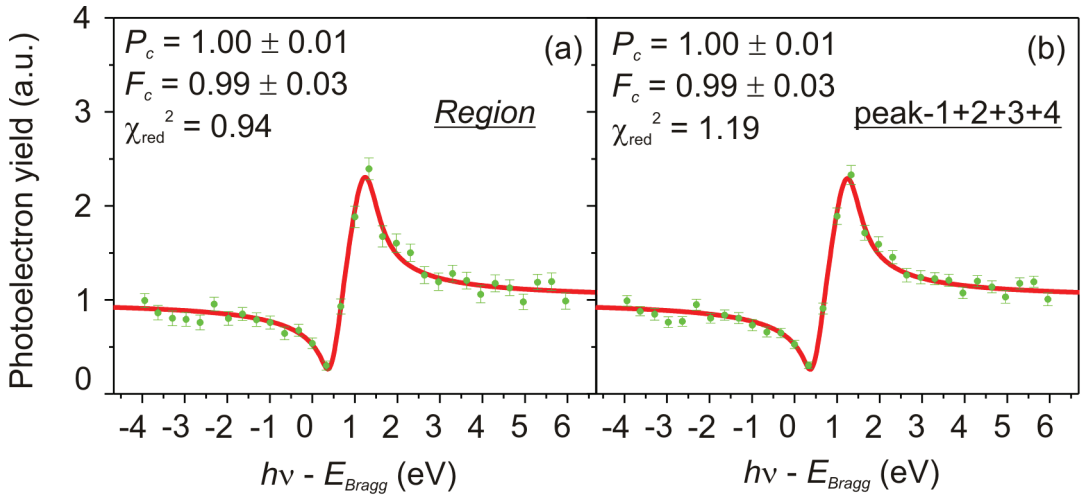


Figure 6.8: Photoelectron yield (green dots and relative error bars) and corresponding fitting curve (red) of the *Region* signal (a) and peak-1+2+3+4 (see text) (b) relative to data set Clean-3 (Table 6.4), displayed as a function of the photon energy relative to the Bragg energy (2627 eV). Results of the fit: coherent position (P_c), coherent fraction (F_c), and reduced χ^2, are reported in the figure.

each component independently and in addition the *Region* signal, i.e., the whole spectrum after background subtraction. We find that structural parameters of the single components are equal to those of their sum peak-1+2+3+4. Moreover, the coherent position and coherent fraction of the *Region* are in perfect agreement with those derived from the fitting model, as it is obvious from the values reported in Table 6.4 and plotted in Figure 6.7. Figure 6.8a,b shows two examples of photoelectron yield curves that are nearly indistinguishable, although corresponding to the two different signals, *Region* and peak-1+2+3+4, respectively. Furthermore, the Argand diagram representation of *Region* and peak-1+2+3+4 results shows overlapping data points and an average located at the $P_c = 1$, $F_c = 1$ point. This confirms that the peaks in question are plasmon peaks arising from Ag3*d* lines. We have now an XPS model, including energy window and background type, that can be transferred to the N1*s* spectra of AB and TBA in order to extract the nitrogen component.

6.3.3 Azobenzene

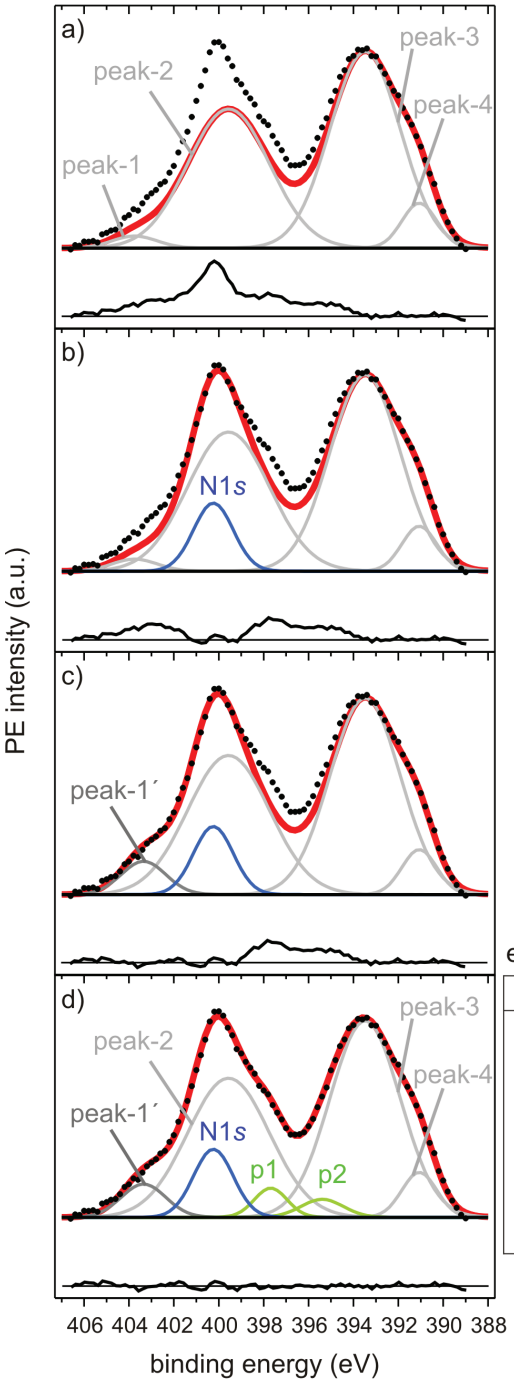
In the following section, NIXSW results of azobenzene molecules adsorbed on the Ag(111) substrate are presented. In particular, the N1*s* and C1*s* XPS models are derived and discussed, after which we focus our attention on the corresponding photoelectron yield profiles and structural parameters.

6.3.3.1 Nitrogen

The first step towards the extraction of N1*s* PE intensity has been already achieved with the definition of the Ag3*d*-plasmons model described in section 6.3.2.2. Analogous to the Ag plasmon case, the sum of all N1*s*+Ag3*d*-plasmons spectra of the three XSW data sets (Figure 6.9a-d), measured on AB/Ag(111), is adopted as a reference spectrum where N1*s* model is developed. The idea is to subtract Ag3*d*-plasmons XPS model (Figure 6.6) from the N1*s*+Ag3*d*-plasmons spectrum and find the binding energy position and FWHM of the N1*s* component, to then extract its photoelectron yield profile and the corresponding structural parameters.

XPS fitting model

After subtracting the Ag3*d*-plasmons XPS model from the N1*s*+Ag3*d*-plasmons spectra, the residuals in Figure 6.9a show that a large portion of the PE signal is still not accounted for. The most prominent missing component is at approximately 400 eV, thus attributed to the N1*s* core-level peak,[139,140] as shown in Figure 6.9b. Despite the insertion of a new component, the residuals (Figure 6.9b) reveal the presence of at least three more contributions not yet included in the fitting. One of them is at the high binding energy tail of the spectrum at approximately the same position of peak-1 of the plasmon model; hence rather than adding a new component, peak-1 of Ag3*d*-plasmons model is modified as follows. The intensity constraint of peak-1 relative to peak-3 is removed, and its position is left free to vary within ± 0.5 eV around its original value. The peak modified in this way is renamed as peak-1′ (Figure 6.9c). Finally, the fit of the N1*s*+Ag3*d*-plasmons spectrum is also improved in the central region through the insertion of two additional minor peaks, called p1 and p2. Judging from the residuals of Figure 6.9d, the XPS model constructed in this way and summarized in Figure 6.9e accurately describes our reference spectrum.



e)

Name	Pos.	FWHM	%Area
N1*s*	400.24	2.08	8.28
p1	397.69	1.72	2.93
p2	395.40	2.21	2.32
peak-1´	403.35	2.33	4.51
peak-2	399.56	4.29	34.88
peak-3	393.48	3.69	42.29
peak-4	391.07	1.82	4.78

Figure 6.9: (a)-(d): sum of 93 XSW-XPS spectra of N1*s*+Ag-plasmons acquired in three XSW data sets (AB-1, AB-2, AB-3, see Table 6.5). Ag3*d*-plasmons (peak-1, peak-2, peak-3, peak-4, see section 6.3.2.2): light gray line. N1*s*: blue line. peak-1′: dark gray line. p1, p2: green line. Background: straight black line. Residuals (black line below each spectrum) result from the subtraction of the whole spectrum (black dots) and the sum of all fitting components (thick red line). Table (e): position (eV), FWHM (eV), and relative area (%) of the fitting components N1*s*, p1, p2, peak-1′, peak-2, peak-3, peak-4 of model in panel d.

In comparison with the Ag3*d*-plasmons model of the bare Ag crystal (Figure 6.6c), the fitting model of the N1*s*+Ag3*d*-plasmons spectrum has four additional components: N1*s*, peak-1′, p1 and p2. Their physical origin is discussed below based on NIXSW results. However, even before analyzing the results, the different nature of the component assigned to the N1*s* core level compared to the remaining components is clearly revealed in Figure 6.10. In fact, a significant change in its intensity occurs between off-Bragg and on-Bragg conditions. This is already a strong indication in support of our assignment of the component at 400 eV (blue) to N1*s*, while the other components originate from the Ag3*d* plasmons. Note also the noise of the single XSW-XPS spectra reported in Figure 6.10. Because of the low signal-to-noise ratio, the fitting model was developed for the summed spectra (Figure 6.9).

Photoelectron yield

The fitting model of Figure 6.9d is applied to each XSW-XPS spectrum after constraining all positions and FWHMs, plus the area of peak-2 and peak-4 relative to peak-3, as discussed in section 6.3.2.2. On the other hand, the areas of peak-1′, N1*s*, p1, p2 and peak-3 are free to be fitted. The following photoelectron yield signals are investigated: N1*s*; peak-1′; peak-2+3+4 (= peak-2 + peak-3 + peak-4), summed because their intensities are constrained to each other; p1+2 (= p1 + p2). In this latter case, we decided to sum the two components for two reasons. First, in some data sets, p1 and/or p2 photoelectron yield is 0 at some given photon energies, hence the corresponding standard deviation of such data points is also 0 and χ^2 diverges. To prevent this occurrence, the areas of the two components are summed, because their sum is always greater than 0. Second, due to the proximity of the two peaks and due to their binding energy positions which correspond to Ag plasmons, it is very likely that they belong to the same species, presumably Ag. It is thus reasonable to evaluate the sum of these two minor components.

Figure 6.11 shows the photoelectron yield profiles of the four analyzed signals (data set AB-2, Table 6.5). At first glance, it is evident that peak-2+3+4 and p1+2, and peak-1′ have a substrate-like profile, while the N1*s* curve exhibits a very different behavior. The larger error bars of p1+2 and peak-1′ data points follow from the small signal-to-noise ratio of the N1*s*+Ag3*d*-plasmons spectra, which introduce a large error into the smaller fit components. For a better overview of the NIXSW results that are summarized in Table 6.5, a visual representation is offered by the Argand

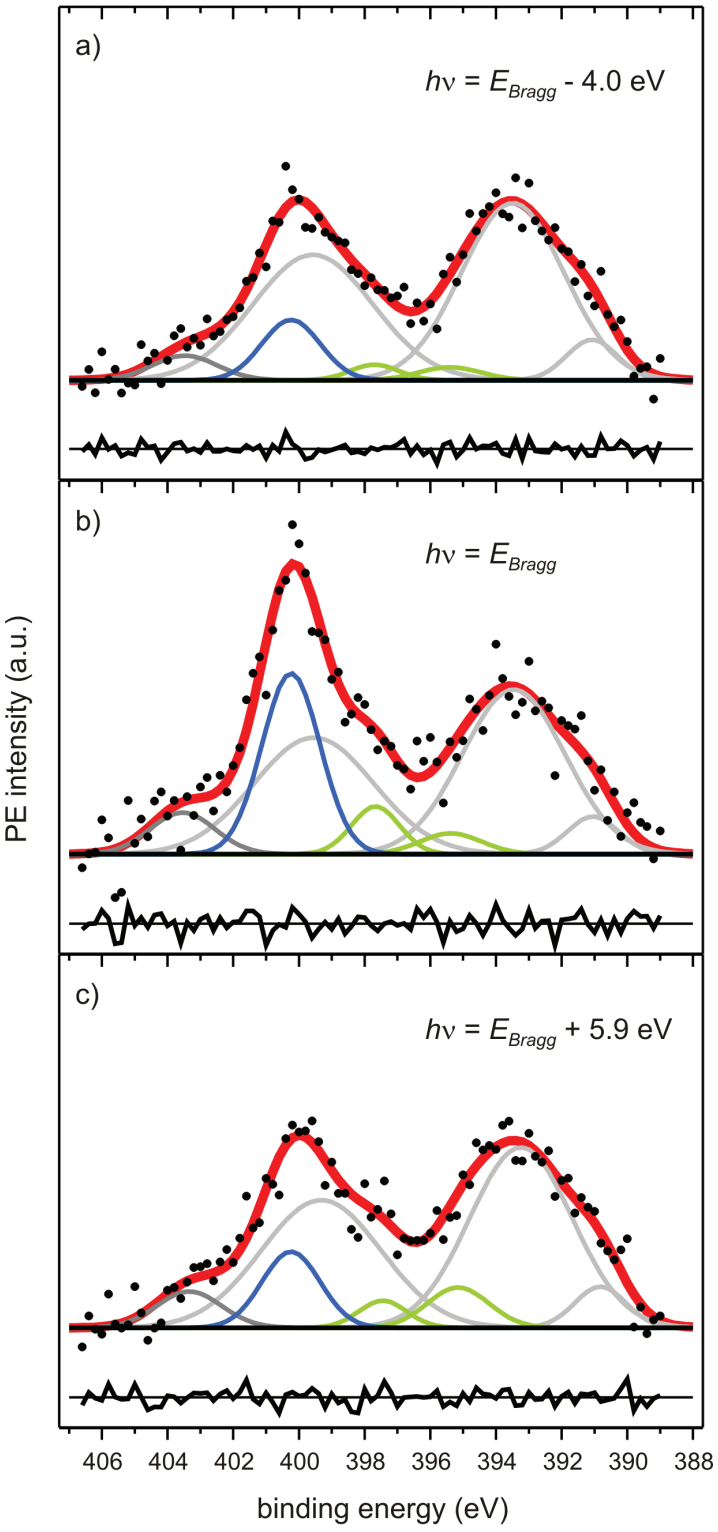


Figure 6.10: (a)-(c): XSW-XPS spectra of N1s+Ag-plasmons, extracted from XSW data set AB-2 (see Table 6.5), measured at the photon energy $h\nu$ specified in each panel relatively to $E_{Bragg} = 2634$ eV (see section 6.2.2). Each spectrum is normalized to the corresponding background value at 388 eV. For peak assignment and color code see Figure 6.9d and corresponding caption.

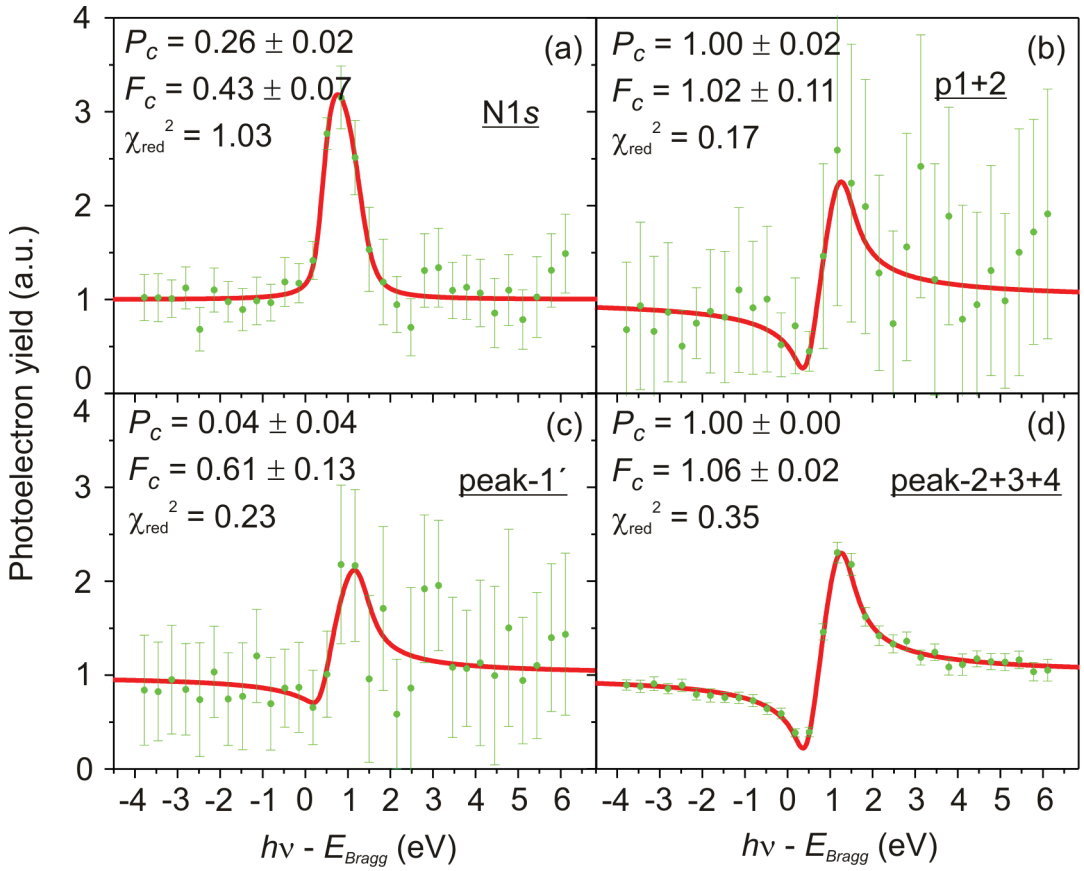


Figure 6.11: Photoelectron yield (green dots and relative error bars) and corresponding fitting curve (red) of N1*s* (a), p1+2 (see text) (b), peak-1′ (c), peak-2+3+4 (see text) of data set AB-2 (Table 6.5), displayed as a function of the photon energy relative to the Bragg energy (2634 eV). Results of the fit: coherent position (P_c), coherent fraction (F_c), and reduced χ^2, are reported in the figure.

diagram in Figure 6.12. The N1*s* data points (Figure 6.12a) have well-defined coherent position $P_c = 0.26 \pm 0.02$, and a coherent fraction of $F_c = 0.48 \pm 0.12$, characterized by a 10% larger scatter around the average. On the other hand, the structural parameters of peak-2+3+4 in all data sets (Figure 6.12d) cluster around the typical substrate values of $P_c = 0$ and $F_c = 1$. The same conclusion applies to p1+2 (Figure 6.12b), which is characterized by a coherent position of 0.05 ± 0.05, although with a smaller coherent fraction (0.86 ± 0.15) and much larger error bars for the reasons discussed above. Finally, the results for peak-1′ (Figure 6.12c) deviate slightly more from the silver structural parameters. In fact, the corresponding average values $P_c = 0.08 \pm 0.05$ and $F_c = 0.70 \pm 0.14$ suggest a possible minor contribution of the N1*s* PE intensity to the peak-1′ component. Indeed, N1*s* spectra of TBA/Au(111),[141] where no substrate plasmon peaks appear, reveal the presence of a nitrogen shake-up satellite at approximately 3 eV higher binding energy than the main photoemission line (399 eV). However, due to the small relative area of peak-1′

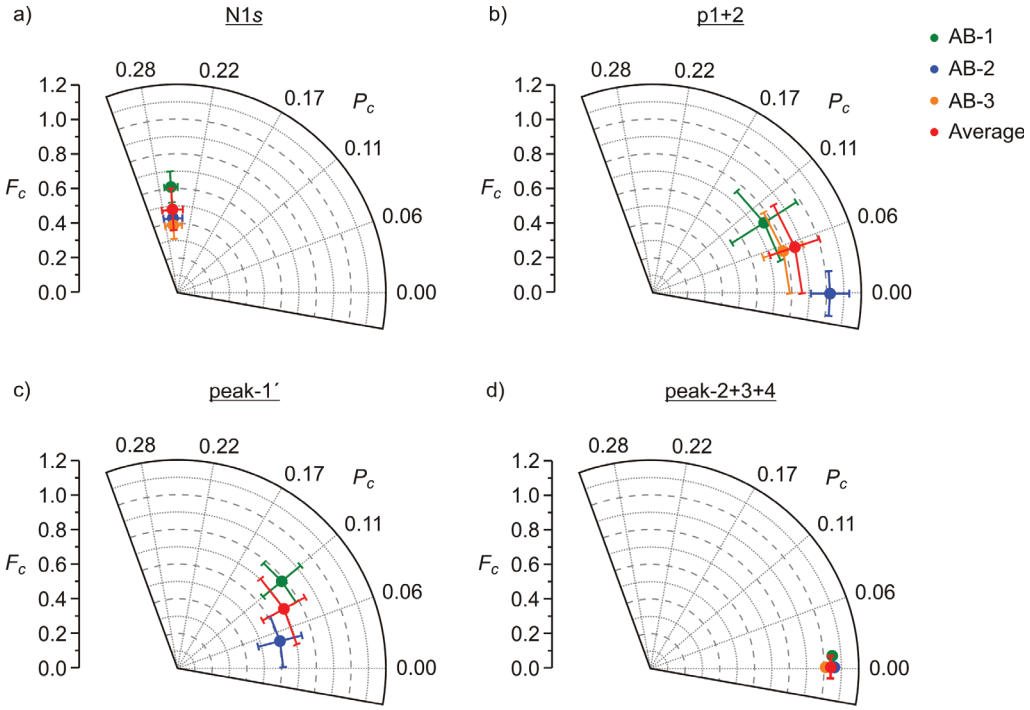


Figure 6.12: Argand diagram of N1*s* (a), p1+2 (see text) (b), peak-1′ (c), peak-2+3+4 (see text) structural parameters (P_c, F_c), with corresponding error bars, of data sets specified in the legend and reported in Table 6.5.

and due to the small signal-to-noise ratio, no further investigations to differentiate possible contributions from different species that may be present in peak-1′ are performed.

To conclude, the average height of nitrogen atoms is 2.97 Å ± 0.04 Å with a coherent fraction of approximately 50%. These experimental findings will be discussed together with the carbon structural parameters in section 6.4.1, where a comprehensive picture of AB adsorption geometry is derived.

N1s+Ag3d-plasmons results												
component	N1s			p1+2			peak-1′			peak-2+3+4		
data set	P_c	d_c	F_c	P_c	d_c	F_c	P_c	d_c	F_c	P_c	d_c	F_c
AB-1	0.26 (1)	2.97 (2)	0.61 (9)	0.09 (5)	2.57 (12)	0.76 (22)	0.11 (3)	2.61 (7)	0.78 (14)	0.01 (0)	2.38 (0)	1.05 (2)
AB-2	0.26 (2)	2.97 (5)	0.43 (7)	0.00 (2)	2.36 (5)	1.02 (11)	0.04 (4)	2.45 (9)	0.61 (13)	0.00 (0)	2.36 (0)	1.06 (2)
AB-3	0.26 (2)	2.97 (5)	0.39 (8)	0.05 (5)	2.47 (12)	0.79 (12)	-	-	-	0.00 (0)	2.36 (0)	1.01 (2)
Average	0.26 (2)	2.97 (4)	0.48 (12)	0.05 (5)	2.47 (11)	0.86 (15)	0.08 (5)	2.53 (12)	0.70 (14)	0.00 (1)	2.36 (1)	1.04 (2)

Table 6.5: N1s and Ag3d-plasmons fitted values of coherent position (P_c), coherent fraction (F_c) and vertical distance d_c (Å) from the Bragg plane, calculated as $P_c \times d_{\mathrm{Ag(111)}}$ or $(P_c + 1) \times d_{\mathrm{Ag(111)}}$ ($d_{\mathrm{Ag(111)}} = 2.3552$ Å) depending on whether P_c is closer to 1 or 0, are reported for each XSW data set. peak-1′ of AB-3 is missing because at one photon energy, its area equals 0; thus χ^2 diverges and no fitting parameters can be found.

6.3.3.2 Carbon

The C1*s* spectrum reported in Figure 6.13a, resulting from the sum of 10 fast-XPS spectra (section 6.2.2) in order to increase the statistics, consists of one peak at 284.8 eV with FWHM = 1.9 eV, followed by a broad tail at higher binding energies, attributed to inelastically scattered electrons. Although carbon atoms of azobenzene are not all in the same chemical state, the *Region* signal is taken as representative of the whole carbon contribution, because no chemically shifted PE components are discernible in the spectra in Figure 6.13a. *Region* is the integrated PE intensity of the C1*s* spectrum after background subtraction. The background, defined within the energy window marked by the two dotted lines in Figure 6.13a, is of linear type. Since no differentiation of carbon species is possible, the resulting structural parameters correspond to the average of all carbon atoms of the AB molecule.

An example of the C1*s* photoelectron yield is reported in Figure 6.13b. The profile reminds one of the N1*s* profile presented above (Figure 6.11a). Indeed, the respective structural parameters are similar. The polar plot representation (Figure 6.14) of all experimental results that are also summarized in Table 6.6 shows a small scatter of data points around the average value $P_c = 0.27 \pm 0.02$, $F_c = 0.34 \pm 0.03$. The lower coherent fraction of carbon atoms compared to that of nitrogens (0.48 ± 0.12) suggests a distribution of carbon atoms across the spaces between the extended Bragg planes, thus a lower vertical order. In particular, a deviation of the flat gas-phase geometry of azobenzene with the presence of tilted phenyl rings would be consistent

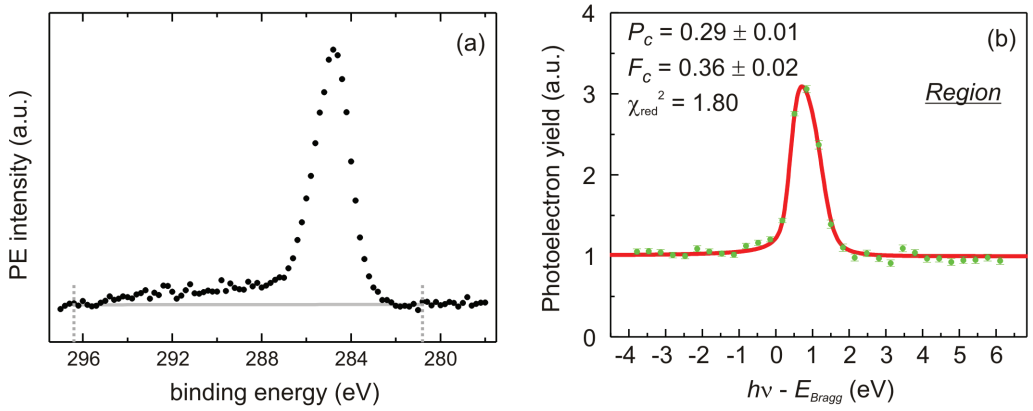


Figure 6.13: (a): sum of 10 fast-XPS spectra (black dots, see aquisition parameters in Table 6.1) measured at $h\nu = 2617$ eV; background: gray line. (b): photoelectron yield (green dots and relative error bars) and corresponding fitting curve (red) of C1*s* of data set AB-2 (Table 6.6), displayed as a function of the photon energy relative to the Bragg energy (2634 eV). Results of the fit: coherent position (P_c), coherent fraction (F_c), and reduced χ^2 are reported in the figure.

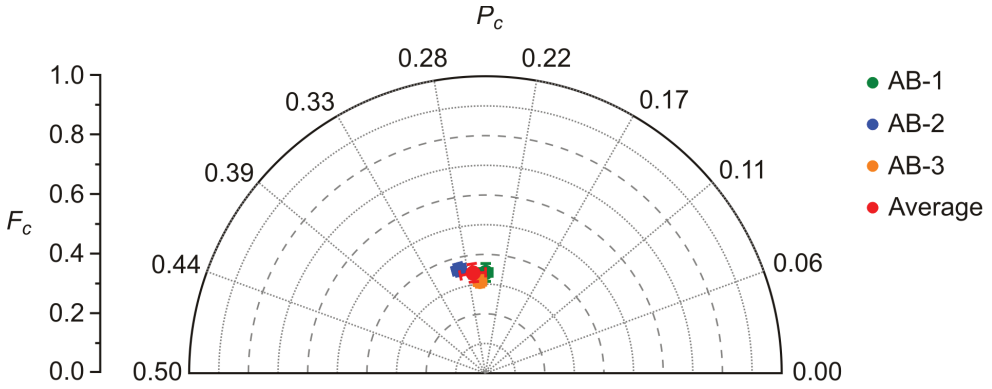


Figure 6.14: Argand diagram of C1*s* structural parameters (P_c, F_c), with relative error bars, of data sets reported in Table 6.6.

C1s results			
	C1*s Region*		
data set	P_c	d_c	F_c
AB-1	0.25 (1)	2.94 (2)	0.34 (3)
AB-2	0.29 (1)	3.04 (2)	0.36 (2)
AB-3	0.26 (1)	2.97 (2)	0.31 (2)
Average	0.27 (2)	2.98 (5)	0.34 (3)

Table 6.6: C1*s* fitted values of coherent position (P_c), coherent fraction (F_c) and vertical distance d_c (Å) from the surface Bragg plane, calculated as $(P_c + 1) \times d_{\mathrm{Ag(111)}}$ ($d_{\mathrm{Ag(111)}} = 2.3552$ Å), are reported for each C1*s* XSW data set.

with a lower coherent fraction of carbon atoms compared to the nitrogens. In section 6.4.1, the adsorption geometry of AB molecules on Ag(111) will be retrieved on the basis of nitrogen and carbon NIXSW results.

6.3.4 TBA

In analogy to section 6.3.3 for azobenzene, nitrogen and carbon NIXSW results of TBA molecules adsorbed on Ag(111) are presented below. We will adopt a N1s fitting model similar to the one of azobenzene, and will then focus on the photoelectron yields and structural parameters corresponding to each component. Finally, C1s data are reported. For the discussion of TBA adsorption geometry, please refer to section 6.4.2.

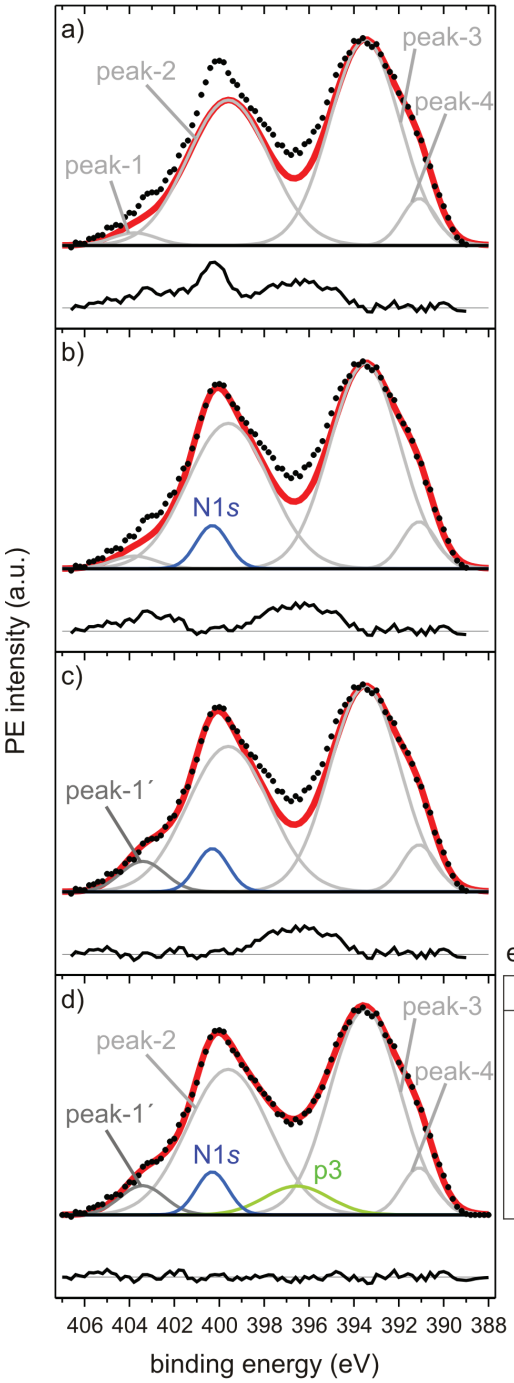
6.3.4.1 Nitrogen

In analogy to the N1s+Ag3d-plasmons spectrum of azobenzene (section 6.3.3.1), the Ag3d-plasmons model of bare Ag, described in section 6.3.2.2, is transferred to the corresponding TBA spectrum and the N1s peak is obtained by subtraction. Subsequently, the corresponding photoelectron yields are analyzed and the structural parameters fitted.

XPS fitting model

The reference spectrum (Figure 6.15) on which the N1s+Ag3d-plasmons model is developed results from the sum of all XSW-XPS spectra of the two measured XSW data sets. The sum of XSW-XPS spectra does not alter the relative intensity of peaks with the same nature; hence we can still apply the Ag3d-plasmons model found for the bare Ag (Figure 6.6c). This fit is shown in Figure 6.15a. From the analysis of the corresponding residuals, it is possible to deduce the presence of at least three additional components. Similarly to the AB spectrum in Figure 6.9, we introduce three additional peaks, i.e., N1s, peak-1$'$ and p3. Judging from the analysis of the residuals of Figure 6.15d, the XPS fitting model summarized in Figure 6.15e describes our N1s+Ag3d-plasmons reference spectrum very well.

The nature of the newly introduced components will be evaluated on the basis of the corresponding photoelectron yield fits. However, from the spectra reported in Figure 6.16a-c a significant difference in the intensity of the N1s peak at off-Bragg and on-Bragg, compared to the other components, is already evident. This already represents an indication of different behaviors of nitrogen and silver atoms within the XSW field, presumably due to different positions with respect to the Bragg plane.



e)

Name	Pos.	FWHM	%Area
N1*s*	400.31	1.68	4.24
p3	396.55	3.36	5.69
peak-1´	403.42	2.33	3.99
peak-2	399.60	4.29	36.64
peak-3	393.51	3.69	44.42
peak-4	391.10	1.82	5.02

Figure 6.15: (a)-(d): sum of 62 XSW-XPS spectra of N1*s*+Ag-plasmons acquired in two XSW data sets (TBA-1, TBA-2, see Table 6.7). Ag3*d*-plasmons (peak-1, peak-2, peak-3, peak-4, see section 6.3.2.2): light gray line. N1*s*: blue line. peak-1′: dark gray line. p3: green line. Background: straight black line. Residuals (black line below each spectrum) result from the subtraction of the whole spectrum (black dots) and the sum of all fitting components (*Envelope*, thick red line). Table (e): position (eV), FWHM (eV), and relative area (%) of the fitting components N1*s*, p3, peak-1′, peak-2, peak-3, peak-4.

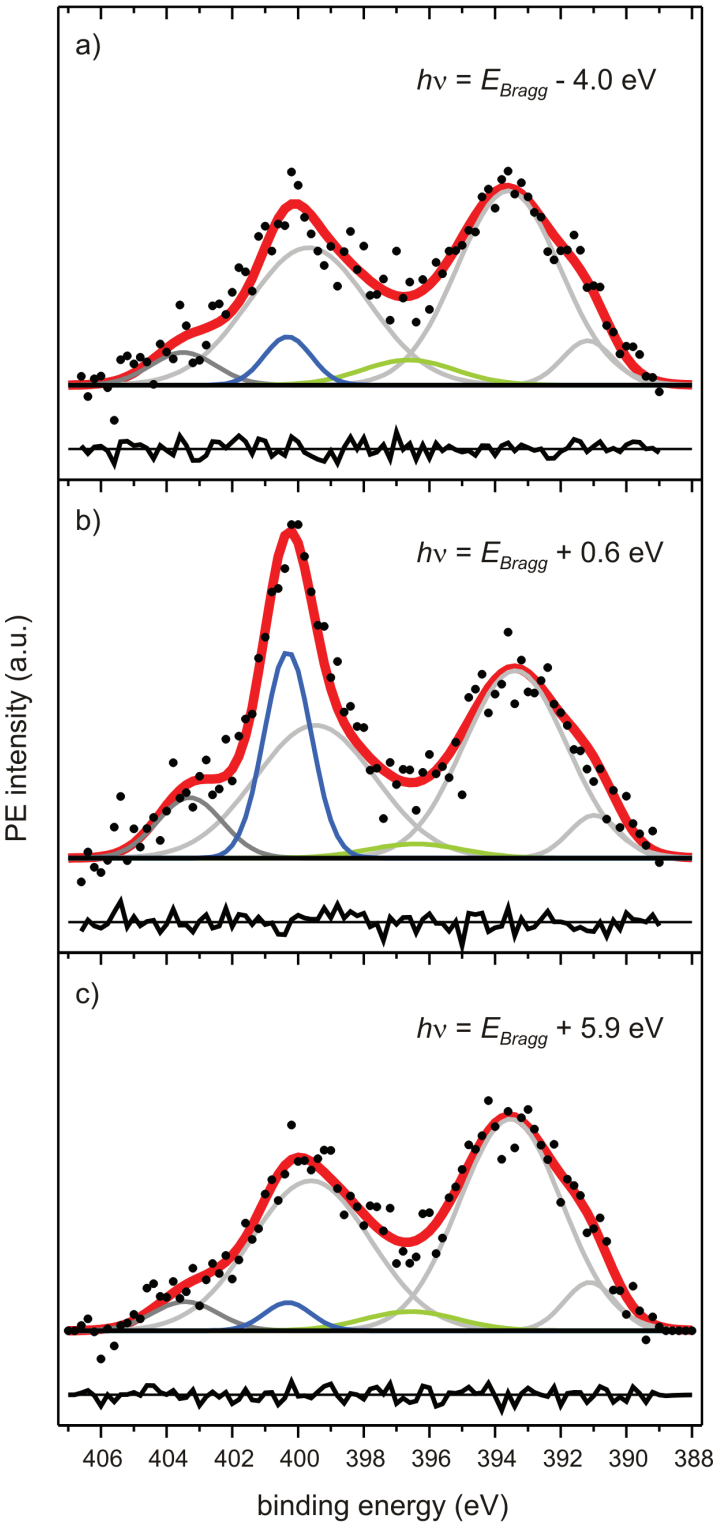


Figure 6.16: (a)-(c): XSW-XPS spectra of N1s+Ag3d-plasmons, extracted from XSW data set TBA-1 (see Table 6.7), measured at the photon energy $h\nu$ specified in each panel relative to $E_{Bragg} = 2627$ eV (section 6.2.2). Each spectrum is normalized to the corresponding background value at 388 eV. For peak assignment and color code, see Figure 6.15d and relative caption.

Photoelectron yield

N1s+Ag3d-plasmons XSW-XPS spectra are fitted with the XPS model detailed above (Figure 6.15d,e) and the following signals are analyzed: N1s, p3, peak-1′ and peak-2+3+4 (= peak-1 + peak-2 + peak-3). Figure 6.17 shows examples of photoelectron yield profiles for each of the signals under investigation. The very different behavior of the N1s curve (Figure 6.17a) compared to the others (Figure 6.17b-d) is evident from inspection alone. Another interesting remark concerns the size of the error bars. In case of N1s, p3, peak-1′ error bars are much larger than for peak-2+3+4: this occurrence is attributed to the small signal-to-noise ratio of the first components, as opposite to the latter one. Consequently, even a slight variation of their fitting components area of the Monte Carlo-simulated raw spectra (see section 3.5) results in a large relative difference.

The Argand diagram in Figure 6.18 offers a visual representation of results summarized in Table 6.7. The N1s signal shows a well-defined coherent position and fraction, equal to 0.32 ± 0.03 and 0.66 ± 0.15, respectively. TBA nitrogen atoms are thus at 3.10 ± 0.06 Å above the surface, 0.13 Å higher than in the case of AB, and with a coherent fraction about 20% larger. In contrast, the structural parameters of peak-2+3+4, $P_c = 1.00 \pm 0.01$ and $F_c = 1.02 \pm 0.02$, exhibit the typical substrate behavior. Clearly, a value of coherent fraction greater than 1 has no physical meaning. It simply results from the best fit of P_c and F_c without setting any constraints on the boundaries of the fitting parameters. However, since the the discrepancy from the F_c upper limit is negligible (2%), it does not represent an issue for the interpretation of our results. Similar substrate-like profiles result for p3 (Figure 6.17b) and by peak-1′ (Figure 6.17c), although in the latter case, the coherent fraction is approximately 20% lower and error bars are notably larger. The lower fraction might be a direct consequence of the inclusion of the N1s signal into the peak-1′, as already seen for azobenzene (section 6.3.3.1), while the larger error bars are related to the small absolute intensity of the component, as discussed above.

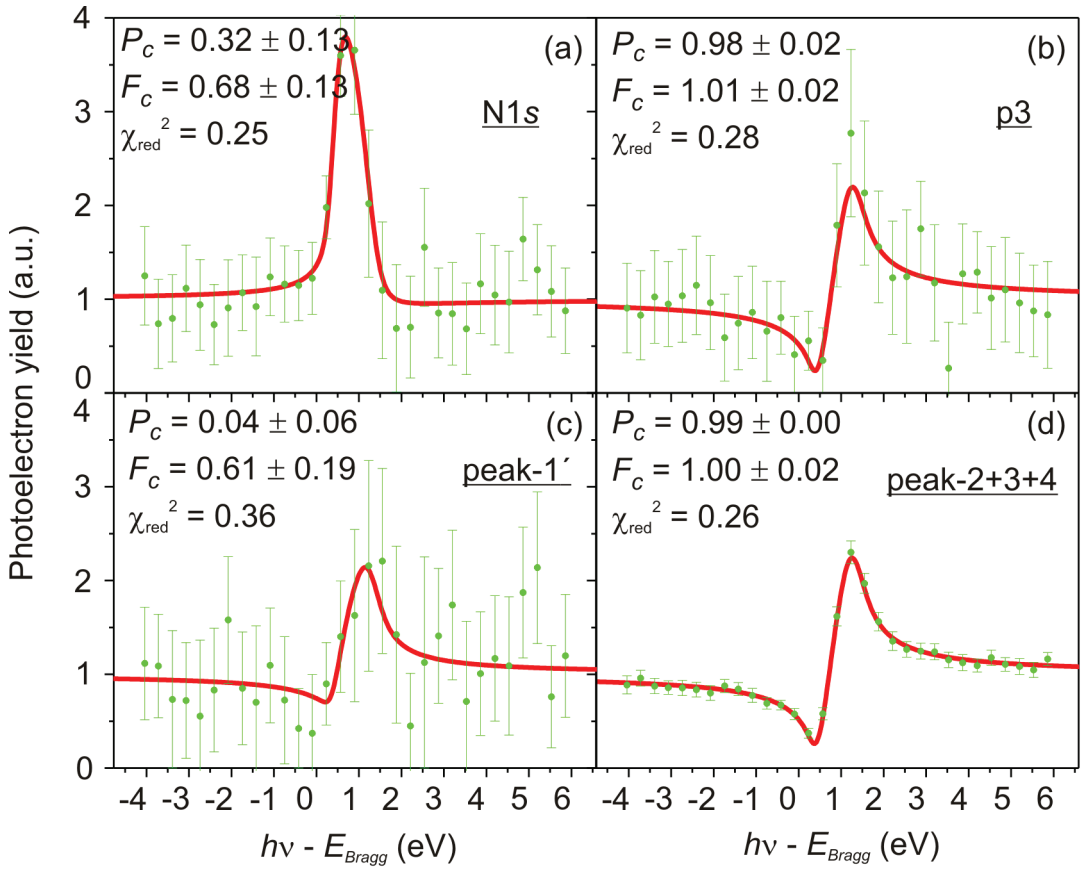


Figure 6.17: Photoelectron yield (green dots and relative error bars) and corresponding fitting curve (red) of N1*s* (a), p3 (b), peak-1′ (c), peak-2+3+4 (see text) of data set TBA-1 (Table 6.5), displayed as a function of the photon energy relative to the Bragg energy (2627 eV). Results of the fit: coherent position (P_c), coherent fraction (F_c), and reduced χ^2, are reported in the figure.

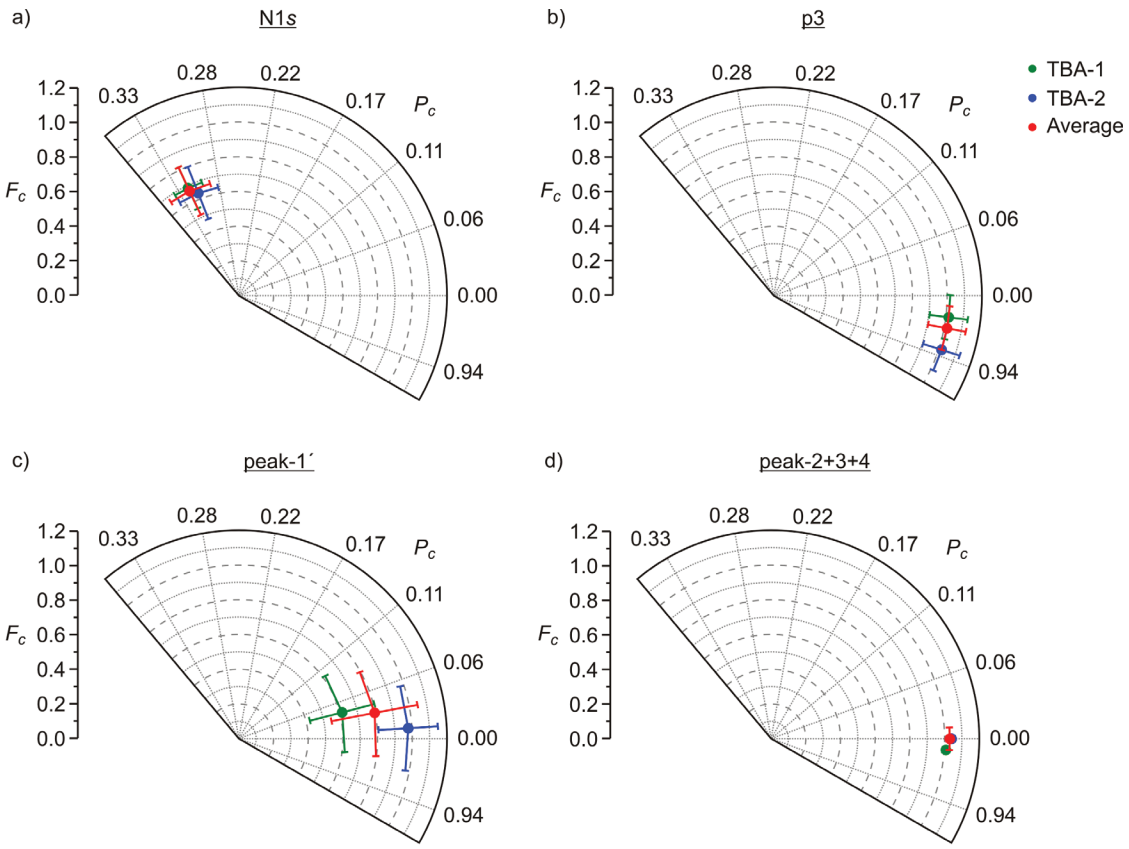


Figure 6.18: Argand diagram of N1s (a), p3 (b), peak-1′ (c), peak-2+3+4 (see text) structural parameters (P_c, F_c), with corresponding error bars, of data sets specified in the legend and reported in Table 6.7.

N1s+Ag3d-plasmons results												
component	N1s			p3			peak-1′			peak-2+3+4		
data set	P_c	d_c	F_c	P_c	d_c	F_c	P_c	d_c	F_c	P_c	d_c	F_c
AB-1	0.32 (2)	3.11 (5)	0.68 (13)	0.98 (2)	2.31 (5)	1.01 (11)	0.04 (6)	2.45 (14)	0.61 (19)	0.99 (0)	2.34 (0)	1.00 (2)
AB-2	0.31 (3)	3.09 (7)	0.63 (16)	0.95 (2)	2.24 (5)	1.01 (11)	0.01 (4)	2.38 (9)	0.97 (17)	1.00 (0)	2.36 (0)	1.03 (2)
Average	0.32 (3)	3.10 (6)	0.66 (15)	0.97 (2)	2.28 (5)	1.01 (11)	0.03 (5)	2.42 (12)	0.79 (25)	1.00 (1)	2.35 (2)	1.02 (2)

Table 6.7: N1s and Ag3d-plasmons fitted values of coherent position (P_c), coherent fraction (F_c) and the vertical distance d_c (Å) from the next Bragg plane underneath, calculated as $P_c \times d_{\mathrm{Ag(111)}}$ or $(P_c + 1) \times d_{\mathrm{Ag(111)}}$ ($d_{\mathrm{Ag(111)}} = 2.3593$ Å) depending on whether P_c is closer to 1 or 0, are reported for each XSW data set.

6.3.4.2 Carbon

The same considerations as for the C1*s* spectrum of azobenzene (section 6.3.3.2) also apply to the case of TBA. In fact, although TBA molecule contains several chemically different carbon species, especially carbons of phenyl rings and *tert*-butyl groups, chemical shifts are not large enough to be resolved by our electron analyzer. In particular, the C1*s* spectrum consists of a peak at 285 eV with FWHM of 1.83 eV and a broad tail at higher binding energies, assigned to inelastically scattered electrons (section 4.2.4).

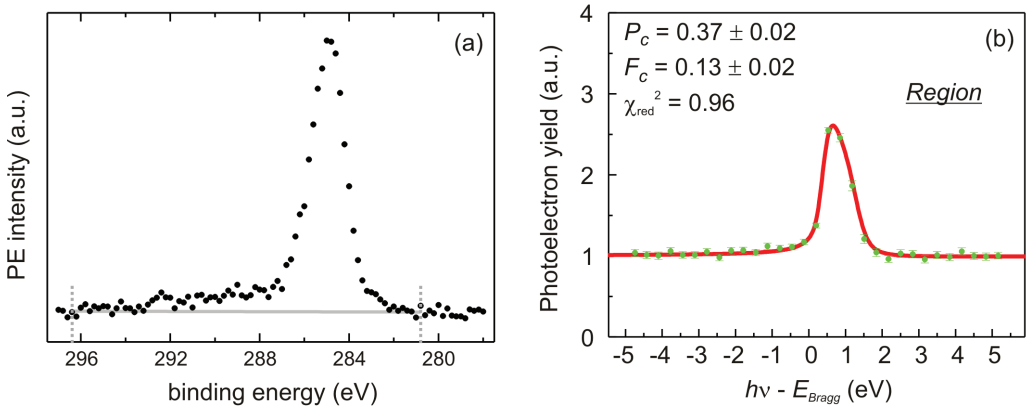


Figure 6.19: (a): sum of 2 C1*s* fast-XPS spectra (black dots, see acquisition parameters in Table 6.1) measured at $h\nu = 2617$ eV; background: gray line. (b): photoelectron yield (green dots and relative error bars) and corresponding fitting curve (red) of C1*s* of data set TBA-1 (Table 6.8), displayed as a function of the photon energy relative to the Bragg energy (2627 eV). Results of the fit: coherent position (P_c), coherent fraction (F_c), and reduced χ^2, are reported in the figure.

Due to the impossibility of differentiating carbon species, the photoelectron yield signal analyzed is given by the integrated PE intensity after background subtraction

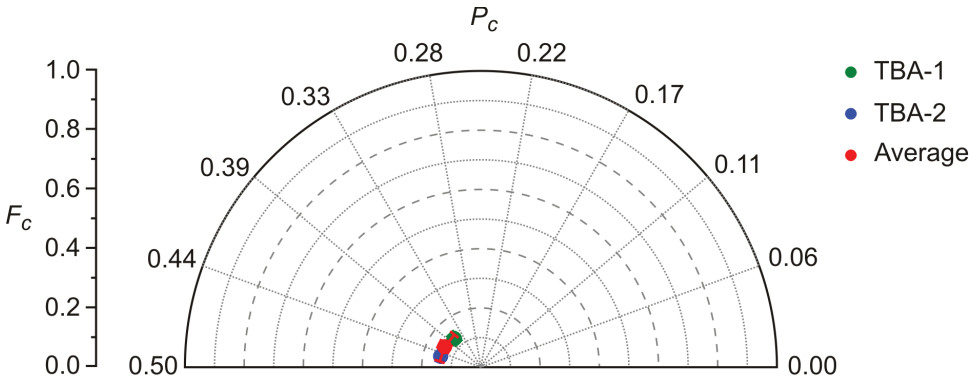


Figure 6.20: Argand diagram of C1*s* structural parameters (P_c, F_c), with relative error bars, of data sets reported in Table 6.8.

C1s results			
	C1*s Region*		
data set	P_c	d_c	F_c
AB-1	0.37 (2)	3.23 (5)	0.13 (2)
AB-2	0.46 (2)	3.44 (5)	0.14 (1)
Average	0.42 (6)	3.34 (15)	0.14 (2)

Table 6.8: Fitted values of coherent position (P_c), coherent fraction (F_c) and the vertical distance d_c (Å) from the surface Bragg plane calculated as $(P_c + 1) \times d_{\mathrm{Ag(111)}}$ ($d_{\mathrm{Ag(111)}} = 2.3593$ Å), are reported for each C1*s* XSW data set.

(*Region*). The background of C1*s* spectra is linear and the energy window is defined by the two dotted lines shown in Figure 6.8. An example of C1*s* photoelectron yield is reported in Figure 6.19b. The Argand diagram representation of all C1*s* results (Figure 6.20), also summarized in Table 6.8, reveals a very low coherent fraction of $F_c = 0.14 \pm 0.02$, coupled to a coherent position of $P_c = 0.42 \pm 0.06$. This corresponds to an average height of carbon atoms equal to 3.34 ± 0.15 Å. Both the larger average distance of carbons from the surface and the lower coherent fraction are consistent with the bulky TBA molecular structure as compared to azobenzene, due to the presence of the *tert*-butyl groups. In section 6.4.2, the adsorption geometry of TBA/Ag(111) is derived and the role played by the "spacer leg" groups is discussed in more detail.

6.4 Discussion

Carbon and nitrogen NIXSW results regarding azobenzene (section 6.3.3) and TBA (section 6.3.4) are discussed in sections 6.4.1 and 6.4.2, respectively. In particular, a novel analysis scheme is introduced and employed to extract further information concerning the adsorption geometry of azobenzene and TBA on Ag(111), besides the average adsorption heights. Experimental results are then compared with DFT calculations and a bonding mechanism of the molecule to the surface is proposed.

6.4.1 Discussion of azobenzene experimental results

6.4.1.1 Introduction

For the purpose of the discussion, azobenzene can be decomposed into the azo (-N=N-) bridge and the phenyl (-C_6H_5) ring moieties. This conceptual subdivision of the molecule is also supported by the fact that HOMO and LUMO predominantly consist of the N lone pairs and the π^* orbital of the -N=N- moiety, respectively.[142] Therefore, the molecular orbitals that are chemically interacting with the substrate in the adsorbate state are mainly located at the nitrogen atoms, suggesting a substantial difference between the azo bridge and the closed-shell phenyl rings. The latter indeed are expected to be mainly involved in long-range dispersive interactions with the metal surface.

With this conceptual decomposition of azobenzene in mind, we can qualitatively discuss the azobenzene-substrate interactions, characterized primarily by the balance among the following four major contributions:

- the vdW interactions between the phenyl rings and the metal,
- the Pauli repulsion between the phenyl rings and the substrate,
- a possible covalent bond between the nitrogen atoms and the Ag surface atoms,
- a possible energetic penalty due to the distortion of the planar gas-phase molecular geometry.

In case of the flat *trans* isomer of azobenzene (Figure 6.1a), the second and the third contributions are in competition, because the covalent bond N-Ag tends to bring the molecule closer to the surface, where the phenyl rings may already experience a

substantial Pauli repulsion and thus lift away from the surface to form a butterfly-like configuration (Figures 6.21 and 6.2a). On the other hand, attractive vdW forces tend to pull the molecule closer to the surface, decreasing both the phenyl ring tilt angle $\widetilde{\omega}$ (Figure 6.21) and the nitrogen adsorption height $d_c\,(N)$, as well as the energetic cost for the molecular distortion. These two parameters, $\widetilde{\omega}$ and $d_c\,(N)$, are therefore sensitive to the balance between the N-Ag covalent interaction and the dispersive phenyl-substrate interactions. Their determination will allow the magnitude of the different binding forces acting at the azobenzene/Ag(111) interface to be assessed.

NIXSW AB results			
	P_c	d_c (Å)	F_c
N	0.26 (2)	2.97 (4)	0.48 (12)
C	0.27 (2)	2.98 (5)	0.34 (3)

Table 6.9: Summary of NIXSW experimental results of carbon and nitrogen of AB/Ag(111). In particular, coherent position (P_c), corresponding adsorption height d_c and coherent fraction (F_c) derived from N1s and C1s lines are reported (section 6.3.3).

6.4.1.2 A novel interpretative scheme of NIXSW results

NIXSW provides the structural parameters (P_c, F_c) of nitrogen and carbon atoms of azobenzene/Ag(111) (Table 6.9). Due to the small chemical core-level shifts, it is not possible to directly differentiate carbon atoms of the phenyl rings, as it was done e.g., for PTCDA/Ag(110) (section 4.3.1.2) and TPA/Cu(100) (section 7.3.1). Moreover, since the adsorption geometry is not known a priori and the molecule could possibly extend over more than a Bragg plane spacing, the modulo 1 ambiguity of P_c (section 2.5) does not allow consideration of the carbon coherent position as the average vertical position. In order to overcome this deficiency and determine the tilt angle $\widetilde{\omega}$ of azobenzene in the adsorbate state, a novel analysis scheme is developed. In particular, different molecular configurations are simulated and the corresponding coherent positions and coherent fractions are calculated as they would result from a NIXSW experiment. The ultimate goal is to determine the adsorption geometries of azobenzene that are consistent with NIXSW data.

The simulations of the azobenzene conformation primarily aim to investigate the following two degrees of freedom:

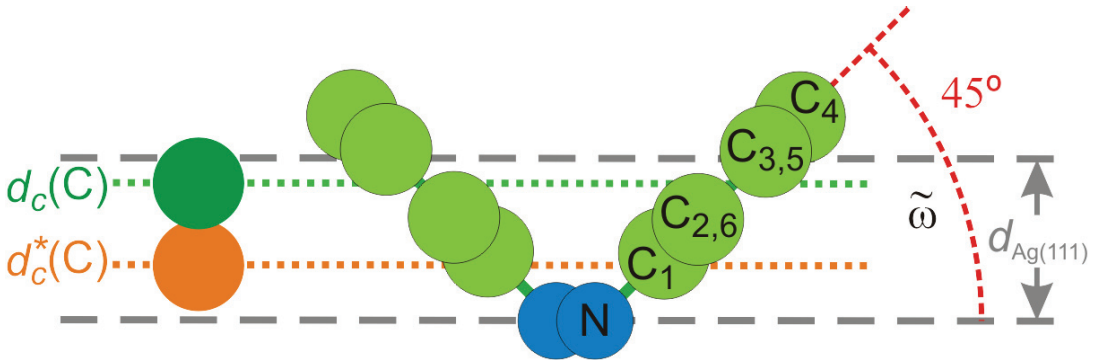


Figure 6.21: Adsorption model of azobenzene *trans*-isomer in the symmetric butterfly geometry (side view) with the nitrogen atoms placed at the Bragg plane and the tilt angle $\widetilde{\omega} = 45°$ (dashed red arc). d_c is the average distance of carbon atoms (center of phenyl ring, dark green circle and dotted green line at 1.98 Å) from the Bragg plane. d_c^* is the distance of carbon atoms (center of phenyl ring, orange circle and dotted orange line at 0.81 Å) from the Bragg plane corresponding to the coherent position $P_c^* = 0.34$ derived from the sum in the Argand diagram of single carbon atoms positions (Figure 6.23). The Bragg plane spacing is $d_{\mathrm{Ag(111)}} = 2.3552$ Å (section 6.2.1).

- the tilt angle $\widetilde{\omega}$ between the plane of the phenyl ring, including the N atom directly bonded to it, and the (111) Bragg plane (Figure 6.21),
- the rotation angle β of the phenyl ring around the N-C_4 axis (Figure 6.28a and 6.29).

The assumption behind the simplified azobenzene model of Figure 6.21 and Figure 6.28 is that the phenyl ring and the N atom, to which it is directly bound, lie in the same plane, which may be tilted relative to the surface. According to DFT calculations[143] the distortion of azobenzene is more complex. Namely, the center of rotation $\widetilde{\omega}$ is C_1 rather than N and the axis around which the phenyl ring rotates in β is C_1-C_4 rather than N-C_4. However, an additional minor tilt of the N-C_1 axis occurs as the phenyl moiety lifts from the molecular plane. Therefore, for simplicity, azobenzene is modeled as described above and illustrated in Figure 6.21. The same argument will apply for $\widetilde{\omega}$ of TBA molecule (section 6.4.2.3).

We focus first on the tilt angle $\widetilde{\omega}$. Figure 6.21 shows a simplified model of azobenzene with the two nitrogen atoms located at the Bragg plane and the two symmetric phenyl rings tilted at $\widetilde{\omega} = 45°$. In order to determine the effect of $\widetilde{\omega}$ on the structural parameters of carbon, the phenyl ring tilt angle is varied from $-5°$ to $90°$ and for each configuration two parameters are calculated:

- The first parameter is the average distance d_c (C) of carbon atoms, i.e., the center of the phenyl ring, from the Bragg plane. The dotted green line and the dark green

circle in Figure 6.21 mark the center of the phenyl ring. This is the distance that we are interested in and that we may naively expect to measure with NIXSW.

- The second parameter is the average distance $d_c^*(\mathrm{C})$ of carbon atoms derived from the sum of the vectors representing the positions of the single carbon atoms in the Argand diagram. The dotted orange line and the orange circle in Figure 6.21 mark the height corresponding to $d_c^*(\mathrm{C})$ (Figure 6.24a). Remarkably, $d_c^*(\mathrm{C}) \neq d_c(\mathrm{C})$. This second parameter represents what would actually result from a NIXSW experiment, if AB adsorbs as depicted in Figure 6.21. The procedure followed to calculate $d_c^*(\mathrm{C})$ is described in detail below.

Definition of $P_c(\mathrm{C})$ and $d_c(\mathrm{C})$

In order to determine the sum of the single carbon contributions in the Argand diagram, the vertical and lateral positions of all phenyl ring carbon atoms need to be defined. The lateral positions of carbon atoms within the phenyl ring are assumed to be identical to the ones in the crystal structure of *trans*-azobenzene.[144] Once the relative lateral positions of carbons in the phenyl ring are fixed, the distance $d_c(\mathrm{C_i})$ (where i = 1, 2, 3, 4, 5, 6) of each carbon atom from the Bragg plane is calculated for each configuration of azobenzene and converted into a coherent position by the following formula (see section 2.5):

$$P_c(\mathrm{C_i}) = \frac{d_c(\mathrm{C_i})}{d_{\mathrm{Ag(111)}}} \tag{6.3}$$

where $d_{\mathrm{Ag(111)}} = 2.3552$ Å. The average distance of carbon atoms from the Bragg plane is given by:

$$d_c(\mathrm{C}) = \frac{1}{n}\sum_{i=1}^{n} d_c(\mathrm{C_i}), \tag{6.4}$$

where n is the number of averaged carbon atoms. In our case $n = 6$, i.e., the number of carbon atoms in the phenyl ring. As a consequence, the corresponding coherent position is:

$$P_c(\mathrm{C}) = \frac{d_c(\mathrm{C})}{d_{\mathrm{Ag(111)}}} = \frac{\frac{1}{n}\sum_{i=1}^{n} d_c(\mathrm{C_i})}{d_{\mathrm{Ag(111)}}}. \tag{6.5}$$

Definition of $P_c^*(\mathrm{C})$ and $d_c^*(\mathrm{C})$

The position of the six phenyl ring carbon atoms can be represented by the respective vectors in the Argand diagram. A vector in the Argand diagram represents a Fourier

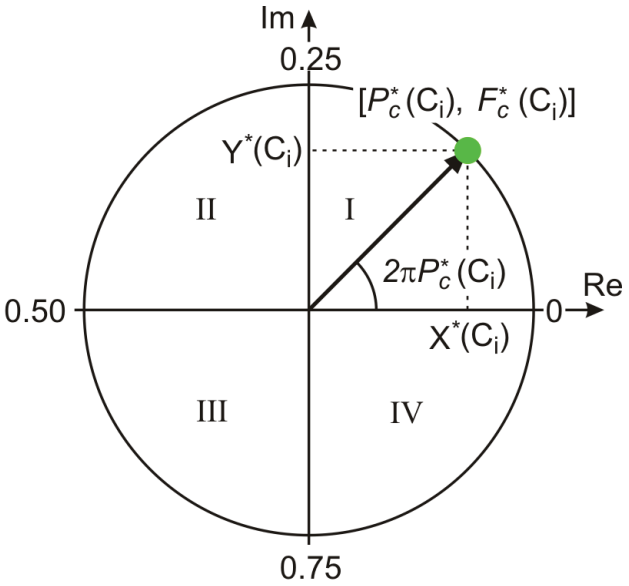


Figure 6.22: Argand diagram of a single carbon atom with polar coordinates $[P_c^*(\mathrm{C_i}), F_c^*(\mathrm{C_i})]$ and Cartesian coordinates $[\mathrm{X}^*(\mathrm{C_i}), \mathrm{Y}^*(\mathrm{C_i})]$, represented by a vector forming an angle $2\pi P_c^*(\mathrm{C_i})$ with the positive real axis. Each quadrant of the Argand diagram is labeled from I to IV, and coherent position values are also marked in the figure.

component of the corresponding atomic site distribution projected along the reciprocal vector $\boldsymbol{H}$ (section 2.5), and can be expressed as:

$$F_c^*(\mathrm{C_i}) \exp\left(2\pi i P_c^*(\mathrm{C_i})\right), \tag{6.6}$$

whose amplitude and phase are defined by $F_c^*(\mathrm{C_i})$ and $P_c^*(\mathrm{C_i})$, respectively. Therefore, each Fourier component defines coherent position and coherent fraction of a single carbon atom $\mathrm{C_i}$ in the Argand diagram (Figure 6.22). From now on, the symbol "*" refers to parameters defined or calculated for Argand diagram representation (e.g., Figure 6.22), whereas parameters without the symbol "*" correspond to values geometrically derived in real space (e.g., Figure 6.21).

NIXSW provides structural parameters (P_c, F_c) corresponding to the vector sum of all different adsorption sites of the same element. Therefore, to simulate NIXSW results, different vectors in the Argand diagram need to be summed. In order to practically calculate the *Sum* vector, the polar coordinates of the Argand diagram are transformed into Cartesian coordinates:

$$\begin{cases} \mathrm{X}^*(\mathrm{C_i}) = F_c^*(\mathrm{C_i}) \cos\left[2\pi P_c^*(\mathrm{C_i})\right] \\ \mathrm{Y}^*(\mathrm{C_i}) = F_c^*(\mathrm{C_i}) \sin\left[2\pi P_c^*(\mathrm{C_i})\right] \end{cases} \tag{6.7}$$

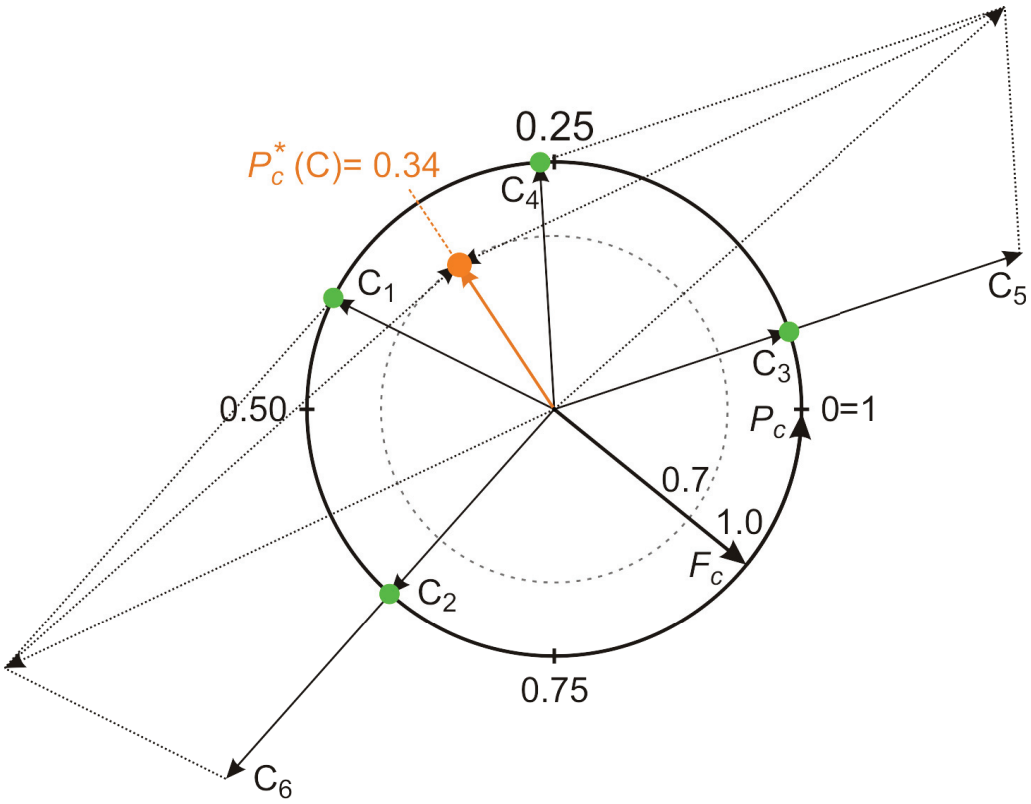


Figure 6.23: Carbon Argand diagram for AB adsorption configuration shown in Figure 6.21 with green circles representing the individual contributions of carbon atoms C_1-C_6 (assuming $F_c^* = (C_i)\,1$) and their *Sum* vector (orange) with $P_c^*(C) = 0.34$.

where $2\pi P_c^*(C_i)$ is the coherent position $P_c^*(C_i)$ expressed in radians, i.e., the angle of the vector with positive real axis, as shown in Figure 6.22. The sum of $X^*(C_i)$ and $Y^*(C_i)$ coordinates yields $X^*(C)$ and $Y^*(C)$; hence the corresponding coherent position and coherent fraction of the *Sum* vector are:

$$P_c^*(C) = \frac{1}{2\pi} \times \begin{cases} \arctan\left(\frac{Y^*(C)}{X^*(C)}\right) & X^*(C) > 0 \\ \arctan\left(\frac{Y^*(C)}{X^*(C)}\right) + \pi & X^*(C) < 0 \end{cases} \tag{6.8}$$

$$F_c^*(C) = \frac{1}{n} \times \sqrt{[X^*(C)]^2 + [Y^*(C)]^2} \tag{6.9}$$

where the division by n in equation 6.9 stands for the normalization by the number of vectors summed, so that $F_c^*(C) \in [0, 1]$ (section 2.5). Since the function arctan has values in the interval $\left(-\frac{\pi}{2}, \frac{\pi}{2}\right)$, and is thus in the I and IV quadrant of the Argand diagram (Figure 6.22), in order to retrieve all possible values of P_c^*, the sign of $X^*(C)$ has to be monitored. In particular, if $X^*(C) < 0$, the *Sum* vector is in the II and III quadrant, although $\arctan\left(\frac{Y^*(C)}{X^*(C)}\right)$ results in the IV and I quadrant,

respectively, therefore π has to be added to obtain the correct value of $P_c^*(\mathrm{C})$.

Figure 6.23 shows the vectors corresponding to carbon atoms of azobenzene with $\widetilde{\omega} = 45°$ as in Figure 6.21 and assuming $F_c^*(\mathrm{C_i}) = 1$. Since the rotation angle β is fixed to 0°, the vertical positions of atoms C_2 and C_6 are identical (Figures 6.21 and 6.29b). The same is true for C_3 and C_5. For this reason, C_2 and C_6 vectors coincide, as do C_3 and C_5 vectors (Figure 6.23). The sum of the six C_i vectors in the Argand diagram yields the *Sum* vector at coherent position $P_c^*(\mathrm{C})$ and coherent fraction $F_c^*(\mathrm{C})$, from which

$$d_c^*(\mathrm{C}) = P_c^*(\mathrm{C}) \times d_{\mathrm{Ag}(111)} \tag{6.10}$$

follows. This parameter would result from an NIXSW experiment on a layer of azobenzene molecules with adsorption geometry as in Figure 6.21, i.e., with the azo (-N=N-) bridge at the Bragg plane and $\widetilde{\omega} = 45°$. Note that this parameter is not the average distance of carbon atoms from the Bragg plane.

Dependence of the coherent position on the tilt angle $\widetilde{\omega}$

Having defined both pairs $[P_c(\mathrm{C}), d_c(\mathrm{C})]$ in equations 6.5, 6.4, and $[P_c^*(\mathrm{C}), d_c^*(\mathrm{C})]$ in equations 6.8, 6.10, their behavior as a function of the tilt angle $\widetilde{\omega}$, shown in Figure 6.24a, is investigated. For angles $-5° \leq \widetilde{\omega} \leq 40°$ $d_c(\mathrm{C})$ and $d_c^*(\mathrm{C})$ perfectly coincide, as one would expect. However, for $\widetilde{\omega} > 40°$ the two parameters differ by $d_{\mathrm{Ag}(111)}/2$. Since $d_c(\mathrm{C})$ is directly derived from the average of carbon atom positions corresponding to a specific adsorption geometry, its values are correct by definition. As a consequence, we conclude that a direct conversion of the coherent position $P_c^*(\mathrm{C})$ into an adsorption height $d_c^*(\mathrm{C})$ according to equation 6.10 leads to incorrect values of the average carbon adsorption height. This result is initially very surprising, because it apparently contradicts the concept of coherent position itself, usually interpreted as being representative of the average distance of atoms of a certain species from the Bragg plane (section 2.5). As it will be explained below, this idea is still valid in general, although the average vertical position in the real space may not correspond to the position obtained by NIXSW.

Since we understood that the origin of the deviation between $d_c(\mathrm{C})$ and $d_c^*(\mathrm{C})$ follows from the sum of the single carbon Fourier components, the coherent position $P_c^*(\mathrm{C})$ of the *Sum* vector is displayed as a function of the tilt angle $\widetilde{\omega}$ (Figure 6.24b). Here too, for $\widetilde{\omega} > 40°$ $P_c^*(\mathrm{C})$ deviates significantly from $P_c(\mathrm{C})$, i.e., the coherent position derived from $d_c(\mathrm{C})$ through equation 6.3. Interestingly, the difference

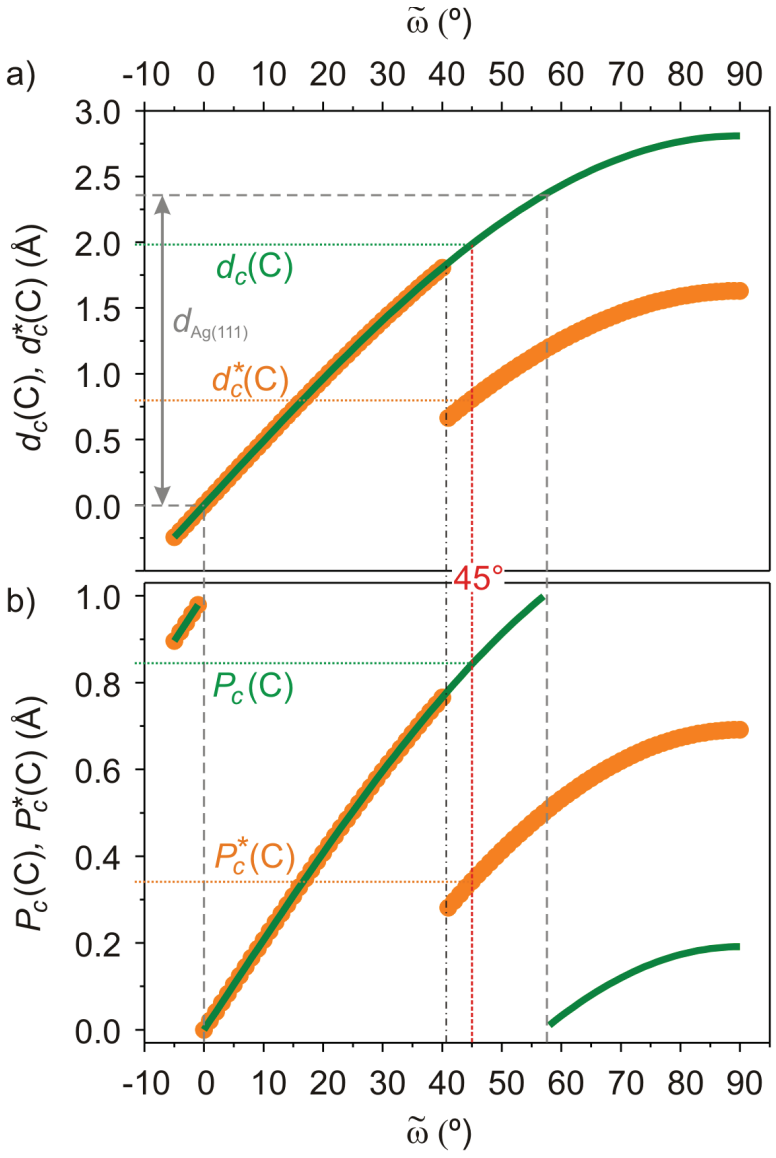


Figure 6.24: (a): actual average distance d_c (C) of carbon atoms from the Bragg plane underneath (green line) and the distance d_c^* (C) derived from the *Sum* (orange circles) of the single carbon contributions in the Argand diagram (Figure 6.23), displayed as a function of the tilt angle $\widetilde{\omega}$. (b): coherent position $P_c = d_c/d_{\mathrm{Ag(111)}}$ corresponding to the actual distance d_c (green line) and coherent position P_c^* derived from the vector sum (orange circles) of individual carbon atoms contributions displayed as a function of the tilt angle $\widetilde{\omega}$. The angles and the corresponding distances, at which the center of a phenyl ring crosses the Bragg plane, are marked with vertical dashed gray lines. The 45° angle case shown in Figure 6.21 is marked with a vertical dotted red line. The angle ($\approx 40°$) above which the actual average carbon distance d_c (C) and the distance derived from Argand sum d_c^* (C) are not coincident is marked with a dashed-dotted black line. The coherent position P_c^* (C) = 0.34 and the distance d_c^* (C) = 0.81 Å, corresponding to the *Sum* vector of Figure 6.23 relative to AB adsorption configuration shown in Figure 6.21, are marked with dotted orange lines.

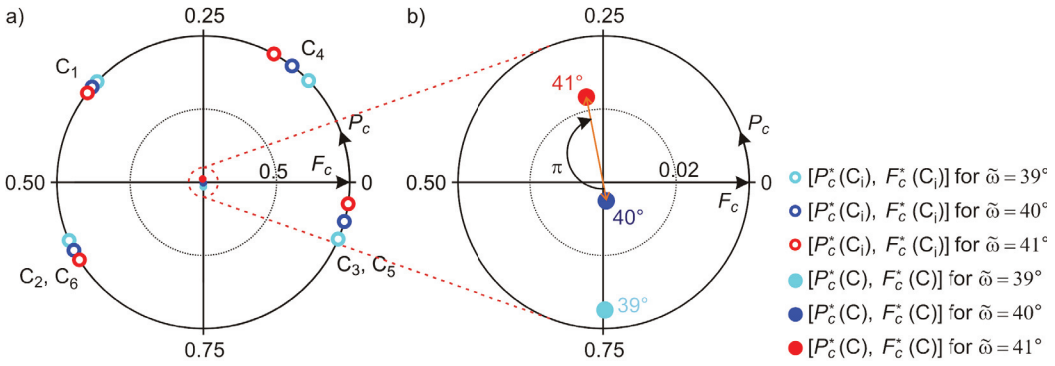


Figure 6.25: (a): Argand diagram of the calculated $[P_c^*(\mathrm{C_i}), F_c^*(\mathrm{C_i})]$ corresponding to $\widetilde{\omega} = 39°$ (light blue), 40° (dark blue) and 41° (red). (b): enlarged Argand diagram with the respective *Sum* vectors of the single carbon vectors plotted in panel (a) and corresponding to each of the three $\widetilde{\omega}$.

between the two coherent positions is equal to 0.50, as can be clearly seen in Figure 6.25b, where the carbon *Sum* vector flips from the IV to the II quadrant as the tilt angle goes from 40° to 41°. The jump in coherent position $P_c^*(\mathrm{C})$ and consequently in $d_c^*(\mathrm{C})$ occurs at approximately 40° when the contribution of carbon atoms $\mathrm{C_4}$, which have already crossed the Bragg plane at $\widetilde{\omega} = 35°$, is now large enough to cause the overturning of the *Sum* vector with a shift of π. In fact, if part of the phenyl ring is in one Bragg spacing and part in the following, there will be carbon atoms directly below ($\mathrm{C_3}$, $\mathrm{C_5}$) and directly above ($\mathrm{C_4}$) the Bragg plane in between that are very close in the real space (Figure 6.21). However, these C atoms will have very different coherent positions due to the modulo 1 periodicity of P_c, corresponding to the 2π periodicity of the phase of a Fourier component (expression 6.6 and section 2.5) in the Argand diagram.

In summary, if the phenyl ring of azobenzene extends over two Bragg spacings, $d_c^*(\mathrm{C})$ may not coincide with $d_c(\mathrm{C})$, which leads to a discrepancy between the actual average vertical position of carbon atoms and the result of NIXSW experiments. In other words, if azobenzene adsorbs with $\widetilde{\omega} > 40°$, the average distance of carbon atoms, derived from the carbon coherent position, does not correspond to the real average distance from the Ag(111) surface. The cause of this divergence is the modulo 1 uncertainty of the coherent position. This represents a very important result for the interpretation of NIXSW structural parameters of large organic molecules which may adsorb in a non-flat geometry. In the following, a solution to the above presented possible inconsistency between NIXSW results and actual adsorption geometry is proposed and applied to azobenzene/Ag(111).

Vector analysis in the Argand diagram

The strategy to determine the tilt angle of azobenzene/Ag(111) involves comparing the behavior of the simulated $[P_c^*(\mathrm{C}),\ F_c^*(\mathrm{C})]$ with the corresponding experimental values. Figure 6.26a shows the carbon *Sum* as the tilt angle varies from 0° to 90°, assuming that the nitrogen atoms are at the Bragg plane as in Figure 6.21 and $F_c^*(\mathrm{C_i}) = 1$ (light gray curve). As $\widetilde{\omega}$ varies, the *Sum* vector draws a spiral in the Argand diagram. In particular, it starts from ($P_c = 0$, $F_c = 1$) for $\widetilde{\omega} = 0°$ with the molecule perfectly flat (Figure 6.26c). As $\widetilde{\omega}$ increases, P_c increases while F_c decreases, because the center of the phenyl ring lifts from the Bragg plane and carbon atoms have different vertical positions; hence the lower carbon coherent fraction follows. This trend continues until the *Sum* vector reaches the center of the Argand diagram ($P_c = 0$, $F_c = 0$), at approximately $\widetilde{\omega} > 40°$. After this point, the vector jumps from the IV to the II quadrant and for greater tilt angles, its P_c and F_c continue to increase. The reason for this latter increase in carbon coherent fraction for $40° < \widetilde{\omega} \leq 90°$ results from the fact that when the phenyl ring crosses the upper Bragg plane, carbon atoms C_3, C_5 and C_4 in the upper Bragg spacing have P_c increasingly closer to those of C_1, C_2 and C_6 in the lower Bragg spacing, respectively (Figure 6.26b). As a result, the overall coherent fraction of the carbon signal will increase,

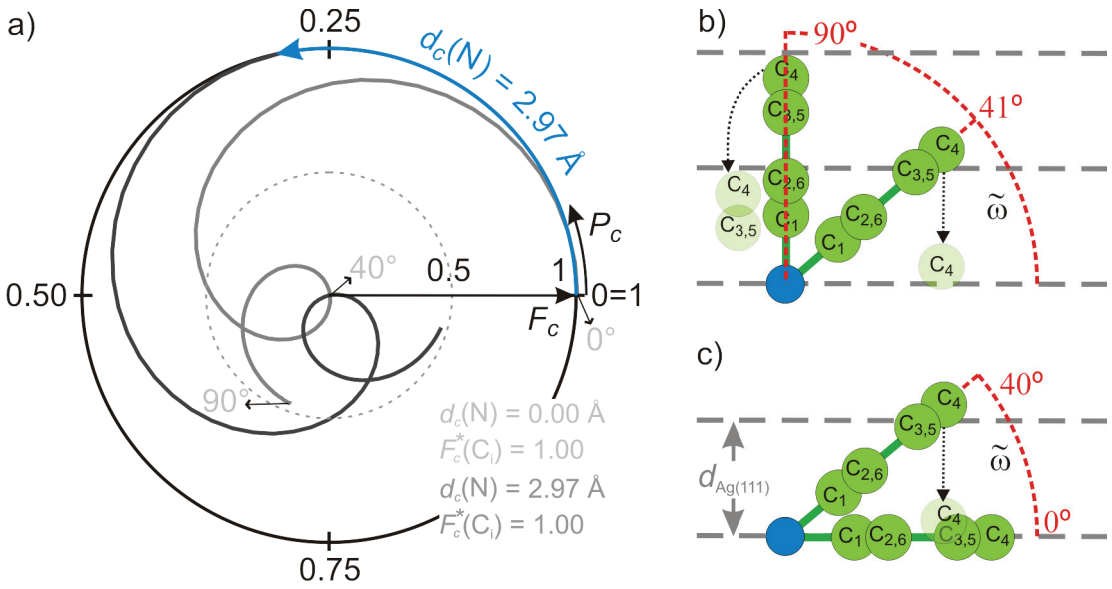


Figure 6.26: (a): Argand diagram of the calculated $P_c^*(\mathrm{C})$ and $F_c^*(\mathrm{C})$ for the carbon signal (*Sum*) as $\widetilde{\omega}$ varies from 0° to 90°. Each of the three spirals (light gray, dark gray, red lines) corresponds to a different set of initial parameters reported in the legend. A change in $d_c(N)$ implies the rotation of the spiral around the center. Schematic representation (side view) of one phenyl ring at $\widetilde{\omega} = 41°$ (b), at $\widetilde{\omega} = 90°$ (b), at $\widetilde{\omega} = 0°$ (c) and at $\widetilde{\omega} = 40°$ (c). Shaded green circles mark the effective position of carbon atoms in the upper Bragg spacing translated in the lower Bragg spacing.

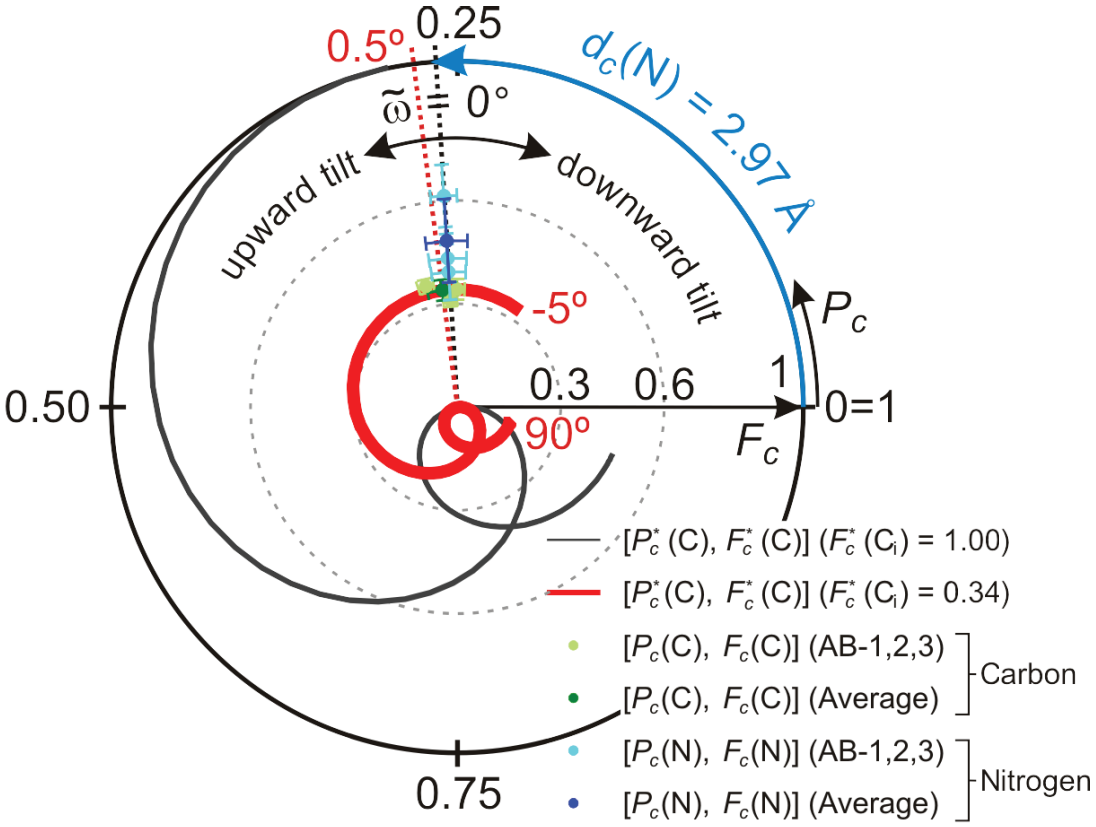


Figure 6.27: Argand diagram of carbon and nitrogen P_c and F_c as derived from experiments (light green and light blue circles), and the corresponding average point (dark green and dark blue circles). The dark gray and red spirals represent the calculated P_c^* (C) and F_c^* (C) of carbon for F_c^* (C$_i$) = 1.00 and 0.34, respectively, where $d_c\,(N) = 3.07$ Å, and as $\tilde{\omega}$ varies from $-5°$ to 90°. Positive [negative] $\tilde{\omega}$ correspond to upward [downward] tilt of the azobenzene phenyl rings.

because carbon atoms will not be distributed at four different vertical positions from the Bragg plane, but will instead cluster around two effective heights, as illustrated in the extreme case of $\tilde{\omega} = 90°$.

All of the simulations presented above are based on the assumption of having the nitrogen atoms located at the Bragg plane as shown in Figures 6.21 and 6.26b,c. If nitrogen atoms are shifted to the vertical position found by NIXSW, i.e., 2.97 Å above the surface Bragg plane, the spiral described by the *Sum* vector undergoes a rigid rotation around the origin (dark gray line in Figure 6.26a). This follows from the direct proportionality between the adsorption height and the coherent position (equation 6.10). If the starting vertical position of the molecule is altered, each single carbon vector also undergoes a corresponding rotation in the Argand diagram; thus the behavior of the *Sum* vector as a function of $\tilde{\omega}$ will not be affected.

For $\widetilde{\omega} = 0°$, carbon and nitrogen atoms have the same adsorption height, hence, the same coherent position marked in Figure 6.27 by the dotted black line passing through the experimental average nitrogen data point (dark blue). In order to determine the tilt angle $\widetilde{\omega}$ corresponding to the intersection of the simulated structural parameters with the experimental average carbon data point (dark green), the dark gray spiral in Figure 6.27 has to be rescaled. This operation is carried out by changing $F_c^*(\mathrm{C_i})$, i.e., the amplitude of each Fourier component (see expression 6.6). The result of changing $F_c^*(\mathrm{C_i})$ is a rescaling of the whole spiral without altering the corresponding coherent position $P_c^*(\mathrm{C})$. In particular, the intersection of the simulated carbon signal for $0° \leq \widetilde{\omega} \leq 90°$ (red spiral) and the experimental carbon data points (green circles) is unique and it occurs for $\widetilde{\omega} = 0.5 \pm 1.0°$, with a coherent fraction of the single carbon atoms equal to $F_c^*(\mathrm{C_i}) = 0.34$, as shown in Figure 6.27.

Influence of the roation angle β on the structural parameters

The lower coherent fraction of the carbon signal compared to the nitrogen one (Table 6.9) cannot be attributed to the phenyl tilt angle of azobenzene, as it has just been shown that the molecule adsorbs practically flat ($0.5 \pm 1.0°$) on the Ag(111) surface. The lower F_c of carbon could be then due to the rotation angle β between the plane of the phenyl ring and the (111) Bragg plane (Figure 6.28a). The Argand diagram in Figure 6.28b shows the effect of rotation angles $\beta = 5°$, $10°$, $15°$, $20°$ of the phenyl ring with tilt angle $\widetilde{\omega} = 0°$, $1°$, $2°$, $3°$ on the carbon *Sum* vector $[P_c^*(\mathrm{C}),\ F_c^*(\mathrm{C})]$. A similar effect is registered for each of the four different $\widetilde{\omega}$ configurations investigated. In particular, the carbon coherent fraction progressively decreases as β increases, dropping by approximately 40% for $\beta = 20°$, while the coherent position slightly increases by 0.01 for $\beta = 15°$ and $20°$. The experimental F_c of carbon (0.34 ± 0.03) is 30% lower than the coherent fraction of nitrogen atoms (0.48 ± 0.12). This decrease in the carbon coherent fraction can be rationalized by a rotation angle β of approximately 17° with a tilt angle $\widetilde{\omega} = 0.5°$, and $F_c^*(\mathrm{C_i}) = 0.48$ $[= F_c(\mathrm{N})]$. In summary, by means of the vector analysis in the Argand diagram we derived the tilt angle $\widetilde{\omega}$ ($0.5°$) and the rotation angle β ($17°$) that are consistent with the experimental structural parameters (P_c, F_c) of carbon and nitrogen (Table 6.9), and without the need to invoke a differential coherent fraction for different elements of the same molecule.

A possible explanation of the generally low coherent fraction of carbon and nitrogen atoms ($\lesssim 50\%$) may be the diffusion of the azobenzene molecules on the

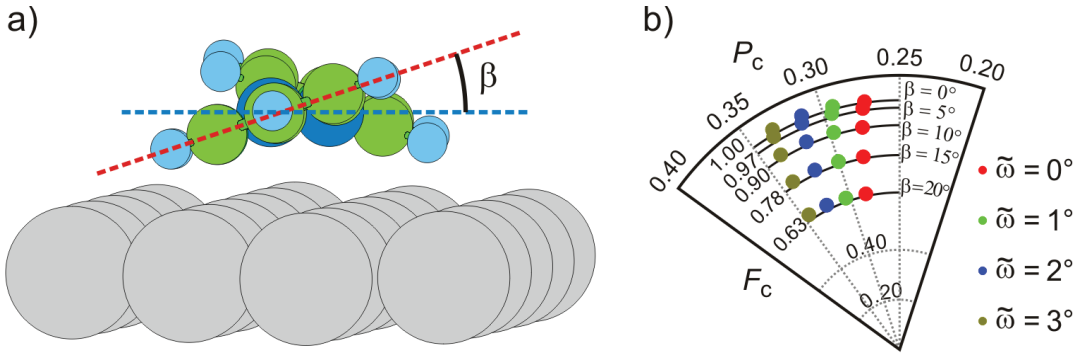


Figure 6.28: (a): scale model of azobenzene/Ag(111) with $\widetilde{\omega} = 3°$ and $\beta = 20°$, where β is the angle between the horizontal plane (dashed blue line) and the plane of the phenyl ring (dashed red line). (b): Argand diagram of AB carbon signal for phenyl ring tilt angle $\widetilde{\omega} = 0°, 1°, 2°, 3°$ and phenyl ring rotation angle $\beta = 0°, 5°, 10°, 15°, 20°$.

Ag(111) surface. Already at temperatures greater than 50 K azobenzene molecules cannot be detected the STM tip on the less reactive Au(111) surface because they diffuse.[145] Even on the more reactive Cu(110) surface azobenzene molecule diffuse already at 168 K as observed by time-lapsed STM images.[146] Therefore, it is likely that azobenzene diffuses at 210 K (section 6.2.1) on the Ag(111) surface, leading to incoherently distributed phenyl carbons contribute to the coherent fraction decrease, as extensively argued in section 4.4.1. However, it is not clear why the molecular diffusion should affect more the carbon than the nitrogen coherent fraction. For this reason the adsorption geometry with $\beta = 17°$ seems more plausible than the one with $\beta = 0°$.

6.4.1.3 NIXSW adsorption model of azobenzene/Ag(111)

From the vector analysis in the Argand diagram, two possible adsorption geometries of azobenzene/Ag(111) are found:

(a) According to the first adsorption model, azobenzene adsorbs essentially flat with a small upward tilt angle $\widetilde{\omega} = 0.5 \pm 1.0°$ and rotation angle $\beta = 0°$, as shown in Figure 6.29a. For this geometry, the coherent fraction of the single carbon atoms is $F_c^*(\mathrm{C_i}) = 0.34$, approximately 30% smaller than the coherent fraction of the nitrogen atoms, $F_c^*(\mathrm{N}) = 0.48$. This lower coherent fraction for the single carbon atoms is necessary to rationalize the experimental coherent fraction of the carbon signal (Table 6.9).

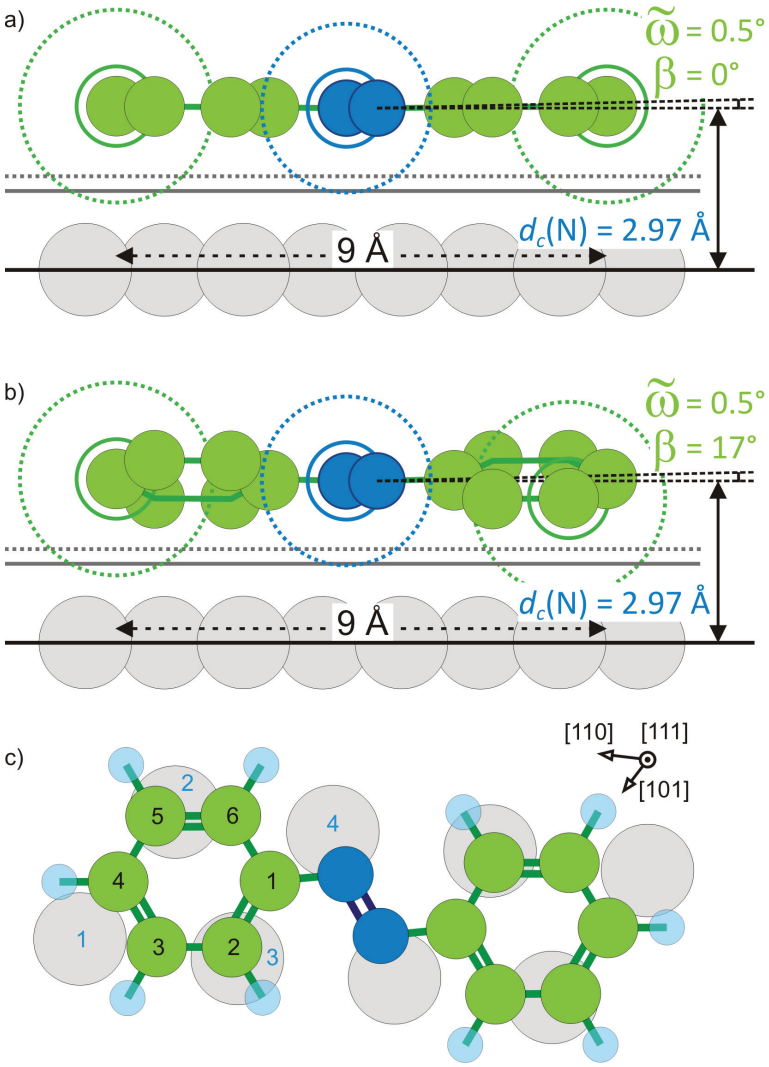
(b) Another possible adsorption geometry consists of a flat-lying azobenzene molecule with tilt angle $\widetilde{\omega} = 0.5 \pm 1.0°$, but with a pronounced rotation angle $\beta = 17°$, as shown in Figure 6.29b. This configuration perfectly reproduces the experimental structural parameters (P_c, F_c) of AB/Ag(111) (Table 6.9), without the need for a differential coherent fraction for carbon and nitrogen. In fact, this adsorption geometry is consistent with a coherent fraction common to each single atom $F_c^*(\mathrm{C_i}) = F_c^*(\mathrm{N_i}) = 0.48$. We can therefore interpret it as the fraction of the azobenzene molecules that coherently adsorb on the Ag(111) surface (section 4.4.1).

We note that in both cases (a) and (b) azobenzene adsorbs in the *trans* isomer conformation (Figure 6.1a), in agreement with STM images revealing the presence of *trans*-azobenzene on Au(111)[28,145,147] and on Cu(110).[146]

In order to better assess the interaction of azobenzene with the Ag(111) substrate, and possibly to conclude which of the adsorption geometries presented above is more plausible, the interatomic distance between atoms of the molecule and the Ag surface atoms are compared with the corresponding sum of covalent radii and vdW radii (Table 6.10). To estimate the interatomic distances, the adsorption site of azobenzene is assumed to be the one predicted by the DFT calculations,[142] i.e., azobenzene is oriented along the [110] direction with the center at the bridge site as shown in Figure 6.29c.

The interatomic distances reported in Figure 6.29d reveal that the smallest distances d_i(C-Ag) are 3.03 Å (model (a)) and 2.69 Å (model (b)), 39% and 23% larger respectively than the lower limit represented by the sum of the corresponding cova-

lent radii (2.18 Å). Since even the smallest d_i(C-Ag) are well above the sum of the corresponding covalent radii (2.18 Å), we conclude that both adsorption geometries are plausible, and neither of them can be excluded on the basis of being unphysical.



d)

β	0°	17°
X-Ag	d_i(X-Ag)	d_i(X-Ag)
N-Ag	3.11	3.11
C_1-Ag_4	3.35	3.35
C_2-Ag_3	3.03	3.39
C_3-Ag_1	3.36	3.67
C_4-Ag_1	3.30	3.29
C_5-Ag_2	3.05	2.69
C_6-Ag_2	3.20	2.87
$\overline{d_i(\text{N-Ag})}$	3.11	3.11
$\overline{d_i(\text{C-Ag})}$	3.21	3.21

Figure 6.29: (a): adsorption geometry (side view) of azobenzene/Ag(111) corresponding to model (a), with $\widetilde{\omega} = 0.5°$, $\beta = 0°$ and $F_c^*(\text{C}_\text{i}) = 0.34$. (b): adsorption geometry (side view) of azobenzene/Ag(111) corresponding to model (b), with $\widetilde{\omega} = 0.5°$, $\beta = 17°$ and $F_c^*(\text{C}_\text{i}) = F_c^*(\text{N}) = 0.48$. Color code: blue → nitrogen, green → carbon, gray → silver. Filled circles indicate atomic positions, solid lines indicate covalent radii[91] (C: 0.73 Å; N: 0.71 Å; Ag: 1.45 Å), dotted lines indicate vdW radii[92] (C: 1.77 Å; N: 1.55 Å; Ag: 1.72 Å). The distance of nitrogen atoms from the surface Bragg plane d_c(N), the tilt angle of the phenyl rings $\widetilde{\omega}$ and the length of of azobenzene *trans*-isomer[148] are explicitly marked in the figure. (c): adsorption site (top view) of azobenzene/Ag(111) as it results from DFT calculations performed by E. R. McNellis, A. D. Baghi (Fritz Haber Institute), J. Meyer and K. Reuter (TU München).[142] (d): interatomic distances of nitrogen and carbon atoms from the nearest Ag atom, assuming the lateral position of azobenzene with respect to the substrate as in panel b and the vertical position resulting from models (a) and (b), respectively.

X	$r^{\mathrm{X}}_{cov} + r^{\mathrm{Ag}}_{cov}$	$r^{\mathrm{X}}_{vdW} + r^{\mathrm{Ag}}_{vdW}$	$\overline{d_i(\text{X-Ag})}$	% of $(r^{\mathrm{X}}_{cov} + r^{\mathrm{Ag}}_{cov})$	% of $(r^{\mathrm{X}}_{vdW} + r^{\mathrm{Ag}}_{vdW})$
C	2.18	3.49	3.21	147	92
N	2.16	3.27	3.11	144	95

Table 6.10: Sum of covalent radii[91] $r^{\mathrm{X}}_{cov} + r^{\mathrm{Ag}}_{cov}$, sum of vdW radii[92] $r^{\mathrm{X}}_{vdW} + r^{\mathrm{Ag}}_{vdW}$ and average interatomic distances $\overline{d_i(\text{X-Ag})}$ (X = C, N) for azobenzene/Ag(111) are reported, followed by the percentage of the interatomic distances with respect to the sum of covalent radii and the sum of vdW radii.

If we look at the molecule as a complex, we observe that in both adsorption geometries the average interatomic distance of carbon and nitrogen atoms from the nearest Ag atom is $\overline{d_i(\text{C-Ag})} = 3.21$ Å and $\overline{d_i(\text{N-Ag})} = 3.11$ Å, respectively (Figure 6.29d). These values are 47% and 44% larger than the corresponding sum of covalent radii (Table 6.10) respectively; therefore there is no indication of a significant chemical interaction between the molecule and the substrate, except for the slightly lower adsorption height of nitrogen atoms compared to the carbon average adsorption height. At the same time, $\overline{d_i(\text{C-Ag})}$ and $\overline{d_i(\text{N-Ag})}$ are 8% and 5% lower than the corresponding sum of vdW radii (Table 6.10) respectively. Therefore, we conclude that azobenzene molecule is mainly physisorbed on the Ag(111) surface, to which it appears to be bound primarily by long-range vdW forces. The scenario described here is very different from that of PTCDA/Ag(110) (chapter 4) and TPA/Cu(100) (chapter 7) where, instead, a rather strong chemical contribution to the molecule-substrate interaction is found. From the flat adsorption geometry of azobenzene on Ag(111), we exclude a prominent role of the N-Ag covalent bond that would lead to a pronounced butterfly-like configuration, and we attribute the reduced importance of covalent bonding to (1) the counteracting presence of attractive vdW forces that tend to pull the phenyl rings closer to the surface and (2) the lower energetic penalty of a nearly flat bonding geometry compared to a distorted configuration with a larger tilt angle $\widetilde{\omega}$.

6.4.1.4 Comparison of NIXSW and DFT adsorption models

DFT calculations strongly support the scenario just described and the importance of vdW interactions at the azobenzene/Ag(111) interface. In fact, if the bare GGA-PBE functional is employed, completely disregarding dispersive vdW forces, the molecule floats at 3.64 Å above the Ag surface with an adsorption energy of only −0.11 eV (red curve in Figure 6.30).[142] In sharp contrast, if vdW interactions are

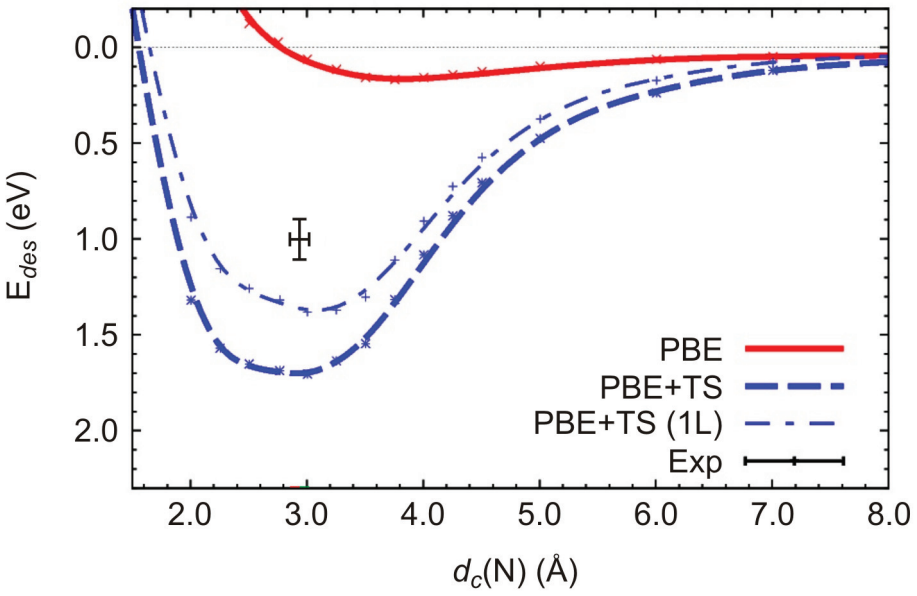


Figure 6.30: Figure from ref.[4] Desorption energy curves, computed with the bare DFT-PBE (red line) and with the DFT-PBE-D scheme (dashed blue line). The PBE-D curve corresponding to calculations with the substrate slab reduced to the topmost layer (1L) is indicated with the dashed-dotted blue line. The black data point marks experimental values (NIXSW, TPD) and errors.

taken into account at the semiempirical level (PBE+TS functional,[149] dashed blue line in Figure 6.30), the molecule is pulled further down to 2.98 Å above the surface and adsorbs with tilt angle $\widetilde{\omega} = 3°$ and rotation angle $\beta = 3°$,[4,143] in good agreement with the adsorption geometry (a) (Figure 6.29a). Therefore, DFT calculations (PBE functional) confirm that N-Ag covalent bonding alone is not sufficient to bind the molecule to the surface, as testified by the very large adsorption height and the very low adsorption energy. On the other hand, if dispersive vdW interactions are included (PBE+TS functional), the optimized geometry of azobenzene/Ag(111) matches the experimental adsorption geometry (a) derived from NIXSW experiments very well. In particular, not only the vertical position of the azo (-N=N-) bridge fits perfectly with $d_c(N)$ within the errors, but also the slight upward tilt of the phenyl rings $\widetilde{\omega} = 3°$ and their rotation angle $\beta = 3°$ is consistent with model (a), i.e., $\widetilde{\omega} = 0.5 \pm 1.0°$ and $\beta = 0°$. Note that the starting geometry of azobenzene for DFT calculations is that of the gas phase *trans*-isomer, and the influence of the angles $\widetilde{\omega}$ and β on the adsorption energy is not specifically tested.

In summary, the inclusion of dispersive vdW interactions in the DFT calculations brings the molecule closer to the surface, also enabling the chemical interaction be-

tween the nitrogen atoms and the surface. This attractive interaction brings the slightly elongated azo bridge even closer to the surface at a distance at which the Pauli-repelled phenyl rings start to tilt upward forming a butterfly-like configuration. The larger binding energy predicted by PBE+TS calculations, compared to experimental adsorption energy measured by TPD,[4] is due to the strictly pairwise evaluation of the dispersive interactions. In fact, the TS scheme has an intrinsic shortcoming, namely that interaction of all atom pairs is summed without taking into account the screening of dispersive interactions between adsorbate atoms and deeper substrate atoms. To mimic the screening effect, the substrate slab of DFT calculations is reduced to the topmost layer [PBE+TS(1L)], considering that the screening length of Ag is on the order of the interlayer distance. The resulting adsorption energy (dashed-dotted blue curve in Figure 6.30) is now much closer to the experimental value, essentially without affecting the optimized geometry of azobenzene.[4]

The combination of NIXSW experiments and DFT calculations allows us to conclude that vdW interactions play an important role for azobenzene/Ag(111), and benchmarks different semiempirical dispersion correction approaches.[4] In particular, the TS semiempirical correction scheme proves to be an efficient way to accurately predict the adsorption geometry, albeit with a sizable overbinding that can be assigned to the neglected screening. The same trend was also shown for another system, PTCDA/Ag(111), obtaining results in good agreement with experiments[2] and high-level theory calculations.[150]

The good agreement between the theoretical calculations and the adsorption geometry (a) derived from NIXSW results is based on the assumption that carbon and nitrogen atoms, although part of the same molecule, have different coherent fractions. The large discrepancy of approximately 30% between the carbon and nitrogen coherent fraction of azobenzene cannot be explained with a quantitative argument, but qualitative arguments such as diffusion and thermal vibrations can be invoked to rationalize this differential behavior. In this context, the adsorption geometry (b), with rotation angle $\beta = 17°$ may represent a valid alternative, albeit the agreement with DFT calculations is worse. In fact, adsorption geometry (b) is consistent with NIXSW results (Table 6.9), as well as adsorption model (a), but it has carbon and nitrogen atoms with the same coherent fraction, as one may initially expect. Furthermore, besides the two extreme cases of $\beta = 0°$ and $\beta = 17°$, there can be many other possible adsorption geometries with $0° \leq \beta \leq 17°$, so that for a lower

rotation angle β, the lower coherent fraction of the single carbon atoms compared to the nitrogen ones may be explained by a more or less relevant effect of the thermal vibrations of the phenyl rings.

To conclude, we wish to highlight how a critical analysis of NIXSW results sheds light on structural details hidden behind the average structural parameters (P_c, F_c). Even if a conclusive adsorption model of AB/Ag(111) cannot be proposed, several possible geometries are discussed. For this purpose, we suggest performing NEXAFS experiments to clarify the orientation of the phenyl rings, and determine whether it is closer to the adsorption geometry (a) ($\beta = 0°$) or (b) ($\beta = 17°$). This result would also indirectly provide deeper understanding of the azobenzene coherent fraction.

6.4.2 Discussion of TBA experimental results

6.4.2.1 Introduction

NIXSW experimental results, presented in section 6.3.4, and summarized in Table 6.11, show a sizable difference, more pronounced than for azobenzene/Ag(111) (Table 6.9), between the structural parameters (P_c, F_c) of carbon and those of nitrogen. In particular, the relatively high $F_c\,(\mathrm{N}) = 0.66 \pm 0.15$ indicates a unique adsorption site and the same adsorption height for the two nitrogen atoms, whose distance from the surface Bragg plane is equal to 3.10 ± 0.06 Å. On the other hand, the carbon signal exhibits a much lower coherent fraction (0.14 ± 0.02) and the average distance of the atoms from the surface Bragg plane is 3.34 ± 0.15 Å; thus 0.24 Å larger than the nitrogen surface distance.

NIXSW TBA results			
	P_c	d_c (Å)	F_c
N	0.32 (3)	3.10 (6)	0.66 (15)
C	0.42 (6)	3.34 (15)	0.14 (2)

Table 6.11: Summary of carbon and nitrogen NIXSW structural parameters of TBA/Ag(111): coherent position P_c, corresponding adsorption height d_c and coherent fraction F_c derived from N1*s* and C1*s* lines (section 6.3.4).

Based on the structural parameters reported in Table 6.11, one can intuitively picture TBA adsorbed on the Ag(111) surface with the azo (-N=N-) bridge lying flat parallel to the surface and the phenyl ring together with the *tert*-butyl (TB) groups slightly upward tilted, resulting in an average vertical position of carbon atoms 0.24 Å above the nitrogen atoms (Figure 6.31). The tilt of the phenyl rings and the additional presence of TB carbon atoms, schematically drawn in Figure 6.31, would also qualitatively rationalize the fact that $F_c\,(\mathrm{C})$ is approximately five times lower than $F_c\,(\mathrm{N})$, while for azobenzene $F_c\,(\mathrm{C})$ is only 30% lower than $F_c\,(\mathrm{N})$.

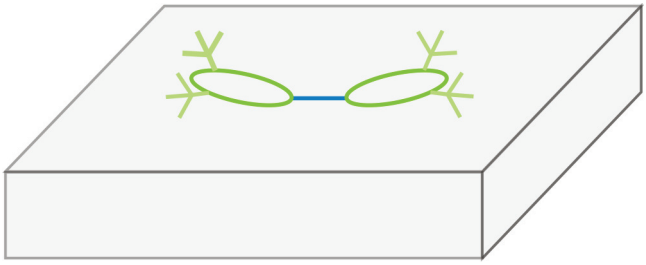


Figure 6.31: Schematic adsorption geometry of TBA/Ag(111) resulting from a first interpretation of NIXSW C and N structural parameters in Table 6.11.

The adsorption model described above is based on a direct conversion of the coherent position in adsorption height [$d_c = (P_c + 1) \times d_{\mathrm{Ag(111)}}$]. However, from the interpretative scheme of NIXSW results, introduced in section 6.4.1.2, we learned that in the presence of strongly bent molecules that extend over more than one Bragg spacing, e.g., $d_{\mathrm{Ag(111)}} = 2.3593$ Å, the coherent position as derived from the NIXSW fit may not correspond to the real average vertical position of a certain atomic species. Therefore, to confirm the qualitative adsorption geometry sketched in Figure 6.31, a more quantitative analysis, similar to the one presented for azobenzene in section 6.4.1.2, is necessary.

To proceed with a more quantitative analysis, a TBA structural model employed as a reference for further simulations of different adsorption geometries is required. The goal is to simulate the NIXSW structural parameters (P_c, F_c) of the corresponding TBA configurations and compare them with the experimental ones. Because of the complex structure of TBA and the additional degrees of freedom compared to azobenzene, it is not trivial to develop a structural model, especially as far as TB groups are concerned. As a consequence, we consider as our reference geometry of TBA/Ag(111) the optimized structure resulting from DFT calculations, presented in section 6.4.2.2 below.

6.4.2.2 Comparison of NIXSW results with DFT calculations

DFT calculations of TBA/Ag(111) are performed exactly as described for the corresponding calculations on the Au(111) surface.[151] In particular, Figure 6.32 shows the optimized geometry of *trans*-TBA/Ag(111) obtained with the use of PBE+TS functional in order to take into account the dispersive vdW interactions at a semiempirical level.[143,151] The two nitrogen atoms appear at the same height, 3.11 Å, above the surface, while the phenyl rings have a tilt angle of $\widetilde{\omega} = 9°$. The larger tilt angle in comparison with azobenzene/Ag(111)[143] ($\widetilde{\omega} = 3°$) is attributed to the presence of the bulky TB groups that lift the two extremities of the molecule off the Ag surface. Another important structural parameter characterizing the TBA adsorption geometry is the orientation of the TB groups. This parameter is extensively investigated in section 6.4.2.3.

If we compare the DFT optimized geometry of TBA/Ag(111) with NIXSW results, we note an excellent agreement of the nitrogen adsorption height, equal to 3.11 Å

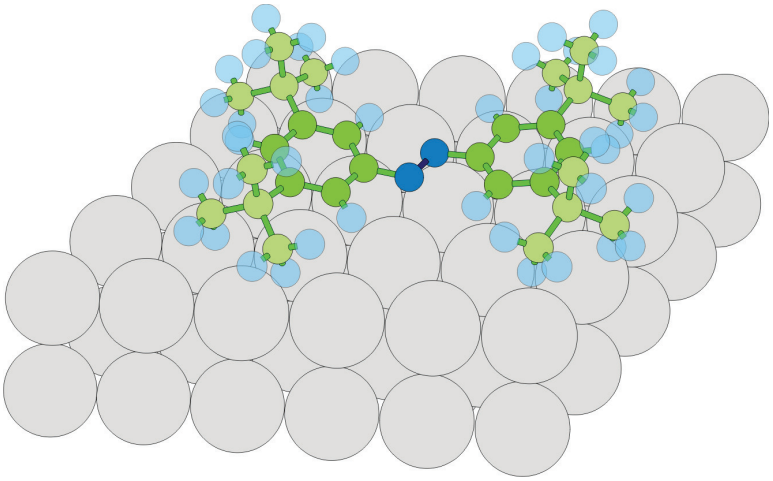


Figure 6.32: Optimized geometry of TBA/Ag(111) as it results from DFT calculation with the employment of PBE+TS functional,[143,149] already introduced in section 6.4.1.4 for AB/Ag(111). The optimization of the present geometry was performed by E. R. McNellis, A. D. Baghi (Fritz Haber Institute), J. Meyer and K. Reuter (TU München), details of the calculations are reported in refs.[3,142] Color code: dark blue → nitrogen, green → phenyl ring carbon, light green → *tert*-butyl group (TB) carbon, transparent light blue → hydrogen.

(theory) and 3.10 ± 0.06 Å (experiments), respectively. The simulation of NIXSW results for carbon atoms of the calculated TBA/Ag(111) geometry (Figure 6.32) provides $P_c\,(\mathrm{C}) = 0.47$ and $F_c\,(\mathrm{C}) = 0.14$ with $F_c^*\,(\mathrm{C_i}) = 0.18$ (see section 6.4.1.2), equal within the errors to the experimental C structural parameters [$P_c\,(\mathrm{C}) = 0.42 \pm 0.06$ and $F_c\,(\mathrm{C}) = 0.14 \pm 0.02$] (Table 6.11). From the comparison of vdW-corrected DFT calculations of TBA/Ag(111) and the corresponding NIXSW results, two conclusions can be drawn. First, the remarkable agreement of the calculated azo bridge adsorption height and the experimental $d_c\,(\mathrm{N})$ indicates that TBA adsorbs in the *trans* isomer configuration (Figure 6.32), instead of the *cis* configuration, for which nitrogen atoms are predicted at 2.59 Å.[152] Second, the agreement between the calculated adsorption geometry of the phenyl rings plus TB groups and NIXSW results is based on a coherent fraction of the single carbon atoms $F_c^*\,(\mathrm{C_i}) = 0.18$, approximately 70% lower than nitrogen coherent fraction $F_c^*\,(\mathrm{N}) = 0.66 \pm 0.15$ (for azobenzene it is 30% lower). This represents a major flaw of the DFT structural model reported in Figure 6.32. For this reason, in the following section we look for other possible adsorption models in agreement with the experimental NIXSW results.

6.4.2.3 NIXSW simulations of TBA/Ag(111)

In order to verify whether there are other possible adsorption geometries consistent with the experimental results and/or to rule out any other configuration different from the one predicted by DFT calculations, the influence of multiple degrees of freedom of the TBA molecule on the NIXSW results is investigated. All simulations are based on the structure resulting from DFT calculations, slightly vertically translated to bring the azo bridge to the experimental adsorption height, 3.10 Å (Table 6.11). Three different orientations of the TB groups are tested:

- TB-down, where two legs (C-CH_3) point downward and one points upward,
- TB-up, where two legs point upward and one points downward,
- TB-up/down, where two of the four groups are TB-up and two are TB-down.

For the above-listed configurations of TBA, two structural parameters are investigated:

- The tilt angle $\widetilde{\omega}$ between the plane of the phenyl ring, including the N atom to which it is directly bound, and the surface normal, as illustrated in Figure 6.33. This definition of the tilt angle is identical to that of azobenzene in section 6.4.1.2. Here too, we note that according to DFT calculations, the phenyl ring and the nitrogen atoms do not lie on the same plane in the presence of a tilt angle greater than zero. However, for the sake of simplicity, we assume them to be coplanar.
- The angle γ between the vector C_C-C_0 and the normal to the plane of the three TB carbon atoms C_1, C_2 and C_3, as illustrated in Figure 6.35.

In particular, the effect of $\widetilde{\omega}$ on $[P_c\,(\mathrm{C}),\, F_c\,(\mathrm{C})]$ is studied for each of the TB configurations, while the minor influence of γ on the simulated NIXSW results is investigated only for the TB-down configuration.

TB-down configuration: influence of $\widetilde{\omega}$ and γ on $[P_c^*\,(\mathrm{C}),\, F_c^*\,(\mathrm{C})]$

Figure 6.33 shows a side view of the TB-down configuration with the nitrogen atoms at 3.10 Å and the tilt angle of the phenyl rings $\widetilde{\omega}$ indicated in the figure. The behavior of $[P_c^*\,(\mathrm{C}),\, F_c^*\,(\mathrm{C})]$, as $\widetilde{\omega}$ varies between $-5°$ and $90°$, is marked by the red spiral in Figure 6.34a. The intersection with the average carbon structural parameter (dark green circle) occurs for the TBA geometry corresponding to $\widetilde{\omega} = 7°$, with $F_c^*\,(\mathrm{C_i}) = 0.18$. The slightly lower tilt angle of the experimental results compared

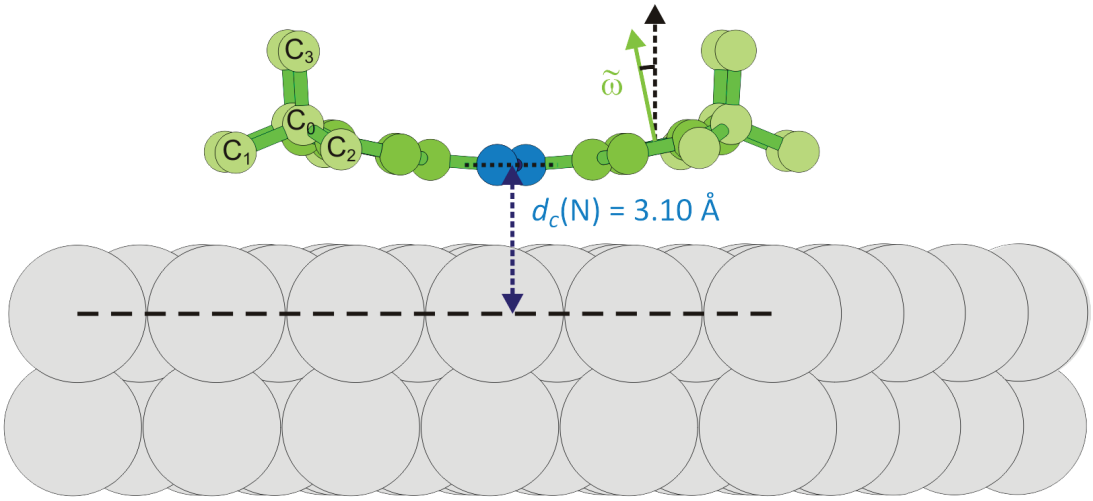


Figure 6.33: TB-down configuration of TBA/Ag(111) with nitrogen atoms located at 3.10 Å from the surface Bragg plane (section 6.3.4.1) and the molecular adsorption geometry as in Figure 6.32. The tilt angle $\widetilde{\omega}$ between the plane of the phenyl ring, including the nitrogen directly bound to it, and the normal to the Ag surface is marked in the figure. Hydrogen atoms are not drawn in order to facilitate the visualization of TB carbons.

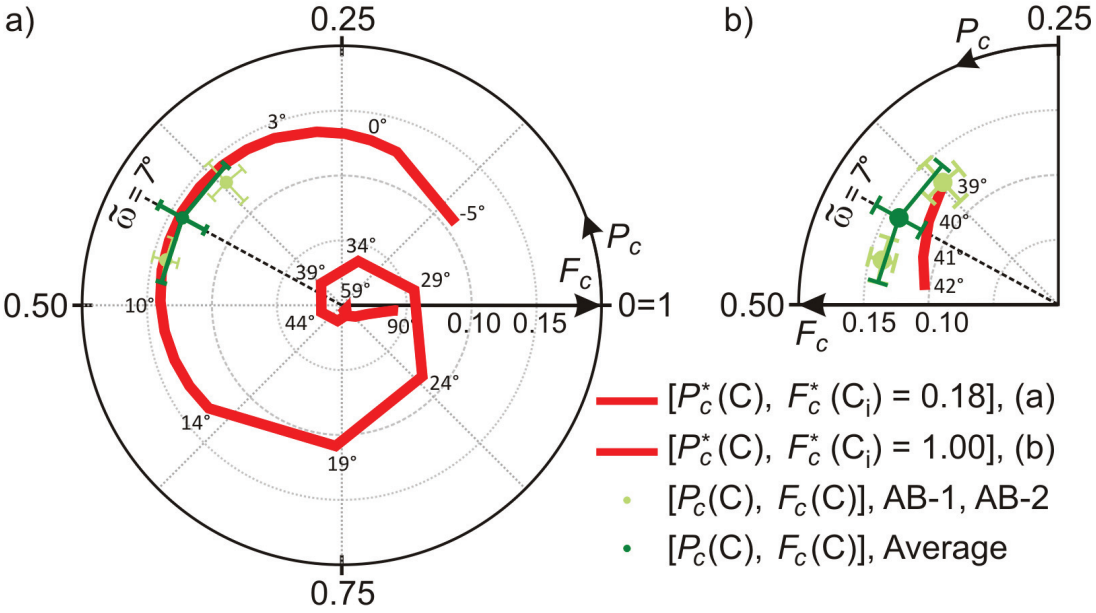


Figure 6.34: Red spiral: Argand diagram of the calculated $[P_c^*(\mathrm{C}), F_c^*(\mathrm{C})]$ with $F_c^*(\mathrm{C_i}) = 0.18$ (a) and $F_c^*(\mathrm{C_i}) = 1.00$ (b) for the carbon signal (*Sum*) of the TB-down configuration as $\widetilde{\omega}$ varies from $-5°$ to $90°$. Step size is of $1°$ in proximity of the experimental data points, while it is larger otherwise. Some selected values of $\widetilde{\omega}$ are marked next to the corresponding points of the spiral. Light green circles: Argand diagram of carbon P_c and F_c as derived from NIXSW experiments (section 6.3.4.2). Dark green circle: the average of experimental data points.

to the DFT calculations ($\widetilde{\omega} = 9°$, section 6.4.2.2) suggests an even stronger vdW attraction of the phenyl ring and TB groups to the substrate. Despite the presence of the TB group, the small tilt angle indicates an essentially flat-lying molecule with all carbon atoms located at vertical positions within 0.65 Å, except the four C_3 carbon atoms lying 1.54 Å above C_0 atoms (Figure 6.33). As a consequence, the inner structure of TBA with $\widetilde{\omega} = 7°$ is not sufficiently bent to justify a reduction of the coherent fraction because of the vertical displacement of carbon atoms within the molecule. In fact, the experimental $F_c^*(\mathrm{C}) = 0.14$ results from a coherent fraction of the single carbon atoms equal to $F_c^*(\mathrm{C_i}) = 0.18$. Therefore, the coherent fraction decrease due to the vertical displacement of carbon atoms within each TBA molecule is approximately 0.04 (22%). The intrinsic low coherent fraction of carbons may be explained by the presence of molecules in different adsorption geometries and/or by diffusion on the surface (section 4.4.1). NIXSW experiments on TBA/Ag(111) are indeed performed at room temperature (section 6.2.1); thus a significant portion of diffusing molecules can be expected, with a corresponding relatively large amount of molecules contributing to the incoherent part of the molecular layer, which ultimately leads to a lower F_c. Nevertheless, these arguments do not rationalize the differential coherent fraction of carbon and nitrogen. In the following, we will see how this shortcoming is overcome by other adsorption geometries.

The $P_c = 0.42$ radius of the Argand diagram in Figure 6.34a crosses the red spiral in two points, one corresponding to $\widetilde{\omega} = 7°$ (just discussed) and the other one at approximately 40°. However, the corresponding inner trace of the spiral does not intersect the experimental average point, not even if $F_c^*(\mathrm{C_i}) = 1$, as illustrated in Figure 6.34b. We can therefore conclude that our NIXSW structural parameters are consistent with TB-down configuration of TBA adsorbed on Ag(111) only with $\widetilde{\omega} = 7°$. Furthermore, the small tilt angle is also in qualitative agreement with NEXAFS data of TBA adsorbed on the Au(111) surface, where $\widetilde{\omega} = 4 \pm 4°$ was measured.[141]

Next, the effect of the angle γ on the TB-down configuration of TBA is investigated. In particular, we start from the reference structure of the DFT calculations (Figure 6.32) in which the TB group C_0-C_1-C_2-C_3 is rotated around the vector with origin in C_0, normal to C_C-C_0 and parallel to the Bragg plane. Positive angles γ, as the one shown in Figure 6.35, correspond to an upward tilt of both the lower and the upper legs away from the surface, leading thus to a greater P_c and smaller F_c. On the other hand, negative γ correspond to a downward tilt of the whole TB

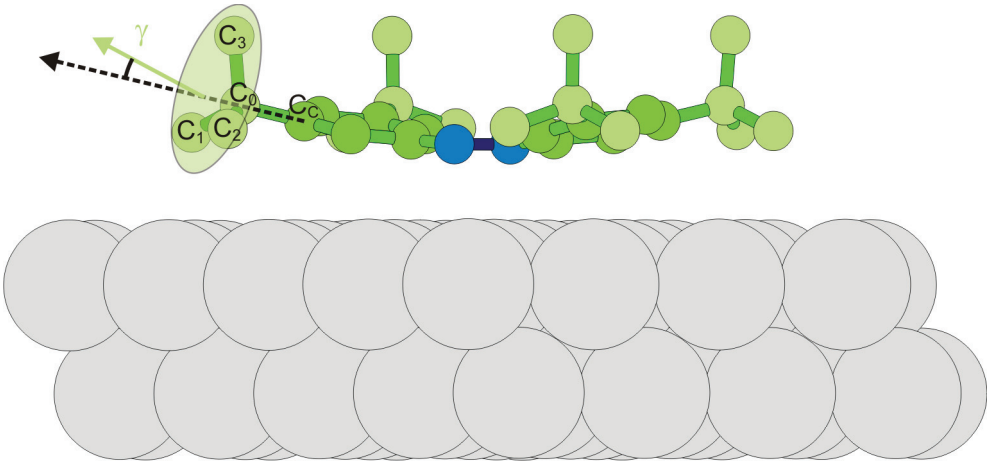


Figure 6.35: Side view of TBA/Ag(111) to highlight the angle γ between the normal to the plane defined by the TB carbon atoms C_1, C_2, C_3 and the vector C_C-C_0.

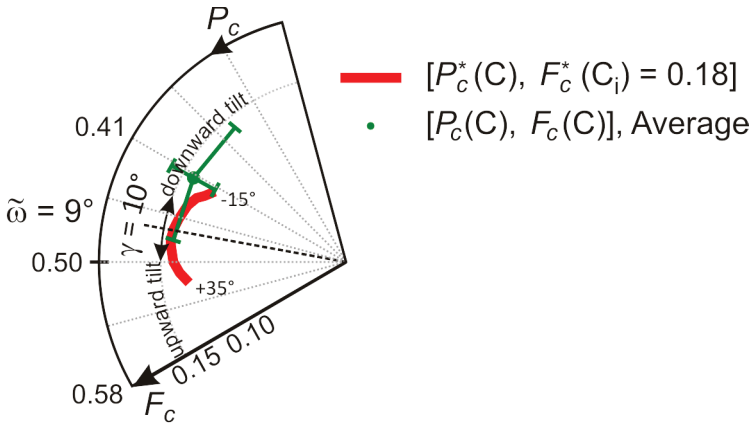


Figure 6.36: Argand diagram of the calculated $[P_c^*(\mathrm{C}), F_c^*(\mathrm{C})]$ with $F_c^*(\mathrm{C_i}) = 0.18$ (red spiral) for the carbon signal (Sum) as γ varies from $-15°$ to $35°$, for $\widetilde{\omega} = 9°$. Argand diagram of the average carbon P_c and F_c (dark green circle) as derived from NIXSW experiments (section 6.3.4.2).

groups closer to the surface, with consequent decrease of both P_c and F_c.

DFT calculations show that γ increases by 10° going from the gas-phase TBA to TBA/Ag(111). A further increase of γ to favor a closer surface distance of the phenyl rings can thus be expected. For example, a possible alternative to the geometry of $\widetilde{\omega} = 7°$ and $\gamma = 10°$, i.e., as in DFT calculations, is an even lower $\widetilde{\omega}$ with correspondingly higher γ leading to a smaller surface distance of the phenyl rings. In this latter scenario, to compensate for the lower $F_c^*(\mathrm{C})$ associated with a larger γ (see Figure 6.36) of the simulated structure, $F_c^*(\mathrm{C_i})$ would increase to allow the intersection with the experimental data point. In particular, for $\widetilde{\omega} = 3°$ the intersection with the experimental average carbon point occurs for $\gamma = +35°$ and $F_c^*(\mathrm{C_i}) = 0.20$, slightly larger than $F_c^*(\mathrm{C_i}) = 0.18$ corresponding to $\widetilde{\omega} = 7°$ and $\gamma = 0°$.

TB-up configuration: influence of $\widetilde{\omega}$ on $[P_c^*(\mathrm{C}), F_c^*(\mathrm{C})]$

In the absence of DFT calculations leading to the TB-up configuration, we construct the adsorption geometry in Figure 6.37 from the rotation of TB-down groups (Figure 6.33) by 60° around the vector $\mathrm{C_C}$-$\mathrm{C_0}$. As $\widetilde{\omega}$ of this TBA configuration varies

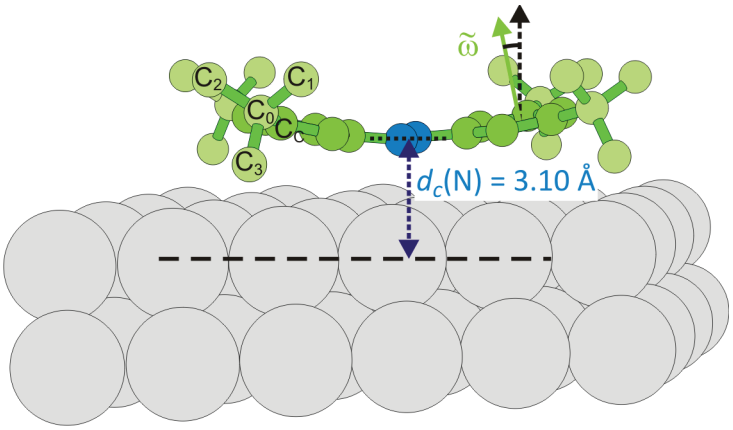


Figure 6.37: Structural model of TB-up configuration of TBA/Ag(111). The adsorption geometry is exactly as in Figure 6.33 with the exception of TB groups, here pointing down to the surface. TB groups are rotated by 60° around the vector $\mathrm{C_C}$-$\mathrm{C_0}$ (Figure 6.35), compared to the TB-down configuration of Figure 6.33. $\widetilde{\omega}$ is illustrated in the figure and defined as in Figure 6.33.

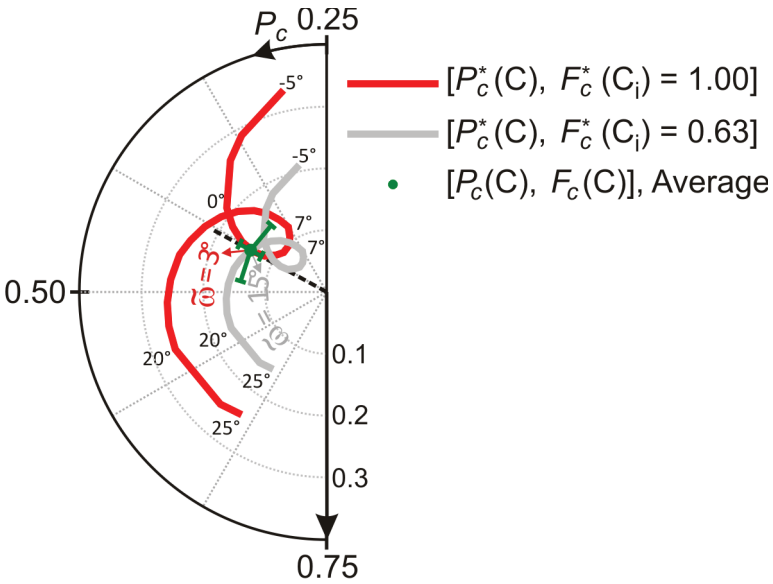


Figure 6.38: Argand diagram of the calculated $[P_c^*(\mathrm{C}), F_c^*(\mathrm{C})]$ with $F_c^*(\mathrm{C_i}) = 1.00$ (red spiral) and $F_c^*(\mathrm{C_i}) = 0.63$ (gray spiral) for the carbon signal (*Sum*) of TB-up configuration as $\widetilde{\omega}$ varies from −5° to 25°. Argand diagram of the average carbon P_c and F_c (dark green circle) as derived from NIXSW experiments (section 6.3.4.2). The values of the tilt angle corresponding to the intersection of the calculated spiral with the experimental data point are equal to 3° and 15°, for the red and the gray spiral, respectively.

between −5° and 25°, the simulated [P_c^* (C), F_c^* (C)] trace follows the red and gray spirals in Figure 6.38 for F_c^* (C_i) = 1.00 and 0.63, respectively. The intersection of the NIXSW data point (dark green circle) with the red spiral corresponds to a tilt angle $\widetilde{\omega} = 3°$. However, this TBA adsorption geometry can be reasonably excluded because it implies a coherent fraction of each carbon species equal to 1, as the bulk Ag atoms. In other words, this would mean that each carbon species has exactly the same vertical position in all TBA molecules adsorbed at the Ag(111) surface: a rather unrealistic scenario if we consider the presence of molecules adsorbed at defects or step edges or diffusing on the surface. The P_c (C) = 0.42 radius in the Argand diagram of Figure 6.38 also intersects the red spiral in a second point at a larger $\widetilde{\omega}$. To obtain the intersection with the experimental average point (green circle), the amplitude [F_c (C)] of the red spiral with F_c^* (C_i) = 1.00 has to be rescaled. With the coherent fraction of the single carbon species F_c^* (C_i) = 0.63, the gray spiral is obtained and the corresponding overlap with the NIXSW average carbon data point occurs at $\widetilde{\omega} = 15°$.

The agreement between NIXSW structural parameters and the TB-up configuration with a tilt angle $\widetilde{\omega} = 15°$ and F_c^* (C_i) = 0.63 is intriguing and leads to the following conclusions:

- First, the agreement between NIXSW data and TB-up configuration for $\widetilde{\omega} = 15°$ occurs for a coherent fraction of the single carbon atoms F_c^* (C_i) = 0.63, identical to that of nitrogen atoms (0.66 ± 0.15) within the errors (Table 6.11). In this case we can therefore talk about the coherent fraction of the molecule as a whole, since F_c^* (C_i) ≈ F_c^* (N_i), and the lower F_c (C) directly and exclusively results from the presence of carbon atoms located at different vertical positions above the surface. This represents a strong argument in favor of the TBA configuration with TB-up, instead of TB-down.
- Second, interestingly, the simulated trace of the carbon signal in the TB-up configuration intersects the experimental average carbon data point at the point corresponding to $\widetilde{\omega} = 15°$. The larger tilt angle compared to the TB-down configuration is consistent with the presence of the lower TB leg that effectively introduces a spacing 0.30 Å larger than the two lower TB legs of the TB-down configuration. This structural consistency indeed corroborates the plausibility of the TB-up configuration.

TB-up/down configuration: influence of $\widetilde{\omega}$ on [P_c^* (C), F_c^* (C)]

To conclude our sequence of the investigated TBA configurations, we focus on the TBA molecule illustrated in Figure 6.39, characterized by two TB-down and two TB-up groups. In this way, we implicitly also consider the situation where one half of the molecules is TB-up and the other half is TB-down. The red spiral in Figure 6.40 represents the behavior of the calculated [P_c^* (C), F_c^* (C)] of the TBA adsorption geometries simulated for $0° \leq \widetilde{\omega} \leq 90°$. The only possible intersection with the experimental average carbon data point occurs for $\widetilde{\omega} = 7°$, as for the TB-down

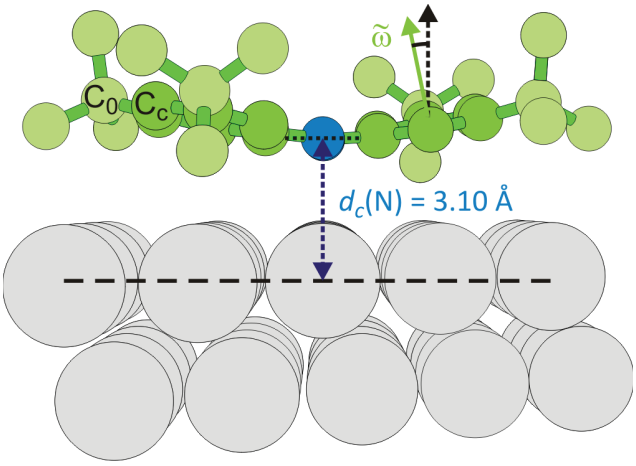


Figure 6.39: TB-up/down configuration of TBA/Ag(111), where TB groups are alternatively rotated by 60° around the vector C_C-C_0, compared to the TB-up configuration of Figure 6.37. $\widetilde{\omega}$ is illustrated in the figure and defined as in Figure 6.37.

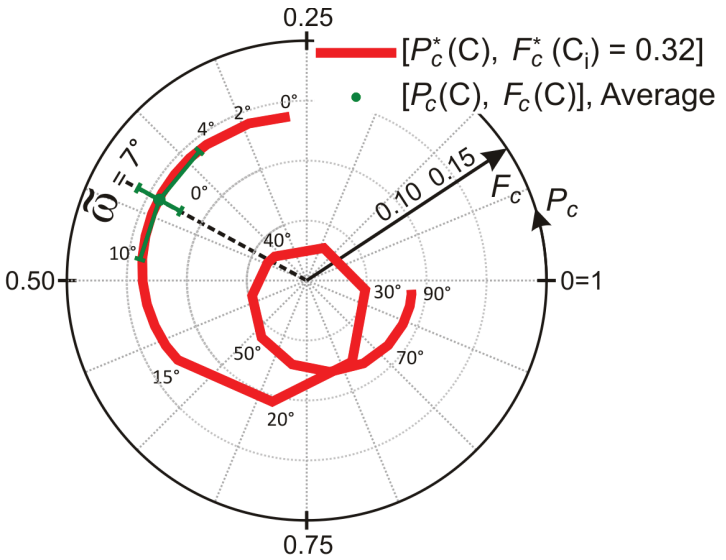


Figure 6.40: Argand diagram of the calculated [P_c^* (C), F_c^* (C)] with F_c^* (C_i) = 0.32 (red spiral) for the carbon signal (*Sum*) as $\widetilde{\omega}$ varies from 0° to 90°. Argand diagram of the average carbon P_c and F_c (dark green circle) as derived from NIXSW experiments (section 6.3.4.2).

configuration, but here with $F_c^*(\mathrm{C_i}) = 0.32$. Interestingly, this coherent fraction is similar to the one found for the single carbon atoms of azobenzene (section 6.4.1.2), according to model (a).

However, in this case too, there is a sizable difference between $F_c^*(\mathrm{C_i}) = 0.32$ and $F_c^*(\mathrm{N_i}) = 0.66$. Therefore, the TB-up/down configuration, as well as the TB-down configuration requires additional arguments to explain the discrepancy between the coherent fraction of carbon and nitrogen atoms of the same molecule.

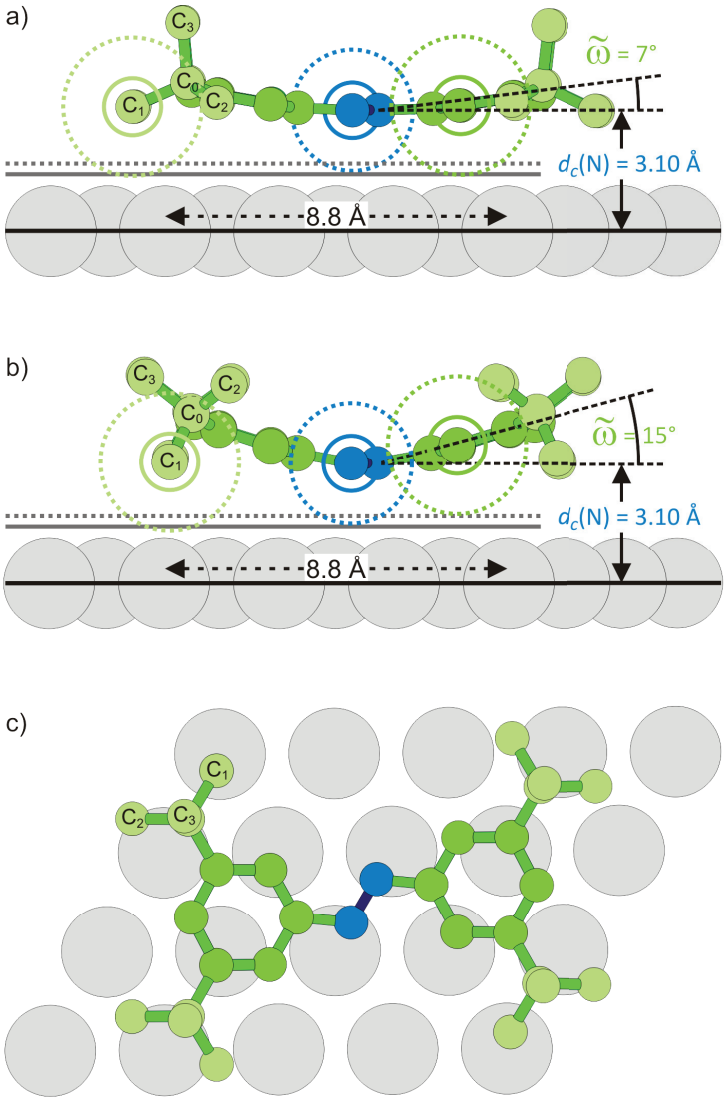
6.4.2.4 NIXSW adsorption model of TBA/Ag(111)

In this section, the main results of the NIXSW simulations are discussed. In particular, our attention is focused on the TBA configurations, i.e., TB-down and TB-up, consistent with the experimental results. We will argue why each of them is a plausible adsorption model and also point out the weak points. Finally, on the basis of the structural model, the switching functionality of TBA/Ag(111) is discussed.

The TBA configuration TB-down, i.e., with two of the three *tert*-butyl legs pointing towards the surface, is the one resulting from DFT-D calculations and is the one used as a reference for the NIXSW simulations reported in section 6.4.2.3. The TB-down configuration is expected to be the most energetically favorable because it minimizes the adsorption height of *tert*-butyl and phenyl carbons, which are attracted to the substrate via dispersive interactions. In fact, in the TB-down configurations predicted by theory,[152] the two legs pointing to the surface are almost parallel to the plane of the molecule, while the third leg points straight upwards, as illustrated in Figure 6.32 and 6.33. Besides maximizing the energy gain from vdW interactions, the TB-down configuration also minimizes the energetic penalty due to the distortion of the gas-phase planar geometry. In fact, the DFT-optimized geometry is only slightly distorted with $\widetilde{\omega} = 9°$ and $\gamma = 10°$ compared to $\widetilde{\omega} = 0°$ and $\gamma = 0°$ typical of the gas-phase geometry.

By tuning only the tilt angle $\widetilde{\omega}$, we find that the TB-down configuration in agreement with NIXSW data has $\widetilde{\omega} = 7°$ and $F_c^*(\mathrm{C_i}) = 0.18$, as shown in Figure 6.41a. If then γ is also allowed to vary, another possible geometry has $\widetilde{\omega} = 3°$, $\gamma = 35°$ and $F_c^*(\mathrm{C_i}) = 0.20$ (section 6.4.2.3). Since the latter two adsorption geometries are similar to each other, we focus only on the former one.

We remark a slightly lower tilt angle $\widetilde{\omega}$ compared to the DFT-D calculations. This suggests an even stronger vdW interaction that pulls the phenyl rings closer to the



d)

X-Ag	d_i(X-Ag)
$\overline{d_i(\text{N-Ag})}$	3.21
$\overline{d_i(C_{ph},C_{TB\text{-}0,1,2}\text{-Ag})}$	3.58
$\overline{d_i(C_{TB\text{-}3}\text{-Ag})}$	5.44

e)

X-Ag	d_i(X-Ag)
$\overline{d_i(\text{N-Ag})}$	3.21
$\overline{d_i(C_{ph},C_{TB\text{-}0,1}\text{-Ag})}$	3.66
$\overline{d_i(C_{TB\text{-}1}\text{-Ag})}$	3.20
$\overline{d_i(C_{TB\text{-}2,3}\text{-Ag})}$	5.24

Figure 6.41: (a): adsorption geometry (side view) of the TB-down configuration of TBA/Ag(111) with $\widetilde{\omega} = 7°$. (b): adsorption geometry (side view) of the TB-up configuration of TBA/Ag(111) with $\widetilde{\omega} = 15°$. Filled circles indicate atomic positions, solid lines indicate covalent radii[91] (C: 0.73 Å; N: 0.71 Å; Ag: 1.45 Å), dotted lines indicate van der Waals radii[92] (C: 1.77 Å; N: 1.55 Å; Ag: 1.72 Å). The distance of nitrogen atoms from the surface Bragg plane d_c (N) and the tilt angle of the phenyl rings $\widetilde{\omega}$ are explicitly marked in panels a and b. (c): adsorption site (top view) of azobenzene/Ag(111) as it results from DFT calculations performed by E. R. McNellis, A. D. Baghi (Fritz Haber Institute), J. Meyer and K. Reuter (TU München).[142] (d) and (e): average interatomic distances of nitrogen and carbon atoms from the nearest Ag atom, assuming the lateral position of TBA with respect to the substrate as in panel c and the vertical position resulting from NIXSW experiments and simulations as in panels (a) and (b), respectively.

X	$r^{X}_{cov} + r^{Ag}_{cov}$	$r^{X}_{vdW} + r^{Ag}_{vdW}$	$\overline{d_i(\text{X-Ag})}$	% of $(r^{X}_{cov} + r^{Ag}_{cov})$	% of $(r^{X}_{vdW} + r^{Ag}_{vdW})$
C	2.18	3.49	3.58 [3.66]	164 [168]	102 [105]
N	2.16	3.27	3.21	148	98

Table 6.12: Sum of covalent radii[91] $r^{X}_{cov} + r^{Ag}_{cov}$, sum of vdW radii[92] $r^{X}_{vdW} + r^{Ag}_{vdW}$ and average interatomic distances $\overline{d_i(\text{X-Ag})}$ (X = C, N) for TBA/Ag(111) are reported, followed by the percentage of the interatomic distances with respect to the sum of covalent radii and the sum of vdW radii.

surface. In order to discuss the molecule-substrate interaction in a more quantitative way, the interatomic distances d_i(X-Ag), where X = N, C, are calculated. We find that for nitrogens, the average distance from the surface is $\overline{d_i(\text{N-Ag})} = 3.21$ Å, whereas for carbons $\overline{d_i(\text{C-Ag})} = 3.58$ Å, excluding from the average the carbon atoms C_3 of the TB leg pointing to the vacuum and located at 5.44 Å above the Ag surface (Figure 6.41d). Both N and C average interatomic distances from the nearest Ag atoms are larger than the sum of the corresponding sum of covalent radii, 48% and 64%, respectively (Table 6.12). At the same time, both carbon and nitrogen atoms are approximately at the vdW interaction limit, represented by the sum of the vdW atomic radii of TBA and Ag atoms. In particular, nitrogen atoms are slightly below, while the average carbon height is slightly above the sum of the vdW radii.

The adsorption model illustrated in Figure 6.41a shows an essentially flat TBA molecule adsorbed on Ag(111). A weak covalent bond between nitrogen and surface Ag atoms can explain the fact that the azo (-N=N-) bridge is slightly closer to the surface. At the same time, the butterfly-like configuration of TBA ($\widetilde{\omega} = 7°$) results from the competition between the steric hindrance of the TB groups that tend to lift the molecule from the surface, and the vdW attraction that instead pulls the molecule closer to the surface.

The agreement between theoretical calculations and NIXSW results occurs only if vdW dispersion forces are taken into account, albeit at a semiempirical level (PBE+TS).[143,149] In fact, if the pure PBE functional is employed, the molecule would be floating on the surface at adsorption height 3.86 Å. This result further confirms the importance of the dispersion interactions for large organic molecules with highly polarizable conjugated ring system, e.g., azobenzene,[4] TBA,[3,151] PTCDA,[4] adsorbed on metal surfaces, as already discussed in section 6.4.1.4.

The assumption behind the statement that the TB-down configuration, shown in

Figure 6.41a, is consistent with NIXSW results and is a coherent fraction for the single carbon atoms approximately one third of the nitrogen coherent fraction. NIXSW experiments provide $F_c\,(\mathrm{C}) = 0.14 \pm 0.02$ for carbon and $F_c\,(\mathrm{N}) = 0.66 \pm 0.15$ for nitrogen. Since the TB-down configuration matches the experimental carbon coherent position for $\widetilde{\omega} = 7°$, the molecule is substantially flat. As a consequence, the small distortion of the molecule does not cause a large decrease in the single carbon coherent fraction, which indeed results $F_c^*\,(\mathrm{C_i}) = 0.18$. Since the large discrepancy between the coherent fraction of carbon and nitrogen of the same TBA molecule cannot be easily explained, the plausibility of the entire adsorption model is questioned.

A valid alternative model that solves this latter major flaw of the TB-down configuration is the adsorption geometry with two *tert*-butyl legs pointing to the vacuum and one to the surface, i.e., the TB-up configuration. Figure 6.41b shows the TB-up configuration consistent with NIXSW results with $\widetilde{\omega} = 15°$ and $F_c^*\,(\mathrm{C_i}) = 0.63$. Interestingly, for this configuration, the vertical displacement of the carbon atoms is such that the experimental average carbon coherent fraction $F_c\,(\mathrm{C}) = 0.14$ results from the single carbon coherent fraction $F_c^*\,(\mathrm{C_i}) = 0.63$ that is equal within the error to the $F_c\,(\mathrm{N}) = 0.66 \pm 0.15$. Therefore, we can talk about coherent fraction of the TBA molecule, and the decrease of the measured carbon coherent fraction simply follows from the vertical distribution of carbon atoms through the Bragg plane spacing.

The larger tilt angle $\widetilde{\omega} = 15°$ is interpreted as a direct consequence of the lower *tert*-butyl leg acting as a spacer. In fact, for $\widetilde{\omega} = 7°$, as in DFT calculations, the TB-up configuration would have the carbon atoms $\mathrm{C_1}$ at 2.55 Å from the Ag surface, i.e., only 17% larger than the corresponding sum of covalent radii. On the other hand, for $\widetilde{\omega} = 15°$ $\mathrm{C_1}$ is 3.20 Å above the surface.

While the TB-up configuration leads to a larger tilt angle $\widetilde{\omega}$, the vdW interaction is still rather strong. In fact, the evidence that phenyl rings and the azo bridge are pulled down closer to the surface to form a pronounced butterfly geometry is attributed to the dispersive attraction with the metal surface. If we look at the average adsorption height of the phenyl ring, $\mathrm{C_0}$ and $\mathrm{C_1}$ TB carbons, $d_i\,(\mathrm{C_{ph}}, \mathrm{C_{TB-0,1}} - Ag) = 3.66$ Å, we note that it is only 0.08 Å greater than $d_i\,(\mathrm{C_{ph}}, \mathrm{C_{TB-0,1,2}} - Ag) = 3.58$ Å of the TB-down configuration (Figure 6.41d,e), while the nitrogen atoms are at exactly the same distance (3.21 Å) from the surface. The main difference with the TB-down configuration is in the *tert*-butyl group atoms. In fact, in the TB-up configuration, $\mathrm{C_1}$ is 0.25 Å lower than $\mathrm{C_2}$ and $\mathrm{C_3}$ in the

TB-down configuration, while C_1 and C_2 are 0.20 Å higher than C_3 in the TB-down configuration. Therefore, the same conclusions regarding the molecule-substrate interaction also apply here, although in this case a larger energetic penalty due to the distortion of the gas-phase planar geometry may be expected.

In summary, two different adsorption models are presented and discussed. A conclusive adsorption geometry cannot be proposed only on the base of NIXSW. However, it should be highlighted that the TB-up configuration seems more plausible and does not require additional qualitative and questionable arguments to rationalize the differential coherent fraction of TBA as in the TB-down configuration. We also propose here, as for azobenzene, NEXAFS experiments to determine the tilt angle $\widetilde{\omega}$ of TBA phenyl rings and consequently the corresponding adsorption geometry on the basis of NIXSW results.

To conclude, independently from the adsorption model, the fact that the azo bridge of *trans*-TBA/Ag(111) is only 0.13 Å larger than for azobenzene, strongly contradicts the concept of the *tert*-butyl groups as a strategy for geometrically decoupling the molecule from the substrate. In fact, a much larger d_c (N) distance difference of 1.70 Å is expected from the gas-phase molecular geometries of azobenzene and TBA.[3,151] Experimental and theoretical results rationalize the non-switching behavior of azobenzene and TBA on Ag(111) as a failure of the "spacer legs" strategy to decouple geometrically the molecules from the substrate. Nevertheless, DFT calculations, proven to have predictive power for both azobenzene and TBA on the Ag(111) surface, show that on the Au(111) surface as well, the height difference of the two molecules -N=N- unit is negligible. Therefore, we can use the geometrical argument to explain the low switching probability of azobenzene on Ag and Au and of TBA on Ag; however, why the same argument does not hold for TBA/Au(111), where light-induced switching can be achieved, remains unanswered.[6,29] Tegeder et al.[29] propose that in addition to the geometric coupling, the electronic coupling to the surface also plays a crucial role in understanding the switching mechanism. In particular, they consider the energetic position of the metal *d*-band with respect to the molecular HOMO to be the fundamental difference between Ag and Au.[3,153] In fact, the hole created by a photon in the Au *d*-band relaxes to the top of the band and then transfers to the HOMO of TBA, leading to the conformational change from the *trans*- to the *cis*-isomer. In the case of Ag, as the *d*-band lies approximately 2 eV lower than in the Au, the transfer of the hole is not so efficient; hence the switching does not occur.

6.5 Conclusions

The main conclusions following from data analysis (section 6.3) and discussion (section 6.4) of NIXSW experiments performed on azobenzene/Ag(111) and TBA/Ag(111) are summarized here. In order to interpret NIXSW structural data of the two investigated molecules, a novel analysis scheme, i.e., the vector analysis in the Argand diagram, is developed (section 6.4.1.2) and leads to two main results:

- NIXSW structural parameters of large organic molecules extending over more than one Bragg plane spacing (e.g., $d_{\mathrm{Ag(111)}}$) may not directly correspond to the real average adsorption height of a certain atomic species. The ultimate reason for this is the modulo 1 periodicity of the coherent position P_c (section 6.4.1.2). This finding has important implications in the analysis of NIXSW data regarding systems whose orientation with respect to the substrate is a priori unknown. In these cases, the vector analysis is thus necessary to avoid incorrect interpretation of the measured structural parameters.

- While the vector analysis in the Argand diagram can be required to properly interpret NIXSW data of strongly bent adsorbed molecules, its benefits are also valuable for molecules presumed to be flat-lying. In fact, it consists of independently probing different degrees of freedom of the molecular geometry, providing a quantitative estimate of the (P_c, F_c) variations as one or more selected structural parameters (e.g., the tilt angle $\widetilde{\omega}$, the angle γ, the TB orientation) change. The comparison of the simulated molecular conformations with the experimental results can then provide a unique adsorption geometry consistent with NIXSW structural parameters, or, alternatively, a set of possible configurations (whose number increase with the complexity of the molecule), all in agreement with the experiments. In this latter case, the comparison with other experimental results and DFT calculations can shed light on the most plausible adsorption geometry.

The application of the vector analysis to AB/Ag(111) NIXSW data primarily yields two adsorption geometries both in agreement with NIXSW results, albeit with different structural parameters, i.e., tilt angle $\widetilde{\omega}$, rotation angle β and coherent fraction of the single carbon atom $F_c^*\,(\mathrm{C_i})$. The common features of both models are the position of the nitrogen atoms $d_c\,(\mathrm{N}) = 2.97 \pm 0.04$ Å, the phenyl ring tilt angle $\widetilde{\omega} = 0.5 \pm 1.0°$ and the average position of the carbon atoms $d_c\,(\mathrm{C}) = 2.98 \pm 0.04$ Å. The differences are in the rotation angle β, 0° in one case and 17° in the other case, and in $F_c^*\,(\mathrm{C_i})$, equal to 0.34 and 0.48 [$= F_c\,(\mathrm{N})$], respectively.

In the case of the more complex TBA molecule, the vector analysis allows its multiple degrees of freedom to be investigated, yielding several possible geometries, all consistent with NIXSW results. They have in common the distance of the nitrogen atoms from the surface, i.e., 3.10 ± 0.06 Å and the average adsorption height of the carbon atoms, i.e., 3.34 ± 0.15 Å. The main difference is in the orientation of the *tert*-butyl groups. We investigated the TB-down and the TB-up configurations (section 6.4.2.3) in more detail. As a result of a different TB orientation, a different tilt angle $\widetilde{\omega}$ follows: 7° and 15°, respectively. However, the most fundamental diversity is in the coherent fraction of the single carbon atoms, in one case, $F_c^*(\mathrm{C_i}) = 0.18$, while in the other case $F_c^*(\mathrm{C_i}) = 0.63 \approx F_c(\mathrm{N})$.

Both for AB/Ag(111) and for TBA/Ag(111), we propose different possible adsorption geometries and express a cautious preference for those characterized by the same coherent fraction for carbon and nitrogen atoms of the same molecule.

The comparison of experimental adsorption geometry with DFT calculations employing different functionals, namely pure PBE and PBE-D (dispersion corrected), allows the crucial role played by vdW interactions at the AB/Ag and TBA/Ag inter-

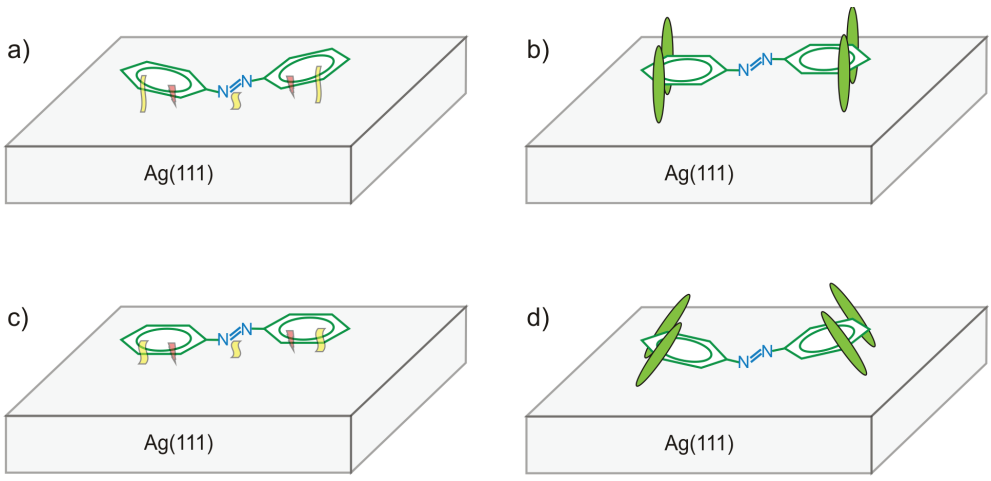


Figure 6.42: (a): Schematic representation of azobenzene/Ag(111) based on the expectation that the azo (-N=N-) bridge interacts chemically with the Ag atoms (yellow symbol), bringing the phenyl rings in the Pauli repulsive regime (red symbol), thereby leading to a butterfly-like configuration (sections 6.4.1 and 6.4.1.3) in which phenyl rings are vdW attracted to the substrate (yellow symbol). (b): Schematic representation of TBA/Ag(111) based on the "spacer leg" groups strategy of decoupling the photo-active moiety (-N=N-) from the surface. Schematic representation of azobenzene/Ag(111) (c) and TBA/Ag(111) (d) resulting from NIXSW experiments and in agreement with DFT calculations.

faces to be highlighted. Moreover, NIXSW data benchmark different semiempirical correction schemes, finding the one proposed by Tkatchenko and Scheffler[149] to be the most accurate in predicting the structure of AB/Ag(111) and TBA/Ag(111), although with a sizable overestimation of the adsorption energy (section 6.4.1.4). This shortcoming is assigned to the lack of metallic screening in the strictly pairwise evaluation of the dispersive interactions.[4]

Finally, the small height difference (0.13 Å) of the -N=N- moiety for azobenzene and TBA absorbed on Ag(111) represents the experimental proof that the strategy of decoupling the molecules from the substrate (Figure 6.42b), aimed at restoring the switching functionality, by means of the *tert*-butyl groups as "spacer legs", fails (Figure 6.42d). At the same time, this important results for the understanding of the switching mechanism in the adsorbate state suggests the necessity of taking into account both geometrical and electronic properties of the molecule-substrate complex for successful and technologically relevant tuning of the switching functionality.

7 Terephthalic acid on Cu(100)

7.1 Introduction

Terephthalic acid (TPA, see Figure 7.1) is known for being a very effective ligand for metal-organic networks at surfaces[33,34] and, more recently, as a binding layer in organic photovoltaics devices.[154] The adsorption and self-assembly of TPA was investigated on many different metal surfaces: Pt(111),[155] Pd(111),[156] Ag(111),[157] Au(111).[158] In those systems, the highly ordered molecular layer was attributed to the head-to-tail and/or side-to-side intermolecular coupling by formation of hydrogen bonds. In contrast, if the interaction with the underlying substrate is very strong, through the formation of covalent bonds, TPA adsorbs randomly, as occurs on the Si(111)-7 x 7 surface[157] due to the high density of dangling bonds. As a common feature of the substrates mentioned so far, TPA adsorbs in a flat-lying geometry, while on Cu(110)[159,160] and TiO_2,[154] as the monolayer regime is approached, it adsorbs upright. In this way, due to the selective reactivity of the functional group located at the vacuum interface, a functionalized surface is generated.

TPA is also the basic unit of a prototypical metal-organic coordination network with iron on the Cu(100) surface.[33,34] These supramolecular coordination structures

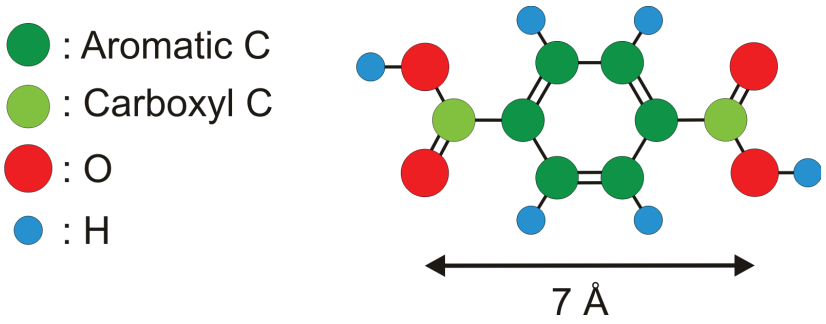


Figure 7.1: Molecular structure of terephthalic acid [1,4-benzenedicarboxylic acid, $C_6H_4(COOH)_2$]. Color code: aromatic carbons → dark green; carboxyl carbons → light green; oxygens → red; hydrogens → blue.

offer enormous possibilities for the nanometer-scale patterning of solid surfaces with specific structure as well as tailored physical and chemical properties. In order to better control and tune the geometric, electronic and magnetic properties[7,31,35] of these metal-organic networks, it is essential to deeply understand the adsorbate-adsorbate and adsorbate-substrate interactions of the pure molecular phase at a metallic surface.

To this end, in this chapter we investigate TPA on the Cu(100) surface. From XPS,[161] STM[161] and LEED[5] measurements, we know that doubly deprotonated TPA (= TPA^{-2}) forms a well-ordered structure with a 3×3 unit cell commensurate with the copper substrate underneath. Based on the lateral arrangement of the molecules resulting from the STM images[161] and on the flat adsorption geometry resulting from NEXAFS measurements,[161] H-bonding was proposed as the stabilization force of TPA islands (Figure 7.2).[161] However, a recent HREELS study[5] did not find any evidence of direct intermolecular H-bonding. Instead, it revealed the presence of an adsorbate-substrate interaction, indicating the bonding to the substrate as a probable driving force for the ordering of TPA through a stress field induced in the surface top layers.[162]

Previously, supramolecular self-organization on metal surfaces was believed to be directed primarily by hydrogen bonds or by coordination bonds.[31] We also propose here a substrate-mediated self-ordering[162] of TPA on the Cu(100) surface, based on experimental structural information, supported by theoretical calculations.[163] Ad-

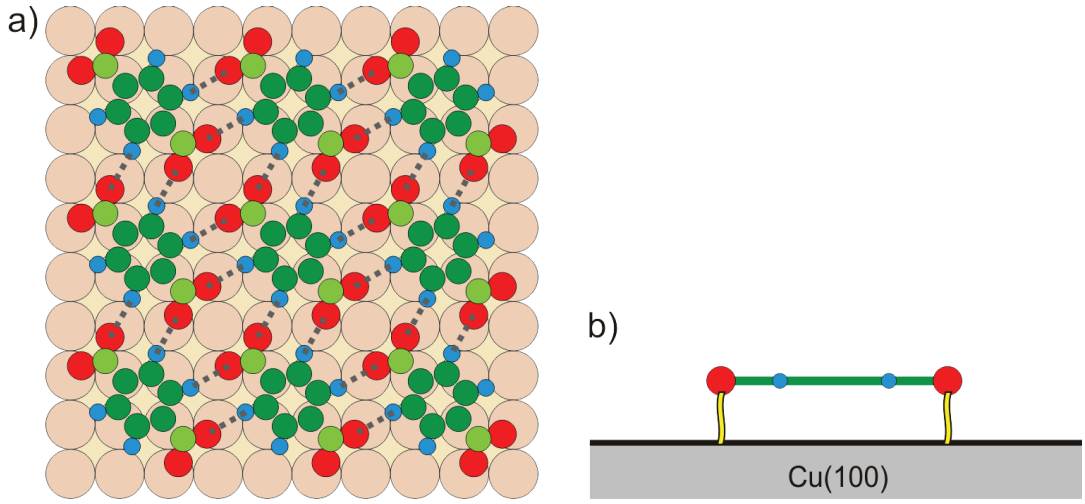


Figure 7.2: (a): top view of hydrogen-bonded deprotonated TPA molecules adsorbed on Cu(100). (b): side view schematic representation of deprotonated TPA/Cu(100) resulting from STM, XPS and NEXAFS data.[161]

sorption heights measured by NIXSW offer further insight into the interaction of the molecule with the substrate and the comparison with DFT results highlights a new shortcoming of the PBE functional.[164] The understanding of this prototypical system thus represents a fundamental basis for the development of highly-ordered organic molecules at metal surfaces.

7.2 Experimental details

This section is divided into four parts. In the first part, experimental details about the preparation of the TPA layer and an estimate of its coverage are reported. In the second part, acquisition parameters of photoemission spectra, recorded during XSW experiments, are summarized and discussed. In the third and fourth parts, the background properties of XPS spectra and the line shapes of the C1*s* fitting components respectively are described. The experiments were performed at the beamline ID32 (ESRF, Grenoble) together with S. Subach (Forschungszentrum Jülich), A. Langner, S. Stepanow (Max Planck Institute for Solid State Research, Stuttgart) and H. Adler, S. Tait (Indiana University).

7.2.1 Sample preparation and coverage estimation

The goal of this chapter is to investigate the interaction between deprotonated TPA molecules (see Figure 7.3b) and the Cu(100) surface. To this end, a sub-monolayer needs to be prepared in order not to mix contributions from molecules in direct contact with the substrate and from molecules in the second layer.

We first focus on the procedure to follow in order to obtain deprotonated TPA molecules. STM and XPS studies[161] show that TPA molecules present three different phases for substrate temperatures in the range 190 K–400 K. The deprotonation of TPA molecules, i.e., transformation of the carboxyl groups into carboxylate upon H^+ detachment, starts gradually at room temperature and is completed upon 400 K annealing. Hence, after TPA deposition, the sample is annealed at 400 K for several minutes in order to obtain a uniform layer of deprotonated TPA molecules, all in the same chemical state. To obtain a sub-monolayer of deprotonated TPA molecules and estimate its coverage, we first prepare a reference monolayer and subsequently

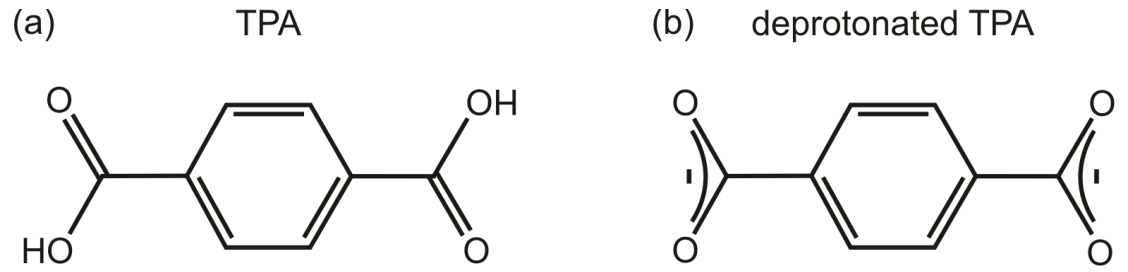


Figure 7.3: Molecular model of terephthalic acid (a), and doubly deprotonated terephthalic acid (b).

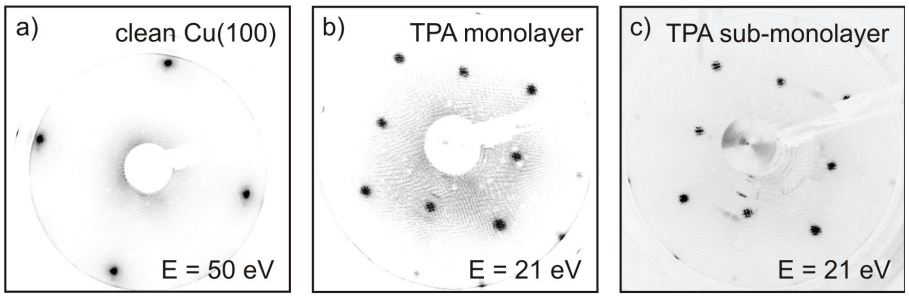


Figure 7.4: LEED images of the clean Cu(100) substrate (a), a monolayer TPA/Cu(100) (b), and a sub-monolayer TPA/Cu(100) (c). Energy (E) of the incident electron beam is also reported in the figures.

reduce the deposition time in order to achieve the desired coverage. This procedure is described below.

Before deposition, the Cu(100) crystal is prepared by repeated cycles of Ar^+ sputtering, followed by annealing at 800 K (see Figure 7.4a). Subsequently, organic molecular beam epitaxy from a Knudsen-cell evaporator is used to deposit TPA (99.9 %, purchased from Sigma Aldrich) for 30 minutes on a Cu(100) substrate kept at 420 K, and then TPA is annealed at the same temperature for 5 minutes (see Table 7.1). The molecular layer obtained is considered to be our monolayer reference of deprotonated TPA, for the following reasons:

First, from some preliminary and yet unpublished results[165] of temperature programmed desorption of TPA/Cu(100), there are indications of a second layer desorption peak at approximately 380 K. Therefore, by annealing at a temperature 40 K higher, the second layer should be fully desorbed. However, an additional compressed layer structure appears in the full monolayer; hence to prevent this, the right amount of TPA is directly deposited instead of desorbing multilayers.

Second and more important, a HREELS study[5] revealed that the bilayer presents

TPA coverage estimation				
preparation	deposition time [min]	T_sample [K]	T_annealing [K]	Coverage [ML]
monolayer	30	420	420	1.00 ± 0.01
sub-monolayer	20	310	400	0.79 ± 0.07

Table 7.1: Coverage estimation, expressed in monolayers (ML), of two different preparations of TPA on Cu(100). Deposition time, sample temperature during deposition and annealing temperature after evaporation of the molecules are also reported in the table.

OH and C=O stretch modes that are characteristic of intact TPA (Figure 7.3a) and absent in the first layer. This indicates that in the second layer, TPA does not undergo a deprotonation process that is induced by the substrate. Moreover, thanks to a detailed XPS study[161] of intact and deprotonated TPA adsorbed on Cu(100) (Figure 7.5a, top and bottom spectra, respectively), it is straightforward to distinguish the two TPA species just by inspection of C1*s* and O1*s* PE spectra. In

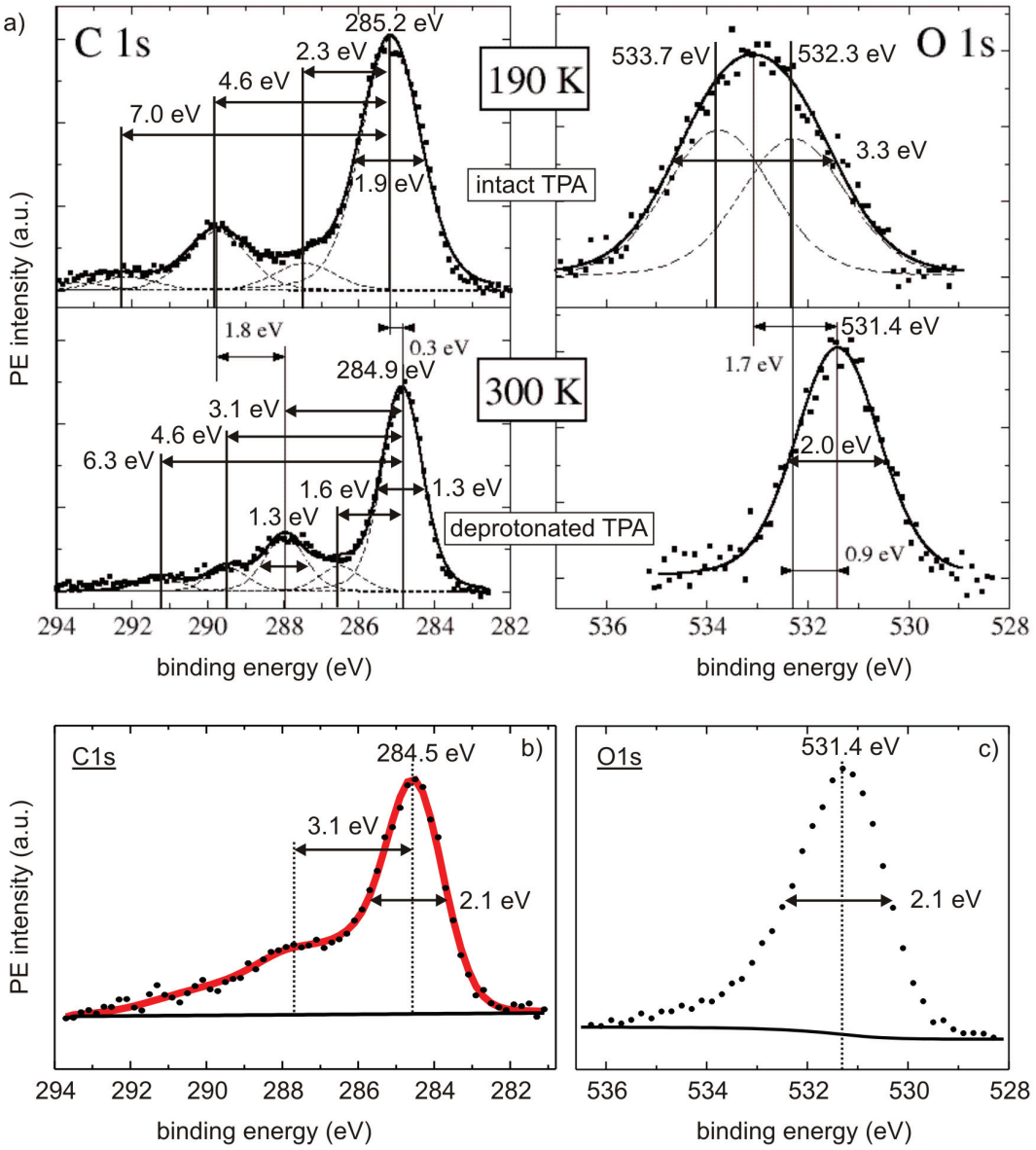


Figure 7.5: (a): figure from Stepanow et al.,[161] PE spectra C1*s* and O1*s* for a TPA layer prepared and measured at 190 K (upper graphs), and after annealing at 400 K for 30 min and measured at 300 K (lower graphs). C1*s* (b) and O1*s* (c) PE spectra of the TPA monolayer preparation. Each spectrum (black dots) in (b) and (c) is given by the sum of three fast-XPS (see section 7.2.2). The background is indicated by a black line and the envelope of all fitting components by the red line.

fact, since both C1s and O1s spectra (Figure 7.5b,c) of the present study have peak positions and FWHM very similar to the deprotonated TPA molecule (Figure 7.5a, bottom spectra), and there is no evidence of intact molecules in the second layer, we conclude that we have indeed achieved our goal of preparing a reference monolayer of deprotonated TPA.

In order to prepare a sub-monolayer, TPA is deposited for 20 minutes on a Cu(100) crystal held at room temperature and subsequently annealed at 400 K for a few minutes (see Table 7.1). The corresponding LEED pattern, shown in Figure 7.4c, represents the 3×3 molecular superstructure. From the comparison of the corresponding C_C/C_{Cu} ratio with the monolayer reference (Table 7.1), a TPA coverage of 0.79 ± 0.07 follows (see section 4.2.1). This coverage is ideal for NIXSW experiments because it is below the monolayer limit but still large enough to have a sufficiently strong photoemission signal to allow differential analysis of carbon species within the same TPA molecule, as described in section 7.3.1.

7.2.2 XPS acquisition parameters of NIXSW experiments

Acquisition parameters of the PE spectra are summarized in Table 7.2 for each of the recorded lines. Three different kind of photoemission spectra are considered.

- The first, fast-XPS, is measured at relatively high pass energy (94 eV) and with a small number of repeats (2). These spectra are acquired in order to check the integrity of the molecular layer before and after XSW experiments.

XPS data acquisition parameters									
element	C1s			O1s			Cu2p		CuLMM
XPS type	fast	HR	XSW	fast	HR	XSW	fast	XSW	XSW
$h\nu$ window [eV]	-	-	6	-	-	6	-	6	6
$h\nu$ step [eV]	-	-	0.15	-	-	0.15	-	0.15	0.15
E_k window [eV]	20	16	17	20	16	15	20	45	30
E_k step [eV]	0.2	0.2	0.3	0.2	0.2	0.3	0.2	0.3	0.3
time/step [ms]	500	500	500	500	500	500	500	500	50
pass energy [eV]	94	47	94	94	47	94	94	94	94
repeats	2	30	4	2	20	4	2	1	2

Table 7.2: Data acquisition parameters of fast, high resolution (HR), and XSW photoemission spectra measured on TPA/Cu(100). Photon energy window, photon energy step, kinetic energy window, kinetic energy step, time per step, pass energy and number of repeats are reported for PE spectra of lines C1s, O1s, Cu2p, CuLMM.

- The second, HR-XPS, is measured at lower pass energy (47 eV) and higher number of repeats (30) in order to have higher resolution and better statistics at the same time. In fact, these spectra are used to develop the XPS fitting model consisting of the several components into which, for instance, the C1s spectrum can be decomposed.

- The third, the PE spectra of a standing wave experiments (XSW-XPS), are recorded at the same pass energy as the fast-XPS (94 eV), but with a higher number of repeats (4) in order to achieve better statistics and a larger energy step (0.3 eV) in order to decrease the acquisition time.

The photon energy window (6 eV) and its energy step (0.15 eV) are chosen identically for each XSW experiment. On the other hand, the kinetic energy window of the XSW-XPS spectra differs depending on the element. The largest value, 45 eV, is for the two core lines Cu2$p_{3/2}$ and Cu2$p_{1/2}$, separated from each other by 20 eV. It follows then the broad Auger CuLMM peak with an energy window of 30 eV. Finally, while only one O1s species is present, in order to differentiate the two chemically shifted carbon peaks, the C1s spectrum is recorded in an energy window that is slightly bigger. Since high statistics are not required for the CuLMM peak, a lower acquisition time per energy step, 50 ms instead of 500 ms, is selected. For analogous reasons, the number of repeats of the copper signals is set to 1 or 2, instead of 4, as for carbon and oxygen spectra, where higher statistics is required, due to the lower signal-to-noise ratio, for better determination of their structural parameters.

7.2.3 XPS background

Two aspects of the background definition procedure are discussed here: the background type and the $AvWidth$ (Table 7.3), i.e., the number of data points averaged to determine the edge intensities of the background (see section 4.2.3).

For C1s spectra, a linear background is chosen because there is no evidence for

element	C1s	O1s	Cu2p	CuLMM
BG type	linear	Shirley	Shirley	Shirley
$AvWidth$	3	5	5	4

Table 7.3: Background type and $AvWidth$ of C1s, O1s, Cu2p, CuLMM PE spectra measured during XSW experiments.

a Shirley background or any other type of non-linear background (Figures 7.5b and 7.7). The corresponding $AvWidth$ is set to 3 in order to maximize the energy window in which the background is defined and without including signal contributions in the average for defining the background edge points. O1s spectra have a shallow Shirley type background (Figure 7.5c), with $AvWidth = 5$. Thanks to the smaller width of the oxygen signal with respect to the corresponding energy window (Figure 7.11a), it is possible for O1s PE spectra to average a higher number of points for the definition of the background edge intensities than for C1s PE spectra, in which the carbon signal occupies essentially all the acquired energy window (Figure 7.7a). The same arguments are valid for Cu2p and CuLMM lines. Furthermore, in these last two cases the Shirley background is even more pronounced.

7.2.4 Line shapes of the fitting components

The line shapes of core-level peaks were discussed in section 4.2.4. In this experiment, only the C1s spectrum is decomposed into multiple fitting components representative of carbon atoms in different chemical states. Main peaks are fitted with a Voigt function, approximated by a linear combination of a Gaussian (90%) and a Lorentzian (10%), while a pure Gaussian function is adopted for satellite components. The parameters reported above minimize the standard deviation of the residuals of the fit. Both oxygen and copper photoemission peaks are not decomposed into several components since there are no chemically shifted species to differentiate; instead *Region*, i.e., spectrum area after background subtraction, is considered to be the photoelectron yield signal.

7.3 Experimental results

In this section, NIXSW results of TPA carbon and oxygen atoms and of the copper substrate are presented. Particular attention is paid to the development of the XPS fitting model for the C1*s* PE spectrum and to the comparison of Cu2*p* and CuLMM structural parameters. The resulting adsorption geometry of TPA/Cu(100) and the interpretation of the adsorbate-adsorbate and adsorbate-metal interactions are discussed in section 7.4.

7.3.1 Carbon

XPS fitting model

In order to develop a fitting model for the C1*s* XSW-XPS spectra, three steps are followed. First, the C1*s* high resolution photoemission spectrum[161] of TPA/Cu(100) is analyzed and taken as our reference spectrum. Second, a fitting model is developed for C1*s* HR-XPS of present work (section 7.2.2). As a third and final step, the latter model is transferred to XSW-XPS spectra and the corresponding structural parameters are found.

The C1*s* PE spectrum measured by Stepanow et al.[161] (Figure 7.6) is decomposed by the authors in five components. The most intense peak at 284.9 eV is attributed to the aromatic ring carbons; the smaller peak at 1.6 eV higher binding energy is ascribed to possible final state effects or partial decomposition of the TPA molecules at defects on the copper surface; the component at 288 eV is assigned to carbon atoms of the carboxylate groups; the smaller peak at approximately 289.5 eV is not discussed; finally, the last high-energy component is attributed to a π-π^* shakeup transition of the aromatic system. We will see how some of the open questions about the origin and the nature of the fitting components will be answered in the present section.

The HR-XPS reported in Figure 7.7a consists of an intense photoemission line, followed by a smaller and clearly resolved peak and finally a broad tail at high binding energies. Following the model of the higher resolution spectrum described above,[161] HR-XPS is also decomposed in five components: *Aro-Main*, *Aro-Sat*, *Carb-Main*, *Carb-Sat* and *Sat*. In particular, we tentatively introduce two main components plus their corresponding satellite peaks (section 4.2.4), representing carbon atoms

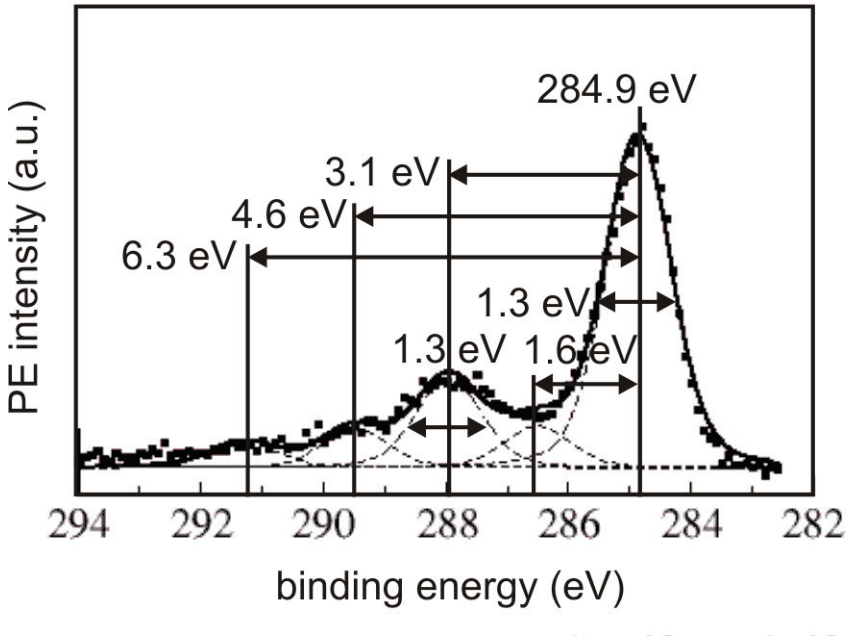


Figure 7.6: Figure from Stepanow et al.:[161] C1*s* PE spectrum of a TPA layer prepared at 190 K, annealed at 400 K for 30 min, and measured at 300 K (see section 7.2.1).

of the aromatic ring and of the carboxylate groups, respectively. The higher binding energy of *Carb-Main* compared to *Aro-Main* can be rationalized in an initial state picture. In fact, carboxylate carbons are bound to oxygen atoms which are more electronegative than carbon atoms forming the aromatic ring. Finally, at higher binding energy, the spectrum is modeled by a satellite peak, discussed in more detail below.

Before fitting HR-XPS, the positions of *Aro-Sat*, *Carb-Main*, *Carb-Sat* and *Sat* are fixed at +1.6 eV, +3.1 eV, +4.6 eV, +6.3 eV respectively relative to *Aro-Main* position, which is left free to be fitted. The relative positions listed above follow from C1*s* spectrum[161] reported in Figure 7.6. Moreover, in order to prevent some of the peaks from having an unphysically large width upon fitting, *Carb-Main* and *Carb-Sat* FWHM are constrained to be equal to *Aro-Main* and *Aro-Sat* FWHM, respectively. Given these constraints, HR-XPS is fitted and provides the model of Figure 7.7a with the features reported in the corresponding inset table. As a result of the fit, the area ratio $(Aro\text{-}Main + Aro\text{-}Sat)/(Carb\text{-}Main + Carb\text{-}Sat)$ is equal to 3. Therefore, the fitting model just described is consistent with the stoichiometry of TPA, consisting of 6 aromatic carbons and 2 carboxylate carbons.

As already discussed in section 7.2.2, HR-XPS and XSW-XPS are measured with different acquisition settings, in particular with different pass energies (47 eV and

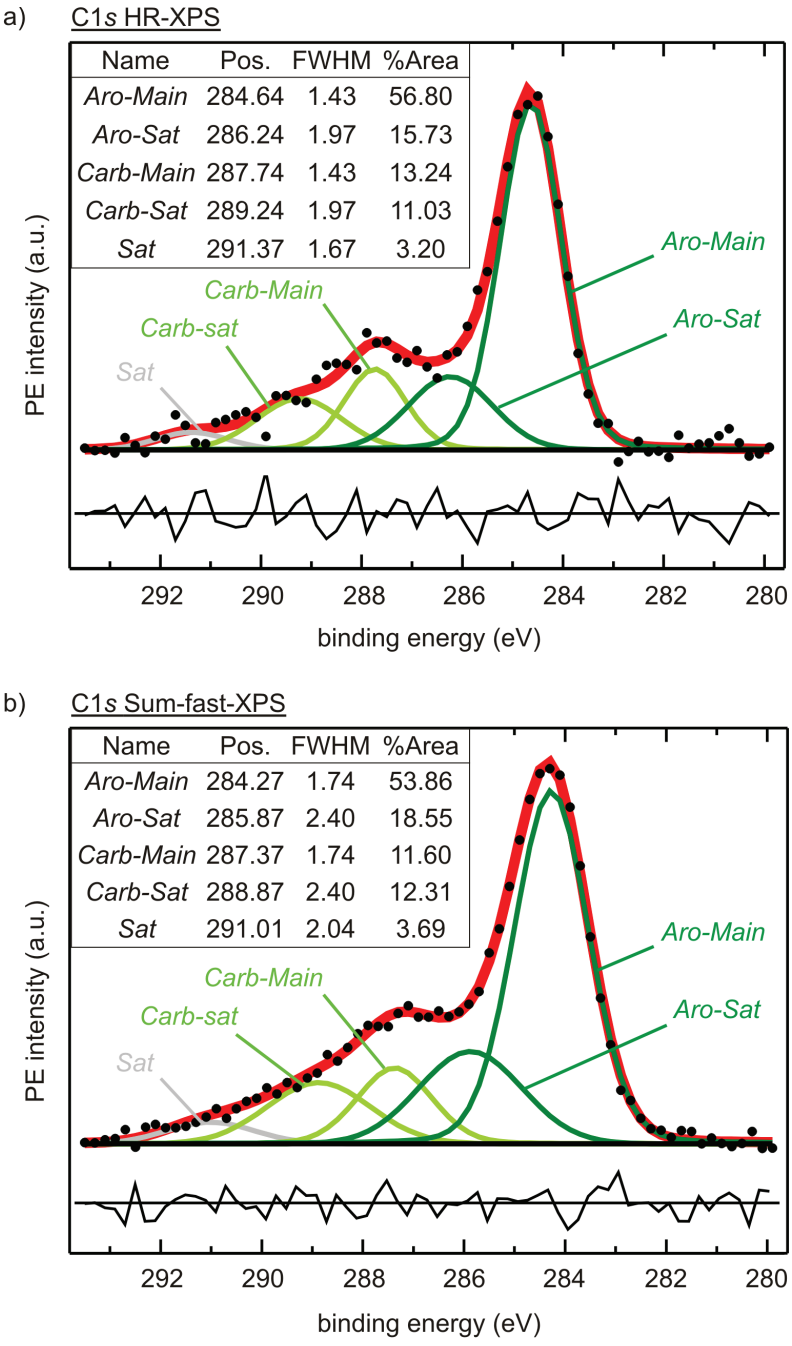


Figure 7.7: (a): C1*s* HR-XPS (pass energy = 47 eV, energy window = 16 eV, energy step = 0.2 eV, time/step = 500 ms, repeats = 30) measured at $h\nu = 3416$ eV. (b): C1*s* Sum-fast-XPS (pass energy = 94 eV, energy window = 20 eV, energy step = 0.2 eV, time/step = 500 ms, repeats = 31) measured at $h\nu = 3416$ eV. In the top-left table of both (a) and (b): position (eV), FWHM (eV), and relative area (%) of the fitting components *Aro-Main* and *Aro-Sat* (green line), *Carb-Main* and *Carb-Sat* (light green line), *Sat* (gray line) are reported. Background: thick black line. Residuals (thin black line below the spectrum) result from the subtraction of the whole spectrum (black dots) and the sum of all components (thick red line).

94 eV, respectively). Therefore, the HR-XPS fitting cannot be directly transferred to XSW-XPS data and needs to be adapted to a PE spectrum measured with similar settings as XSW-XPS. According to Table 7.2, fast-XPS is also acquired with pass energy equal to 94 eV. In order to increase the statistics, we consider the sum of seven fast-XPS spectrum (Figure 7.7b). From the comparison of the main peak of HR-XPS (Figure 7.7a) and of Sum-fast-XPS (Figure 7.7b), we estimate that the FWHM in the latter spectrum is approximately 1.22 times larger than in HR-XPS. As a consequence, the HR-XPS fitting model is then applied to Sum-fast-XPS with the same constraints discussed above, but with the FWHM of all components increased by a factor of 1.22. In this case too, the stoichiometry of the molecule is reflected by the area ratio of the fitting components.

Finally, we note that, for better consistency of the models relative to spectra acquired with different settings, the same energy window, linear background and $AvWidth$ (section 4.2.3) are defined for each kind of C1s spectrum: HR-XPS, fast-XPS and XSW-XPS. The model described above is then applied to XSW-XPS spectra, and the corresponding photoelectron yield and structural parameters are presented below.

Photoelectron yield

Since the areas of the five components described above are independent of each other, the corresponding photoelectron yields are also analyzed for each of the three available NIXSW data sets. A summary of all structural parameters (P_c, F_c) is reported in Table 7.4. Results relative to Sat are not presented there, because due to the very

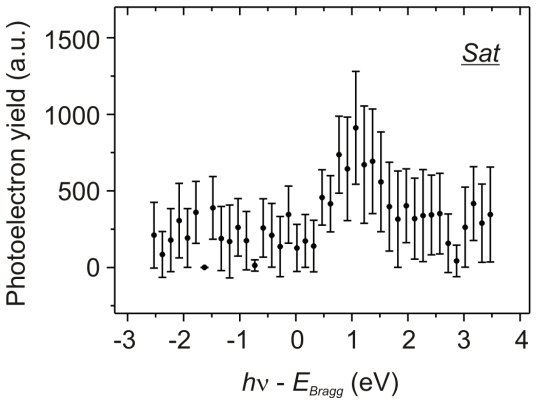


Figure 7.8: Photoelectron yield (black dots and relative error bars) of *Sat* (data set 1) displayed as a function of the photon energy relative to the Bragg energy, after normalization by the photon beam intensity.

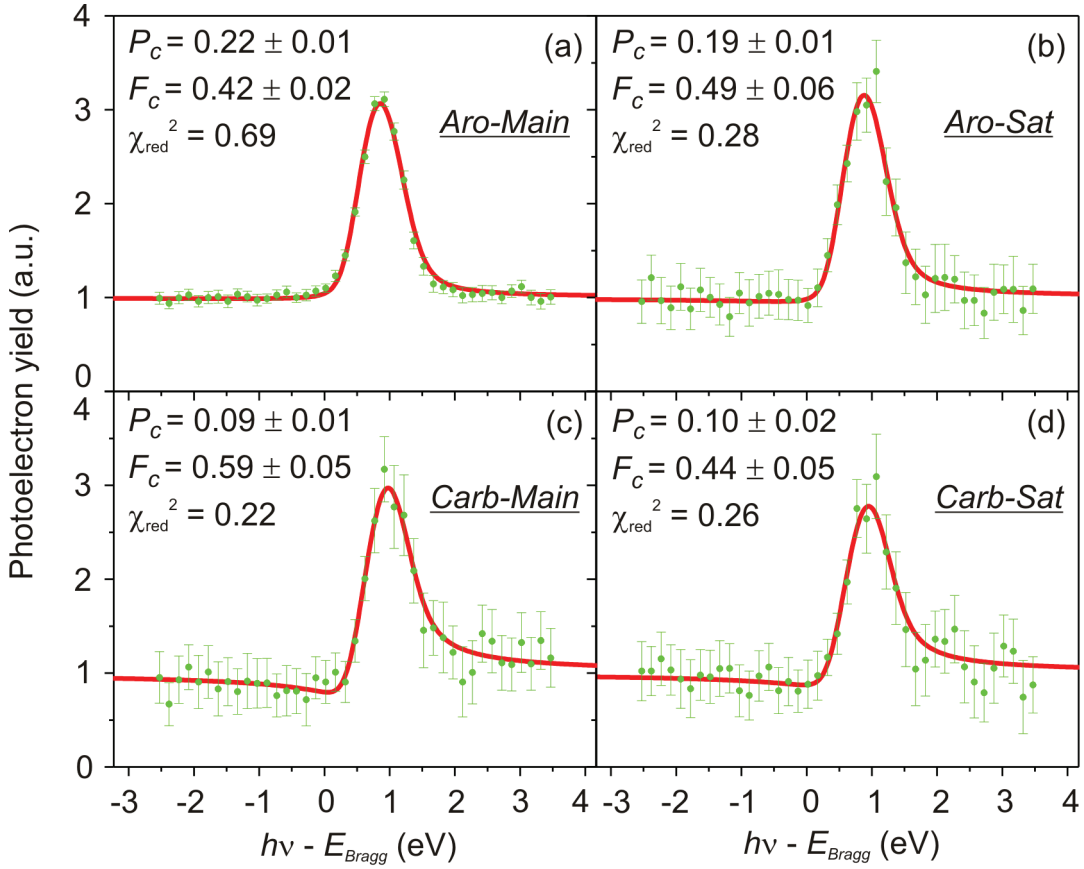


Figure 7.9: Photoelectron yield (green dots and relative error bars, data set 1 in Table 7.4) of *Aro-Main* (a), *Aro-Sat* (b), *Carb-Main* (c), *Carb-Sat* (d) displayed as a function of the photon energy relative to the Bragg energy (3427.63 eV). Fitting curve (red) together with results of the fit: coherent position (P_c), coherent fraction (F_c), and reduced χ^2 are also reported in the figure.

small signal-to-noise ratio, the corresponding photoelectron yield profiles do not provide any structural information, as suggested by the large scatter of data points in Figure 7.8. In contrast, the remaining four signals exhibit well-defined profiles, as shown in Figure 7.9. From a first inspection, we note that *Aro-Main* and *Aro-Sat* are characterized by similar photoelectron yields, and also *Carb-Main* and *Carb-Sat* profiles show some similarities. Moreover, *Aro-Sat*, *Carb-Main* and *Carb-Sat* have a common feature, i.e., larger error bars than *Aro-Main*. This follows from the larger signal-to-noise ratio of the most intense component as compared to the others. However, for each signal, the scatter of the data points around the fitting curve is rather small, as testified by the reduced χ^2 whose value is equal to or lower than 1.

Looking more closely at the average values from Table 7.4, we see that indeed *Aro-Main* and *Aro-Sat* both have identical P_c and F_c within the error. The main difference between the two is the size of the corresponding error bars, as shown in

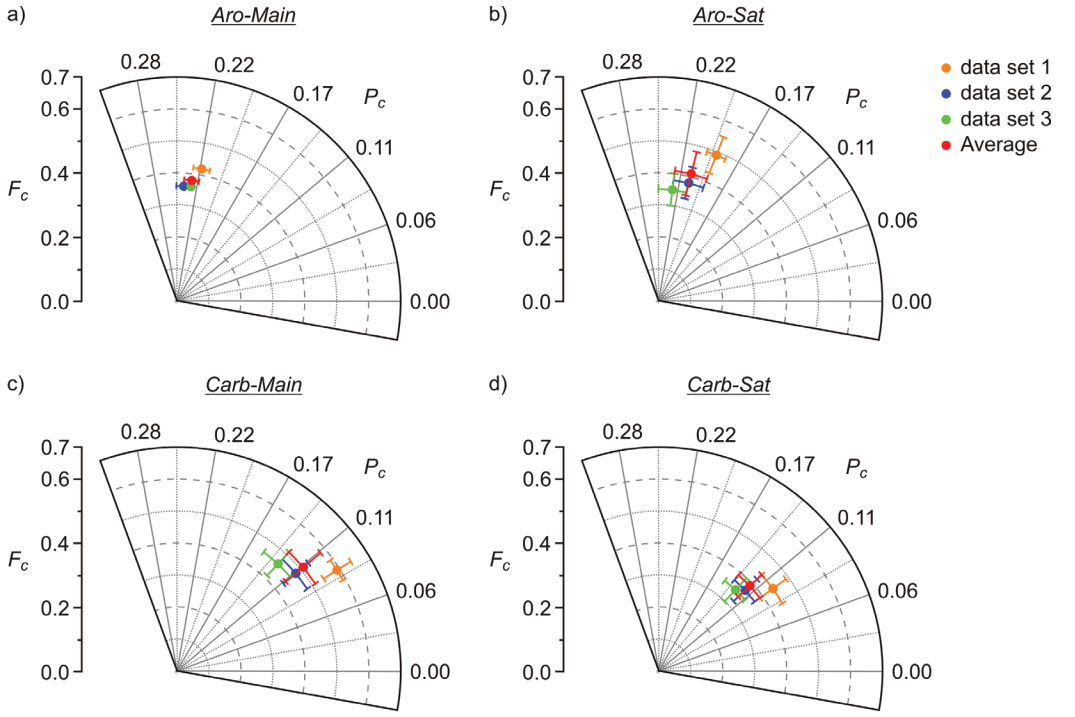


Figure 7.10: Argand diagram of *Aro-Main*, *Aro-Sat*, *Carb-Main* and *Carb-Sat* structural parameters (P_c, F_c) with relative error bars of data sets 1 (orange), 2 (blue), 3 (green) and their average (red).

the Argand diagrams of Figure 7.10a,b. This conclusively proves that *Aro-Main* and *Aro-Sat* have the same structural properties and originate from the same carbon atoms of TPA aromatic ring. Hence, on the basis of this result, *Aro-Sat* represents a satellite peak of *Aro-Main*, appearing at higher binding energies because of inelastic shakeup processes (section 4.2.4). Having established that *Aro-Main* and *Aro-Sat* carry the same structural information, we refer to the average values of *Aro-Main*, $P_c = 0.23 \pm 0.01$ and $F_c = 0.38 \pm 0.03$, as representative of the aromatic carbons position.

On the other hand, *Carb-Main* and *Carb-Sat* have the similar coherent positions (0.11±0.02 and 0.12±0.02), while their coherent fractions (0.51±0.07 and 0.39±0.05, respectively) are different. The difference between NIXSW positions of *Aro-Main* and *Carb-Main* confirm the conclusion from Figure 7.7a that the peak at 284.64 eV and 287.74 eV correspond to different carbon species.

The lower F_c of *Carb-Sat* (Figure 7.10b,c) suggests that this component results from the superposition of multiple contributions. In particular, a satellite peak of the carboxylate carbons is expected to occur in that energy region. However, as

already seen for *Aro-Sat*, satellite peaks carry the same structural information of the corresponding main components, without altering either P_c nor F_c. Therefore, there must be another signal which decreases the coherent fraction without affecting the coherent position. We assign this role to carboxylate carbons of TPA molecules adsorbed at the step edges. In fact, STM experiments reveal that TPA molecules adsorb flat at step edges preferably with one carboxylate group facing the step.[166] Thereby, oxygen atoms of TPA at steps edges will be in a rather different chemical environment as compared to inside an island. As a consequence, the carbon atoms bound to them will be also indirectly affected. They may experience a chemical shift towards higher binding energy, hence their presence in correspondence of *Carb-Sat*, and result at different adsorption heights depending on the local chemical environment. For the reasons explained above and to be consistent with what was already done for the aromatic carbons, the structural parameters representative of the average carboxylate carbons adsorption height are those of *Carb-Main* (Table 7.4).

To conclude, C1*s* NIXSW data show that deprotonated TPA molecules adsorb on Cu(100) with their aromatic rings at 2.22 ± 0.02 Å [$= (1 + P_c) \times d_{\mathrm{Cu(200)}}$, where $d_{\mathrm{Cu(200)}} = 1.807$ Å] and the carboxylate carbons at 2.01 ± 0.04 Å above the surface (Table 7.4). The gas-phase planar geometry of the molecule is thus bent upon adsorption on the copper surface. Moreover, the 25% lower F_c of the aromatic carbons compared to the carboxylate ones suggests a further distortion of the carbon ring. We refer to section 7.4.1 for a more detailed discussion of the TPA adsorption geometry, which also includes oxygen data to which we now turn.

C1s results												
C1s	*Aro-Main*			*Aro-Sat*			*Carb-Main*			*Carb-Sat*		
data set	P_c	d_c	F_c	P_c	d_c	F_c	P_c	d_c	F_c	P_c	d_c	F_c
1	0.22 (1)	2.21 (2)	0.42 (2)	0.19 (1)	2.15 (2)	0.49 (6)	0.09 (1)	1.97 (2)	0.59 (5)	0.10 (2)	1.99 (4)	0.44 (5)
2	0.24 (1)	2.24 (2)	0.36 (2)	0.21 (2)	2.19 (4)	0.38(5)	0.11 (2)	2.01 (4)	0.48 (5)	0.12 (2)	2.02 (4)	0.37 (5)
3	0.23 (0)	2.22 (0)	0.36 (1)	0.23 (2)	2.22 (4)	0.35(5)	0.13 (2)	2.04 (4)	0.46 (5)	0.13 (2)	2.04 (4)	0.35 (5)
Average	0.23 (1)	2.22 (2)	0.38 (3)	0.21 (2)	2.19 (4)	0.41(7)	0.11 (2)	2.01 (4)	0.51 (7)	0.12 (2)	2.02 (4)	0.39 (5)

Table 7.4: Coherent position (P_c), coherent fraction (F_c) and adsorption height d_c (Å), calculated as $(P_c+1)\times d_{\mathrm{Cu(200)}}$ (where $d_{\mathrm{Cu(200)}} =$ 1.807 Å) are reported for each data set labeled from 1 to 3, followed by the average values of all data sets. $d_{\mathrm{Cu(200)}}$ is the distance between two (200) Cu planes and is calculated as $d_{\mathrm{Cu(200)}} = a_{\mathrm{Cu}}/2$, where $a_{\mathrm{Cu}} = 3.6149$ Å [167] is the Cu lattice constant at room temperature.

7.3.2 Oxygen

In the case of intact TPA molecules adsorbed on Cu(100) two different chemical species of oxygen are present in each of the two acid groups of TPA: one which forms a double bond with a carbon atom and another which is bound to one hydrogen and one carbon atom (see Figure 7.3a). Photoemission spectroscopy can distinguish between the two oxygen species, since they are chemically shifted by about 1.5 eV, as shown by Stepanow et al.[161] (see Figure 7.5a top right panel). However, if TPA is deprotonated (Figure 7.3b), as in our experiments (section 7.2.1), both O atoms of the carboxylate group have the same bonding to the C atom; hence only one oxygen species is expected in the corresponding PE spectra. In fact, both the PE spectrum reported by Stepanow et al.[161] and the PE spectra of the present study reveal the presence of only one O1*s* peak of FWHM $\approx$ 2 eV at 531.4 eV, as is shown in Figure 7.5a (bottom right panel) and in Figure 7.5c, respectively.

In submonolayer TPA on Cu(100), on which NIXSW measurements were carried out, all molecules are deprotonated after annealing at 400 K (section 7.2.1), hence all oxygen atoms are in the same chemical environment[5,161] and presumably also at the same adsorption height. The asymmetric shape of O1*s* HR-XPS (Figure 7.11a) is assigned to the O1*s* satellite peak (section 4.2.4), yielding the tail in the PE intensity at high binding energies. In fact, an attempt to fit the O1*s* spectrum with two

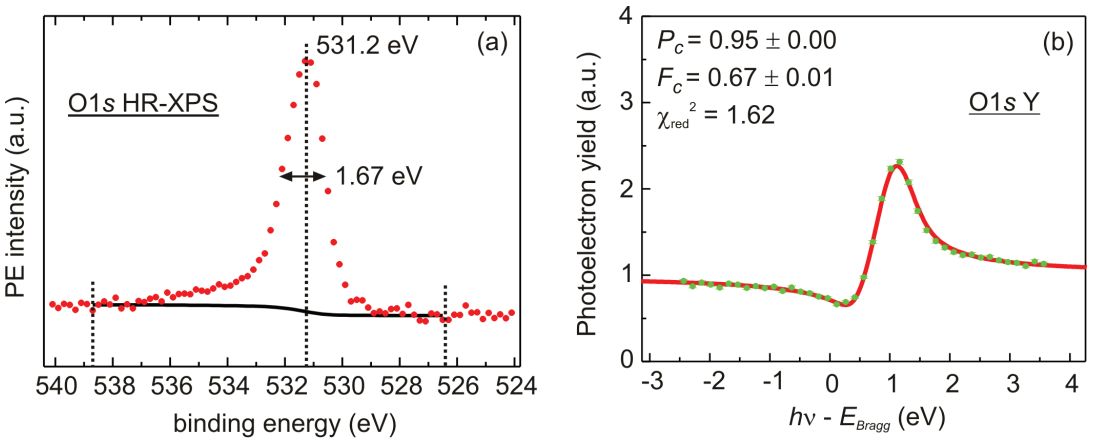


Figure 7.11: (a): O1*s* HR-XPS (red dots) (pass energy = 47 eV, energy window = 16 eV, energy step = 0.2 eV, time/step = 500 ms, repeats = 20) measured at hν = 3416 eV; background: black line. (b): Photoelectron yield (green dots and relative error bars, data set 3, Table 7.5) of O1*s* *Region* as a function of the photon energy relative to the Bragg energy (3427.84 eV). Fitting curve (red) together with results of the fit: coherent position (P_c), coherent fraction (F_c), and reduced χ^2 are reported in the figure.

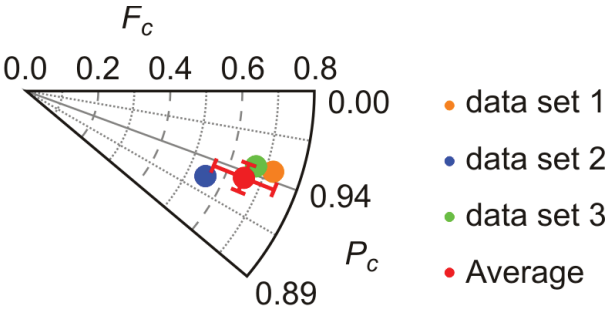


Figure 7.12: Argand diagram of O1*s* *Region* structural parameters (P_c, F_c) with relative error bars of data sets 1 (orange), 2 (blue), 3 (green) and their average (red).

components, *Main* and *Sat*, located at the dominant photoemission peak and in the high binding energy tail, respectively, provides identical structural parameters for both signals within the error, also equal to *Region* results (Table 7.5). This is a further indication that there are no oxygen species to differentiate. Although oxygen atoms of TPA at step edges may be in a slightly different chemical environment and likely at different vertical positions, as compared to those inside an island, this difference is not revealed by NIXSW, probably due to the small fraction of molecules at the step edges. Therefore, the entire O1*s* PE intensity after background subtraction (*Region*, section 4.2.3) is taken as the oxygen photoelectron yield. An example (data set 3) of O1*s* photoelectron yield is reported in Figure 7.11b, where the small error bars follow from the high signal-to-noise ratio of the O1*s* PE spectrum (Figure 7.11a).

Three NIXSW data sets are measured and the corresponding structural parameters are summarized in Table 7.5 and in the Argand diagram of Figure 7.12. All data sets yield similar coherent positions but different coherent fractions. In fact, the coherent fraction of data set 2 (0.55 ± 0.01) is approximately 20% smaller than F_c of the other two data sets (≈ 0.70), although all experiments are performed on

O1*s* results			
O1*s*	*Region*		
data set	P_c	d_c	F_c
1	0.95 (0)	1.72 (0)	0.72 (1)
2	0.93 (0)	1.68 (0)	0.55 (1)
3	0.95 (0)	1.72 (0)	0.67 (1)
Average	0.94 (1)	1.70 (2)	0.65 (9)

Table 7.5: Coherent position (P_c), coherent fraction (F_c) and adsorption height d_c (Å), calculated as $P_c \times d_{\mathrm{Cu(200)}}$ (where $d_{\mathrm{Cu(200)}} = 1.807$ Å), are reported for each O1*s* XSW data set labeled from 1 to 3, followed by the average values of all data sets.

the same sample preparation. Since coherent fractions are relatively high, compared to $F_c = 0.38 \pm 0.03$ of the aromatic carbons, and considering that coherent positions do not scatter significantly, in the following we will refer to the average values of all the measured data sets, i.e., $P_c = 0.94 \pm 0.01$ and $F_c = 0.65 \pm 0.09$. The corresponding adsorption height of oxygen atoms is then given by $P_c \times d_{\mathrm{Cu(200)}} = 1.70 \pm 0.02$ Å (where $d_{\mathrm{Cu(200)}} = 1.807$ Å). If one substrate interlayer spacing $d_{\mathrm{Cu(200)}}$ is added, then oxygens would result at 3.52 ± 0.02 Å, approximately 1.5 Å above the carbons of the carboxylate groups. This possibility can be therefore confidently excluded because it is implausible. To conclude, we note that the relatively high coherent fraction of 0.65 ± 0.09 suggests a unique adsorption for oxygen atoms, as expected from the symmetry of deprotonated TPA (Figure 7.3b) and from the analysis of the O1*s* PE spectrum.

7.3.3 Copper

Two different copper signals are measured: the Cu2$p_{3/2}$ core-level line, and the CuLMM Auger line. As was already discussed in section 3.4.2, in order to fit the structural parameters P_c and F_c accurately, it is necessary to take into account the angular dependence of the photoemission through the nondipolar correction parameters, which enter directly into the expression for the photoelectron yield generated by an x-ray standing wave (equation 3.46). While the expression for the nondipolar parameters in case of photoemission from an initial s-state is known,[18,44] the effect of the angular dependence of photoemission from an initial state different than s, e.g., p or d, on the XSW formula has not yet been formulated. In contrast, an Auger monitored XSW experiment does not need nondipolar correction terms, because the Auger process is independent of the direction of the primary photon beam; hence, there is no forward/backward asymmetry (section 3.4.3). As a consequence, in the case of an Auger peak, the expression of the photoelectron yield generated by a standing wave field (equation 2.17) is strictly exact without taking into account nondipolar parameters. Therefore, the structural parameters of the CuLMM Auger signal can be used as a reference to assess the role of nondipolar terms on the Cu2p signal. In the following, we first discuss the results corresponding to the Cu2$p_{3/2}$ line, and then the ones corresponding to the CuLMM Auger peak.

Figure 7.13a shows a PE spectrum of the Cu2$p_{3/2}$ core level and indicates the energy window (between the two dotted lines) in which the corresponding photoelectron yield, i.e., PE intensity after background subtraction (*Region*), is defined. As there is no analytical expression for the nondipolar parameters of an initial p state, two different sets of values are tested. First, the XSW formula developed for initial s state is assumed to also be valid for Cu2p. Nondipolar parameters are consequently calculated under the assumption of $\Delta = 0$, because they are not defined for an initial p state (see section 3.4.2, equation 3.51). We refer to this set of values as the approximated nondipolar parameters (*approx ndp*). Second, Cu2p experimental photoelectron yield is fitted within the framework of the dipole approximation, disregarding the higher order terms completely. We refer to this set of values as *no ndp*. The structural parameters of the Cu2p signal, resulting from the use of the two sets of nondipolar parameters described above, are summarized in Table 7.6 together with their average values. The corresponding photoelectron yield profiles and fitting curves (data set 2) are reported in Figure 7.13c,d. At first glance, they look identical, although a closer look at the central profile region in panels c and d of Figure 7.13

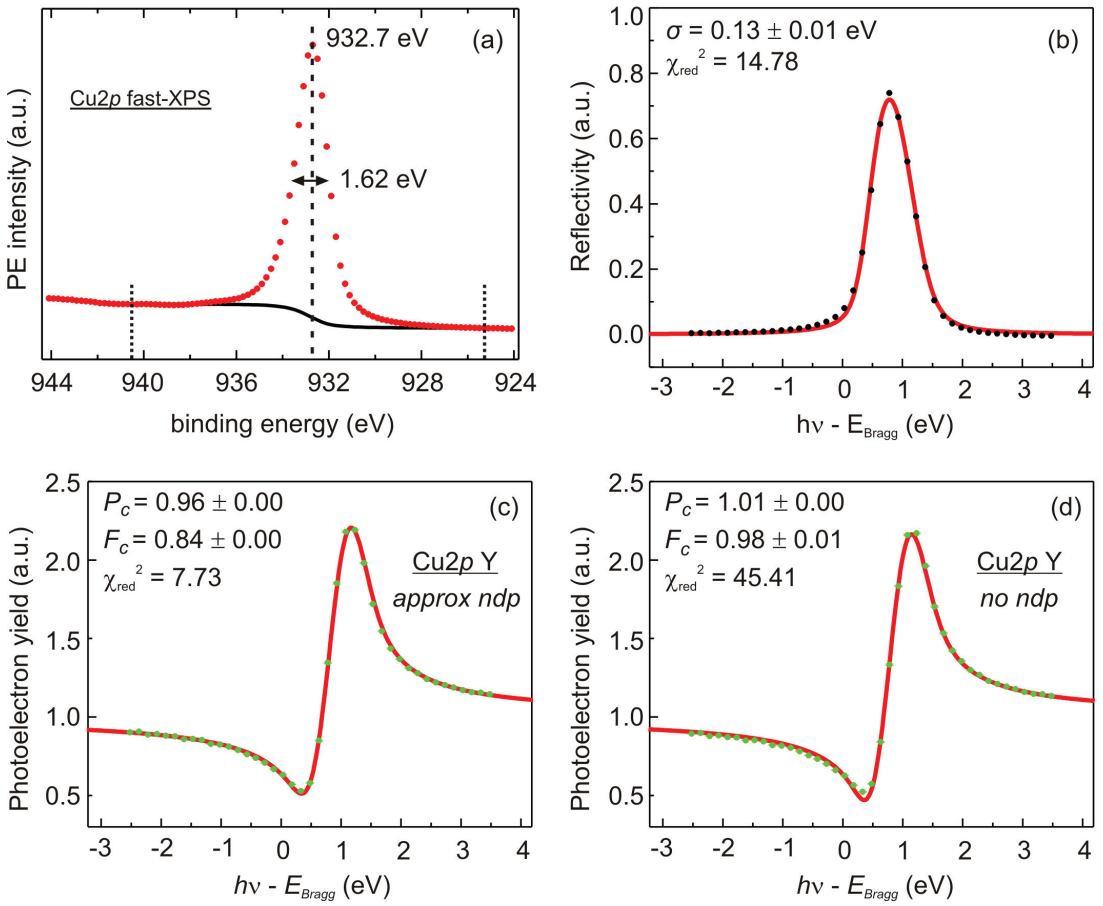


Figure 7.13: (a): Cu2*p* fast-XPS (red dots) (pass energy = 94 eV, energy window = 20 eV, energy step = 0.2 eV, time/step = 500 ms, repeats = 2) measured at hν = 3416 eV; background: black line. The region energy window where electron yield is defined is marked by the two dotted lines. (b): X-ray beam reflectivity (black dots) corresponding to experimental data displayed panels c and d. Fitting curve (red), fitted width σ of the Gaussian function (see section 3.3), and reduced χ^2 are also reported on the plot. (c-d): Cu2*p* photoelectron yield (green dots and relative error bars, data ses 2, Table 7.6), fitted using *approx ndp* (c) and *no ndp* (d) parameters displayed as a function of the photon energy relative to the Bragg energy (3427.77 eV). Fitting curve (red) together with results of the fit: coherent position (P_c), coherent fraction (F_c), and reduced χ^2, are reported in the figure.

reveals a better fit if *approx ndp* are used. This is also testified by the reduced χ^2 which turns out to be a factor six smaller compared to the case when *no ndp* are employed. Coherent fraction and position, resulting from the *approx ndp*, are both lower, 17% and 6% respectively, compared to the values obtained by disregarding nondipolar terms. The lower F_c and P_c follow directly from the analytical expression of the XSW formula (equation 3.46). Structural parameters of the copper substrate independent of the nondipolar parameters are given by the CuLMM signal, to which we now turn.

Cu results						
Cu	approximated ndp			no ndp		
data set	P_c	d_c	F_c	P_c	d_c	F_c
Cu2p 1	0.95 (0)	1.72 (0)	0.85 (0)	1.00 (0)	1.81 (0)	0.97 (1)
Cu2p 2	0.96 (0)	1.73 (0)	0.84 (0)	1.01 (0)	1.83 (0)	0.98 (1)
Average Cu2p	0.955 (5)	1.73 (1)	0.845 (5)	1.005 (5)	1.82 (1)	0.975 (5)
CuLMM				0.99 (0)	1.79 (0)	0.89 (1)

Table 7.6: Coherent position (P_c), coherent fraction (F_c) and vertical distance from the Bragg plane beneath d_c (Å), calculated as $P_c \times d_{Cu(200)}$ (where $d_{Cu(200)} = 1.807$ Å) are reported for each Cu2p XSW data set labeled 1 and 2, followed by the average values of the two data sets, and results of the CuLMM Auger signal.

Figure 7.14a shows the first Auger spectrum of an NIXSW scan recorded at photon energy 3425.25 eV. From the kinetic energy scale of the Auger electrons we can expect a probing depth of about 20 Å,[37] thus about 11 Cu layers. The coherent position, 0.99, is typical of metal surfaces,[168] while the coherent fraction, 0.89, is approximately 10% smaller than what is usually expected for single substrate crystals. At the same time, the small value of reduced χ^2 testifies the good quality of the fit, which corroborates the accuracy of structural parameters just presented. Furthermore, CuLMM results are also in perfect agreement with analogous values from Cafolla et al.[169] ($P_c = 0.99 \pm 0.02$, $F_c = 0.91 \pm 0.04$). In section 7.4.2 we will see that DFT calculations predict a buckling of the Cu surface upon TPA adsorption; however this occurrence can only rationalize a decrease in the coherent fraction of Cu of a

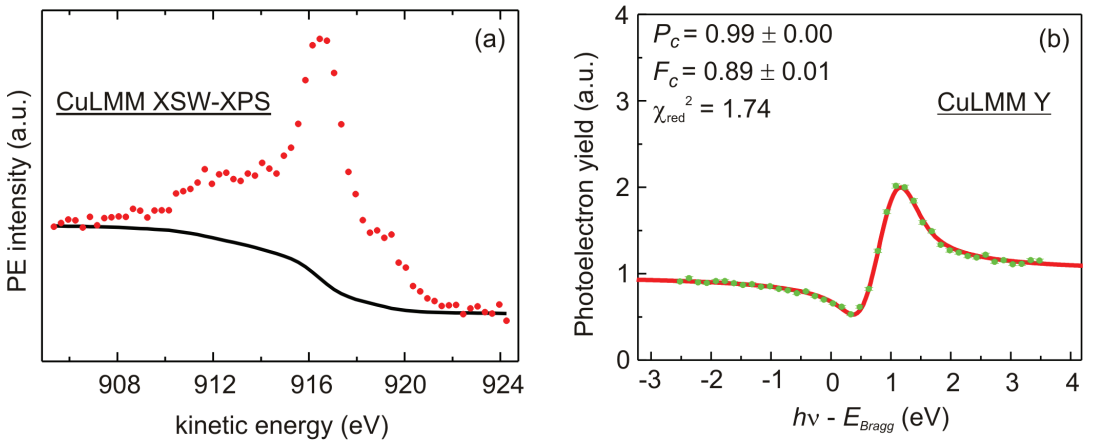


Figure 7.14: (a): CuLMM Auger spectrum (red dots) (pass energy = 94 eV, energy window = 30 eV, energy step = 0.3 eV, time/step = 50 ms, repeats = 2) measured at hν = 3425.25 eV; background: black line. (b): Photoelectron yield (green dots and relative error bars) of CuLMM region as a function of the photon energy relative to the Bragg energy (3427.77 eV). Fitting curve (red) together with results of the fit: coherent position (P_c), coherent fraction (F_c), and reduced χ^2 are reported in the figure.

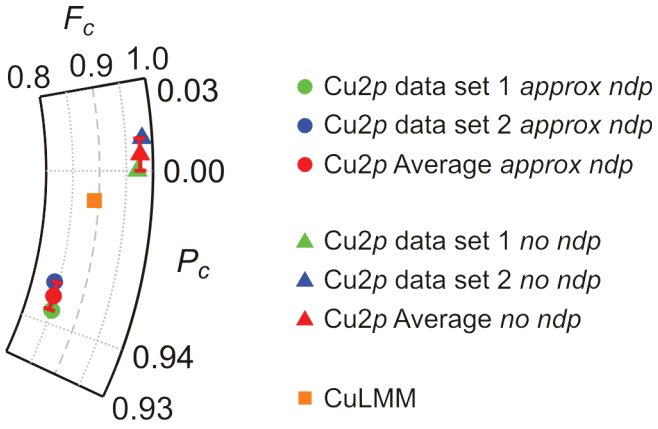


Figure 7.15: Argand diagram of Cu2*p* structural parameters (P_c, F_c) with relative error bars of data sets 1 (green), 2 (blue) and their average (red), resulting from the employment of approximated nondipolar parameters (circles), and no nondipolar parameters (triangles). CuLMM data point is marked by the orange square.

few percent, with respect to the ideal value of 1, and not of 10%, as the CuLMM signal reveals. To this end, a significant contribution to decrease the substrate coherent fraction can follow from the mosaicity of the Cu crystal that indeed leads to a broadening of the reflectivity curve (Figure 7.13b), $\sigma = 0.13 \pm 0.01$ eV, comparable with that of the Ag(110) crystal reflectivity profile (Figure 5.12c), $\sigma = 0.18 \pm 0.01$ eV, coupled to an average coherent fraction of the Auger signal $F_c = 0.88$.

A summary of all copper results presented above is reported in Figure 7.15. Structural parameters of Cu2*p*, using both sets of *ndp* values, are located relatively far from the CuLMM data point. In particular, P_c of the CuLMM data set is closer to P_c (Cu2*p*) resulting from the *no ndp* approach, while F_c of the CuLMM data set is closer to F_c (Cu2*p*) resulting from the *approx ndp* approach. We can therefore conclude that nondipolar terms play an important role in describing the photoelectron yield of core level in an initial non-*s* state and can considerably affect the resulting structural parameters, especially F_c, in agreement with other studies.[18,47]

Finally, since we cannot conclude anything from the Auger XSW signal about the surface relaxation of the Cu surface, as CuLMM line is not surface sensitive enough (see section 7.3.3), we will consider two cases. First, the surface does not relax and the topmost Cu layer is at the Bragg position. Second, the surface relaxes and, according to experiments[169,170] and calculations,[171] the topmost layer is expected to be 0.05 Å below the corresponding Bragg plane.

7.4 Discussion

In this section, the adsorption geometry of TPA on Cu(100) is discussed on the basis of NIXSW results presented in section 7.3. From the comparison with DFT calculations, a deeper insight into the molecule-metal and molecule-molecule interactions is achieved and an adsorption model for deprotonated TPA on Cu(100) is proposed.

7.4.1 Adsorption geomety of deprotonated TPA on Cu(100)

The discussion of the adsorption geometry of deprotonated TPA is based on the structural data measured by NIXSW (section 7.3) and summarized in Table 7.7. According to NIXSW measurements, the aromatic ring of TPA lies at 2.22 Å above the surface Bragg plane, the carbon atoms of the carboxylate groups are 0.21 Å lower, and the oxygen atoms are even closer to the surface, only 1.70 Å above the surface Bragg plane. This results in an arc-like geometry of TPA with the carboxylate groups pointing towards the surface, as is illustrated in Figure 7.16a,b. More-

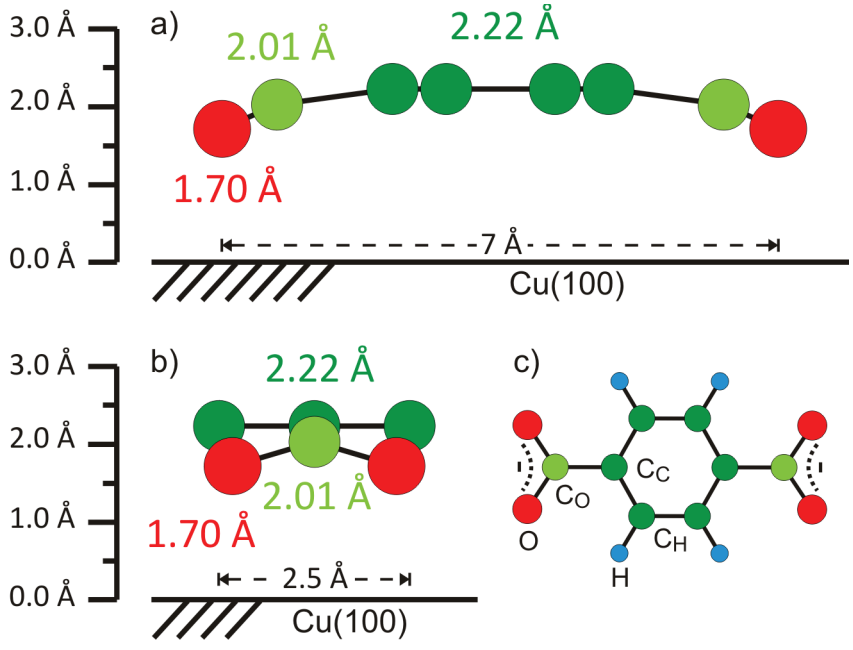


Figure 7.16: (c): ball-and-stick molecular model of deprotonated TPA, where nomenclature of different atomic species is specified. Long side view (a) and short side view (b) of the structural model of TPA adsorbed on Cu(100) as results from NIXSW experiments. Adsorption heights are reported following the same color code of the atoms: oxygens (red), carboxylate carbons (light green), aromatic carbons (dark green), hydrogens (light blue).

TPA results			
element	P_c	d_c (Å)	F_c
C_{aro}	0.23 (1)	2.22 (2)	0.38 (3)
C_O	0.11 (2)	2.01 (4)	0.51 (7)
O	0.94 (1)	1.70 (2)	0.65 (9)
Cu	0.99 (0)	1.79 (0)	0.89 (1)

Table 7.7: Summary of NIXSW experimental results of carbon and oxygen signals of deprotonated TPA and copper substrate. In particular, coherent position (P_c), corresponding adsorption height d_c and coherent fraction (F_c) of aromatic carbon C_{aro} (*Aro-Main*), carboxylate carbon C_O (*Carb-Main*), oxygen (*Region*) and copper (CuLMM) are reported.

over, the 25% lower coherent fraction of the aromatic signal compared to the carboxylate signal indicates a deviation of the aromatic ring from the perfectly flat gas-phase structure, and suggests a further distortion of the carbon backbone.

Simulations of the aromatic ring distortion

In order to prove our conjecture and to estimate the vertical displacement of atoms consistent with the lower F_c of the aromatic C compared to the carboxylate C, we simulate a deformation of the C-ring based on the following two assumptions:
1) $P_c(C_C) = P_c(C_O) = 0.11$
2) $F_c(C_H) = F_c(C_C) = F_c(C_O) = 0.51$.
We calculate that the coherent position of C_H atoms that leads to the measured coherent fraction of the aromatic ring (0.38) and is in agreement with the two equations above is $P_c(C_H) = 0.36$. However, the weighted average coherent position of $P_c(C_C) = 0.11$ and $P_c(C_H) = 0.36$ does not correspond to the measured one, $P_c(C_{aro}) = 0.23$. Therefore, from this calculation we learn that:

- $\Delta P_c = P_c(C_H) - P_c(C_C) = 0.36 - 0.11 = 0.25$ could explain a reduction in the aromatic ring coherent fraction of 25% with respect to the coherent fraction of the single carbon atoms (assumed to be 0.51). This result is independent of the absolute values of $P_c(C_H)$ and $P_c(C_C)$.
- However, $\Delta P_c = 0.25$ is not compatible with both assumption 1) and $P_c(C_{aro}) = 0.23$ (Table 7.7).

We now go one step further and seek the coherent positions $P_c(C_C)$ and $P_c(C_H)$ whose weighted average is the measured value 0.23 (Table 7.7), under the assumption that C_C and C_H atoms are within one Bragg plane spacing, and under the

additional constraint that the corresponding decrease in the coherent fraction is 25%. In mathematical terms, we are looking for the two values $P_c\,(\mathrm{C_C})$ and $P_c\,(\mathrm{C_H})$ that satisfy the following equations:

$$\begin{cases} P_c\,(\mathrm{C_{aro}}) = (1/3)\,[2P_c\,(\mathrm{C_H}) + P_c\,(\mathrm{C_C})] = 0.23 \\ \Delta P_c = P_c\,(\mathrm{C_H}) - P_c\,(\mathrm{C_C}) = 0.25 \end{cases} . \tag{7.1}$$

The results are $P_c\,(\mathrm{C_C}) = 0.05$ (1.91 Å) and $P_c\,(\mathrm{C_H}) = 0.30$ (2.36 Å). Since $P_c\,(\mathrm{C_C})$ turns out to be lower than $P_c\,(\mathrm{C_O})$, we consider this TPA configuration, illustrated in Figure 7.17a, to be rather unrealistic. Hence, we conclude that the lower F_c of the aromatic signal cannot be exclusively attributed to the vertical displacement of atoms within the aromatic ring. Another reason may be the different adsorption geometry of TPA at surface steps as compared to inside an island, although the fraction of molecules at the step edges is expected to be much lower than inside an island. Furthermore, the molecular diffusion among islands can also be considered to be a likely cause of low coherent fraction as explained in section 4.4.1.

Having learned that the whole F_c reduction from $\mathrm{C_{aro}}$ to $\mathrm{C_O}$ cannot be ascribed to the inner distortion of the aromatic ring, we aim to calculate the maximal decrease of F_c consistent with the measured structural parameters. The equations to fulfill are:

$$\begin{cases} P_c\,(\mathrm{C_C}) = P_c\,(\mathrm{C_O}) = 0.11 \\ P_c\,(\mathrm{C_{aro}}) = (1/3)\,[2P_c\,(\mathrm{C_H}) + P_c\,(\mathrm{C_C})] = 0.23. \end{cases} \tag{7.2}$$

The solution is $P_c\,(\mathrm{C_H}) = 0.29$ (2.35 Å), as illustrated in Figure 7.17b, and the corresponding decrease in the aromatic ring coherent fraction is 14% [$F_c\,(\mathrm{C_{aro}}) = 0.44$].

Finally, we calculate the structural parameters of the TPA aromatic ring so that the carbon vertical displacement can rationalize an F_c decrease of 10% with respect to $F_c\,(\mathrm{C_C}) = F_c\,(\mathrm{C_H}) = F_c\,(\mathrm{C_O}) = 0.51$. Therefore, the constraints to fulfill are the following:

$$\begin{cases} F_c\,(\mathrm{C_{aro}}) = 0.90F_c\,(\mathrm{C_O}) = 0.46 \\ P_c\,(\mathrm{C_{aro}}) = (1/3)\,[2P_c\,(\mathrm{C_H}) + P_c\,(\mathrm{C_C})] = 0.23 \end{cases} \tag{7.3}$$

The resulting structural parameters, illustrated in Figure 7.17c, are $P_c\,(\mathrm{C_C}) = 0.13$ (2.06 Å) and $P_c\,(\mathrm{C_C}) = 0.28$ (2.33 Å). In section 7.4.2, we will see that this is the same trend of the carbon vertical positions as obtained from DFT calculations.
After discussing the structural parameters of the TPA carbon species, we turn to

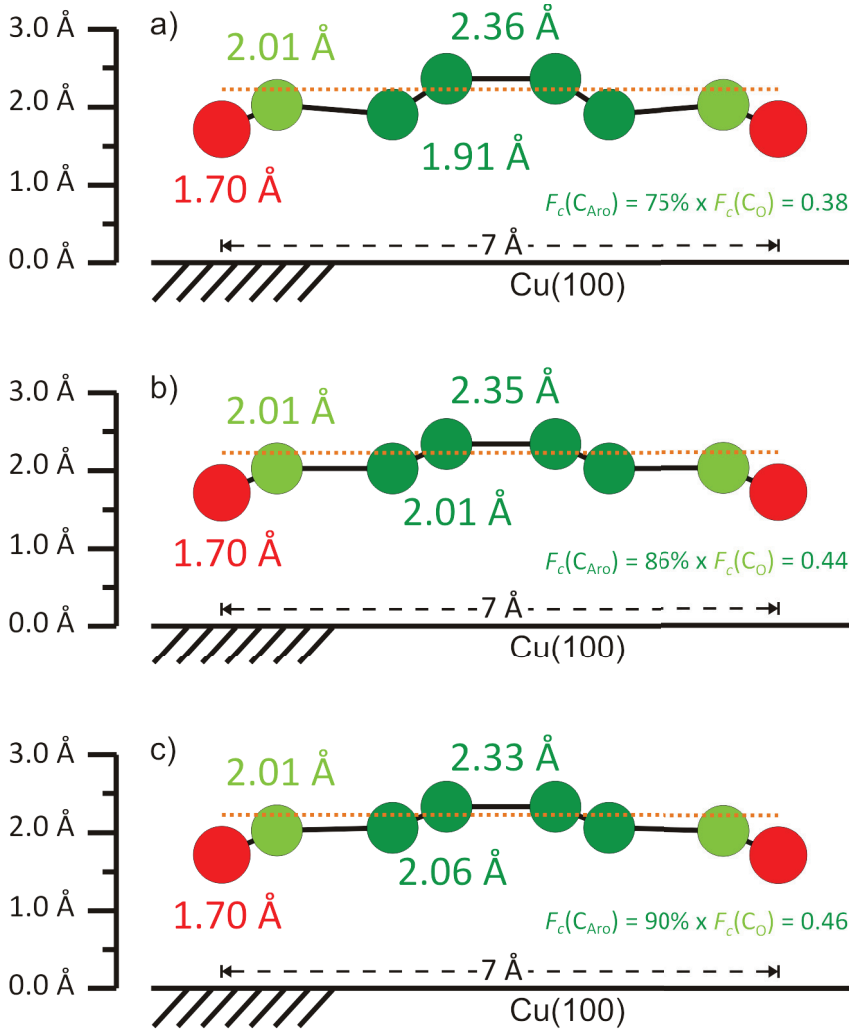


Figure 7.17: Long side view of TPA structural model with O and C_O at the experimental adsorption heights (Table 7.7), while C_C and C_H vertical positions result from three different simulations keeping the average coherent position constant and equal to $P_c\,(C_{aro}) = 0.23$. (a): the aromatic ring is distorted so that the coherent fraction coincides with the experimental value $P_c\,(C_{aro}) = 0.38$ (Table 7.7). (b): the aromatic ring is distorted so that C_C atoms are at the same adsorption height as carboxylate carbons and the resulting coherent fraction is 86% of the C_O coherent fraction. (c): the distortion of the aromatic ring is consistent with a coherent fraction equal to 90% of $F_c\,(C_O)$.

the oxygen results. As discussed in section 7.3.2, the O1*s* PE spectrum consists of only one peak (see Figure 7.11a) and there are no indications of additional components representing different oxygen species. Therefore, from inspection of the O1*s* spectrum, one would expect only one oxygen species. In fact, the relatively high coherent fraction ($F_c = 0.65 \pm 0.09$), compared to that of carbons ($\lesssim 0.50$), indicates a well-defined adsorption site. Moreover, the small distance of 1.70 ± 0.02 Å from the surface Bragg plane suggests the presence of a strong interaction between

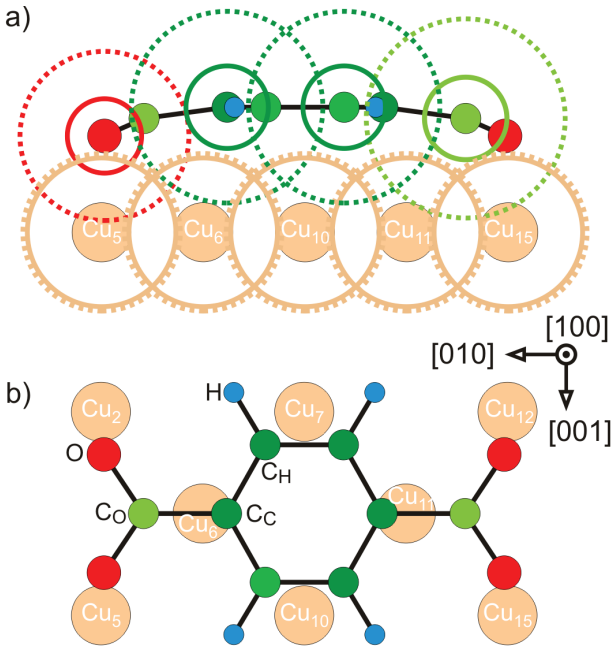
the oxygen atoms of TPA and the copper atoms underneath, as shown in Figure 7.16b.

Molecule-metal interactions

For a more quantitative analysis of the interaction between deprotonated TPA molecules and the copper surface, we calculate the interatomic distance between TPA carbon and oxygen atoms and the nearest surface copper atoms. In order to calculate these distances, the lateral position of TPA relative to the Cu(100) has to be defined. Although there are no conclusive experimental data which reveal the adsorption site of TPA on Cu(100) in the 3×3 superstructure, there are several strong indications, discussed below, pointing to the hollow site as the most favorable one.

STM investigations[161] reveal that TPA molecules, assembled in the 3×3 phase under study, are oriented with their long molecular axes along the [010] direction (see Figure 7.18b). Along this direction, the three highest symmetry adsorption sites for TPA are the hollow site, with the center of the molecule at the hollow surface position, the on-top site, with the center of the molecule on top of a Cu atom, and the bridge site, with the TPA center half way between two adjacent Cu atoms along the [011] direction. As mentioned above, the small adsorption height of oxygen atoms (Figure 7.16a,b and Table 7.7) suggests a strong interaction with the copper substrate; therefore the hollow adsorption site is more plausible than on-top or bridge sites, because it minimizes the O-Cu distance and strengthens the bonding of TPA carboxylate groups with the Cu surface atoms. In support of our hypothesis, according to DFT-PBE-D calculations[163] presented in section 7.4.2, the hollow site is more favorable than the on-top site by approximately 1.4 eV. Furthermore, even in the absence of the functional groups that interact with the substrate, the hollow site is still preferred, as revealed by DFT calculations for benzene/Cu(100), which show that benzene adsorbs at the hollow site.[163,172] In light of the arguments listed above, the remaining discussion is based on the deprotonated TPA molecule adsorbed at the hollow site of Cu(100), as shown in Figure 7.18b and in Figure 7.21.

Before calculating the interatomic distances between atoms of TPA and the copper surface atoms, the positions of the latter have to be defined. Two different scenarios are considered. In the first case, the (unrelaxed) surface Cu atoms are located at the surface Bragg plane, i.e., at their ideal bulk positions, and we will refer to them as Cu_B. In the second case, the topmost Cu layer is assumed to relax by approximately 0.05 Å, as derived from theory[171] and experiments,[169,170] and the



c)

X-Cu	d_i(X-Cu_B)	d_i(X-Cu_r)
O-Cu_2	1.86	1.91
C_O-Cu_6	2.27	2.31
C_C-Cu_6	2.26	2.31
C_H-Cu_7	2.40	2.45
$\overline{d_i(\text{O-Cu})}$	1.86	1.91
$\overline{d_i(\text{C-Cu})}$	2.33	2.38

Figure 7.18: (a): scale model of the long side view of TPA adsorbed on the topmost layer of Cu(100). Filled circles indicate atomic positions, solid lines indicate covalent radii[91] (C: 0.73 Å; O: 0.66 Å; Cu: 1.32 Å), dotted lines indicate vdW radii[92] (C-aliphatic: 1.70 Å; C-aromatic: 1.77 Å; O: 1.50 Å; Cu: 1.40 Å). (b): top view of TPA/Cu(100), see text for the discussion regarding the lateral position of TPA with respect to Cu substrate. (c): interatomic distances between atoms of TPA and the corresponding nearest neighbor Cu atom, assuming the topmost Cu layer at the Bragg plane position (Cu_B) and relaxed of 0.05 Å[169–171] ((Cu_r)).

corresponding nomenclature is Cu_r.

The vertical positions of TPA atoms are known from NIXSW (Figure 7.18b), while the lateral positions are assumed to be as in the gas-phase molecule. The resulting interatomic distances of carbon [d_i (C-Cu)] and oxygen [d_i (O-Cu)] atoms from the nearest surface Cu atoms underneath are reported in Figure 7.18c, where Cu = Cu_B or Cu_r. In the following section, values corresponding to Cu_r atoms are reported in square brackets. From the symmetry of deprotonated TPA at the hollow adsorption site, the same distance for all four oxygen atoms d_i (O-Cu) = 1.86 Å [1.91 Å] follows. On the other hand, the different interatomic distances of carbon atoms from the nearest Cu atoms yield the average value d_i (C-Cu) = 2.33 Å [2.38 Å].

In order to assess how strong the interaction between TPA and the copper substrate is, the average interatomic distances $\overline{d_i(\text{X-Cu})}$ are compared with the sum of covalent radii $r^{\text{X}}_{cov} + r^{\text{Cu}}_{cov}$ and the sum of vdW radii $r^{\text{X}}_{vdW} + r^{\text{Cu}}_{vdW}$ (Figure 7.18a), where X represents either carbon (C) or oxygen (O) atoms. From the values reported in Table

X	$r^{\mathrm{X}}_{cov} + r^{\mathrm{Cu}}_{cov}$	$r^{\mathrm{X}}_{vdW} + r^{\mathrm{Cu}}_{vdW}$	$\overline{d_i(\text{X-Cu}_\text{B})}$ [$\overline{d_i(\text{X-Cu}_\text{r})}$]	% of $(r^{\mathrm{X}}_{cov} + r^{\mathrm{Cu}}_{cov})$	% of $(r^{\mathrm{X}}_{vdW} + r^{\mathrm{Cu}}_{vdW})$
C	2.05	3.15	2.33 [2.38]	114 [116]	74 [76]
O	1.98	2.90	1.86 [1.91]	94 [96]	64 [66]

Table 7.8: Sum of covalent radii[91] $r^{\mathrm{O}}_{cov} + r^{\mathrm{Cu}}_{cov}$, sum of vdW radii[92] $r^{\mathrm{O}}_{vdW} + r^{\mathrm{Cu}}_{vdW}$ and average interatomic distances $\overline{d_i(\text{C-Cu}_\text{B})}$ [$\overline{d_i(\text{O-Cu}_\text{r})}$] for TPA/Cu(100) are reported, followed by the percentage of the interatomic distances with respect to the sum of covalent radii and the sum of vdW radii.

7.8 we note that the average interatomic distance $\overline{d_i(\text{O-Cu})} = 1.86$ Å [1.91 Å] is 6% [4%] (0.11 Å [0.08 Å]) smaller than the sum of covalent radii $r^{\mathrm{O}}_{cov} + r^{\mathrm{Cu}}_{cov} = 1.98$ Å. At the same time, the average interatomic distance $\overline{d_i(\text{C-Cu})} = 2.33$ Å [2.38 Å] is 26% [24%] (0.82 Å [0.76 Å]) smaller than the sum of vdW radii $r^{\mathrm{X}}_{vdW} + r^{\mathrm{Cu}}_{vdW} = 3.15$ Å and only 14% [16%] larger than the sum of covalent radii $r^{\mathrm{O}}_{cov} + r^{\mathrm{Cu}}_{cov} = 2.05$ Å. In summary, on the one hand, the distance of TPA oxygen atoms from Cu atoms is even below the lower limit of the covalent bond length, and on the other hand, the average distance of TPA carbon atoms from Cu atoms is substantially below the upper limit of the vdW interaction length, as shown in Figure 7.18a.

From the analysis of the interatomic distances d_i presented above, we propose that TPA adsorption on Cu(100) is mainly mediated by the four following components:

- carboxylate groups of deprotonated TPA form chemical bonds with the surface Cu atoms, as testified by $\overline{d_i(\text{O-Cu})}$ even smaller than $r^{\mathrm{O}}_{cov} + r^{\mathrm{Cu}}_{cov}$;
- the closed-shell aromatic ring is attracted by vdW forces towards the copper substrate and is pulled down by the carboxylate groups towards the Pauli repulsion regime, as shown by $\overline{d_i(\text{C-Cu})}$ smaller than $r^{\mathrm{C}}_{vdW} + r^{\mathrm{Cu}}_{vdW}$;
- the distortion of the gas-phase planar geometry upon adsorption on Cu(100) is ascribed to the competition between the functional groups interaction that tend to pull TPA closer to the surface and the Pauli repulsion between occupied molecular and substrate orbitals;
- finally, the overall small adsorption height of deprotonated TPA on Cu(100) is also attributed to the presumably strong electrostatic interaction between the double negative charge carried by the molecule and the image charges in the substrate.

The adsorption model presented above focuses on the molecule-substrate interaction, but not yet on the molecule-molecule interactions, which we will discuss below.

Molecule-molecule interactions

The adsorption model available so far is based on STM, XPS and NEXFAS measurements[161] and is summarized below. STM[34,161] showed that TPA molecules form well-ordered 3×3 commensurate structures on the Cu(100) surface (section 7.2.1) oriented along the [010] direction. Since no further chemical information or evidence of bond formation can be provided by STM imaging, the driving force for the stabilization of the molecular islands is attributed to direct intermolecular interaction, namely hydrogen bonding between oxygen and hydrogen atoms of neighboring molecules, as shown in Figure 7.21. In particular, according to this model,[161] each TPA molecule is involved in eight H-bonds (four as a donor and four as an acceptor) with four other molecules. Therefore, the energy gain that leads the self-assembly of TPA in a structure ordered in this manner is assigned to this bond formation. To support this conjecture based on STM images, NEXAFS experiments[161] are performed and reveal a very strong dichroism for π^* resonances of both the aromatic and the carboxyl carbons with almost completely vanishing but still non-zero intensity at normal photon incidence (90°). Two possible interpretations of the small residual intensity still present in the 90° NEXAFS spectra are offered. On the one hand, most TPA molecules can be flat-lying and some of them, for instance those adsorbed at step edges, have a completely different geometry to justify the residual intensity. On the other hand, all the molecules may be tilted by 5° relative to the surface. The first interpretation, preferred by the authors of ref.[161], goes hand in hand with the idea of having the molecular layer interconnected by hydrogen bonds, which are in turn maximized if the H-bond angle is close to 180°.[173]

On the basis of the present NIXSW data, a third possible interpretation of the NEXAFS spectra is suggested. Specifically, the intensity of the π^* resonances of both the aromatic and the carboxylate carbons in the 90° spectrum could be due to the bending of the carbon backbone of TPA molecules upon adsorption on Cu(100). In particular, a non-planar geometry of the aromatic ring can be inferred from the lower coherent fraction of the aromatic contribution compared to the carboxylate contribution (Table 7.7), whereas the bending of the carboxylate groups arises directly from our structural data shown in Figure 7.16a.

Furthermore, NIXSW data do not seem to support the idea of H-bonding as a fundamental component in the stabilization of TPA islands on Cu(100), as is argued below. In general,[173,174] the smaller the H-bond angle, the weaker the bond itself. In particular, due to the bending of the functional groups towards the surface, the

H-bond angle (CH$\cdots$O) decreases compared to the case in which molecules adsorb completely flat, if H atoms are assumed to be at the same height as the aromatic carbons. Therefore, a weaker H-bonding is expected for the distorted TPA in comparison with the flat-lying molecule. Moreover, the interatomic distance d_i(H-O) between H and O of two neighboring molecules is approximately 2.36 Å, assuming that hydrogens are at the same height as the aromatic ring. In order to estimate the strength of CH$\cdots$O interaction, we compare d_i(H-O) to the H-bond distances of two other systems. The first H-bond, between -COO^- group (acceptor) and H of H_2O (donor), provides d_i(H-O) = 1.86 Å.[173] The second one, between (C,C)C_{sp^2}-H (donor) and O of H_2O (acceptor), gives d_i(H-O) = 2.55 Å.[173] The distance d_i(H-O) = 2.36 Å estimated on the basis of NIXSW data is much closer to the H-O distance of the second system in which relatively weak H-bonding takes place.

We can therefore conclude that NIXSW structural data of deprotonated TPA/Cu(100) provide evidence of a rather strong interaction between oxygen atoms of the carboxylate groups and the surface Cu atoms underneath. This interaction between the functional groups and the substrate brings the whole molecule closer to the surface, well into the Pauli repulsion regime. As a result of the delicate balance between these two interaction channels, the molecule bends in an arc-like geometry, qualitatively consistent with the above-discussed re-interpretation of NEXAFS data.[161] However, in contrast with the current understanding of TPA self-assembly, mainly ascribed to intermolecular H-bonding,[161] NIXSW data instead appear to suggest a stabilization of TPA islands primarily driven by the molecule-metal interaction through O-Cu chemical bonding.

Our conjecture is supported by HREELS experiments on TPA/Cu(100).[5] In fact, a vibrational mode which is seen in the first TPA layer and whose intensity does not increase in the bilayer is assigned to the Cu-O stretch mode. This mode indicates a bonding of the oxygen atoms to the Cu surface atoms. At the same time, no experimental evidence was found for the H-bonding between molecules, although a perturbation of CH modes in presence of H-bonds can be expected and is indeed reported for other hydrogen-bonded systems.[173,175]

For a deeper understanding of the adsorption model presented above and in order to assess the role played by molecule-metal and molecule-molecule interactions, DFT calculations of TPA/Cu(100) were performed.[163] In the section below, the most significant results are discussed and compared to experimental data.

7.4.2 Comparison of NIXSW data with DFT calculations

DFT calculations were performed by J. Jelic and K. Reuter[163] (TU München) with the CASTEP code using the PBE functional[164] and a modified version of it according to the semiempirical correction scheme developed by Tkatchenko and Scheffler.[149] This latter functional is called PBE-D since it takes long-range dispersion forces into account. The substrate of both PBE and PBE-D calculations is modeled with a 3×3 slab consisting of four layers. The two bottom layers are kept fixed and the two upper layers are allowed to relax.

Figure 7.19b,c and Table 7.9 report the distances from the surface Bragg plane, d_{PBE} and $d_{\mathrm{PBE-D}}$ of TPA/Cu(100) resulting from PBE and PBE-D calculations, respectively. Both functionals yield the largest vertical distance from the Cu surface for C_H atoms, followed in order by C_C, C_O and finally O atoms, the latter being the closest to the surface. In particular, $d_{\mathrm{PBE-D}}$ distances turn out to be 6.9% lower on average than d_{PBE}. In comparison with NIXSW results (Table 7.9), DFT calculations simultaneously overestimate the O adsorption height, while they underestimate the C vertical position. As a result, the adsorption geometries resulting from DFT calculations (Figure 7.19b,c) are much less deformed than the one found in NIXSW (Figure 7.19a). In fact, the vertical distances between C_H and O atoms, $\Delta d_{\mathrm{PBE}}\,(C_H - O) = 0.22$ Å and $\Delta d_{\mathrm{PBE-D}}\,(C_H - O) = 0.15$ Å are 2.4 and 3.5 times smaller respectively than $\Delta d_{c,\mathrm{NIXSW}}\,(C_H - O) = 0.52$ Å.

Comparison NIXSW–DFT: adsorption heights					
	NIXSW	PBE		PBE-D	
element	d_c (Å)	d_{PBE} (Å)	% of d_c	$d_{\mathrm{PBE-D}}$ (Å)	% of d_c
O	1.70	1.91	112	1.76	104
C_O	2.01	1.97	98	1.83	91
C_C	2.22	2.03	91	1.90	85
C_H	2.22	2.13	96	2.01	91
H	-	2.30	-	2.22	-

Table 7.9: Adsorption heights, i.e., vertical distances from the surface-extended Bragg plane, of oxygen, C_O, C_C, C_H carbon species (Figure 7.18b) resulting from NIXSW measurements, PBE and PBE-D calculations (performed by J. Jelic and K. Reuter, TU München). Both absolute values d_c, d_{PBE}, $d_{\mathrm{PBE-D}}$ (Å) and percentage values (%) of d_c are reported. Since it is not possible to differentiate carbon species within the aromatic ring by NIXSW, d_c of C_C and C_H are assumed to be equal.

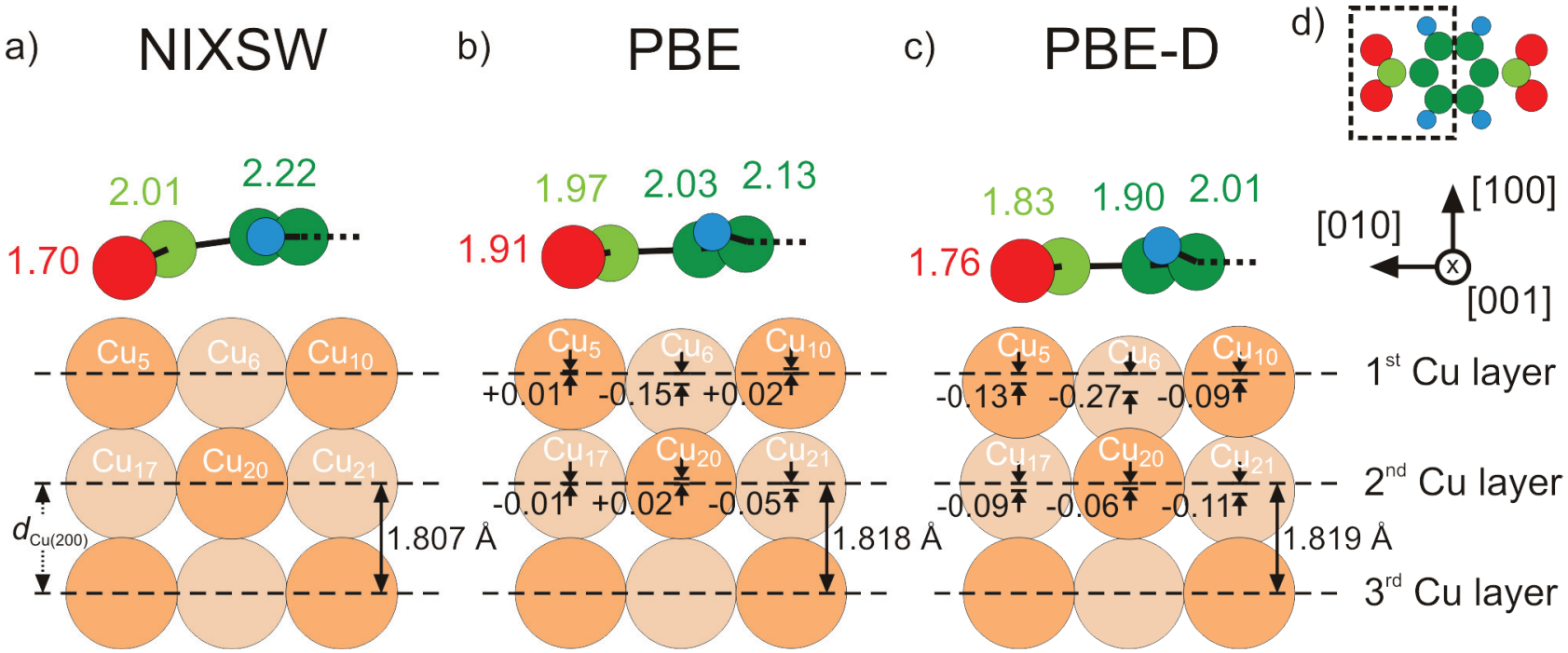


Figure 7.19: Side view of TPA/Cu(100) scale model, as measured by NIXSW (a), as calculated, by J. Jelic and K. Reuter (TU München), by means of DFT-PBE (b) and DFT-PBE-D (c). Thanks to the D_{2h} symmetry of the molecule, only one half, highlighted by the dashed black line in panel (d), is displayed in panels (a)-(c), the remaining half (not shown) is equivalent. Adsorption heights (Å) of oxygen (red), C_O (light green), C_C and C_H (dark green) are marked in the figure with corresponding font color, and they are calculated with respect to the topmost unrelaxed Cu layer. The dashed black lines crossing the substrate Cu atoms indicate the position of the first three extended Bragg planes (equal to the unrelaxed Cu planes), whose spacing $d_{Cu(200)}$ is also reported. The spacing values of PBE and PBE-D calculations follow from the optimized Cu bulk structure, while the spacing value used for NIXSW data was found experimentally.[167] The values (black font) next to the distance arrows on top of the substrate atoms refer to the distances of corresponding Cu atoms from the nearest Bragg plane. Positive [negative] values refer to Cu atoms above [below] the corresponding Bragg plane. Substrate atoms are numbered (white font) according to notation of Figure 7.18b. Cu atoms in the foreground are displayed in darker color, while those in the background are in lighter color. Crystallographic directions of the substrate are reported below panel (d).

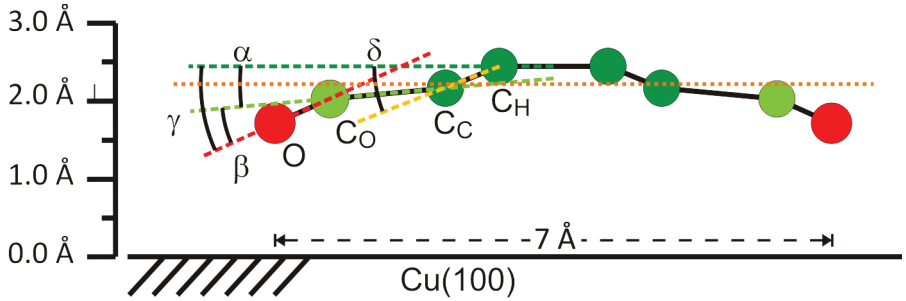


Figure 7.20: Side view of TPA/Cu(100), where O (red circle), C_O (light green circle) and C_{aro} (orange dotted line) are at the vertical positions obtained from NIXSW (Table 7.7), while C_C and C_H (dark green circles) do not correspond to either experiment or to calculations. Their position is meant to highlight the four angles described below in the figure. α is the angle between C_O-C_C vector and C_H plane. β is the angle between O-C_O-O plane and C_O-C_C vector. γ is the angle between O-C_O-O plane and C_H plane. δ is the angle between C_C-C_H vector and C_H plane.

Comparison NIXSW–DFT: tilt angles			
angle (°)	NIXSW	PBE	PBE-D
α	8.1	2.3	2.6
β	15.0	3.8	3.3
γ	23.1	6.1	5.9
δ	10.9	3.4	4.5

Table 7.10: Values of angles α, β, γ and δ (Figure 7.20) of the TPA adsorption geometry resulting from NIXSW experiments, PBE and PBE-D calculations (Figure 7.19), performed by J. Jelic and K. Reuter (TU München). Concerning NIXSW angles: α, β and γ are calculated assuming C_C and C_H to be located at the average adsorption height of the aromatic ring (2.22 Å), while δ is calculated assuming $d_c\,(C_C) = 2.06$ Å and $d_c\,(C_H) = 2.33$ Å as in Figure 7.17c, characterized by a distortion of the ring corresponding to a 10% decrease in the coherent fraction $F_c\,(C_H) = F_c\,(C_C) = F_c\,(C_O) = 0.51$.

The stronger distortion of the adsorbed TPA molecule as measured by NIXSW is confirmed by the following structural parameters. Figure 7.20 illustrates four angles, α, β, γ and δ introduced to characterize and quantify the deformation of the molecule. In particular, α is the angle between the C_O-C_H vector and the plane of C_H atoms, β is the angle between the O-C_O-O plane and the C_O-C_C vector, γ is the dihedral angle between the O-C_O-O plane and the plane of C_H atoms. Since the position of C_H atoms cannot be determined by NIXSW, angles α, β and γ of the NIXSW column in Table 7.10 are calculated with respect to the plane of the aromatic carbon atoms (dotted orange line), while the δ value refers to the simulated aromatic ring structure of Figure 7.17c. The angles calculated for PBE and PBE-D adsorption geometries are approximately 3.6 times smaller than those corresponding to NIXSW configuration. This confirms the distortion of the molecule derived from

Comparison NIXSW–DFT: interatomic distances					
	NIXSW	PBE		PBE-D	
element	$d_{i,\mathrm{Cu_r}}$ (Å)	$d_{i,\mathrm{PBE}}$ (Å)	% of d_i	$d_{i,\mathrm{PBE-D}}$ (Å)	% of d_i
O	1.91	2.02	106	2.02	106
C_O	2.31	2.41	104	2.40	104
C_C	2.31	2.20	95	2.19	95
C_H	2.45	2.31	94	2.31	94
H	-	2.65	-	2.67	-

Table 7.11: Interatomic distances of oxygen, C_O, C_C, C_H carbon species resulting from NIXSW measurements (Figure 7.18), PBE and PBE-D calculations (performed by J. Jelic and K. Reuter, TU München), from the nearest Cu atom, assuming a 0.05 Å-relaxed topmost Cu layer for NIXSW values. Both absolute values $d_{i,\mathrm{Cu_r}}$, $d_{i,\mathrm{PBE}}$, $d_{i,\mathrm{PBE-D}}$ (Å) and percentage values (%) of $d_{i,\mathrm{Cu_r}}$ are reported. Since it is not possible to differentiate carbon species within the aromatic ring by NIXSW, we assume that $d_c\,(\mathrm{C_C}) = d_c\,(\mathrm{C_H}) = d_c\,(\mathrm{C_{aro}})$.

the atomic adsorption heights.

From a closer inspection of Figure 7.19b,c we note a sizable relaxation and buckling of the topmost Cu atoms, which is stronger for the PBE-D substrate than for the PBE one. Considering the different positions of the substrate atoms, the interatomic distances between TPA atoms and the nearest Cu atoms thus represent a more interesting parameter than the vertical distance from the surface Bragg plane, because they give a direct estimation of the molecule-substrate interaction (section 7.4.1). Table 7.11 reports the interatomic distances TPA-Cu $d_{i,\mathrm{Cu_r}}$ calculated for the 0.05 Å inward-relaxed topmost Cu layer (Figure 7.18c), together with the analogous distances calculated for DFT adsorption structures, $d_{i,\mathrm{PBE}}$ and $d_{i,\mathrm{PBE-D}}$. The carboxylate functional group (O-C_O-O) results closer to the surface while the aromatic ring is farther away from the surface compared to both DFT predictions. Moreover, the fact that $d_{i,\mathrm{PBE}}$ and $d_{i,\mathrm{PBE-D}}$ are identical indicates that the molecule-substrate interaction resulting from PBE functional is not altered by the dispersion correction term, in fact the corresponding relative distance remains constant.

From the analysis and the comparison of the NIXSW and DFT TPA/Cu(100) adsorption geometries, the following conclusions can be drawn:

- Apparently the vdW correction term does not play a dominant role for TPA adsorbed on Cu(100). This can be deduced from the relatively small height difference, approximately 0.14 Å, with respect to PBE calculations and the corresponding small adsorption energy difference. In fact, the PBE-D adsorption

energy of TPA/Cu(100), 6.79 eV, is only 30% larger than that predicted by DFT-PBE (5.30 eV). In other systems, e.g., benzene/Cu(100), azobenzene/Ag(111) and TBA/Ag(111), the semiempirical correction term brings a significant percentage increase of the molecular adsorption energy compared to the bare PBE calculations, 0.03 eV → 1.32 eV (4400%),[163] 0.2 eV → 1.7 eV (850%),[4] and 0.13 eV → 2.91 eV (2238%),[152] respectively. Therefore, considering the small effect of the vdW correction term on the adsorption geometry and energy, we conclude that vdW interactions do not play such an important role within the TPA-Cu interaction. This can be explained by the fact that already at the PBE level of theory, the molecule is in the chemisorption regime, while at the same DFT-PBE level, azobenzene and TBA molecules float at 3.64 Å[4] and 3.86 Å[152], respectively. Only the inclusion of vdW dispersion term pulls the latter molecules closer to the surface, at 2.98 Å[4] and 3.11 Å[152] respectively, distances at which they can interact with the underlying Ag(111) substrate (chapter 6). In contrast, for TPA/Cu(100), the dispersion term represents only a small correction to the PBE result and does not significantly affect either the molecular structure or the energetics.

- In particular, the slightly lower distance (≈ 0.14 Å) of the molecule from the substrate, according to PBE-D, goes hand in hand with a similar inward relaxation of the topmost Cu layer. Therefore, the dispersion forces do not alter the interatomic distances TPA-Cu and do not increase the bending of TPA molecule, which, in so doing, remains far from the experimental results. In summary, the dispersion term does not offset the discrepancies between DFT-PBE and NIXSW results.

- The main difference between experimental and theoretical adsorption geometry remains the overall bending of the deprotonated TPA molecule adsorbed on Cu(100). In particular, the differential chemistry of the molecule, with the carboxylate groups strongly interacting with the surface through the O-Cu covalent bonds, and the central aromatic ring being pushed away from the surface due to Pauli repulsion cannot be properly described by PBE calculations. In fact, the rather flat adsorption geometry of TPA/Cu(100) predicted by DFT-PBE suggests the existence of another shortcoming, beyond the lack of vdW interactions. The evidence of the above-discussed deficiency in the PBE functional for the description of molecule-metal interfaces represents the first step in improving density functional theory towards a better predictive quality of these systems.

With the aim of shedding light on the role played by molecule-molecule interactions within the TPA-Cu interfaces, further DFT calculations have been performed and the main results are presented below.

DFT calculations of different TPA configurations

As already discussed above, the H · · · O distance (2.36 Å) and CH · · · O angle (160°), derived from NIXSW data, do not support the notion of a prominent contribution of H-bonding in the stabilization of TPA islands. The corresponding values of H · · · O distance and CH · · · O angle derived from PBE and PBE-D calculations (Table 7.12) are in good agreement with the estimates based on NIXSW data lacking the H positions. In order to investigate the intermolecular interactions and to assess the role played by H-bonding in the formation of well-ordered 3×3 domains of deprotonated TPA molecules on the Cu(100) surface,[161] additional DFT calculations are performed.[163]

Comparison NIXSW–DFT: H-bonds			
	NIXSW	PBE	PBE-D
CH–C-ring angle	-	10.4	11.3
H · · · O distance	2.36	2.27	2.31
CH · · · O angle	160°	155°	153°

Table 7.12: Summary of distances and angles characterizing H-bonds between two TPA molecules, with TPA adsorption geometry as measured by NIXSW and as calculated by PBE and PBE-D functionals (by J. Jelic and K. Reuter, TU München). In particular, we report the angle between CH vector and the plane of C_H atoms, the distance between H and O atoms of neighboring molecules, and the CH · · · O angle between CH and O of neighboring molecules. NIXSW values are calculated assuming H atoms to be at the same height as C_{aro} carbon atoms (Table 7.7).

In particular, a larger 6×6 slab (Figure 7.21, gray dashed line) is employed and three different configurations of TPA molecules are considered:

- A single molecule at adsorption site (0,0), as illustrated in Figure 7.21 and schematically in Figure 7.22a.
- Two molecules located at adsorption sites (0,0) and (1,1) respectively, as illustrated in Figure 7.21 and schematically in Figure 7.22b. This is the "head-to-head" configuration since the "heads" of two neighboring molecules face each other.
- Two molecules located at adsorption sites (0,0) and (0,1) respectively, as illustrated in Figure 7.21 and schematically in Figure 7.22c. This is the "side-to-side" configuration because the sides of two neighboring molecules are next to each other.
- The full-layer configuration (Figure 7.21 and Figure 7.22d) is calculated with a 3×3 slab, i.e., the fundamental unit cell of the 3×3 TPA superstructure, and cor-

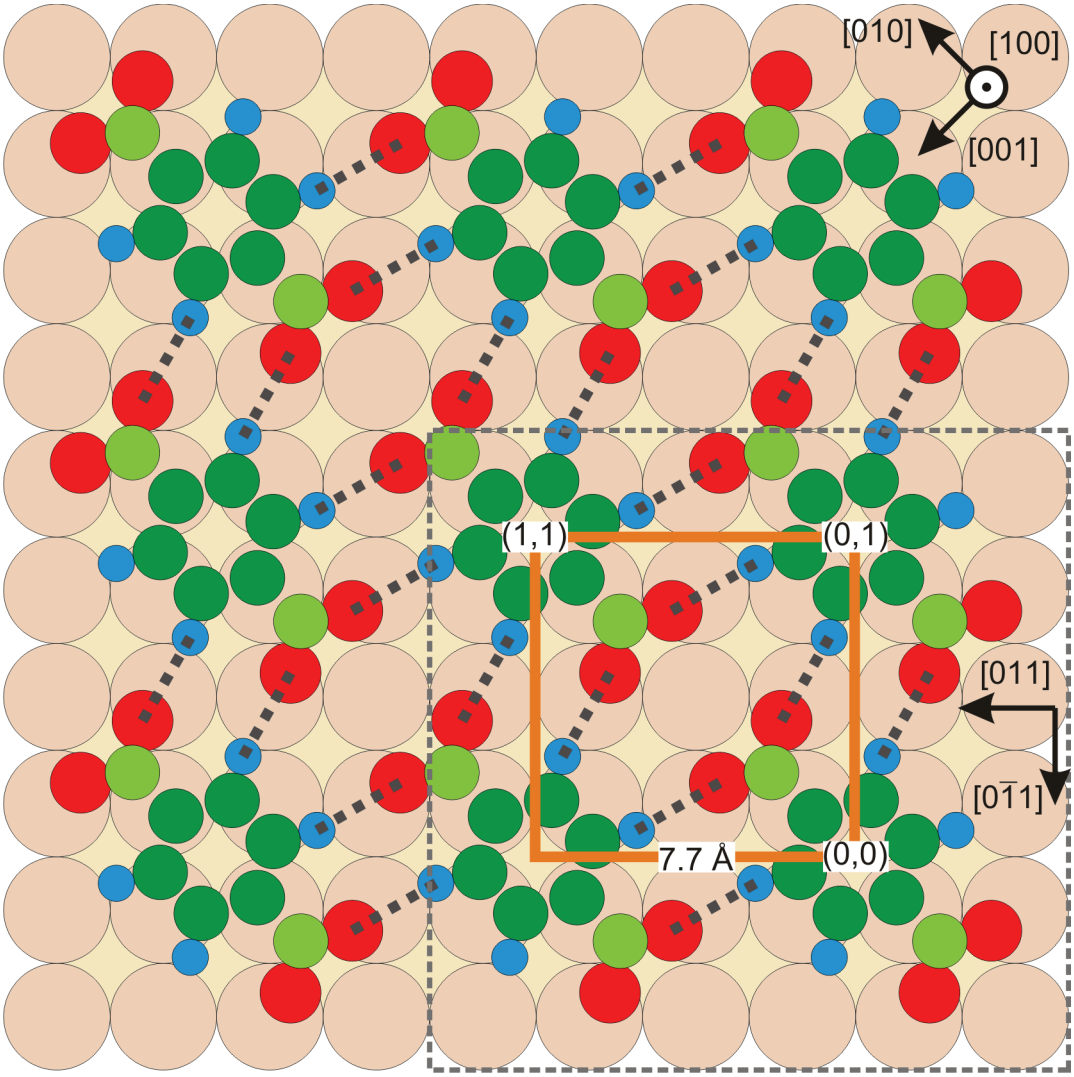


Figure 7.21: Top view of full coverage TPA/Cu(100) based on LEED measurements (see Figure 7.4c) and STM experiments.[161] The 7.7×7.7 Å square unit cell is marked by the solid orange line. Hydrogen bonds are highlighted by the dotted gray lines connecting H and O atoms of neighboring molecules. The adsorption sites of three molecules are labeled with (0,0), (0,1), (1,1), respectively, and they will be referred to in the text. The dashed gray square indicates the surface area (6×6 Cu atoms) of the substrate slab used in PBE and PBE-D calculations of single molecule, head-to-head and side-to-side configurations (performed by J. Jelic and K. Reuter, TU München). Substrate crystallographic directions are reported at the upper and at the lower right corners.

responding structural parameters (Table 7.9-7.12 and Figure 7.19) are discussed above.

The goal of calculating the molecular configurations listed above is to determine how the local environment affects the adsorption energy and geometry of TPA molecules. Table 7.13 summarizes all the adsorption energies per molecule of each TPA configu-

TPA adsorption energies per molecule				
	single molecule	head-to-head	side-to-side	full layer
PBE	5.18	5.22	5.26	5.50
PBE-D	6.27	6.36	6.47	6.79

Table 7.13: Adsorption energies of deprotonated TPA in four different configurations: single molecule, head-to-head, side-to-side and full layer, calculated using PBE and PBE-D functionals by J. Jelic and K. Reuter (TU München).

ration. We note that the adsorption energies resulting from the PBE-D calculations are always greater than those corresponding to the bare PBE calculations. This follows from the definition of the dispersion correction term.[4,149] At the same time, the trend of adsorption energies is the same for PBE and PBE-D calculations. In particular, TPA in a full layer has the largest adsorption energy, followed by the side-to-side and the head-to-head configurations, and finally the single molecule without any neighbor is characterized by the lowest adsorption energy. Interestingly, the energy difference between the largest and the smallest values is only 6% (PBE) [8% (PBE-D)]. This already indicates that the main contribution to the binding energy of deprotonated TPA on Cu(100) comes from the interaction with the substrate, and that intermolecular interactions add a relatively small bonding energy to the entire system. In the following, each TPA configuration and the corresponding adsorption energies, calculated with PBE and PBE-D functionals, are discussed in detail (PBE-D values are reported in square brackets).

In the head-to-head configuration, the negatively charged carboxylate groups face each other, hence no H-bonding can occur. However, an increase in adsorption energy of 0.04 eV [0.09 eV], compared to the single molecule configuration, is registered (Figure 7.22 a $\rightarrow$ b). We attribute this energy gain (E_S) upon adsorption of a second molecule to the decrease in the surface energy, which in turn follows from the substantial modification of the Cu surface beneath and nearby the first adsorbed deprotonated TPA. In fact, the chemical bond between O of carboxylate groups and the surface Cu atoms, on one hand, and the Pauli repulsion between substrate and the molecular occupied orbitals, on the other, induce a significant rearrangement of the topmost Cu atoms. The consequent stress field in the copper surface reduces the energetic cost for altering the unperturbed positions of Cu atoms nearby an adsorbed molecule, upon adsorption of another molecule. The buckling of the Cu surface, as resulting from the DFT calculations, is shown in Figure 7.19b,c (side view) and in Figure 7.23 (top view). In particular, PBE calculations reveal that Cu atoms beneath O atoms are slightly upward 0.01 Å (0.06 Å) shifted with respect

to the unrelaxed (0.05 Å-relaxed) topmost surface layer. As a consequence, some of the neighboring Cu atoms are pushed down into the substrate and some others up towards the vacuum, leading to a different rearrangement of Cu atoms along the different crystallographic directions with higher and deeper rows of Cu atoms oriented along [010] direction and alternating along [001] direction (Figure 7.23) to form a stress field wave within the topmost Cu layer. Because of the different surface buckling along [010] and [0$\bar{1}$1] directions, it is plausible to expect corresponding different adsorption energy gains E_S mediated by the substrate, $E_{S,h-h}$ and $E_{S,s-s}$, respectively for head-to-head and side-to-side configurations. However, since we can estimate E_S only in the head-to-head configuration (1 S interaction/molecule, Figure 7.22b and Table 7.14), we will assume it to be approximately the same in the side-to-side configuration as well, hence:

$$E_{S,s-s} \approx E_{S,h-h} \approx 0.04 \text{ eV } [0.09 \text{ eV}]. \tag{7.4}$$

The larger energy gain from the single molecule to the side-to-side configuration, $\Delta E_{s\rightarrow s-s} = 0.08$ eV [0.20 eV], as compared to the head-to-head configuration, $\Delta E_{s\rightarrow h-h}$ = 0.04 eV [0.09 eV], is attributed to the H bonds between CH and O of the two neighboring molecules. Under the assumption of equation 7.4, we derive the energy per H-bond between two deprotonated TPA molecules:

$$E_H = \frac{\Delta E_{s\rightarrow s-s} - E_{S,s-s}}{2} = 0.02 \text{ eV } [0.055 \text{ eV}]. \tag{7.5}$$

Apart from the larger adsorption energy of the side-to-side configuration another indication of the presence of H-bonding comes from the adsorption heights of O and H atoms. In fact, O and H atoms involved in H-bonds between two neighboring molecules in the side-to-side configuration are found to be 0.05 Å higher and 0.02 Å lower respectively than O and H atoms of the same molecules but not involved in H-bonding. A similar trend is registered from the comparison of O and H atoms of single molecule and full-layer TPA configurations, calculated with both PBE and PBE-D functionals. This structural modification confirms that molecules aligned along [0$\bar{1}$1] direction, and for symmetry also along [011] direction, are H-bonded.

Finally, the full-layer configuration is characterized by four H-bonds and 2.5 substrate-mediated interactions per molecule (Table 7.14). Assuming, as above, that the energy gain due to the substrate mediated interactions (equation 7.4) is the same independent of the interaction direction, and under the assumption that it is additive, we

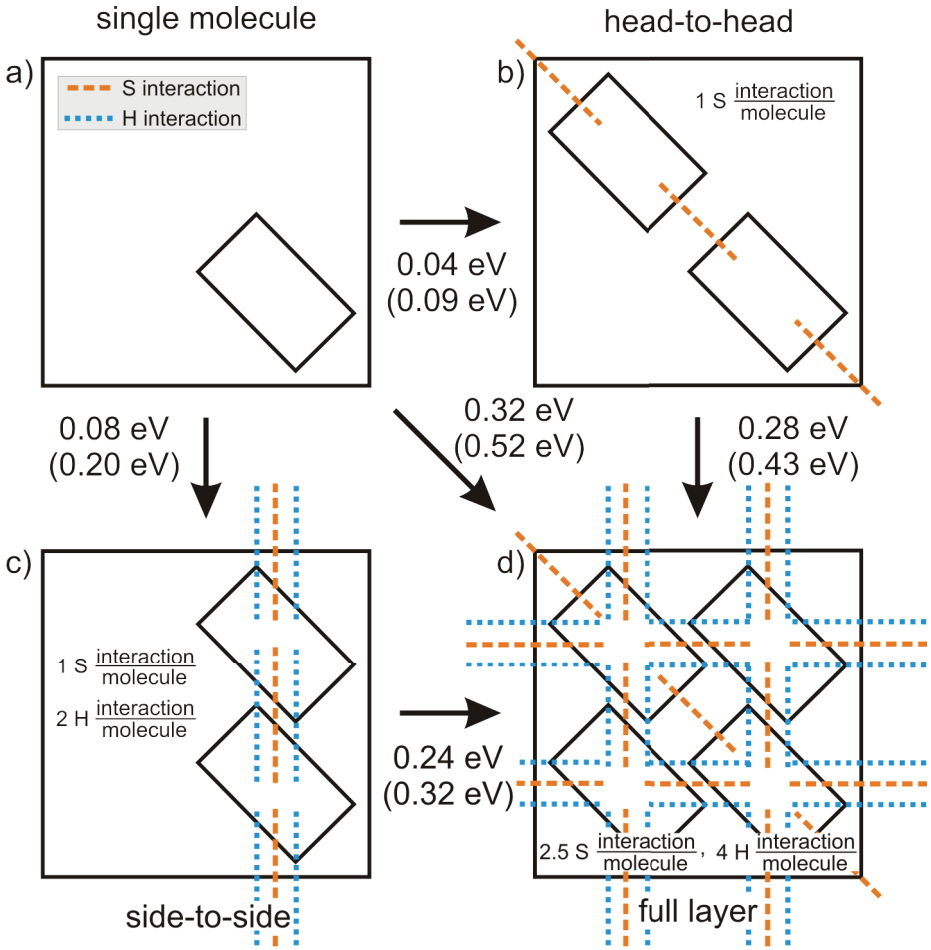


Figure 7.22: Schematic representation of single molecule (a), head-to-head (b), side-to-side (c) and full layer (d) configurations. Substrate mediated and hydrogen interactions are marked with dashed orange lines and dotted blue lines, respectively. Adsorption energy differences, according to PBE and PBE-D (in brackets) calculations (performed by J. Jelic and K. Reuter, TU München), are reported next to the arrows indicating the transition. For each of the panels (b), (c) and (d) the number of substrate-mediated and hydrogen interactions is specified according to values summarized in Table 7.14.

	H interaction	S interaction	ΔE (PBE)	ΔE (PBE-D)
single	0	0	-	-
head-to-head	0	1	0.04	0.09
side-to-side	2	1	0.08	0.20
full layer	4	2.5	0.32	0.52

Table 7.14: Number of substrate-mediated (S) and hydrogen (H) interactions in the four TPA configurations (Figure 7.22), single molecule, head-to-head, side-to-side, full layer, followed by the adsorption energy differences with respect to the single molecule adsorption energy (Table 7.13).

can express the energy gain from the single molecule to the full-layer configuration

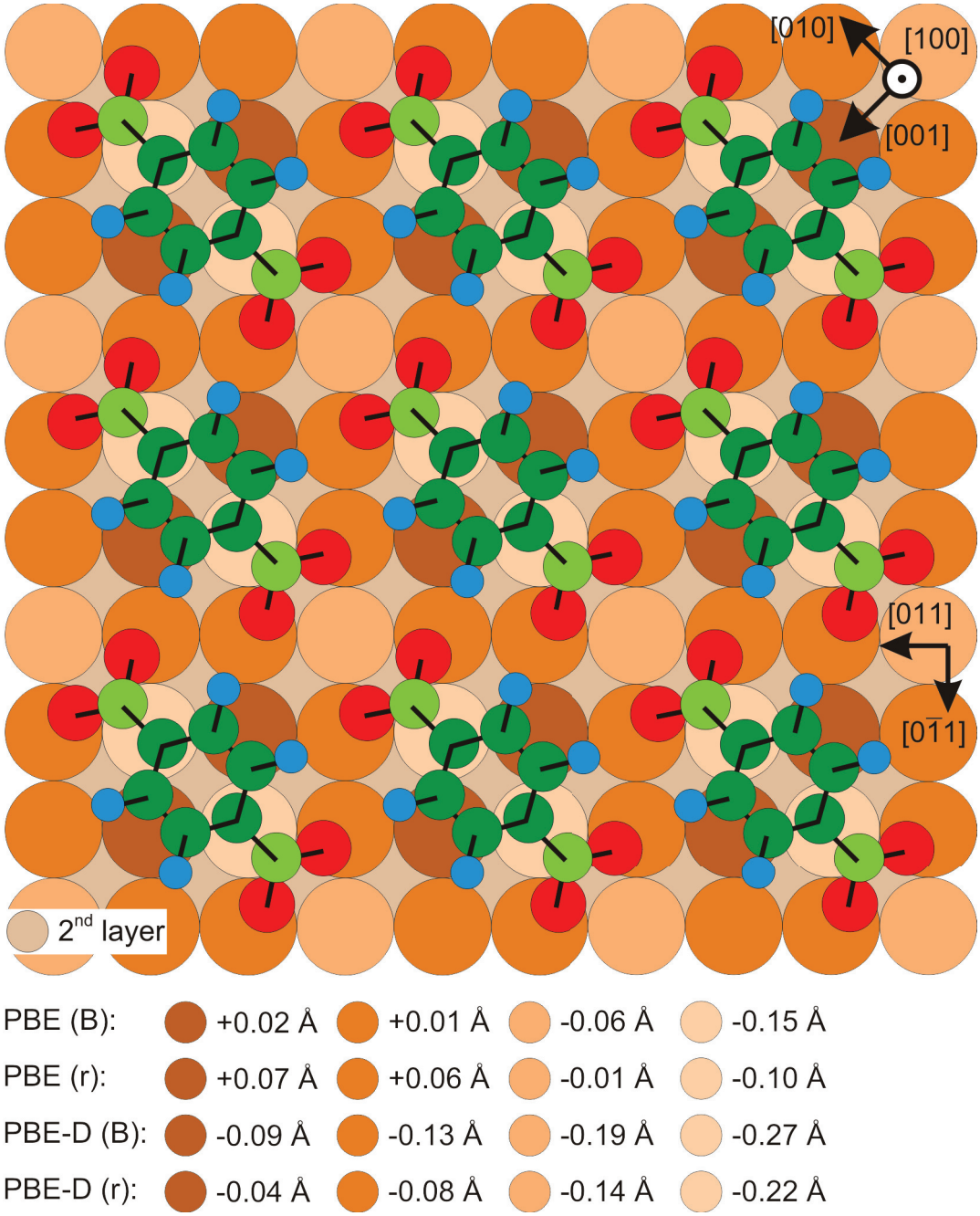


Figure 7.23: Top view of deprotonated TPA adsorbed on Cu(100) and the buckling of the Cu atoms in the topmost substrate layer, according to PBE and PBE-D calculations (Figure 7.19b,c) performed by J. Jelic and K. Reuter (TU München). The vertical displacements of Cu atoms reported in the legend are relative to the Bragg plane (B) or to the 0.05 Å lower position of the relaxed topmost layer (r). Cu atoms of different colors are at a different vertical distance from the ideal unrelaxed position of the Bragg plane (B) or from the relaxed layer position (r). Darker colors correspond to higher positions, as indicated in the legend. Bonds between atoms of TPA are explicitly drawn to highlight the different adsorption heights of O (red), C_O (light green), C_C and C_H (green), H (blue).

as:

$$\Delta E_{s\rightarrow f-l} = 2.5E_S + 4E_H = 0.18 \text{ eV } [0.445 \text{ eV}]. \quad (7.6)$$

The latter values are 44% and 14% smaller respectively than the corresponding calculated values (Table 7.14). We ascribe the discrepancy with the theoretical results to the simplicity of the model employed (Figure 7.22), which is based on the above-described assumptions which may not be strictly valid. In particular, the different buckling of the Cu surface along [010] and [0$\bar{1}$1] directions suggests different energy gains mediated by the substrate for head-to-head and side-to-side configurations. If we then recast equations 7.4, 7.5 and 7.6, assuming that $E_{S,s-s} \neq E_{S,h-h}$:

$$E_{S,h-h} = 0.04 \text{ eV } [0.09 \text{ eV}] \quad (7.7)$$

$$E_{S,s-s} + 2E_H = 0.08 \text{ eV } [0.20 \text{ eV}] \quad (7.8)$$

$$E_{S,s-s} + 2E_H = 0.16 \text{ eV } [0.26 \text{ eV}] - (1/4)E_{S,h-h} \quad (7.9)$$

we can clearly observe that equation 7.8 and equation 7.9 are linearly dependent and there is no solution ($E_{S,h-h}$, $E_{S,s-s}$, E_H) that satisfies the three equations simultaneously. We therefore conclude that the three energy contributions do not sum linearly, as we implicitly assumed in our model and in the set of equations 7.5–7.9.

On the basis of the results reported above, we can conclude that DFT calculations suggest the presence of H-bonding, as predicted from STM images,[161] and of substrate-mediated interactions, as expected from NIXSW structural data (section 7.4.1). This last interaction channel was already found to be predominant for TCNQ/Cu(100).[162] In that case, TCNQ undergoes charge transfer from the surface, with consequent larger conformational freedom[176] and strong interaction of the cyano groups with Cu atoms, which, in absence of H-bonding, lead to the anisotropic island growth.

The latter example reinforces the idea that the substrate-mediated energy gain can play a significant role in the formation of molecular islands. Nevertheless, in the case of TPA/Cu(100) the co-presence of H-bonding does not allow their relative contribution to be more accurately quantified, although DFT calculations strongly suggest their co-existence in the formation of large and exceedingly ordered domains of deprotonated TPA on the Cu(100) surface.

7.5 Conclusions

NIXSW data, presented in section 7.3, provide a detailed adsorption geometry of deprotonated TPA on the Cu(100) surface. The significant distortion of the gas-phase planar geometry (Figure 7.16) reflects the competition between two main interactions:

- the O-Cu bonds with a strong chemical character, as suggested by the interatomic distance smaller than the sum of the corresponding covalent radii,
- the Pauli repulsion experienced by the aromatic ring when it is pulled closer to the surface by the carboxylate groups.

The deformation of the carbon backbone is also suggested by the lower F_c (Table 7.7), compared to the carboxylate C, and is estimated on the basis of NIXSW simulations (Figure 7.17).

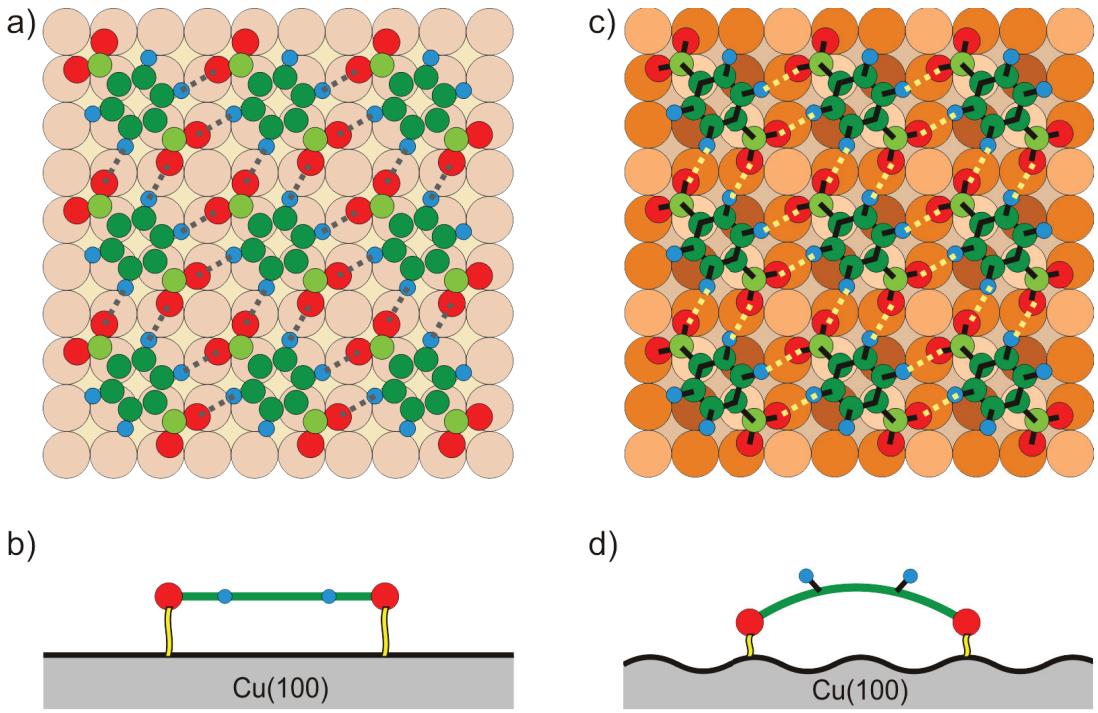


Figure 7.24: Top view (a) and schematic side view (b) of flat-lying deprotonated TPA molecules adsorbed on Cu(100), where H-bonding is highlighted by the dotted gray lines. This model results from STM and NEXAFS data.[161] Top view (c) and schematic side view (d) of deprotonated TPA adsorbed on Cu(100), where both H-bonding and buckling of the surface leading to substrate mediated intermolecular interactions are highlighted respectively by the dotted yellow lines and the colored Cu atoms (Figure 7.23). This model results from NIXSW data and DFT calculations,[163] supported by HREELS.[5]

Interestingly, the differential chemistry of the deprotonated TPA molecule cannot be accurately predicted by DFT-PBE calculations, which instead provide a much flatter adsorption geometry for TPA/Cu(100). This significant qualitative difference between experimental and theoretical results indicates the presence of a shortcoming in the PBE functional for the description of this and probably similar strongly interacting organic molecules at metal surfaces.

Moreover, the flaw of DFT calculations is not due to the lack of vdW dispersion forces. In fact, their inclusion in the form of semiempirical corrections (PBE-D), already proven to be accurate for several systems,[3,4] does not heal the disagreement with NIXSW adsorption geometry. In contrast, PBE-D calculations yield the same molecule-substrate interatomic distances (Table 7.11) and very similar structural properties (Table 7.10 and 7.12).

In order to investigate the intermolecular interactions, further DFT calculations of different TPA configurations are carried out and indicate the presence of both H-bonding and substrate-mediated interactions. This result is in qualitative agreement with the model based on STM and NEXAFS data,[161] which proposes H-bonded flat-lying TPA molecules (Figure 7.24a,b), and also confirms the presence of a substrate-mediated interaction, suggested on the basis of a HREELS study,[5] and in agreement with the strong distortion of TPA (Figure 7.24d) reflecting a significant molecule-substrate interaction, proven by NIXSW data.

We can therefore conclude that this NIXSW study helps shed light on the complex molecule-substrate and molecule-molecule interactions of TPA/Cu(100). The idea of H-bonded flat-lying TPA molecules based on STM and NEXAFS data[161] is partly revised in light of NIXSW structural data, supported by DFT calculations[163] and HREELS.[5] According to the present scenario, TPA molecules adsorb in an arc-like geometry with the carboxylate groups pointing towards the surface and both H-bonding and substrate-mediated interactions are ascribed as the stabilizing forces of the molecular islands. This deeper insight in the molecule-substrate interface represents the basis for understanding how interactions change upon deposition of an external metal to form the technologically relevant metal-organic networks.

8 Summary and conclusions

In this study, several molecule-metal interfaces are investigated in order to gain a deeper understanding of the elementary processes governing organic molecules at metal surfaces. In particular, with the aim of assessing the role played by the substrate within molecule-metal interfaces, the extensively studied PTCDA molecule is investigated on the Ag(110) surface (chapter 4). In this way, the series of experiments on the other low indices Ag surfaces, i.e., (111) and (100), has been completed. The adsorption heights resulting from NIXSW experiments, and analyzed by the newly developed open-source program Torricelli (chapter 3 and appendix A), yield two main outcomes. First, the perylene core is closer to the more open Ag(110) surface, at 2.59 Å, with respect to the less reactive Ag(100), Ag(111), and Au(111) substrates, where the perylene core is at 2.84 Å,[1] 2.86 Å[2] and 3.27 Å,[177] respectively. Second, both carboxylic and anhydride oxygen atoms appear below the carbon backbone and have the same interatomic distance (2.45 Å) from the Ag atoms underneath (section 4.4.2). In contrast, on the more closed-packed surfaces, anhydride oxygens are further away from the surface compared to the carboxylic oxygens suggesting a weaker molecule-metal interaction. This evidence suggests that the local bonds of the molecular functional groups pull the molecule closer to the surface and cause a stronger distortion of the gas-phase planar geometry. As a result, the influence of the substrate on the geometric and chemical properties of a molecule-metal interface is proved. Specifically, the more reactive the substrate, the stronger the molecule-metal interaction and the more distorted the molecular geometry. Moreover, the adsorption geometry of PTCDA/Ag(110) confirms the bonding mechanism, proposed for PTCDA/Ag(111),[2,93,178] based on charge transfer to the LUMO, mainly located at the perylene core, and the chemical interaction of the functional groups with the substrate atoms.

The prototypical molecular unit TPA, typically used in 2D metal-organic networks, experiences an relevant modification of the gas-phase molecular geometry induced by the substrate when adsorbs on Cu(100). In fact, upon adsorption, TPA undergoes

a deprotonation process, as testified by XPS (section 7.2.1). Furthermore, NIXSW experiments reveal a significantly distorted molecular geometry with the carboxylate groups covalently bound to the Cu atoms underneath and the carbon backbone bent due to the competition between the chemically interacting end groups and the Pauli-repelled C-ring (section 7.4.1). The arc-like geometry and the interatomic distance O-Cu, below the sum of the corresponding covalent radii, indicate a direct bonding to the metal surface, in agreement with HREELS measurements.[5] Both pieces of evidence suggest the presence of a substrate-mediated interaction, apart from the intermolecular H-bonding, as a stabilizing force of the long-range ordered molecular islands. This conjecture is supported by DFT calculations aimed to determine the adsorption energy of TPA in different local environments (section 7.4.2).

Having highlighted the influence of the substrate on the geometry and chemistry of a molecule-metal interface, we go one step further and show how the interaction of an organic molecule with a metal substrate can be tuned. For this purpose, K is deposited on PTCDA/Ag(110) and the sample is subsequently annealed. A combined study of the K+PTCDA/Ag(110) interface by means of NIXSW, XPS, UPS, LEED and STM provides the following results: The anhydride groups of PTCDA unbind from the surface and lift by approximately 0.30 Å, due to the presence of K atoms underneath, while the perylene core is only 0.05 Å higher because of a still reactive surface, in comparison with the bare molecular phase (section 5.2.3). Upon K deposition, the Ag(110) surface undergoes a reconstruction mediated by PTCDA and activated by annealing. In fact, alternated up- and down- reconstructed Ag terraces, where K atoms are embedded, appear covered by single or double rows of PTCDA molecules (section 5.6). Therefore, on the one hand, the molecule-metal interaction is tuned, and on the other hand the interface is nanopatterned with the characteristic unit length defined by the size of the adsorbed molecule (section 5.4.3.4). This indicates that the surface is not passive and shows that alkali metal-induced reconstruction can be guided by organic molecules.

Among the functional organic molecules, the potential applications[24,25] of the molecular switches have attracted relevant scientific interest. In order to understand the functionality of the molecular switches adsorbed on metal surfaces, AB/Ag(111) and TBA/Ag(111) are investigated by means of NIXSW (chapter 6). The *tert*-butyl groups of TBA were believed to act as "spacer legs" and thus lift the molecule from the surface, enabling the switching in the solid state phase as well.[28,29,130,131] Surprisingly, the photochromic moiety (-N=N-) of TBA results only 0.13 Å further away

from the surface compared to AB.[3] Therefore, NIXSW bonding distances disprove the widely accepted strategy of the geometric decoupling of the molecular switches as a way to recover their functionality in the adsorbed state.

For a deeper understanding of the interaction channels between the molecular switches and the Ag(111) surface, NIXSW bonding distances are employed to benchmark different DFT approaches. Interestingly, the agreement between measured and calculated nitrogen adsorption heights is excellent only if van der Waals interactions are taken into account, although as a semiempirical correction term to the PBE functional.[3,4] This testifies to the significant role played by dispersive attractive interactions, especially for molecules with closed-shell phenyl rings as AB and TBA adsorbed on a closed-packed surface as Ag(111). In contrast, the chemistry of a rather strongly chemisorbed molecule, i.e., TPA/Cu(100), is not accurately described by the DFT-PBE functional; nor does the vdW semiempirical correction offset this shortcoming. This case study reveals a flaw in the PBE functional, also for such apparently simple system. Hopefully, this disagreement between theory and experiments will motivate further theoretical studies for improving the understanding of this prototypical molecule-metal interface.

Finally, for a more accurate determination of the adsorption geometry of large organic molecules, e.g., AB and TBA, the respective molecular degrees of freedom are investigated by means of the newly developed vector analysis in the Argand diagram (section 6.4.1.2). This powerful analysis tool allows structural details that are otherwise inscrutable to be determined and represents a valuable reference for judging theoretical predictions. In general, the vector analysis in the Argand diagram is necessary to retrieve the adsorption geometry of molecules extending over more than one Bragg spacing d_{hkl}. In fact, in this case, because of the modulo 1 ambiguity, the coherent position may not correspond to the real space average of the single atomic vertical positions (section 6.4.1.2). To calculate the latter parameter, the simulated atomic vertical positions must be summed in the Argand diagram and compared to NIXSW structural parameters. As a result, with this method, the bonding conformation of a broader range of organic molecules can be obtained with great accuracy. In particular, the vector analysis provides detailed bonding conformations of AB and TBA (sections 6.4.1.3 and 6.4.2.4) in perfect agreement with NIXSW and with a unique coherent fraction for the whole molecule. In summary, this deeper analysis of NIXSW data is a method (i) for learning about fine details of the adsorbed molecule, beyond the average vertical position, (ii) for benchmarking different DFT schemes,

and finally (iii) for better understanding the molecule-substrate interaction through a more detailed knowledge of the interface geometry.

A Technical details and code of Torricelli

A.1 Introduction

This appendix contains the most important parts of Torricelli code which are relevant for understanding the program and the *physics* behind it. It is subdivided into six sections, one for each of the modules forming Torricelli:

- preparing reflectivity and electron yield profiles for fitting,
- fitting the reflectivity,
- calculating the ideal reflectivity,
- calculating the structure factors,
- fitting the electron yield profile: coherent position and fraction,
- calculating nondipolar correction parameters,
- fitting the electron yield profile: the asymmetry parameter Q.

The lines reported below appear at the beginning of each source file and concern the license with which the program is released and the libraries imported and employed throughout the code.

```
1  # Copyright (C) 2010 Giuseppe Mercurio
2  # This file is part of Torricelli.~Torricelli is free software: you can
3  # redistribute it and/or modify it under the terms of the GNU General Public
4  # License as published by the Free Software Foundation, either version 3 of the
5  # License, or (at your option) any later version.~Torricelli is distributed in
6  # the hope that it will be useful, but WITHOUT ANY WARRANTY; without even the
7  # implied warranty of MERCHANTABILITY or FITNESS FOR A PARTICULAR PURPOSE.~
8  # See the GNU General Public License for more details.~You should have received
9  # a copy of the GNU General Public License along with Torricelli.~If not, see
10 # <http://www.gnu.org/licenses/>.
11 import pylab as pl
12 import scipy as sp
13 import numpy as np
```

```
14 from numpy import *
15 import matplotlib
16 import scipy.optimize
17 import os
```

A.2 Preparing reflectivity and electron yield profiles for fitting

A.2.1 Technical details

The main function of the first section of Torricelli is to import the raw experimental data (reflectivity and absorption profile) and normalize them by the intensity of the incoming x-ray beam. The output files will be then object of the respective fitting, as explained in sections A.3 and A.6. We will now see in detail all the operations carried out in this section of the program.

First of all, the user is asked to select or create a directory in which all the files created by Torricelli will be saved. Subsequently, the reflectivity and the absorption profile files are imported:

- The first consists of three columns: the experimental energy scale, the quantity proportional to the reflectivity R (section 2.6) and the quantity proportional to the intensity of the beam.
- The second consists of at least three columns, namely the photon energy scale (obviously equal to that of reflectivity); the absorption yield for each photon energy, and, finally, the corresponding standard deviation. The number of columns of the electron yield file is proportional to the number of fitting components forming the XPS model of a given spectrum. Specifically, in the presence of multiple components, there will be two more columns (electron yield plus corresponding standard deviation) for each additional fitting component. For details regarding the calculation of the standard deviation associated with the electron yield we refer to section 3.5.

Often XPS fitting models are developed to differentiate two or more atomic species and, at the same time, may consist of two or more components for each atomic species. Therefore, it would be desirable, on the one hand, to separately analyze components of different species belonging to the same spectrum and, on the other

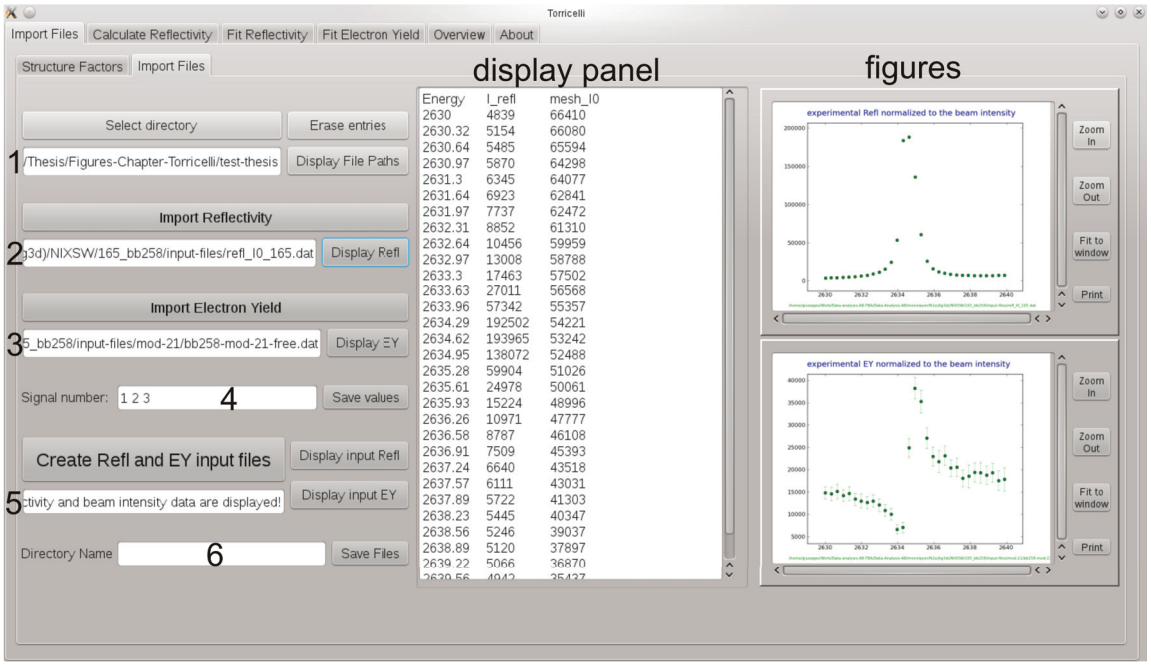


Figure A.1: "Import Files" section of Torricelli. On the left, all the buttons and text boxes are grouped. Text boxes are numbered from 1 to 6, of which 4 and 6 are input boxes while the rest are output boxes. The central region of the section is occupied by the display panel where text files can be visualized. On the right, there are two figure panels, to display the reflectivity and the electron yield after normalization by the intensity of the incoming beam.

hand, to sum components of the same species within the same spectrum. Both requests are fulfilled by Torricelli through the option "Signal number". In order to specify the electron yields to fit, the following convention is adopted. If we consider an electron yield file with four different signals, to select the first, the second, the third or the fourth one, the user should type 0, 1, 2 or 3 respectively. This nomenclature follows from the fact that often the first signal of the EY file is the *Region* (integrated area of the whole spectrum after background subtraction), while component areas come usually afterward. In the example reported in Figure 3.17, 1, 2 and 3 correspond to three fitting components of the XPS spectrum. If we are interested in analyzing their sum, we simply type in the "Signal number" text box "1 2 3" (separated by one space). The button "Save values" creates a file where the signal numbers specified above are stored. This file is then used by the "Create Refl and EY input file" function.

Finally, the button "Create Refl and EY input file" executes the following operations:

- First, the electron yield specified in "Signal number" is normalized by the intensity

of the incoming x-ray beam. If more than one signal is selected, the sum of the corresponding electron yields of the the specified components is normalized by the intensity of the incoming x-ray beam. This operation is carried out for the whole column of values, in other words, for each photon energy scanned during the NIXSW experiment (see section A.2.2, lines 30–55).

- Second, the reflectivity values are normalized by the intensity of the incoming x-ray beam and the corresponding standard deviation is calculated (see section A.2.2, lines 61–67). Assuming a Poisson distribution, the standard deviation is given by the square root of each reflectivity value.
- Third, the two resulting normalized signals are plotted as a function of the photon energy, and will be subsequently fitted as discussed in section A.3 and A.6.

The file path of the selected directory, where all files created by Torricelli are saved, is displayed in text box 1. The button "Display File Paths" enables visualization on the central display panel of the saved file paths. Text boxes 2 and 3 show the file path of the imported experimental files, whose content can be displayed in the central panel by clicking the corresponding buttons "Display Refl" and "Display EY". The buttons "Display input Refl" and "Display input EY" allow the visualization in the central display panel of the normalized reflectivity and electron yield text files, whose plots are reported in the corresponding windows on the right hand side of the section. The figures can also be zoomed in/out and printed, which is the case for all figure panels in Torricelli.

Other features present throughout the program are reported below. Each section has a text box (in this case 5), where comments regarding the operation just executed are reported. Moreover, Torricelli provides the user with the opportunity to save all the files created within each section in a separate folder, located in the same original selected directory, with the name specified in the "Directory Name" text box. This option can be useful if the user wants to compare results after changing some parameters or start with the analysis of a new set of data without changing the main directory. Finally, the button "Erase entries" deletes the content of each text box and allows the user to start over from the beginning.

A.2.2 Code

```
1 class Make_Files(object):
2 # the function consisting of the main program is defined
3     def run(self):
```

```
# the file containing the file paths is imported and read
        file_path_file = "./parameters/file_path.dat"
        file_path = sp.loadtxt (file_path_file, dtype = str, usecols=(2,))
# the experimental reflectivity (Refl) file (3 columns: energy, reflectivity,
# beam intensity) is read
        data_r = sp.loadtxt (file_path[0], dtype = "float", skiprows=1)
# the experimental photoelectron yield (EY) file (consisting of a variable
# number of columns depending on the number of components) is read
        data_ey = sp.loadtxt (file_path[1], dtype = "float", skiprows=3)
# the signal_file, containing the information about the number of column
# (signals) to sum is read.
        signal_file = sp.loadtxt (file_path[2], dtype = str)
        l = len(signal_file)
        signal_num = sp.zeros(7)
        sig_num = sp.zeros(7)
        col_num = sp.zeros(7)
# the beam intensity column is stored in i0 and its average in i0ave
        i0 = data_r[:,2]
        i0ave = sum(data_r[:,2])/len(data_r[:,2])
# a new file "ey_exp_1.dat" is created. "ey_exp_1" contains the energy values,
# the EY data and the corresponding standard deviation (STD). EY column can be
# only one signal (l=2) or the sum of multiple signals (l>2) specified by the
# user. It is possible to sum up to 7 different signals, corresponding to an
# equal number of fitting components. This file will be used by the
# "ideal_refl.py" in section A.3 to rescale the energy around 0, and then by
# "fit_EY.py" in section A.6 for the fitting of EY.
        if l == 2:
                for i in range (l-1):
                        sig_num[i] = int(signal_file[i+1])
# conversion of the signal number into a column number
                        col_num[i] = (2*sig_num[i]) +1
                fp = open ("./data/ey_exp_1.dat", "w")
                for i in range (len (data_ey[:, 0])):
                    x = data_ey[i, 0]
                    y = data_ey[i, col_num[0]]/i0[i]*i0ave
                    err = data_ey[i, col_num[0]+1]/i0[i]*i0ave
                    fp.write ("%+f        %+f        %+f\n" % (x, y, err))
                fp.close ()
# the following "if" condition sums two signals
        elif l == 3:
                for i in range (l-1):
                        sig_num[i] = int(signal_file[i+1])
                        col_num[i] = (2*sig_num[i]) +1
                fp = open ("./data/ey_exp_1.dat", "w")
                for i in range (len (data_ey[:, 0])):
                    x = data_ey[i, 0]
                    y = (data_ey[i, col_num[0]]+data_ey[i,
                        col_num[1]])/i0[i]*i0ave
                    err = (data_ey[i, col_num[0]+1]+data_ey[i,
                          col_num[1]+1])/i0[i]*i0ave
                    fp.write ("%+f        %+f        %+f\n" % (x, y, err))
                fp.close ()
# there are five more "if" conditions (not reported here) in order to sum up to
# seven signals.
# the file "refl_exp_1.dat" containing the reflectivity normalized to the beam
# intensity and the corresponding standard deviation (square root of each data
# point) is created
        fp = open ("./data/refl_exp_1.dat", "w")
        for i in range (len (data_r[:,0])):
            x = data_r[i,0]
            y = data_r[i,1]/i0[i]*i0ave
            err = sp.sqrt(data_r[i,1]/i0[i]*i0ave)
            fp.write ("%+f        %+e        %+f\n" % (x, y, err))
        fp.close ()
```

```
68  # the files "ey_exp_1.dat" and "refl_exp_1.dat", containing the experimental
69  # data normalized to the beam intensity and the corresponding standard
70  # deviations, are then plotted and saved both as figure and as text file.
71  # Moreover, both absolute paths are saved in the file "file_path.dat". The
72  # code of the operations listed above is here omitted and can be found in the
73  # original version of the code.
```

A.3 Fitting the reflectivity

A.3.1 Technical details

The fitting of the experimental reflectivity is carried out by the SciPy (scientific library for Python) function optimize.leastsq[179] (section A.3.2, lines 116–126) that minimizes the sum of squares of a given function, in our case, the difference (divided by the experimental standard deviation) between experimental reflectivity and the fitting function (section A.3.2, lines 9–60). As already mentioned in section 3.3, there are four fitting parameters: σ, N, ΔR and ΔE. Therefore, before running the actual fitting, the initial values of the fitting parameters must be specified in text boxes 1–4 (Figure A.2). This operation is performed by the "Set suggested Fit parameters". The default values that will appear are $\sigma = 0.1$, $\Delta E = -0.7$, N is equal to the largest experimental reflectivity value, and ΔR is equal to the opposite of the first experimental reflectivity value. The choice of this set of initial values

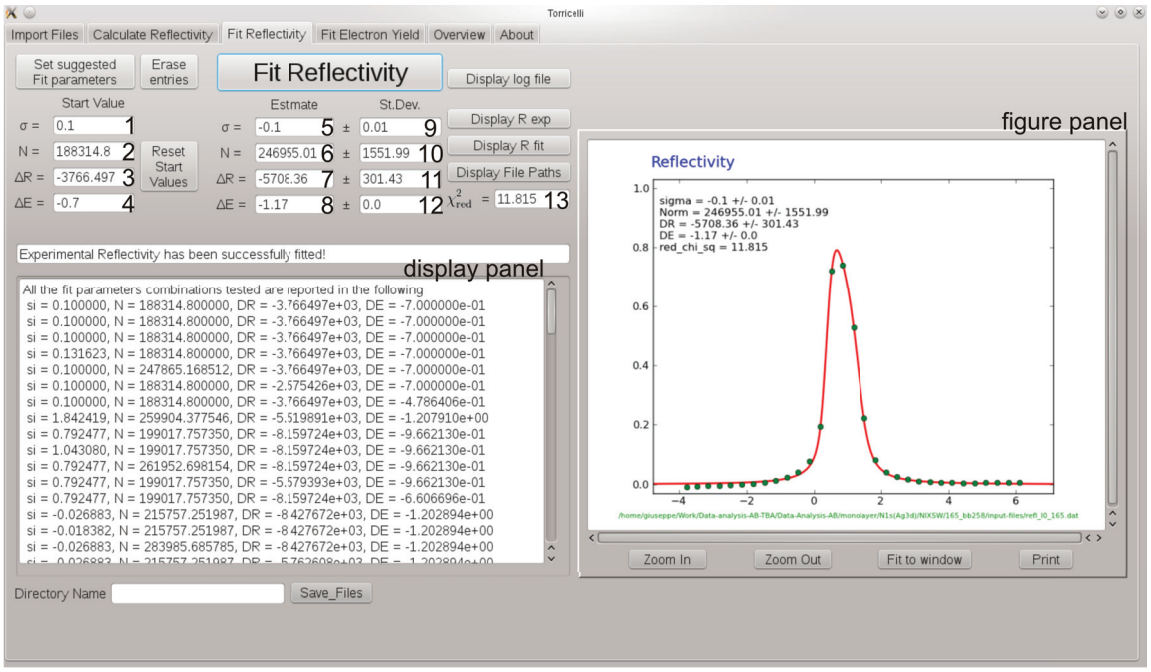


Figure A.2: "Fit Reflectivity" section of Torricelli.

has, in our case, always led to convergence of the fit. However the user can reset the initial fitting parameters and save the changes by clicking the "Reset Start Values" button.

The fitting routine is activated by clicking the "Fit Reflectivity" button. The fitted parameter values (section A.3.2, lines 127–131) will appear in text boxes 5–8, while the corresponding standard deviations (section A.3.2, lines 149–153) will be in text boxes 9–12. Finally, the resulting χ^2_{red} (reduced χ^2), i.e., χ^2 divided by the degrees of freedom (section A.3.2, lines 132–136), is shown in text box 13. The resulting fitting function and the experimental reflectivity are plotted in the figure panel on the right.

Moreover, as a result of the fit, the display panel shows all the combinations of fitting parameters tested by the fitting routine. In the same display panel it is possible to see the text file of the experimental reflectivity ("Display R exp" button), of the fitting function ("Display R fit" button), and of the file paths of all the files used by Torricelli ("Display File Paths" button).

A.3.2 Code

```
1  class Fit_Refl(object):
2  # The function "gauss" returns the Gaussian function with area normalized to 1.
3  # The function "gauss" has two input parameters: sigma and an array of energy
4      def gauss (self, sigma, energy):
5          g = sp.exp (-energy**2 / (2*sigma**2))        # the Gaussian is defined
6          norm = sum (g)                # the area of the Gaussian is calculated
7  # the Gaussian function normalized to its own area is returned as output
8          return g/norm
9  # Definition of the function "diff" which returns the difference between the
10 # experimental values and the calculated ones, normalized to the STD (standard
11 # deviation) of the experimental data. The "diff" function returns an array of
12 # values which are then squared and then summed, and this sum is minimized by
13 # the function sp.optimize.leastsq
14     def diff (self, params, xy, data):
15 # the four fitting parameters are initialized to the values resulting from the
16 # previous fitting iteration or, if it is the first iteration, to the values
17 # given as starting parameters by the user through the GUI
18         sigma = params[0]
19         Norm = params[1]
20         DR = params[2]
21         DE = params[3]
22 # the following function "gauss_xy" is employed to fit the experimental
23 # reflectivity. The fitting function consists essentially of the convolution of
24 # the so-called theoretical reflectivity (given by the convolution of the sample
25 # crystal reflectivity and the square of the monochromator crystal reflectivity,
26 # see section A.3) and the Gaussian function defined above. There are three
27 # fitting parameters: "Norm" is a factor which multiplies the above described
28 # convoluted functions; "sigma" is the width of the Gaussian function (see
29 # above); "DR" is a reflectivity offset.
30         gauss_xy = Norm * sp.convolve (xy[:, 1], self.gauss(sigma, xy[:, 0]),
31                                        mode = "same") - DR
32 # the fourth fitting parameter is "DE", a shift in the energy scale of the
```

```
33  # fitting function
34  # an array of energy values is created:
35          x_min = min (xy[:, 0])                  # minimum energy value of the array
36          x_max = max (xy[:, 0])                  # maximum energy value of the array
37          dx = (x_max - x_min) / len (gauss_xy)         # energy step of the array
38  # x is a new array of energy values shifted by DE: this will correspond to an
39  # energy shift of the fitting function
40          x = sp.arange (x_min, x_max, dx) + DE
41  # an array containing the experimental reflectivity values is created
42          n_data = data[:, 1]
43  # array that contains the fitting function values
44          y_m = sp.zeros(len (n_data))
45  # the following "for" loop looks for the value of the fitting function
46  # corresponding to the closest calculated energy value to the experimental one,
47  # for each experimental energy value
48          for i in range (len (data[:, 0])):
49  # the i^th experimental energy is read from the experimental reflectivity file
50              data_x = data[i, 0]
51  # x_lo = x[x > data_x][0] returns the smallest (lo->lowest) calculated energy
52  # value which is greater than data_x
53  # x_hi = x[x < data_x][len (x[x < data_x]) - 1] returns the largest
54  # (hi->highest) calculated energy value which is smaller than data_x
55  # y_lo is the fitting function value corresponding to x_lo
56              y_lo = gauss_xy[pl.find ((x > data_x))[0]]
57  # y_hi is the fitting function value corresponding to x_hi
58              y_hi = gauss_xy[pl.find ((x < data_x))[len (x[x < data_x]) - 1]]
59  # y_m is the average of the two values y_lo and y_hi
60              y_m[i] = (y_lo + y_hi)*0.5
61  # the following two lines save each combination of the fitting parameters
62  # tested at each iteration in a log file
63          fp = open ("./data/log_refl_fit.dat", "a")
64          fp.write (" si = %f, N = %f, DR = %+e, DE = %+e\n" % (sigma,Norm,DR,DE))
65  # the "diff" function returns the difference between the experimental value
66  # "n_data" and the value of the fitting function "y_m", divided by the largest
67  # square root of the experimental reflectivity values (saved in the second
68  # column of the file), for each experimental energy. The choice of taking the
69  # largest square root as a standard deviation is to be more conservative in the
70  # error estimation, and in order not to weight reflectivity values of the tail
71  # and of the peak differently. The assumption is that the reflectivity signal
72  # follows the Poisson statistic, therefore the standard deviation is equal to
73  # the square root of the counts.
74          return (n_data - y_m) / max(data[:, 2])
75  # The function consisting of the main program is in the following defined:
76      def run(self):
77  # the log file, where all combination of the fitting parameters are saved is
78  # created here
79          fp = open ("./data/log_refl_fit.dat", "w")
80          fp.write ("All the fit parameters combinations tested are reported in
81                     the following\n")
82          fp.close ()
83  # the "file_path.dat" file is imported and read
84          file_path_file = "./parameters/file_path.dat"
85          file_path = sp.loadtxt (file_path_file, dtype = str, usecols=(2,))
86  # file path of the experimental reflectivity "refl_exp.dat"
87          exp_file = file_path[10]
88  # file path of the theoretical reflectivity ("refl_cr_mono.dat"), i.e. the convo-
89  # lution of the sample crystal reflectivity and the square of the monochromator
90  # crystal reflectivity (with area normalized to 1, section A.3.2, lines 312-314)
91          theor_file = file_path[8]
92  # the content of the files just uploaded is saved in two new variables
93          data = sp.loadtxt (exp_file, dtype = "float")
94          xy = sp.loadtxt (theor_file, dtype = "float")
95  # path of the file containing the starting fitting parameters, this file
96  # contains the input values from the user inserted through the GUI
97          start_fit_par_file = file_path[12]
```

```
98  # the content of the files just uploaded is read
99          start_fit_par = sp.loadtxt (start_fit_par_file,dtype=float,usecols=(1,))
100 # initial values of the fitting parameters
101         sigma = float(start_fit_par[0])
102         Norm = float(start_fit_par[1])
103         DR = float(start_fit_par[2])
104         DE = float(start_fit_par[3])
105 # convolution of the theoretical reflectivity (R_cr * R_mo^2) and the Gaussian
106 # function with the initial sigma value
107         gauss_xy = sp.convolve (xy[:, 1], self.gauss(sigma, xy[:, 0]))
108 # the experimental reflectivity and the fitting function corresponding to the
109 # initial fitting parameters are plotted (code omitted)
110 # the vector containing the starting fitting parameters is initialized
111         params = sp.zeros (4)
112         params[0] = sigma
113         params[1] = Norm
114         params[2] = DR
115         params[3] = DE
116 # the following function minimizes the sum of the squares of the function
117 # "diff". "sp.optimize.leastsq" calls the function "diff" and in turn the Gauss
118 # function iteratively.
119         params, cov_x, info, msg, ierr = sp.optimize.leastsq ( \
120             self.diff, \
121             params, \
122             args = (xy, data), \
123             ftol = 1e-24, \
124             full_output = 1, \
125             epsfcn = 1e-1 \
126             )
127 # The parameters fitted by sp.optimize.leastsq
128         sigma = params[0]
129         Norm = params[1]
130         DR = params[2]
131         DE = params[3]
132 # degrees of freedom (dof) = N-P, where N is the number of data points being
133 # fitted and P is the number of fitted parameters.
134         dof = len(data[:,0]) - len(params)
135 # reduced chi^2 = chi^2 / dof
136         chi_sq = sum (self.diff(params, xy, data)**2)/dof
137 # covariance matrix: obtained by multiplying the matrix "cov_x" (output of
138 # "sp.optimize.leastsq") times the residual standard deviation, i.e. the
139 # reduced chi_sq calculated above
140         cov = chi_sq * np.diag(cov_x)
141 # the diagonal of the covariance matrix contains the variance of the fitted
142 # parameters, therefore the corresponding standard deviation is given by the
143 # square root of the diagonal of the covariance matrix, as calculated in the
144 # "for" loop below
145 # the uncertainty associated to the four fitting parameters is saved in "err"
146         err = [0,0,0,0]
147         for i in range(4):
148           err[i]=sp.sqrt(cov[i])
149 # name of the errors:
150         stdev_sigma = round(err[0],2)
151         stdev_Norm = round(err[1],2)
152         stdev_DR = round(err[2],2)
153         stdev_DE = round(err[3],2)
154 # calculation of the fitting function gauss_xy with the parameters resulting
155 # from the fit
156         gauss_xy = sp.convolve (xy[:, 1], self.gauss(sigma, xy[:, 0]), "same")
157         x_min = min (xy[:, 0])
158         x_max = max (xy[:, 0])
159         dx = (x_max - x_min) / len (gauss_xy)
```

```
160         r_path = os.path.abspath(file_path[0])
161 # experimental reflectivity and the fitting curve are plotted (only the three
162 # most significant lines of the code are reported)
163         pl.plot (sp.arange (x_min, x_max, dx), gauss_xy, linewidth=2, color='r')
164 # plot of the experimental reflectivity
165         pl.plot (data[:, 0] - DE, (data[:, 1] + DR)/Norm, "o")
166 # setting of the axes
167         pl.axis ([min (data[:, 0] - DE) - 1, max (data[:, 0] - DE) + 1, -0.03,
168                                                 1.03])
169 # output files of this section (code is omitted):
170 # "en_theo_fit.dat": file containing the energy scale after the fit, with the
171 # fitted shift DE;
172 # "R_theo_fit.dat": file containing the fitting curve "gauss_xy" with the fitted
173 # parameters "sigma" as a function of the energy scale shifted by "DE"
174 # "R_exp_fit.dat": file containing the experimental reflectivity shifted by the
175 # vertical offset "DR" and normalized by "Norm" as a function of the the energy
176 # scale shifted by "DE".
177 # The experimental reflectivity is imported to retrieve the value c by which the
178 # absolute energy scale has been shifted before fitting in order to bring it
179 # around 0
180         refl_exp_file = file_path[3]
181         data_r = sp.loadtxt (refl_exp_file, dtype = "float")
182 # the constant energy subtracted to the absolute energy scale in order to bring
183 # it around 0
184         c = ( min (data_r[:,0]) + ( max (data_r[:,0]) - min (data_r[:,0]) )/2 )
185 # the following output files (code is omitted) are analogous files as
186 # before but with the absolute experimental energy scale:
187 # "en_theo_fit_abs.dat": file containing the absolute energy scale shifted by DE
188 # "R_theo_fit_abs.dat": file containing the fitting curve "gauss_xy" with the
189 # fitted parameters "sigma" as a function of the absolute energy scale shifted
190 # by "DE";
191 # "R_exp_fit_abs.dat": file containing the experimental reflectivity shifted by
192 # the vertical offset "DR" and normalized by "Norm" as a function of the the
193 # absolute energy scale shifted by "DE".
194 # A vector containing the fitted parameters "sigma" and "DE" is created. Its
195 # file path is saved and it will be used to in the photoelectron yield fit (code
196 # omitted).
197 # The Bragg energy is defined:
198         Bragg_En = c+DE
199 # The file "fitted_refl_par.dat" to save the fitted parameters and the reduce
200 # chi^2 is created (code omitted).
```

A.4 Calculating the ideal reflectivity

A.4.1 Technical details

The "Calculate Reflectivity" section of Torricelli employs the formula reported and discussed in section 3.3.2 to calculate the reflectivity and phase of the sample and of the monochromator crystal.

The input file that can be loaded by clicking the "Import prm file" button consists of all the information about the crystal needed to calculate the reflectivity and the phase, e.g., lattice constant, Bragg spacing and structure factors. This input file

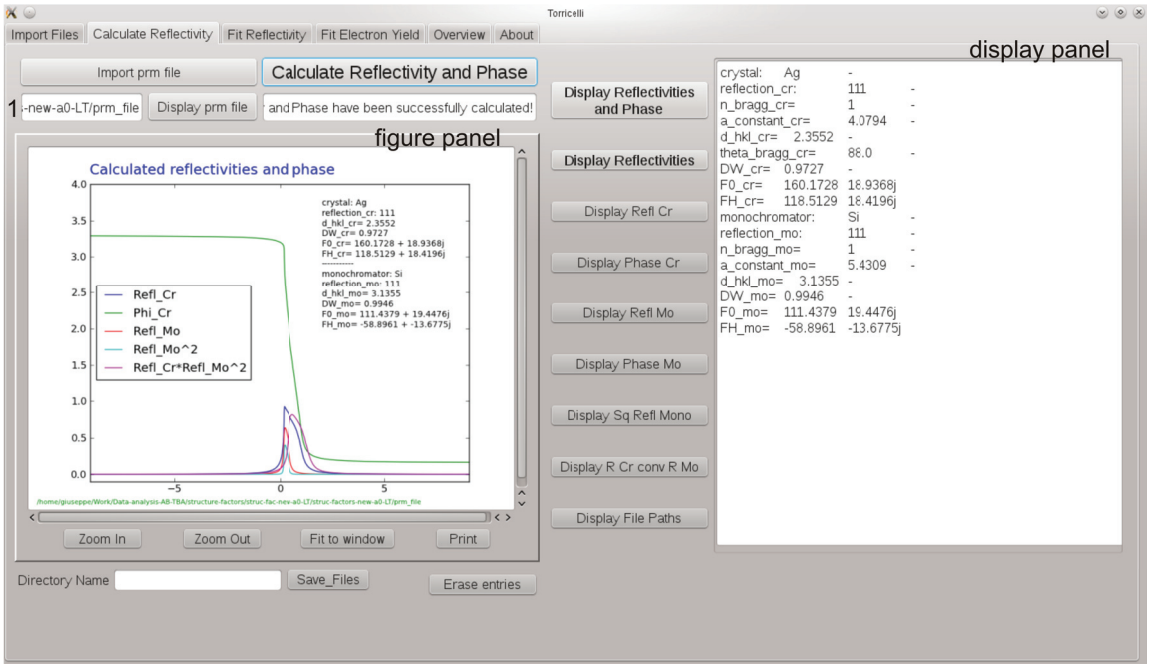


Figure A.3: "Calculate Reflectivity" section of Torricelli.

can be created by Torricelli itself as explained in sections 3.3.3, where a detailed description of how structure factors are calculated is provided. Text box 1 (Figure A.3) shows the file path of the input file and its content can be shown in the display panel by clicking the "Display prm file" button.

The calculations of the reflectivity and phase are activated by clicking the "Calculate Reflectivity and Phase" button. As a result, the figure panel will show the plot of R_{sa}, Φ_{sa}, R_{mo}, R^2_{mo}, $R_{sa} \otimes R^2_{mo}$ and the corresponding text files can be visualized in the display panel by clicking the respective button next to it (see Figure A.3).

A.4.2 Code

```
# The formula used to calculate reflectivity and phase come from the following
# three references:
# 1) B. W. Batterman and H. Cole, Dynamical diffraction of X rays by perfect
# crystals, Rev. Mod. Phys. (1964), in short: Batterman64RMP36_681;
# 2) D. P. Woodruff, Normal incidence x-ray standing wave determination of
# adsorbate structures, Progress in Surface Science 57(1), 1 (1998), in short:
# Woodruff98PiSS57_1;
# 3) J. Zegenhagen, Surface structure determination with x-ray standing waves,
# Surface Science Reports 18(7-8), 202 (1993), in short: Zegenhagen93SSR18_202.
class Ideal_Refl(object):
# the function consisting of the main program is defined
    def run(self):
# the "file_path.dat" file is imported
        file_path_file = "./parameters/file_path.dat"
```

```
# the "file_path.dat" file is read
        file_path = sp.loadtxt (file_path_file, dtype = str, usecols=(2,))
# the parameter file containing the information about the crystals is read
# name and reflection of the crystal
        par_name_cr = sp.loadtxt (file_path[5], dtype = str, usecols=(1,))
# all the real parameters
        par_r_cr = sp.loadtxt (file_path[5],dtype=str, usecols=(1,), skiprows=2)
# all the imaginary parameters
        par_i_cr = sp.loadtxt (file_path[5],dtype=str, usecols=(2,), skiprows=7)
# the crystal parameters
# sample crystal name
        crystal = par_name_cr[0]
# sample Bragg reflection
        reflection_cr = par_name_cr[1]
# order of Bragg reflection (this is a read-only value, it does not affect any
# formula, it is here for completeness)
        n_bragg_cr = int(par_r_cr[0])
# lattice constant of the sample crystal
        a_constant_cr = float(par_r_cr[1])
# distance between two consecutive Bragg planes of the sample crystal
        d_hkl_cr = float(par_r_cr[2])
# angle theta between the photon beam direction and the surface plane
        theta_bragg_cr = float(par_r_cr[3]) * sp.pi / 180
# Debye-Waller factor, this value is also read-only, it is not used in the rest
# of the code, because it is already included in the structure factors!
        DW_cr = float(par_r_cr[4])
# structure factor for forward scattering
        F0_cr = float(par_r_cr[5]) + complex(par_i_cr[0])
# structure factor for the H=(hkl) reflection
        FH_cr = float(par_r_cr[6]) + complex(par_i_cr[1])
# relation valid for centrosymmetric crystals having the origin of the Bravais
# lattice at the symmetry center
        FH_bar_cr = FH_cr
# b parameter (see Batterman64RMP36_681). It is defined as b= gamma_0/gamma_H,
# where gamma_0=n*s_0, and gamma_H=n*s_H are the direction cosines of the
# incident and diffracted beams with respect to the incident surface (n is the
# normal to the surface, s_0 and s_H are the unit vectors in the incident and
# diffraction beam directions). For the symmetric Bragg reflection (b=-1). b
# negative indicates a Bragg reflection: entrance and exit beams through the
# same surface. Here b=-1 is a fixed value.
        b_cr = -1
# The parameter file containing the information about the monochromator is read
# Comments are omitted because the same parameters described above for the
# sample crystal are here reported for the monochromator crystal:
        par_name_mo = sp.loadtxt (file_path[5], dtype = str, usecols=(1,),
                                  skiprows = 9)
        par_r_mo = sp.loadtxt (file_path[5],dtype=str,usecols=(1,), skiprows=11)
        par_i_mo = sp.loadtxt (file_path[5],dtype=str,usecols=(2,), skiprows=15)
# the monochromator parameters
        monochromator = par_name_mo[0]
        reflection_mo = par_name_mo[1]
        n_bragg_mo = int(par_r_mo[0])
        a_constant_mo = float(par_r_mo[1])
        d_hkl_mo = float(par_r_mo[2])
        DW_mo = float(par_r_mo[3])
        F0_mo = float(par_r_mo[4]) + complex(par_i_mo[0])
        FH_mo = float(par_r_mo[5]) + complex(par_i_mo[1])
        FH_bar_mo = FH_mo
        b_mo = -1
# Constants and corresponding units
        planck_constant = 4.13566733e-15        # ev*s
        light_speed = 2.99792458e18               # Ang*s^-1
        electron_charge = 1.602176487e-19       # C=A*s
# unit of epsilon_0: F/m=(C/V)/m=(s^4*A^2)/(m^-3*kg)=(s^4*A^2)/(1e30*Ang^-3*kg)
        epsilon_0 = 8.854187817e-12/1e30
```

```
80          electron_mass = 9.10938215e-31                # kg
81          elelctron_radius = 2.8179402894e-5        # Ang
82  # lambda, Bragg energy, gamma of the sample crystal:
83  # "lambda_Bragg" is the wavelength corresponding to the Bragg energy
84  # ("energy_bragg"), calculated as in the "Calculate Structure Factors" section,
85  # using the experimental angle "theta_Bragg_energy" calculated from
86  # "lambda_bragg"
87          lambda_bragg = 2 * d_hkl_cr * sp.sin (theta_bragg_cr) / n_bragg_cr
88  # Bragg energy
89          energy_bragg = planck_constant * light_speed / lambda_bragg
90  # gamma parameter of the sample crystal at the Bragg energy (see
91  # Batterman64RMP36_681)
92          gamma_cr = (elelctron_radius * lambda_bragg**2)/(sp.pi*a_constant_cr**3)
93  # lambda, Bragg energy, gamma of the monochromator crystal:
94  # theta Bragg for the monochromator is derived knowing the lambda_bragg
95  # (Bragg_energy is defined by the sample crystal) and the Bragg plane distance
96  # d_hkl of the monochromator
97          theta_bragg_mo = sp.arcsin( (n_bragg_mo * lambda_bragg)/(2 * d_hkl_mo) )
98  # gamma parameter of the monochromator crystal at the Bragg energy
99  # (see Batterman64RMP36_681)
100         gamma_mo = (elelctron_radius * lambda_bragg**2)/(sp.pi*a_constant_mo**3)
101 # an array of theoretical energy values is generated, then for each of this
102 # energy values the ideal reflectivity and phase is calculated
103 # the minimum and the maximum values of this energy interval could be reduced in
104 # order to speed up the calculation, provided that it is always bigger than the
105 # experimental energy range
106         x_min = -10
107         x_max = 10
108 # energy step of this theoretical array of energies
109         dx = 0.02
110 # array of energies
111         en_delta = sp.arange (x_min, x_max + dx, dx)
112 # first absolute energy value corresponding to the smallest energy values of the
113 # array
114         en_first = energy_bragg + x_min
115 # array of zeros having the same length of the en_delta array: here the
116 # reflectivity values will be stored
117         refl_cr = sp.zeros ( len (en_delta) )
118 # array of zeros having the same length of the en_delta array: here the phase
119 # values will be stored
120         phi_cr = sp.zeros ( len (en_delta) )
121 # array of zeros having the same length of the en_delta array: here the
122 # reflectivity values will be stored
123         refl_mo = sp.zeros ( len (en_delta) )
124 # array of zeros having the same length of the en_delta array: here the phase
125 # values will be stored
126         phi_mo = sp.zeros ( len (en_delta) )
127 # beginning of the loop "for" where all the reflectivity and phase values are
128 # calculated:
129 # the index i goes from 0 to the total number of energies in the defined
130 # theoretical energy range
131         for i in range (int((x_max-x_min)/dx) +1):
132 # first value of absolute energy
133                 en = en_first + dx*i
134 # corresponding first value of delta energy (= absolute energy - E_Bragg)
135                 en_delta[i]
136 # the goal of this loop "for" is to calculate the modulo squared of the ratio of
137 # the complex field amplitudes (diffracted/incident) according to the formula
138 # 103 and 104 of Batterman64RMP36_681 (see also formula 2.3 of
139 # Woodruff98PiSS57_1). Furthermore, the phase has to be calculated, for this
140 # purpose formulas 2.10, 2.11, 2.12 of Zegenhagen93SSR18_202 have been followed.
141 # eta is calculated according to formula 2.4 of Woodruff98PiSS57_1. This
142 # parameter is a measure of how far the scattering conditions are from the
143 # midpoint of the Darwin reflectivity curve. |P| multiplies gamma_cr in the
144 # denominator, and P is a polarization factor which is always unity for NIXSW
145 # (sigma polarization), although at a more general incidence angle and in
```

```
146 # pi-polarization this factor is cos(2*theta_Bragg).
147                 eta_cr = ( -2 * ( en_delta[i] / en )*(sp.sin(theta_bragg_cr))**2
148                           + gamma_cr * F0_cr ) / ( gamma_cr * sp.sqrt( FH_cr *
149                           FH_bar_cr ) )
150 # real part of eta_cr
151                 eta_r_cr = sp.real(eta_cr)
152 # imaginary part of eta_cr
153                 eta_i_cr = sp.imag(eta_cr)
154 # eta is calculated for the monochromator crystal as described above
155                 eta_mo = ( -2 * ( en_delta[i] / en ) *
156                           (sp.sin(theta_bragg_mo))**2 + gamma_mo * F0_mo ) /
157                           ( gamma_mo * sp.sqrt( FH_mo * FH_bar_mo ) )
158 # real part of eta_mo
159                 eta_r_mo = sp.real(eta_mo)
160 # imaginary part of eta_mo
161                 eta_i_mo = sp.imag(eta_mo)
162 # sqrt(eta**2 -1) is calculated (for the sample crystal)
163                 eta_temp1_cr = sp.sqrt( eta_cr**2 - 1 )
164 # sqrt(eta**2 -1) is calculated (for the monochromator crystal)
165                 eta_temp1_mo = sp.sqrt( eta_mo**2 - 1 )
166 # calculation of the positive and negative solution eta +/- sqrt(eta**2 -1) for
167 # the sample crystal
168 # positive solution
169                 eta_temp2_plus_cr = eta_cr + eta_temp1_cr
170 # real part of the positive solution
171                 Re_eta_temp2_plus_cr = sp.real(eta_temp2_plus_cr)
172 # imaginary part of the positive solution
173                 Im_eta_temp2_plus_cr = sp.imag(eta_temp2_plus_cr)
174 # negative solution
175                 eta_temp2_minus_cr = eta_cr - eta_temp1_cr
176 # real part of the negative solution
177                 Re_eta_temp2_minus_cr = sp.real(eta_temp2_minus_cr)
178 # imaginary part of the negative solution
179                 Im_eta_temp2_minus_cr = sp.imag(eta_temp2_minus_cr)
180 # calculation of the positive and negative solution eta +/- sqrt(eta**2 -1) for
181 # the monochromator crystal
182 # positive solution
183                 eta_temp2_plus_mo = eta_mo + eta_temp1_mo
184 # real part of the positive solution
185                 Re_eta_temp2_plus_mo = sp.real(eta_temp2_plus_mo)
186 # imaginary part of the positive solution
187                 Im_eta_temp2_plus_mo = sp.imag(eta_temp2_plus_mo)
188 # negative solution
189                 eta_temp2_minus_mo = eta_mo - eta_temp1_mo
190 # real part of the negative solution
191                 Re_eta_temp2_minus_mo = sp.real(eta_temp2_minus_mo)
192 # imaginary part of the negative solution
193                 Im_eta_temp2_minus_mo = sp.imag(eta_temp2_minus_mo)
194 # calculation of the positive and negative solutions of the reflectivity of the
195 # sample crystal. |b| = 1 and F_H/F_H_bar = 1
196 # positive solution
197                 refl_plus_cr = (sp.absolute(eta_temp2_plus_cr))**2
198 # negative solution
199                 refl_minus_cr = (sp.absolute(eta_temp2_minus_cr))**2
200 # calculation of the positive and negative solutions of the reflectivity of the
201 # monochromator crystal. |b| = 1 and F_H/F_H_bar = 1
202 # positive solution
203                 refl_plus_mo = (sp.absolute(eta_temp2_plus_mo))**2
204 # negative solution
205                 refl_minus_mo = (sp.absolute(eta_temp2_minus_mo))**2
206 # calculation of the phase according to formula 2.10, 2.11, 2.12 of
207 # Zegenhagen93SSR18_202. The phase will depend on the sign of the Re(EH/E0) ->
208 # Re(sqrt(abs(b=-1))*eta_temp2_plus), Re(sqrt(abs(b=1))*eta_temp2_minus), where
209 # sqrt(abs(-1)) = 1 or -1. Both positive and negative solutions are considered
```

```
# in order to check which is the physical one. The result is that only the (-1)
# solution gives a physical continuous solution of the phase without any
# singularities, otherwise present in the positive solution. In the formula 2.3
# Woodruff98PSS57_1 the sign minus for the ratio of the field amplitudes is
# directly reported.
# The positive and negative solution of Re(EH/E0) and Im(EH/E0) of the sample
# crystal, with sqrt(abs(-1)) = -1
# real part of the ratio of the field amplitudes (positive solution)
                Re_EH_E0_plus_cr = (-1) * Re_eta_temp2_plus_cr
# imaginary part of the ratio of the field amplitudes (positive solution)
                Im_EH_E0_plus_cr = (-1) * Im_eta_temp2_plus_cr
# real part of the ratio of the field amplitudes (negative solution)
                Re_EH_E0_minus_cr = (-1) * Re_eta_temp2_minus_cr
# imaginary part of the ratio of the field amplitudes (negative solution)
                Im_EH_E0_minus_cr = (-1) * Im_eta_temp2_minus_cr
# calculation of the phase phi for the sample crystal:
# positive solution
                phi_temp1_plus_cr = sp.arctan(Im_EH_E0_plus_cr/Re_EH_E0_plus_cr)
# negative solution
                phi_temp1_minus_cr = sp.arctan(Im_EH_E0_minus_cr/Re_EH_E0_minus_cr)
# the sign of the ratio of the field amplitudes (positive solution) is checked
# in order to determine the corresponding phase value
                if Re_EH_E0_plus_cr < 0:
                        phi_temp2_plus_cr = phi_temp1_plus_cr + sp.pi
                elif Re_EH_E0_plus_cr > 0:
                        phi_temp2_plus_cr = phi_temp1_plus_cr
# the sign of the ratio of the field amplitudes (negative solution) is checked
# in order to determine the corresponding phase value
                if Re_EH_E0_minus_cr < 0:
                        phi_temp2_minus_cr = phi_temp1_minus_cr + sp.pi
                elif Re_EH_E0_minus_cr > 0:
                        phi_temp2_minus_cr = phi_temp1_minus_cr
# The following "if" statements are meant to define which one between the
# positive and the negative is the physical solution for reflectivity and phase
# of the sample crystal.
# The condition is such that if the positive solution of the reflectivity is
# smaller than 1 and the negative solution is greater than 1 for that particular
# i^th energy, then the positive solution of reflectivity and phase will be
# considered
                if refl_plus_cr < 1 :
                        if refl_minus_cr > 1 :
                                refl_cr[i] = refl_plus_cr
                                phi_cr[i] = phi_temp2_plus_cr
# vice versa if the negative solution of the reflectivity is smaller than 1 and
# the positive solution is greater than 1 for that particular i^th energy, then
# the negative solution of reflectivity and phase will be considered
                if refl_plus_cr > 1 :
                        if refl_minus_cr < 1 :
                                refl_cr[i] = refl_minus_cr
                                phi_cr[i] = phi_temp2_minus_cr
# the following condition applies in case both positive and negative solutions
# are unphysical because the reflectivity is greater than 1
                if refl_plus_cr > 1 :
                        if refl_minus_cr > 1 :
                                refl_cr[i] = -1 # arbitrarly chosen value of -1
                                phi_cr[i] = -1  # arbitrarly chosen value of -1
# the positive and negative solution of Re(EH/E0) and Im(EH/E0) of the
# monochromator crystal, with sqrt(abs(-1)) = -1.
# The same comments made for the sample crystal parameters apply in the
# following for the monochromator parameters, therefore they are omitted, and
# only the code is reported.
                Re_EH_E0_plus_mo = (-1) * Re_eta_temp2_plus_mo
                Im_EH_E0_plus_mo = (-1) * Im_eta_temp2_plus_mo
                Re_EH_E0_minus_mo = (-1) * Re_eta_temp2_minus_mo
                Im_EH_E0_minus_mo = (-1) * Im_eta_temp2_minus_mo
```

```
# calculation of the phase phi for the monochromator crystal:
                phi_temp1_plus_mo = sp.arctan(Im_EH_E0_plus_mo/Re_EH_E0_plus_mo)
                phi_temp1_minus_mo = sp.arctan(Im_EH_E0_minus_mo/Re_EH_E0_minus_mo)
# the sign of the ratio of the field amplitudes (positive and negative
# solutions) is checked in order to determine the corresponding phase value
                if Re_EH_E0_plus_mo < 0:
                        phi_temp2_plus_mo = phi_temp1_plus_mo + sp.pi
                elif Re_EH_E0_plus_mo > 0:
                        phi_temp2_plus_mo = phi_temp1_plus_mo
                if Re_EH_E0_minus_mo < 0:
                        phi_temp2_minus_mo = phi_temp1_minus_mo + sp.pi
                elif Re_EH_E0_minus_mo > 0:
                        phi_temp2_minus_mo = phi_temp1_minus_mo
# The following "if" statements are meant to define which one between the
# positive and the negative is the physical solution for reflectivity and phase
# of the monochromator crystal:
                if refl_plus_mo < 1 :
                        if refl_minus_mo > 1 :
                                refl_mo[i] = refl_plus_mo
                                phi_mo[i] = phi_temp2_plus_mo
                if refl_plus_mo > 1 :
                        if refl_minus_mo < 1 :
                                refl_mo[i] = refl_minus_mo
                                phi_mo[i] = phi_temp2_minus_mo
                if refl_plus_mo > 1 :
                        if refl_minus_mo > 1 :
                                refl_mo[i] = -1 # arbitrarly chosen value of -1
                                phi_mo[i] = -1  # arbitrarly chosen value of -1
# end of the "for" loop.
# At end of the loop the reflectivity and phase for both the sample and the
# monochromator crystals are calculated for each of the energy values of the
# theoretical energy range.
# The reflectivity and the phase of the sample crystal and the
# reflectivity of the monochromator are plotted (code omitted)
# The square of the monochromator reflectivity is calculated
        sq_refl_mo = refl_mo**2
# and then plotted (code omitted)
# the area of sq_refl_mo is normalized to 1, so that it will not affect the
# area of the the sample crystal reflectivity when they are convoluted
        sq_refl_mo_norm = sq_refl_mo/sum(sq_refl_mo)
# convolution of the sample crystal reflectivity with the square of the
# monochromator reflectivity having area normalized to 1.
        refl_cr_conv_sq_mo = sp.convolve (refl_cr, sq_refl_mo_norm, mode='same')
# convolution of the sample crystal phase with the square of the monochromator
# reflectivity having area normalized to 1. This convolution is calculated only
# in order to check how much this convolution affect the phase term, but it will
# not be used in the rest of the program
        phi_cr_conv_sq_mo =  sp.convolve ( phi_cr, sq_refl_mo_norm, mode = 'same')
# all the crystal information including the structure factors are read:
        prm_path = os.path.abspath(file_path[5])
# sample crystal information
        crystal = par_name_cr[0]                # sample crystal name
        reflection_cr = par_name_cr[1]              # sample Bragg reflection
        n_bragg_cr = int(par_r_cr[0])               # order of Bragg reflection
# lattice constant of the sample crystal
        a_constant_cr = float(par_r_cr[1])
# Bragg planes distance of the sample crystal
        d_hkl_cr = float(par_r_cr[2])
# angle theta between the photon beam direction and the surface plane
        theta_bragg_cr = float(par_r_cr[3]) * sp.pi / 180
# Debye-Waller factor, this value is also read-only, it is not used in the rest
# of the code, because it is already included in the structure factors!
        DW_cr = float(par_r_cr[4])
# structure factor for forward scattering
```

```
339         F0_cr = float(par_r_cr[5]) + complex(par_i_cr[0])
340 # structure factor for the H=(hkl) reflection
341         FH_cr = float(par_r_cr[6]) + complex(par_i_cr[1])
342 # relation valid for centrosymmetric crystals having the origin of the Bravais
343 # lattice at the symmetry center
344         FH_bar_cr = FH_cr
345 # monochromator crystal information (comments are omitted because analogous to
346 # the ones of the sample crystal above)
347         monochromator = par_name_mo[0]
348         reflection_mo = par_name_mo[1]
349         n_bragg_mo = int(par_r_mo[0])
350         a_constant_mo = float(par_r_mo[1])
351         d_hkl_mo = float(par_r_mo[2])
352         DW_mo = float(par_r_mo[3])
353         F0_mo = float(par_r_mo[4]) + complex(par_i_mo[0])
354         FH_mo = float(par_r_mo[5]) + complex(par_i_mo[1])
355         FH_bar_mo = FH_mo
356 # the ideal sample crystal reflectivity, the ideal monochromator crystal
357 # reflectivity, the square of the monochromator reflectivity, and the
358 # convolution of the sample reflectivity and the square of the monochromator
359 # reflectivity are plotted (code omitted).
360 # The following output files, containing results of reflectivities and phases
361 # are created:
362 # file containing the reflectivity of the sample crystal
363 # file containing the phase of the sample crystal reflectivity
364 # file containing the reflectivity of the monochromator crystal
365 # file containing the phase of the monochromator crystal reflectivity
366 # file containing the square of the reflectivity of the monochromator
367 # whose area is normalized to 1
368 # file containing the convolution of the sample crystal reflectivity and
369 # the square of the monochromator crystal reflectivities
370 # experimental reflectivity and photoelectron yield data from section A.1 are
371 # imported in order to rescale the energy axis from the absolute values to the
372 # values around 0
373 # the normalized reflectivity from section A.1 is imported
374         data_r = sp.loadtxt (file_path[3], dtype = "float")
375 # experimental energies are rescaled and transformed to a relative energy scale,
376 # where 0 corresponds to the mean experimental energy value.
377         data_r[:,0] = data_r[:,0] - ( min (data_r[:,0]) + ( max (data_r[:,0]) -
378                                       min (data_r[:,0]) )/2 )
379 # the reflectivity with the modified energy scale is plotted (code omitted)
380 # the reflectivity with the modified energy scale is saved and will be the input
381 # for the reflectivity fit function (code omitted)
382 # the normalized photoelectron yield from section A.1 is imported
383         data_ey = sp.loadtxt (file_path[4], dtype = "float")
384 # experimental energies are rescaled as for the reflectivity above
385         data_ey[:,0] = data_r[:,0]
386 # the photoelectron yield with the modified energy scale is plotted (code
387 # omitted)
388 # the photoelectron yield with the modified energy scale is saved and will be
389 # the input for the photoelectron yield fit function (code omitted)
390 # the paths of the following files used for the fit of the experimental
391 # reflectivity and the photoelectron yield are saved in "file_path.dat":
392 # "refl_cr.dat": the ideal sample reflectivity;
393 # "phi_cr.dat": the phase of the ideal sample reflectivity;
394 # "refl_cr_mono.dat": the ideal monochromator reflectivity;
395 # "sq_refl_mo_norm.dat": the square of the ideal monochromator reflectivity;
396 # "refl_exp.dat": the experimental reflectivity with the energy scale shifted
397 # around 0;
398 # "ey_exp.dat": the experimental photoelectron yield with the energy scale
399 # shifted around 0.
```

A.5 Calculating the structure factors

A.5.1 Technical details

The "Structure Factors" section of Torricelli, shown in Figure A.4 appears rather involved due to the many text boxes and buttons. In fact, there are many input and output parameters, the latter resulting from the use of equations reported in section 3.3.3.

First of all, the user is asked to select a directory in which all the files created in this section are saved. Subsequently, in both the "sample" and "monochromator" subsections, three files need to be uploaded:

- The "crystal file", containing information about the crystal, i.e., the name, the atomic number, the lattice constant, the atomic weight, the Debye temperature, and four parameters needed to determine the Debye-Waller factor according to Sears and Shelley.[43] As the sample crystal file is uploaded, text boxes 6, 10 and 15 fill with the corresponding values. The angle θ is also initialized to 88°, i.e., typical of NIXSW experiments and the sample temperature is set to 300 K. Both the latter

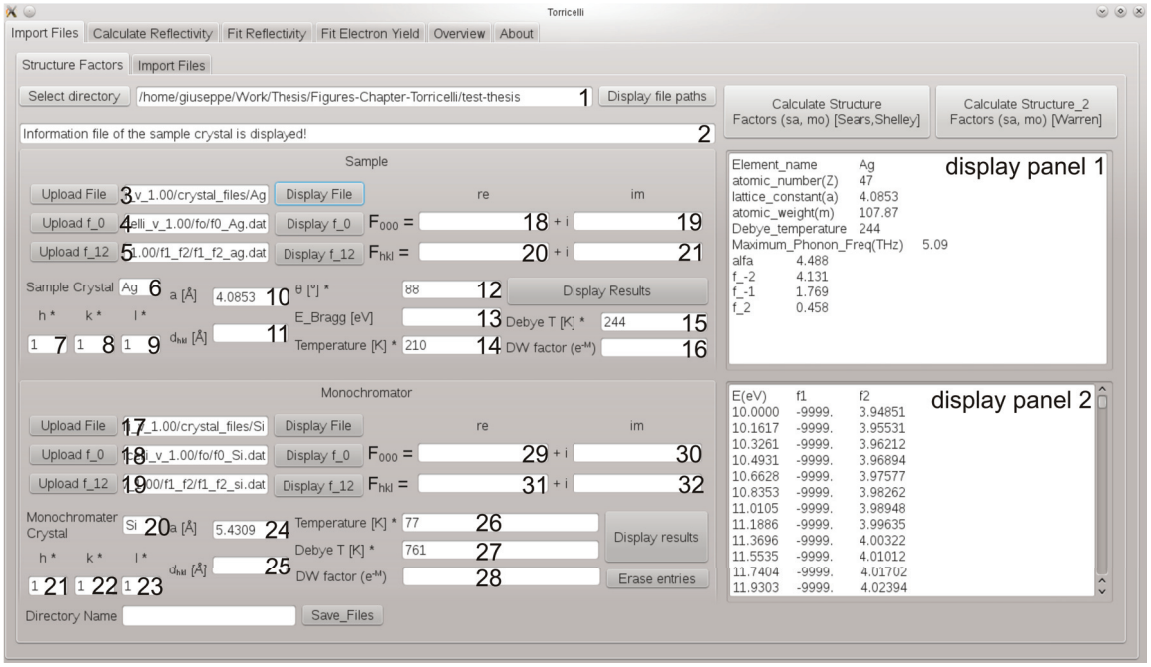


Figure A.4: "Structure Factors" section of Torricelli after importing the input files. Display panel 1 shows the sample crystal file, while display panel 2 shows the file containing the atomic scattering factors $f_1(0)$ and $f_2(0)$ of the monochromator Si crystal.

parameter and the Debye temperature can be reset by the user. Analogously, as the monochromator crystal file is uploaded, text boxes 20–24, 26, 27 are filled with the corresponding values that are characteristic of the experimental set-up at ID32 (ESRF) (section 2.6).

- The file containing the tabulated atomic form factors[40] as a function of $\frac{sin\theta}{\lambda} = \frac{1}{2d_{hkl}}$.
- The file containing the angular-independent scattering factors $f_1(0)$ and $f_2(0)$ tabulated as a function of the photon energy.[42]

As each file above is uploaded, its content appears in "Display panel 1" and "Display panel 2". To redisplay them it is sufficient to click the corresponding buttons beside text boxes 3, 4, 5 (sample) and 17, 18, 19 (monochromator), where the respective file path is shown.

Once all the information about the crystal and its scattering factors is uploaded, the Miller indices of the reflection to be investigated must be selected. Note that all the parameters marked with the "*" symbol can be modified by the user and are read by Torricelli.

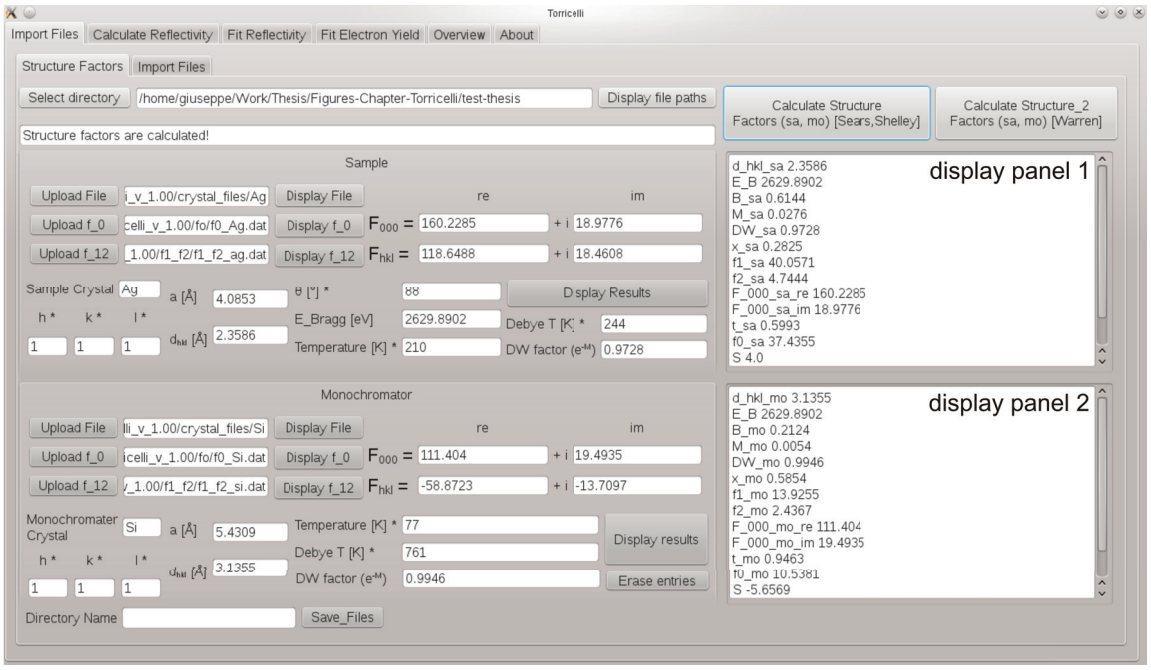


Figure A.5: "Structure Factors" section of Torricelli after the calculations of the structure factors. Display panel 1 and 2 show the calculated parameters of the sample and the monochromator crystals, respectively.

At this point it is possible to calculate the structure factors by clicking one of the two buttons at the upper right corner of the page in Figure A.4. The difference between the two approaches in the calculation of the Debye-Waller factor is explained in section 3.3.3.

As a result of the calculations, the text boxes in both sample and monochromator subsection regarding d_{hkl}, E_{Bragg}, the Debye-Waller factor and the structure factors contain now the calculated values (Figure A.5). At the same time, the "parameter" (prm) files are created and displayed in the corresponding display panel 1 and 2 (Figure A.5). These two files are then merged into a file that can be directly uploaded in section "Calculate Reflectivity" (section A.4.1) in order to calculate the reflectivities and phases of sample and monochromator crystals.

Moreover, the user can save the results in another folder by clicking the "Save Files" button (at the bottom in Figure A.5), after selecting a name for the new directory, and repeat the calculations with some changes to investigate e.g., the effect of the temperature on the reflectivity or to calculate E_{Bragg} for a given hkl-reflection. Also for this purpose the "Structure Factors" section is located even before "Import Files", since it may be actually used even before experiments are performed.

A.5.2 Code

```
# The following code is used to calculate the structure factors F_H.
# Two different approaches for calculating the Debye-Waller (DW) factor are
# employed:
# method 1) "run_sa_mo" calculates the structure factors and DW factor
# is calculated according to the formula from the book B.E. Warren, x-ray
# diffraction, (pag. 189), Dover, New York (1969)
# method 2) "run_sa_mo_2" calculates the structure factors and DW factor is
# calculated according to the formula from the publication V.F. Sears, S.A.
# Shelley, Acta Cryst., A47, 441-446 (1991).
class Structure_Factors(object):
# the function for calculating the structure factors is defined
    def run_sa_mo(self):
# file paths are imported
        file_paths = sp.loadtxt ("./struc_fac/file_path_s_fac.dat", dtype = str,
                                 usecols=(2,))
# in the following all the files needed to calculate the structure factors
# are imported
# file containing general information about the sample crystal
        sa_file = sp.loadtxt (file_paths[0], dtype = str, usecols=(1,))
# file containing the f0 values for the sample crystal, i.e. the atomic form
# factors. Reference: Maslen et al., International Tables for Crystallography,
# Volume C, (table 6.1.1.1)
        f0_sa_file = sp.loadtxt (file_paths[1], dtype = float, skiprows = 1)
# file containing the atomic scattering factors f1 and f2 of the sample crystal.
```

```
# Reference: B.L. Henke, E.M. Gullikson, and J.C. Davis. X-ray interactions:
# photoabsorption, scattering, transmission, and reflection at E=50-30000 eV,
# Z=1-92, Atomic Data and Nuclear Data Tables, Vol. 54 (no.2), 181-342 (1993)
        f12_sa_file = sp.loadtxt (file_paths[2], dtype = float, skiprows = 1)
# file containing general information about the monochromator crystal
        mo_file = sp.loadtxt (file_paths[3], dtype = str, usecols=(1,))
# file containing the f0 values for the monochromator crystal, i.e. the atomic
# form factors. Reference: Maslen et al., International Tables for
# Crystallography, Volume C, (table 6.1.1.1)
        f0_mo_file = sp.loadtxt (file_paths[4], dtype = float, skiprows = 1)
# file containing the atomic scattering factors f1 and f2 of the monochromator
# crystal. Reference: B.L. Henke, E.M. Gullikson, and J.C. Davis. X-ray
# interactions: photoabsorption, scattering, transmission, and reflection at
# E=50-30000 eV, Z=1-92, Atomic Data and Nuclear Data Tables, Vol. 54 (no.2),
# 181-342 (1993)
        f12_mo_file = sp.loadtxt (file_paths[5], dtype = float, skiprows = 1)
# this file contains the input data from the user: reflection Miller Indices,
# angle of incidence, temperature of the crystals, Debye temperature if
# different from the default one.
        input_data = sp.loadtxt (file_paths[6], dtype = float, usecols=(1,))
# The input data are read
        h_sa = input_data[0]
        k_sa = input_data[1]
        l_sa = input_data[2]
        theta = input_data[3]
        temp_sa = input_data[4]
        debyeT_sa = input_data[5]
        h_mo = input_data[6]
        k_mo = input_data[7]
        l_mo = input_data[8]
        temp_mo = input_data[9]
        debyeT_mo = input_data[10]
# the atomic number (Z), the lattice constant (a), the atomic weight (m) are
# read from the input files
        z_sa = float(sa_file[1])
        a_sa = float(sa_file[2])
        m_sa = float(sa_file[3])
        z_mo = float(mo_file[1])
        a_mo = float(mo_file[2])
        m_mo = float(mo_file[3])
# the Planck constant and speed of light are defined
        planck_constant = 4.13566733e-15        ## ev*s
        light_speed = 2.99792458e18                ## Ang*s^-1
###### structure factors of the sample crystal ################################
# distance between two consecutive Bragg planes of the hkl reflection
        d_hkl_sa = sp.sqrt(1/((h_sa/a_sa)**2 + (k_sa/a_sa)**2 + (l_sa/a_sa)**2))
# wavelength corresponding to the Bragg energy, calculated using the input angle
# value, and the calculated d_hkl
        lamba_B = 2*d_hkl_sa*sp.sin(theta * sp.pi / 180)
# Bragg energy
        E_B = planck_constant*light_speed/lamba_B
# constants for the calculation of the Debye-Waller factor in the units
# expressed on the side
        # Planck constant
        h = 6.626068e-21        ## ang^2 * g * s^-1
        # Boltzmann constant
        k = 1.3806503e-10        ## ang^2 * g * s^-2 * K^-1
        # Avogadro number
        N_A = 6.02214179e23        ## mol^-1, m_sa/N_A is in [gm]
# variable which enters into DW formula
        x_sa = debyeT_sa/temp_sa
# the following factor M_sa plays a role only if the reflection is not the 000
# (forward scattering) and is calculated as follows
```

```
88          M_sa = ((6*(h**2)*temp_sa)/((m_sa/N_A)*k*(debyeT_sa)**2))*(1 +
89                    (x_sa**2)/36 - (x_sa**4)/3600)*(1/(2*d_hkl_sa)**2)
90  # DW factor is calculated
91          DW_sa = sp.exp(-M_sa)
92  # reflection 000
93  # the atomic scattering factors f1 anf f2 for both the 000 and hkl reflection at
94  # the E_B are in the following calculated (delta_f0_000 = Z-f0_000 = 0, because
95  # f0_000 = Z)
96          size_f12_sa_file = size(f12_sa_file[:,0])
97  # "for" loop to find the two energy values closer to the Bragg energy in order
98  # to find the corresponding tabulated f1 and f2 values
99          for i in range (0,size_f12_sa_file) :
100                 if f12_sa_file[i,0] > E_B :
101                         en_sa_l = f12_sa_file[i-1,0]
102                         en_sa_h = f12_sa_file[i,0]
103                         break
104 # energy value interpolated between the two energies closest to the Bragg energy
105         x_sa = (E_B - en_sa_l)/(en_sa_h - en_sa_l)
106 # the values of f1 and f2 corresponding to the interpolated energy value
107         f1_sa = x_sa * f12_sa_file[i,1] + (1-x_sa) * f12_sa_file[i-1,1]
108         f2_sa = x_sa * f12_sa_file[i,2] + (1-x_sa) * f12_sa_file[i-1,2]
109 # the structure factor at 000 are given by 4*f = 4*(f1_sa + i*f2_sa)
110         F_000_sa_re = 4*f1_sa
111         F_000_sa_im = 4*f2_sa
112 # reflection hkl
113 # f0 at 1/2d_hkl is here calculated
114         t = 1/(2*d_hkl_sa)
115         size_f0_sa_file = size(f0_sa_file[:,0])
116         for i in range (0,size_f0_sa_file) :
117                 if f0_sa_file[i,0] > t :
118                         t_l = f0_sa_file[i-1,0]
119                         t_h = f0_sa_file[i,0]
120                         break
121 # the values of f0, f1 and f2 are interpolated
122         t_sa = (t - t_l)/(t_h - t_l)
123         f0_sa = t_sa * f0_sa_file[i,1] + (1-t_sa) * f0_sa_file[i-1,1]
124 # in the two following expressions the Debye-Waller factor is taken into account
125         f_hkl_sa_re = ( f1_sa - ( z_sa - f0_sa ) ) * DW_sa
126         f_hkl_sa_im = f2_sa * DW_sa
127 # S factor is defined in the following way: S = Sum exp(2*pi*H*ri) =
128 # exp(2*pi*H*r_1) + exp(2*pi*H*r_2) + exp(2*pi*H*r_3) + exp(2*pi*H*r_4)
129 # H = (h, k, l) is the vector defined by the reflection these are the vectors
130 # defining the positions of the atoms in the unit cell: r_1 = (0,0,0), r_2 =
131 # (1/2 ,1/2, 0), r_3 = (1/2, 0, 1/2), r_4 = (0, 1/2, 1/2).
132 # a, b, c, d are the results of the products H*ri, for i = 1, 2, 3, 4
133         a = h_sa*0 + k_sa*0 + l_sa*0
134         b = h_sa*0.5 + k_sa*0.5 + l_sa*0
135         c = h_sa*0.5 + k_sa*0 + l_sa*0.5
136         d = h_sa*0 + k_sa*0.5 + l_sa*0.5
137 # S is calculated
138         S = sp.exp(2j*sp.pi*a) + sp.exp(2j*sp.pi*b) + sp.exp(2j*sp.pi*c) +
139             sp.exp(2j*sp.pi*d)
140 # the following "if" condition is set in order to overcome calculation
141 # approximations. For example, sin(2*pi) = 2.44e-16 and not exactly 0.
142 # The following "if" condition sets to 0 any value smaller than 1e-10.
143         if sp.imag(S) < 1e-10:
144                 S = sp.real(S)
145                 print "S is real"
146                 F_hkl_sa_re = f_hkl_sa_re * S
147                 F_hkl_sa_im = f_hkl_sa_im * S
148         else :
149                 S_re = sp.real(S)
150                 S_im = sp.imag(S)
151                 print "S is complex"
152 # since S is complex and (a+ib)*(c+id) = (ac-bd) +i(ad+bc), then (f_hkl_sa_re +
153 # i*f_hkl_sa_im)*(S_re +i*S_im):
```

```
154                 F_hkl_sa_re = f_hkl_sa_re*S_re - f_hkl_sa_im*S_im
155                 F_hkl_sa_im = f_hkl_sa_re*S_im + f_hkl_sa_im*S_re
156 # the file "result_sa.dat" containg all the results (atomic form factor,
157 # scattering factors, DW factors, structure factors and intermidiate results) is
158 # created
159         fp = open("./struc_fac/result_sa.dat", "w")
160         fp.write("d_hkl_sa %s\nE_B %s\nM_sa %s\nDW_sa %s\nx_sa %s\nf1_sa
161 %s\nf2_sa %s\nF_000_sa_re %s\nF_000_sa_im %s\nt_sa %s\nf0_sa %s\nS
162 %s\nF_hkl_sa_re %s\nF_hkl_sa_im %s" % (round(d_hkl_sa, 4),round(E_B,
163 4),round(M_sa, 4),round(DW_sa, 4),round(x_sa, 4),round(f1_sa, 4),round(f2_sa,
164 4),round(F_000_sa_re, 4),round(F_000_sa_im, 4),round(t_sa, 4),round(f0_sa,
165 4),round(S, 4),round(F_hkl_sa_re, 4),round(F_hkl_sa_im, 4)))
166         fp.close()
167 # the path of "result_sa.dat" is written in "file_path_s_fac.dat" (code omitted)

168 # The same approach seen above for the sample crystal is used for the crystal
169 # monochromator
170 ######        structure factors of the monochromator crystal  ######################
171 # distance between two consecutive Bragg planes of the hkl reflection
172         d_hkl_mo = sp.sqrt(1/((h_mo/a_mo)**2 + (k_mo/a_mo)**2 + (l_mo/a_mo)**2))
173 # variable which enters into DW formula
174         x_mo = debyeT_mo/temp_mo
175 # this factor plays a role only if the reflection is not the 000 (forward
176 # scattering)
177         M_mo = ((6*(h**2)*temp_mo)/((m_mo/N_A)*k*(debyeT_mo)**2))*(1 +
178                 (x_mo**2)/36 - (x_mo**4)/3600)*(1/(2*d_hkl_mo)**2)
179 # DW factor is calculated
180         DW_mo = sp.exp(-M_mo)
181 # reflection 000
182 # the atomic scattering factors f1 anf f2 for both the 000 and hkl reflection at
183 # the E_B are in the following calculated (delta_f0_000 = Z-f0_000 = 0, because
184 # f0_000 = Z)
185         size_f12_mo_file = size(f12_mo_file[:,0])
186 # "for" loop to find the two energy values closer to the Bragg energy in order
187 # to find the conrresponding tabulated f1 and f2 values
188         for i in range (0,size_f12_mo_file) :
189                 if f12_mo_file[i,0] > E_B :
190                         en_mo_l = f12_mo_file[i-1,0]
191                         en_mo_h = f12_mo_file[i,0]
192                         break
193 # energy value interpolated between the two energies closest to the Bragg energy
194         x_mo = (E_B - en_mo_l)/(en_mo_h - en_mo_l)
195 # the values of f1 and f2 corresponding to the interpolated energy value
196         f1_mo = x_mo * f12_mo_file[i,1] + (1-x_mo) * f12_mo_file[i-1,1]
197         f2_mo = x_mo * f12_mo_file[i,2] + (1-x_mo) * f12_mo_file[i-1,2]
198 # the structure factor at 000 are given by 4*f = 4*(f1_sa + i*f2_sa)
199         F_000_mo_re = 8*f1_mo
200         F_000_mo_im = 8*f2_mo
201 # reflection hkl
202 # the f0 at 1/2d_hkl is here calculated
203         t = 1/(2*d_hkl_mo)
204         size_f0_mo_file = size(f0_mo_file[:,0])
205         for i in range (0,size_f0_mo_file) :
206                 if f0_mo_file[i,0] > t :
207                         t_l = f0_mo_file[i-1,0]
208                         t_h = f0_mo_file[i,0]
209                         break
210 # the values of f0, f1 and f2 are interpolated
211         t_mo = (t - t_l)/(t_h - t_l)
212         f0_mo = t_mo * f0_mo_file[i,1] + (1-t_mo) * f0_mo_file[i-1,1]
213 # in the two following expressions the Debye-Waller factor is taken into account
214         f_hkl_mo_re = ( f1_mo - ( z_mo - f0_mo ) ) * DW_mo
215         f_hkl_mo_im = f2_mo * DW_mo
216 # S factor is defined in the following way: S = Sum exp(2*pi*H*ri), H=(111),
```

```
# r_1 = -1/8 -1/8 -1/8, r_2 = 3/8 3/8 -1/8, r_3 = 3/8 -1/8 3/8, r_4 = -1/8 3/8
# 3/8, r_5 = 1/8 1/8 1/8, r_6 = 5/8 5/8 1/8, r_7 = 5/8 1/8 5/8, r_8 = 1/8 5/8
# 5/8
        S = 8*sp.cos(0.75*sp.pi)        # 3/4=0.75
        F_hkl_mo_re = f_hkl_mo_re * S
        F_hkl_mo_im = f_hkl_mo_im * S
# the file "result_mo.dat" containg all the results (atomic form factor,
# scattering factors, DW factors, structure factors and intermidiate results) is
# created.
        fp = open("./struc_fac/result_mo.dat", "w")
        fp.write("d_hkl_mo %s\nE_B %s\nM_mo %s\nDW_mo %s\nx_mo %s\nf1_mo
%s\nf2_mo %s\nF_000_mo_re %s\nF_000_mo_im %s\nt_mo %s\nf0_mo %s\nS
%s\nF_hkl_mo_re %s\nF_hkl_mo_im %s" % (round(d_hkl_mo, 4),round(E_B,
4),round(M_mo, 4),round(DW_mo, 4),round(x_mo, 4),round(f1_mo, 4),round(f2_mo,
4),round(F_000_mo_re, 4),round(F_000_mo_im, 4),round(t_mo, 4),round(f0_mo,
4),round(S, 4),round(F_hkl_mo_re, 4),round(F_hkl_mo_im, 4)))
        fp.close()
# the path of "result_sa.dat" is written in "file_path_s_fac.dat" (code omitted)
# In the following the "prm_file.dat" is created and its file path saved
# (warning! structure factors are already multiplied by the DW factor, therefore
# in the ideal Refl file they will not be multiplied again).
# In other words, the DW factor written in this file, is there for information
# and it will not be used for additional calculations later in the program.
        fp = open("./struc_fac/prm_file.dat", "w")
        fp.write("crystal:%s-\nreflection_cr:%s%s%s-\nn_bragg_cr=1-\
na_constant_cr=%s-\nd_hkl_cr=%s-\ntheta_bragg_cr=%s-\nDW_cr=%s-\nF0_cr=
%s%sj\nFH_cr=%s%sj\nmonochromator:%s-\nreflection_mo:%s%s%s-\nn_bragg_mo=1-\
na_constant_mo=%s-\nd_hkl_mo=%s-\nDW_mo=%s-\nF0_mo=%s%sj\nFH_mo=%s%sj" %\
(sa_file[0],int(input_data[0]),int(input_data[1]),int(input_data[2]),round(float
(sa_file[2]),4),round(d_hkl_sa,4),theta,round(DW_sa,4),round(F_000_sa_re,4),
round(F_000_sa_im,4),round(F_hkl_sa_re,4),round(F_hkl_sa_im,4),mo_file[0],int(
input_data[6]),int(input_data[7]),int(input_data[8]),round(float(mo_file[2]),4),
round(d_hkl_mo,4),round(DW_mo,4),round(F_000_mo_re,4),round(F_000_mo_im,4),round
(F_hkl_mo_re,4),round(F_hkl_mo_im,4)))
        fp.close()
# the path of "prm_file.dat" is written in "file_path_s_fac.dat" (code omitted)
################################################################################
################################################################################
################################################################################
################################################################################
################################################################################
# The following code calculates also the structure factors using the Debye
# Waller factors calculated according to Sears and Shelley, method 2).
    def run_sa_mo_2(self):
# All the files needed to calculate the structure factors are imported. Since
# they are identical to what already seen for method 1) the corresponding code
# is here omitted.
# In addition to what already seen in method 1) the following information need
# to be imported as well: phonon frequency, alfa, f_-2, f_-1, f_2, results of
# the fit of the experiemtal J(y) integral with two functions (see reference
# Sears and Shelly)
        freq_nu_sa = float(sa_file[5])
        alfa_sa = float(sa_file[6])
        f_min2_sa = float(sa_file[7])
        f_min1_sa = float(sa_file[8])
        f_2_sa = float(sa_file[9])
        freq_nu_mo = float(mo_file[5])
        alfa_mo = float(mo_file[6])
        f_min_2_mo = float(mo_file[7])
        f_min1_mo = float(mo_file[8])
        f_2_mo = float(mo_file[9])
# the only difference with method 1) is in DW defined as follows:
# variable which enters into the J(y) integral
        y_sa = temp_sa/debyeT_sa
```

```
281 # The J(y) integral is calculated using the experimental temperature of the
282 # crystal
283         if y_sa < 0.2 :
284             J_sa = f_min1_sa + ((sp.pi**2)/3)*alfa_sa*(y_sa**2)
285         else :
286             J_sa = 2*f_min2_sa + 1/(6*y_sa) - f_2_sa/(360*(y_sa**2))
287 # B and M factors are calculated
288         B_sa  = (39.904/(m_sa*freq_nu_sa))*J_sa
289         M_sa = B_sa*(1/(2*d_hkl_sa)**2)
290 # DW factor is calculated
291         DW_sa = sp.exp(-M_sa)
292 # from this point on the code follows as above in method 1).
293 # also for the monochromator structure factors, the corresponding DW is
294 # defined as follows:
295 # variable which enters into the J(y) integral
296         y_mo = temp_mo/debyeT_mo
297 # the J(y) integral is calculated using the experimental temperature of the
298 # crystal
299         if y_mo < 0.2 :
300             J_mo = f_min1_mo + ((sp.pi**2)/3)*alfa_mo*(y_mo**2)
301         else :
302             J_mo = 2*f_min2_mo + 1/(6*y_mo) - f_2_mo/(360*(y_mo**2))
303 # B and M factors are calculated
304         B_mo  = (39.904/(m_mo*freq_nu_mo))*J_mo
305         M_mo = B_mo*(1/(2*d_hkl_mo)**2)
306 # DW factor is calculated
307         DW_mo = sp.exp(-M_mo)
308 # from this point on the code follows as above in method 1).
```

A.6 Fitting the electron yield profile: coherent position and fraction

A.6.1 Technical details

The "Fit F_c and P_c" section of Torricelli, before carrying out the actual fitting of the experimental electron yield selected in section "Import Files", requires the input (from the user) of the nondipolar parameters and the initial values of the fitting parameters. To this purpose, the "Set and Save suggested parameters" button sets the nondipolar parameters to $S_R = 1$, $|S_i| = 1$, $\Psi = 0$ and the fitting parameters to ($P_c = 0.5$, $F_c = 0.5$) while the normalization factor is set to the first electron yield value. The user can modify each of the input parameters and save the changes by clicking the corresponding "Reset" buttons (Figure A.6). Note that in case the "Nondipolar Parameters" section is used before the "Fit Fc and Pc" one, then the nondipolar parameters are set to the values calculated in the corresponding section.

The fitting of the experimental electron yield is activated by clicking the "Fit Electron Yield" button and is carried out by the SciPy (scientific library for Python) function optimize.leastsq[179] (section A.6.2, lines 132–140) that minimizes the sum of squares of a given function, in our case the difference (divided by the experimental standard deviation) between experimental electron yield and the fitting function (section A.6.2, lines 33–92).

As a result of the fit, the best fit values of the three fitting parameters (section A.6.2, lines 141–144) and the respective standard deviations (section A.6.2, lines 163–166) are reported in the text boxes 9–11 and 12–14, respectively. The standard deviations of the parameters are calculated as the square root of the diagonal values of the covariance matrix (section A.6.2, lines 161–162). In turn, the covariance matrix comes from the product of an estimate of the Jacobian matrix around the solution (output of optimize.leastsq[179]) times the residual standard deviation (section A.6.2, lines 151–154), i.e., the reduced χ^2 (section A.6.2, lines 145–150), whose value is reported in the text box 15.

In analogy with the "Fit Reflectivity" section the list of all tested combinations of the fitting parameters (N, P_c, F_c) is reported in the display panel in Figure A.7. At the same time, the plot of the experimental electron yield together with the

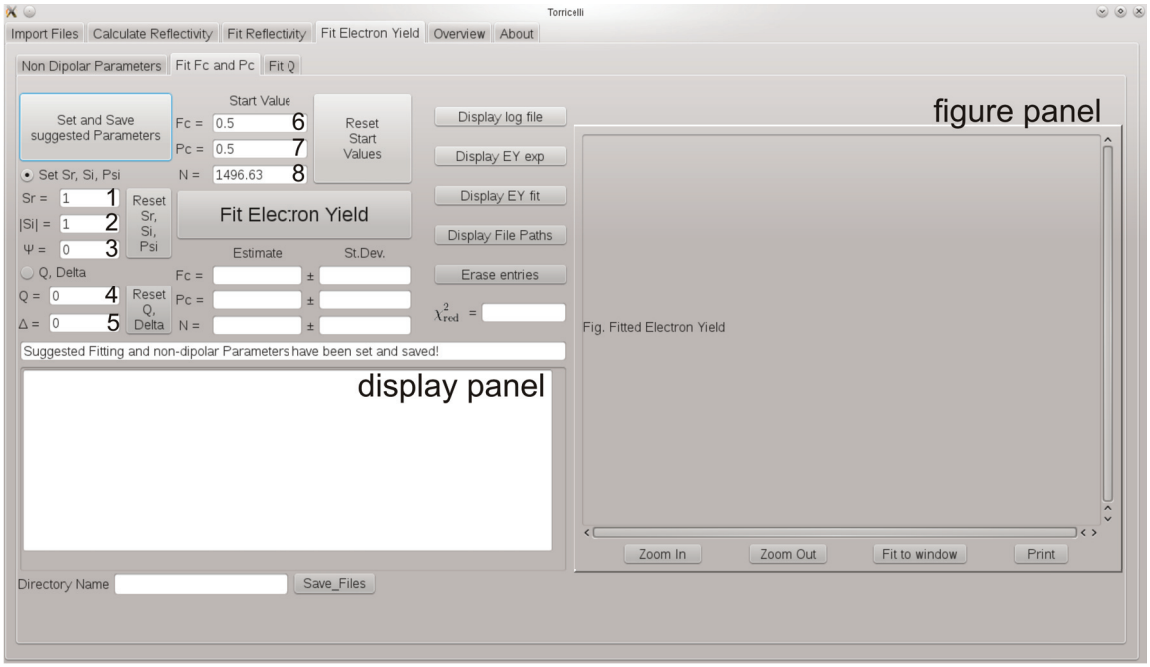


Figure A.6: "Fit Fc and Pc" section of Torricelli after setting the suggested initial fitting parameters.

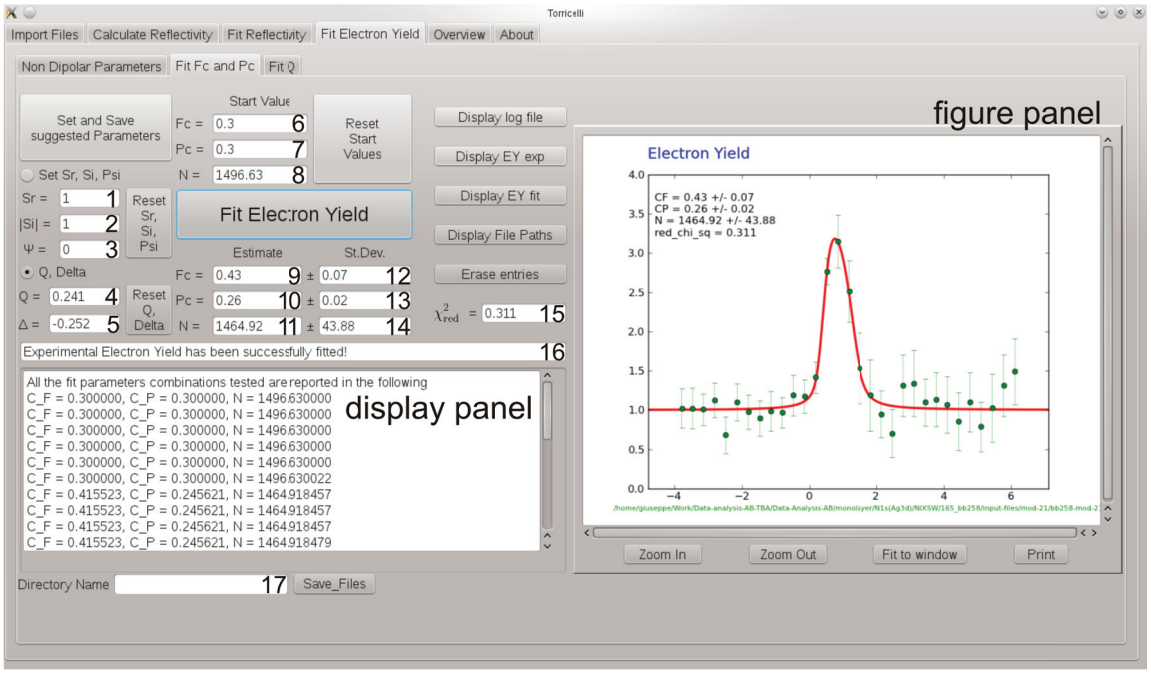


Figure A.7: "Fit Fc and Pc" section of Torricelli after the experimental electron yield is fitted.

resulting fitting function is shown in the figure panel of Figure A.7.

In case the fitting fails, the user can modify the initial fitting parameters and repeat it again. Instead, if the fitting succeeds, the user may still wish to save the previous results in another directory through the "Save Files" button (located at the bottom of Figure A.7) and repeat the fitting again to test e.g., how robust the results are with respect to the initial parameters or to test the effect of different nondipolar parameters on (P_c, F_c).

A.6.2 Code

```
class Fit_EY (object):
# the function that sets the non dipolar parameters is in the following defined
    def setndp(self):
# the file "file_path.dat" is imported
        file_path_file = "./parameters/file_path.dat"
        file_path = sp.loadtxt (file_path_file, dtype = str, usecols=(2,))
# the file where non dipolar parameters are saved is imported
        ndp_file = file_path[14]
        non_dip_par = sp.loadtxt (ndp_file, dtype = float, usecols=(1,))
# the following "if" statements distinguish between (Sr, Si, Psi) and (Q, Delta)
# and in case (Q, Delta) are given by the user then (Sr, Si, Psi) are calculated
        if len(non_dip_par) == 3:
                self.Sr = non_dip_par[0]
                self.Si = non_dip_par[1]
                self.Psi = non_dip_par[2]
        elif len(non_dip_par) == 2:
```

```
                q = non_dip_par[0]
                d = non_dip_par[1]
                self.Sr = (1+q)/(1-q)
                self.Si = sqrt(1+(q**2)*sp.tan(d)**2)/(1-q)
                self.Psi = sp.arctan(q*sp.tan(d))

# the fitting function of the experimental electron yield is defined
    def func (self,C_F, C_P, N, refl, phi): \
        return N * (1 + \
        self.Sr * refl + \
        2 * C_F * sp.sqrt (refl) * self.Si * sp.cos(phi-2*sp.pi*C_P+self.Psi) )
# this function returns the Gaussian function with area normalized to 1:
# the function has two input parameters: sigma and array of energy
    def gauss (self, sigma, energy):
        g = sp.exp (-energy**2 / (2*sigma**2))
        norm = sum (g)
        return g/norm
# Definition of the function "diff" which returns the difference between the
# experimental values and the calculated ones, normalized by the STD (standard
# deviation) of the experimental data. The "diff" function returns
# an array of values which are then squared and then summed, and this sum is
# minimized by the function sp.optimize.leastsq.
    def diff (self, params, data, energy, refl, phi, sigma, DE, sq_refl):
# fitting parameters from the vector "params" determined in the previous
# iteration, or in case it is the first iteration it contains the initial
# values of the fitting parameters set by the user
        C_F = params[0]
        C_P = params[1]
        N = params[2]
# function representing the ideal electron yield (before convolution)
        vec_func = self.func (C_F, C_P, N, refl, phi)
# gauss function with the fitted "sigma" value and the energy array
        vec_gauss = self.gauss (sigma, energy)
# convolution of ideal electron yield and the square of the monochromator
# reflectivity normalized
        vec_conv_1 = sp.convolve (vec_func, sq_refl, mode = 'same')
# convolution of vec_conv_1 and the Gaussian function
        vec_conv = sp.convolve (vec_conv_1, vec_gauss, mode = 'same')
# an array of energy values is created:
        x_min = min (energy)
        x_max = max (energy)
        dx = (x_max - x_min) / len (vec_conv)
# new array of energy values shifted by DE corresponding to an energy shift of
# the fitting function
        x = sp.arange (x_min, x_max, dx) + DE
# an array containing the experimental electron yield values is created
        y = data[:, 1]
# array that contains the fitting function values
        y_m = sp.zeros (len (y))
# array that contains the standard deviation of the experimental electron yield
        y_err = data[:, 2]
# the following "for" loop looks for the values of the fitting function
# corresponding to the closest energy values with respect to the ones of the
# experimental electron yield
        for i in range (len (data[:, 0])):
# the i^th experimental energy is read from the experimental electron yield
            data_x = data[i, 0]
# x_hi is the largest (hi->highest) calculated energy value that is smaller
# than data_x
# x_hi = x[x > data_x][0]
# x_lo is the smallest (lo->lowest) calculated energy value that is greater
# than data_x
# x_lo = x[x < data_x][len (x[x < data_x]) - 1]
# y_hi is the fitting function value corresponding to x_hi
            y_hi = vec_conv[pl.find ((x > data_x))[0]]
```

```
# y_lo is the fitting function value corresponding to x_lo
            y_lo = vec_conv[pl.find ((x < data_x))[len (x[x < data_x]) - 1]]
# y_m is the average of the two values y_lo and y_hi
            y_m[i] = (y_hi + y_lo)*0.5
# the following two lines save each combination of the fitting parameters
# tested at each iteration in a log file
        fp = open ("./data/log_ey_fit.dat", "a")
        fp.write ("C_F = %f, C_P = %f, N = %f\n" % (C_F, C_P, N))
# "diff" function returns the difference between the experimental value "y" and
# the value of the fitting function "y_m". The difference is then divided by the
# corresponding standard deviation, for each experimental energy
        return ( y - y_m )/y_err
# the function consisting of the main program is in the following defined:
    def run(self):
# the log file, where all combination of the fitting parameters are saved, is
# created here
        fp = open ("./data/log_ey_fit.dat", "w")
        fp.write ("All the fit parameters combinations tested are reported in
                   the following\n")
        fp.close ()
# the "file_path.dat" file is imported and read
        file_path_file = "./parameters/file_path.dat"
        file_path = sp.loadtxt (file_path_file, dtype = str, usecols=(2,))
# file path of the following files:
        data_file = file_path[11]         # "ey_exp.dat"
        sq_refl_file = file_path[9]          # "sq_refl_mo_norm.dat"
        refl_file = file_path[6]         # "refl_cr.dat"
        phi_file = file_path[7]                  # "phi_cr_ey.dat"
# fitting parameters "sigma" and "DE" obtained from the fit of the reflectivity
        fit_file = file_path[13]
# starting fitting parameters ("Pc" and "Fc")
        EY_Fit_Par_file = file_path[15]
# the content of the files just uploaded is saved into new variables
        energy = sp.loadtxt (refl_file, dtype = float, usecols=(0,))
        data = sp.loadtxt (data_file, dtype = float)
        sq_refl = sp.loadtxt (sq_refl_file, dtype = float, usecols=(1,))
        refl = sp.loadtxt (refl_file, dtype = float, usecols=(1,))
        phi = sp.loadtxt (phi_file, dtype = float, usecols=(1,))
        EY_Fit_Par = sp.loadtxt (EY_Fit_Par_file, dtype = float, usecols=(1,))
        fit = sp.loadtxt (fit_file, dtype = float, usecols=(1,))
# values of "sigma" and "DE" resulting from the fit of the reflectivity
        sigma = fit[0]
        DE = fit[1]
# the initial values of the fitting parameters set by the user
        C_F = EY_Fit_Par[0]
        C_P = EY_Fit_Par[1]
# the starting value of the normalization factor "N" is always the first value
# of the electron yield
        N = data[0,1]
# the vector containing the starting fitting parameters
        params_initial = [C_F, C_P, N]
# the following function minimizes the sum of the squares of the function
# "diff". "sp.optimize.leastsq" calls the function "diff" at each iteration.
        params, cov_x, info, msg, ierr = sp.optimize.leastsq ( \
            self.diff, \
            params_initial, \
            args = (data, energy, refl, phi, sigma, DE, sq_refl), \
            ftol = 1e-12, \
            full_output = 1 \
            )
# The parameters fitted by sp.optimize.leastsq
        C_F = params[0]
        C_P = params[1]
        N = params[2]
```

```
145  # degree of freedom (dof) = N-P, where N is the number of fitted data points of
146  # the electron yield) and P is the number of fitted parameters, in our case 3
147          dof = len(data[:,0]) - len(params)
148  # reduced chi^2 = chi^2 / dof
149          chi_sq = sum (self.diff(params, data, energy, refl, phi, sigma, DE,
150                                  sq_refl)**2)/dof
151  # covariance matrix: obtained by multiplying the matrix "cov_x" (output of
152  # "sp.optimize.leastsq") times the residual standard deviation, i.e. the
153  # reduced chi_sq calculated above
154          cov = chi_sq * np.diag(cov_x)
155  # the diagonal of the covariance matrix contains the variance of the fitted
156  # parameters, therefore the corresponding standard deviation is given by the
157  # square root of the diagonal of the covariance matrix, as calculated in the
158  # "for" loop below
159  # the uncertainty associated to the three fitting parameters is saved in "err"
160          err = [0,0,0]
161          for i in range(3):
162            err[i]=sp.sqrt(cov[i])
163  # one variable for each standard deviation is defined
164          stdev_CF = round(err[0],2)
165          stdev_CP = round(err[1],2)
166          stdev_N = round(err[2],2)
167  # vec_func is calculated with the fitted parameters
168          vec_func = self.func (C_F, C_P, N, refl, phi)
169  # the Gaussian function is recalled again
170          vec_gauss = self.gauss (sigma, energy)
171  # vec_conv_1 is calculated using the fitted parameters
172          vec_conv_1 = sp.convolve (vec_func, sq_refl, mode = 'same')
173  # vec_conv is calculated using the fitted parameters
174          vec_conv = sp.convolve (vec_conv_1, vec_gauss, mode = 'same')
175  # the array of energies is set again
176          x_min = min (energy)
177          x_max = max (energy)
178          dx = (x_max - x_min) / len (vec_conv)
179          x = sp.arange (x_min, x_max, dx)
180  # experimental electron yield and the fitting curve are plotted (only the
181  # most significant lines of the code are reported)
182  # plot of the fitting function
183          pl.plot (x, vec_conv/N, linewidth=2.5, color='r')
184  # plot of the experimental values with corresponding error bars
185          pl.errorbar (data[:, 0] - DE, data[:, 1]/N, data[:, 2]/N, fmt = 'o',
186                       linewidth=0.3, capsize = 3, barsabove=True)
187  # setting of the energy axes
188          pl.axis ([min(data[:,0] - DE)-1, max(data[:,0] - DE)+1, 0, 4])
189  # a figure of the experimental data and fitting curve is created (code omitted)
190  # two output files are created:
191  # "ey_theo_fit.dat": vec_conv/N (energy)
192  # "ey_exp_fit.dat": data[i, 1]/N (data[i, 0] - DE)
193  # The experimental reflectivity is imported to retrieve the value c by which the
194  # absolute energy scale has been shifted before fitting in order to bring it
195  # around the value of 0.
196          refl_exp_file = file_path[3]
197          data_r = sp.loadtxt (refl_exp_file, dtype = "float")
198  # the constant energy subtracted to the absolute energy scale in order to bring
199  # it around 0.
200          c = ( min (data_r[:,0]) + ( max (data_r[:,0]) - min (data_r[:,0]) )/2 )
201  # two output files are created:
202  # "ey_theo_fit_abs.dat": vec_conv/N (energy + DE + c)
203  # "ey_exp_fit_abs.dat": data[i, 1]/N (data[i, 0] + c)
204  # the Bragg energy is defined:
205          Bragg_En = c+DE
206  # a file containing the fitted values is created
```

```
207         fp = open ("./data/fitted_ey_par.dat", "w")
208         fp.write ("CF %f%f\nCP %f%f\nN %f%f\nChi_sq %f-\nBragg_Energy %f-\n"%
209                   (round(C_F, 2), stdev_CF, round(C_P, 2), stdev_CP, round(N,2),
210                   stdev_N, round(chi_sq, 3), round(Bragg_En, 3)))
211         fp.close ()
```

A.7 Calculating the nondipolar correction parameters

A.7.1 Technical details

In order to calculate the nondipolar parameters we need to upload a text file (shown in the "display panel" in Figure A.8) containing the binding energy of the core level and the γ values with the corresponding kinetic energy. As the text file is uploaded, the value of θ_p (text box 3) is set to 45°, since this corresponds to our experimental set-up (section 2.6). However, this value can be modified by the user before saving all the input parameters. Subsequently, the value of the Bragg energy and of the phase shifts δ_p and δ_d need to be inserted in the corresponding text boxes 2, 4, 5, and saved by clicking the " Save Parameters" button. Finally the nondipolar parameters

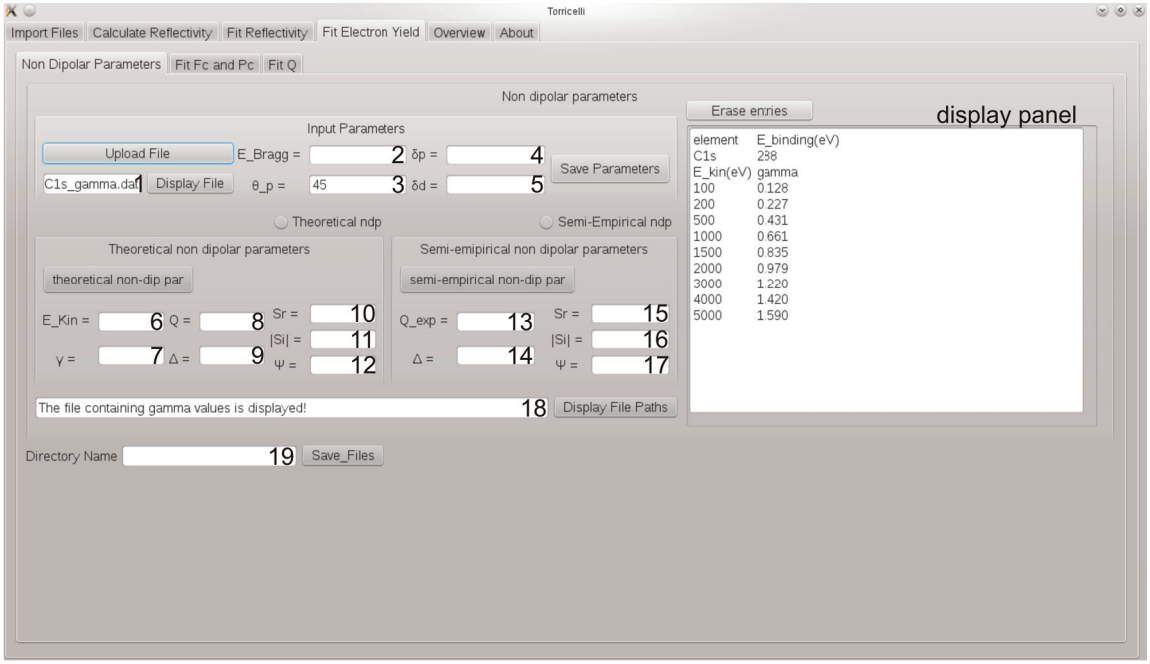


Figure A.8: "Non Dipolar Parameters" section of Torricelli after uploading the file containing the γ values and corresponding kinetic energies, shown in the display panel.

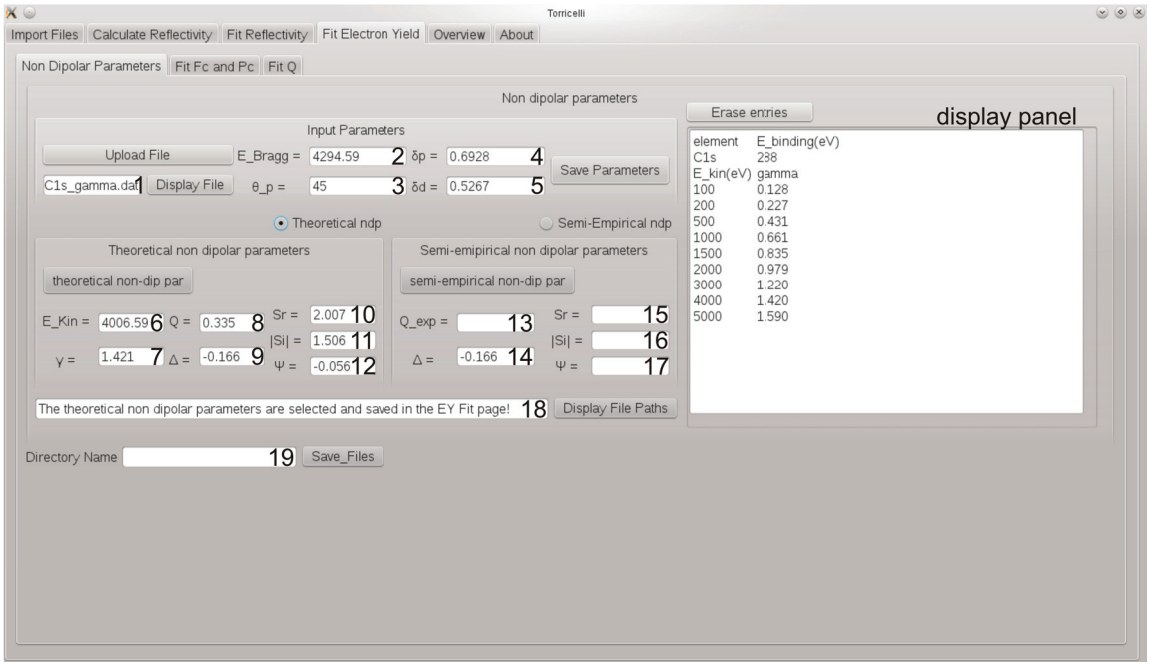


Figure A.9: "Nondipolar Parameters" section of Torricelli after inserting the other input parameters and once calculations are carried out.

can be calculated (section A.7.2, lines 42-49) by clicking the "theoretical non-dip par" button, and results are shown in text boxes 6–12 (Figure A.9).

If the asymmetry parameter Q is known from experiments, the parameters S_R, $|S_i|$, Ψ are calculated (section A.7.2, lines 76–79) by clicking the "semi-empirical non-dip par" button.

The nondipolar parameters calculated above are then directly copied into the corresponding text boxes of the "Fit Fc and Pc" section by clicking the toggle button "Theoretical ndp" or "Semi-Empirical ndp".

Finally, calculations can be saved ("Save Files" button) in a separate folder whose name is specified in the text box "Directory Name" and new calculations can be performed.

A.7.2 Code

```
1 class Non_Dip_Par(object):
2 # The formula for calculating S_R, |S_I|, Psi and Delta are taken from
3 # equations 10, 11, 12 of reference J.J. Lee et al., Surface Science, 494 (2001)
4 # 166-182, in the following called "Lee01SS494_166".
5 # The expression of Q is taken from reference I. Vartanyants at al., Nuclear
6 # Instruments and Methods in Physics Research A 547 (2005) 196-207, in the
```

```
# following called "Vartanyants05NIaMiPRSAASDaAE547_196".
# Gamma values are taken from reference Trzhaskovskaya et al., Atomic Data and
# Nuclear Data Tables 77 (2001) 97-159 and 82 (2002) 257-311, in the following
# called "Trzhaskovskaya01ADaNDT77_97"
# The function that calculates the theoretical non dipolar parameters is defined
    def run_theo(self):
# the file "file_path.dat" is imported
        file_path_file = "./non_dip_par/file_path_par.dat"
            file_path = sp.loadtxt (file_path_file, dtype = str, usecols=(2,))
# the gamma file, containing the name of the element, its binding energy, and
# the corresponding gamma values as a function of the kinetic energy, is read
        gamma_file = sp.loadtxt (file_path[0], dtype = str)
# the input parameters file, containing E_Bragg, theta_p, delta_d and delta_p
# is read
        input_par = sp.loadtxt (file_path[1], dtype = float, usecols=(1,))
# all the parameters needed to calculate the non dipolar parameters are saved in
# local variables
        E_b = float(gamma_file[1,1])
        E_Bragg = float(input_par[0])
        theta_p = float(input_par[1])
        delta_p = float(input_par[2])
        delta_d = float(input_par[3])
        E_kin_exp = E_Bragg - E_b
# the tabulated kinetic energy values (from "Trzhaskovskaya01ADaNDT77_97")
# corresponding to gamma values and closest # to "E_kin_exp" are found
        for i in range (3, 12):
                if float(gamma_file[i,0]) > E_kin_exp :
                        E_kin_l = float(gamma_file[i-1,0])
                        E_kin_h = float(gamma_file[i,0])
                        count = i-1
                        break
        x = (E_kin_h - E_kin_exp)/(E_kin_h - E_kin_l)
# the gamma values (from "Trzhaskovskaya01ADaNDT77_97") are interpolated to
# find the closest value corresponding to "E_kin_exp"
        gamma = x*float(gamma_file[count,1]) + (1-x)*float(gamma_file[count+1,1])
# "Q" (from "Vartanyants05NIaMiPRSAASDaAE547_196") and "Delta"
# (from "Lee01SS494_166") are calculated
        Q = (gamma/3)*sp.cos(theta_p*sp.pi/180)
        Delta = delta_d - delta_p
# "Sr", "|Si|" and "Psi" (from "Lee01SS494_166") are calculated
        Sr = (1+Q)/(1-Q)
        Si = (sp.sqrt(1+(Q**2)*(sp.tan(Delta))**2))/(1-Q)
        Psi = sp.arctan(Q*tan(Delta))
# the file containing the non dipolar parameters calculated above is created
        fp = open ("./non_dip_par/ndp_theo.dat", "w")
        a = round(E_kin_exp, 3)
        b = round(gamma, 3)
        c = round(Q, 3)
        d = round(Delta, 3)
        e = round(Sr, 3)
        f = round(Si, 3)
        g = round(Psi, 3)
        fp.write ( "E_kin_exp%f\ngamma%f\nQ%f\nDelta%f\nSr%f\nSi%f\nPsi        %f" %
                 (a, b, c, d, e, f, g) )
        fp.close ()
# the file path of "ndp_theo.dat" is saved (code omitted)
# the function for calculating the semi-empirical non dipolar parameters is in
# the following defined:
    def run_exp(self):
# the file "file_path.dat" is imported
        file_path_file = "./non_dip_par/file_path_par.dat"
            file_path = sp.loadtxt (file_path_file, dtype = str, usecols=(2,))
# the file containing the "Q" value resulting from the fit of the photoelectron
# yield and the theoretical "Delta" value is read
```

```
71          semi_emp_ndp = sp.loadtxt (file_path[3], dtype = str, usecols=(1,))
72  # the interesting values from the file just uploaded are saved in two local
73  # variables
74          Q_exp = float(semi_emp_ndp[0])
75          Delta = float(semi_emp_ndp[1])
76  # "Sr", "|Si|" and "Psi" (from "Lee01SS494_166") are calculated
77          Sr = (1+Q_exp)/(1-Q_exp)
78          Si = (sp.sqrt(1+(Q_exp**2)*(sp.tan(Delta))**2))/(1-Q_exp)
79          Psi = sp.arctan(Q_exp*tan(Delta))
80  # the file containing the non dipolar parameters calculated above is created
81          fp = open ("./non_dip_par/ndp_exp.dat", "w")
82          h = round(Sr, 3)
83          j = round(Si, 3)
84          k = round(Psi, 3)
85          fp.write ("Sr%f\nSi%f\nPsi%f\nQ%f\nDelta %f" % (h, j, k,round(Q_exp,3),
86                                                          round(Delta, 3)) )
87          fp.close ()
88  # the file path of "ndp_exp.dat" is saved (code omitted)
```

A.8 Fitting the electron yield profile: the asymmetry parameter Q

A.8.1 Technical details

Analogous to the "Fit Fc and Pc" and the "Fit Reflectivity" section, here too, before the actual fitting, the initial parameters must be provided to the program. When the "Set suggested Fit Parameters" button is clicked the first value of the electron yield is set as N, while the asymmetry parameter is fixed to $Q = 0.2$. If initial values are changed, the new input must be saved by clicking the "Reset Start Values" button.

The fitting is activated by the "Fit Electron Yield" button and is carried out by the same function "optimize.leastsquare" (section A.8.2, lines 47–55) already mentioned in sections A.6.1 and A.3.1. The fitted values together with the corresponding standard deviations are reported in text boxes 3–6, while the χ^2_{red} value occupies the text box 7. All the combinations of fitting parameters tested can be visualized in the display panel, while the experimental electron yield with the resulting fitting curve is displayed in the figure panel (Figure A.10). As in any other section of the program, data can be saved in a separate folder, whose name in specified in text box 9, by clicking the "Save Files" button.

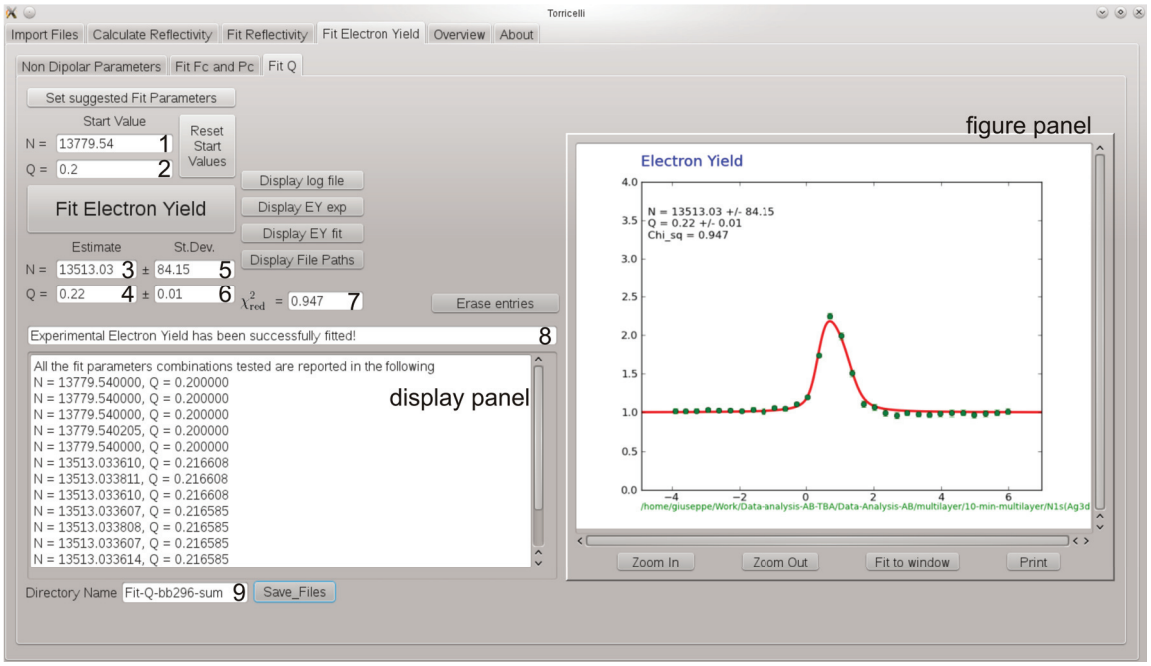


Figure A.10: "Fit Q" section of Torricelli.

A.8.2 Code

```
class Fit_EY (object):
# The function fitting the electron yield in order to find the non dipolar
# paramter "Q" is in the following defined
    def func_Q (self, N, Q, refl): \
        return N*(1 + \
        refl*(1+Q)/(1-Q) \
        )

# the function to be squared summed and minimized is defined in the following
    def diff_Q (self, params, data, energy, refl, sigma, DE, sq_refl):
# the values of the fitting parameters from the previous iteration, or if it is
# the first one, as they are defined by the user
        N = params[0]
        Q = params[1]
# function representing the ideal electron yield (before convolution)
        vec_func = self.func_Q (N, Q, refl)
# since the rest of the "diff_Q" function is exactly as the "diff" function
# defined in section A.5.2, the corresponding code is omitted and we jump to the
# output value
# "diff_Q" function returns the difference between the experimental value "y"
# and the value of the fitting function "y_m", divided by the corresponding
# standard deviation, for each experimental energy.
        return ( y - y_m )/y_err

# The function consisting of the main program is in the following defined:
    def run_Q(self):
# also here a log file is created, and all the files imported in the "run"
# function above are imported also here, therefore the corresponding code is
# not reported. One exception is the file containing the initial parameters:
        EY_Fit_Q_Par_file = file_path[14]        # it contains "N" and "Q"

# the content of the files is read
        energy = sp.loadtxt (refl_file, dtype = float, usecols=(0,))
        data = sp.loadtxt (data_file, dtype = float)
        sq_refl = sp.loadtxt (sq_refl_file, dtype = float, usecols=(1,))
```

```
        refl = sp.loadtxt (refl_file, dtype = float, usecols=(1,))
        fit = sp.loadtxt (fit_file, dtype = float, usecols=(1,))
        EY_Fit_Q_Par = sp.loadtxt (EY_Fit_Q_Par_file, dtype = float,
                                   usecols=(1,))
# values of "sigma" and "DE" as found in the fit of the reflectivity
        sigma = fit[0]
        DE = fit[1]
# initial values of the fitting parameters set by the user:
# the initial value of the normalization factor "N" is always the first value of
# the electron yield
        N = EY_Fit_Q_Par[0]
        Q = EY_Fit_Q_Par[1]
# the vector containing the initial fitting parameters
        params_initial = [N, Q]
# the following function minimizes the sum of the squares of the function
# "diff_Q". "sp.optimize.leastsq" calls the function "diff_Q" at each iteration.
        params, cov_x, info, msg, ierr = sp.optimize.leastsq ( \
            self.diff_Q, \
            params_initial, \
            args = (data, energy, refl, sigma, DE, sq_refl), \
            ftol = 1e-12, \
            full_output = 1 \
            )
# The parameters fitted by sp.optimize.leastsq
        N = params[0]
        Q = params[1]
# degree of freedom (dof) = N-P, where N is the number of fitted data points
# being fitted and P is the number of fitted parameters
        dof = len(data[:,0]) - len(params)
# reduced chi^2 = chi^2 / dof
        chi_sq = sum (self.diff_Q(params, data, energy, refl, sigma, DE,
                                  sq_refl)**2)/dof
# covariance matrix: obtained by multiplying the matrix "cov_x" (output of
# "sp.optimize.leastsq") times the residual standard deviation, i.e. the
# reduced chi_sq calculated above
        cov = chi_sq * np.diag(cov_x)
# the diagonal of the covariance matrix contains the variance of the fitted
# parameters, therefore the corresponding standard deviation is given by the
# square root of the diagonal of the covariance matrix, as calculated in the
# "for" loop below
# the uncertainty associated with the two fitting parameters is saved in "err"
        err = [0,0]
        for i in range(2):
          err[i]=sp.sqrt(cov[i])
# one variable for each standard deviation is defined
        stdev_N = round(err[0],2)
        stdev_Q = round(err[1],2)
# vec_func is calculated with the fitted parameters
        vec_func = self.func_Q (N, Q, refl)
# the Gaussian function is recalled again
        vec_gauss = self.gauss (sigma, energy)
# vec_conv_1 is calcualted using the fitted parameters
        vec_conv_1 = sp.convolve (vec_func, sq_refl, mode = 'same')
# vec_conv is calculated using the fitted parameters
        vec_conv = sp.convolve (vec_conv_1, vec_gauss, mode = 'same')
# the array of energies is set again
        x_min = min (energy)
        x_max = max (energy)
        dx = (x_max - x_min) / len (vec_conv)
        x = sp.arange (x_min, x_max, dx)
# experimental electron yield and the fitting curve are plotted (only the
# most significant lines of the code are reported)
# plot of the fitting function
        pl.plot (x, vec_conv/N, linewidth=2.5, color='r')
```

```
97  # plot of the experimental values with corresponding error bars
98          pl.errorbar (data[:, 0] - DE, data[:, 1]/N, data[:, 2]/N, fmt = 'o',
99                       linewidth=0.3, capsize = 3, barsabove=True)
100 # setting of the energy axis
101         pl.axis ([min(data[:,0] - DE)-1, max(data[:,0] - DE)+1, 0, 4])
102 # a figure of the experimental data and fitting curve is created (code omitted)
103 # The rest of the code is analogous to the "run" function (section A.5.2, line
104 # 94) therefore it is not reported here. The further operation carried out by
105 # the program are described as follows:
106 # four output files are created:
107 # "ey_theo_fit_q.dat": vec_conv/N (energy)
108 # "ey_exp_fit_q.dat": data[i, 1]/N (data[i, 0] - DE)
109 # "ey_theo_fit_q_abs.dat": vec_conv/N (energy + DE + c)
110 # "ey_exp_fit_q_abs.dat": data[i, 1]/N (data[i, 0] + c).
```

Bibliography

[1] M. Willenbockel, O. Bauer, S. Soubatch, M. Sokolowski, and F. S. Tautz, *Personal communication.*

[2] A. Hauschild, K. Karki, B. C. C. Cowie, M. Rohlfing, F. S. Tautz, and M. Sokolowski, *Molecular Distortions and Chemical Bonding of a Large π-Conjugated Molecule on a Metal Surface*, Phys. Rev. Lett. **94**, 036106 (2005).

[3] E. R. McNellis, G. Mercurio, S. Hagen, F. Leyssner, J. Meyer, S. Soubatch, M. Wolf, K. Reuter, P. Tegeder, and F. S. Tautz, *Bulky spacer groups - A valid strategy to control the coupling of functional molecules to surfaces?*, Chemical Physics Letters **499**, 247 (2010).

[4] G. Mercurio, E. R. McNellis, I. Martin, S. Hagen, F. Leyssner, S. Soubatch, J. Meyer, M. Wolf, P. Tegeder, F. S. Tautz, and K. Reuter, *Structure and Energetics of Azobenzene on Ag(111): Benchmarking Semiempirical Dispersion Correction Approaches*, Phys. Rev. Lett. **104**, 036102 (2010).

[5] Y. Ge, H. Adler, A. Theertham, L. L. Kesmodel, and S. L. Tait, *Adsorption and Bonding of First Layer and Bilayer Terephthalic Acid on the Cu(100) Surface by High-Resolution Electron Energy Loss Spectroscopy*, Langmuir **26**, 16325 (2010).

[6] M. Wolf and P. Tegeder, *Reversible molecular switching at a metal surface: A case study of tetra-tert-butyl-azobenzene on Au(111)*, Surface Science **603**, 1506 (2009).

[7] J. V. Barth, G. Costantini, and K. Kern, *Engineering atomic and molecular nanostructures at surfaces*, Nature **437**, 671 (2005).

[8] S. R. Forrest and M. E. Thompson, *Introduction: Organic Electronics and Optoelectronics*, Chemical Reviews **107**, 923 (2007).

[9] D. Wöhrle and D. Meissner, *Organic Solar Cells*, Advanced Materials **3**, 129 (1991).

[10] C. Dimitrakopoulos and P. Malenfant, *Organic Thin Film Transistors for Large Area Electronics*, Advanced Materials **14**, 99 (2002).

[11] H. E. Katz, *Recent Advances in Semiconductor Performance and Printing Processes for Organic Transistor-Based Electronics*, Chemistry of Materials **16**, 4748 (2004).

[12] Y. Shen, A. R. Hosseini, M. H. Wong, and G. G. Malliaras, *How To Make Ohmic Contacts to Organic Semiconductors*, ChemPhysChem **5**, 16 (2004).

[13] P. M. Beaujuge and J. M. J. Fréchet, *Molecular Design and Ordering Effects in π-Functional Materials for Transistor and Solar Cell Applications*, Journal of the American Chemical Society **133**, 20009 (2011).

[14] Y. Xue and M. A. Ratner, *Microscopic study of electrical transport through individual molecules with metallic contacts. II. Effect of the interface structure*, Phys. Rev. B **68**, 115407 (2003).

[15] G. Heimel, L. Romaner, E. Zojer, and J.-L. Brédas, *Toward Control of the Metal-Organic Interfacial Electronic Structure in Molecular Electronics: A First-Principles Study on Self-Assembled Monolayers of π-Conjugated Molecules on Noble Metals*, Nano Letters **7**, 932 (2007).

[16] A. H. Flood, J. F. Stoddart, D. W. Steuerman, and J. R. Heath, *Whence Molecular Electronics?*, Science **306**, 2055 (2004).

[17] A. Kahn, N. Koch, and W. Gao, *Electronic structure and electrical properties of interfaces between metals and π-conjugated molecular films*, Journal of Polymer Science Part B: Polymer Physics **41**, 2529 (2003).

[18] J. J. Lee, C. J. Fisher, D. P. Woodruff, M. G. Roper, R. G. Jones, and B. C. C. Cowie, *Non-dipole effects in photoelectron-monitored X-ray standing wave experiments: characterisation and calibration*, Surface Science **494**, 166 (2001).

[19] A. Gerlach, F. Schreiber, S. Sellner, H. Dosch, I. A. Vartanyants, B. C. C. Cowie, T.-L. Lee, and J. Zegenhagen, *Adsorption-induced distortion of F_{16}CuPc on Cu(111) and Ag(111): An x-ray standing wave study*, Phys. Rev. B **71**, 205425 (2005).

[20] B. W. Batterman and H. Cole, *Dynamical Diffraction of X Rays by Perfect Crystals*, Rev. Mod. Phys. **36**, 681 (1964).

[21] D. P. Woodruff, *Normal incidence X-ray standing wave determination of adsorbate structures*, Progress in Surface Science **57**, 1 (1998).

[22] J. Zegenhagen, *Surface structure determination with X-ray standing waves*, Surface Science Reports **18**, 202 (1993).

[23] F. S. Tautz, *Structure and bonding of large aromatic molecules on noble metal surfaces: The example of PTCDA*, Progress in Surface Science **82**, 479 (2007).

[24] Z. F. Liu, K. Hashimoto, and A. Fujishima, *Photoelectrochemical information storage using azobenzene derivative*, Nature **347**, 658 (1990).

[25] Y. Yu, M. Nakano, and T. Ikeda, *Photomechanics: Directed bending of a polymer film by light*, Nature **425**, 145 (2003).

[26] P. P. Birnbaum and D. W. G. Style, *The photo-isomerization of some azobenzene derivatives*, Trans. Faraday Soc. **50**, 1192 (1954).

[27] T. Hugel, N. B. Holland, A. Cattani, L. Moroder, M. Seitz, and H. E. Gaub, *Single-Molecule Optomechanical Cycle*, Science **296**, 1103 (2002).

[28] M. J. Comstock, N. Levy, A. Kirakosian, J. Cho, F. Lauterwasser, J. H. Harvey, D. A. Strubbe, J. M. J. Fréchet, D. Trauner, S. G. Louie, and M. F. Crommie, *Reversible Photomechanical Switching of Individual Engineered Molecules at a Metallic Surface*, Phys. Rev. Lett. **99**, 038301 (2007).

[29] S. Hagen, F. Leyssner, D. Nandi, M. Wolf, and P. Tegeder, *Reversible switching of tetra-tert-butyl-azobenzene on a Au(111) surface induced by light and thermal activation*, Chemical Physics Letters **444**, 85 (2007).

[30] P. Tegeder, S. Hagen, F. Leyssner, M. Peters, S. Hecht, T. Klamroth, P. Saalfrank, and M. Wolf, *Electronic structure of the molecular switch tetra-tert-butyl-azobenzene adsorbed on Ag(111)*, Applied Physics A: Materials Science & Processing **88**, 465 (2007).

[31] A. Langner, S. L. Tait, N. Lin, C. Rajadurai, M. Ruben, and K. Kern, *Self-recognition and self-selection in multicomponent supramolecular coordination networks on surfaces*, Proceedings of the National Academy of Sciences of the United States of America **104**, 17927 (2007).

[32] S. L. Tait, A. Langner, N. Lin, S. Stepanow, C. Rajadurai, M. Ruben, and K. Kern, *One-Dimensional Self-Assembled Molecular Chains on Cu(100): Interplay between Surface-Assisted Coordination Chemistry and Substrate Commensurability*, The Journal of Physical Chemistry C **111**, 10982 (2007).

[33] S. L. Tait, Y. Wang, G. Costantini, N. Lin, A. Baraldi, F. Esch, L. Petaccia, S. Lizzit, and K. Kern, *Metal-Organic Coordination Interactions in Fe-Terephthalic Acid Networks on Cu(100)*, Journal of the American Chemical Society **130**, 2108 (2008).

[34] M. A. Lingenfelder, H. Spillmann, A. Dmitriev, S. Stepanow, N. Lin, J. V. Barth, and K. Kern, *Towards Surface-Supported Supramolecular Architectures: Tailored Coordination Assembly of 1,4-Benzenedicarboxylate and Fe on Cu(100)*, Chemistry – A European Journal **10**, 1913 (2004).

[35] P. Gambardella, S. Stepanow, A. Dmitriev, F. M. F. Honolka, Janand de Groot, S. S. Lingenfelder, Magaliand Gupta, D. D. Sarma, P. Bencok, S. Stanescu, Stefanand Clair, S. Pons, A. P. Lin, Nianand Seitsonen, H. Brune, J. V. Barth, and K. Kern, *Supramolecular control of the magnetic anisotropy in two-dimensional high-spin Fe arrays at a metal interface*, Nat Mater **8**, 189 (2009).

[36] D. P. Woodruff, *Surface structure determination using x-ray standing waves*, Reports on Progress in Physics **68**, 743 (2005).

[37] M. P. Seah and W. A. Dench, *Quantitative electron spectroscopy of surfaces: A standard data base for electron inelastic mean free paths in solids*, Surface and Interface Analysis **1**, 2 (1979).

[38] A. Caticha and S. Caticha-Ellis, *Dynamical theory of x-ray diffraction at Bragg angles near $\pi/2$*, Phys. Rev. B **25**, 971 (1982).

[39] J. Zegenhagen, *X-ray standing waves imaging*, Surface Science **554**, 77 (2004).

[40] E. N. Maslen, A. G. Fox, and M. A. O'Keefe, *International Table for Crystallography, Volume C* (KLUVER ACADEMIC PUBLISHERS, 1993).

[41] B. E. Warren, *X-ray diffraction* (Dover, 1990).

[42] B. L. Henke, E. M. Gullikson, and J. C. Davis, *X-Ray Interactions: Photoabsorption, Scattering, Transmission, and Reflection at E = 50-30,000 eV, Z = 1-92*, Atomic Data and Nuclear Data Tables **54**, 181 (1993).

[43] V. F. Sears and S. A. Shelley, *Debye–Waller factor for elemental crystals*, Acta Crystallographica Section A **47**, 441 (1991).

[44] I. A. Vartanyants and J. Zegenhagen, *Photoelectric scattering from an X-ray interference field*, Solid State Communications **113**, 299 (1999).

[45] G. J. Jackson, B. C. C. Cowie, D. P. Woodruff, R. G. Jones, M. S. Kariapper, C. Fisher, A. S. Y. Chan, and M. Butterfield, *Atomic Quadrupolar Photoemission Asymmetry Parameters from a Solid State Measurement*, Phys. Rev. Lett. **84**, 2346 (2000).

[46] E. J. Nelson, J. C. Woicik, P. Pianetta, I. A. Vartanyants, and J. W. Cooper, *Quadrupole effects in core and valence photoelectron emission from crystalline germanium measured via a spatially modulated x-ray interference field*, Phys. Rev. B **65**, 165219 (2002).

[47] I. Vartanyants, T.-L. Lee, S. Thiess, and J. Zegenhagen, *Non-dipole effects in X-ray standing wave photoelectron spectroscopy experiments*, Nuclear Instruments and Methods in Physics Research Section A: Accelerators, Spectrometers, Detectors and Associated Equipment **547**, 196 (2005).

[48] M. B. Trzhaskovskaya, V. I. Nefedov, and V. G. Yarzhemsky, *Photoelectron angular distribution parameters for elements Z=1 to Z=54 in the photoelectron energy range 100-5000 eV*, Atomic Data and Nuclear Data Tables **77**, 97 (2001).

[49] M. B. Trzhaskovskaya, V. I. Nefedov, and V. G. Yarzhemsky, *Photoelectron angular distribution parameters for elements Z=55 to Z=100 in the photoelectron energy range 100-5000 eV*, Atomic Data and Nuclear Data Tables **82**, 257 (2002).

[50] A. Jablonski, F. Salvat, and C. J. Powell, Tech. Rep., *NIST Electron Elastic-Scattering Cross-Section Database*, Version 3.1, National Institute of Standards and Technology, Gaithersburg, MD (2003).

[51] P. J. Cumpson and M. P. Seah, *Random uncertainties in AES and XPS: I: Uncertainties in peak energies, intensities and areas derived from peak synthesis*, Surface and Interface Analysis **18**, 345 (1992).

[52] N. Fairley, *CasaXPS*, URL `http://www.casaxps.com/`.

[53] J. R. Taylor, *An introduction to error analysis: the study of uncertainties in physical measurements* (University Science Books, 1997).

[54] N. Fairley, *Peak Fitting Statistics* (2011), URL `http://www.casaxps.com/help_manual/curve_fitting_polymers.htm`.

[55] W. H. Press, S. A. Teukolsky, W. T. Vetterling, and B. P. Flannery, *Numerical Recipes in C* (Cambridge University Press, 1992).

[56] S. Evans, *Estimation of the uncertainties associated with XPS peak intensity determination*, Surface and Interface Analysis **18**, 323 (1992).

[57] K. Harrison and L. B. Hazell, *The determination of uncertainties in quantitative XPS/AES and its impact on data acquisition strategy*, Surface and Interface Analysis **18**, 368 (1992).

[58] T. Dobbertin, M. Kroeger, D. Heithecker, D. Schneider, D. Metzdorf, H. Neuner, E. Becker, H.-H. Johannes, and W. Kowalsky, *Inverted top-emitting organic light-emitting diodes using sputter-deposited anodes*, Applied Physics Letters **82**, 284 (2003).

[59] Y. Gao, L. Wang, D. Zhang, L. Duan, G. Dong, and Y. Qiu, *Bright single-active layer small-molecular organic light-emitting diodes with a polytetrafluoroethylene barrier*, Applied Physics Letters **82**, 155 (2003).

[60] J.-S. Kim, F. Cacialli, and R. Friend, *Surface conditioning of indium-tin oxide anodes for organic light-emitting diodes*, Thin Solid Films **445**, 358 (2003).

[61] B. D'Andrade, R. Holmes, and S. Forrest, *Efficient Organic Electrophosphorescent White-Light-Emitting Device with a Triple Doped Emissive Layer*, Advanced Materials **16**, 624 (2004).

[62] W. Rieß, T. A. Beierlein, and H. Riel, *Optimizing OLED Structures for a-Si Display Applications via Combinatorial Methods and Enhanced Outcoupling*, Physica Status Solidi A **201**, 1360 (2004).

[63] H. E. Katz, X. M. Hong, A. Dodabalapur, and R. Sarpeshkar, *Organic field-effect transistors with polarizable gate insulators*, Journal of Applied Physics **91**, 1572 (2002).

[64] H. Sandberg, O. Henze, A. F. Kilbinger, H. Sirringhaus, W. J. Feast, and R. H. Friend, *Oligoethyleneoxide functionalised sexithiophene organic field effect transistors*, Synthetic Metals **137**, 885 (2003).

[65] K. Takahashi, N. Kuraya, T. Yamaguchi, T. Komura, and K. Murata, *Three-layer organic solar cell with high-power conversion efficiency of 3.5%*, Solar Energy Materials and Solar Cells **61**, 403 (2000).

[66] B. Maennig, J. Drechsel, D. Gebeyehu, P. Simon, F. Kozlowski, A. Werner, F. Li, S. Grundmann, S. Sonntag, M. Koch, K. Leo, M. Pfeiffer, H. Hoppe, D. Meissner, N. Sariciftci, I. Riedel, V. Dyakonov, and J. Parisi, *Organic p-i-n solar cells*, Applied Physics A: Materials Science & Processing **79**, 1 (2004).

[67] A. Abbasi and R. Scholz, *Ab Initio Calculation of the Dispersion Interaction between a Polyaromatic Molecule and a Noble Metal Substrate: PTCDA on Ag(110)*, The Journal of Physical Chemistry C **113**, 19897 (2009).

[68] M. Böhringer, W. D. Schneider, K. Glöckler, E. Umbach, and R. Berndt, *Adsorption site determination of PTCDA on Ag(110) by manipulation of adatoms*, Surface Science **419**, L95 (1998).

[69] K. Glöckler, C. Seidel, A. Soukopp, M. Sokolowski, E. Umbach, M. Böhringer, R. Berndt, and W. D. Schneider, *Highly ordered structures and submolecular scanning tunnelling microscopy contrast of PTCDA and DM-PBDCI monolayers on Ag(111) and Ag(110)*, Surface Science **405**, 1 (1998).

[70] C. Seidel, C. Awater, X. D. Liu, R. Ellerbrake, and H. Fuchs, *A combined STM, LEED and molecular modelling study of PTCDA grown on Ag(110)*, Surface Science **371**, 123 (1997).

[71] F. S. Tautz, M. Eremtchenko, J. A. Schaefer, M. Sokolowski, V. Shklover, K. Gloeckler, and E. Umbach, *A comparison of the chemisorption behaviour of PTCDA on different Ag surfaces*, Surface Science **502-503**, 176 (2002).

[72] F. S. Tautz, S. Sloboshanin, J. A. Schaefer, R. Scholz, V. Shklover, M. Sokolowski, and E. Umbach, *Vibrational properties of ultrathin PTCDA films on Ag(110)*, Phys. Rev. B **61**, 16933 (2000).

[73] F. S. Tautz, S. Sloboshanin, V. Shklover, R. Scholz, M. Sokolowski, J. A. Schaefer, and E. Umbach, *Substrate influence on the ordering of organic submonolayers: a comparative study of PTCDA on Ag(110) and Ag(111) using HREELS*, Applied Surface Science **166**, 363 (2000).

[74] J. Ziroff, F. Forster, A. Schöll, P. Puschnig, and F. Reinert, *Hybridization of Organic Molecular Orbitals with Substrate States at Interfaces: PTCDA on Silver*, Phys. Rev. Lett. **104**, 233004 (2010).

[75] Y. Zou, L. Kilian, A. Schöll, T. Schmidt, R. Fink, and E. Umbach, *Chemical bonding of PTCDA on Ag surfaces and the formation of interface states*, Surface Science **600**, 1240 (2006).

[76] E. Umbach, K. Glöckler, and M. Sokolowski, *Surface "architecture" with large organic molecules: interface order and epitaxy*, Surface Science **402-404**, 20 (1998).

[77] C. Seidel, J. Poppensieker, and H. Fuchs, *Real-time monitoring of phase transitions of vacuum deposited organic films by molecular beam deposition LEED*, Surface Science **408**, 223 (1998).

[78] D. Braun, A. Schirmeisen, and H. Fuchs, *Molecular growth and sub-molecular resolution of a thin multilayer of PTCDA on Ag(110) observed by scanning tunneling microscopy*, Surface Science **575**, 3 (2005).

[79] M. Cardona and L. Ley, *Photoemission in Solids I*, vol. 26 of *Topics in Applied Physics* (Springer-Verlag, 1978).

[80] A. Hauschild, Ph.D. thesis, *The Adsorption Geometry of PTCDA on Ag(111): an NIXSW Study*, Rheinische Friedrich-Wilhelms-Universität Bonn (2007).

[81] D. A. Shirley, *High-Resolution X-Ray Photoemission Spectrum of the Valence Bands of Gold*, Phys. Rev. B **5**, 4709 (1972).

[82] A. Schöll, Y. Zou, M. Jung, T. Schmidt, R. Fink, and E. Umbach, *Line shapes and satellites in high-resolution x-ray photoelectron spectra of large π-conjugated organic molecules*, The Journal of Chemical Physics **121**, 10260 (2004).

[83] M. Willenbockel, T. Sueyoshi, S. Soubatch, and F. S. Tautz, *Personal communication.*

[84] F. Schreiber, A. Gerlach, N. Koch, E. Zojer, M. Sokolowski, F. S. Tautz, M. Rohlfing, and E. Umbach, *Comment on "Electron Core-Hole Interaction and Its Induced Ionic Structural Relaxation in Molecular Systems under X-Ray Irradiation"*, Phys. Rev. Lett. **99**, 059601 (2007).

[85] I. Kröger, B. Stadtmüller, C. Stadler, J. Ziroff, M. Kochler, A. Stahl, F. Pollinger, T.-L. Lee, J. Zegenhagen, F. Reinert, and C. Kumpf, *Submonolayer growth of copper-phthalocyanine on Ag(111)*, New Journal of Physics **12**, 083038 (2010).

[86] J. Ikonomov, O. Bauer, and M. Sokolowski, *Highly ordered thin films of perylene-3,4,9,10-tetracarboxylic acid dianhydride (PTCDA) on Ag(100)*, Surface Science **602**, 2061 (2008).

[87] J. Ikonomov, P. Bach, R. Merkel, and M. Sokolowski, *Surface diffusion constants of large organic molecules determined from their residence times under a scanning tunneling microscope tip*, Phys. Rev. B **81**, 161412 (2010).

[88] J. Ikonomov, C. H. Schmitz, and M. Sokolowski, *Diffusion-limited island decay of PTCDA on Ag(100): Determination of the intermolecular interaction*, Phys. Rev. B **81**, 195428 (2010).

[89] M. Böhringer, W.-D. Schneider, R. Berndt, K. Glöckler, M. Sokolowski, and E. Umbach, *Corrugation reversal in scanning tunneling microscope images of organic molecules*, Phys. Rev. B **57**, 4081 (1998).

[90] M. J. Frisch, G. W. Trucks, H. B. Schlegel, G. E. Scuseria, M. A. Robb, J. R. Cheeseman, J. A. Montgomery, Jr., T. Vreven, K. N. Kudin, J. C. Burant, J. M. Millam, S. S. Iyengar, J. Tomasi, V. Barone, B. Mennucci, M. Cossi, G. Scalmani, N. Rega, G. A. Petersson, H. Nakatsuji, M. Hada, M. Ehara, K. Toyota, R. Fukuda, J. Hasegawa, M. Ishida, T. Nakajima, Y. Honda, O. Kitao, H. Nakai, M. Klene, X. Li, J. E. Knox, H. P. Hratchian, J. B. Cross, V. Bakken, C. Adamo, J. Jaramillo, R. Gomperts, R. E. Stratmann, O. Yazyev, A. J. Austin, R. Cammi, C. Pomelli, J. W. Ochterski, P. Y. Ayala, K. Morokuma, G. A. Voth, P. Salvador, J. J. Dannenberg, V. G. Zakrzewski, S. Dapprich, A. D. Daniels, M. C. Strain, O. Farkas, D. K. Malick, A. D. Rabuck, K. Raghavachari, J. B. Foresman, J. V. Ortiz, Q. Cui, A. G. Baboul, S. Clifford, J. Cioslowski, B. B. Stefanov, G. Liu, A. Liashenko, P. Piskorz, I. Komaromi, R. L. Martin, D. J. Fox, T. Keith, M. A. Al-Laham, C. Y. Peng, A. Nanayakkara, M. Challacombe, P. M. W. Gill, B. Johnson, W. Chen, M. W. Wong, C. Gonzalez, and J. A. Pople, *Gaussian 03, Revision C.02*, Gaussian, Inc., Wallingford, CT, 2004.

[91] B. Cordero, V. Gomez, A. E. Platero-Prats, M. Reves, J. Echeverria, E. Cremades, F. Barragan, and S. Alvarez, *Covalent radii revisited*, Dalton Trans. pp. 2832–2838 (2008).

[92] A. Bondi, *van der Waals Volumes and Radii*, The Journal of Physical Chemistry **68**, 441 (1964).

[93] M. Rohlfing, R. Temirov, and F. S. Tautz, *Adsorption structure and scanning tunneling data of a prototype organic-inorganic interface: PTCDA on Ag(111)*, Phys. Rev. B **76**, 115421 (2007).

[94] D. A. Verner, D. G. Yakovlev, I. M. Band, and M. B. Trzhaskovskaya, *Subshell Photoionization Cross Sections and Ionization Energies of Atoms and Ions from He to Zn*, Atomic Data and Nuclear Data Tables **55**, 233 (1993).

[95] W. Jacob, E. Bertel, and V. Dose, *Potassium-induced empty electronic states on Ag(110)*, Phys. Rev. B **35**, 5910 (1987).

[96] V. B. Nascimento, E. A. Soares, V. E. de Carvalho, E. L. Lopes, R. Paniago, and C. M. C. de Castilho, *Thermal expansion of the Ag(110) surface studied by low-energy electron diffraction and density-functional theory*, Phys. Rev. B **68**, 245408 (2003).

[97] P. Bayersdorfer, *Spot-Plotter (Version 1.2.1.4)* (2008).

[98] M. Horn-von Hoegen, *Growth of semiconductor layers studied by spot profile analysing low energy electron diffraction*, Zeitschrift für Kristallographie **214**, 591 (1999).

[99] M. Sokolowski, *Personal communication*.

[100] I. Horcas, R. Fernandez, J. M. Gomez-Rodriguez, J. Colchero, J. Gomez-Herrero, and A. M. Baro, *WSXM: A software for scanning probe microscopy and a tool for nanotechnology*, Review of Scientific Instruments **78**, 013705 (2007).

[101] J. V. Barth, R. Schuster, J. Wintterlin, R. J. Behm, and G. Ertl, *Scanning-tunneling-microscopy observation of K-induced reconstructions on Au(110)*, Phys. Rev. B **51**, 4402 (1995).

[102] M. Willenbockel, G. Mercurio, S. Soubatch, and F. S. Tautz, *Personal communication*.

[103] I. G. Hill, A. Rajagopal, A. Kahn, and Y. Hu, *Molecular level alignment at organic semiconductor-metal interfaces*, Applied Physics Letters **73**, 662 (1998).

[104] X. Crispin, V. Geskin, A. Crispin, J. Cornil, R. Lazzaroni, W. R. Salaneck, and J.-L. Brédas, *Characterization of the Interface Dipole at Organic/Metal Interfaces*, Journal of the American Chemical Society **124**, 8131 (2002).

[105] V. De Renzi, R. Rousseau, D. Marchetto, R. Biagi, S. Scandolo, and U. del Pennino, *Metal Work-Function Changes Induced by Organic Adsorbates: A Combined Experimental and Theoretical Study*, Phys. Rev. Lett. **95**, 046804 (2005).

[106] H. Yamane, D. Yoshimura, E. Kawabe, R. Sumii, K. Kanai, Y. Ouchi, N. Ueno, and K. Seki, *Electronic structure at highly ordered organic/metal interfaces: Pentacene on Cu(110)*, Phys. Rev. B **76**, 165436 (2007).

[107] R. Smoluchowski, *Anisotropy of the Electronic Work Function of Metals*, Phys. Rev. **60**, 661 (1941).

[108] M. De Seta and F. Evangelisti, *LUMO band of K-doped C_{60} single phases: A photoemission and yield-spectroscopy study*, Phys. Rev. B **51**, 1096 (1995).

[109] C. Zazza, S. Meloni, A. Palma, M. Knupfer, G. G. Fuentes, and R. Car, *Quasi-One-Dimensional K-O Chain in PTCDA Thin Films: Evidence from First-Principles Calculations*, Phys. Rev. Lett. **98**, 046401 (2007).

[110] T. Sueyoshi, H. Kakuta, M. Ono, K. Sakamoto, S. Kera, and N. Ueno, *Band gap states of copper phthalocyanine thin films induced by nitrogen exposure*, Applied Physics Letters **96**, 093303 (2010).

[111] U. Martinez, L. Giordano, and G. Pacchioni, *Tuning the work function of ultrathin oxide films on metals by adsorption of alkali atoms*, The Journal of Chemical Physics **128**, 164707 (2008).

[112] H. Ibach, *Physics of Surfaces and Interfaces* (Springer, 2006).

[113] K. W. Jacobsen and J. K. Nørskov, *Theory of Alkali-Metal-Induced Reconstruction of fcc (110) Surfaces*, Phys. Rev. Lett. **60**, 2496 (1988).

[114] P. Hofmann, S. Bao, K.-M. Schindler, O. Schaff, M. Polcik, V. Fritzsche, A. Bradshaw, R. Davis, and D. Woodruff, *The potassium-induced reconstruction of Cu(110): the K atom adsorption site*, Surface Science **319**, L7 (1994).

[115] H. Bonzel, A. Bradshaw, and G. Ertl, eds., *Physics and chemistry of alkali metal adsorption* (Elsevier, 1989).

[116] H. Tochihara and S. Mizuno, *Composite surface structures formed by restructuring-type adsorption of alkali-metals on fcc metals*, Progress in Surface Science **58**, 1 (1998).

[117] B. E. Hayden, K. C. Prince, P. J. Davie, G. Paolucci, and A. M. Bradshaw, *Alkali metal-induced reconstruction of Ag(110)*, Solid State Communications **48**, 325 (1983).

[118] J. W. M. Frenken, R. L. Krans, J. F. van der Veen, E. Holub-Krappe, and K. Horn, *Missing-row surface reconstruction of Ag(110) induced by potassium adsorption*, Phys. Rev. Lett. **59**, 2307 (1987).

[119] C. L. Fu and K. M. Ho, *External-charge-induced surface reconstruction on Ag(110)*, Phys. Rev. Lett. **63**, 1617 (1989).

[120] G. A. Somorjai, *The flexible surface. Correlation between reactivity and restructuring ability*, Langmuir **7**, 3176 (1991).

[121] J. Gimzewski, S. Modesti, C. Gerber, and R. Schlittler, *Observation of a new Au(111) reconstruction at the interface of an adsorbed C_{60} overlayer*, Chemical Physics Letters **213**, 401 (1993).

[122] P. W. Murray, M. O. Pedersen, E. Lægsgaard, I. Stensgaard, and F. Besenbacher, *Growth of C_{60} on Cu(110) and Ni(110) surfaces: C_{60}-induced interfacial roughening* , Phys. Rev. B **55**, 9360 (1997).

[123] J. A. Appelbaum and D. R. Hamann, *Electronic structure of the Cu(111) surface*, Solid State Communications **27**, 881 (1978).

[124] B. Hammer, Y. Morikawa, and J. K. Nørskov, *CO Chemisorption at Metal Surfaces and Overlayers*, Phys. Rev. Lett. **76**, 2141 (1996).

[125] M. Schunack, L. Petersen, A. Kühnle, E. Lægsgaard, I. Stensgaard, I. Johannsen, and F. Besenbacher, *Anchoring of Organic Molecules to a Metal Surface: HtBDC on Cu(110)*, Phys. Rev. Lett. **86**, 456 (2001).

[126] L. Kilian, A. Hauschild, R. Temirov, S. Soubatch, A. Schöll, A. Bendounan, F. Reinert, T.-L. Lee, F. S. Tautz, M. Sokolowski, and E. Umbach, *Role of Intermolecular Interactions on the Electronic and Geometric Structure of a Large π-Conjugated Molecule Adsorbed on a Metal Surface*, Phys. Rev. Lett. **100**, 136103 (2008).

[127] A. L. R. Delhey, S. Soubatch, and F. S. Tautz, *Personal communication.*

[128] S. Duhm, A. Gerlach, I. Salzmann, B. Broeker, R. Johnson, F. Schreiber, and N. Koch, *PTCDA on Au(111), Ag(111) and Cu(111): Correlation of interface charge transfer to bonding distance*, Organic Electronics **9**, 111 (2008).

[129] B.-Y. Choi, S.-J. Kahng, S. Kim, H. Kim, H. W. Kim, Y. J. Song, J. Ihm, and Y. Kuk, *Conformational molecular switch of the azobenzene molecule: A scanning tunneling microscopy study*, Phys. Rev. Lett. **96**, 156106 (2006).

[130] M. Alemani, M. V. Peters, S. Hecht, K.-H. Rieder, F. Moresco, and L. Grill, *Electric Field-Induced Isomerization of Azobenzene by STM*, Journal of the American Chemical Society **128**, 14446 (2006).

[131] L. Óvári, M. Wolf, and P. Tegeder, *Reversible Changes in the Vibrational Structure of Tetra-tert-butylazobenzene on a Au(111) Surface Induced by Light*

and Thermal Activation, The Journal of Physical Chemistry C **111**, 15370 (2007).

[132] I. Martin, M. Wolf, and P. Tegeder, *Personal communication.*

[133] R. Kirby, T. A. Hahn, and B. D. Rothrock, *American Institute of Physics Handbook,* 3^{rd} *ed.* (McGrw-Hill, New York, 1963).

[134] H. E. Swanson, M. C. Morris, and E. Evans, *Standard X-ray diffraction Powder Patterns*, National Bureau of Standards Monograph **25(4)**, 3 (1966).

[135] C. Stadler, S. Hansen, F. Pollinger, C. Kumpf, E. Umbach, T.-L. Lee, and J. Zegenhagen, *Structural investigation of the adsorption of SnPc on Ag(111) using normal-incidence x-ray standing waves*, Phys. Rev. B **74**, 035404 (2006).

[136] A. Gerlach, S. Sellner, F. Schreiber, N. Koch, and J. Zegenhagen, *Substrate-dependent bonding distances of PTCDA: A comparative x-ray standing-wave study on Cu(111) and Ag(111)*, Phys. Rev. B **75**, 045401 (2007).

[137] J. Zegenhagen, DARE, personal communication.

[138] J. Leiro, E. Minni, and E. Suoninen, *Study of plasmon structure in XPS spectra of silver and gold*, Journal of Physics F: Metal Physics **13**, 215 (1983).

[139] H. J. Lindberg, B.J., *Molecular spectroscopy by means of ESCA, VI. Group shifts for N, P and as compounds*, Chem. Scr. **7**, 155 (1975).

[140] P. Brant and R. D. Feltham, *X-ray photoelectron spectra of aryldiazo derivatives of transition metals*, Journal of Organometallic Chemistry **120**, C53 (1976).

[141] R. Schmidt, S. Hagen, D. Brete, R. Carley, C. Gahl, J. Dokic, P. Saalfrank, S. Hecht, P. Tegeder, and M. Weinelt, *On the electronic and geometrical structure of the trans- and cis-isomer of tetra-tert-butyl-azobenzene on Au(111)*, Phys. Chem. Chem. Phys. **12**, 4488 (2010).

[142] E. McNellis, J. Meyer, A. D. Baghi, and K. Reuter, *Stabilizing a molecular switch at solid surfaces: A density functional theory study of azobenzene on Cu(111), Ag(111), and Au(111)*, Phys. Rev. B **80**, 035414 (2009).

[143] E. R. McNellis, J. Meyer, and K. Reuter, *Azobenzene at coinage metal surfaces: Role of dispersive van der Waals interactions*, Phys. Rev. B **80**, 205414 (2009).

[144] J. A. Bouwstra, A. Schounten, and J. Kroon, *Structural Studies of the System trans-Azobenzene/trans-Stilbene. I. A Reinvestigation of the Disorder in the Crystal Structure of trans-Azobenzene, $C_{12}H_{10}N_2$*, Acta Crystallographica Section C **39**, 1121 (1983).

[145] M. J. Comstock, J. Cho, A. Kirakosian, and M. F. Crommie, *Manipulation of azobenzene molecules on Au(111) using scanning tunneling microscopy*, Phys. Rev. B **72**, 153414 (2005).

[146] J. A. Miwa, S. Weigelt, H. Gersen, F. Besenbacher, F. Rosei, and T. R. Linderoth, *Azobenzene on Cu(110): Adsorption Site-Dependent Diffusion*, Journal of the American Chemical Society **128**, 3164 (2006).

[147] A. Kirakosian, M. J. Comstock, J. Cho, and M. F. Crommie, *Molecular commensurability with a surface reconstruction: STM study of azobenzene on Au(111)*, Phys. Rev. B **71**, 113409 (2005).

[148] J. J. de Lange, J. M. Robertson, and I. Woodward, *X-Ray Crystal Analysis of Trans-Azobenzene*, Proceedings of the Royal Society of London. Series A. Mathematical and Physical Sciences **171**, 398 (1939).

[149] A. Tkatchenko and M. Scheffler, *Accurate Molecular Van Der Waals Interactions from Ground-State Electron Density and Free-Atom Reference Data*, Phys. Rev. Lett. **102**, 073005 (2009).

[150] M. Rohlfing and T. Bredow, *Binding Energy of Adsorbates on a Noble-Metal Surface: Exchange and Correlation Effects*, Phys. Rev. Lett. **101**, 266106 (2008).

[151] E. R. McNellis, C. Bronner, J. Meyer, M. Weinelt, P. Tegeder, and K. Reuter, *Azobenzene versus 3,3′,5,5′-tetra-tert-butyl-azobenzene (TBA) at Au(111): characterizing the role of spacer groups*, Phys. Chem. Chem. Phys. **12**, 6404 (2010).

[152] E. R. McNellis, J. Meyer, and K. Reuter, *Personal communication.*

[153] S. Hagen, P. Kate, F. Leyssner, D. Nandi, M. Wolf, and P. Tegeder, *Excitation mechanism in the photoisomerization of a surface-bound azobenzene derivative: Role of the metallic substrate*, The Journal of Chemical Physics **129**, 164102 (2008).

[154] P. Rahe, M. Nimmrich, A. Nefedov, M. Naboka, C. Woell, and A. Kuehnle, *Transition of Molecule Orientation during Adsorption of Terephthalic Acid on Rutile TiO_2(110)*, The Journal of Physical Chemistry C **113**, 17471 (2009).

[155] Y.-G. Kim, S.-L. Yau, and K. Itaya, *In Situ Scanning Tunneling Microscopy of Highly Ordered Adlayers of Aromatic Molecules on Well-Defined Pt(111) Electrodes in Solution: Benzoic Acid, Terephthalic Acid, and Pyrazine*, Langmuir **15**, 7810 (1999).

[156] M. E. Cañas-Ventura, F. Klappenberger, S. Clair, S. Pons, K. Kern, H. Brune, T. Strunskus, C. Woell, R. Fasel, and J. V. Barth, *Coexistence of one- and two-dimensional supramolecular assemblies of terephthalic acid on Pd(111) due to self-limiting deprotonation*, The Journal of Chemical Physics **125**, 184710 (2006).

[157] T. Suzuki, T. Lutz, D. Payer, N. Lin, S. L. Tait, G. Costantini, and K. Kern, *Substrate effect on supramolecular self-assembly: from semiconductors to metals*, Phys. Chem. Chem. Phys. **11**, 6498 (2009).

[158] S. Clair, S. Pons, A. P. Seitsonen, H. Brune, K. Kern, and J. V. Barth, *STM Study of Terephthalic Acid Self-Assembly on Au(111): Hydrogen-Bonded Sheets on an Inhomogeneous Substrate*, The Journal of Physical Chemistry B **108**, 14585 (2004).

[159] D. S. Martin, R. J. Cole, and S. Haq, *Creating a functionalized surface: The adsorption of terephthalic acid onto Cu(110)*, Phys. Rev. B **66**, 155427 (2002).

[160] N. Atodiresei, V. Caciuc, K. Schroeder, and S. Blügel, *First-principles investigation of terephthalic acid on Cu(110)*, Phys. Rev. B **76**, 115433 (2007).

[161] S. Stepanow, T. Strunskus, M. Lingenfelder, A. Dmitriev, H. Spillmann, N. Lin, J. V. Barth, C. Wöll, and K. Kern, *Deprotonation-Driven Phase Transformations in Terephthalic Acid Self-Assembly on Cu(100)*, The Journal of Physical Chemistry B **108**, 19392 (2004).

[162] T. Tseng, C. Urban, Y. Wang, R. Otero, S. L. Tait, A. Manuel, D. Écija, M. Trelka, J. M. Gallego, N. Lin, M. Konuma, U. Starke, A. Nefedov, A. Langner, C. Wöll, M. A. Herranz, F. Martín, N. Martín, K. Kern, and R. Miranda, *Charge-transfer-induced structural rearrangements at both sides of organic/metal interfaces*, Nat Chem **2**, 374 (2010).

[163] J. Jelic and K. Reuter, *Personal communication.*

[164] J. P. Perdew, K. Burke, and M. Ernzerhof, *Generalized Gradient Approximation Made Simple*, Phys. Rev. Lett. **77**, 3865 (1996).

[165] S. L. Tait, *Personal communication.*

[166] S. Stepanow and K. Kern, *Personal communication.*

[167] M. E. Straumanis and L. S. Yu, *Lattice parameters, densities, expansion coefficients and perfection of structure of Cu and of Cu–In α phase*, Acta Crystallographica Section A **25**, 676 (1969).

[168] F. Allegretti, D. Woodruff, V. Dhanak, C. Mariani, F. Bussolotti, and S. D'Addato, *Self-assembly of an aromatic thiolate on Cu(100): The local adsorption site*, Surface Science **598**, 253 (2005).

[169] A. A. Cafolla, E. McLoughlin, E. AlShamaileh, P. Guaino, G. Sheerin, D. Carty, T. McEvoy, C. Barnes, V. Dhanak, and A. Santoni, *Observation of an anti-phase domain structure in the Cu(100)/Sn surface alloy system*, Surface Science **544**, 121 (2003).

[170] S. Walter, V. Blum, L. Hammer, S. Müller, K. Heinz, and M. Giesen, *The role of an energy-dependent inner potential in quantitative low-energy electron diffraction*, Surface Science **458**, 155 (2000).

[171] A. Groß, *Theoretical Surface Science* (Springer, 2009).

[172] N. Lorente, M. F. G. Hedouin, R. E. Palmer, and M. Persson, *Chemisorption of benzene and STM dehydrogenation products on Cu(100)*, Phys. Rev. B **68**, 155401 (2003).

[173] T. Steiner, *The Hydrogen Bond in the Solid State*, Angewandte Chemie International Edition **41**, 48 (2002).

[174] G. A. Jeffrey, *An Introduction to Hydrogen Bonding* (Oxford University Press, 1997).

[175] B. T. Lutz, J. Jacob, and J. H. van der Maas, *Vibrational spectroscopic characteristics of $=C—H\cdots O$ and $N—H\cdots\pi$ interaction in crystalline N-(2,6-dimethylphenyl)-5-methylisoxazole-3-carboxamide*, Vibrational Spectroscopy **12**, 197 (1996).

[176] B. Milián, R. Pou-Amérigo, R. Viruela, and E. Ortí, *A theoretical study of neutral and reduced tetracyano-p-quinodimethane (TCNQ)*, Journal of Molecular Structure: THEOCHEM **709**, 97 (2004).

[177] S. K. M. Henze, O. Bauer, T.-L. Lee, M. Sokolowski, and F. Tautz, *Vertical bonding distances of PTCDA on Au(111) and Ag(111): Relation to the bonding type*, Surface Science **601**, 1566 (2007).

[178] A. Hauschild, R. Temirov, S. Soubatch, O. Bauer, A. Schöll, B. C. C. Cowie, T.-L. Lee, F. S. Tautz, and M. Sokolowski, *Normal-incidence x-ray standing-wave determination of the adsorption geometry of PTCDA on Ag(111): Comparison of the ordered room-temperature and disordered low-temperature phases*, Phys. Rev. B **81**, 125432 (2010).

[179] *Numpy and scipy documentation*, URL `http://docs.scipy.org/doc/scipy/reference/generated/scipy.optimize.leastsq.html`.

Publications

1. **Structure and energetics of azobenzene at Ag(111): Benchmarking semi-empirical dispersion correction approaches.**
   G. Mercurio, E. McNellis, I. Martin, S. Hagen, F. Leyssner, S. Soubatch, J. Meyer, M. Wolf, P. Tegeder, F. S. Tautz, K. Reuter.
   ESRF Highlights 2010

2. **Bulky Spacer Groups – A Valid Strategy to Control the Coupling of Functional Molecules to Surfaces?**
   E.R. McNellis, **G. Mercurio**, S. Hagen, F. Leyssner, J. Meyer, S. Soubatch, M. Wolf, K. Reuter, P. Tegeder, and F. S. Tautz.
   Chemical Physics Letters, **499** (2010) 247-249.

3. **Structure and energetics of azobenzene at Ag(111): Benchmarking semi-empirical dispersion correction approaches.**
   G. Mercurio, E. McNellis, I. Martin, S. Hagen, F. Leyssner, S. Soubatch, J. Meyer, M. Wolf, P. Tegeder, F. S. Tautz, K. Reuter.
   Physical Review Letters, **104** (2010) 036102.

4. **Free volume fraction and nanoholes shapes in polyvinyl acetate.**
   G. Consolati, **G. Mercurio**, F. Quasso.
   Chemical Physics Letters, **475**, (2009) 54.

Conference contributions

1. **Alkali induced nanopatterning of Ag(110) surface mediated by molecular adsorbate.**
   G. Mercurio, O. Bauer, M. Willenbockel, B. Fiedler, C. Weiss, R. Temirov, S. Soubatch, M. Sokolowski, F. S. Tautz.
   Oral presentation.
   DPG (Deutsche Physikalische Gesellschaft) Spring Meeting, Dresden (Germany), 13–18.03.2011.

2. **Alkali-induced nanopatterning of the PTCDA/Ag(110) interface.**
   G. Mercurio, O. Bauer, C. Weiss, B. Fiedler, A. Delhey, R. Temirov, S. Soubatch, M. Sokolowski, F. S. Tautz.
   Poster presentation.
   Nanoelectronics days 2010, Aachen (Germany), 04–07.10.2010.

3. **Structure and Energetics of azobenzene derivatives at Ag(111).**
   G. Mercurio, E.R. McNellis, I. Martin, S. Hagen, F. Leyssner, S. Soubatch, J. Meyer, M. Wolf, P. Tegeder, F. S. Tautz, and K. Reuter.
   Oral presentation
   IVC-18 (International Vacuum Congress), Beijing (China), 23–27.08.2010.

4. **Alkali-induced nanopatterning of the PTCDA/Ag(110) interface.**
   G. Mercurio, O. Bauer, C. Weiss, B. Fiedler, A. Delhey, R. Temirov, S. Soubatch, M. Sokolowski, F. S. Tautz.
   Poster presentation.
   IVC-18 (International Vacuum Congress), Beijing (China), 23–27.08.2010.

5. **Structure and Energetics of azobenzene on Ag(111).**
   G. Mercurio, E.R. McNellis, I. Martin, S. Hagen, F. Leyssner, S. Soubatch, J. Meyer, M. Wolf, P. Tegeder, F. S. Tautz, and K. Reuter.
   Oral presentation.
   DPG (Deutsche Physikalische Gesellschaft) Spring Meeting, Regensburg (Germany), 21–26.04.2010.

6. **Adsorption geometry of molecular switches.**
   G. Mercurio, E.R. McNellis, I. Martin, S. Hagen, F. Leyssner, S. Soubatch, J. Meyer, M. Wolf, P. Tegeder, F. S. Tautz, and K. Reuter.
   Oral presentation.
   ACSIN-10 (10th International Conference on Atomically Controlled Surfaces, Interfaces and Nanostructures), Granada (Spain), 21–25.09.2009.

7. **Normal Incidence X-ray Standing Wave: Method and Applications.**
   G. Mercurio, O. Bauer, S. Hagen, F. Leyssner, E.R. McNellis, P. Tegeder, S. Soubatch, K. Reuter, M. Wolf, M. Sokolowski, F. S. Tautz.
   Poster presentation.
   JARA-FIT Science Days, Schleiden (Germany), 05–06.06.2009.

8. **Normal Incidence X-ray Standing Wave: Method and Applications.**
   G. Mercurio, O. Bauer, S. Hagen, F. Leyssner, E.R. McNellis, P. Tegeder, S. Soubatch, K. Reuter, M. Wolf, M. Sokolowski, F. S. Tautz.
   Poster presentation.
   HERCULES (Higher Education Course for Users of Large Experimental Systems), Grenoble (France), 01.03–04.04.2009.

Curriculum Vitae

Giuseppe Mercurio
born on August 10th, 1984 in Cinquefrondi (Reggio Calabria), Italy.
Nationality: Italian.

Education

1997–2002: Liceo Scientifico (secondary school focusing on sciences), Cittanova (Reggio Calabria), Italy.

2002–2005: Bachelor of Science study in Physics Engineering at Politecnico di Milano (Milan), Italy.

2005: Bachelor of Science degree with final mark 103/110.
Thesis: "Measurement of the Positronium contact density in chiral materials".
Advisor: Prof. G. Consolati.

2005–2007: Master of Science study in Physics Engineering at Politecnico di Milano (Milan), Italy.

2007: Master of Science degree in Physics Engineering with final mark 107/110.
Thesis title: "Study of the specific free volume of two polymeric materials by means of positron annihilation lifetime spectroscopy and dilatometry".
Advisor: Prof. G. Consolati.

2008–2011: PhD student at Peter Grünberg Institute-3, Forschungszentrum Jülich.
Thesis title: "Study of Molecule-Metal Interfaces by Means of the Normal Incidence X-ray Standing Wave Technique".
Advisor: Prof. Dr. F. S. Tautz.

since 02/2012: Postdoc at Peter Grünberg Institute-3, Forschungszentrum Jülich.

1. **Soft Matter**
   From Synthetic to Biological Materials
   Lecture manuscripts of the 39th IFF Spring School March 3 – 14, 2008
   Jülich, Germany
   edited by J.K.G. Dhont, G. Gompper, G. Nägele, D. Richter, R.G. Winkler (2008),
   c. 1000 pages
   ISBN: 978-3-89336-517-3

2. **Structural analysis of diblock copolymer nanotemplates using grazing incidence scattering**
   by D. Korolkov (2008), III, 167 pages
   ISBN: 978-3-89336-522-7

3. **Thermal Nonequilibrium**
   Thermal forces in fluid mixtures
   Lecture Notes of the 8th International Meeting on Thermodiffusion,
   9 – 13 June 2008, Bonn, Germany
   edited by S. Wiegand, W. Köhler (2008), 300 pages
   ISBN: 978-3-89336-523-4

4. **Synthesis of CMR manganites and ordering phenomena in complex transition metal oxides**
   by H. Li (2008), IV, 176 pages
   ISBN: 978-3-89336-527-2

5. **Neutron Scattering**
   Lectures of the JCNS Laboratory Course held at the Forschungszentrum Jülich and the research reactor FRM II of TU Munich
   edited by R. Zorn, Th. Brückel, D. Richter (2008), ca. 500 pages
   ISBN: 978-3-89336-532-6

6. **Ultrafast Magnetization Dynamics**
   by S. Woodford (2008), 130 pages
   ISBN: 978-3-89336-536-4

7. **Role of Surface Roughness inTribology: from Atomic to Macroscopic Scale**
   by C. Yang (2008), VII, 166 pages
   ISBN: 978-3-89336-537-1

8. **Strahl- und Spindynamik von Hadronenstrahlen in Mittelenergie-Ringbeschleunigern**
   von A. Lehrach (2008), II, 171 Seiten
   ISBN: 978-3-89336-548-7

9. **Phase Behaviour of Proteins and Colloid-Polymer Mixtures**
   by C. Gögelein (2008), II, 147 pages
   ISBN: 978-3-89336-555-5

10. **Spintronics – From GMR to Quantum Information**
    Lecture Notes of the 40th IFF Spring School March 9 – 20, 2009
    Jülich, Germany
    edited by St. Blügel, D. Bürgler, M. Morgenstern, C. M. Schneider,
    R. Waser (2009), c. 1000 pages
    ISBN: 978-3-89336-559-3

11. **ANKE / PAX Workshop on SPIN Physics**
    JINR, Dubna, Russia / June 22. – 26, 2009
    Org. Committee: A. Kacharava, V. Komarov, A. Kulikov, P. Lenisa, R. Rathmann,
    H. Ströher (2009), CD-ROM
    ISBN: 978-3-89336-586-9

12. **Entwicklung einer Nanotechnologie-Plattform für die Herstellung Crossbar-basierter Speicherarchitekturen**
    von M. Meier (2009), 135 Seiten
    ISBN: 978-3-89336-598-2

13. **Electronic Oxides –**
    Correlation Phenomena, Exotic Phases and Novel Functionalities
    Lecture Notes of the 41st IFF Spring School March 8 – 19, 2010
    Jülich, Germany
    edited by St. Blügel, T. Brückel, R. Waser, C.M. Schneider (2010), ca. 1000 pages
    ISBN: 978-3-89336-609-5

14. **4th Georgian-German School and Workshop in Basic Science**
    Tbilisi, Georgia / May 3 – 7, 2010
    Org. Committee: E. Abrosimova, R. Botchorishvili, A. Kacharava, M. Nioradze,
    A. Prangishvili, H. Ströher (2010); CD-ROM
    ISBN: 978-3-89336-629-3

15. **Neutron Scattering**
    Lectures of the JCNS Laboratory Course held at Forschungszentrum Jülich and the research reactor FRM II of TU Munich
    edited by Th. Brückel, G. Heger, D. Richter, G. Roth and R. Zorn (2010),
    ca 350 pages
    ISBN: 978-3-89336-635-4

16. **Ab *initio* investigations of magnetic properties of ultrathin transition-metal films on *4d* substrates**
    by A. Al-Zubi (2010), II, 143 pages
    ISBN: 978-3-89336-641-5

17. **Investigation of a metal-organic interface realization and understanding of a molecular switch**
    by O. Neucheva (2010), 134 pages
    ISBN: 978-3-89336-650-7

18. **Reine Spinströme in lateralen Spinventilen, *in situ* Erzeugung und Nachweis**
von J. Mennig (2010), V, 95 Seiten
ISBN: 978-3-89336-684-2

19. **Nanoimprint Lithographie als Methode zur chemischen Oberflächenstrukturierung für Anwendungen in der Bioelektronik**
von S. Gilles (2010), II, 169 Seiten
ISBN: 978-3-89336-686-6

20. **Macromolecular Systems in Soft- and Living-Matter**
Lecture Notes of the 42nd IFF Spring School 2011 February 14 – 25, 2011 Jülich, Germany
edited by J. K.G. Dhont, G. Gompper, P. R.Lang, D. Richter, M. Ripoll, D. Willbold, R. Zorn (2011), ca. 1000 pages
ISBN: 978-3-89336-688-0

21. **The spin structure of magnetic nanoparticles and in magnetic nanostructures**
by S. Disch (2011), V, 342 pages
ISBN: 978-3-89336-704-7

22. **Element-selective and time-resolved magnetic investigations in the extreme ultraviolet range**
by P. Grychtol (2011), xii, 144 pages
ISBN: 978-3-89336-706-1

23. **Spin-Transfer Torque Induced Dynamics of Magnetic Vortices in Nanopillars**
by V. Sluka (2011), 121 pages
ISBN: 978-3-89336-717-7

24. **Adsorption von Phthalocyaninen auf Edelmetalloberflächen**
von I. Kröger (2011), vi, 206 Seiten
ISBN: 978-3-89336-720-7

25. **Time-Resolved Single Molecule FRET Studies on Folding/Unfolding Transitions and on Functional Conformational Changes of Phosphoglycerate Kinase**
by T. Rosenkranz (2011), III, 139 pages
ISBN: 978-3-89336-721-4

26. **NMR solution structures of the MIoK1 cyclic nucleotide-gated ion channel binding domain**
by S. Schünke (2011), VI, (getr. pag.)
ISBN: 978-3-89336-722-1

27. **Neutron Scattering**
    Lectures of the JCNS Laboratory Course held at Forschungszentrum Jülich and the research reactor FRM II of TU Munich
    edited by Th. Brückel, G. Heger, D. Richter, G. Roth and R. Zorn (2011), ca 350 pages
    ISBN: 978-3-89336-725-2

28. **Neutron Scattering**
    Experiment Manuals of the JCNS Laborator Course held at Forschungszentrum Jülich and the research reactorFRM II of TU Munich
    edited by Th. Brückel, G. Heger, D. Richter, G. Roth and R. Zorn (2011), ca. 180 pages
    ISBN: 978-3-89336-726-9

29. **Silicon nanowire transistor arrays for biomolecular detection**
    by X.T.Vu (2011), vii, 174 pages
    ISBN: 978-3-89336-739-9

30. **Interactions between parallel carbon nanotube quantum dots**
    by K. Goß (2011), viii, 139 pages
    ISBN: 978-3-89336-740-5

31. **Effect of spin-orbit scattering on transport properties of low-dimensional dilute alloys**
    by S. Heers (2011), viii, 216 pages
    ISBN: 978-3-89336-747-4

32. **Charged colloids and proteins: Structure, diffusion, and rheology**
    by M. Heinen (2011), xii, 186 pages
    ISBN: 978-3-89336-751-1

33. **Scattering Methods for Condensed Matter Research: Towards Novel Applications at Future Sources**
    Lecture Notes of the 43rd IFF Spring School 2012
    March 5 – 16, 2012 Jülich, Germany
    edited by M. Angst, T. Brückel, D. Richter, R. Zorn ca. 1000 pages
    ISBN: 978-3-89336-759-7

34. **Single-Site Green Function of the Dirac Equation for Full-Potential Electron Scattering**
    by P. Kordt (2012), 138 pages
    ISBN: 978-3-89336-760-3

35. **Time Resolved Single Molecule Fluorescence Spectroscopy on Surface Tethered and Freely Diffusing Proteins**
    by D. Atta (2012), iv, 126 pages
    ISBN: 978-3-89336-763-4

36. **Fabrication and Utilization of Mechanically Controllable Break Junction for Bioelectronics**
by D. Xiang (2012), 129 pages
ISBN: 978-3-89336-769-6

37. **Contact Mechanics and Friction of Elastic Solids on Hard and Rough Substrates**
by B. Lorenz (2012), iv, 121 pages
ISBN: 978-3-89336-779-5

38. **Ab initio Calculations of Spin-Wave Excitation Spectra from Time-Dependent Density-Functional Theory**
by M. Niesert (2012), 146 pages
ISBN: 978-3-89336-786-3

39. **Neutron Scattering**
Lectures of the JCNS Laboratory Course held at Forschungszentrum Jülich and the research reactor FRM II of TU Munich
edited by Th. Brückel, G. Heger, D. Richter, G. Roth and R. Zorn (2012),
ca 350 pages
ISBN: 978-3-89336-789-4

40. **Neutron Scattering**
Experiment Manuals of the JCNS Laborator Course held at Forschungszentrum Jülich and the research reactorFRM II of TU Munich
edited by Th. Brückel, G. Heger, D. Richter, G. Roth and R. Zorn (2012),
ca. 175 pages
ISBN: 978-3-89336-790-0

41. **Influence of a shear flow on colloidal depletion interaction**
by C. July (2012), xviii, 105 pages
ISBN: 978-3-89336-791-7

42. **NMR studies on the isolated C39 peptidase-like domain of ABC transporter Haemolysin B from *E. coli*: Investigation of the solution structure and the binding interface with HlyA**
by J. Lecher (2012), 126 pages
ISBN: 978-3-89336-793-1

43. **Spin Correlations and Excitations in Spin-frustrated Molecular and Molecule-based Magnets**
by Z. Fu (2012), 208 pages
ISBN: 978-3-89336-797-9

44. **Crystal and spin structure and their relation to physical properties in some geometrical and spin spiral multiferroics**
by N. K. Chogondahalli Muniraju (2012), iii, 190 pages
ISBN: 978-3-89336-802-0

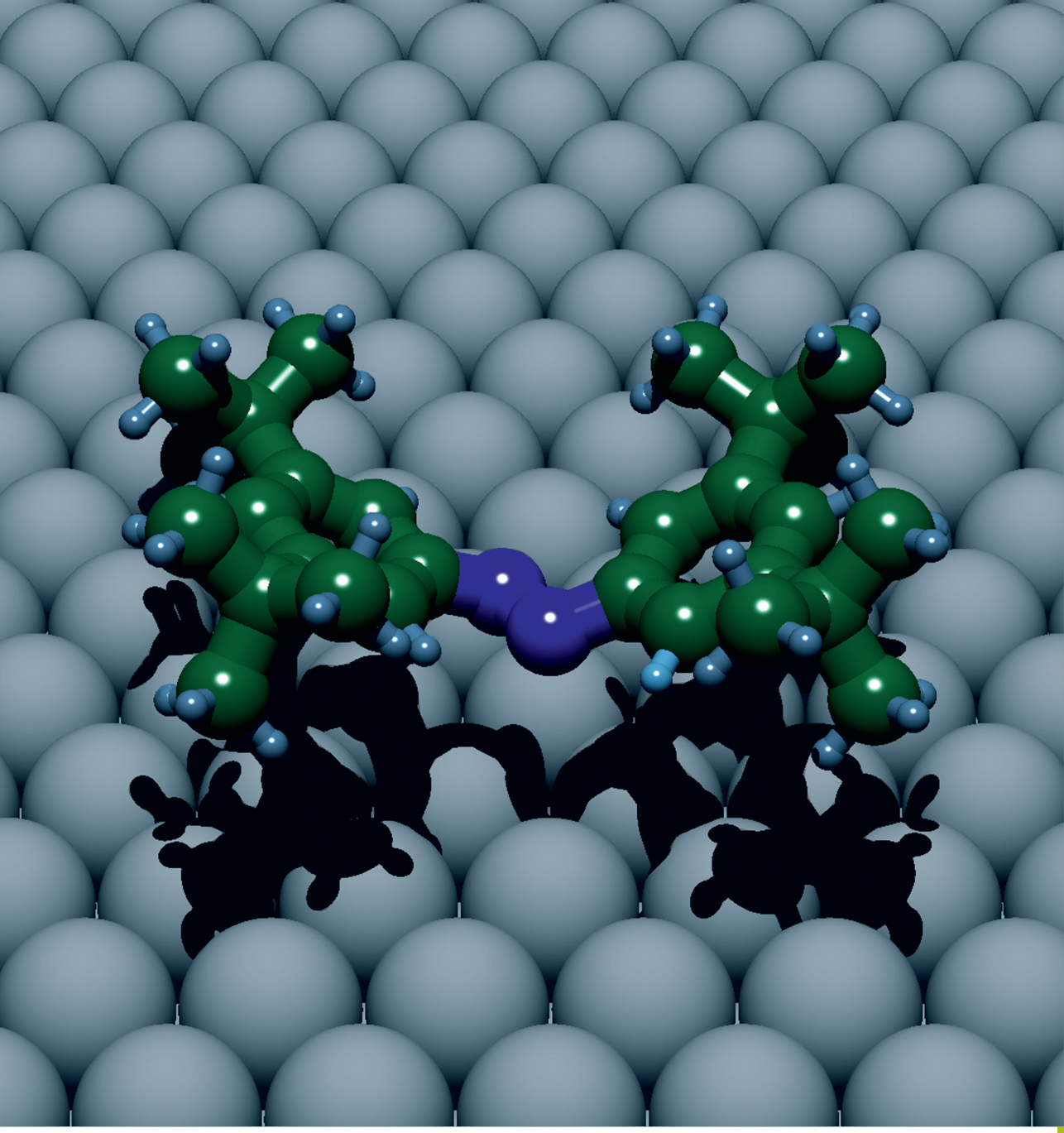
45. **Multiferroicity in oxide thin films and heterostructures**
by A. Glavic (2012), xi, 152 pages
ISBN: 978-3-89336-803-7

46. **German Neutron Scattering Conference 2012**
September 24 -26, 2012. Gustav-Stresemann-Institut, Bonn, Germany
edited by Th. Brückel (2012)
ISBN: 978-3-89336-807-5

47. **STM beyond vacuum tunnelling: Scanning Tunnelling Hydrogen Microscopy as a route to ultra-high resolution**
by C. Weiss (2012), II, 165 pages
ISBN: 978-3-89336-813-6

48. **High Temperature Radio-Frequency Superconducting Quantum Interference Device System for Detection of Magnetic Nanoparticles**
by A. Pretzell (2012), 122 pages
ISBN: 978-3-89336-814-3

49. **Study of Molecule-Metal Interfaces by Means of the Normal Incidence X-ray Standing Wave Technique**
by G. Mercurio (2012), XXII, 361 pages
ISBN: 978-3-89336-816-7



Schlüsseltechnologien / Key Technologies
Band / Volume 49
ISBN 978-3-89336-816-7

JÜLICH
FORSCHUNGSZENTRUM